Sergio Lopes Viana
Maria Custódia Machado Ribeiro
Bruno Beber Machado

Joint Imaging in Childhood and Adolescence

Springer

Sergio Lopes Viana • Maria Custódia Machado Ribeiro
Bruno Beber Machado

Joint Imaging in Childhood and Adolescence

Springer

Sergio Lopes Viana, MD
Hospital da Criança de Brasília – Jose Alencar
Clínica Vila Rica
Brasília
Brazil

Maria Custódia Machado Ribeiro, MD, MSC
Hospital da Criança de Brasília – Jose Alencar
Hospital de Base do Distrito Federal
Brasília
Brazil

Bruno Beber Machado, MD, MSC
Clínica Radiológica Med Imagem
Unimed Sul Capixaba
Santa Casa de Misericordia de
Cachoeiro de Itapemirim
Brazil

ISBN 978-3-642-35875-3 ISBN 978-3-642-35876-0 (eBook)
DOI 10.1007/978-3-642-35876-0
Springer Heidelberg New York Dordrecht London

Library of Congress Control Number: 2013936058

To the loving memory of my parents, Martiniano and Almira, and to Socorro Viana, my mother and my father at the same time.

To Angelica, Maria Fernanda and Vinicius. Sorry for the absent time and thanks for being there for me, making everything worthwhile.

To my family and my friends, for believing in me more than I believe in myself.

SLV

To my son Pedro and my daughter Julia.

To Heloiza, my dear friend, thank you very much for the encouragement and affection.

To Machado, my brother, mentor and counselor.

To my friend Sergio Lopes Viana, for his intelligent and harmonious coordination.

MCMR

To God, who always walks beside me, guiding my steps.

To my beautiful, lovely and patient wife Marina, for her extraordinary love, support and understanding.

To my parents, Eberth and Ana, for showing me the value of work and study.

To my dear friend Sergio Lopes Viana, for his leadership and togetherness.

To all my friends, for their confidence and encouragement.

BBM

Preface

Pediatric radiology is considered the oldest subspecialty of diagnostic imaging. Nevertheless, there has been a steady and progressive decline in the number of pediatric radiologists in the last decades, along with a decreased emphasis on pediatric imaging during the training of radiology residents. On the other hand, advances in technology have provided us with imaging studies whose anatomic detail and diagnostic capabilities are better than ever before. The net result of this is a mismatch between what imaging methods can offer and what is effectively achieved by the radiologists, and this is particularly true in pediatrics: the aversion that many general radiologists present to pediatric studies is proverbial. In most cases, this happens because they are not fully acquainted with the normal appearance of the immature organism, sometimes being even unable to distinguish between normal and abnormal findings.

Many books were already written about pediatric radiology, but only a few were devoted to musculoskeletal imaging. Just a handful was specifically dedicated to the immature joint, especially after the advent of cross-sectional imaging, and that is why our book intends to provide the reader with the basics of articular evaluation of children and adolescents, using a direct and concise approach. The chapters try to follow a logical and linear ordering, so that they can be read in sequence and, at the same time, serve as a reference source. Initially, the book describes the peculiarities of the different imaging modalities in the pediatric patient and the anatomic/developmental uniqueness of the growing skeleton on imaging. The infectious and noninfectious arthritides are discussed in the following chapters, as well as some conditions that are important in the differential diagnosis. The articular and periarticular tumors and pseudotumors of the childhood are also studied, as well as Legg-Calvé-Perthes disease, another important pediatric entity. The chapter on musculoskeletal disorders related to hematologic diseases stresses mainly the importance of the hemophilic arthropathy and abnormalities associated with sickle cell disease. The subsequent chapters are about acute osteoarticular trauma and sports-related lesions, both increasingly found in pediatric patients. Spinal abnormalities inherent to the pediatric age group also deserve their own chapter, as well as some selected dysplastic and developmental abnormalities of the immature joint.

The authors would like to express their gratitude to all those who contributed to this book, providing images of great pictorial value or making a critical review of the manuscript. Many thanks to all in Springer too, for believing in this project, for their professional attitude, and for the cordial mindset. Last but not least, a special "thank you" to Dr. João Luiz Fernandes, one of most prominent Brazilian radiologists, our fellow colleague and mentor. Many of the images in this book were obtained together during years of friendship and mutual collaboration, and many others were kind "gifts" from his personal archive. We gratefully acknowledge his precious help.

In addition to all the foregoing, it goes without saying that even though written only by three authors, this book is the result of several decades of work, depicting the findings of hundreds of patients diagnosed and treated by hundreds of physicians. To all of them, patients and doctors alike, our acknowledgement and our gratefulness.

SLV
MCMR
BBM

Contents

Imaging Methods and the Immature Joint: An Introduction

1

1.1 Introduction

The last decades of the twentieth century and the beginning of the twenty-first century have witnessed unparalleled improvements in diagnostic imaging. Until the 1960s, plain radiographs were the only technique available in this field. In time, however, sophisticated imaging methods were gradually added to the diagnostic arsenal, and even radiographs have entered into the digital arena. Each of these imaging methods has singularities to be considered in the assessment of immature joints, and both the radiologist and the requesting physician must be familiar with them. The requesting physician is supposed to have an open-minded and receptive attitude, consulting the radiologist whenever a doubt arises (e.g., "which imaging method is the most appropriate for this patient in this specific clinical setting?") and providing all the relevant information for each case. Accordingly, the radiologist must perform the requested imaging study and interpret the findings under the light of the clinical picture. Analyzing the images without taking the clinical background into account is dangerous and may lead to an erroneous – and potentially catastrophic – diagnosis.

This chapter is a brief introduction to the most important imaging methods used in the investigation of the immature joint, emphasizing their peculiarities in pediatric patients. It is important to keep in mind that these imaging methods are complementary instead of exclusive, acting in a synergistic way when properly combined.

1.2 Radiographs

Radiographs were always closely associated with the assessment of the locomotor apparatus and its disorders. It is emblematic that the first radiographic study ever made was the image of a hand, the left hand of the wife of Wilhelm Röntgen, the discoverer of the X-rays, in 1895. In its classic form, currently named "conventional" radiography, a radiographic film is placed inside a cassette with intensifying screens and exposed to X-rays. The anatomic structure under study is interposed between the source of the radiation and this cassette. The resulting image translates the different densities of the several body tissues: denser tissues, such as the bone, appear whiter as they absorb the radiation in a higher degree, therefore limiting the amount that effectively reaches the film. Similarly, less dense tissues, such as fat, appear darker. Even though digital radiographs – either obtained with computed radiography (CR) or digital radiography (DR) – take advantage of the same physical principles, they do not rely on X-ray films to produce medical images. On the contrary, a sensor receives the emitted radiation and transmits the electronically obtained information. The generated image is, in fact, a computer file, which can be viewed on the screen of a workstation, archived in many types of digital media, or printed (either on paper or on a medical imaging film). Despite the advantages of the digital modalities over the conventional technique (wider dynamic range, less exposure to radiation, telemedicine capabilities – Fig. 1.1), the training and the experience of the observer are far more important than the technology involved.

The notion that X-rays became outdated after the advent of modern imaging methods has no grounds. Radiographs remain essential and consist in the first line of investigation for patients with articular disorders, so that they must be requested before soliciting any additional imaging study (Fig. 1.2). They are inexpensive and widely available, are not operator dependent, and present good reproducibility. Correct interpretation of imaging studies like ultrasonography and magnetic resonance imaging relies largely on correlation with radiographs. Two or more views are usually obtained, making it easier to determine the location of abnormal findings. Serial radiographs may be used to monitor the course of articular disease and are employed as imaging criteria in several staging and scoring systems (Fig. 1.2). In arthritic patients, for example, radiographs are very suitable for demonstration of established osteoarticular damage, such as cortical erosions, abnormal joint alignment, joint space

S.L. Viana et al., *Joint Imaging in Childhood and Adolescence*,
DOI 10.1007/978-3-642-35876-0_1, © Springer-Verlag Berlin Heidelberg 2013

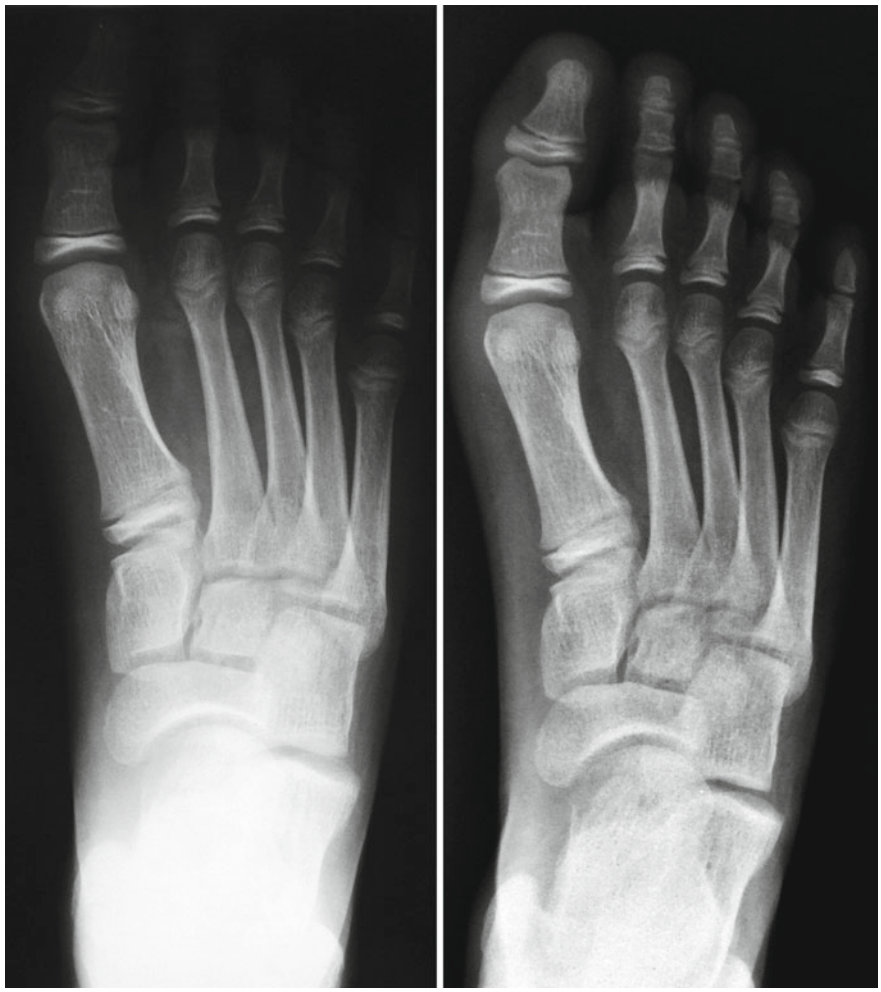

Fig. 1.1 Radiographs of the left foot performed with conventional (*left*) and digital (*right*) techniques. The digital radiograph has wider dynamic range if compared to the conventional one: the toes and the tarsal bones are equally well seen on the former, while only the midfoot is adequately exposed on the latter

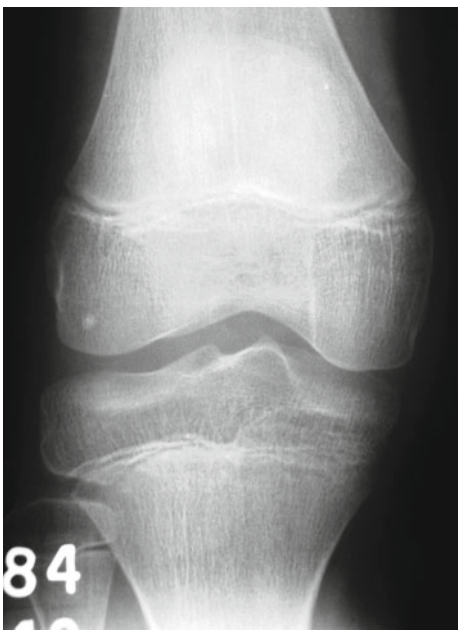

Fig. 1.2 Radiograph of the right knee of a 13-year-old female with juvenile idiopathic arthritis diagnosed one year before. Even though erosions are absent, osteoporosis and subtle increase in the size of the epiphyses are already seen, related to the hyperemic state. This radiograph will serve as a baseline study to monitor disease evolution and treatment response

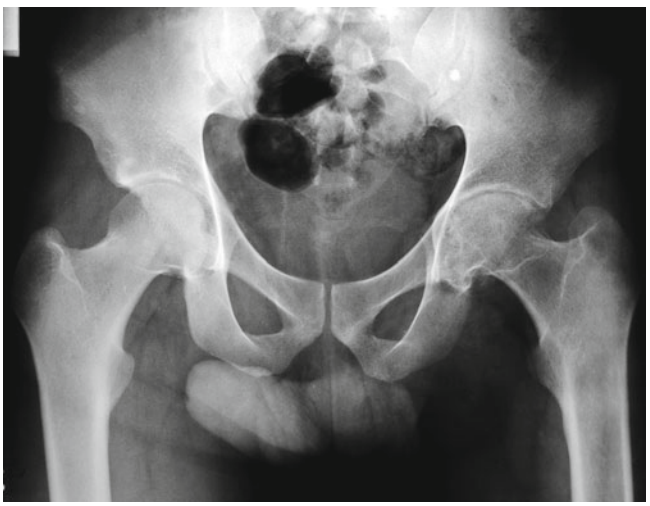

Fig. 1.3 Pelvic radiograph of a 20-year-old male with juvenile idiopathic arthritis since age 15. There is advanced arthritis of the left hip, with regional osteoporosis, erosions of the articular surfaces, narrowing of the joint space, and reduced size of the homolateral femoral head, which is markedly deformed

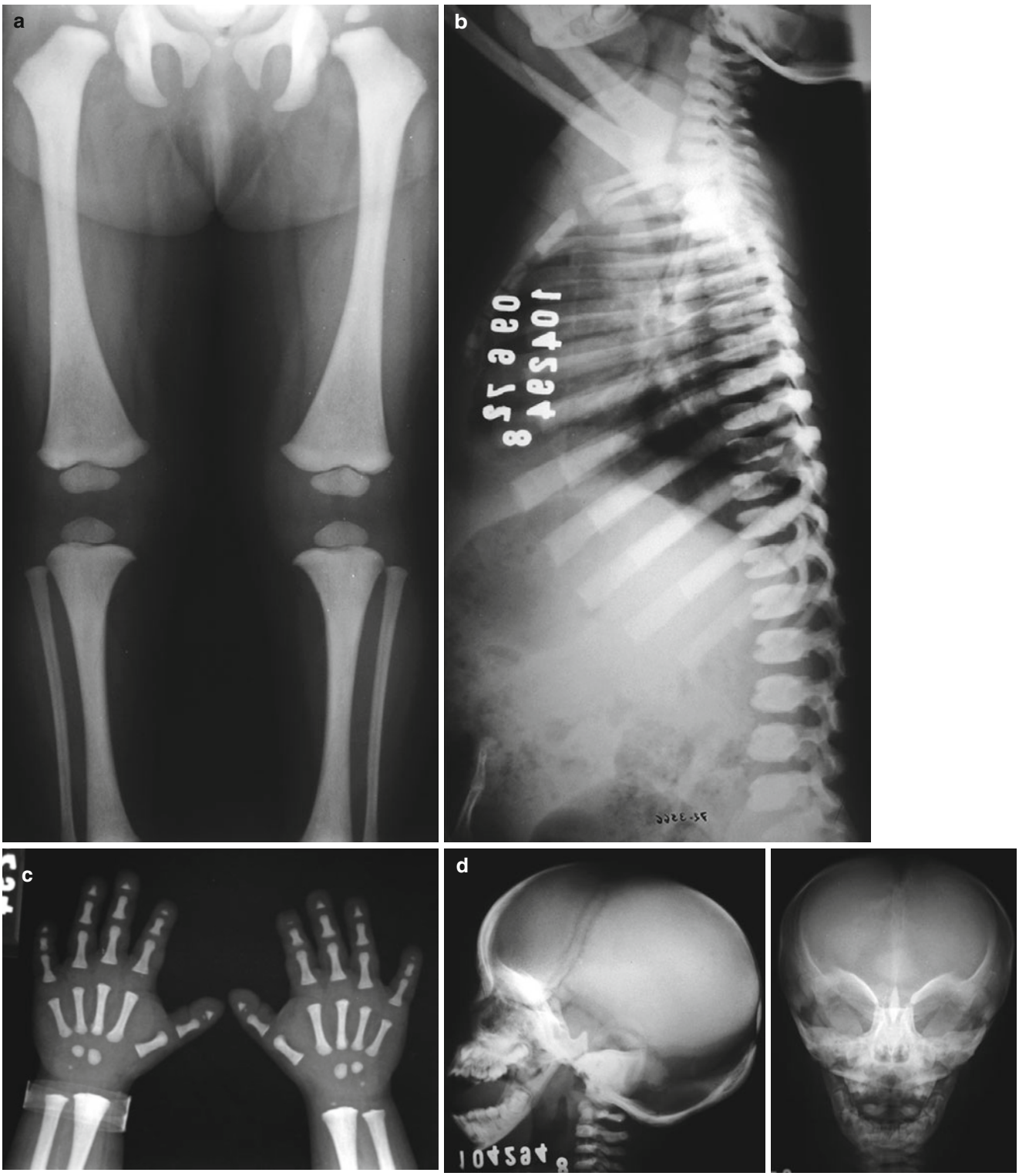

Fig. 1.4 Radiographs of a child with short stature showing generalized increase in bone density, with loss of definition of the corticomedullary junction (**a**, **b**). The fingers are short and stubby and the distal phalanges are hypoplastic (**c**). Craniofacial abnormalities include macrocrania, wide sutures and fontanelles, parieto-occipital bossing, and straightening of the mandibular angles (**d**). These findings are typical of pyknodysostosis, with no need for additional investigation

narrowing, and ankylosis (Fig. 1.3). Moreover, radiographs are often problem-solving by themselves, as several musculoskeletal disorders can be readily diagnosed on X-rays (e.g., bone tumors, fractures, osteomyelitis, congenital malformations, and developmental abnormalities – Figs. 1.4 and 1.5). Disadvantages include the use of ionizing radiation (which is especially deleterious for the immature organism), low sensitivity for the early stages of articular diseases, and

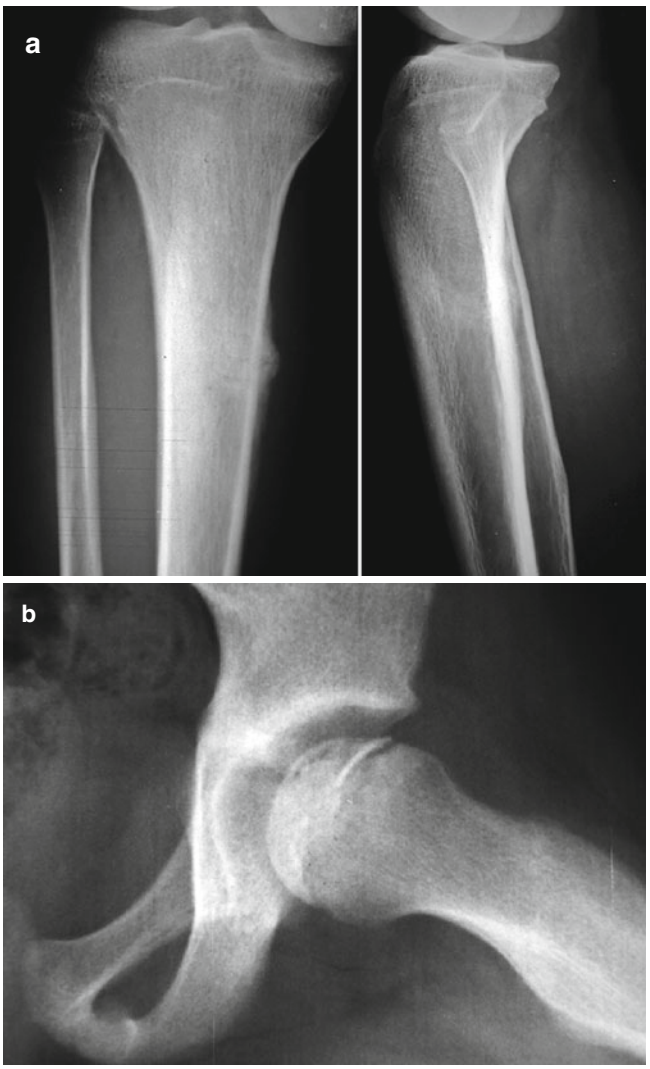

Fig. 1.5 In an appropriate clinical background, some radiographic patterns are almost pathognomonic. However, in most cases these findings usually appear late in the course of the disease, limiting their effectiveness for early diagnosis. In **a**, there is a cortical lucency in the medial aspect of the proximal diaphysis of the right tibia associated with periosteal reaction and bone neoformation, which are highly suggestive of stress fracture in an adolescent runner. In **b**, radiograph of a child with pain in the left hip shows that the femoral head is sclerotic and reduced in size, presenting a curvilinear subchondral lucency (crescent sign), findings that are typical of Legg-Calvé-Perthes disease. In both cases, MRI would be able to establish the diagnosis much earlier

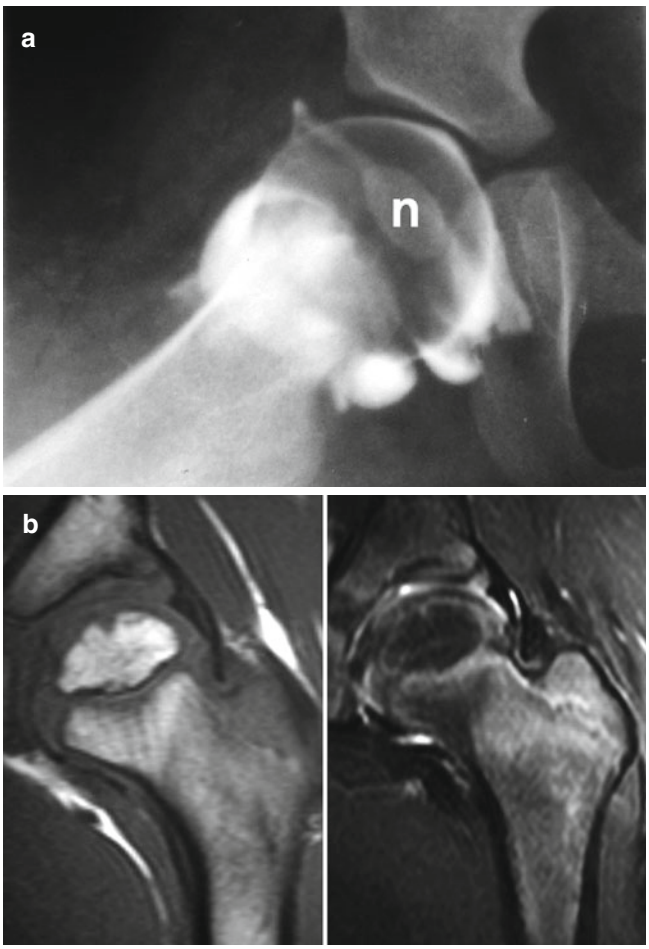

Fig. 1.6 Until the advent of modern imaging methods, only invasive radiographic procedures, such as conventional arthrograms (**a**), were able to demonstrate the epiphyseal cartilage, demanding sedation and intraarticular injection of iodinated contrast. This cartilage is much larger than the mineralized ossification nucleus (*n*), the only portion of the epiphysis that is detectable on radiographs. In (**b**), for comparison, coronal T1-WI (*left*) and fat sat T2-WI (*right*) of the left hip of a 3-year-old child are able to display both calcified and non-calcified structures with high detail and in a noninvasive way, including the epiphyseal cartilage, the acetabular labrum, muscles, and tendons

limited usefulness in the assessment of the soft tissues and anatomically complex joints. Conventional arthrograms and linear tomography (planigraphy) are radiographic techniques that were popular in the past but became obsolete after the advent of cross-sectional imaging, given the higher diagnostic accuracy and the noninvasive nature of the latter (Fig. 1.6).

1.3 Ultrasonography

Ultrasonography (US) has become widely accepted for joint assessment, notably after the introduction of high-frequency transducers. In US, an array of piezoelectric crystals generates a beam of ultrasonic waves that is directed to a given structure, which will reflect them in different degrees, depending on the composition of its tissues. For example, the synovial fluid is a very good conductor of ultrasonic waves, while the cortical bone reflects them almost entirely. The reflections of the ultrasonic beam are transmitted to a computer that will process the obtained data and produce

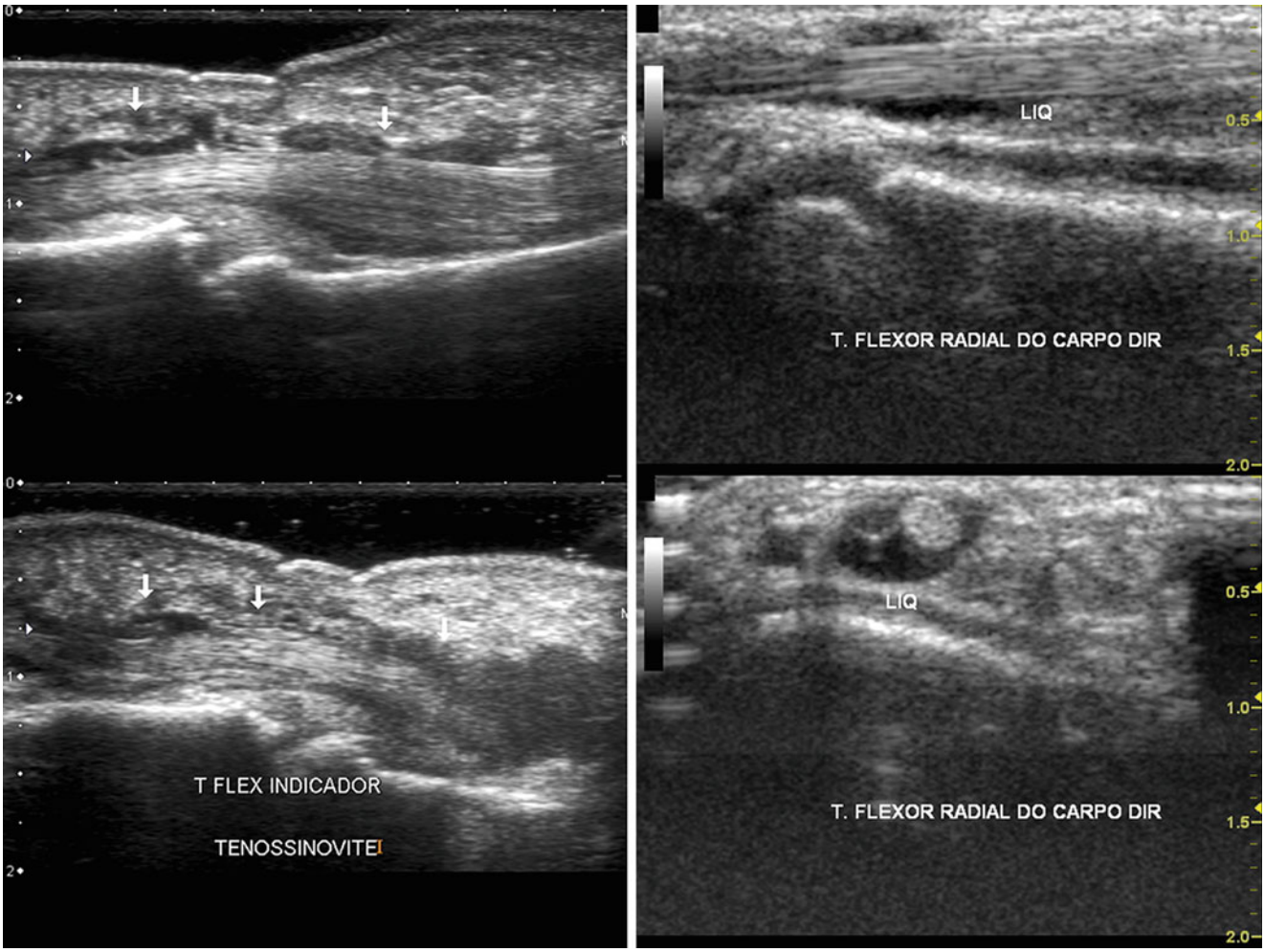

Fig. 1.7 US of two different patients with juvenile idiopathic arthritis and tenosynovitis involving the flexor tendons of the index finger in the first (*left*) and the flexor carpi radialis in the second (*right*). The tendons are elongated on sagittal scans (*left images* and *upper-right image*) and appear as rounded structures on transverse scans (*lower-right image*), with a fibrillar appearance. The synovial fluid in the tendon sheaths appears hypoechogenic, while amorphous echogenic foci are related to synovial thickening and debris. Even a 4-year-old child (first patient) tolerates an US scan very well

real-time images in a screen, therefore providing a unique dynamic characteristic to US. Although excellent for the evaluation of large joints and superficial soft tissues (Figs. 1.7 and 1.8), this study presents limitations in the assessment of deeply seated structures or small/deformed joints, to which the transducer may not fit satisfactorily. In addition, the ultrasonic beam relies on the existence of acoustic "windows" to reach the region of interest. Superficially located osseous abnormalities may occasionally be detected on US, but essentially no information is gathered about the innermost portions of the bones. Doppler US is a technique that detects and measures blood flow in vascular structures, being very useful in the investigation of hyperemic joint diseases and soft-tissue masses and fluid collections (Figs. 1.9 and 1.10).

US is largely used in pediatric patients because it is painless, inexpensive, and widely available; can be performed at the bedside; and does not require special or uncomfortable positioning. The absence of ionizing radiation must also be taken into account in this age group, as serial studies can be performed without risk of damage to the growing organism. It is well tolerated by children, and several joints can be examined expeditiously in a single session. Joint effusion and synovial thickening are readily apparent on US, as well as extension of the inflammatory process to adjacent bursae, synovial sheaths, or cysts (Figs. 1.7, 1.9, and 1.11). The articular cartilage is particularly well seen in large joints (Fig. 1.11). In arthritic patients, the degree of hyperemia can be estimated with Doppler US and monitored in sequential studies, serving as an indicator of disease activity and a marker of treatment response. The dynamic properties of US allow for assessment of a given structure in different spatial planes (Fig. 1.7), evaluation of articular

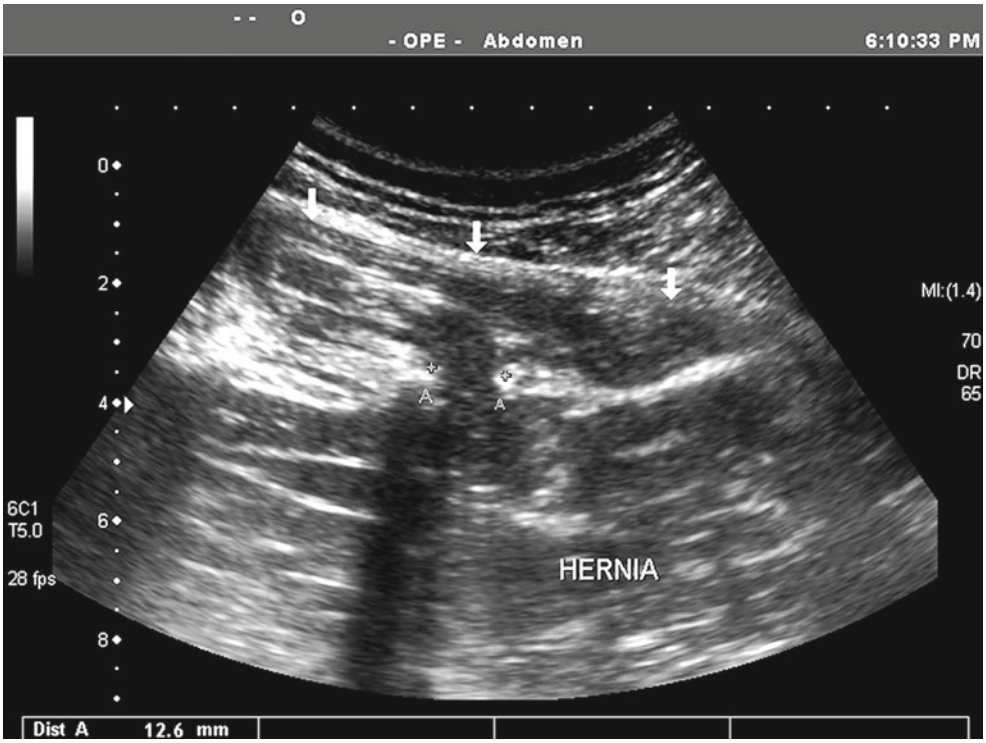

Fig. 1.8 US of an adolescent complaining about a nodule of elastic consistency and variable dimensions in the lumbar region. The image reveals a focal defect of the lumbar aponeurosis measuring 12 mm (calipers) and herniation of paravertebral muscle fibers

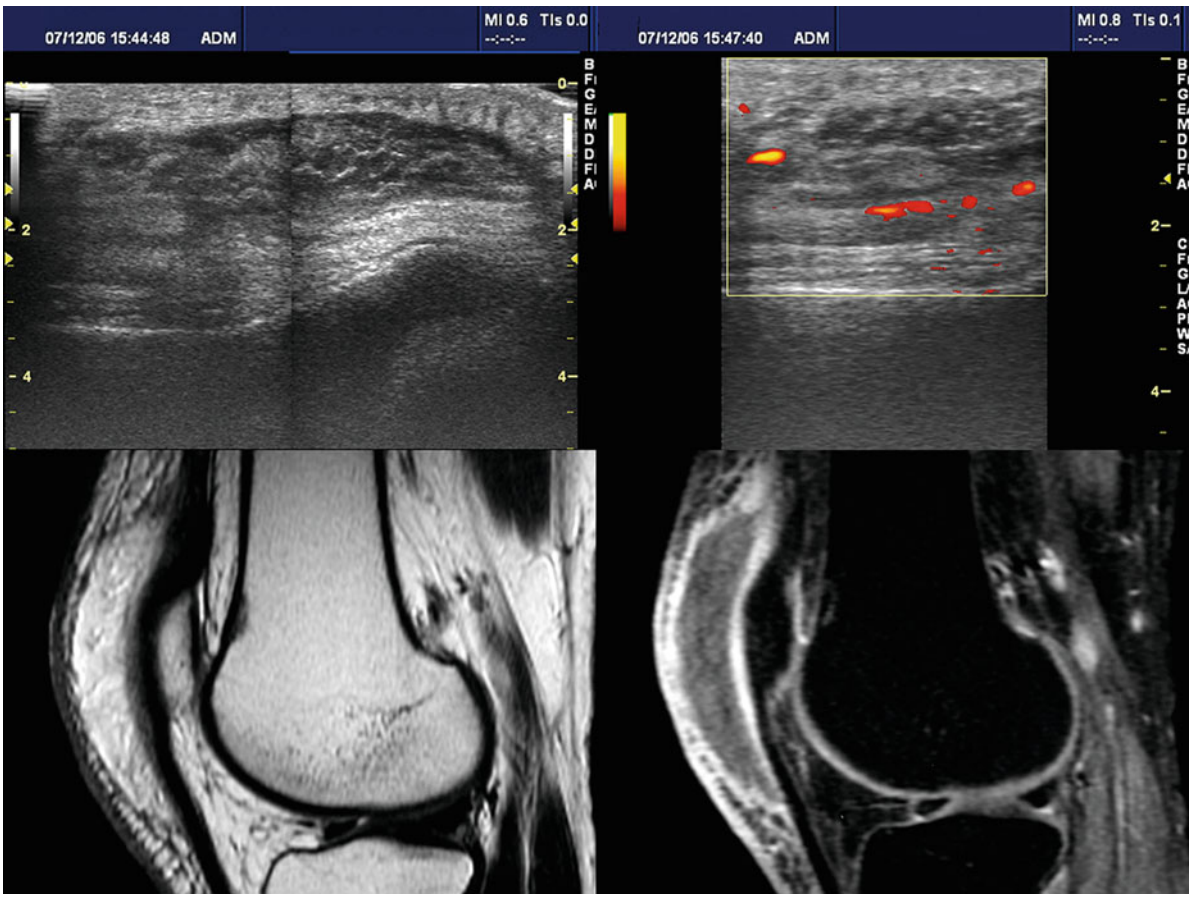

Fig. 1.9 An 18-year-old female with autoimmune hepatitis since age 14 and taking immunosuppressant drugs, presenting with left-sided pyogenic prepatellar bursitis. US scans (*upper row*) reveal thickening of subcutaneous tissue and filling of the prepatellar bursa with heterogeneous hypoechogenic material; peripheral hyperemia is seen on Doppler US (red-yellowish streaks in the second image). In the lower row, T2-WI (*first image*) discloses subcutaneous thickening and filling of prepatellar bursa with heterogeneous content, mostly hyperintense. Post-contrast fat sat T1-WI (*second image*) reveals enhancement of the synovium and of the inflamed subcutaneous tissue, corresponding to the hyperemic zones seen on Doppler. The non-enhancing material inside the bursa corresponds to debris and pus

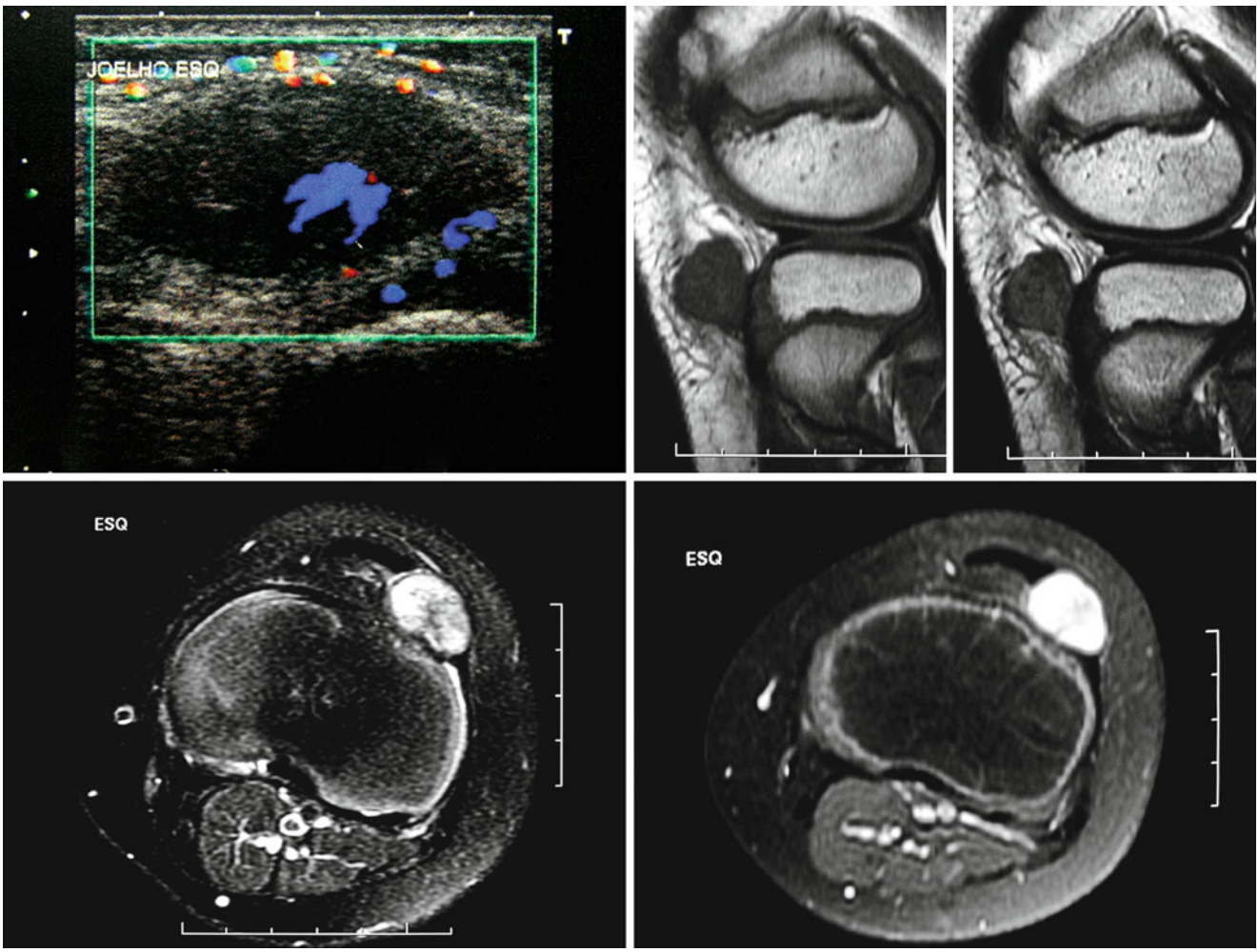

Fig. 1.10 A 9-year-old boy presenting with a painless infrapatellar lump in the anterolateral aspect of the left knee. Doppler US (*upper-left image*) discloses an oval hypoechogenic mass, well delimited, and heterogeneous, with central areas of increased blood flow (lavender). Sagittal T1-WI (*upper-right image*), transverse fat sat T2-WI (*lower-left image*), and post-gadolinium fat sat T1-WI (*lower-right image*) reveal a sharply delimited lesion of heterogeneous appearance, predominantly hypointense on T1-WI and hyperintense on T2-WI, whose epicenter is in the patellar tendon. There is marked post-gadolinium enhancement, as could be inferred from the increased flow seen on Doppler. The histopathological diagnosis was fibroma of the tendon sheath

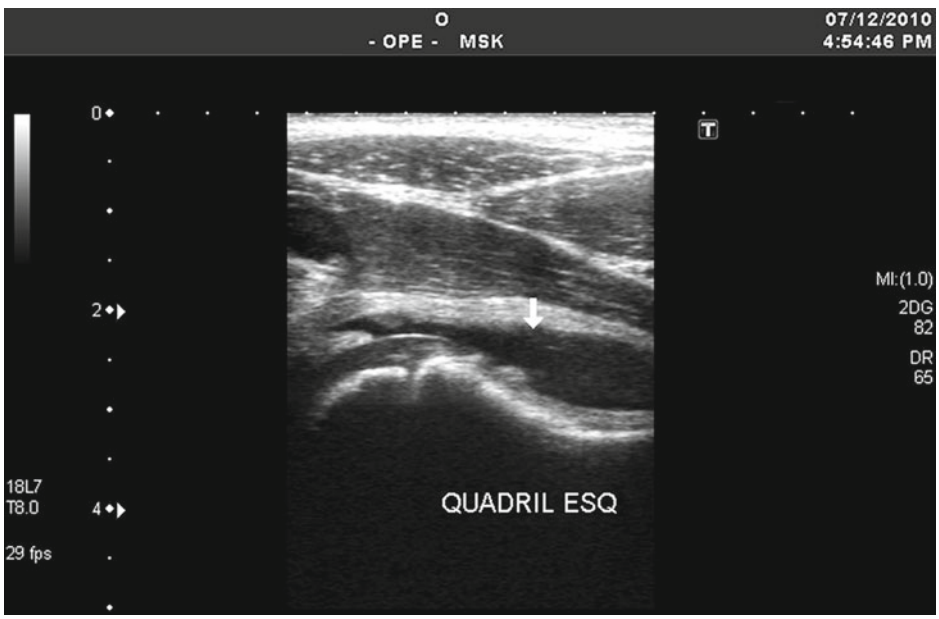

Fig. 1.11 US of a 5-year-old male with transient synovitis of the left hip disclosing synovial thickening and homogeneous synovial effusion. The growth plate and the epiphyseal cartilage are clearly seen as hypoechogenic structures

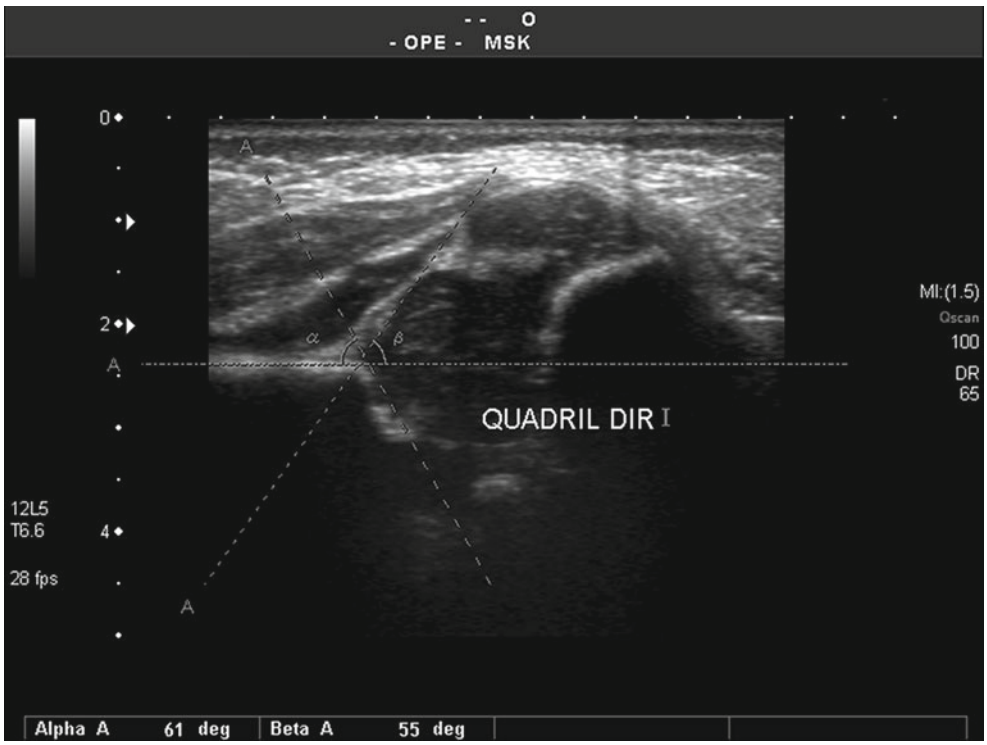

Fig. 1.12 Normal US scan of the right hip of a newborn with suspected developmental dysplasia. Both the femoral head and the acetabulum present preserved shape and size, and the articular relationships are normal (see Chap. 12)

relationships (such as in newborns with suspected developmental dysplasia of the hip – Fig. 1.12), and real-time demonstration of abnormalities that would go unnoticed with other imaging methods, such as tendon dislocations or muscular hernias (Fig. 1.8). Additionally, US is very useful to guide invasive diagnostic and/or therapeutic procedures.

Despite its advantages, US has also some drawbacks, whose importance should not be underestimated. It has limited reproducibility and lacks standardized protocols, requiring specific training of the operator (operator-dependent method) and demanding appropriate equipment, with high-frequency transducers (equipment-dependent method).

1.4 Nuclear Medicine

Scintigraphy is a generic name given to the majority of the nuclear medicine scans. During these studies, a radiopharmaceutical (substance formed by the combination of a radionuclide and a pharmaceutical compound) is administered to the patient and, depending on its properties, it will build up in a given tissue or organ. Such build-up (which is most often due to increased metabolic activity) is registered by detectors in a gamma camera that processes the collected data and produces images based on the pattern of radiation emitted. The different radiopharmaceuticals and techniques available are capable to assess several organs and systems. Whole-body bone scan with technetium-99m

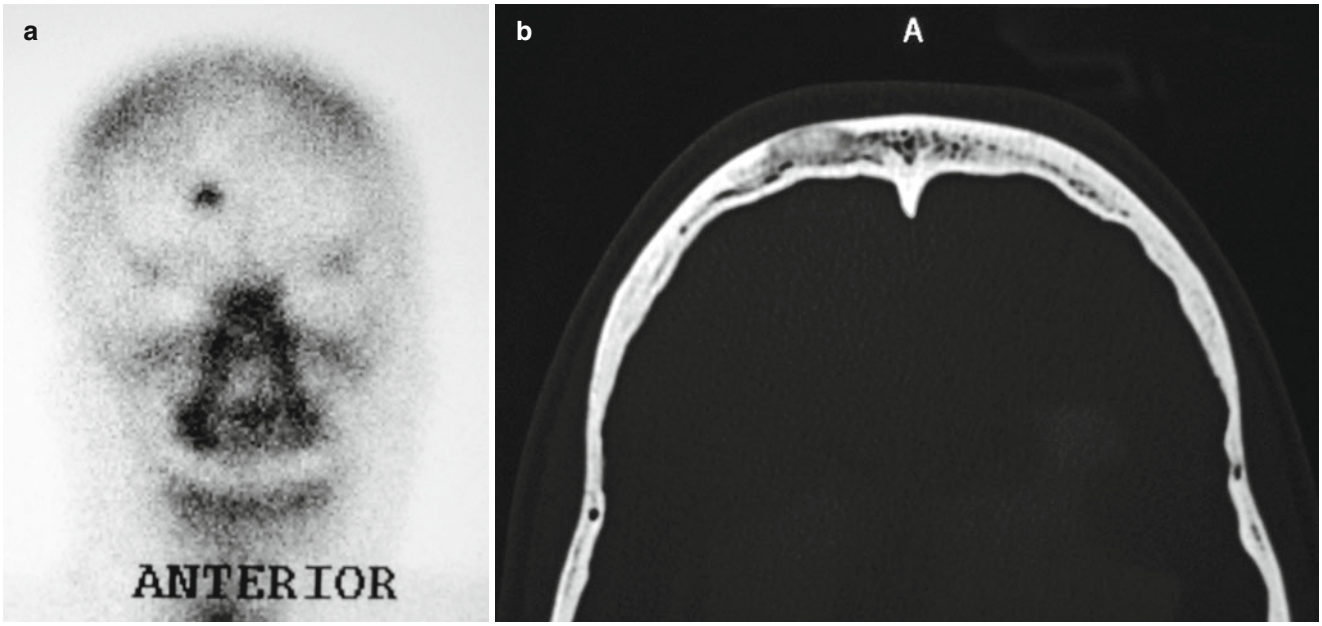

Fig. 1.13 Bone scintigraphy revealing an area of increased uptake projected over the right frontal region (**a**). Though this finding is a reliable indicator of increased metabolic activity, it is far from being specific. CT of the skull of the same patient (**b**) shows a focal area of increased bone density affecting the outer table and the diploe of the right frontal bone, with the "ground glass" appearance typical of fibrous dysplasia. Compare the high spatial resolution of CT with the low level of anatomic detail obtained with bone scintigraphy

compounds is the most important scintigraphic study in musculoskeletal imaging; other radionuclides are used less often, in specific clinical situations. Generally speaking, bone scintigraphy is a highly sensitive study that, if positive, usually indicates the presence of an abnormality. On the other hand, however, its specificity is very low, and it usually requires complementary imaging studies to clarify the real nature of an unexpected area of increased uptake (Figs. 1.13 and 1.14). Furthermore, its spatial resolution is very poor, and sometimes it is not possible to define the precise location of the affected area, such as when very intense carpal or tarsal uptake is found. In children, there is physiological uptake in the normal growth plates – which are juxtaarticular/intraarticular – and in the sacroiliac joints, limiting its usefulness even more (Fig. 1.14). A distinctive feature of bone scintigraphy is its ability to study the whole body in a single study, which is very useful, for example, for screening of occult metastases or "silent" sites of disease in polyarticular arthritis.

While "common" scintigraphies produce planar (two-dimensional) images, single-photon emission computed tomography (SPECT) and positron emission tomography (PET) are nuclear medicine techniques that produce three-dimensional information. An emerging technique blends images obtained with PET and those obtained with computed tomography, known by the acronym PET/CT. This study allows correlation of PET images, which are highly sensitive, with matching computed tomography images, which provide high anatomic resolution. Even though initial results were encouraging, the exact role of this method in the evaluation of articular disease is yet to be established.

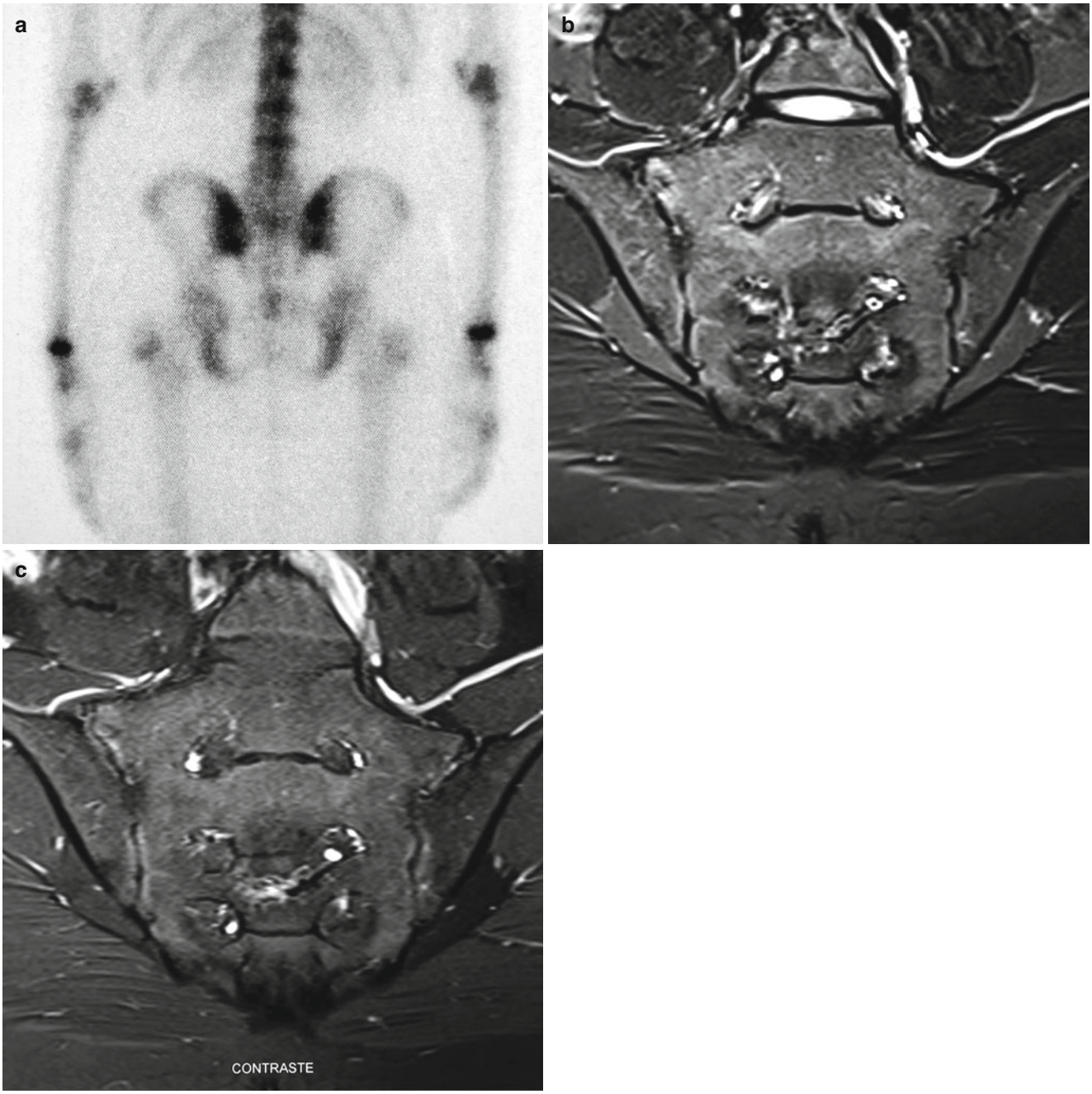

Fig. 1.14 Male adolescent with reactive arthritis. Bone scintigraphy (posterior view, **a**) shows increased uptake in the sacroiliac joints, indicative of sacroiliitis, which is more difficult to evaluate in this age group. Coronal STIR (**b**) and post-contrast fat sat T1-WI (**c**) reveal subchondral marrow edema and and small erosions along the articular surfaces, bilaterally, which show post-gadolinium enhancement. Note the increased uptake in the distal physes of the forearms

1.5 Computed Tomography

After the advent of computed tomography (CT) in the 1970s, this imaging method became widely popular and disseminated throughout the world. To put it briefly, in a modern scanner there are an X-ray tube and an array of detectors that rotate around a moving table, in which the patient is lying. Different tissues have different attenuation coefficients, producing contrast that is noticed by the detectors. The three-dimensional information thus obtained is processed, providing volumetric data to create medical images. Continuous technological progress has led to

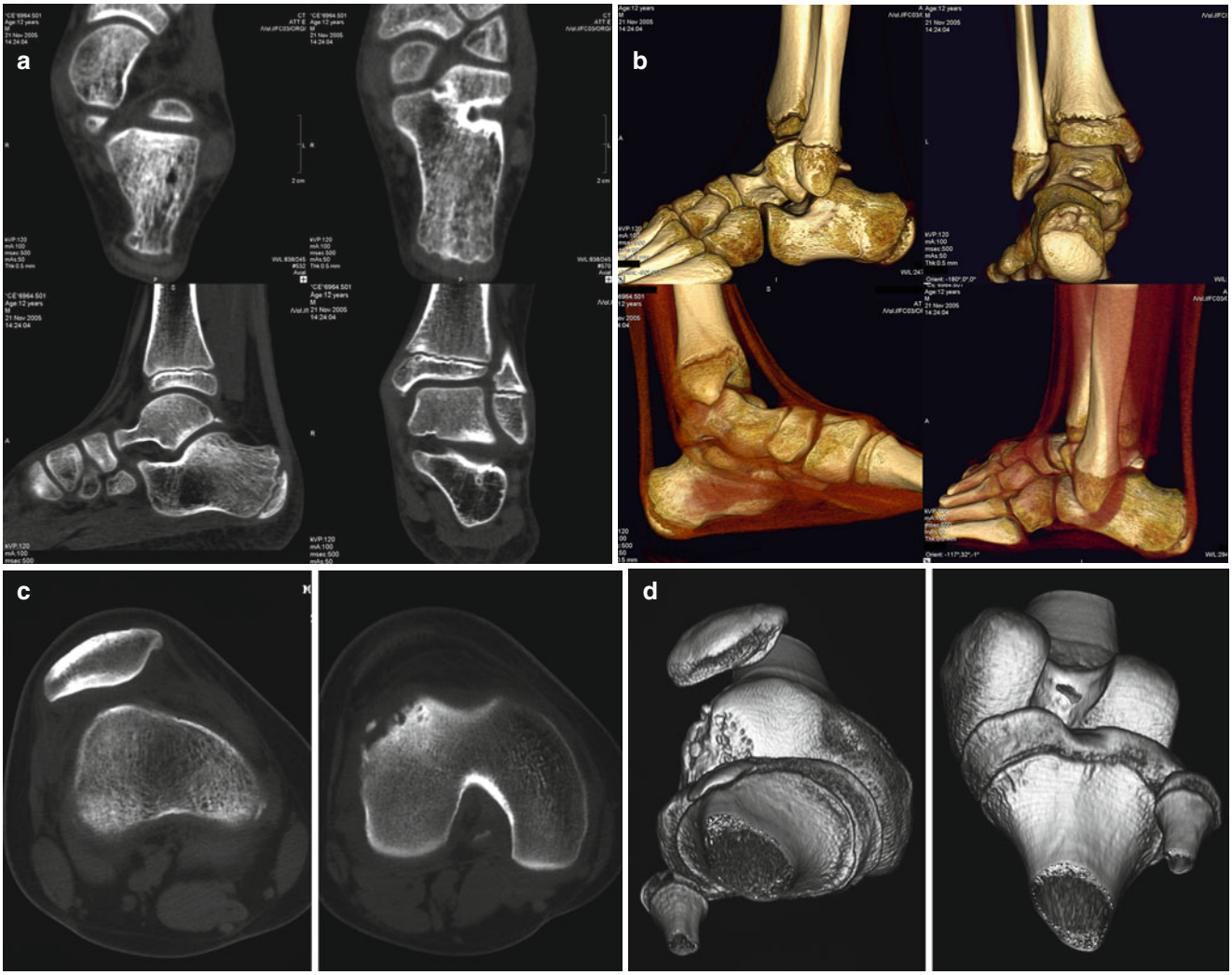

Fig. 1.15 Reformatted CT images (**a**) and volume-rendered reconstructions (**b**) of the left ankle of a healthy 12-year-old male illustrate the multiplanar capabilities of this method, its high spatial definition, and the capacity to highlight different body tissues, like the bones (*upper row*, **b**) and the tendons (*lower row*, **b**). In (**c**), transverse CT images suffice to demonstrate marked trochlear dysplasia and signs of patellofemoral instability in a 12-year-old male, with a large osteochondral lesion in the anterior aspect of the lateral condyle and a bone fragment displaced to the intercondylar notch; nevertheless, volume-rendered reconstructions (**d**) are an elegant way to better display the patellofemoral abnormalities and the relation among the avulsed fragment and the adjacent structures

improved speed of acquisition and image quality in CT scanners, and multidetector computed tomography (MDCT) is currently the state of the art in this imaging field. In MDCT, there is simultaneous acquisition of multiple slices at high speed, with unparalleled spatial resolution. These scanners are coupled to dedicated workstations that generate multiplanar reformatted images and volume-rendered reconstructions (Figs. 1.15, 1.16, 1.17, and 1.18).

CT is the best imaging modality for the assessment of bone anatomy, being capable to detect even very subtle abnormalities, such as incomplete fractures, osseous avulsions, small foci of calcification, tiny cortical erosions, or faint periosteal reaction, with superb detail (Figs. 1.13, 1.16, and 1.17). Radiographic findings can be demonstrated earlier and more accurately with CT, notably in the evaluation of anatomically complex joints. Reformatted images and volume-rendered reconstructions were warmly welcomed by non-radiologists, as they usually find these images more familiar and easier to understand than the transverse sections (Figs. 1.15, 1.16, 1.17, and 1.18). However, in spite of its high spatial resolution, CT has limited usefulness in the evaluation of the soft tissues, and its contrast resolution is lower if compared to magnetic resonance imaging (Fig. 1.16). Furthermore, CT scans deliver ionizing radiation in a non-negligible amount and should be used judiciously in children. Intravenous iodinated contrast is indicated for patients with inflammatory or infectious joint diseases, soft-tissue masses, fluid collections, and tumors/pseudotumors. CT-arthrography is a second-line

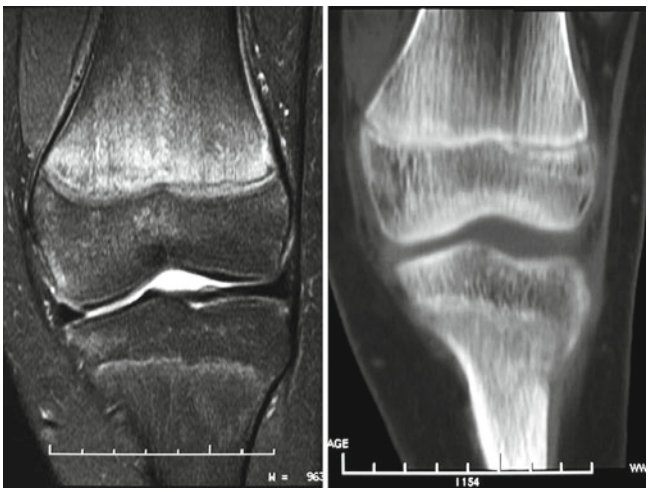

Fig. 1.16 A 12-year-old male with a history of trauma in his left knee one month before, persistent pain, and normal radiographs. Coronal fat sat PD-WI (*left*) shows joint effusion and extensive bone marrow edema pattern in the distal femoral metaphysis, acutely delimited by the growth plate. There is a questionable infraction of the lateral cortex, immediately above the physis, which is widened and hyperintense in its lateral portion. Coronal reformatted CT image (*right*) demonstrates beyond any doubt the suspected fracture and the asymmetric physeal widening. Despite the adequacy of CT for bone assessment, this method has limited usefulness in the evaluation of the soft tissues (compare the level of detail of the intraarticular structures obtained with CT and MRI) and is completely insensitive for bone marrow edema

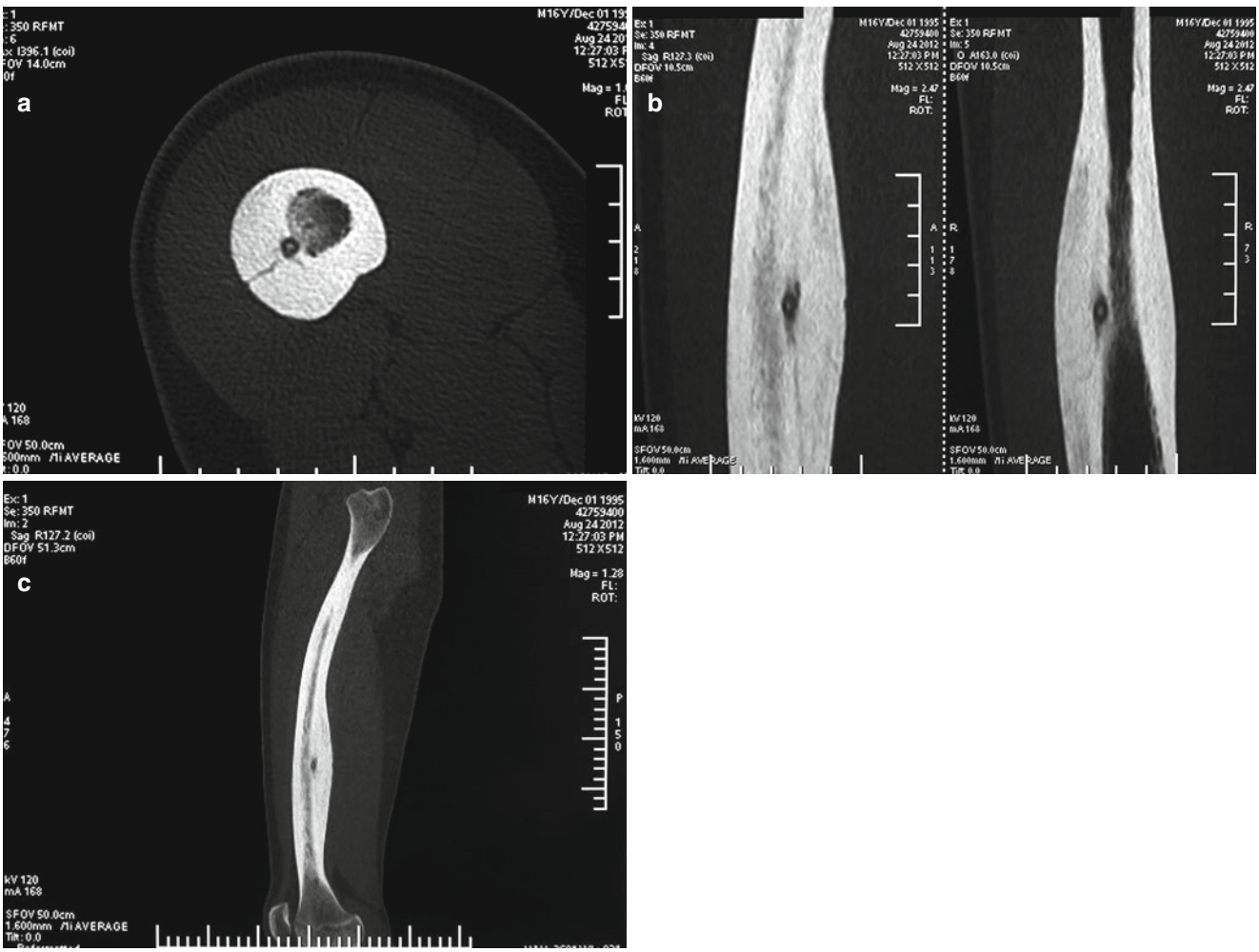

Fig. 1.17 Transverse (**a**) and reformatted (**b** and **c**) CT images of the femur of a 16-year-old male with a diaphyseal osteoid osteoma. Even though the transverse image is sufficient to demonstrate the radiolucent tumoral nidus and a tiny central calcification, the reformatted images help to put in evidence the marked cortical thickening, the endosteal sclerosis, and the diaphyseal bowing that are also present

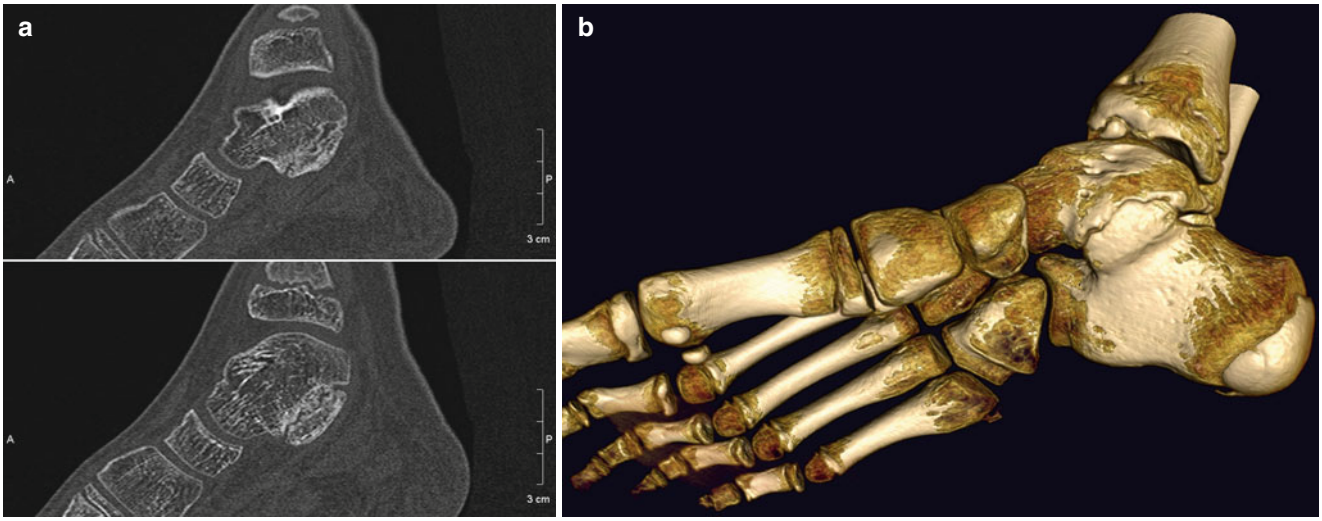

Fig. 1.18 Talocalcaneal coalition in an 11-year-old male. Sagittal reformatted CT images (**a**) are diagnostic, revealing narrowing of the joint space of the middle facet and irregularity of the joint surfaces, as well as sclerosis of the subchondral bone. Nevertheless, most of the non-radiologists will prefer volume-rendered reconstructions (**b**) to envision the anatomic abnormality

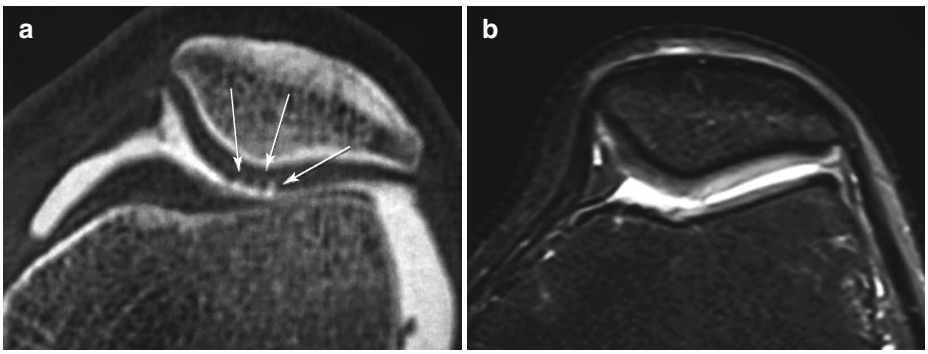

Fig. 1.19 Female adolescent with retropatellar pain in her left knee. CT-arthrography (**a**) reveals irregularity of the surface of the patellar cartilage with great detail (*arrows*), but it is limited for assessment of the cartilaginous substance. Transverse fat sat PD-WI at the same level (**b**) demonstrates the irregular contour of the articular cartilage in a noninvasive way and, in addition, shows abnormal intrasubstance signal intensity

procedure in pediatric radiology, performed after intraarticular injection of iodinated contrast, being useful in selected cases, such as in the assessment of chondral/osteochondral lesions (Fig. 1.19) or to detect non-mineralized intraarticular loose bodies. Even though relatively rare, allergic reactions to iodinated contrast agents do occur, and the fact that these agents are potentially nephrotoxic must be kept in mind (the potential risk-to-benefit ratio should be carefully evaluated, especially in patients with impaired renal function). CT is not the first choice for imaging assessment of most pediatric patients with joint complaints, as US and magnetic resonance imaging are usually more appropriate for clarification of equivocal radiographic findings. CT is usually reserved for traumatic injuries or used as an alternative imaging method for arthritic children that cannot undergo magnetic resonance imaging.

1.6 Magnetic Resonance Imaging

Magnetic resonance imaging (MRI) is currently the most important imaging method in the assessment of the locomotor apparatus. During MRI scanning, the patient is positioned inside a magnet that generates a powerful magnetic field. A radiofrequency energy pulse is delivered to protons spinning in a given frequency (mainly hydrogen protons, the most abundant in the human body), so that they align with the magnetic field. Once this pulse is stopped, protons turn back to their original random status and, by doing so, release a signal that is captured and processed to obtain medical images. Basic sequences include T1-weighted images (T1-WI, more useful to assess the anatomy of the region of interest) and T2-weighted images (T2-WI, more sensitive in the detection of abnormal findings, mostly

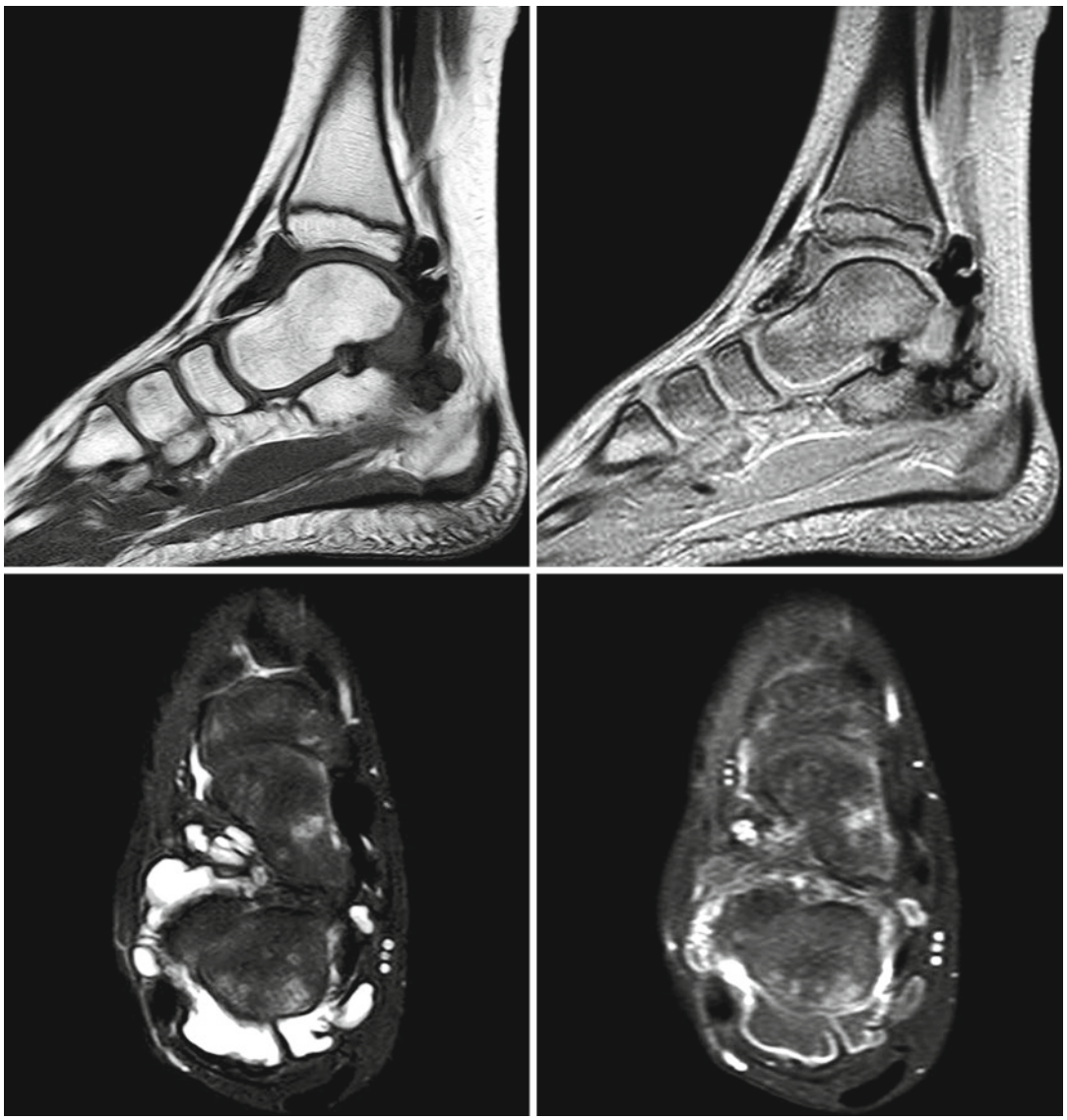

Fig. 1.20 Sagittal T1-WI and gradient-echo image (*upper row*) and transverse fat sat T2-WI and fat sat post-gadolinium T1-WI (*lower row*) of the right ankle of an 11-year-old hemophiliac patient. There is joint effusion and synovial impregnation by hemosiderin, which is markedly hypointense in all sequences, notably T2* (see Chap. 8). Post-gadolinium image discloses a thickened and enhancing synovium, representing active inflammation and hyperemia

when some form of fat suppression is used [fluid-sensitive sequences], such as fat saturation [fat sat] or short-tau inversion-recovery [STIR] images). Proton density-weighted images (PD-WI) are obtained in intermediate-weighted sequences, especially useful for cartilaginous assessment (notably when fat suppression is applied), while gradient-echo sequences (also referred to as T2*) are highly sensitive to the presence of calcifications and hemosiderin (Fig. 1.20). Many other sequences are available, and some of them will be discussed in the following chapters. An in-depth analysis of the technical aspects and the complex physics underlying MRI, however, is beyond the scope of this concise introduction.

MRI is able to obtain images in any conceivable plane, with excellent spatial and contrast resolutions. The absence of ionizing radiation in MRI is especially welcome in pediatric patients. The bones and the soft tissues are equally well studied, and the articular cartilage can be clearly distinguished from the epiphyseal cartilage in the growing skeleton in a noninvasive way (Figs. 1.6, 1.14, 1.19, 1.21, 1.22, 1.23, 1.24, and 1.25). A unique feature of MRI is the ability to demonstrate the so-called bone marrow edema, an

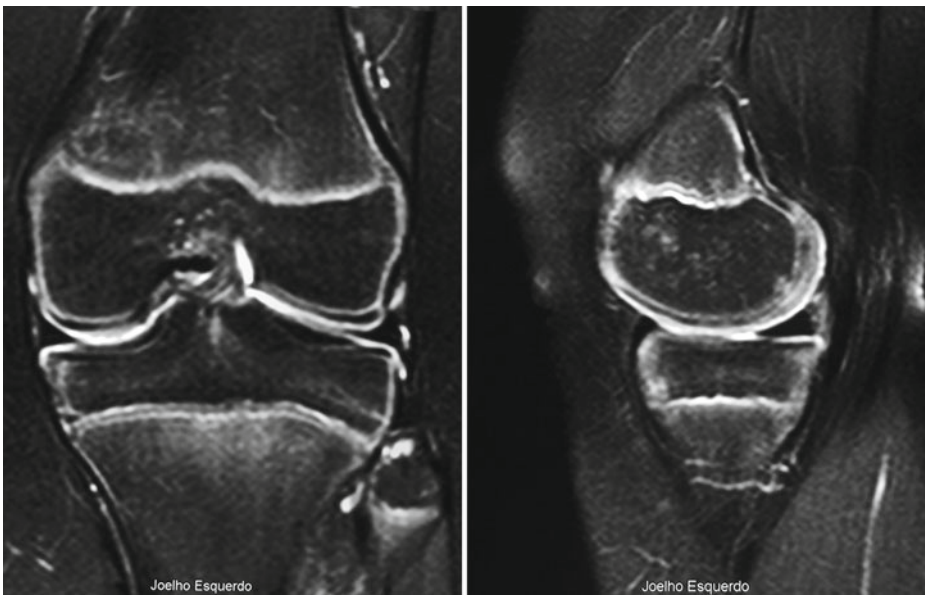

Fig. 1.21 Fat sat PD-WI of the left knee of a healthy 8-year-old child in the coronal (*left*) and sagittal (*right*) planes. MRI is able to assess noninvasively virtually all the osseous and non-osseous structures of the joint, providing excellent anatomic detail

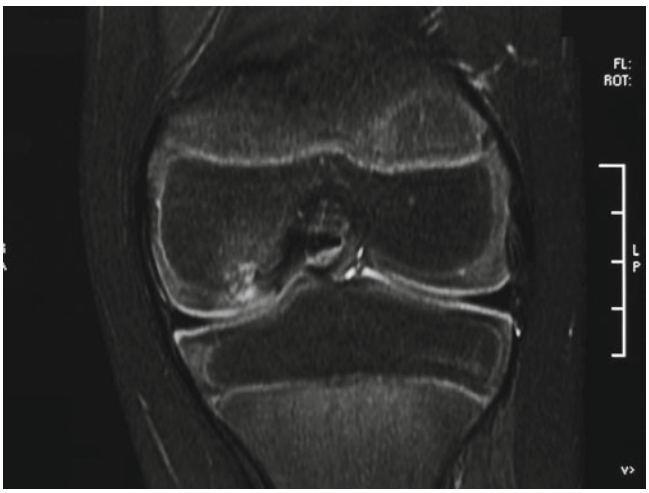

Fig. 1.22 A 9-year-old male with osteochondritis dissecans of the medial femoral condyle. The subchondral bone fragment is clearly seen on a coronal fat sat PD-WI, surrounded by bone marrow edema. Even though the epiphyseal cartilage shows altered signal intensity, there is no discontinuity of the overlying articular cartilage

abnormal pattern of signal intensity in the cancellous bone characterized by low signal intensity on T1-WI and high signal intensity on T2-WI (more evident on fluid-sensitive sequences). Albeit nonspecific, this finding is extremely sensitive and serves as a reliable marker of a subjacent abnormality; it is equivalent to the increased uptake found on bone scintigraphy, but presents higher diagnostic accuracy (Figs. 1.14, 1.22, and 1.24).

MRI uses gadolinium-based compounds as contrast agents, either intravenous or intraarticular (MR-arthrography), taking advantage of the paramagnetic properties of this chemical element. Intravenous contrast is most useful in the assessment of infections (Fig. 1.9), tumoral/pseudotumoral conditions (Fig. 1.10), inflammatory/hyperemic joint diseases (Figs. 1.14, 1.20, and 1.25) and in the postoperative period. The extent and the intensity of post-contrast enhancement parallel the inflammatory activity and can be followed in serial studies: the more severe the inflammation, the more intense the enhancement and vice versa (Fig. 1.25). Post-gadolinium enhancement is also an indicator of neoangiogenesis (usually found in hypervascular neoplastic lesions – Fig. 1.10) or of the presence of anomalous vessels (such as those found in vascular malformations). Unlike iodinated contrast agents, gadolinium-based compounds are not associated to nephrotoxicity. Allergic reactions are extremely uncommon and, when they occur, usually present mild severity.

For all the explained above, MRI is the most complete and sophisticated imaging method in the evaluation of the immature joint, unrivaled as a tool for early diagnosis. MRI can detect abnormalities related to inflammatory arthropathies – such as juvenile idiopathic arthritis and septic arthritis – still in the pre-erosive stage, allowing for a better course and improved prognosis with timely introduction of treatment, before the onset of irreversible changes. Because of its high anatomic resolution, MRI is also very useful in cancer staging and preoperative planning. Given that intravenously administered gadolinium compounds are found inside the joint cavities a few minutes after the injection (notably in inflamed joints), post-contrast sequences should be obtained as soon as possible, in order to distinguish the thickened synovium from the synovial fluid

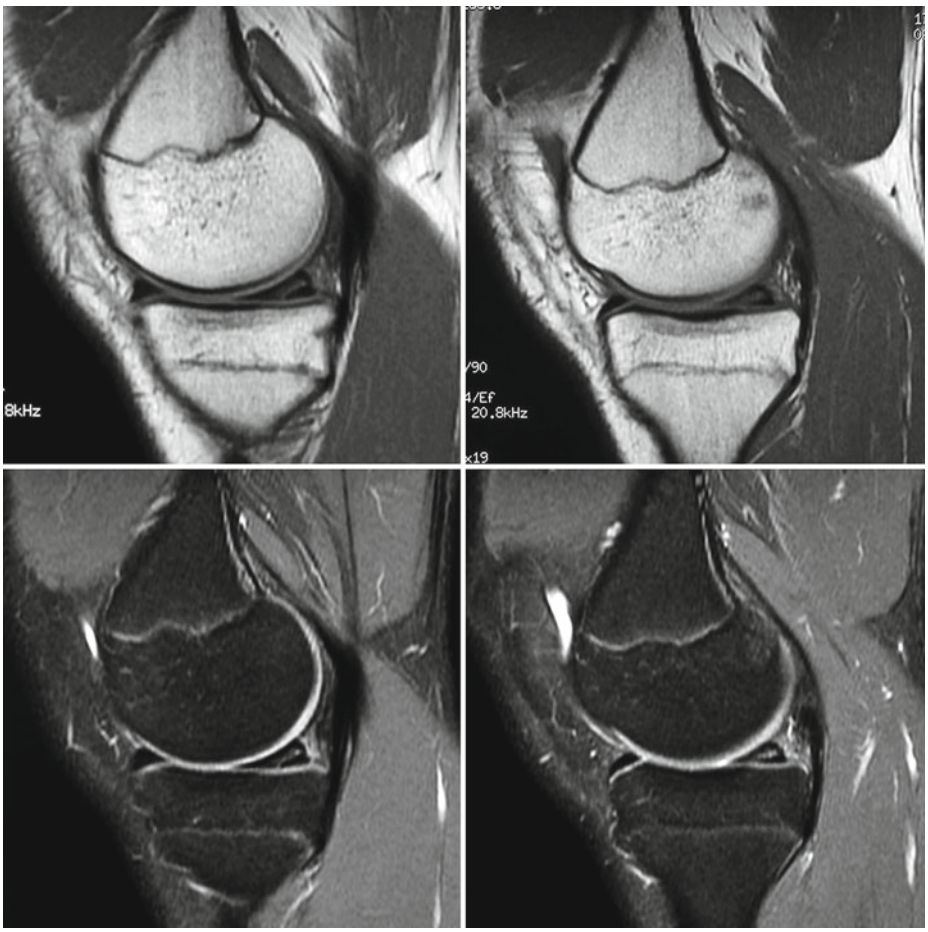

Fig. 1.23 MRI of the left knee of a 16-year-old soccer player. Sagittal T1-WI (*upper row*) and fat sat PD-WI (*lower row*) disclose a non-displaced tear of the posterior horn of the medial meniscus, with transection of the lower surface. Only MRI can demonstrate such abnormality noninvasively and with this level of detail

(Fig. 1.26). Subtle traumatic abnormalities – which are often "occult" on radiographs – may be heralded by areas of bone marrow edema pattern (Fig. 1.24).

Nevertheless, like any imaging modality, MRI also has some limitations and drawbacks. It is an expensive study, whose availability is highly variable worldwide. It is contraindicated for patients with cardiac pacemakers, some types of ferromagnetic intracranial aneurysm clips, and electronic monitoring or life-support devices (like infusion pumps or mechanical ventilators), which are incompatible with a strong magnetic field unless otherwise stated. The time for image acquisition is long, the required position may be uncomfortable, and a few joints – at the maximum – can be examined in a single session and the patient has to stand absolutely still; therefore, individuals unable to cooperate will need sedation, increasing the cost and the risk of the procedure. Although gadolinium-based contrast agents are not nephrotoxic per se, when administered to patients with moderate to severe renal failure (especially those requiring dialysis), they may lead to a rare, progressive, and potentially fatal disease, called nephrogenic systemic fibrosis (NSF), for which no effective treatment exists. Alternative imaging methods should be considered for patients with chronic renal failure if contrast-enhanced MRI is not indispensable; otherwise, informed consent must be obtained from the patient (or its guardian) and from the requesting physician. In order to minimize the risk of NSF, the lowest possible dose of contrast should be used and dialysis must be performed as soon as possible after MRI. Given that NSF is a newly discovered disease, many requesting physicians (and even some radiologists) may not be fully acquainted on the subject.

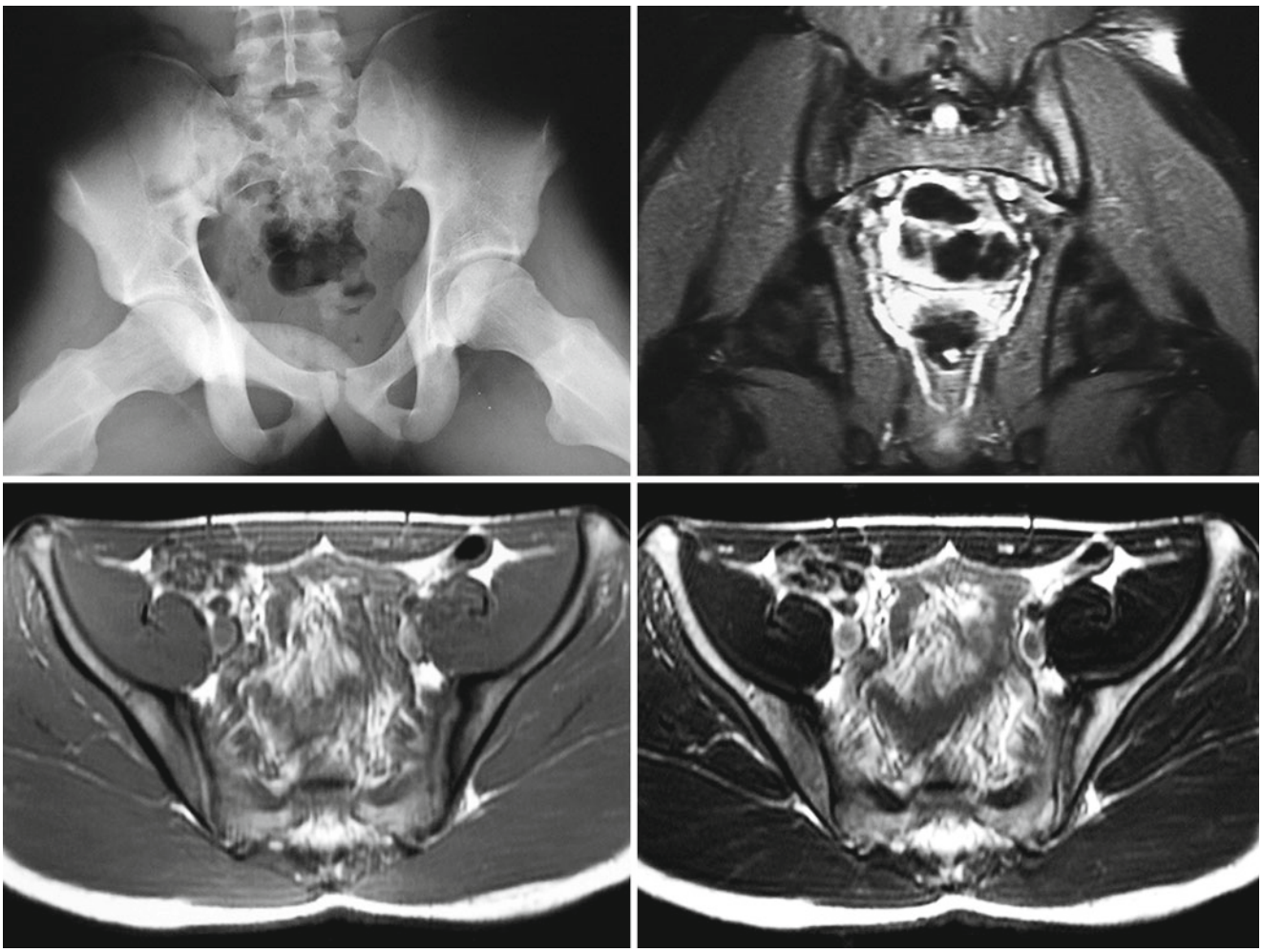

Fig. 1.24 Male adolescent who sustained a traumatic injury to the lumbar region 1 month before (fall during a motocross race) presenting persistent low back pain. Pelvic radiograph (*upper-left image*) failed to disclose any noteworthy abnormalities. However, coronal fat sat T2-WI (*upper-right image*) reveals bone marrow edema adjoining the left sacroiliac joint, with increased signal intensity within the joint space and in the surrounding soft tissues. Transverse T1-WI and T2-WI (*lower row*) show widening of the left sacroiliac joint space and irregularity of the corresponding articular surfaces ("occult" posttraumatic diastasis)

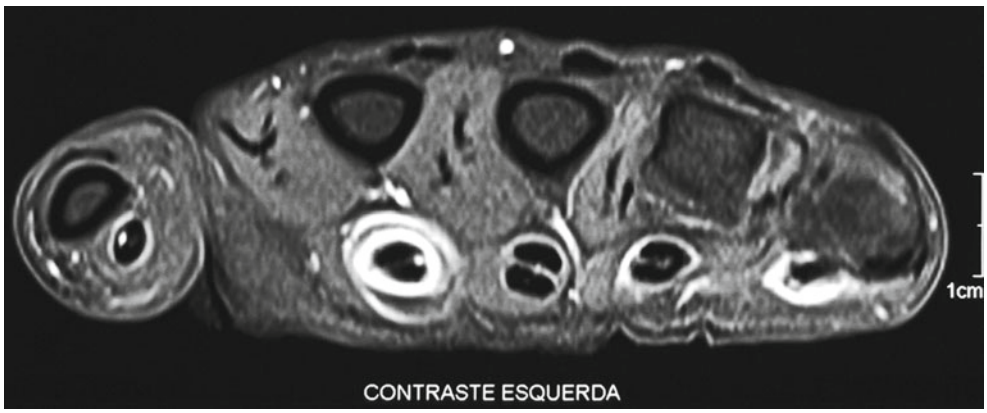

Fig. 1.25 Rheumatoid tenosynovitis in a young patient. Transverse post-gadolinium fat sat T1-WI of the left hand discloses synovial enhancement in the flexor tendon sheaths. Even though all digits are affected, enhancement is more intense in the second and in the fifth flexor sheaths. Involution of this enhancement in subsequent studies is an indicator of good response to the treatment; conversely, progression of the findings indicates worsening of the inflammation

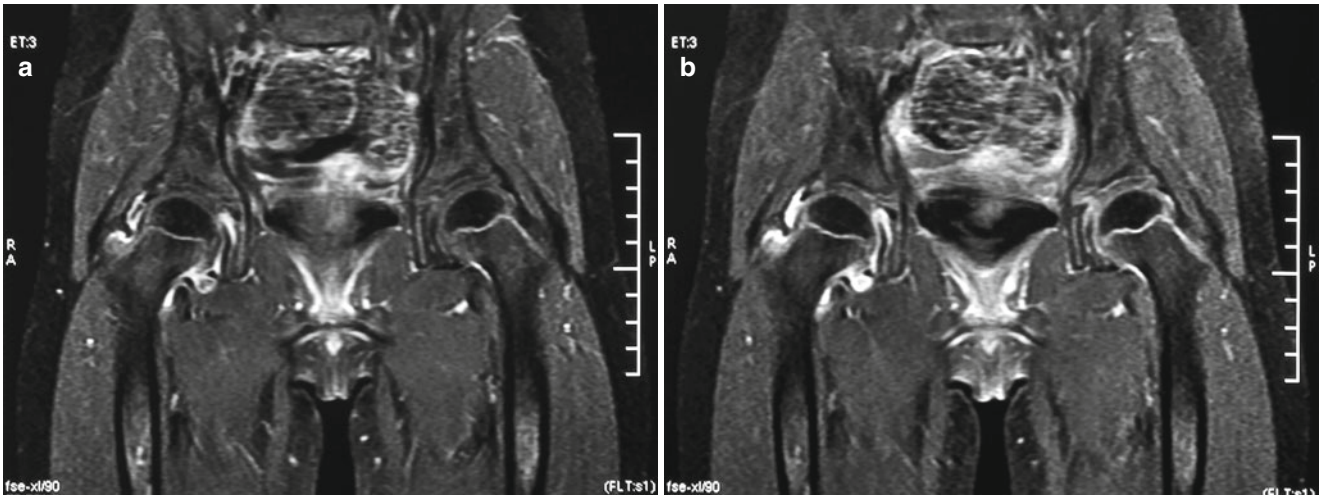

Fig. 1.26 Coronal fat sat T1-WI of the hips of a 6-year-old female with juvenile idiopathic arthritis. The first image (**a**), acquired immediately after intravenous administration of contrast, demonstrates joint effusion and synovial thickening in the right hip, with intense enhancement of the inflamed synovium. The joint fluid can be clearly differentiated from the thickened synovium, mostly adjacent to the acetabular labrum and to the medial cortex of the femoral neck. The second image (**b**), obtained in the same plane several minutes later, reveals diffusion of the contrast to the joint cavity, making it difficult to distinguish the synovial fluid from the synovium

1.7 Dual Energy X-Ray Absorptiometry

Among the several imaging methods able to assess bone mineral density, dual energy X-ray absorptiometry (DEXA) is the most widely used, the most studied, and the more uniformly standardized. In a nutshell, a DEXA scanner is able to interpret the different levels of absorption of X-rays by the different body tissues to estimate the bone mineral density in a given site or in the whole body. The results obtained are quantified in standard deviations and compared with the normal values of a population with similar characteristics (sex, age, and ethnicity), aiming to identify patients with low bone mineral density and increased risk of fractures (Fig. 1.27). Pediatric DEXA is peculiar, differing from that performed in adults as the parameters used are distinct and vary according to the clinical background. The International Society for Clinical Densitometry periodically issues official positions to standardize the procedure, the terms used in the reports, and the uniformity of such reports. These positions are continually updated and are available for the reference of readers on the Internet (www.iscd.org).

Name:	Sex: Female	Height: 155.0 cm
Patient ID: 174819	Ethnicity: Pediatric	Weight: 38.0 kg
DOB: 22 March 1999		Age: 11

Referring Physician:

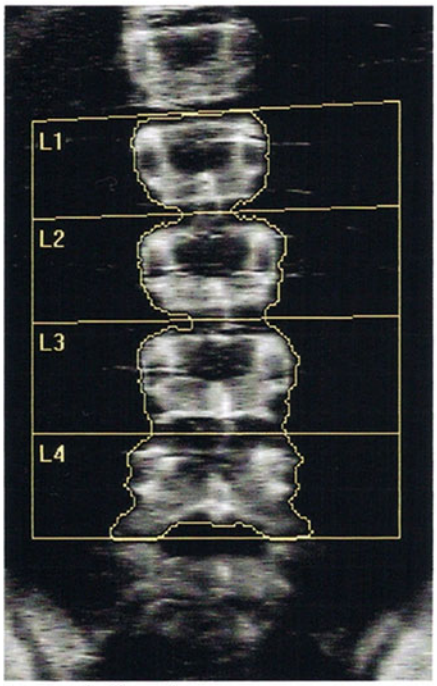

Image not for diagnostic use
k = 1.122, d0 = 52.3
109 x 131

Scan information:

Scan Date: 22 July 2010 ID: A0722100B
Scan Type: f Lumbar Spine
Analysis: 23 July 2010 08:47 Version 12.7.3.2:5
Lumbar Spine
Operator:
Model:
Comment:

DXA results summary:

Region	Area (cm^2)	BMC (g)	BMD (g/cm^2)	T-score	PR (%)	Z-score	AM (%)
L1	10.76	7.46	0.693		76	0.5	109
L2	12.25	8.40	0.685		67	-0.3	96
L3	14.51	10.44	0.719		69	-0.2	98
L4	15.32	10.94	0.714		68	-0.2	97
Total	**52.84**	**37.24**	**0.705**		**70**	**0.0**	**99**

Total BMD CV 1.0 %, ACF = 1.042, BCF = 1.010, TH = 4.885

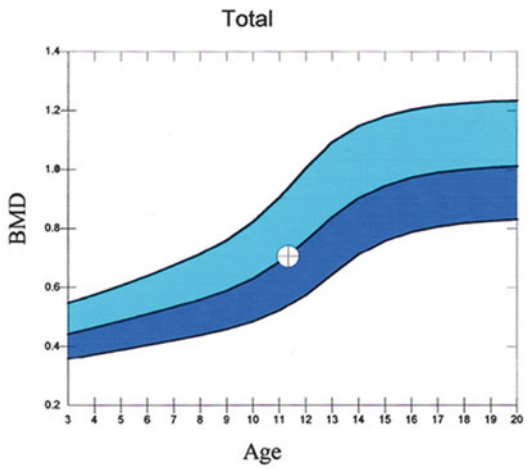

T-score vs. Pediatric Female; Z-score vs. Pediatric Female.

Physician's comment:

Fig. 1.27 DEXA of the lumbar spine (**a**) and of the whole body (**b**) of a healthy 11-year-old female. Bone mineral density (BMD) is within the normal range if compared to a population with similar characteristics (note the graphs in the lower-left corner of the images, in which BMD is plotted, and the charts in *yellow* at right, where the values found are stated). On the other hand, the densitometric data (lumbar spine and whole body) of an 8-year-old female with osteogenesis imperfecta (**c**) reveals marked decrease of the BMD, with consequent increase in the relative risk of fractures

Name:	Sex: Female	Height: 155.0 cm
Patient ID: 174819	Ethnicity: Pediatric	Weight: 39.0 kg
DOB: 22 March 1999		Age: 11

Referring Physician:

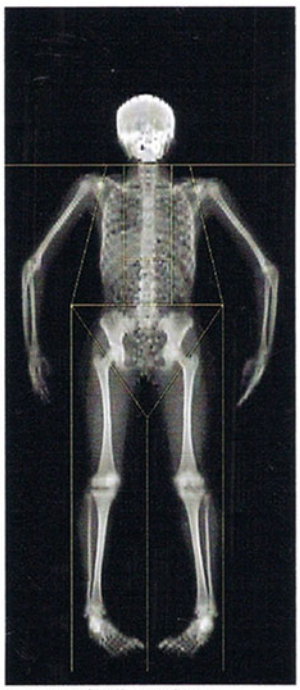

Image not for diagnostic use
k = 1.187, d0 = 51.5
318 x 150

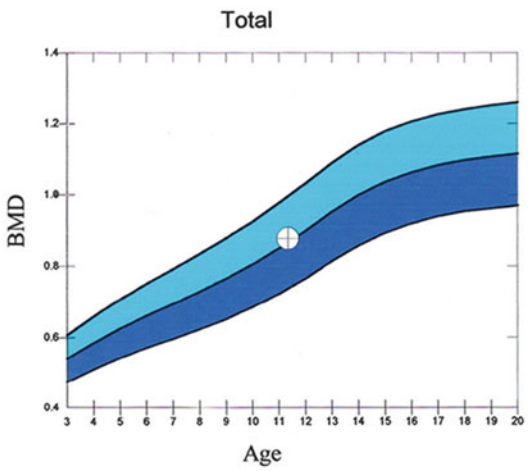

T-score vs. Pediatric Female; Z-score vs. Pediatric Female.

Scan information:

Scan Date: 22 July 2010 ID: A0722100E
Scan Type: a Whole Body
Analysis: 23 July 2010 11:15 Version 12.7.3.2:5
Auto Whole Body
Operator:
Model:
Comment:

DXA results summary:

Region	Area (cm²)	BMC (g)	BMD (g/cm²)	T-score	PR (%)	Z-score	AM (%)
L Arm	151.34	91.63	0.605				
R Arm	150.15	87.80	0.585				
L Ribs	71.91	35.98	0.500				
R Ribs	61.25	29.38	0.480				
T Spine	123.68	69.90	0.565				
L Spine	39.12	32.89	0.841				
Pelvis	188.87	159.41	0.844				
L Leg	270.67	254.12	0.939				
R Leg	252.10	234.43	0.930				
Subtotal	1309.08	995.54	0.760				
Head	205.07	332.67	1.622				
Total	**1514.15**	**1328.21**	**0.877**		**79**	**0.2**	**101**

Total BMD CV 1.0 %, ACF = 1.042, BCF = 1.010

Physician's comment:

Fig. 1.27 (continued)

15/6/1999 8,2 yo female
110,0 cm 16,8 kg

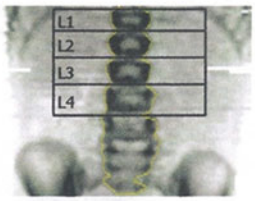

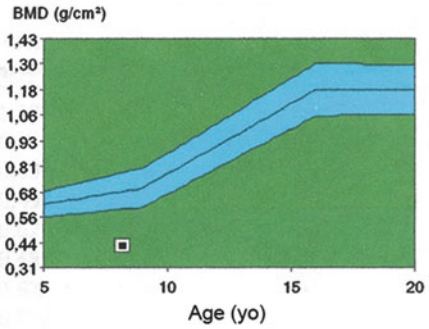

	BMD (g/cm²)	T-Score	Z-Score
L1	0,394	-	-2,8
L2	0,418	-	-3,3
L3	0,451	-	-2,9
L4	0,403	-	-3,4
L1-L4	0,417	-	-3,1

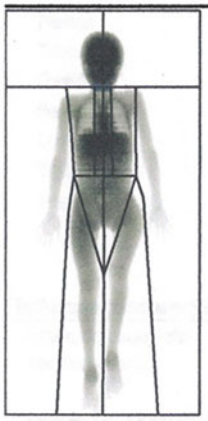

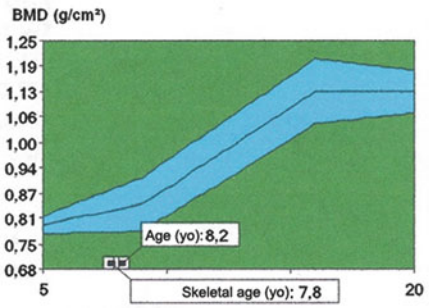

	BMD (g/cm²)	T-Score	Z-Score
Upper limbs	0,487	-	-
Lower limbs	0,581	-	-
Trunk	0,514	-	-
Ribs	0,497	-	-
Pelvis	0,497	-	-
Spine	0,554	-	-
Total	0,697	-	-2,2
Total (head)	0,536	-	-2,5

Fig. 1.27 (continued)

Key Points

- Radiographs are inexpensive, largely available, and useful in the follow-up of already established bone abnormalities. Nonetheless, they are limited for early diagnosis of joint diseases and for the assessment of the soft tissues. Radiographs must always be available before requesting more sophisticated imaging studies.
- US is inexpensive, well tolerated, and sensitive to synovitis and hyperemia, yielding images in real time. However, it is an operator-dependent study, limited to the assessment of superficial structures. Despite its usefulness for the evaluation of the soft tissues, little or no information can be obtained about the bones.
- Bone scintigraphy is highly sensitive, capable to study the entire skeleton in a single study and to detect "occult" sites of multifocal disease (tumors, infection, arthritides). Nonetheless, low specificity and poor spatial resolution limit its usefulness.
- CT has high spatial resolution and multiplanar capabilities, providing excellent assessment of bone anatomy. However, it delivers ionizing radiation and is limited in the evaluation of the soft tissues, and the iodinated contrast agents are potentially nephrotoxic. CT is more useful in the evaluation of osteoarticular trauma or as an alternative to MRI in arthritic children.
- MRI is inherently multiplanar, nonionizing, and highly sensitive, with high spatial and contrast resolutions. It is very useful for early diagnosis of osteoarticular conditions and to monitor the evolution of articular diseases. On the other hand, however, it is expensive, its availability is variable worldwide, and there are some absolute contraindications. Pediatric patients often need sedation.
- DEXA is the method of choice to assess bone mineral density, detecting individuals with increased risk of fractures. However, it is not useful for joint assessment.

Recommended Reading

Allen G, Wilson D, Graham R, Jacob D (2005) Échographie pédiatrique ostéo-articulaire. J Radiol 86(12 Pt 2):1924–1930

Babyn P, Doria AS (2007) Radiologic investigation of rheumatic diseases. Rheum Dis Clin North Am 33(3):403–440

Bianchi ML, Baim S, Bishop NJ, Gordon CM, Hans DB, Langman CB et al (2010) Official positions of the International Society for Clinical Densitometry (ISCD) on DXA evaluation in children and adolescents. Pediatr Nephrol 25(1):37–47

Buchmann RF, Jaramillo D (2004) Imaging of articular disorders in children. Radiol Clin North Am 42(1):151–168

Daldrup-Link HE, Steinbach L (2009) MR imaging of pediatric arthritis. Magn Reson Imaging Clin N Am 17(3):451–467

Damilakis J, Maris TG, Karantanas AH (2007) An update on the assessment of osteoporosis using radiologic techniques. Eur Radiol 17(6):1591–1602

Delle Sedie A, Riente L, Bombardieri S (2008) Limits and perspectives of ultrasound in the diagnosis and management of rheumatic diseases. Mod Rheumatol 18(2):125–131

Fritzsche PJ (2005) Communication: the key to improved patient care. Radiology 234(1):13–14

Hustinx R, Malaise MG (2006) PET imaging of arthritis. PET Clin 1(2):131–139

Imhof H, Mang T (2006) Advances in musculoskeletal radiology: multidetector computed tomography. Orthop Clin North Am 37(3):287–298

Jaramillo D, Laor T (2008) Pediatric musculoskeletal MRI: basic principles to optimize success. Pediatr Radiol 38(4):379–391

Johnson K (2006) Imaging of juvenile idiopathic arthritis. Pediatr Radiol 36(8):743–758

Miller E, Uleryk E, Doria AS (2009) Evidence-based outcomes of studies addressing diagnostic accuracy of MRI of juvenile idiopathic arthritis. AJR Am J Roentgenol 192(5):1209–1218

Nadel HR, Stilwell ME (2001) Nuclear medicine topics in pediatric musculoskeletal disease: techniques and applications. Radiol Clin North Am 39(4):619–651

Schlaudecker JD, Bernheisel CR (2009) Gadolinium-associated nephrogenic systemic fibrosis. Am Fam Physician 80(7):711–714

Peculiar Aspects of the Anatomy and Development of the Growing Skeleton

2

2.1 Introduction

Many radiologists – even experienced and renowned professionals – do not feel comfortable with pediatric studies, including those related to the immature musculoskeletal system. The most important cause of this antipathy is, by far, lack of familiarity with the normal appearance of the growing skeleton and its developmental peculiarities; this unawareness is a barrier both to recognition of normal patterns and to the diagnosis of pathological findings. The purpose of this chapter is to provide the reader with a brief review of the anatomical, histological, and physiological bases of osteoarticular development, which are crucial for interpretation and understanding of pediatric imaging.

2.2 The Immature Epiphysis and the Physis

A unique feature of the immature skeleton is the presence of cartilaginous structures in the extremities of the long bones, namely, the epiphyseal cartilage and the physis (also referred to as primary physis, growth cartilage, or growth plate), which involute with skeletal maturation and are no longer present in the adult organism. These cartilages act together as a functional unit responsible for the longitudinal growth of the bone. On the other hand, the articular cartilage protects and nourishes the subchondral bone of the joint surfaces, and, unlike the physis and the epiphyseal cartilage, it does not disappear, remaining throughout the life course. Radiographs are insensitive to demonstrate these cartilages (Fig. 2.1), and computed tomography and ultrasonography are also limited in their evaluation. Because of its characteristics (see Chap. 1), magnetic resonance imaging (MRI) is the preferred imaging method for assessment of most structures of the immature bone (Fig. 2.2).

The immature epiphysis is situated between the joint cavity and the physis. During the early stages of development, the epiphyses are entirely cartilaginous, serving as precursors for the ossified ends of the long bones. The cartilaginous epiphysis usually display low signal intensity on T1-weighted images (T1-WI) and intermediate to high signal intensity in fluid-sensitive sequences. Transformation of cartilage into bone begins in the inner portion of the epiphysis, the so-called secondary ossification center (the primary ossification centers form the diaphyses of the tubular

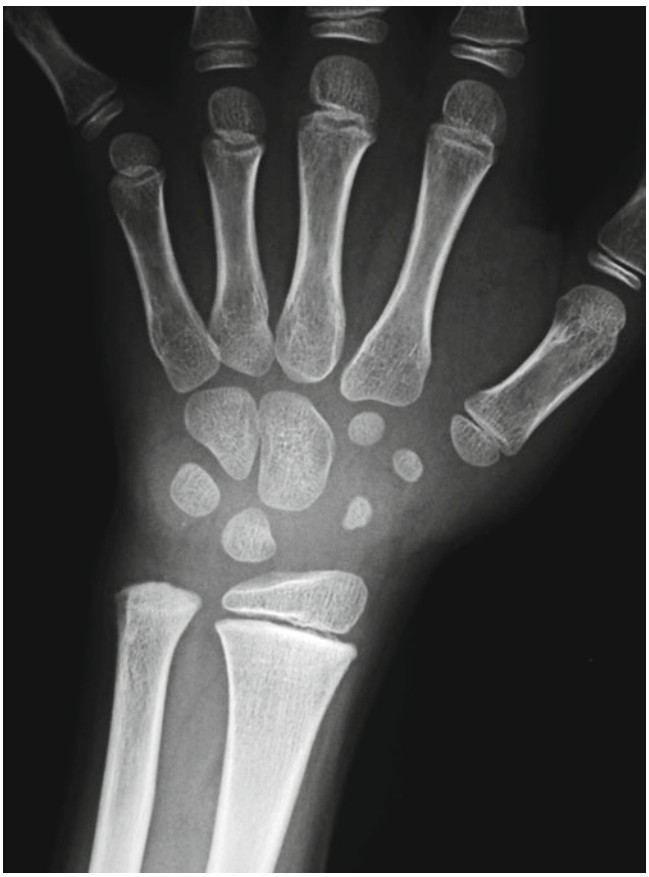

Fig. 2.1 Radiograph of the right wrist of an 8-year-old male showing that ossification has already begun in the carpal bones and in the distal radial epiphysis. However, as radiographs are fairly insensitive for cartilaginous assessment, only an indirect estimate of the thickness of the physes, of the cartilaginous anlage of the carpal bones, and of the epiphyseal cartilages can be made. The distal epiphysis of the ulna is entirely cartilaginous and completely invisible

S.L. Viana et al., *Joint Imaging in Childhood and Adolescence*,
DOI 10.1007/978-3-642-35876-0_2, © Springer-Verlag Berlin Heidelberg 2013

bones during intrauterine life). Ossification may occur in a single center (like in the proximal or distal femoral epiphyses – Fig. 2.3) or, less often, via multiple secondary ossification centers that later coalesce (such as in the distal humerus – Fig. 2.4). The secondary ossification center is surrounded by a specialized structure, the secondary physis, responsible for the endochondral ossification and structurally similar to the primary physis, appearing as a thin layer of high signal intensity on fluid-sensitive sequences (Figs. 2.5 and 2.6). The ossification center, which is round when it first appears, changes to a hemispheric configuration over time: it increases in size and molds to the contour of the epiphysis in which it is settled, at the same time as there is thinning of the epiphyseal cartilage (Fig. 2.7). The epiphyseal

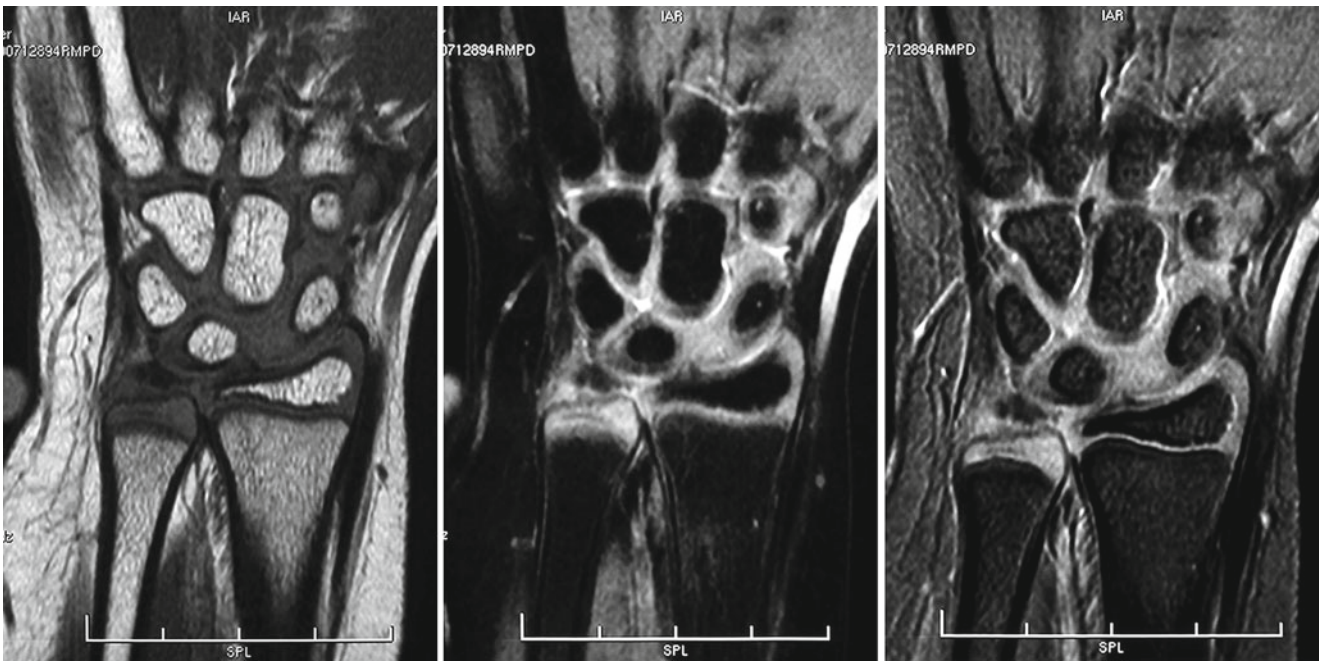

Fig. 2.2 MRI of the right wrist of a young male whose age is similar to that of the child in Fig. 2.1. Coronal T1-WI (*left*), fat sat PD-WI (*center*), and gradient-echo image (*right*) show that the ossified portions of the carpal bones are isointense with the medullary bone seen in the metacarpals, the distal metaphyses of the radius and the ulna, and the ossified portion of the distal epiphysis of the radius. Even though the distal epiphysis of the ulna is entirely cartilaginous, the epiphyseal cartilage is clearly seen, presenting low to intermediate signal intensity on T1-WI and intermediate to high signal intensity in the other sequences; a similar behavior is seen in the cartilaginous anlage of the carpal bones and in the cartilaginous portion of the distal epiphysis of the radius

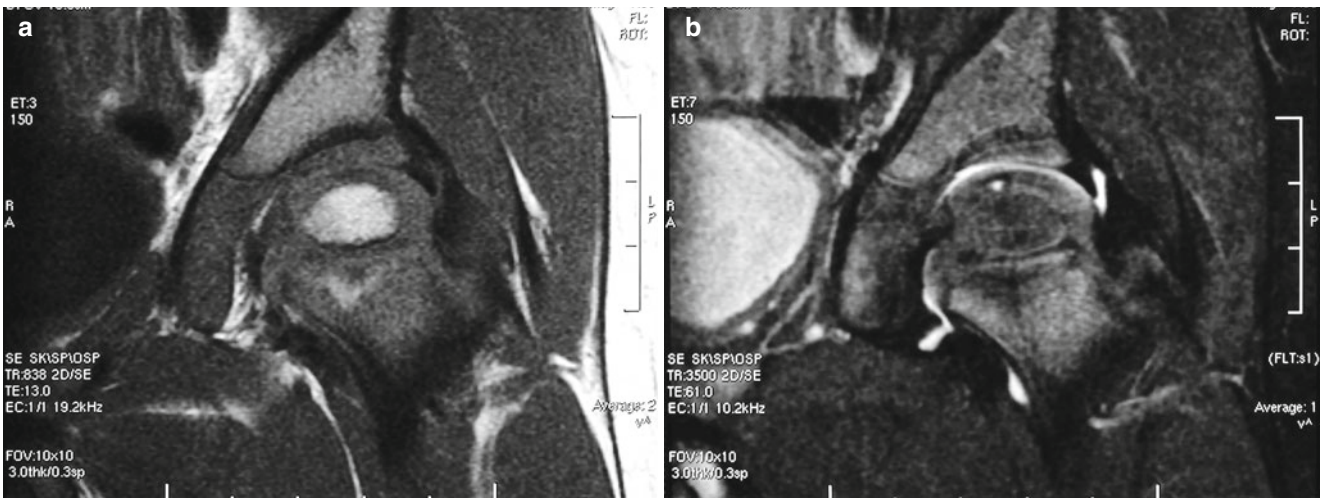

Fig. 2.3 Coronal T1-WI (**a**) and fat sat T2-WI (**b**) of the left hip of a 3-year-old male. The secondary ossification center of the femoral head is already present, whose bone marrow has undergone complete conversion to the fatty type, while the bone marrow of the femoral metaphysis and of the iliac bone presents predominance of the hematopoietic variety. The epiphyseal cartilage is predominantly isointense on T1-WI and shows intermediate signal intensity on fat sat T2-WI. There is a small focus of increased signal intensity on T2-WI in the apex of the epiphyseal cartilage, related to pre-ossification changes. The difference between the signal intensity of the yellow marrow (epiphyseal) and the red marrow (metaphyseal and diaphyseal) is even more striking in sagittal images of the knee of a school-aged child (**c**)

Fig. 2.3 (continued)

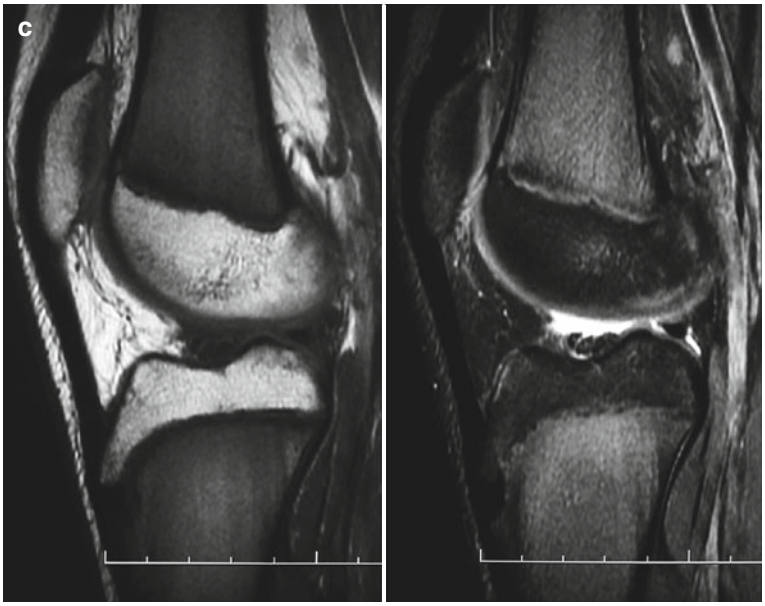

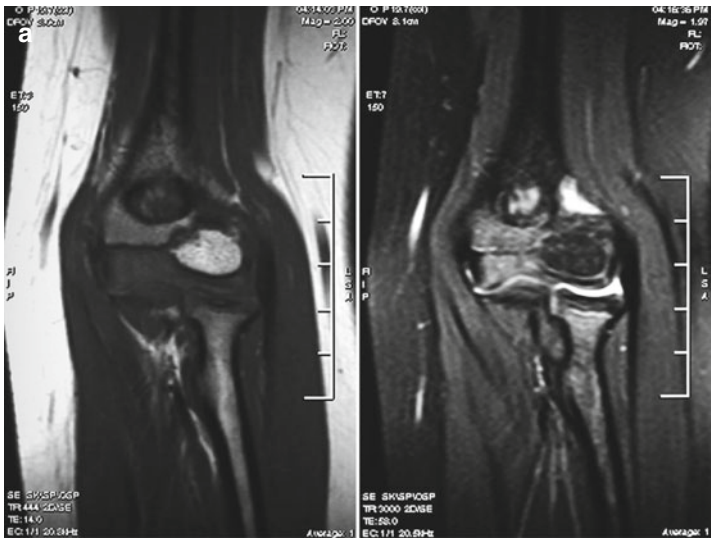

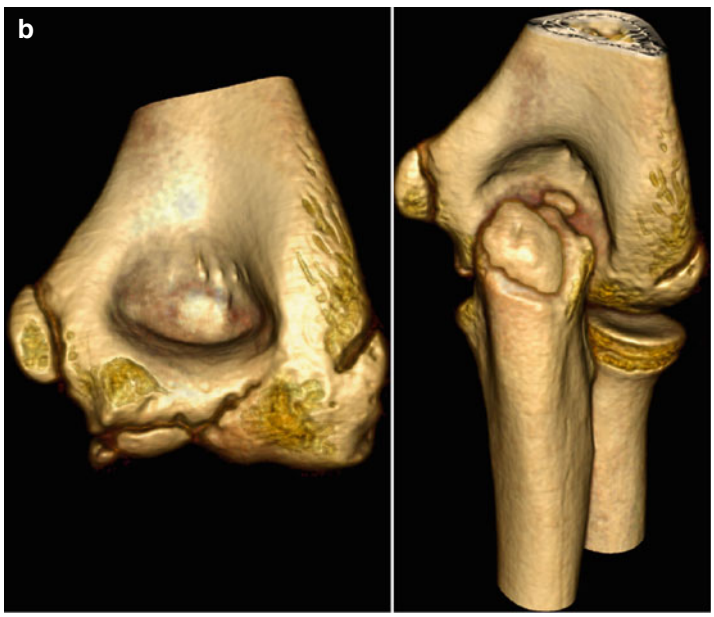

Fig. 2.4 In (**a**), coronal T1-WI (*left*) and fat sat T2-WI (*right*) of the left elbow of a 6-year-old female show that the ossification center of the capitulum is already filled with yellow marrow. The trochlear portion of the distal epiphysis of the humerus is completely cartilaginous, and increased signal intensity is seen in this cartilage on fat sat T2-WI, representing pre-ossification phenomena. In (**b**), volume-rendered CT reconstructions of the left elbow of a 13-year-old male demonstrate that all the ossification centers are ossified, with partial fusion of the ossification center of the capitulum. Despite the excellent anatomic detail of bone provided by CT, very limited information can be obtained with this imaging method about the cartilaginous structures

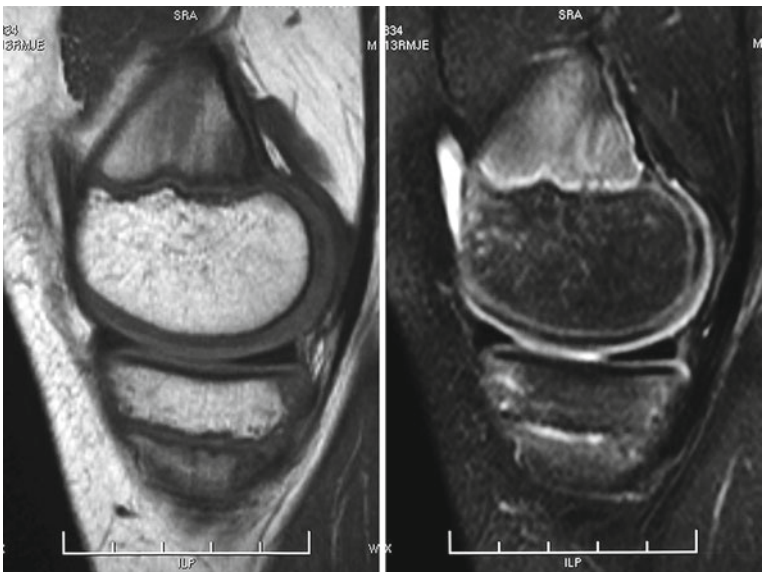

Fig. 2.5 Sagittal T1-WI (*left*) and fat sat T2-WI (*right*) of the right knee of a 13-year-old male. The secondary physis and the articular cartilage of the distal femur are clearly identified on fat sat T2-WI as linear areas of high signal intensity situated between the ossified and the cartilaginous portion of the epiphysis and along the joint surface of the epiphyseal cartilage, respectively. Bone marrow conversion is already completed in the epiphyses, while there is residual red marrow in the metaphyses, with its typical flame-shaped appearance

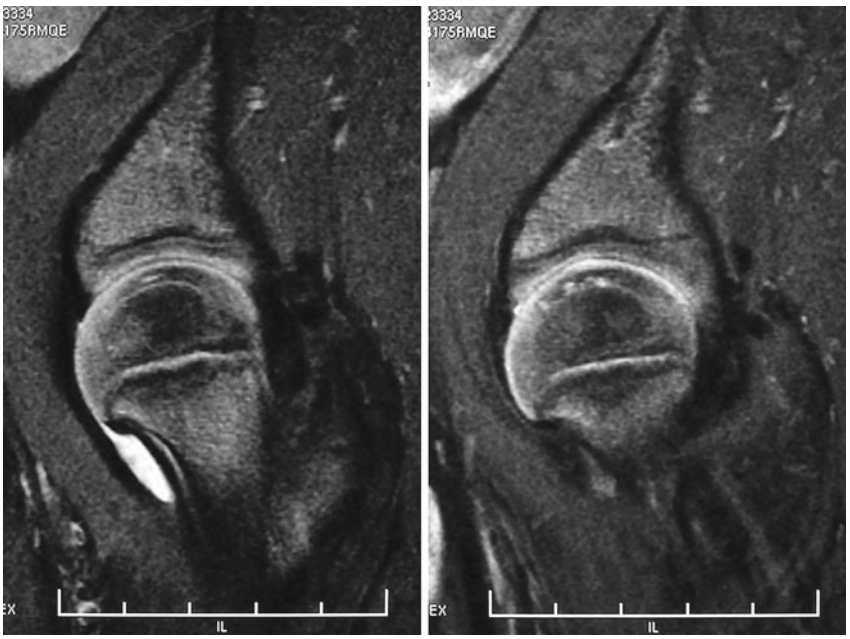

Fig. 2.6 Sagittal fat sat T2-WI of the left hip of a toddler. Although the epiphyseal cartilage displays predominantly intermediate signal intensity, there is low signal intensity in the weight-bearing zone, located in the uppermost portion of the epiphysis. In addition, foci of increased signal intensity are also found in the apex of the epiphyseal cartilage, related to ongoing ossification. The secondary physis appears as a thin hyperintense line surrounding the secondary ossification center, between the latter and the epiphyseal cartilage. The physis and the articular cartilage are also hyperintense if compared to the epiphyseal cartilage

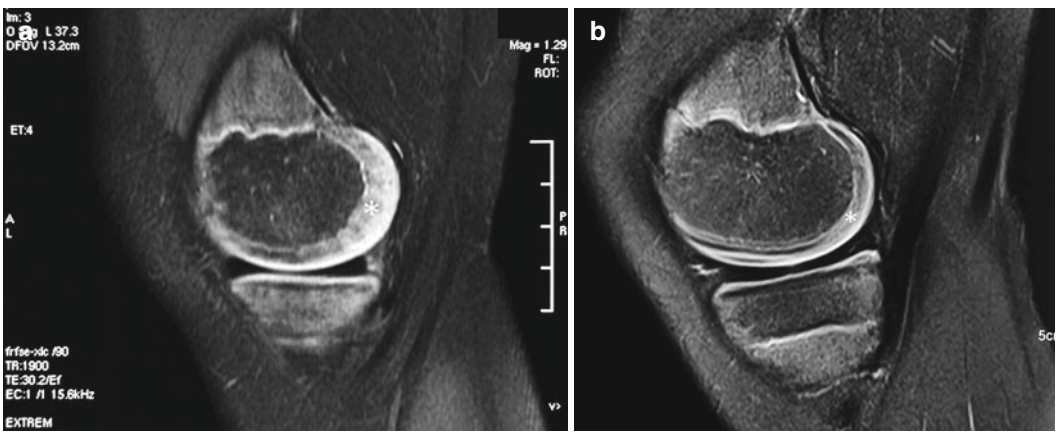

Fig. 2.7 Sagittal PD-WI of the medial femoral condyles of two different children – the first is a 7-year-old subject (**a**) and the second one is a 13-year-old (**b**) – displaying the epiphyseal cartilage (*) as a structure of intermediate signal intensity between the hyperintense articular cartilage and the hypointense secondary ossification center. The ossification center is smaller, and the cartilage is proportionally thicker in younger children

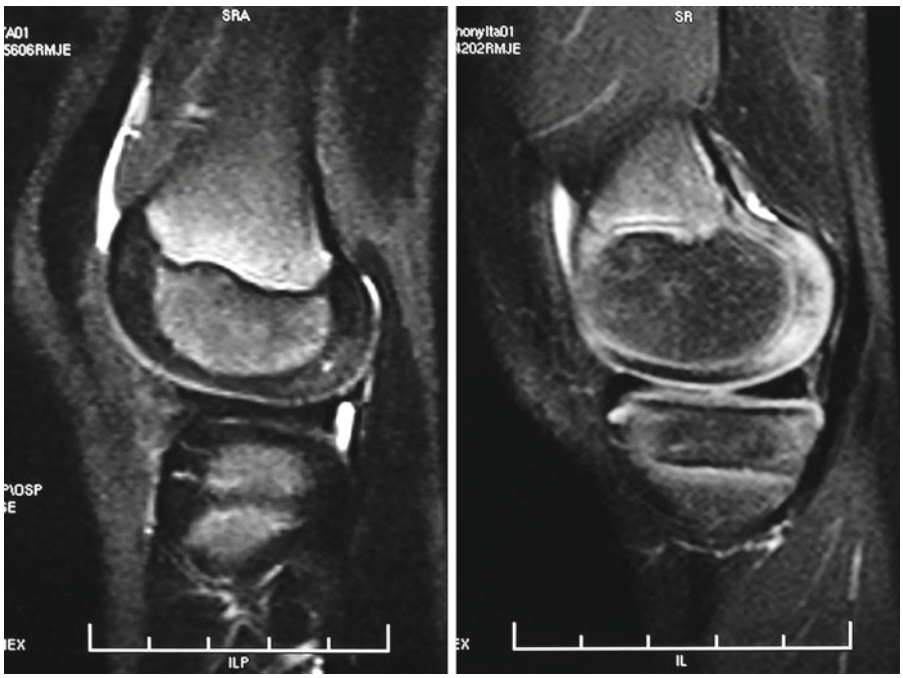

Fig. 2.8 Sagittal fat sat T2-WI of the knees of two different male children, a 5-year-old (*left*) and a 7-year-old (*right*). There is rapid epiphyseal growth over time, with increase in the size of the secondary ossification center and reduction of the thickness of the epiphyseal cartilage. In the first image, marked hyperintensity is present in the primary spongiosa is of the distal femur; a zone of increased signal intensity within the posterior portion of the epiphyseal cartilage of the femoral condyle represents ongoing ossification. The second image also shows hyperintensity of the posterior portion of the epiphyseal cartilage, more diffuse if compared to that seen in the first child. The focal area of decreased signal intensity seen in the weight-bearing zone of the epiphyseal cartilage of the femur in the second image is deprived of significance, typical of ambulating children

cartilage is homogeneous throughout the first year of life, but, as skeleton maturation takes place, focal areas of high signal intensity on T2-WI appear, more evident in the posterior aspect of the femoral condyles. Such areas are more common in preadolescent males and are typically not associated with abnormalities of the subchondral bone, being deprived of significance and representing the earliest stages of endochondral ossification (Figs. 2.3, 2.4, and 2.6). They are initially focal and heterogeneous, becoming more extensive and uniform with time (Fig. 2.8). As the child begins to walk, the weight-bearing portions of the epiphyseal cartilages present a decrease in their signal intensity on T2-WI, more evident in the knees and the hips, also deprived of importance (Figs. 2.6 and 2.8). Irregularity of the secondary ossification centers at the bone/cartilage junction is a normal finding, mostly seen during growth spurts (Fig. 2.9). Accessory ossification centers may also be present, usually adjoining the posterior aspect of the secondary ossification center of the distal femur, not associated with bone marrow edema or abnormalities of the overlying cartilage. The articular cartilage is hardly discernible on T1-WI, appearing as a thin layer of high signal intensity surrounding the immature epiphysis on T2-WI (Figs. 2.5, 2.6, 2.7, and 2.10).

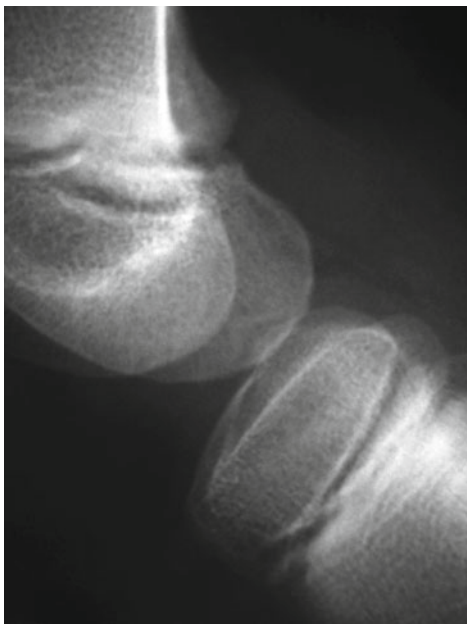

Fig. 2.9 Lateral view of the right knee of a 9-year-old female. The irregular contour of the femoral condyles is a normal finding, related to skeletal maturation

The physis is a specialized area of the bone, situated between the epiphysis and the metaphysis. It is divided into several zones, each one of them with distinct histological appearances and functions in the process of endochondral ossification. The germinal layer (resting zone) abuts the epiphysis and is composed mainly by abundant matrix and loosely organized chondrocytes, providing the cells responsible for growth; lesions of this layer (such as those found in transphyseal fractures, for instance) may lead to arrested bone growth. The proliferating zone is constituted by flattened chondrocytes with intense mitotic activity, which are arranged in columns and separated by bars of chondroid matrix. These columns of cells present continuous migration to the metaphysis, fed by cellular division in their basal portions. Conversely, there is

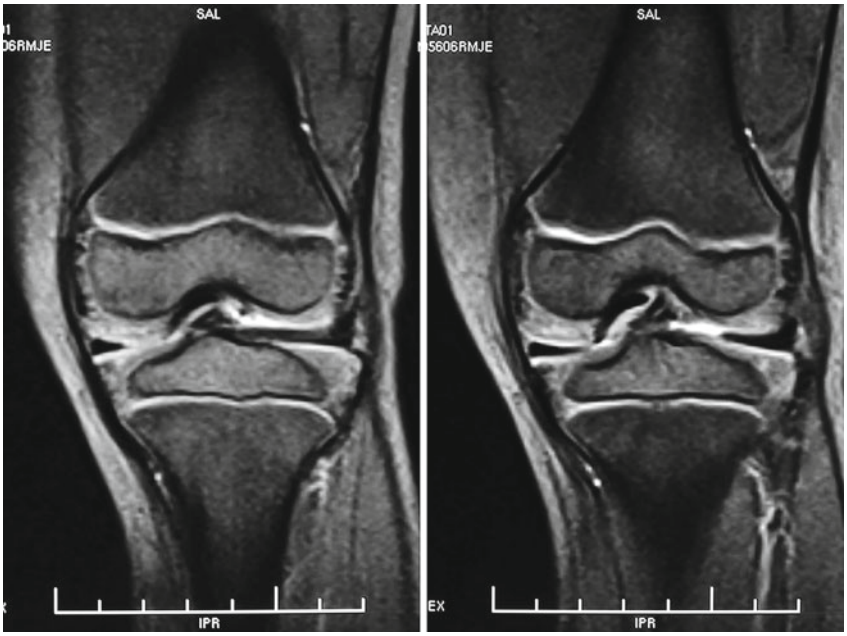

Fig. 2.10 Coronal gradient-echo images of the left knee of a 5-year-old child. The epiphyseal cartilages of the distal femur and of the proximal tibia are clearly distinguished from the adjacent articular cartilages: the latter are noticeably brighter, with signal intensity similar to that of the physeal cartilage. The smooth and regular physes are typical of small children. As the menisci are composed of fibrocartilage, they appear as triangular structures with uniform low signal intensity

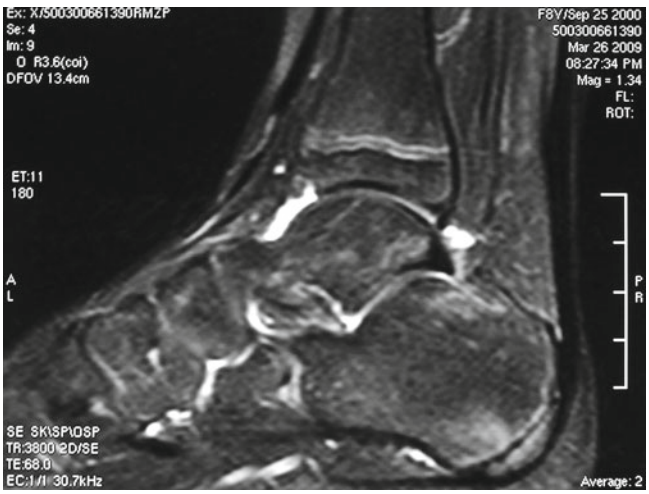

Fig. 2.11 Sagittal fat sat T2-WI of the right ankle of an 8-year-old female. The distal physis of the tibia presents the classic three-layered appearance, with high signal intensity in the physeal cartilage and in the primary spongiosa and an intervening line of low signal intensity corresponding to the provisional calcification zone. The physis is almost flat, a normal finding for the patient's age. Foci of increased signal intensity are seen in the medullary bone of the hindfoot and midfoot representing perivascular residual red marrow, a finding with no significance

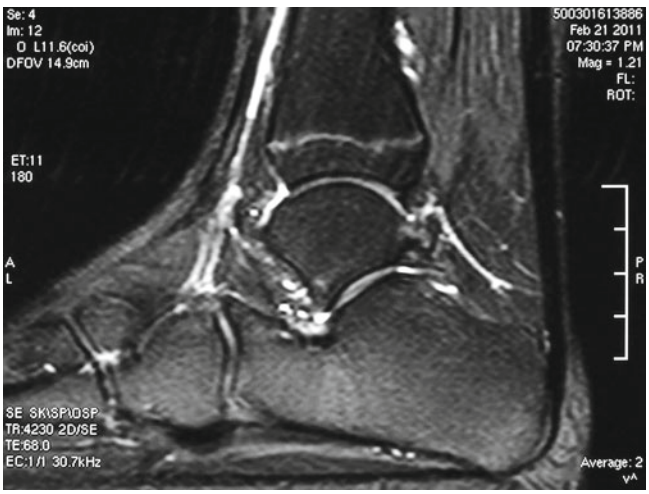

Fig. 2.12 Sagittal fat sat T2-WI of the right ankle of a 12-year-old female. If compared to the child of Fig. 2.11, the distal tibial physis is wavier and presents reduced thickness, findings related to progression of bone maturation. The calcaneal apophysis is already incorporated to the body of the bone

no active cellular division in the hypertrophic cell zone, where the chondrocytes reach their maximum size and undergo vacuolation. Finally, after the death of the chondrocytes and upon production of alkaline phosphatase in the provisional calcification zone, the metaphyseal vessels invade the extracellular matrix, which becomes mineralized and serve as a scaffold for the osteogenesis. These vessels bring osteoprogenitor cells, which differentiate into osteoblasts and form bone in the spaces left behind by the chondrocytes. The thickness of the physis is relatively uniform during growth due to a strict balance between production of cartilage and removal of chondrocytes.

The physes of young children are flat, becoming wavy as the growth advances (Figs. 2.10, 2.11, and 2.12). The primary spongiosa is the portion of the metaphysis adjacent to the physis, composed of newly formed bone, which appears hyperintense on fluid-sensitive sequences (Figs. 2.8,

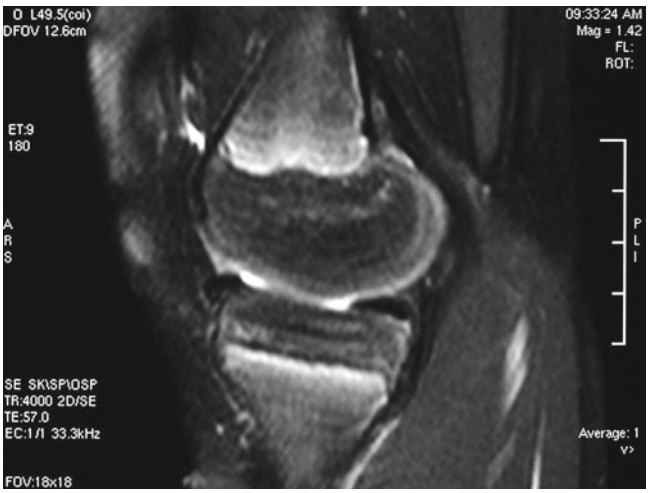

Fig. 2.13 Sagittal T2-WI of the left knee of a 10-year-old male. There is increased signal intensity in the primary spongiosa of the distal femur and proximal tibia, which should not be confused with bone marrow edema pattern

2.11, 2.13, and 2.14). The several physeal zones cannot be discriminated as distinct regions on MRI; nevertheless, the normal physis has a three-layered appearance. In addition to the primary spongiosa, it is possible to distinguish the provisional calcification zone, which is hypointense in all sequences because of its mineralized matrix, and the physeal cartilage itself, which displays intermediate/high signal intensity on fluid-sensitive sequences (Figs. 2.11 and 2.14). Once bone maturation is completed, there is progressive narrowing of the physis until its eventual disappearance (Fig. 2.12), leaving only the physeal scar. Areas of bone marrow edema centered about the physis are occasionally found in adolescents, notably in the knees. Such areas of focal periphyseal edema affect the epiphyseal and the metaphyseal bone marrow and may be occasionally painful, representing the early stages of physeal closure (Fig. 2.15); in the authors' experience, post-contrast enhancement may also be present (Fig. 2.16). They can be found in more than one bone in the same joint or even in more than one joint at the same time. Open physes usually act as barriers between the epiphyseal and metaphyseal vascular beds, limiting the propagation of neoplastic lesions and infections (Fig. 2.17).

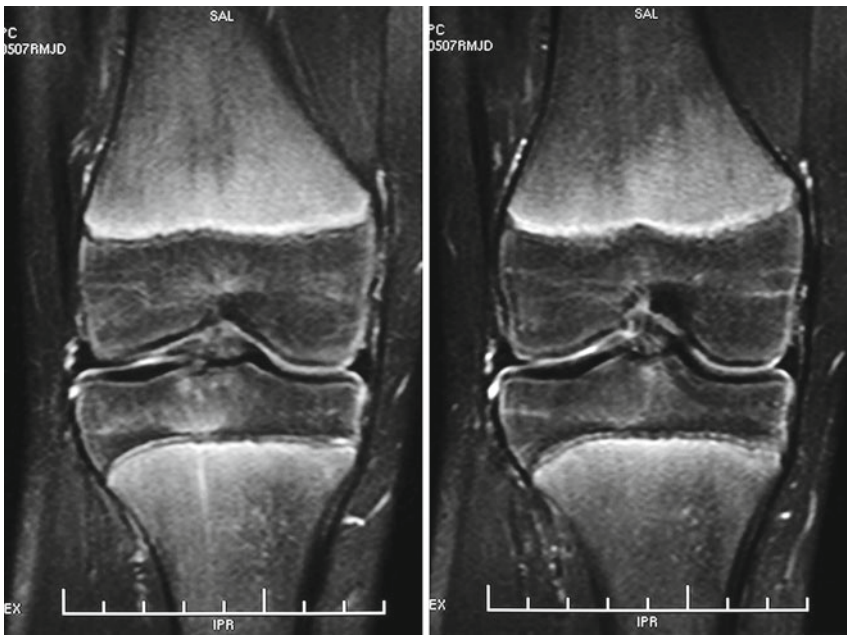

Fig. 2.14 Coronal fat sat T2-WI of the right knee of a 13-year-old male. The physes display their characteristic three-layered appearance, which is more evident in the proximal tibia. Intermediate to high signal intensity can be seen in the flame-shaped red marrow of the metaphyses, notably in the distal femur

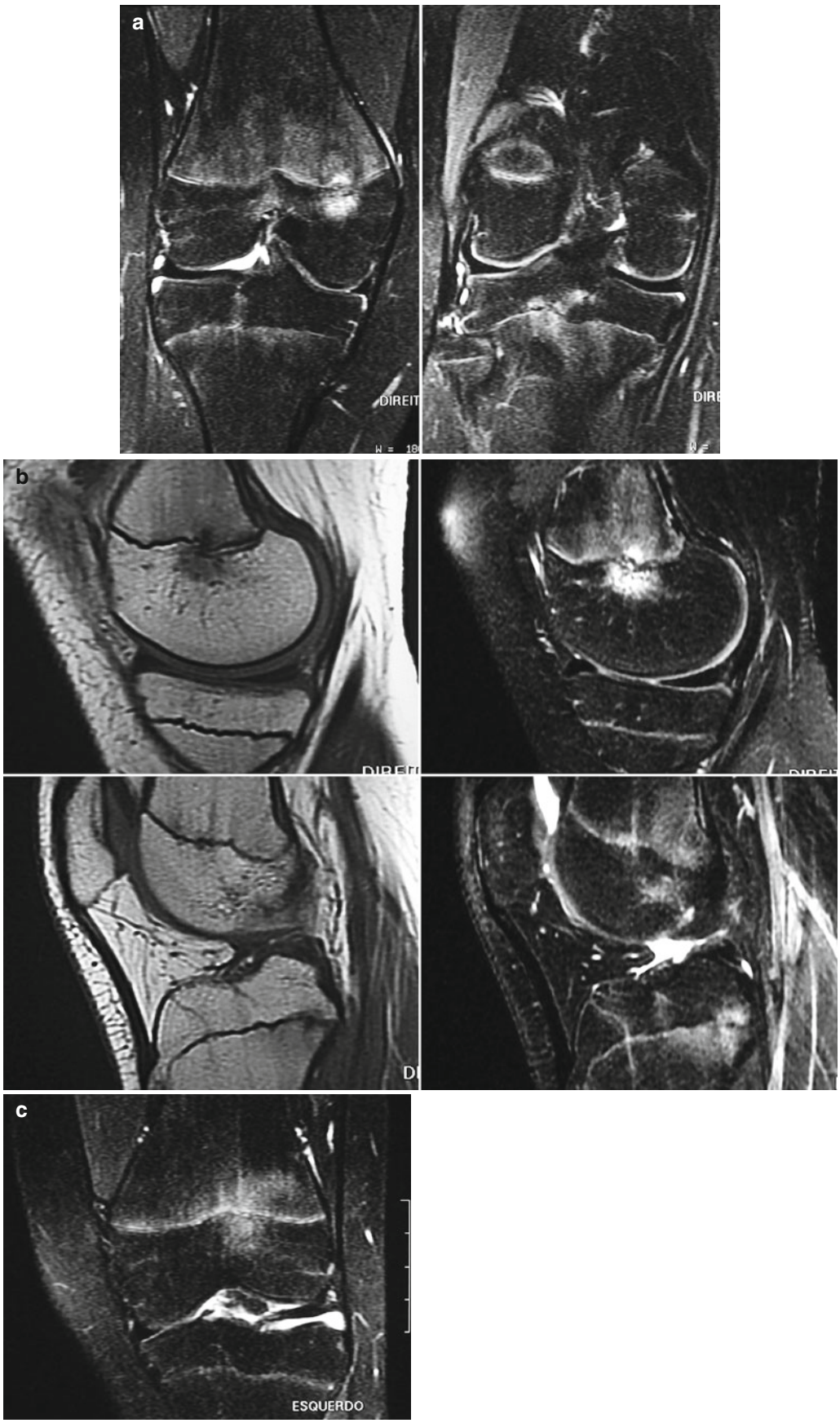

Fig. 2.15 A 14-year-old female complaining of pain in both knees. Coronal fat sat PD-WI (**a**) and sagittal T1-WI (**b**, *upper row*) and fat sat PD-WI (**b**, *lower row*) of the right knee reveal focal areas of bone marrow edema pattern centered about the physes of the distal femur and proximal tibia. Similar findings can be seen in the contralateral femur (**c** and **d**)

Fig. 2.15 (continued)

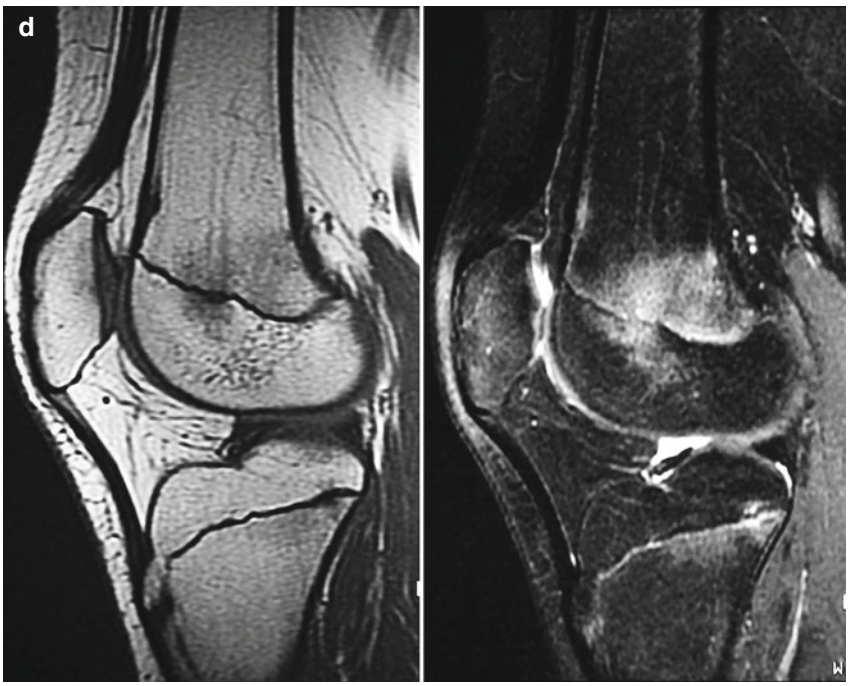

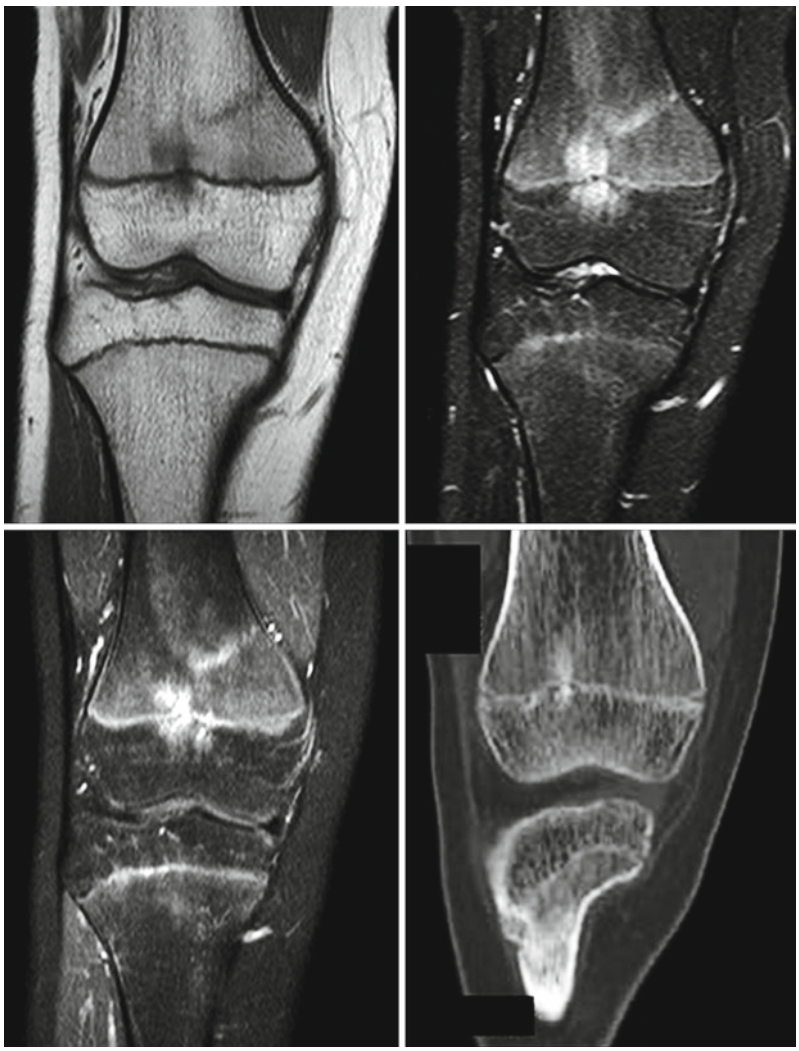

Fig. 2.16 A 13-year-old female complaining of right-sided knee pain. Coronal T1-WI (*upper-left image*) and fat sat T2-WI (*upper-right image*) demonstrate bone marrow edema centered about the distal femoral physis, with questionable physeal narrowing. Post-gadolinium fat sat T1-WI (*lower-left image*) discloses enhancement of the edematous bone marrow, while coronal reformatted CT image of the same knee (*lower-right image*) shows sclerosis of the cancellous bone in the affected area and unequivocal focal narrowing of the growth plate

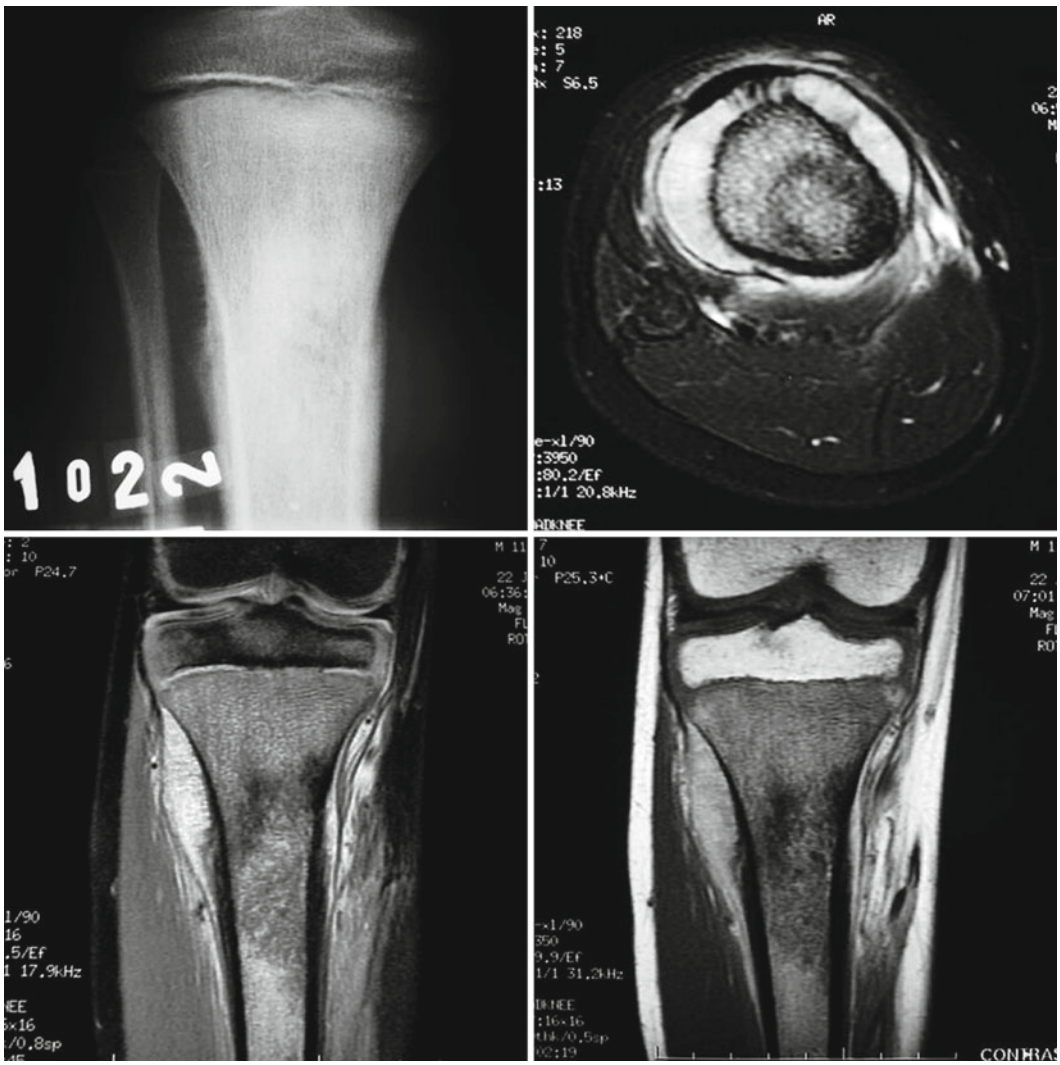

Fig. 2.17 An 11-year-old male with aggressive sarcoma of the right proximal tibia. In addition to an anteroposterior view of the proximal leg (*upper-left image*), transverse fat sat T2-WI (*upper-right image*), coronal fat sat T2-WI (*lower-left image*), and post-gadolinium fat sat T1-WI (*lower-right image*) are also shown. Radiograph reveals heterogeneous bone sclerosis, spiculated periosteal reaction, and an adjacent soft-tissue mass. On MRI, the bone marrow of the proximal metadiaphysis of the tibia is diffusely infiltrated by the tumor, with extensive subperiosteal component. Nonetheless, the proximal tibial epiphysis presents normal signal intensity, as the progression of the sarcoma was halted by the physis

2.3 Pediatric Bone Marrow

The bone marrow is the main hematopoietic organ. As a result of its variable and dynamic composition, its appearance on imaging changes considerably during skeletal maturation. For instance, in newborns, the bone marrow is entirely of the hematopoietic type (red marrow), which presents low signal intensity on T1-WI (similar or higher than that of the skeletal muscle) and intermediate to high signal intensity on fluid-sensitive sequences (Fig. 2.3). The conversion of red marrow to yellow (fatty) marrow in the appendicular skeleton begins in the first year of life and happens expeditiously, following a stereotyped pattern, being almost complete by the time of skeletal maturity. As the yellow marrow is composed mostly by fat, conversion leads to increase in the signal intensity of the bone marrow on T1-WI and signal drop in sequences with fat suppression, a behavior that is similar to that of the subcutaneous tissue. The conversion process starts in the distal portions of the limbs (phalanges of hands and feet) and advances centripetally to the proximal bones (humeri and femora). However, if

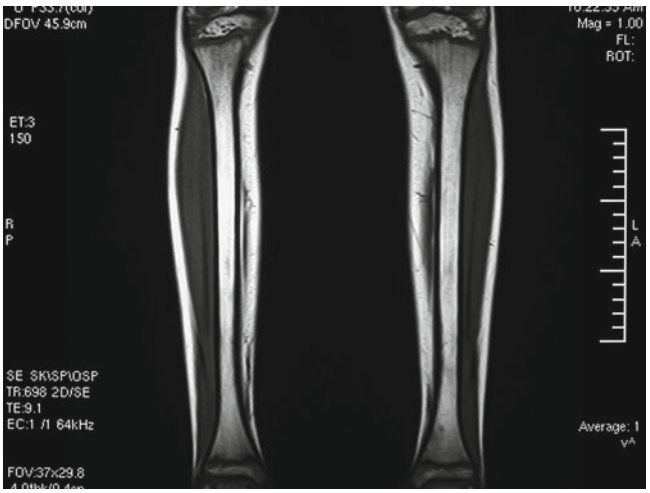

Fig. 2.18 Coronal T1-WI of the legs of a 10-year-old male demonstrating the normal centrifugal pattern of bone marrow conversion, with preponderance of the hyperintense yellow marrow in the tibial diaphysis and residual red marrow predominantly located in the metaphyses, mainly the proximal ones

the long bones are considered individually, the pattern of marrow replacement is centrifugal, beginning in the mid-diaphysis and advancing towards the metaphyses (Fig. 2.18). In the epiphyses, although the bone marrow of the newly formed secondary ossification centers is essentially of the hematopoietic type, conversion takes place within 6 months of their radiographic appearance (Figs. 2.2, 2.3, 2.4, and 2.5). On T1-WI, vertebrae are usually hypointense if compared to disks during the first year of life, becoming isointense/slightly hyperintense from the first to the fifth year and hyperintense from then on. On fluid-sensitive sequences, the signal intensity of the vertebrae presents progressive reduction if compared to the skeletal muscle, going from isointense/slightly hyperintense in young children to hypointense in older individuals. Marrow conversion is progressive and continuous in the axial skeleton, also occurring throughout adult life. In the pelvic bones, marrow conversion is usually more heterogeneous, intertwining areas of red marrow and yellow marrow (Fig. 2.19).

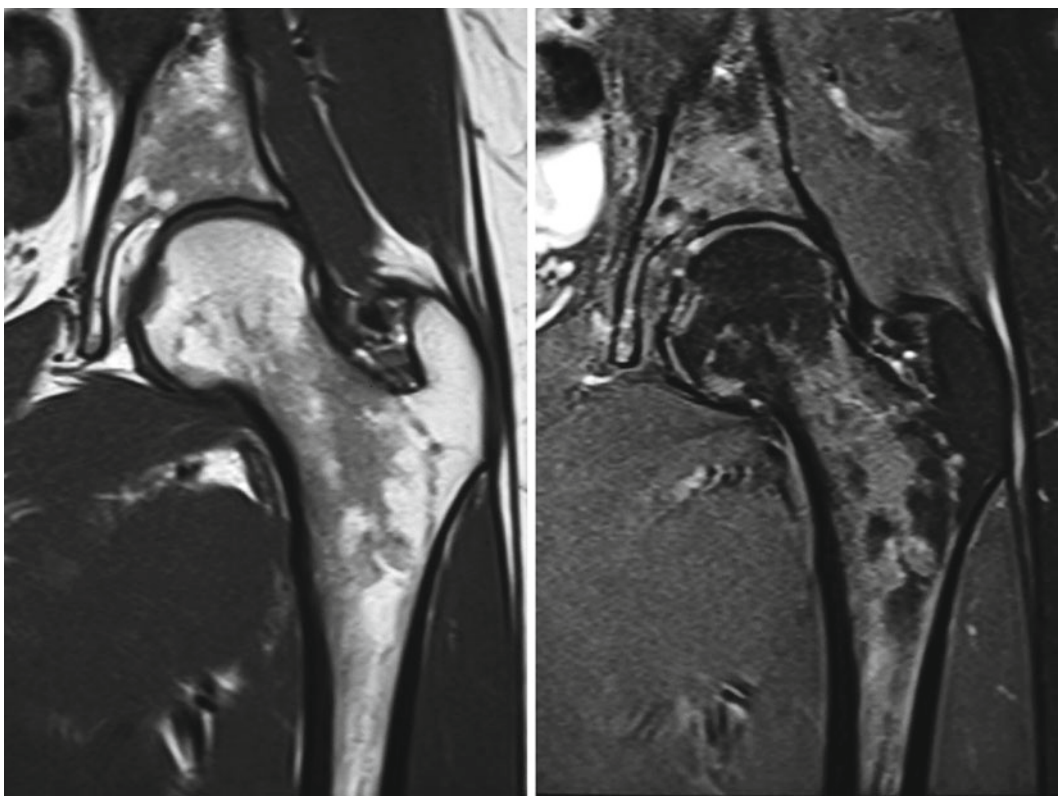

Fig. 2.19 Coronal T1-WI (*left*) and fat sat T2-WI (*right*) of the left hip of a 35-year-old female. There is residual red marrow intertwined with yellow marrow, the former predominantly found in the proximal femoral metadiaphysis and in the iliac bone. Red marrow is no longer present in the femoral epiphysis and in the greater trochanter, which are completely filled by yellow marrow

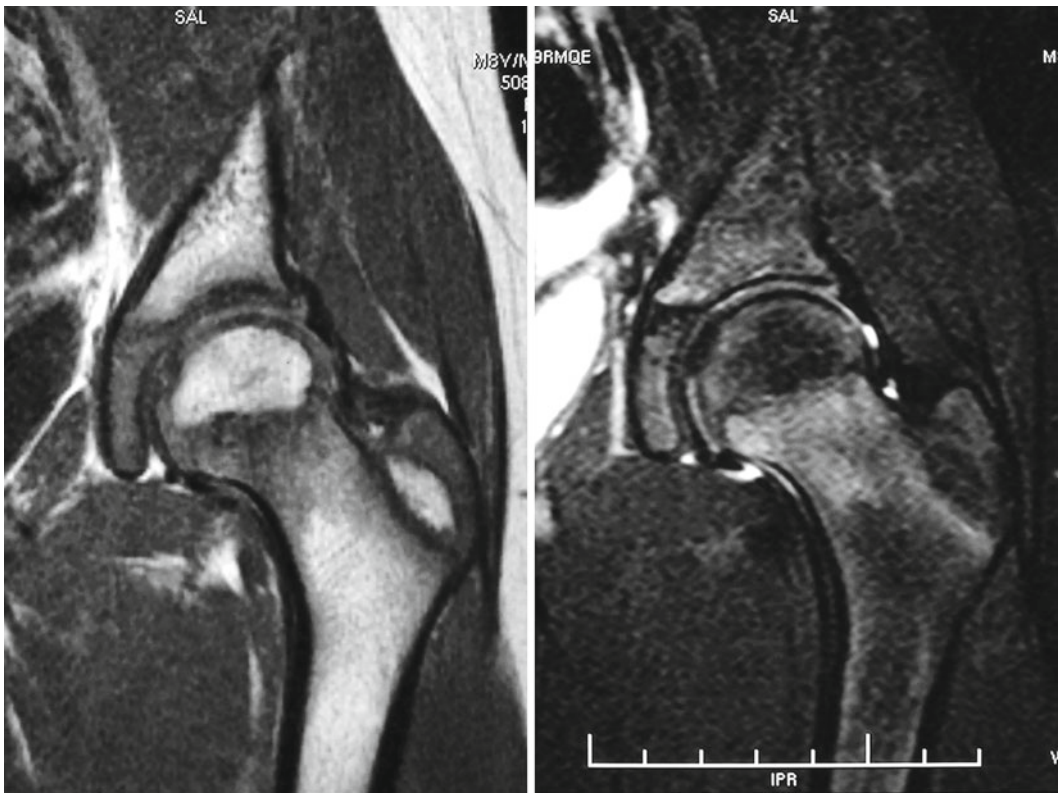

Fig. 2.20 Coronal T1-WI (*left*) and fat sat T2-WI (*right*) of the left hip of an 8-year-old male. A thick cartilaginous anlage is still present in greater trochanter apophysis, while ossification of the femoral head is far more advanced. The secondary ossification center of the femoral epiphysis shows complete conversion to yellow marrow, while red marrow is still predominant in the metaphysis

It is important to keep in mind some normal and peculiar aspects of the pediatric bone marrow that may be mistakenly construed as abnormal. Residual red marrow adjacent to the metaphysis, for instance, has a typical "flame-shaped" appearance, based on the physis and showing imprecise borders; it blends gradually with the adjacent yellow marrow, without trabecular distortion or associated mass effect (Figs. 2.5, 2.14, 2.18, and 2.20). The vast majority of pathologic marrow lesions will display very low signal intensity on T1-WI and marked hyperintensity in fluid-sensitive sequences (Fig. 2.17). T1 is the most important imaging sequence for this kind of assessment, as fluid-sensitive sequences frequently overestimate the signal intensity of the red marrow (Figs. 2.20, 2.21, and 2.22). Residual red marrow is commonly found in the proximal metaphysis of the long bones of young adults and should not be confused with marrow infiltration (Fig. 2.19). Additionally, a significant percentage of asymptomatic children will present residual perivascular islets of red marrow in their ankles and feet, usually bilateral and symmetric, without clinical significance (Fig. 2.11). Post-gadolinium enhancement is found in the normal bone marrow, mainly in the red marrow of young children (Fig. 2.23), and in the primary spongiosa. Physeal enhancement is more prominent than that of the epiphyseal cartilage (Fig. 2.23).

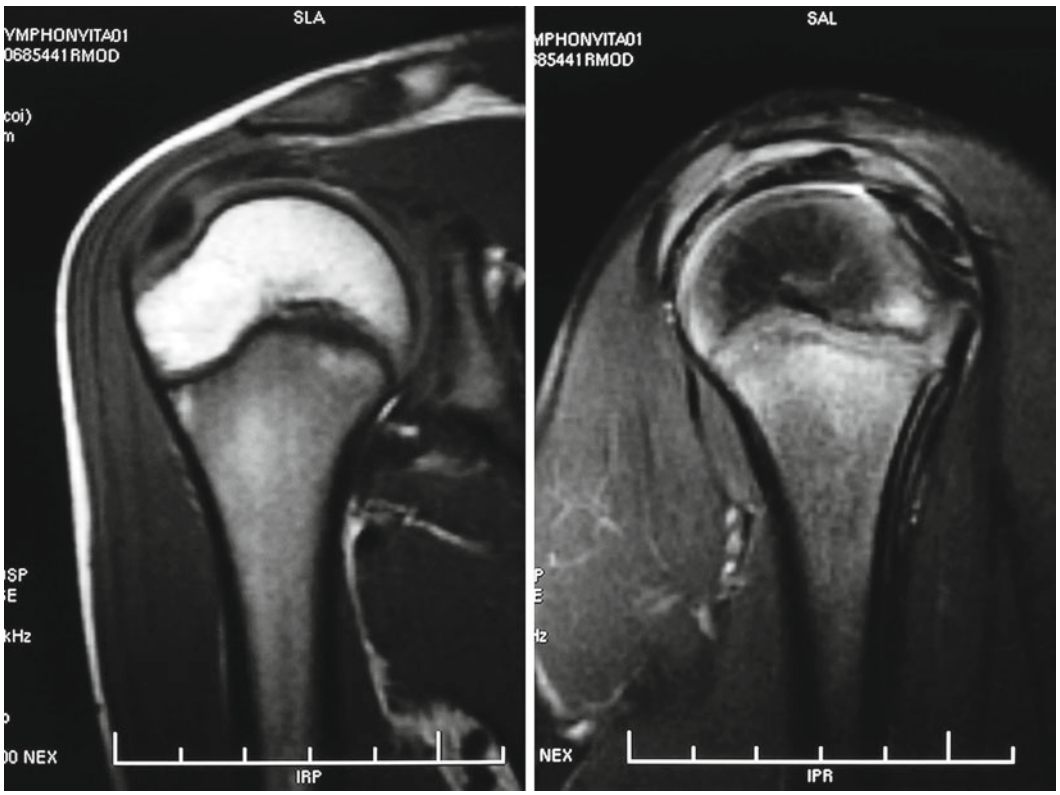

Fig. 2.21 Coronal T1-WI (*left*) and sagittal fat sat T2-WI (*right*) of the right shoulder of a 10-year-old male. The secondary ossification center of the proximal epiphysis of the humerus presents complete bone marrow conversion, and its signal intensity is identical to that of the subcutaneous fat in all sequences. Marrow conversion of the diaphyseal and metaphyseal regions is still happening, with predominance of red marrow in juxtaphyseal areas, characterized by intermediate signal intensity on T1-WI and high signal intensity on fat sat T2-WI

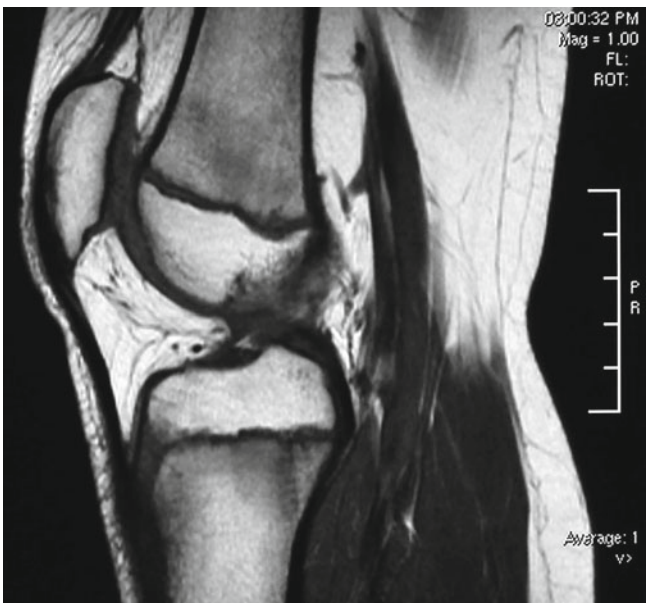

Fig. 2.22 Sagittal T1-WI of the left knee of a 13-year-old male demonstrating the appropriateness of T1-weighted sequences for the assessment of bone marrow. While the epiphyseal yellow marrow presents high signal intensity, similar to that of the subcutaneous fat, metaphyseal red marrow presents low signal intensity. However, red marrow is hyperintense if compared to the skeletal muscle, excluding the possibility of marrow infiltration

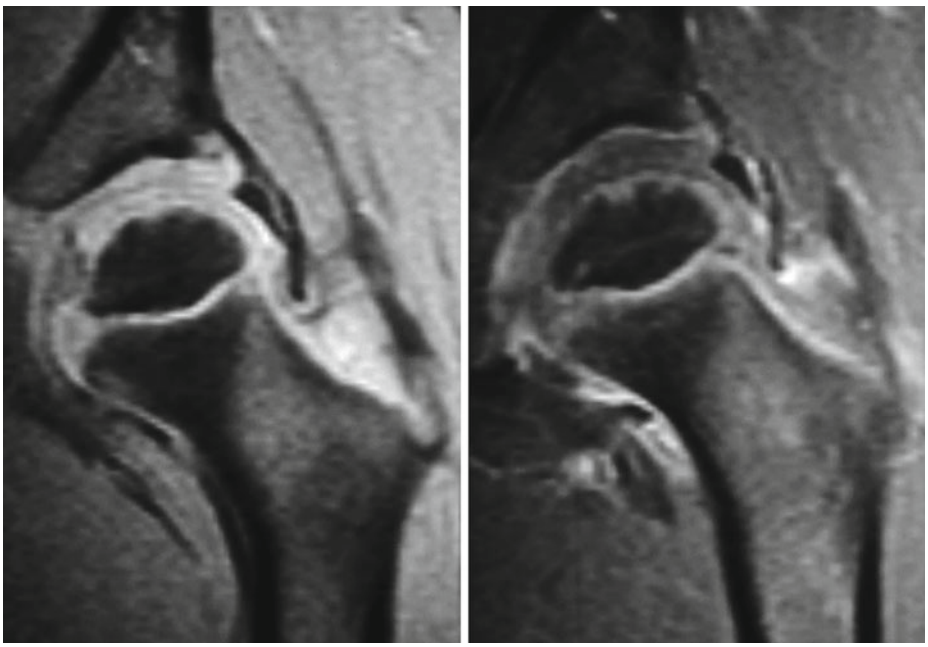

Fig. 2.23 Contrast-enhanced MRI of the left hip of a 13-year-old male, coronal fat sat T1-WI before (*left*) and after (*right*) intravenous administration of gadolinium. Enhancement of the red marrow (mostly diaphyseal) is more intense than that of the yellow marrow (mainly epiphyseal and metaphyseal). Physeal enhancement is more intense than that seen in the epiphyseal cartilage

Key Points

- The epiphyseal cartilage and the physis act together as a functional unit, responsible for longitudinal growth of the bone. The appearance of these structures change along the course of skeletal development, and awareness of these normal changes will avoid erroneous interpretation.
- The epiphysis is entirely cartilaginous in newborns, undergoing progressive ossification that begins in its innermost portion, the secondary ossification center. Changes in the signal intensity of the epiphyseal cartilage related to pre-ossification phenomena should not to be confused with cartilaginous injuries.
- The physis has a typical three-layered appearance on fluid-sensitive sequences, constituted by the hyperintense physeal cartilage, the hypointense provisional calcification zone, and the hyperintense primary spongiosa. In adolescents, areas of focal periphyseal edema can be found and are probably related to closure of the growth plates.
- The appearance of the normal bone marrow changes significantly with growth. In newborns, the marrow is entirely of the hematopoietic type (red), presenting progressive conversion to fatty (yellow) marrow as the skeletal maturation advances. Residual areas of red marrow intertwined with yellow marrow are a major pitfall in MRI interpretation.

Recommended Reading

Barnewolt CE, Shapiro F, Jaramillo D (1997) Normal gadolinium-enhanced MR images of the developing appendicular skeleton: part 1. Cartilaginous epiphysis and physis. AJR Am J Roentgenol 169(1):183–189

Burdiles A, Babyn PS (2009) Pediatric bone marrow MR imaging. Magn Reson Imaging Clin N Am 17(3):391–409

Ecklund K, Jaramillo D (2001) Imaging of growth disturbance in children. Radiol Clin North Am 39(4):823–841

Jans LB, Jaremko JL, Ditchfield M, Verstraete KL (2011) Evolution of femoral condylar ossification at MR imaging: frequency and patient age distribution. Radiology 258(3):880–888

Jaramillo D (2008) Cartilage imaging. Pediatr Radiol 38(Suppl 2):S256–S258

Jaramillo D, Hoffer FA (1992) Cartilaginous epiphysis and growth plate: normal and abnormal MR imaging findings. AJR Am J Roentgenol 158(5):1105–1110

Kan JH (2008) Major pitfalls in musculoskeletal imaging-MRI. Pediatr Radiol 38(Suppl 2):S251–S255

Kellenberger CJ (2009) Pitfalls in paediatric musculoskeletal imaging. Pediatr Radiol 39(Suppl 3):372–381

Khanna PC, Thapa MM (2009) The growing skeleton: MR imaging appearances of developing cartilage. Magn Reson Imaging Clin N Am 17(3):411–421

Laor T, Jaramillo D (2009) MR imaging insights into skeletal maturation: what is normal? Radiology 250(1):28–38

Murphy DT, Moynagh MR, Eustace SJ, Kavanagh EC (2010) Bone marrow. Magn Reson Imaging Clin N Am 18(4):727–735

Parfitt AM, Travers R, Rauch F, Glorieux FH (2000) Structural and cellular changes during bone growth in healthy children. Bone 27(4):487–494

Vande Berg BC, Malghem J, Lecouvet FE, Maldague B (2001) La moelle osseuse normale: aspects dynamiques en imagerie par résonance magnétique. J Radiol 82(2):127–135

Varich LJ, Laor T, Jaramillo D (2000) Normal maturation of the distal femoral epiphyseal cartilage: age-related changes at MR imaging. Radiology 214(3):705–709

Zbojniewicz AM, Laor T (2011) Focal Periphyseal Edema (FOPE) zone on MRI of the adolescent knee: a potentially painful manifestation of physiologic physeal fusion? AJR Am J Roentgenol 197(4):998–1004

Juvenile Idiopathic Arthritis

3

3.1 Introduction

The term juvenile idiopathic arthritis (JIA) encompasses a heterogeneous group of chronic arthritides that share the following features: (1) disease onset before 16 years of age and (2) a minimum duration of 6 weeks. For many years, it was named juvenile rheumatoid arthritis (mainly in the American literature) and chronic juvenile arthritis (mostly in European texts). It is an autoimmune inflammatory disease of unknown etiology that occurs most often in females, whose main target tissue is the synovium. Synovitis is present since the very early stages of JIA, with gradual development of synovial hyperplasia and hypercellular pannus, which eventually erodes cartilage and bone. Even though this diagnosis is essentially a clinical one, recent therapeutic advances have drastically changed the role of imaging in its management. Children with JIA must be diagnosed as soon as possible, aiming at a benign course and a better outcome with timely introduction of treatment. Magnetic resonance imaging is especially useful as it allows for early demonstration of abnormal findings, monitoring of disease progression, and accurate assessment of treatment response.

The classification of JIA is a complex and somewhat controversial issue, and a thorough analysis of it is beyond the scope of this chapter. The following topics will cover the imaging findings of peripheral joint disease in the classic form of JIA. The juvenile spondyloarthropathies will be the discussed in Chap. 4, while spinal involvement in JIA is part of the subject matter of Chap. 11.

3.2 Radiographs

For many decades, radiographs were the only imaging modality available for the assessment of patients with JIA. The accumulated experience with this method is quite vast, so that radiographic findings in advanced disease are characteristic. Nevertheless, radiographs are fairly insensitive for the early stages of arthritides in general, underestimating the real severity of joint damage. This is particularly true for JIA because the epiphyseal cartilage of the long bones is thick and extensive cartilaginous loss must occur before bone erosions become apparent in children. Despite these limitations, radiographs must be requested for all patients as part of the initial assessment (baseline study), being also useful to rule out alternative causes of joint pain.

Early-stage changes, such as synovial thickening and joint effusion, appear on radiographs as nonspecific soft-tissue swelling and obliteration of fat planes (Fig. 3.1). Periarticular soft-tissue swelling is more evident if the joint is surrounded by air and a natural density gradient is therefore present (Fig. 3.2). Findings related to chronic inflammation and hyperemia include juxta-articular osteoporosis (Fig. 3.3), epiphyseal remodeling, and increased size of secondary ossification centers (Fig. 3.4). The hyperemic state may also lead to accelerated skeletal maturation and divergence between bone age – as assessed by radiographs – and the actual chronological age. Bone overgrowth and/or early closure of the growth plates (Figs. 3.4, 3.5, 3.6, and 3.7) can be found, as well as limb-length discrepancy (Fig. 3.8).

S.L. Viana et al., *Joint Imaging in Childhood and Adolescence*,
DOI 10.1007/978-3-642-35876-0_3, © Springer-Verlag Berlin Heidelberg 2013

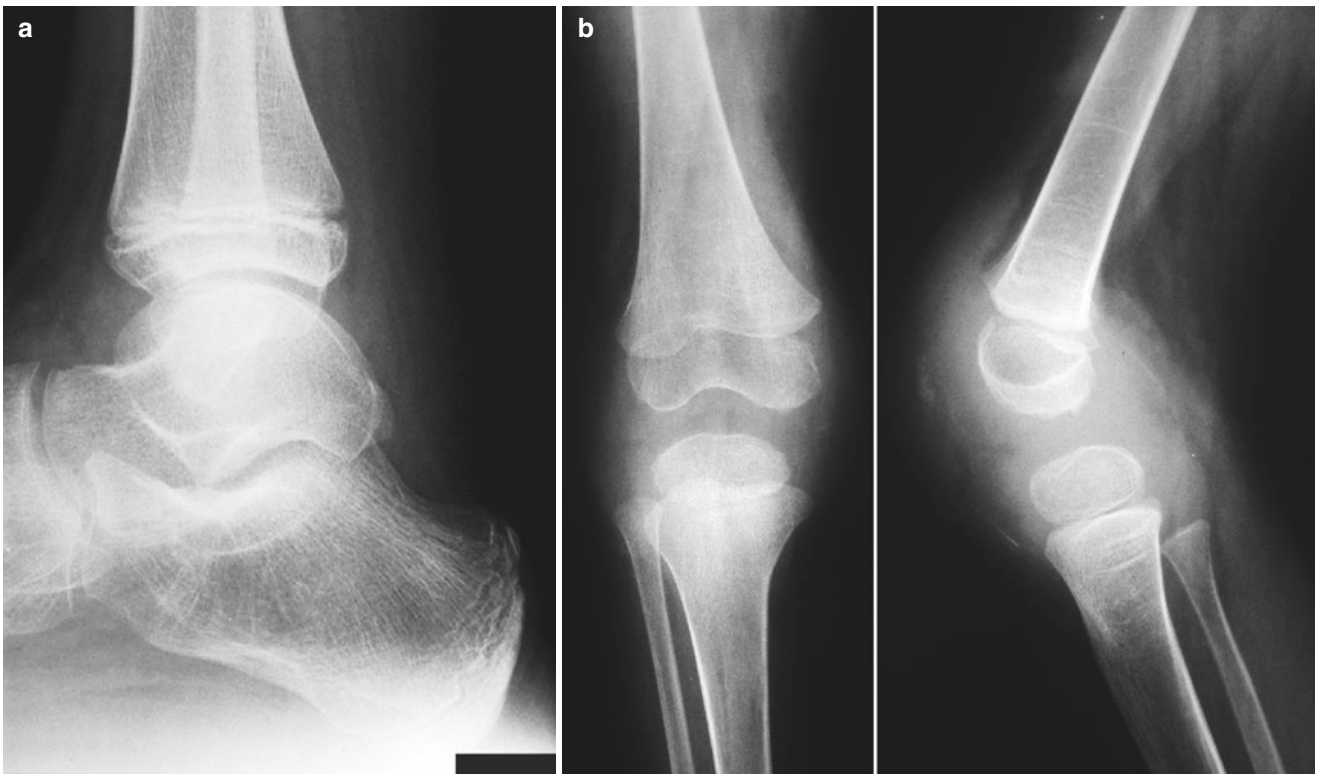

Fig. 3.1 Radiographs of the ankle (**a**) and of the knee (**b**) of two children with JIA showing soft-tissue swelling and displacement of periarticular fat planes. Even though bone erosions are not apparent, osteoporosis is already present, notably in the knee, where soft-tissue swelling is much more prominent

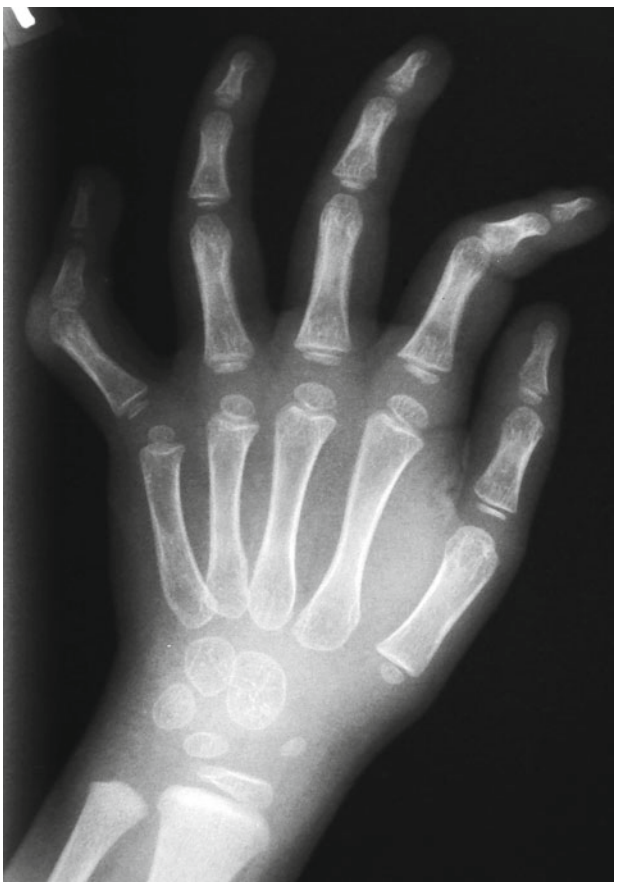

Fig. 3.2 Radiograph of the right hand of a child with JIA. There is soft-tissue swelling adjacent to the proximal interphalangeal joint of the fifth finger, more evident due to the density gradient created by the air/fat interface. Periarticular osteoporosis and periosteal reaction along the diaphyses of the proximal phalanges are also present

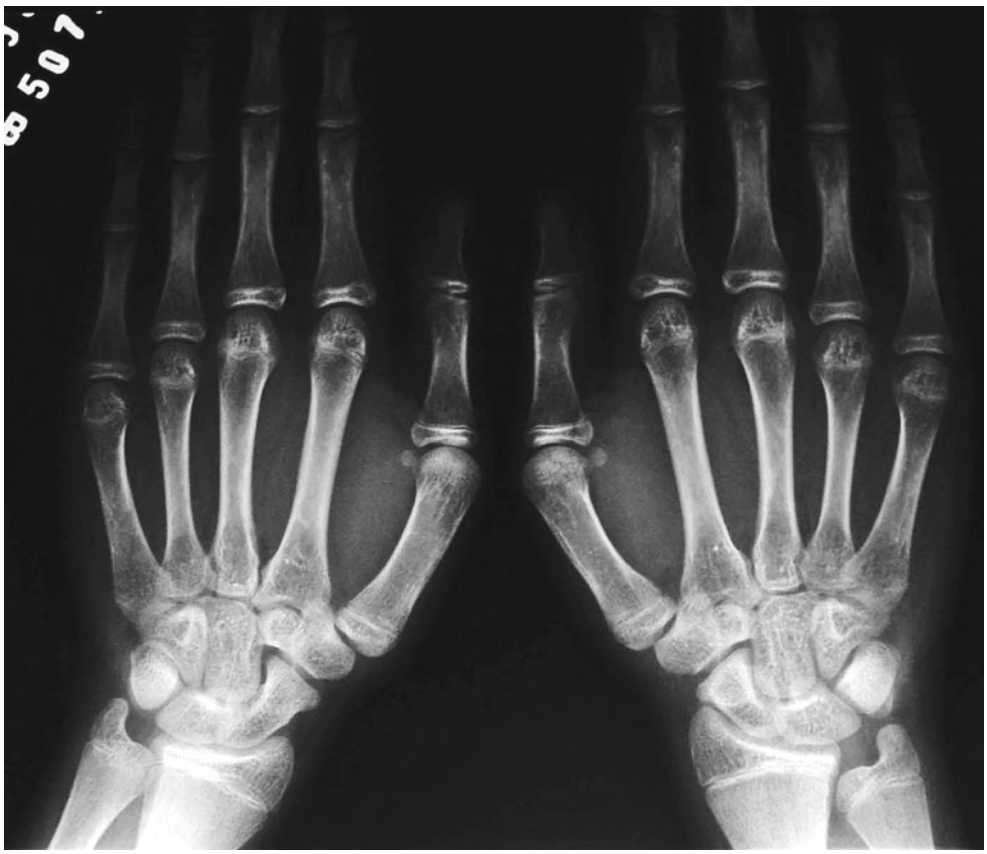

Fig. 3.3 Radiographs of the hands and wrists of a child with early-stage JIA. Symmetric and bilateral periarticular osteoporosis is the main finding, predominantly found in the metacarpophalangeal joints. There is also subtle increase in the size of the epiphyses, mainly in the left wrist, without signs of erosive articular disease

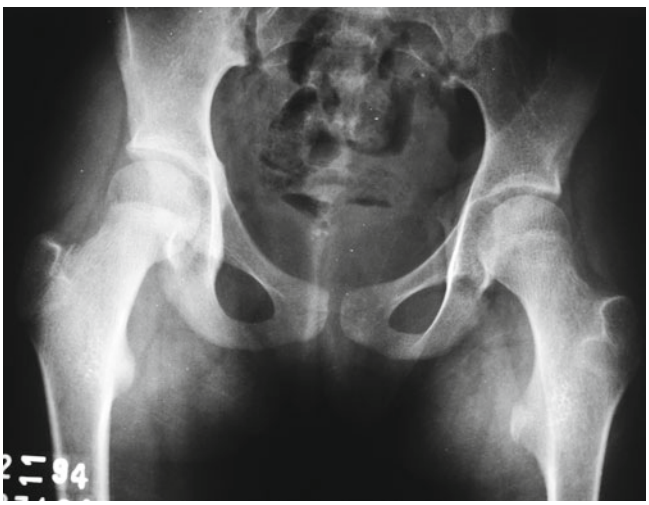

Fig. 3.4 Radiograph of the pelvis of a patient with long-standing JIA displaying findings related to chronic hyperemia. The proximal epiphysis of the right femur shows increased size, while there is diffuse osteoporosis associated with hypoplasia of the bones and early physeal closure at left. Bilateral coxa valga is also present

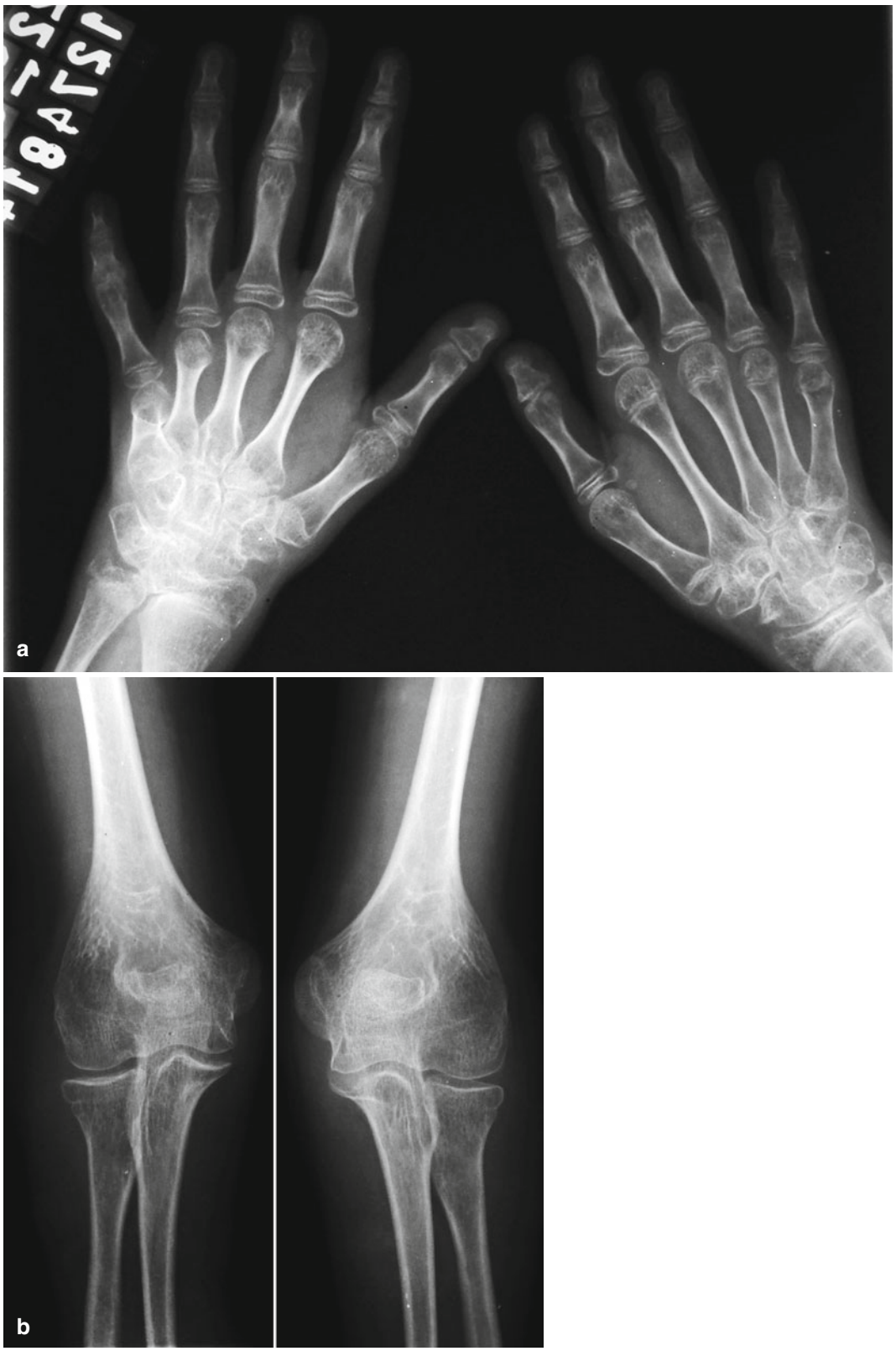

Fig. 3.5 Radiograph of the hands of a patient with long-standing JIA (**a**) discloses acquired bilateral deformity of several digits due to premature and asymmetric closure of the growth plates, with shortening of the second to the fifth metacarpals at right and of the distal phalanges of both thumbs. Diffuse osteoporosis is also present, with abnormal alignment of the carpal bones and increased size of several epiphyses, bilaterally. Narrowing of joint spaces is obvious, mainly in the right radiocarpal joint, with invagination of the adjacent carpal bones. In (**b**), in another child with late-stage JIA, there is growth arrest due to premature closure of most physes in the elbows. Marked periarticular osteoporosis is also present, with increased size of the distal humeral epiphyses, notably in the left elbow

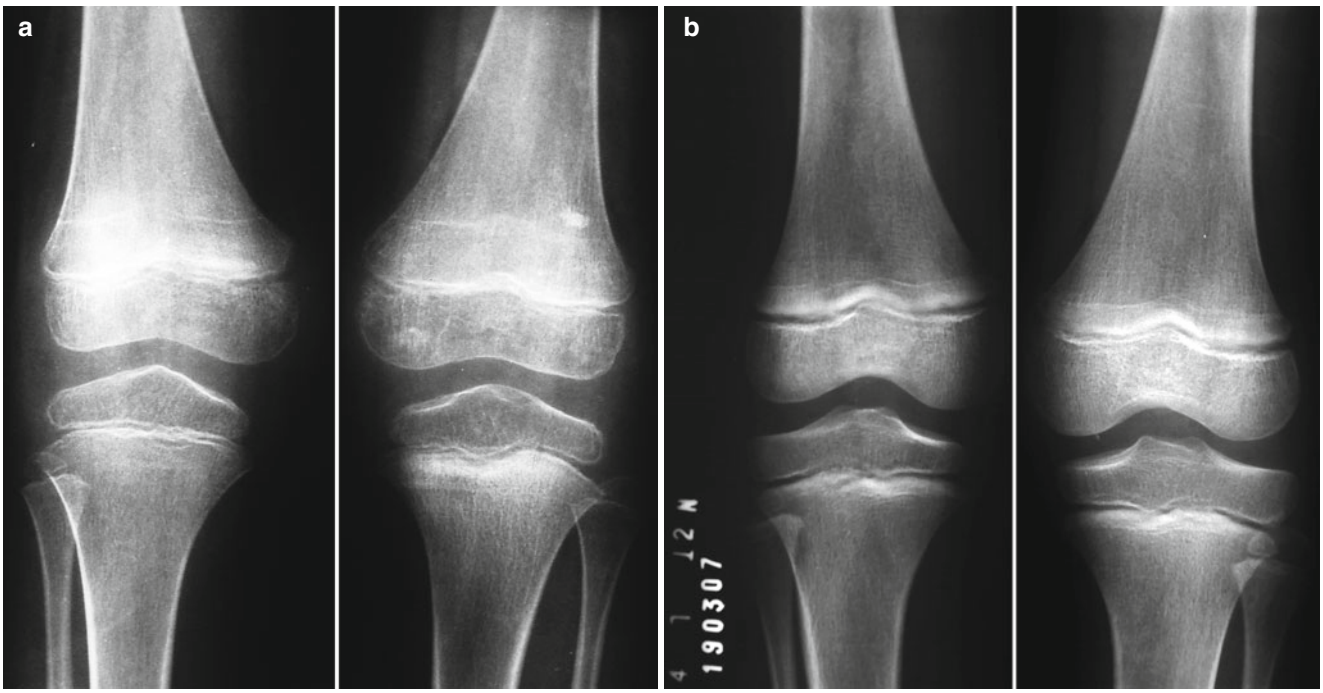

Fig. 3.6 In (**a**), anteroposterior view shows asymmetric growth of the knees, with increased size of the left distal femur when compared to the contralateral (which also displays mild overgrowth); diffuse osteoporosis and growth recovery lines can be seen, bilaterally. In (**b**), only the left knee is affected, with epiphyseal overgrowth of the distal femur and of the proximal tibia and mild homolateral osteoporosis; growth recovery lines are also present

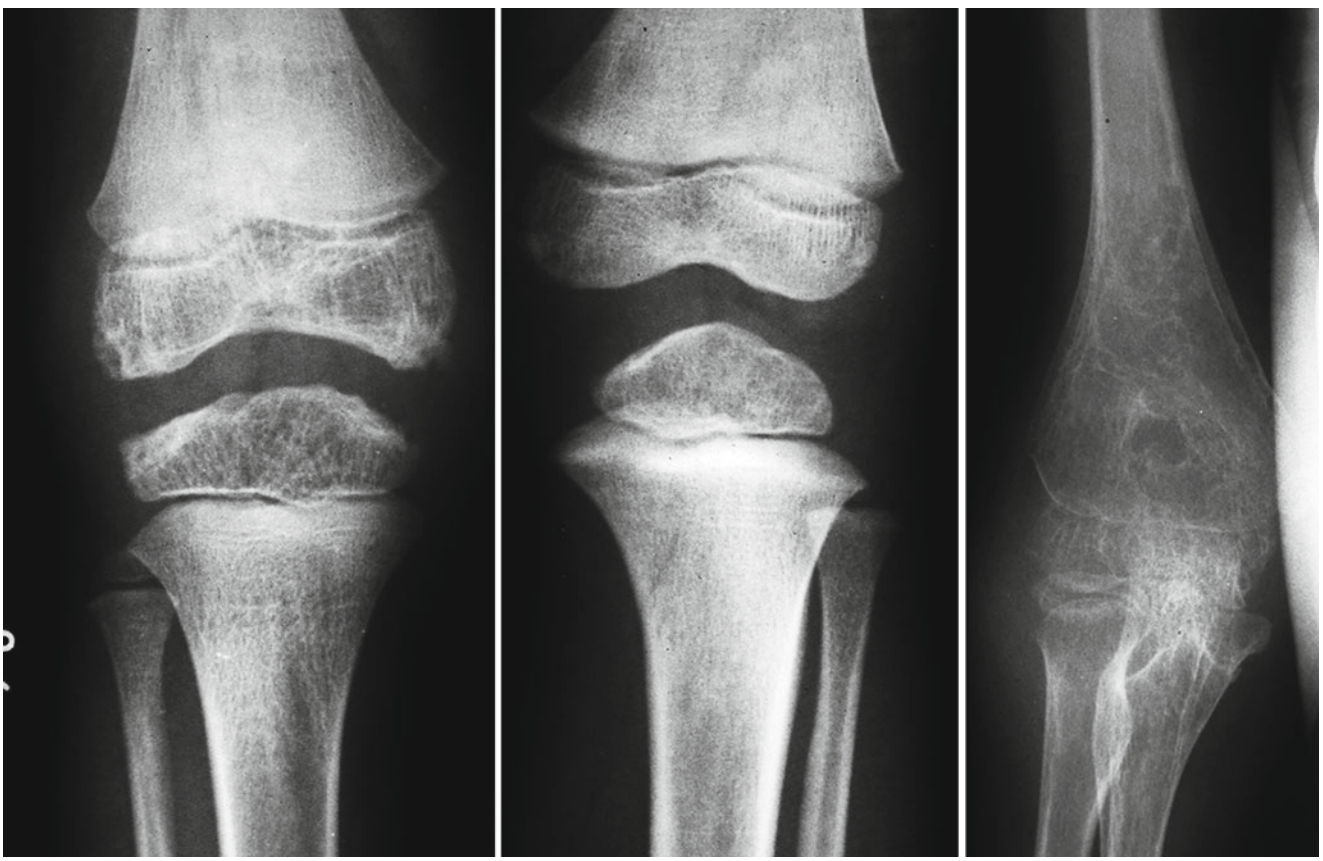

Fig. 3.7 The left image reveals asymmetric bone maturation in the knees of a child with JIA: the epiphyses of the right femur, tibia, and fibula are irregular, bigger, and more developed than the contralateral, and regional osteoporosis is also present. In the right image, there is diffuse osteoporosis of the elbow, marked periosteal reaction along the distal humerus, and epiphyseal overgrowth. Erosive articular disease is evident, mainly in the medial portion of the joint, as well as soft-tissue swelling

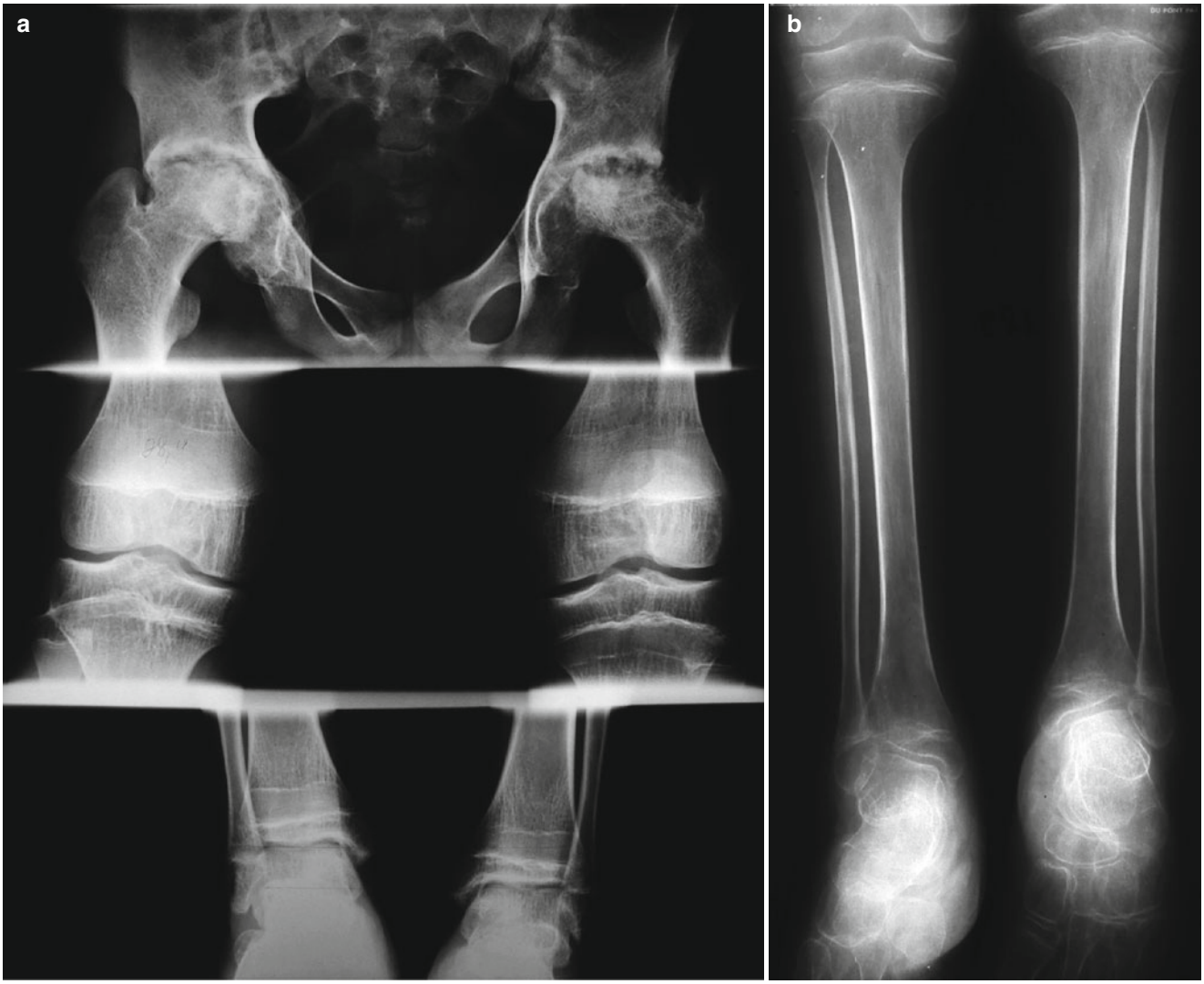

Fig. 3.8 Scanogram of an adolescent with advanced JIA (**a**) demonstrating advanced hip arthritis, bilaterally, more important at left, with widespread erosions and remodeling of the joint surfaces. There is shortening of the right limb, with marked leg-length discrepancy. Growth recovery lines and periarticular osteoporosis can be seen in the knees and ankles. Anteroposterior view of the lower limbs of another patient with JIA (**b**) shows diffuse osteoporosis and increased size of the epiphyses of the knees and ankles; the left limb is shorter than the contralateral as a result of abnormalities above the knee level. Tibiotalar slant can be seen, bilaterally

The so-called joint space seen on radiographs comprises, in fact, the joint cavity itself and non-calcified structures (which are cartilaginous for the most part) interposed between the joint surfaces. This space undergoes slow, progressive, and uniform narrowing due to the action of pannus, which erodes and destroys the cartilaginous structures (Figs. 3.9 and 3.10). Bone erosions are first seen in peripheral sites where the articular cartilage is absent, near to ligament insertions and capsular reflections (Fig. 3.11), presenting centripetal progression. Erosions in the joint surfaces are indicative of advanced disease, which may lead to secondary osteoarthritis (Figs. 3.8, 3.12, and 3.13). Destruction of the joint surfaces may eventually lead to ankylosis, infrequently found nowadays (Fig. 3.14). Periosteal reaction is more frequently encountered in JIA than in the adult form of rheumatoid arthritis, affecting mostly the tubular bones of hands and feet (Figs. 3.2, 3.7, 3.10, 3.14, and 3.15). Bone spurs and enthesophytes are associated with enthesitis (inflammation involving the sites of insertion of tendons, ligaments, and joint capsules).

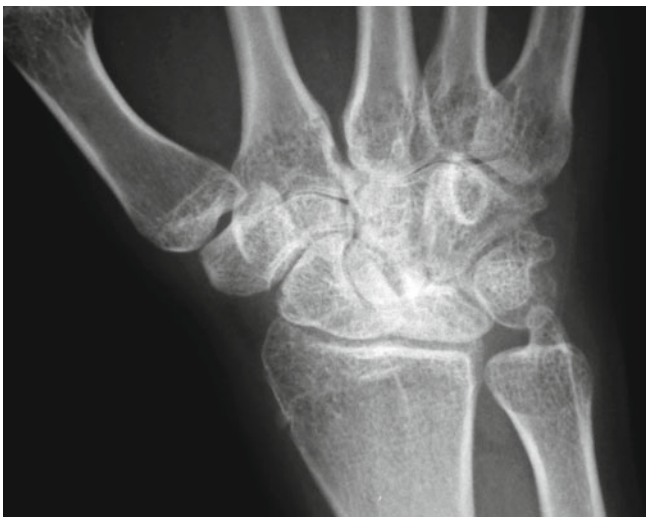

Fig. 3.9 Radiograph of the left wrist of a 16-year-old female with JIA since late childhood. There is mild osteoporosis, with narrowing of the radiocarpal joint space and disorganization of the proximal carpal row; a small cortical erosion can be seen in the distal third of the scaphoid. Despite the absence of extensive bone erosions, these findings are indicative of advanced cartilaginous destruction

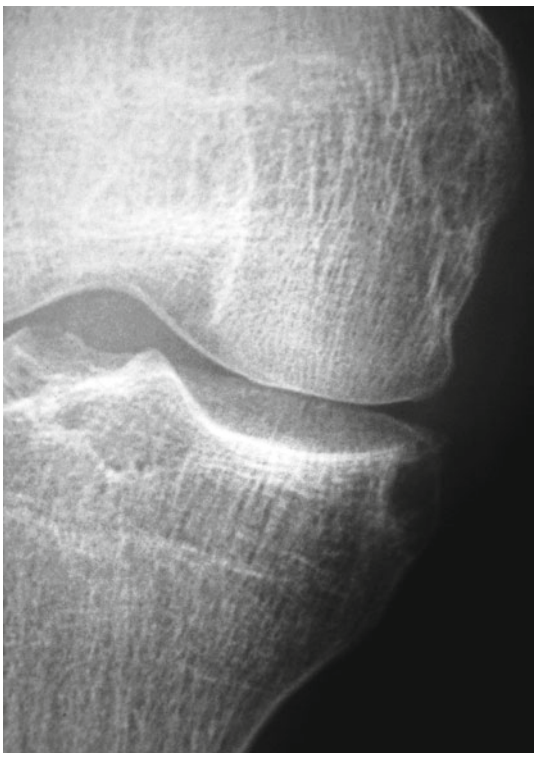

Fig. 3.11 Radiograph of the right knee of an adolescent with JIA and erosive changes. A large peripheral bone erosion can be seen in the proximal tibia, not affecting the joint surface of the adjacent plateau

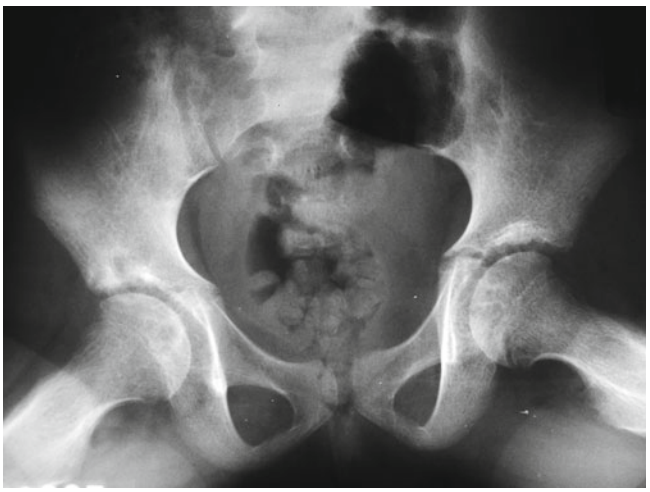

Fig. 3.10 Long-standing JIA affecting both hips, with bone erosions, narrowing of the joint spaces (more important in the right hip), and periarticular osteoporosis. Periosteal reaction is seen along the right femoral neck

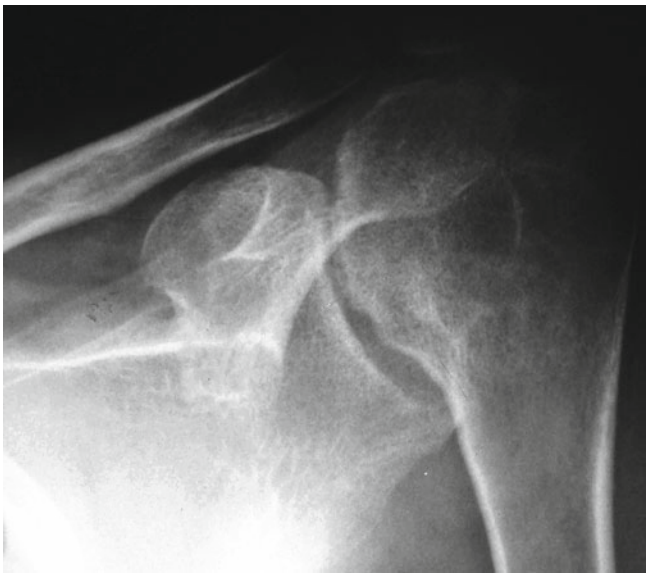

Fig. 3.12 Radiograph of the left shoulder of a patient with long-standing JIA. The joint surface of the humeral head is markedly irregular due to the presence of bone erosions. Cephalic migration of the humeral head is also present, related to complete tear of the rotator cuff. Glenoid deformity and bone remodeling are also evident

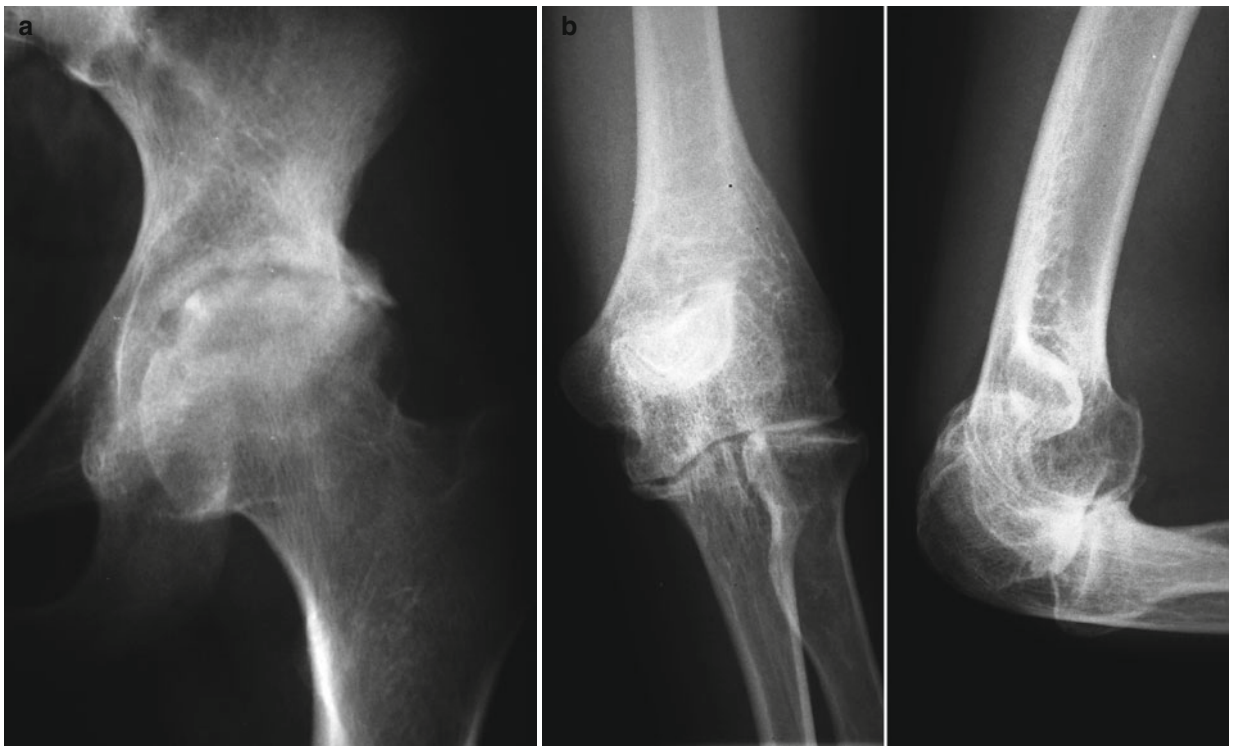

Fig. 3.13 In (**a**), radiograph of the left hip of a patient with advanced JIA demonstrates erosive arthropathy and secondary osteoarthritis due to extensive cartilaginous damage, with marked narrowing of the joint space associated with marginal osteophytes and subchondral sclerosis. In (**b**), radiographs of the left elbow of a 22-year-old patient, suffering from JIA since he was 1 year old, reveal premature osteoarthritis secondary to chronic arthritis

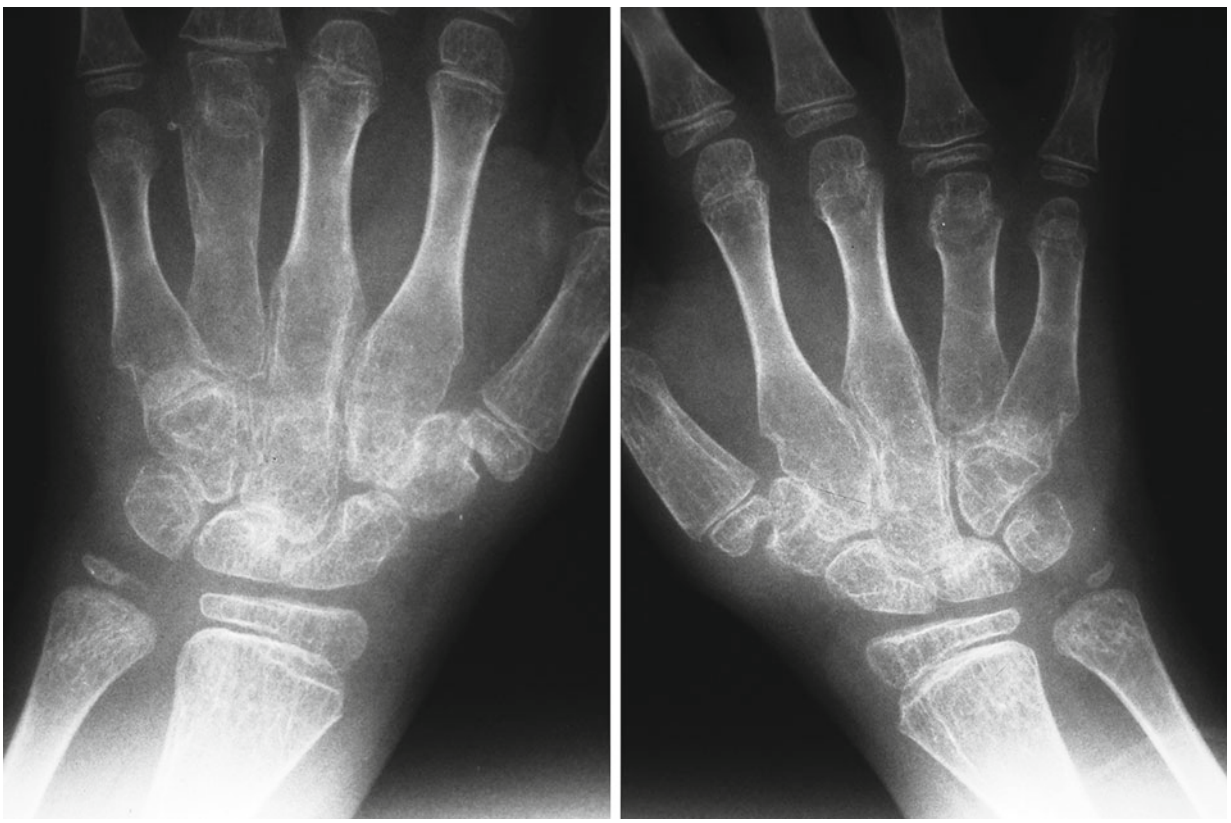

Fig. 3.14 Radiographs of the wrists of a 6-year-old child with JIA since she was 18 months old. There is diffuse osteoporosis and ankylosis of multiple joints, mainly carpometacarpal, as well as bilateral arthritis of the fourth metacarpophalangeal joints, abnormal bone modeling, and solid periosteal reaction in the metacarpal diaphyses

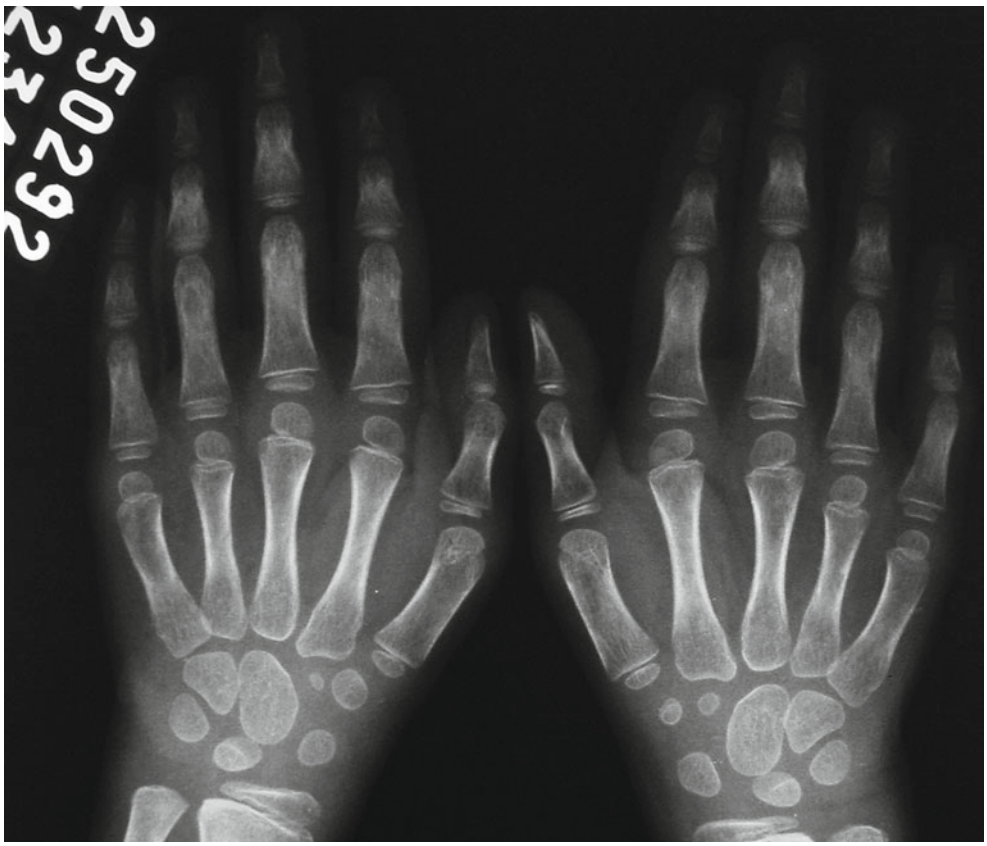

Fig. 3.15 Symmetric and bilateral periostitis can be seen along the proximal and middle phalanges in both hands, notably from the second to the fourth digits. Periarticular osteoporosis is also present in this patient with JIA

In advanced JIA, the association of diffuse osteoporosis (Fig. 3.16) and anomalous biomechanics (caused by changes such as muscle atrophy and abnormal joint alignment) increases the risk of fractures. Radiodense metaphyseal bands can be found in patients to whom bisphosphonates were administered to treat osteoporosis (Fig. 3.17). Growth recovery lines are frequently seen (Figs. 3.5, 3.6, 3.8, and 3.16), mostly in patients with long-standing disease, as well as the "bone-within-bone" appearance, which has a similar meaning (Fig. 3.18). Intra-articular and periarticular soft-tissue calcifications are also common, most often secondary to therapeutic corticosteroid injections (Fig. 3.19). Flexion contractures, varus/valgus deformities, and altered joint alignment are other late-stage complications (Fig. 3.20).

Classic radiographic findings in late-stage JIA of hands and wrists include crowding, altered shape and disorganization of the carpal bones, as well as epiphyseal deformities and brachydactyly (Figs. 3.5 and 3.21). Radial deviation of the affected fingers is more common than the ulnar deviation characteristic of adult-type rheumatoid disease, even though the typical digital deformities commonly found in advanced rheumatoid arthritis – namely, "swan-neck" (hyperextension of the proximal interphalangeal joint and flexion of the distal) and "boutonnière" (hyperflexion of the proximal interphalangeal joint with extension of the distal) – can also be found in JIA. Common findings in the knees include widening of the intercondylar notch (Fig. 3.22) and "squaring" of the patella (Fig. 3.23), similar to those found in hemophiliac children. Tibiotalar slant (medial inclination of the articular surfaces of the ankle) is another finding that can also be seen in JIA and in hemophilia (and in other conditions as well) (Figs. 3.8 and 3.17). Pelvic abnormalities include iliac hypoplasia (Figs. 3.4 and 3.24), abnormal cervical-diaphyseal angle (Fig. 3.4), acetabular protrusion (Fig. 3.25), avascular necrosis of the femoral head (Fig. 3.26), and premature osteoarthritis of the hip (Figs. 3.13 and 3.24). Facial changes related to long-standing JIA comprise micrognathia, increased antegonial notching, malocclusion, abnormal dentition, and shortening of the mandibular body and rami, with "birdlike" facies in advanced cases. Temporomandibular arthritis is not infrequent and may be severe (Fig. 3.27).

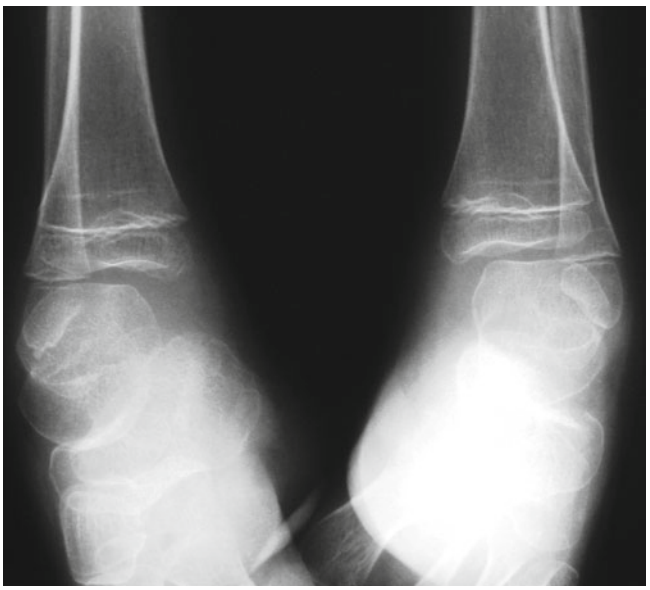

Fig. 3.16 There is marked widespread osteoporosis in both ankles in this patient with long-standing JIA, as well as soft-tissue swelling and growth recovery lines

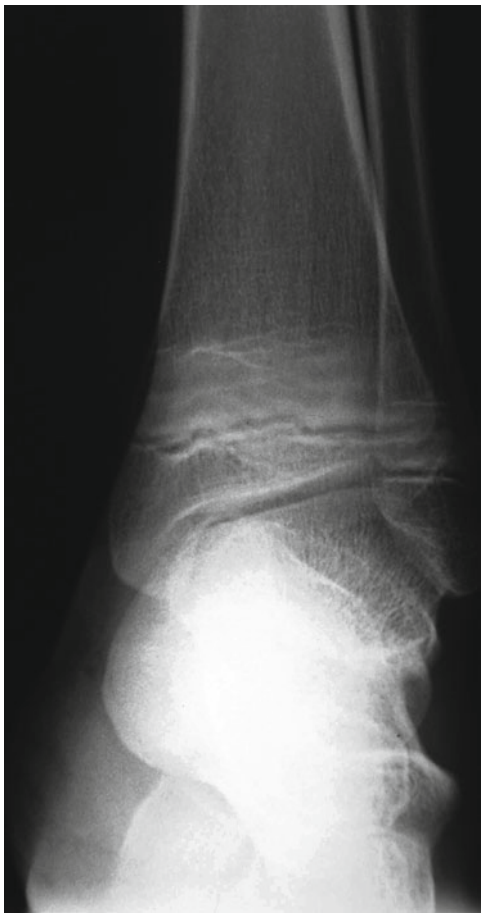

Fig. 3.17 This 14-year-old patient developed diffuse osteoporosis after institution of corticotherapy for treatment of JIA, and treatment with oral alendronate was started. Radiographs taken 10 months later disclosed dense metaphyseal bands in his long bones, here shown in the left ankle. Tibiotalar slant is also evident

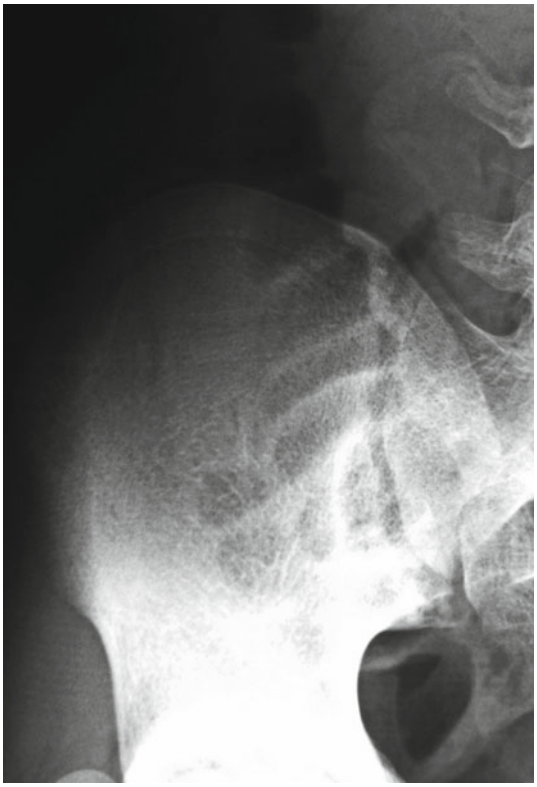

Fig. 3.18 Detail of a pelvic radiograph showing the classic "bone-within-bone" appearance in the right iliac bone of an adolescent with long-standing JIA

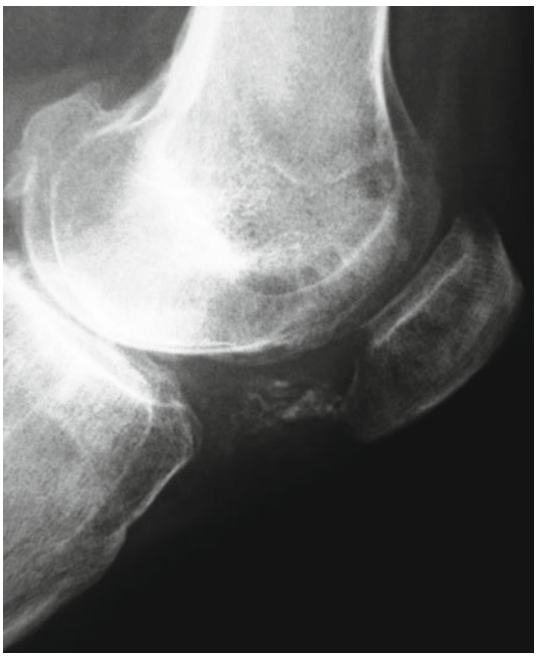

Fig. 3.19 Striated calcifications are seen projected over the infrapatellar fat pad in an adult with late-stage sequelae of JIA who underwent several steroid infiltrations in the knee. The radiographic findings and the clinical data are highly characteristic about the nature of these calcifications, with no need for further investigation

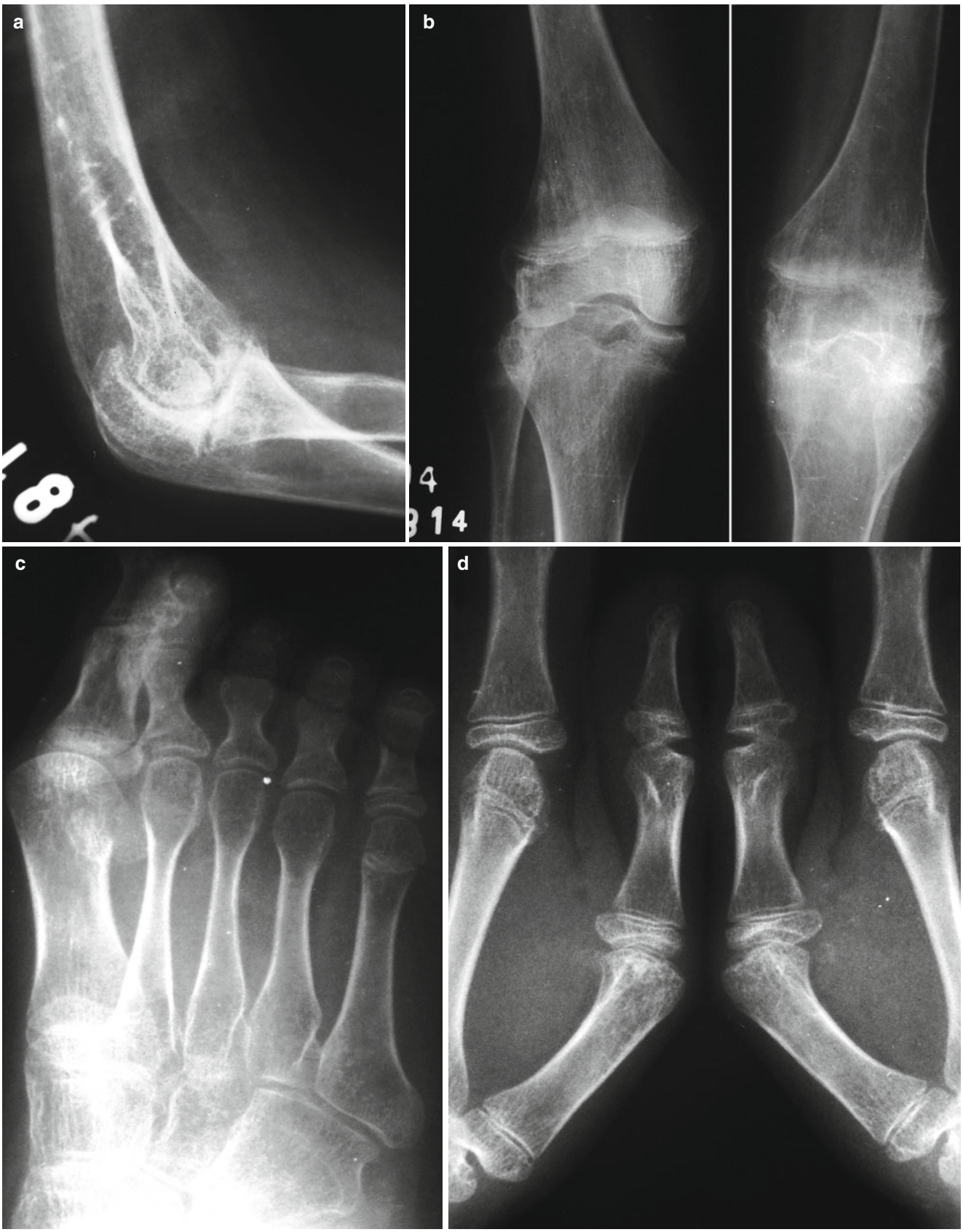

Fig. 3.20 In the patients above, in addition to diffuse osteoporosis and radiographic evidence of arthritis, there is flexion deformity of the left elbow (**a**), both knees (**b**), and the first metatarsophalangeal joint of the left foot (**c**). In (**d**), there is deformity of the heads of the first metacarpals and subluxation of the corresponding metacarpophalangeal joints, more important in the right hand, as well as epiphyseal overgrowth

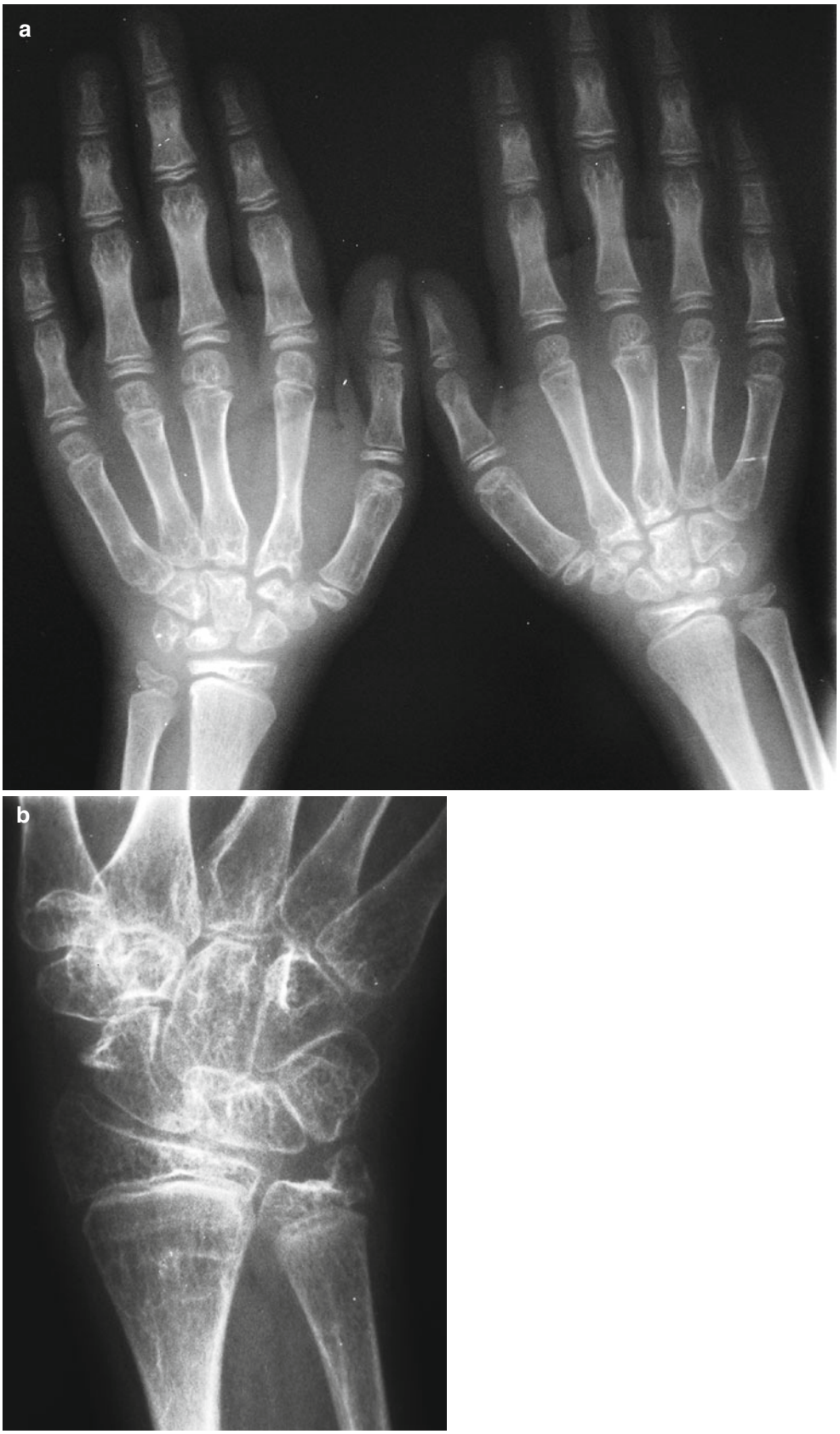

Fig. 3.21 Typical radiographic findings in the hands and wrists of two patients with long-standing JIA. There is crowding of the carpal bones, which present a polyhedric appearance, opposite to the rounded contours that they exhibit in normal children. Diffuse osteoporosis can be seen in both cases, with carpal and metacarpal erosions in (**a**) and increased size of the epiphyses of the distal forearm in (**b**)

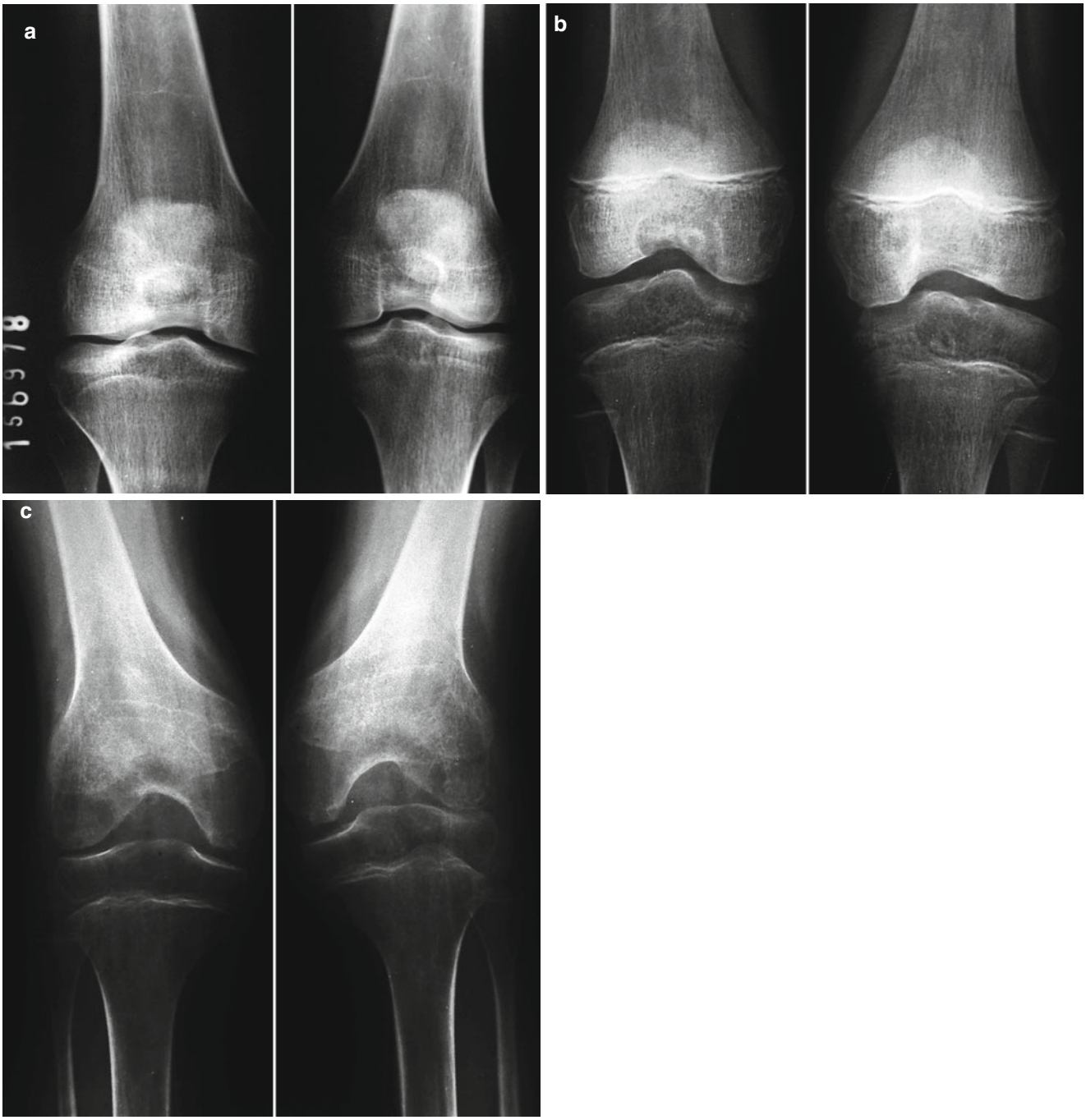

Fig. 3.22 Anteroposterior radiographs of the knees of three different patients with JIA (**a**–**c**). Osteoporosis, epiphyseal remodeling, and widening of the intercondylar notch are found in varied degrees of severity. Bone erosions are also seen, more evident in (**b**)

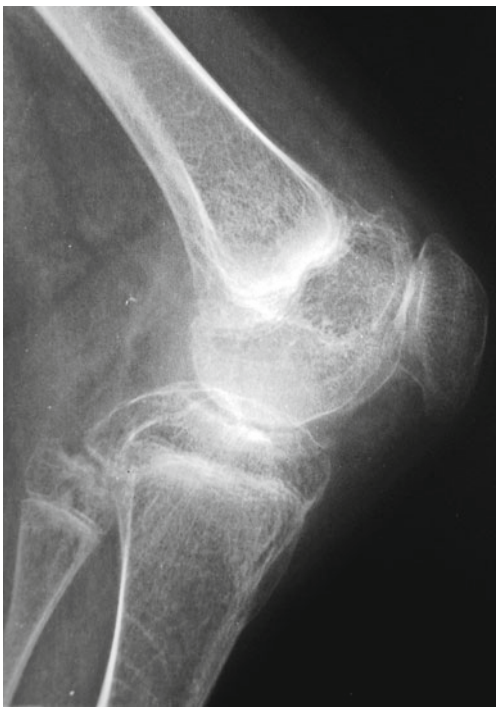

Fig. 3.23 Lateral view of the left knee of a patient with long-standing JIA showing diffuse osteoporosis, markedly increased epiphyseal size, soft-tissue swelling, and patellar "squaring." These findings may be indistinguishable from those associated with hemophilia

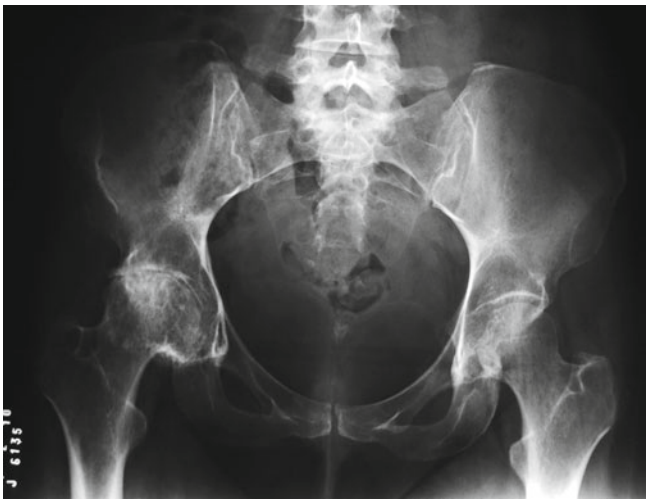

Fig. 3.24 Severely destructive arthropathy of the right hip is evident in this 36-year-old patient with late-stage sequelae of JIA. There is diffuse hypoplasia of the homolateral iliac bone, as well as generalized osteoporosis in the affected hemipelvis

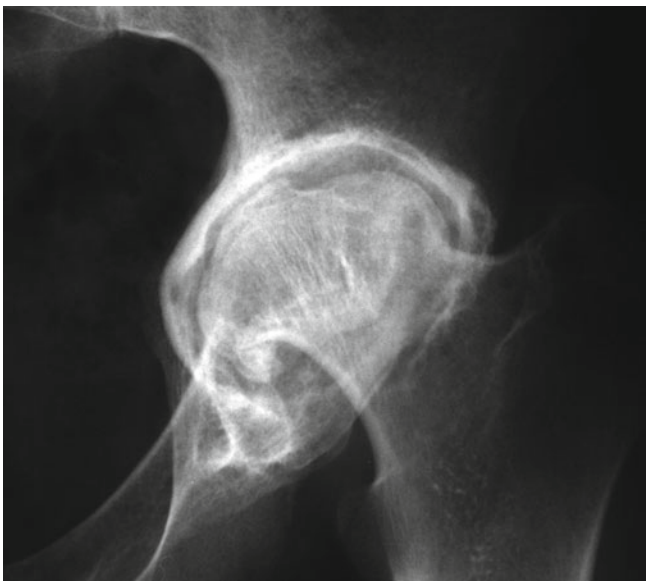

Fig. 3.25 Aggressive arthritis affecting the left hip in a poorly controlled patient with long-standing JIA. Anteroposterior radiograph displays advanced joint destruction, with abnormal shape and irregular contour of the femoral head, bone remodeling, and acetabular protrusion

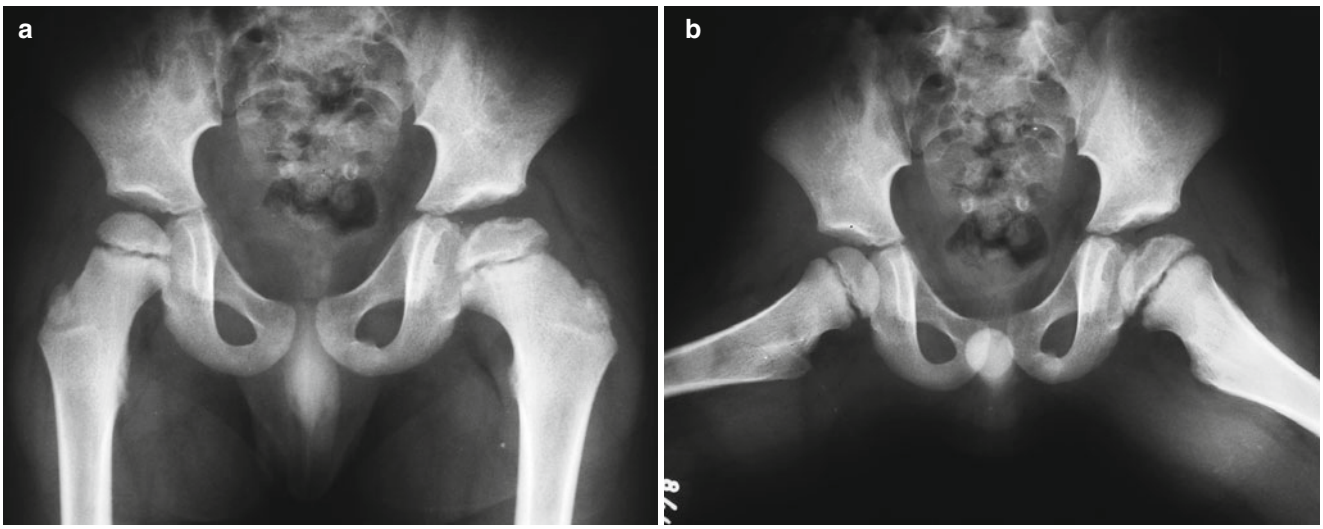

Fig. 3.26 Avascular necrosis of the femoral head is a well-known complication of JIA. Anteroposterior (**a**) and lateral (**b**) views of the hips evidence osteonecrosis of the left femoral head, with bone remodeling, abnormal epiphyseal shape, widening and shortening of the femoral neck, and subchondral lucencies. The articular surface of the right femoral head is irregular, and homolateral coxa valga is also present

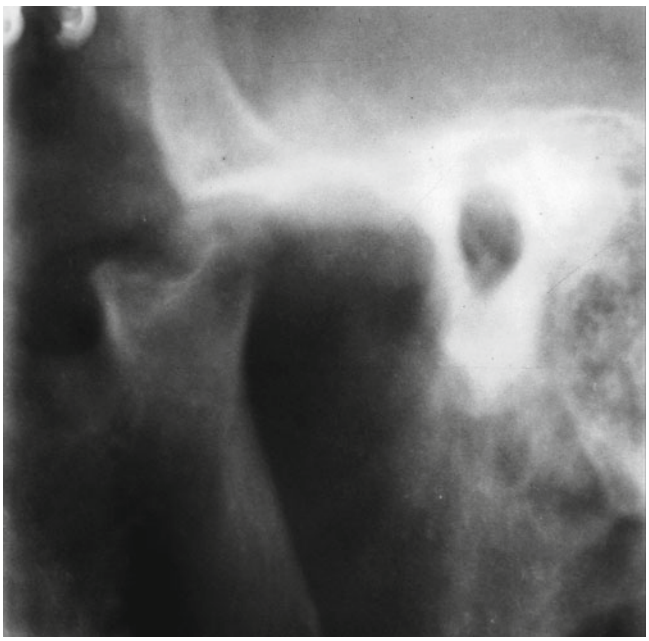

Fig. 3.27 Planigraphy of the right temporomandibular joint (open mouth) of a patient with JIA revealing late-stage arthritic changes, with extensive destruction of the mandibular condyle, bone fragmentation, and erosions of the joint surfaces. Remodeling and enlargement of the glenoid cavity is quite evident, as well as sclerosis of the subchondral bone and flattening of the temporal eminence

3.3 Ultrasonography

Ultrasonography (US) is more sensitive than radiographs for the assessment of initial JIA as it demonstrates abnormalities related to early-stage articular inflammation, such as joint effusion and synovitis. Joint effusion appears hypoechogenic/anechogenic, occasionally with suspended debris, while the thickened synovium is hyperechogenic and hyperemic (Fig. 3.28). Serial studies are useful for monitoring disease evolution and to assess response to treatment: good evolution will lead to involution of joint effusion and of synovial thickening/hyperemia, while the opposite happens in poorly responsive patients. Taking into account the operator-dependent nature of US and the lack of standardized protocols, serial studies should be ideally performed by the same sonographer.

The normal articular cartilage is hypoechogenic, smooth, and well delimited. The inflamed cartilage, however, becomes thickened, irregular, and ill-defined; cartilaginous thinning and erosions can be seen in more advanced stages. US is superior to radiographs for the detection of superficial bone erosions in sites where acoustic windows are available, appearing as focal cortical defects with irregular floor and posterior acoustic enhancement. The tenosynovial component

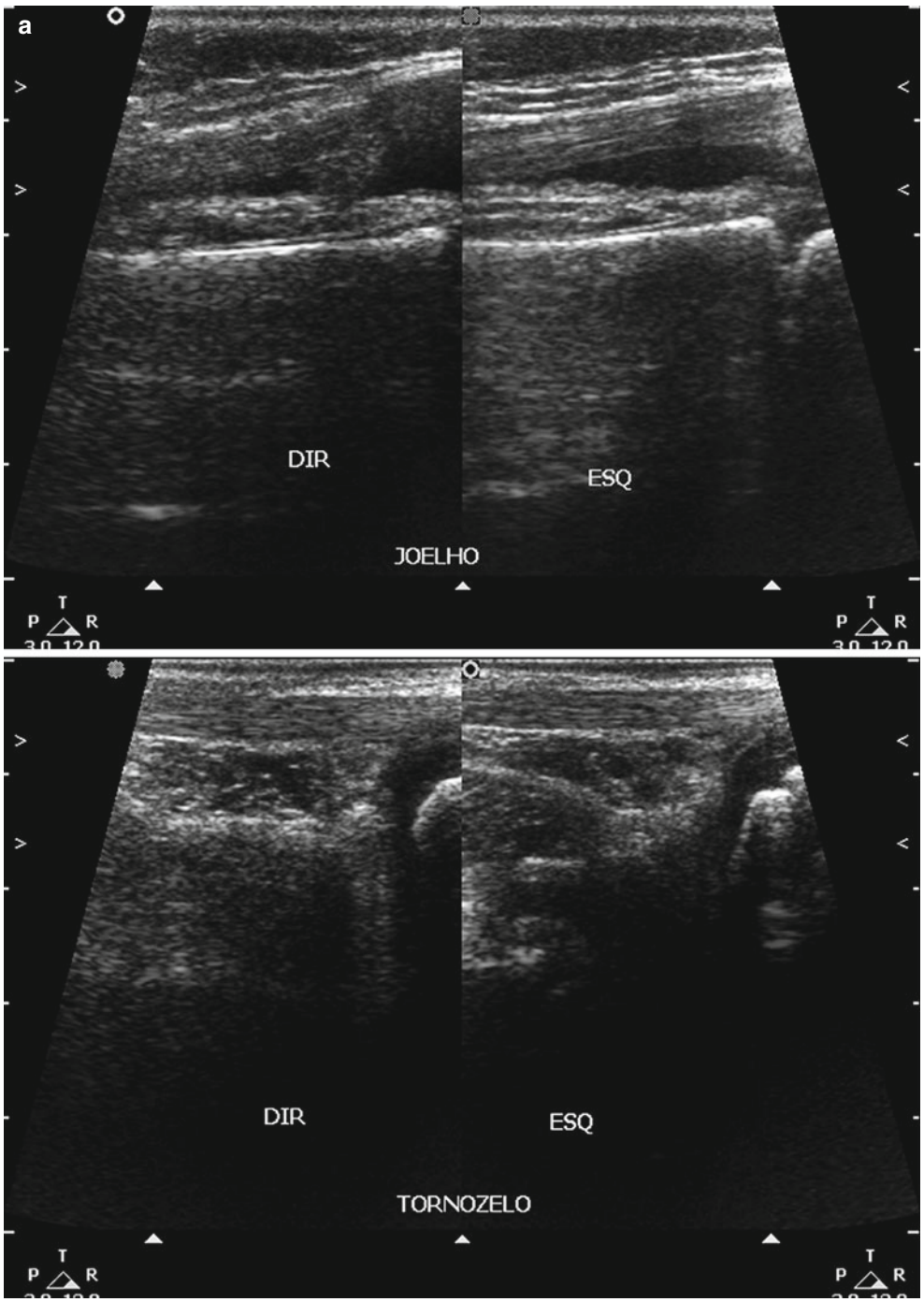

Fig. 3.28 In (**a**), US of the knees (suprapatellar pouches, *upper row*) and of the ankles (*lower row*) of a child with JIA reveals heterogeneous joint effusions in these joints, associated with bilateral and symmetric synovial thickening. In (**b**), US of another patient with JIA discloses a popliteal cyst containing heterogeneous fluid and marked synovial thickening. The thickened synovium displays prominent hyperemia on Doppler US in (**c**), in which areas of increased flow appear *yellow orange* (Courtesy of Dr. Telma Sakuno, Hospital Universitario da UFSC, Florianopolis, Brazil (Fig. 3.28a), and Dr. Maria Montserrat, Clinica Montserrat, Brasilia, Brazil (Fig. 3.28b, c))

Fig. 3.28 (continued)

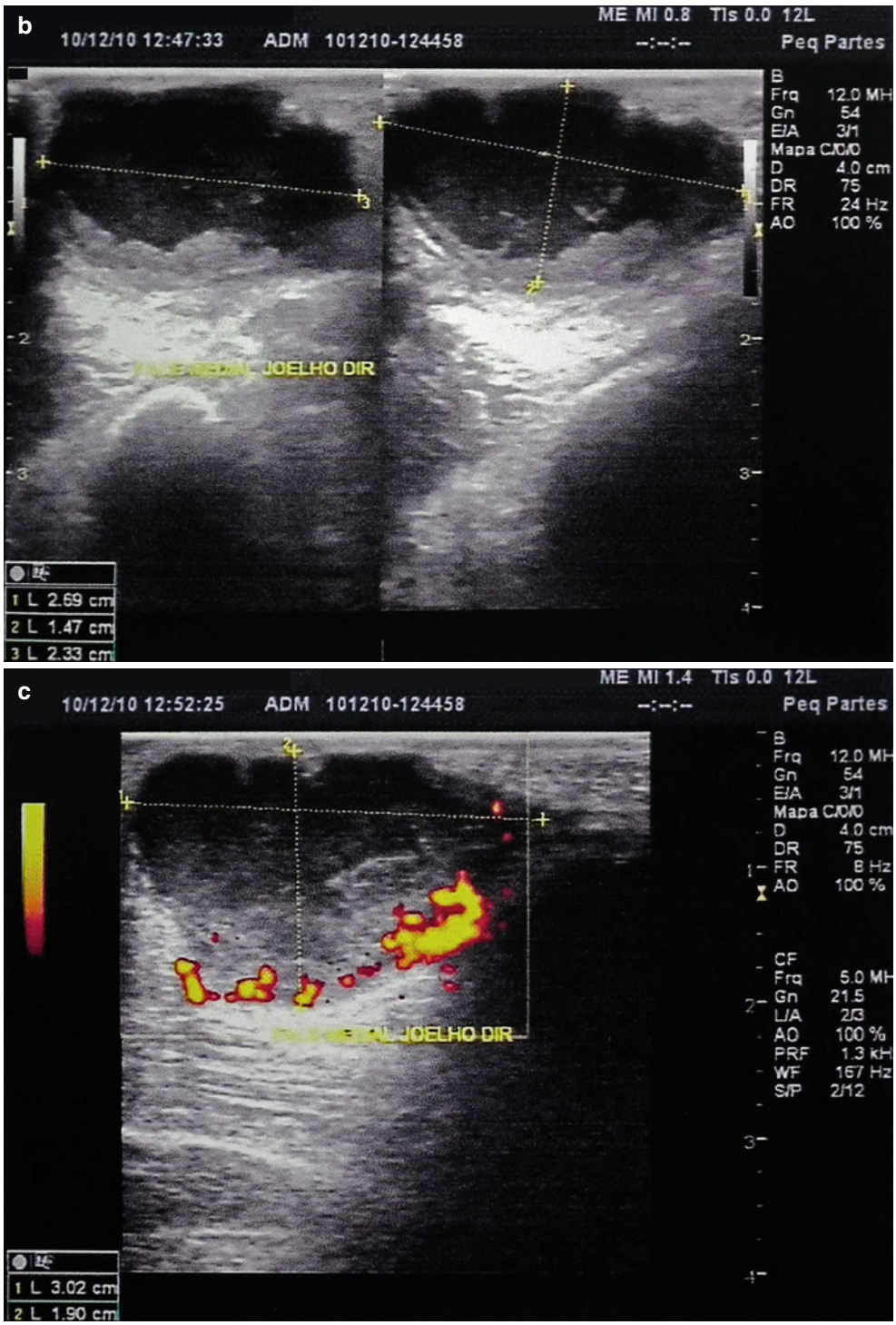

of JIA is particularly well assessed with US, which is able to evaluate the structure of the tendons and the presence of fluid and synovitis within their sheaths (Figs. 1.7 and 3.29). Extension of the inflammation to adjacent bursae and synovial cysts (such as popliteal cysts, which are particularly common in JIA) is usually obvious on US (Fig. 3.28). In addition, US is also is very adequate for guidance of diagnostic or therapeutic joint punctures in children.

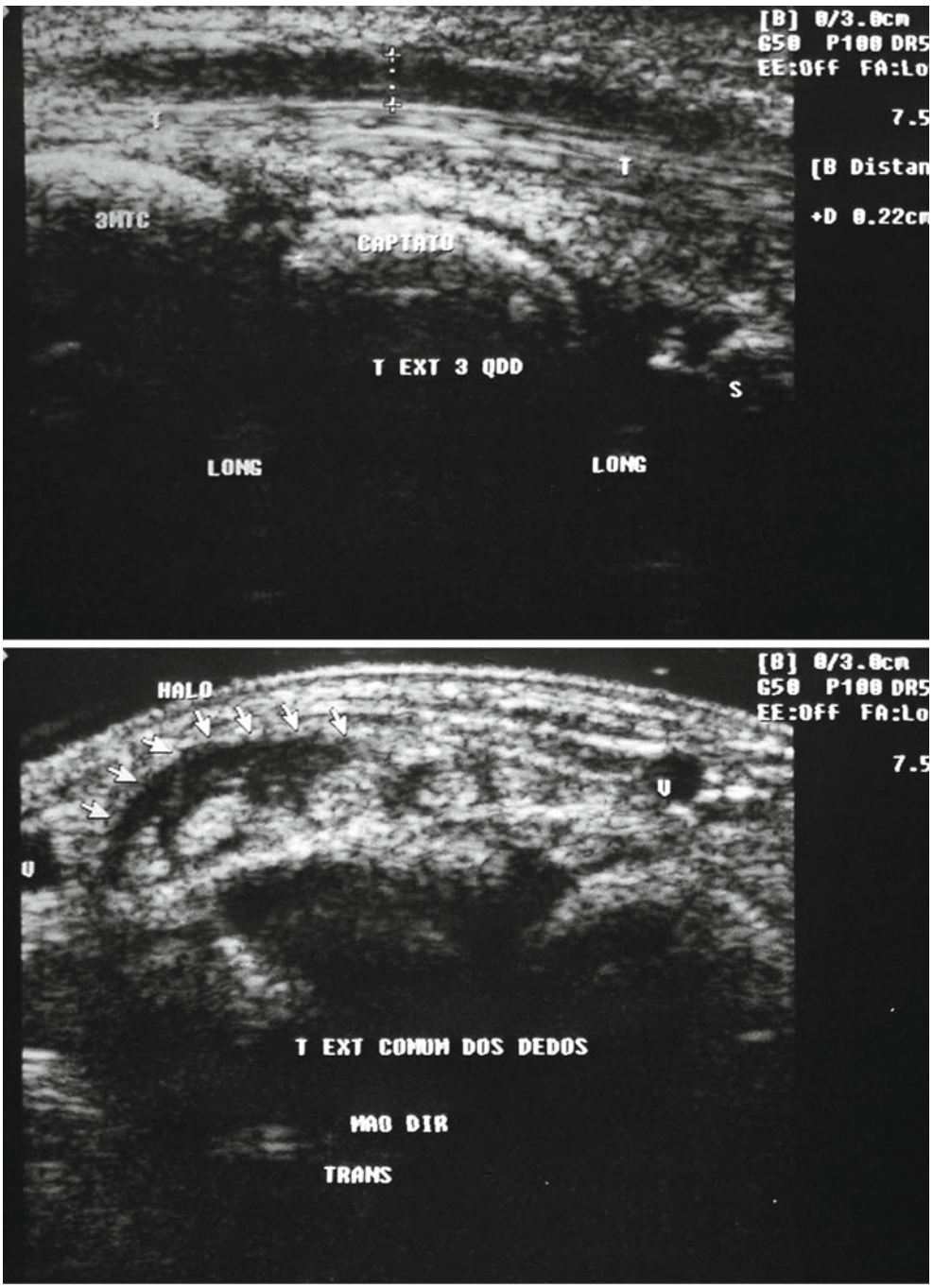

Fig. 3.29 Tenosynovitis of the extensor tendons of the right wrist in an 11-year-old male with JIA. The *upper image* displays a longitudinal scan along the third extensor compartment, while the *lower image* is a transversal section highlighting the fourth compartment. Both images show a hypoechogenic halo surrounding the tendons (calipers and *arrows*), which maintain normal thickness and echogenicity. Histopathological analysis of the hypoechogenic tissue showed chronic hypertrophic synovitis

3.4 Magnetic Resonance Imaging

Magnetic resonance imaging (MRI) is the method of choice for early diagnosis of JIA, mostly because of its multiplanar capabilities, high resolution, and exquisite anatomic detail, providing excellent assessment of the soft tissues and of the bone. Intravenous gadolinium is formally indicated in patients with JIA in order to evaluate the real extent and the severity of arthritis as well as to monitor its evolution in subsequent studies.

Joint effusions usually display low signal intensity on T1-weighted images (T1-WI) and high signal intensity on T2-weighted images (T2-WI) (Figs. 3.30 and 3.31); increased signal intensity on T1-WI and/or decreased signal on T2-WI are indicative of hemarthrosis. The inflamed synovium appears thickened and irregular, most often hypointense on T1-WI and hyperintense on T2-WI; nevertheless, contrast-enhanced fat sat T1-WI are the best to demonstrate synovitis, as the enhancing synovium appears as a bright stripe against the dark background (Figs. 3.30, 3.31, 3.32, 3.33, and 3.34). Progression or involution of synovitis and joint effusion in serial studies provide information about disease evolution and treatment response, just as stated above for US. Prominent periarticular lymph nodes that enhance on post-contrast images may be found, notably in the popliteal fossa (Figs. 3.33 and 3.34).

MRI is able to demonstrate from subtle irregularities of the articular cartilage, seen in the early stages (Figs. 3.31, 3.34, and 3.35), to clear-cut erosions and large areas of osteochondral destruction, which are characteristic of advanced disease (Fig. 3.36). After intravenous injection of gadolinium, inflamed cartilages usually display some degree of enhancement (Fig. 3.34), sometimes with a spoke-wheel pattern caused by prominent epiphyseal vessels (Fig. 3.37). Subchondral areas of bone marrow edema appear on MRI as ill-defined zones of low signal intensity on T1-WI and increased signal intensity on T2-WI, which are more evident on fluid-sensitive sequences, indicative of osteitis and active inflammation (Figs. 3.38, 3.39, and 3.40); such areas commonly exhibit post-contrast enhancement long before the development of bone erosions. Bone erosions are well-delimited cortical defects which are most often hypointense on T1-WI and hyperintense on T2-WI, frequently surrounded by bone marrow edema and displaying post-gadolinium enhancement when active (Figs. 3.35, 3.36, and 3.41). Changes related to joint hyperemia, such as increased size and altered shape of the epiphyses, premature physeal closure, and secondary osteoarthritis (Figs. 3.42 and 3.43), are also clearly seen on MRI.

The inflamed entheses present bone marrow edema pattern associated with edema of the soft tissues and post-gadolinium enhancement, even though enthesophytes and bone spurs are better seen on radiographs. Other soft-tissue changes include inflammation within tendon sheaths, synovial cysts, and periarticular bursae, with fluid distension and synovial thickening (Fig. 3.44). Tenosynovitis affects more frequently the extensor tendons in the wrists and the ankles, though flexor tendons may be affected too (Figs. 1.25 and 3.32); when present, tendon ruptures are usually quite evident. Muscle atrophy and fatty replacement are typical of chronic disease, as well as hypoplasia of the cruciate ligaments and of the menisci (Figs. 3.31 and 3.43).

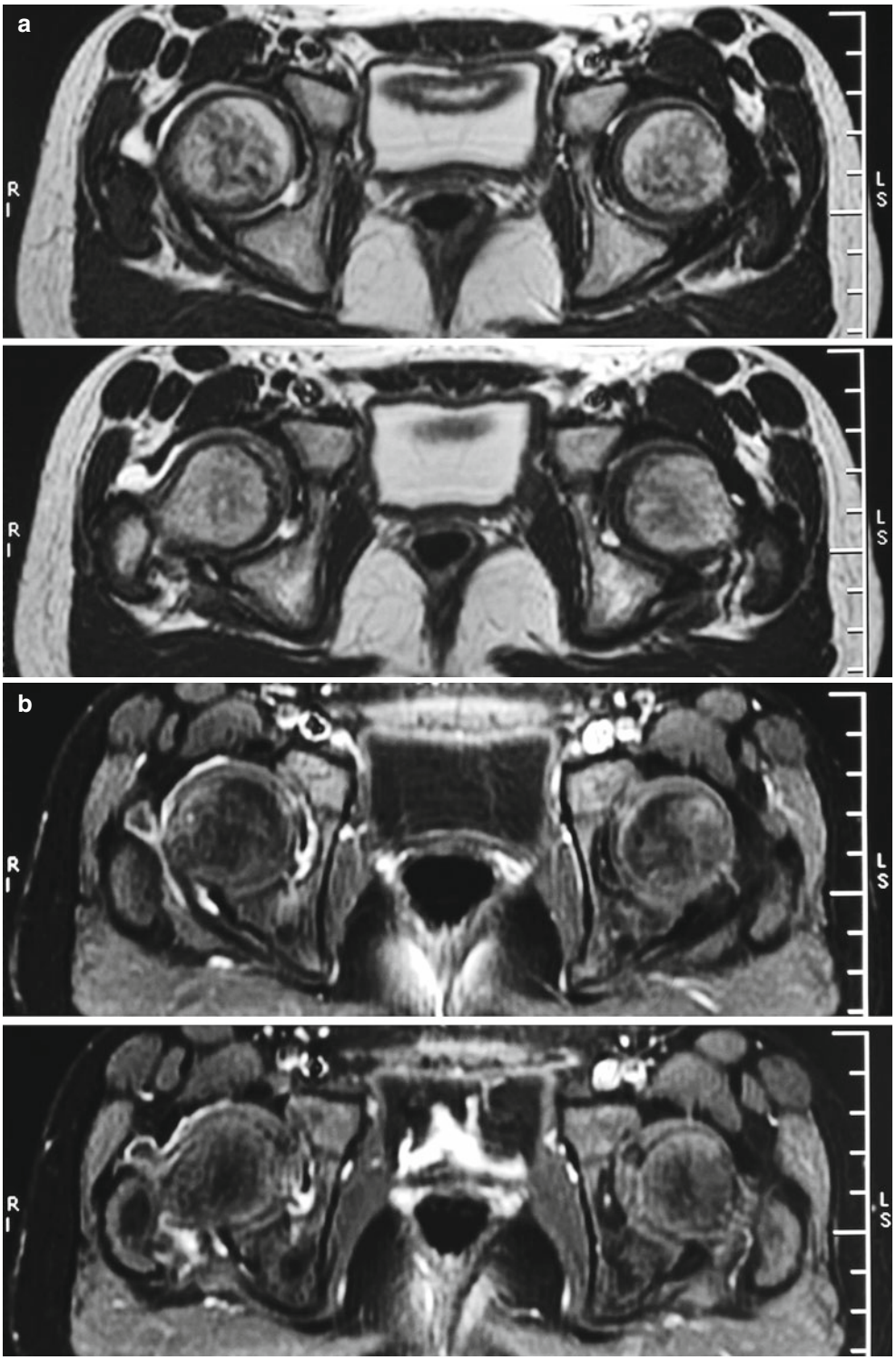

Fig. 3.30 Transverse T2-WI (**a**) and post-gadolinium fat sat T1-WI (**b**) of the hips of a 9-year-old female with long-standing JIA on both knees and arthritis of recent onset on her right hip. It is easier to identify small to moderate joint effusion and synovial thickening at right by comparing the abnormal hip with the contralateral normal one. Synovitis is even more evident on (**b**), appearing as a thin enhancing stripe easily distinguished from the dark synovial fluid. In early-stage arthritis (like in this case), osteitis and erosions are yet absent

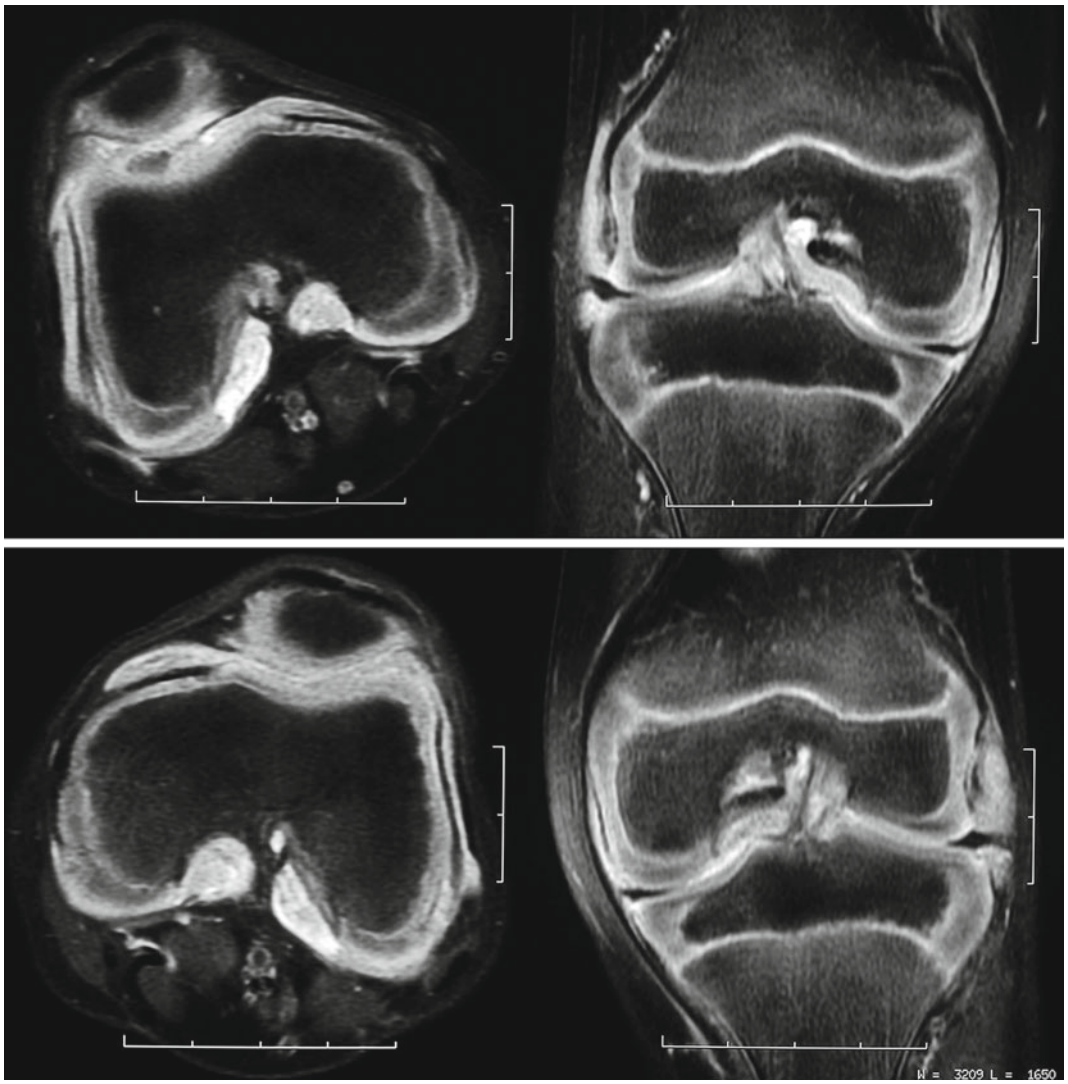

Fig. 3.31 Contrast-enhanced fat sat T1-WI of the knees in the transverse and coronal planes (right knee, *upper row*; left knee, *lower row*). Symmetric and bilateral joint effusion and synovial thickening are present in this 7-year-old male with JIA since age 4, notably in the left knee. The thickened synovium enhances and is more prominent in the intercondylar notches and adjacent to the lateral meniscus of the left knee. Meniscal hypoplasia is also seen in both knees, affecting predominantly the medial menisci. Focal irregularities can be seen in the corners of the tibial epiphyses on coronal images, corresponding to tiny cartilaginous erosions

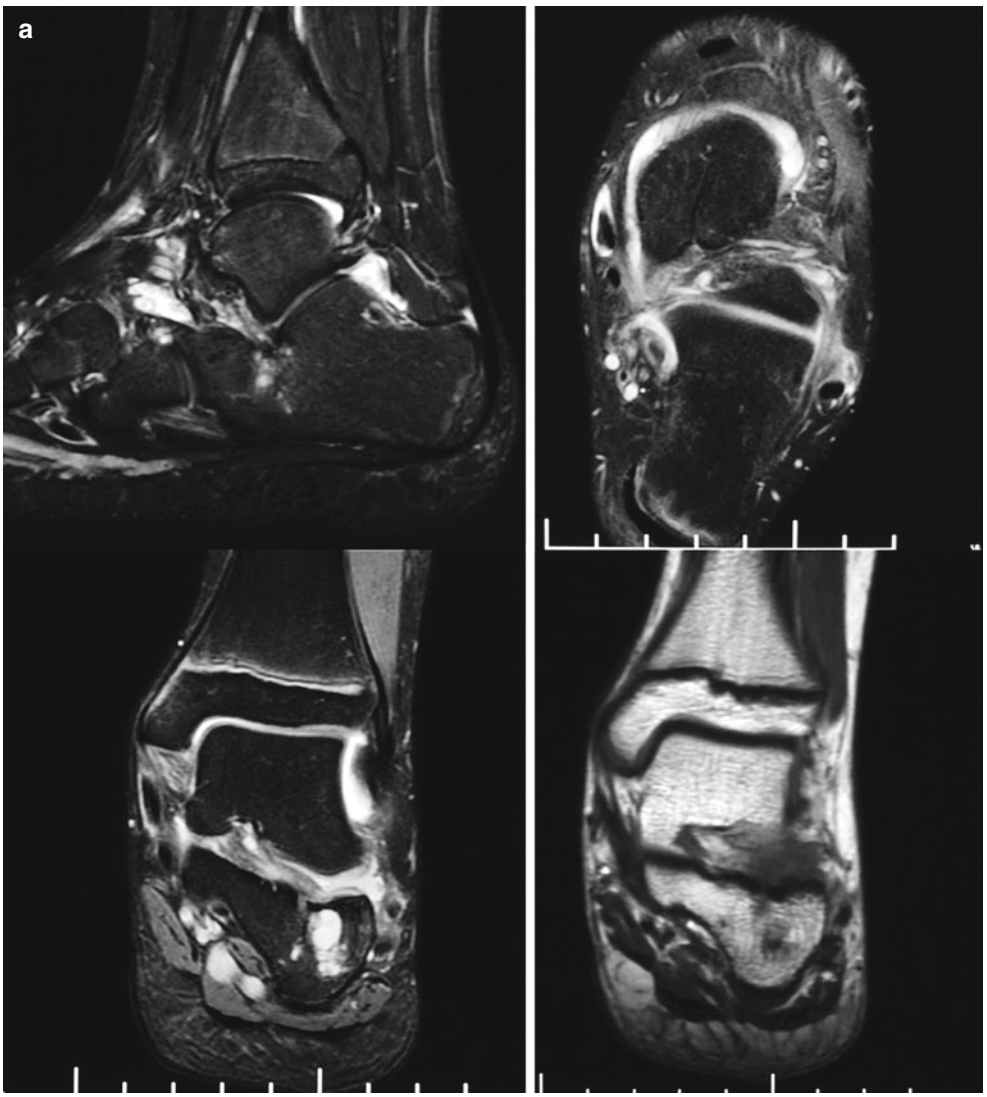

Fig. 3.32 MRI of the left ankle of a child with JIA. In (**a**), images obtained in multiple spatial planes and using different sequences reveal synovitis, joint effusion and subcortical cysts with adjacent bone marrow edema in the tarsal sinus. In (**b**), gadolinium-enhanced fat sat T1-WI display enhancement of the inflamed synovium (allowing it to be distinguished from the synovial fluid) and of the edematous bone. There is tenosynovitis, with fluid distension and contrast enhancement within the sheaths of the fibular tendons and of the posterior tibial tendon. Enhancement of the retrocalcaneal bursa is also present

Fig. 3.32 (continued)

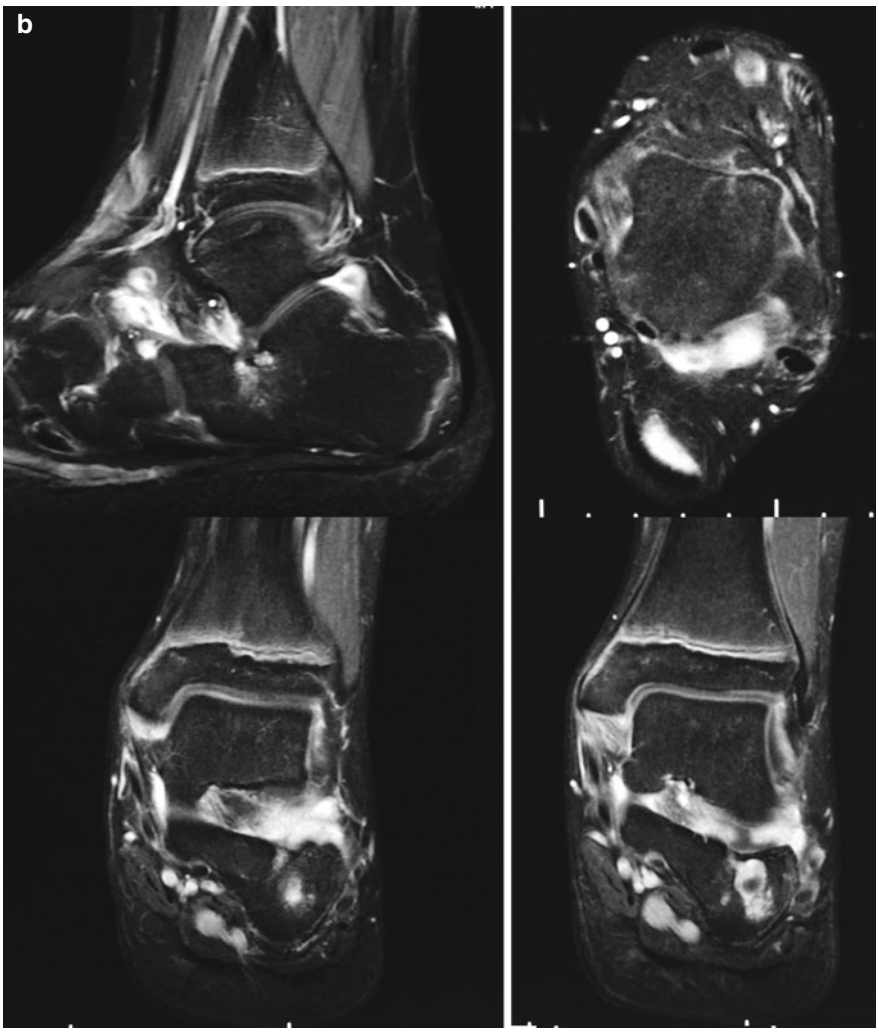

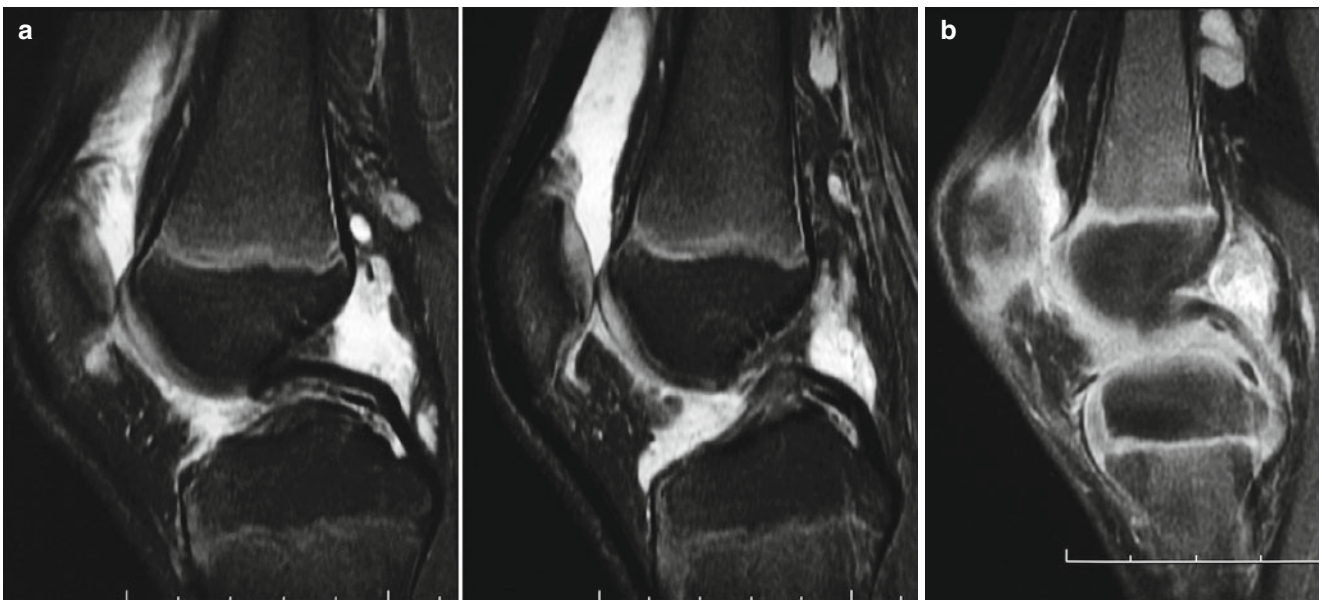

Fig. 3.33 Sagittal fat sat T2-WI of the left knee of a child with JIA (**a**) disclosing a large joint effusion associated with synovial thickening and prominent lymph nodes in the popliteal fossa, posterior to the distal femoral diaphysis, without evidence of erosive arthritis. In another patient, post-contrast fat sat T1-WI of the right knee (**b**) reveal enlarged, enhancing lymph nodes in the popliteal fossa, as well as marked synovitis and joint effusion

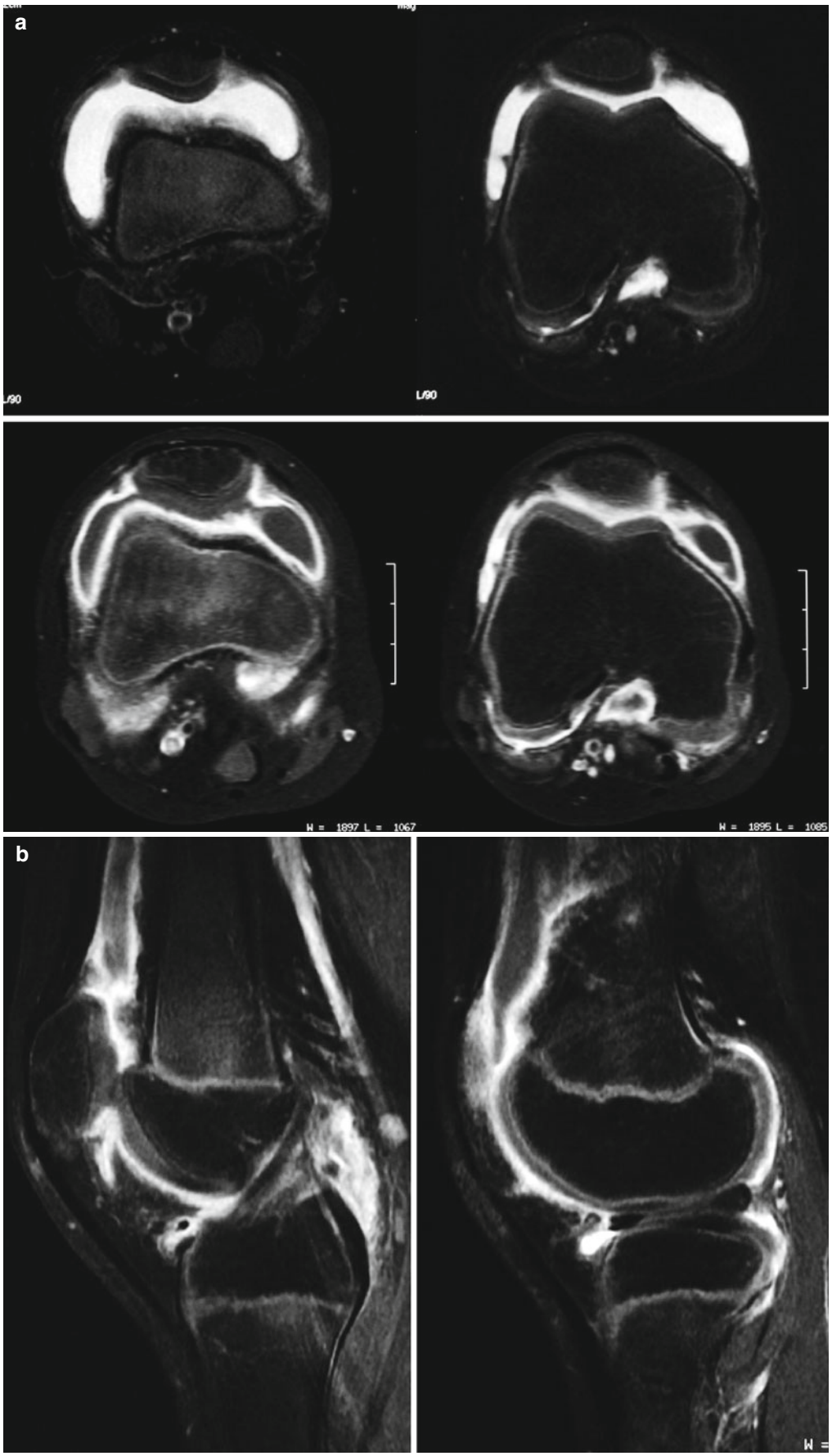
a
L/90
L/90
W = 1897 L = 1067
W = 1895 L = 1085
b
W =

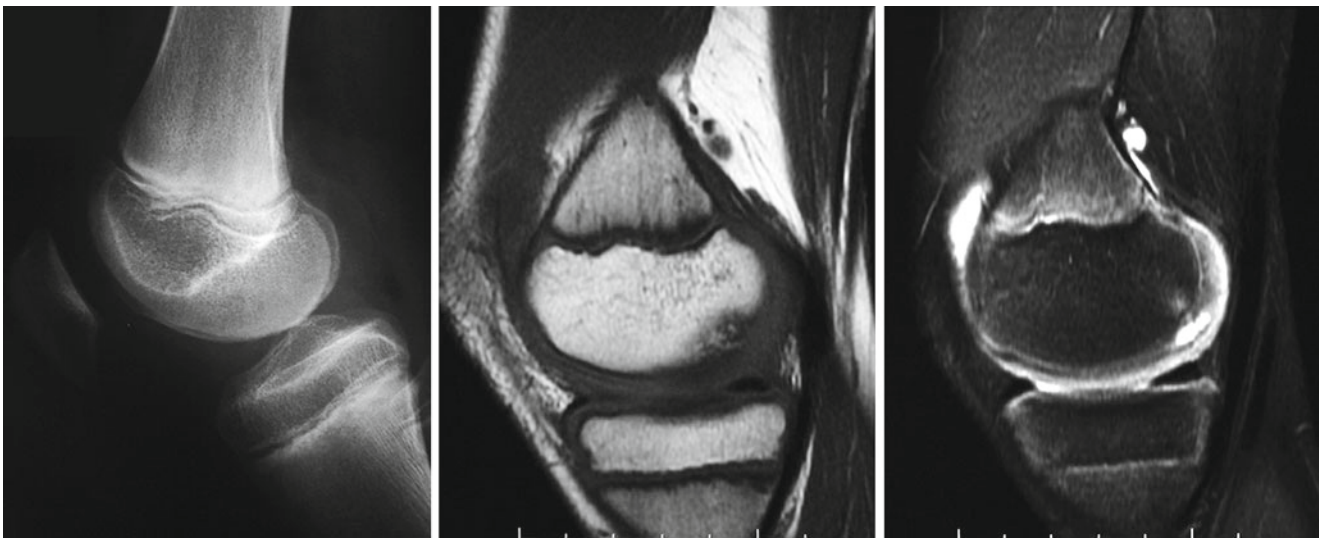

Fig. 3.35 Imaging investigation of the right knee of a child with early JIA. Even though the lateral radiograph is entirely normal (*first image*), sagittal T1-WI (*second image*) and fat sat T2-WI (*third image*) clearly demonstrate a small joint effusion and a cartilaginous erosion affecting the posterior portion of the medial femoral condyle, as well as osteitis and early erosive changes of the subchondral bone; a focal defect of the overlying articular cartilage was also present (not shown in this plane)

Fig. 3.34 Transverse fat sat T2-WI (*upper row*, **a**) and post-gadolinium fat sat T1-WI in the transverse (*lower row*, **a**) and sagittal (**b**) planes of the left knee of a child with JIA. T2-WI demonstrate joint effusion, synovial thickening, and small cartilaginous erosions in the femoral trochlea and in the femoral condyles, with thinning of the cartilage of the lateral condyle. Contrast-enhanced images show that the synovial thickening is even more extensive than initially estimated, as the inflamed synovium can be distinguished from the synovial fluid. Enhancement is also seen in the inflamed cartilages (which present irregular surfaces and superficial erosions) and in popliteal lymph nodes

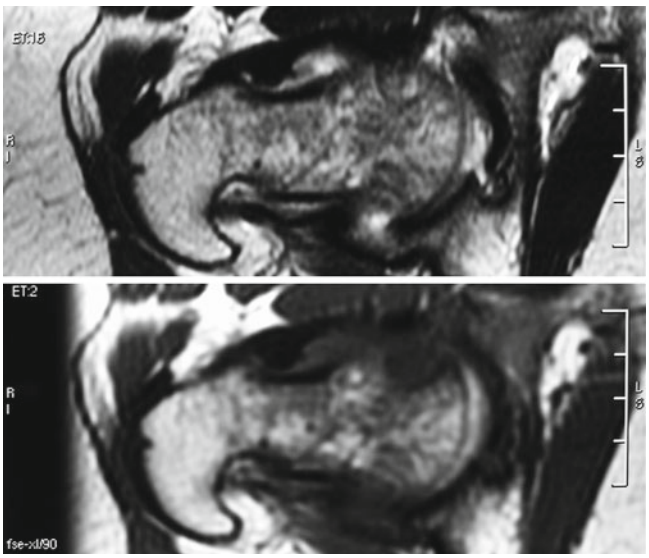

Fig. 3.36 Transverse T2-WI (*upper image*) and T1-WI (*lower image*) of the right hip of a patient with JIA. In addition to joint effusion, there are large bone erosions in the femoral head, filled with thickened synovium and synovial fluid

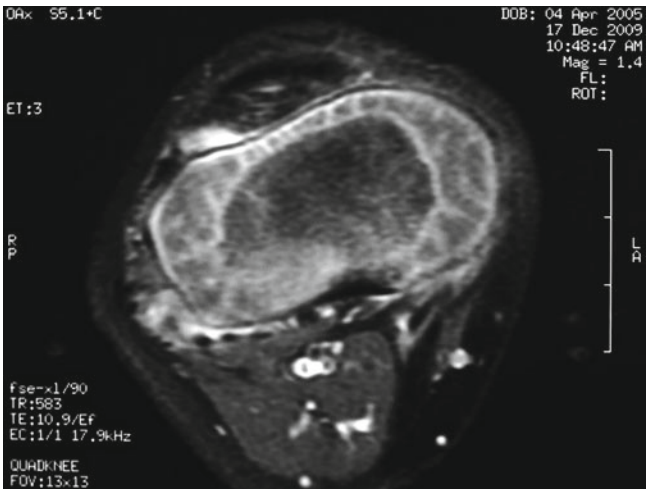

Fig. 3.37 Transverse post-gadolinium fat sat T1-WI of the right knee of a 4-year-old male with JIA. Joint hyperemia led to prominence of epiphyseal vessels of the proximal tibia, causing this bizarre pattern of cartilaginous enhancement

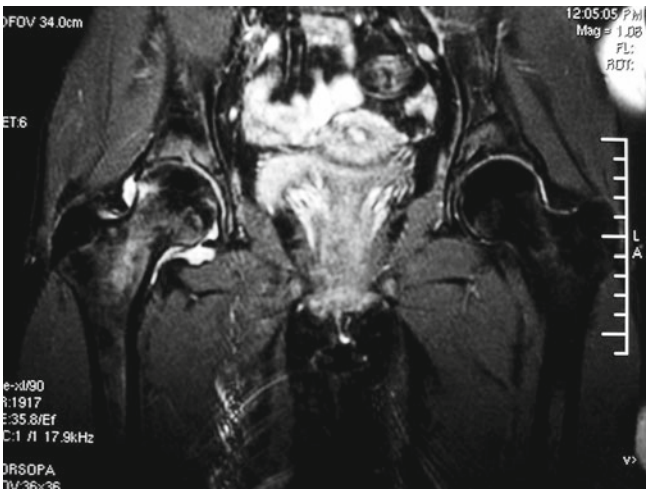

Fig. 3.38 Coronal fat sat PD-WI of the hips of a 19-year-old female with long-standing JIA. There is joint effusion in the right hip, associated with subchondral bone marrow edema in the homolateral acetabulum and in the proximal femur (compare with the normal left hip). A focal area of subcortical osteitis is seen in the lateral portion of the right femoral metaphysis, without associated erosions

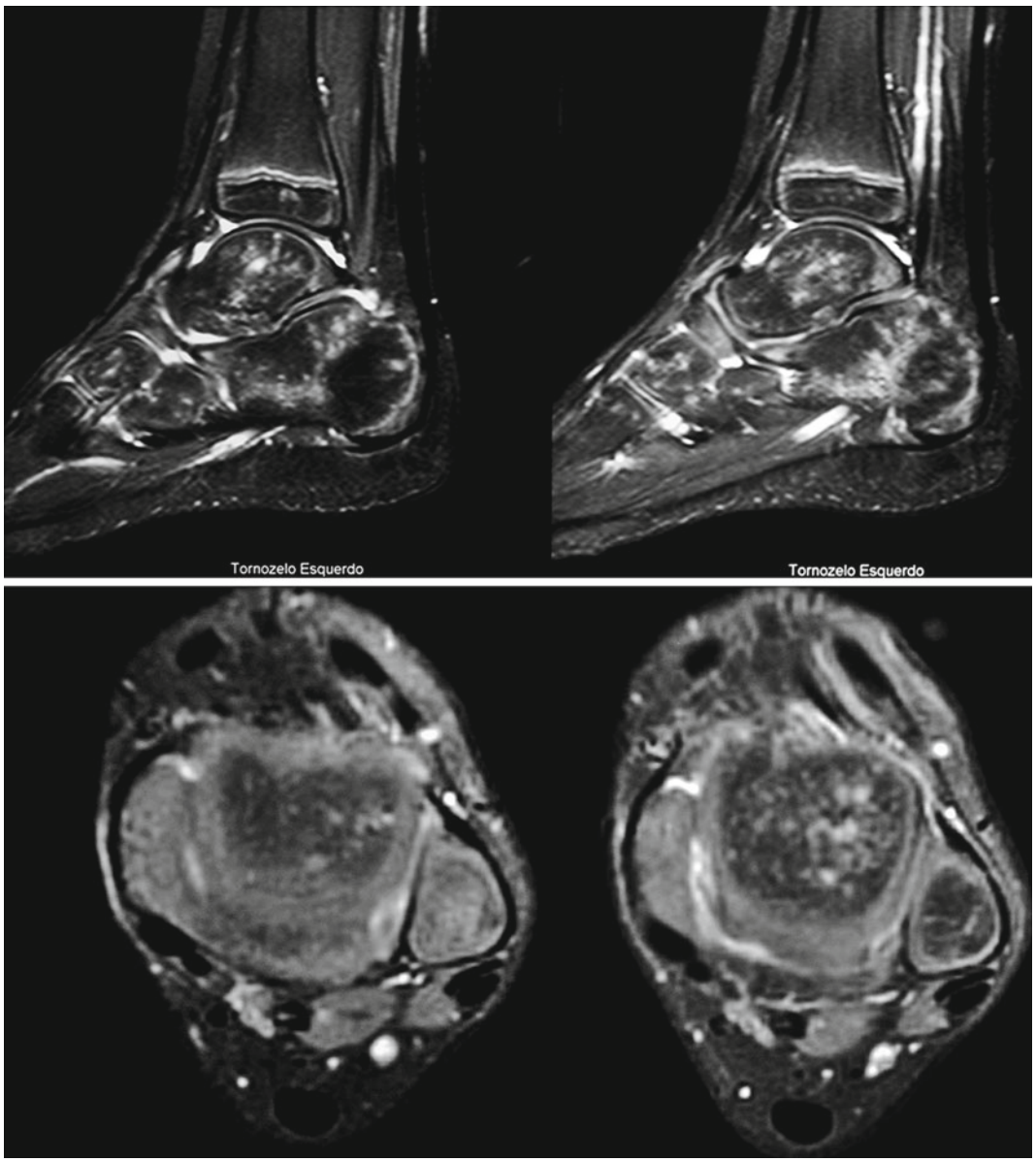

Fig. 3.39 MRI of the left ankle of a child with early JIA. Sagittal fat sat T2-WI (*upper-left image*) reveals a mottled pattern of bone marrow edema affecting the tarsal bones and small tibiotalar joint effusion. Sagittal (*upper-right image*) and transverse (*lower images*) post-gadolinium fat sat T1-WI show enhancement of the edematous bone and of the inflamed synovium, as well as irregularity of the cartilage of the posteromedial portion of the talar dome. Only MRI is able to show these early findings with such a high level of detail

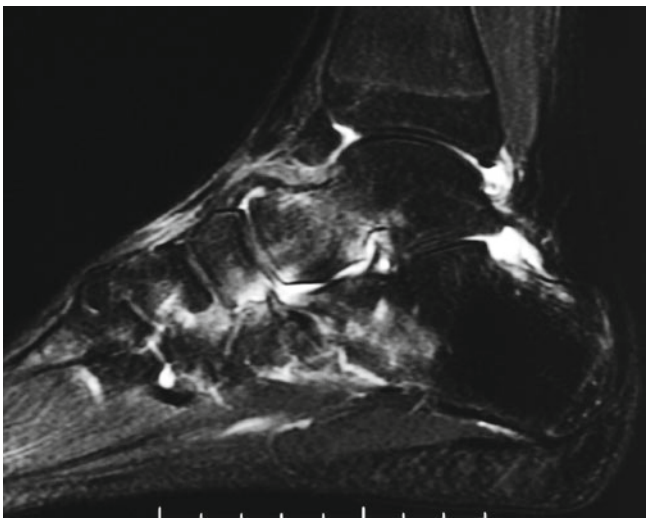

Fig. 3.40 Sagittal fat sat T2-WI of the left ankle of an adolescent with JIA. There are joint effusion and extensive bone marrow edema pattern affecting several tarsal bones. Despite the extent of bone marrow edema, bone erosions are still absent

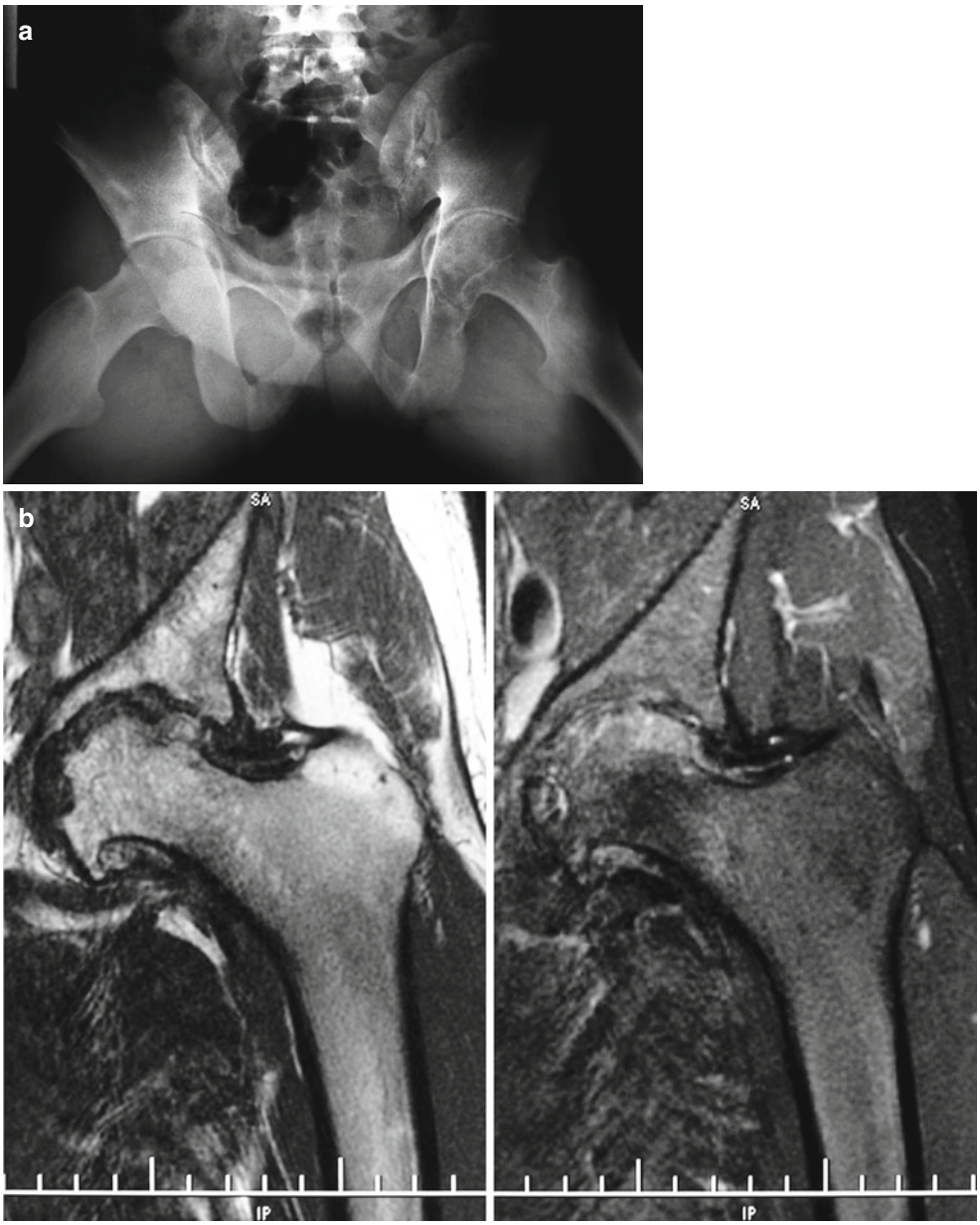

Fig. 3.41 Advanced arthritis of the left hip of a 22-year-old patient suffering from JIA since early adolescence. Anteroposterior view (**a**) discloses marked narrowing of the joint space of the left hip as well as abnormal shape of the femoral head and bone erosions. These findings are evidenced more accurately with MRI (**b**, coronal T1-WI (*left*) and post-gadolinium fat sat T1-WI (*right*)), which reveals extensive cartilaginous destruction, bone erosions, articular incongruity, and secondary osteoarthritis. Enhancing areas are indicative of active inflammation

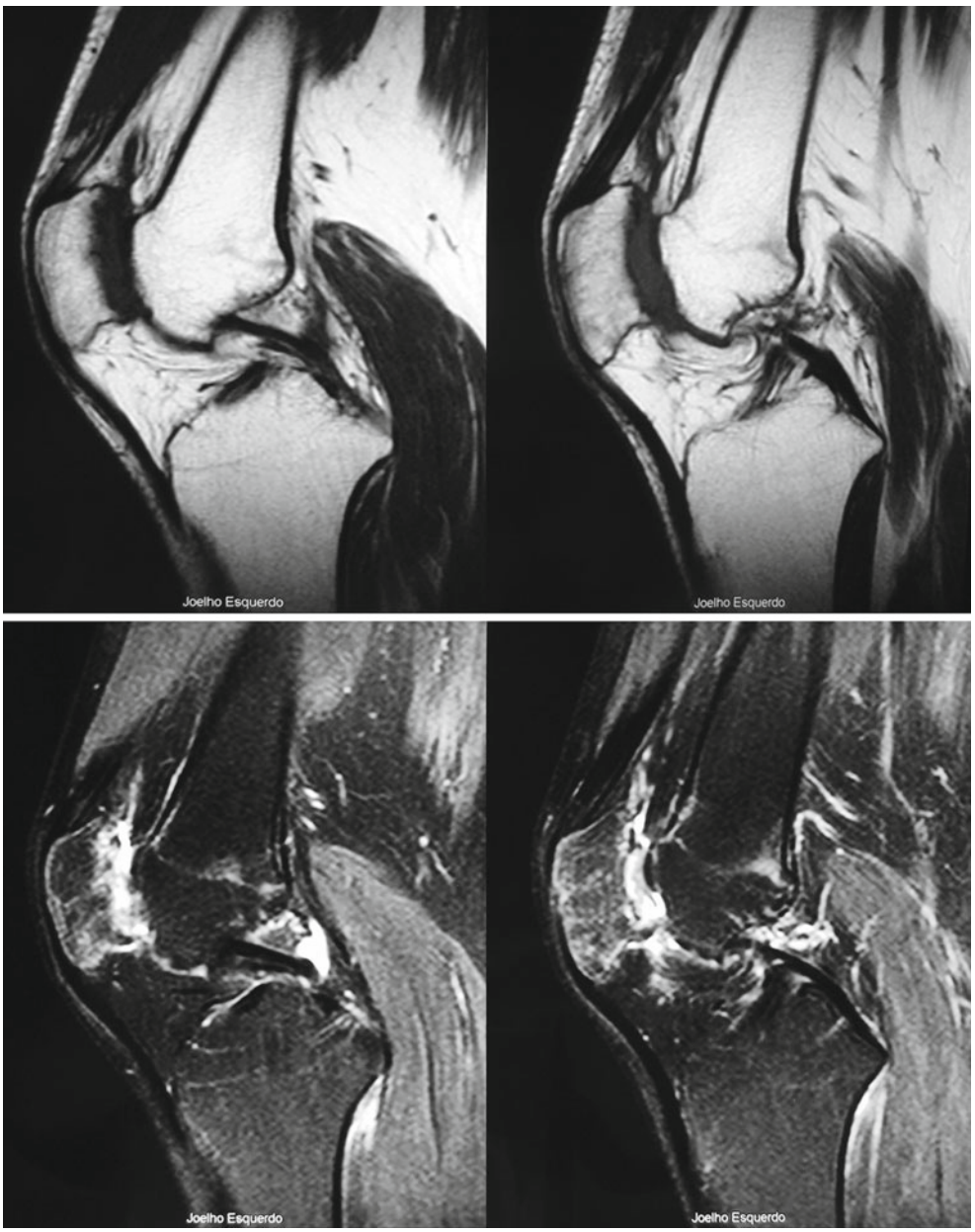

Fig. 3.42 Sagittal T1-WI (*upper images*) and fat sat T2-WI (*lower images*) of the left knee of a young adult with long-standing JIA. There is marked increase in the size of the patella, whose bone marrow is diffusely edematous. In addition, joint effusion and synovitis are also present, with erosions of the femoropatellar joint surfaces

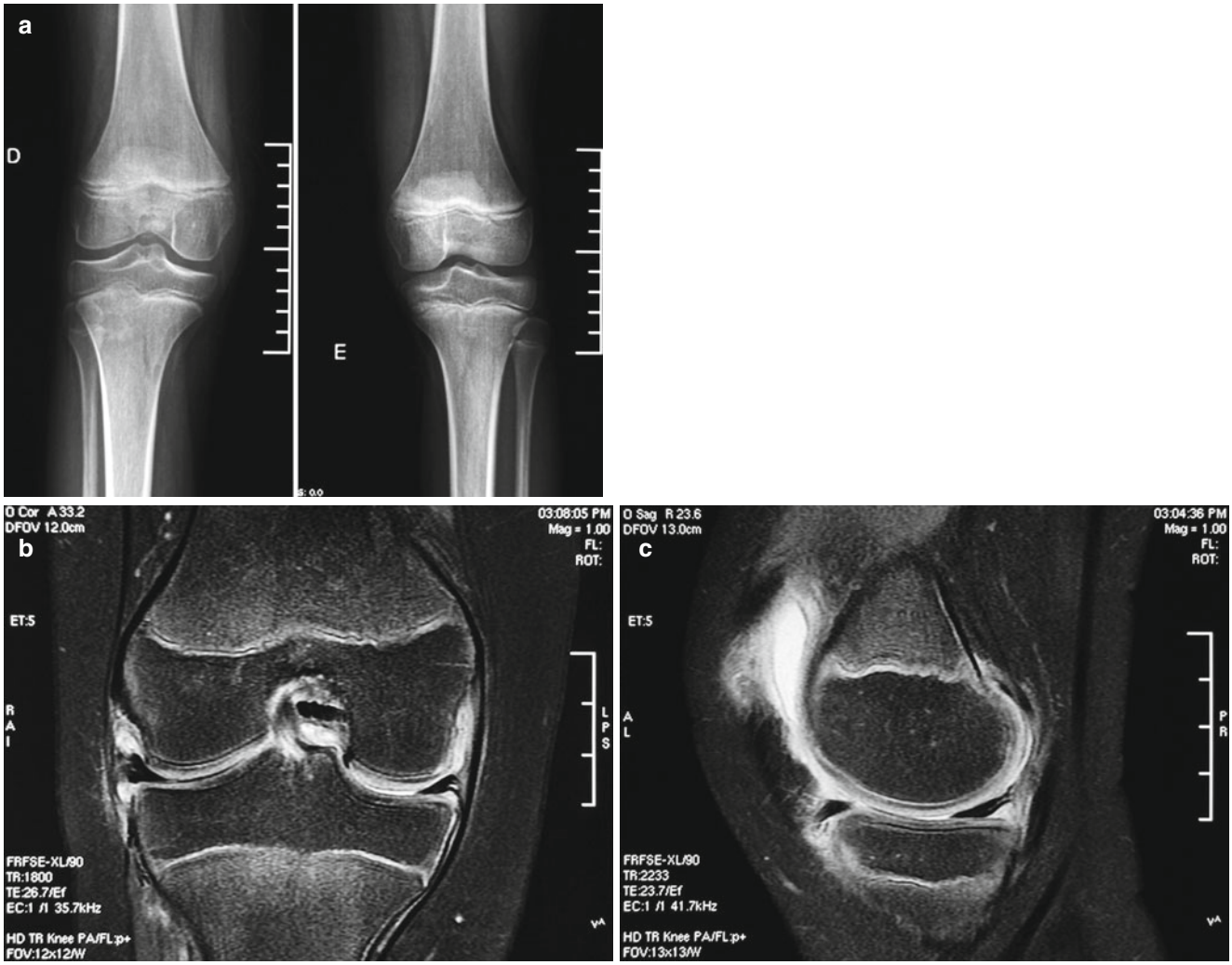

Fig. 3.43 Imaging investigation of the right knee of a 9-year-old female with active JIA. In (**a**), anteroposterior views of both knees demonstrate increased size of the epiphyses of the right distal femur and proximal tibia (compare with the normal left knee). In addition to epiphyseal enlargement, fat sat PD-WI in the coronal (**b**) and sagittal (**c**) planes disclose joint effusion and synovial thickening, as well as mild hypoplasia of the medial meniscus. Despite the active synovitis, erosions and areas of subchondral osteitis are yet absent

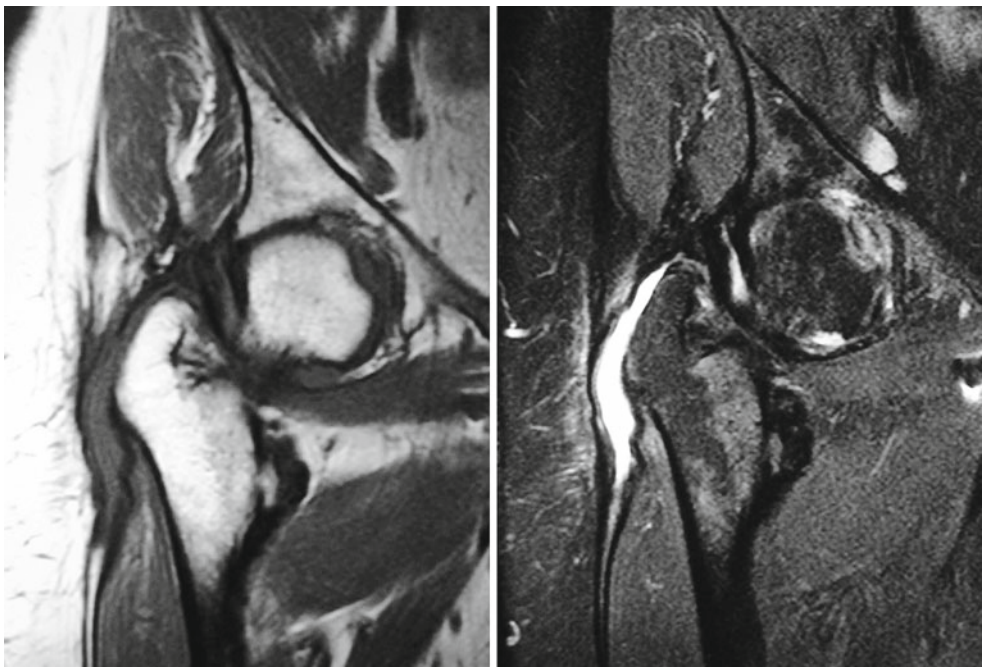

Fig. 3.44 Female patient with long-standing JIA. Coronal T1-WI (*left*) and fat sat T2-WI (*right*) of the right hip disclose narrowing of the joint space and a small joint effusion, in addition to marked fluid distension of the trochanteric bursa. MRI and US are very suitable in the assessment of distended periarticular bursae and other fluid collections

3.5 Computed Tomography

Even though computed tomography (CT) is excellent for bone assessment and for the detection of bone erosions, it is exceptionally requested for patients with JIA, mainly because of its limited accuracy in the evaluation of the soft tissues. Nonetheless, CT may be a useful diagnostic alternative in patients for whom MRI is not available, particularly in the study of anatomically complex joints. In addition, this is the best imaging method for the evaluation of fractures, which may be occasionally present. Intravenous contrast must be administered – just like in MRI – in order to assess the activity of the inflammatory process.

3.6 Nuclear Medicine

Although scintigraphies are highly sensitive in detecting acutely inflamed joints (even when radiographs are still normal), nuclear medicine also plays a limited role in the assessment of JIA. In children, in addition to the poor spatial resolution and low specificity of the images, there are technical issues (see Chap. 1) that limit the interpretation of the scintigraphic studies. Scintigraphies are also inadequate for monitoring disease evolution and for assessment of treatment response.

Key Points

- Timely institution of treatment has the potential to modify the course of JIA, leading to an improved prognosis. Thus, it is essential to diagnose the disease as early as possible, making imaging investigation more important now than ever before.
- Radiographs are suitable for assessment of advanced JIA, in which osteoarticular damage is already established, and the radiographic findings of long-standing disease are considered classic. Nevertheless, this imaging method is inappropriate for early diagnosis and to monitor treatment response.
- US and MRI are useful in the early stages of JIA, as both are able to detect joint effusion, synovitis, and edematous/hyperemic abnormalities of the soft tissues, to which radiographs are fairly insensitive. MRI is superior for the detection of bone erosions and to disclose areas of osteitis (seen as foci of subchondral bone marrow edema) that are present even in the pre-erosive stage. MRI also demonstrates articular structures not seen on US or to which the latter has limited access.
- Doppler US and contrast-enhanced MRI are able to assess treatment response and disease evolution in serial studies, mostly by monitoring joint effusion and synovial inflammation.
- Bone scintigraphy and CT have limited usefulness in the assessment of JIA, and both are usually reserved for exceptional circumstances.

Recommended Reading

Azouz EM (2008) Juvenile idiopathic arthritis: how can the radiologist help the clinician? Pediatr Radiol 38(Suppl 3):S403–S408

Babyn P, Doria AS (2007) Radiologic investigation of rheumatic diseases. Rheum Dis Clin North Am 33(3):403–440

Daldrup-Link HE, Steinbach L (2009) MR imaging of pediatric arthritis. Radiol Clin North Am 47(6):939–955

Johnson K (2006) Imaging of juvenile idiopathic arthritis. Pediatr Radiol 36(8):743–758

Jordan A, McDonagh JE (2006) Juvenile idiopathic arthritis: the paediatric perspective. Pediatr Radiol 36(8):734–742

Karmazyn B, Bowyer SL, Schmidt KM, Ballinger SH, Buckwalter K, Beam TT et al (2007) US findings of metacarpophalangeal joints in children with idiopathic juvenile arthritis. Pediatr Radiol 37(5):475–482

MacKenzie JD, Vasanawala SS (2008) Advances in pediatric MR imaging. Magn Reson Imaging Clin N Am 16(3):385–402

Magni-Manzoni S, Malattia C, Lanni S, Ravelli A (2012) Advances and challenges in imaging in juvenile idiopathic arthritis. Nat Rev Rheumatol 8(6):329–336

Miller E, Uleryk E, Doria AS (2009) Evidence-based outcomes of studies addressing diagnostic accuracy of MRI of juvenile idiopathic arthritis. AJR Am J Roentgenol 192(5):1209–1218

Petty RE, Southwood TR, Manners P, Baum J, Glass DN, Goldenberg J et al (2004) International League of Associations for Rheumatology classification of juvenile idiopathic arthritis: second revision, Edmonton, 2001. J Rheumatol 31(2):390–392

Pruthi S, Thapa MM (2009) Infectious and inflammatory disorders. Magn Reson Imaging Clin N Am 17(3):423–438

Shanmugavel C, Sodhi KS, Sandhu MS, Sidhu R, Singh S, Katariya S et al (2008) Role of power Doppler sonography in evaluation of therapeutic response of the knee in juvenile rheumatoid arthritis. Rheumatol Int 28(6):573–578

Southwood T (2008) Juvenile idiopathic arthritis: clinically relevant imaging in diagnosis and monitoring. Pediatr Radiol 38(Suppl 3):S395–S402

Tattersall R, Rangaraj S (2007) Diagnosing juvenile idiopathic arthritis. Paediatr Child Health 18(2):85–89

Workie DW, Graham TB, Laor T, Rajagopal A, O'Brien KJ, Bommer WA et al (2007) Quantitative MR characterization of disease activity in the knee in children with juvenile idiopathic arthritis: a longitudinal pilot study. Pediatr Radiol 37(6): 535–543

Juvenile Spondyloarthropathies and Pediatric Collagen Vascular Disorders

4

4.1 Introduction

The juvenile spondyloarthropathies comprise a group of conditions characterized by inflammation of the sacroiliac joints and of the spine, association with HLA-B27 antigen, and disease onset before age 16. This group encompasses juvenile ankylosing spondylitis, juvenile psoriatic arthritis, reactive arthritis, arthritis associated with inflammatory bowel disease, and the undifferentiated forms of spondyloarthropathy. In addition to the axial skeleton, the juvenile spondyloarthropathies also affect the peripheral joints, mostly in the lower extremities, and prominent enthesopathy is often present. Peripheral arthritis usually predominates during the initial stage and sacroiliitis/spondylitis are late findings, so that children with early-stage juvenile spondyloarthropathies may be incorrectly diagnosed as having classic juvenile idiopathic arthritis. Classic radiographic criteria employed for adult-type disease are fairly insensitive for early diagnosis of juvenile spondyloarthropathies. Therefore, imaging methods such as ultrasonography (US) and magnetic resonance imaging (MRI), which are more sensitive, have become more and more important, given that early diagnosis and timely introduction of treatment are paramount for improved outcome and better quality of life.

Pediatric collagen vascular disorders are multisystemic autoimmune diseases of unknown etiology, which are similar in many ways to their adult counterparts. Nonetheless, peculiarities in the presentation and in the evolution of the juvenile forms of collagen diseases make them unique, thus deserving separate study. Even though osteoarticular manifestations are not the more relevant in most patients, some imaging findings are quite typical, and it is important for the radiologist to be acquainted with them. The following paragraphs will discuss the major juvenile spondyloarthropathies and the juvenile forms of dermatomyositis, systemic lupus erythematous, scleroderma, and mixed connective tissue disease.

4.2 Juvenile Spondyloarthropathies

4.2.1 Juvenile Ankylosing Spondylitis

Juvenile ankylosing spondylitis (JAS) is more frequent in males, and disease onset usually occurs between the end of childhood and the first years of adolescence. Arthritis and enthesitis (inflammation involving the sites of insertion of tendons, ligaments, and joint capsules) are the more important articular manifestations in JAS. In contradistinction to the adult form of ankylosing spondylitis, in which axial involvement predominates from the start, in JAS, years (or even decades) may elapse before spondylitis and sacroiliitis become evident.

Arthritis is more common in large joints – mainly in the lower extremities – and the peripheral small joints are involved less often. If compared to that found in adult-type ankylosing spondylitis, articular disease in JAS usually follows a more severe course, with unrelenting arthritis, disability, and occasional need for joint replacement (Figs. 4.1 and 4.2). Radiographic findings related to peripheral arthritis include progressive narrowing of joint space and bone erosions of late appearance (Fig. 4.1). MRI is the method of choice for early diagnosis, demonstrating joint effusion, synovial thickening, and inflammation of the soft tissues and of the bones (Fig. 4.1), even in the pre-erosive stage. US is also able to demonstrate joint effusion, synovitis, and soft-tissue swelling as soon as they appear. Enthesitis is frequently found in the insertions of the plantar fascia, of the knee extensor mechanism, and of the Achilles tendon. Enthesitis-related radiographic findings include periosteal reaction, bone spurs, and enthesophytes, as well as sclerosis and lucent areas in the adjacent bone. Periostitis is more common in the hands, while enthesophytes are more frequently seen in the tarsal bones (Fig. 4.1). The affected tendon appears thickened and heterogeneous on US and on MRI, with increased perfusion on Doppler US and post-gadolinium enhancement.

S.L. Viana et al., *Joint Imaging in Childhood and Adolescence*,
DOI 10.1007/978-3-642-35876-0_4, © Springer-Verlag Berlin Heidelberg 2013

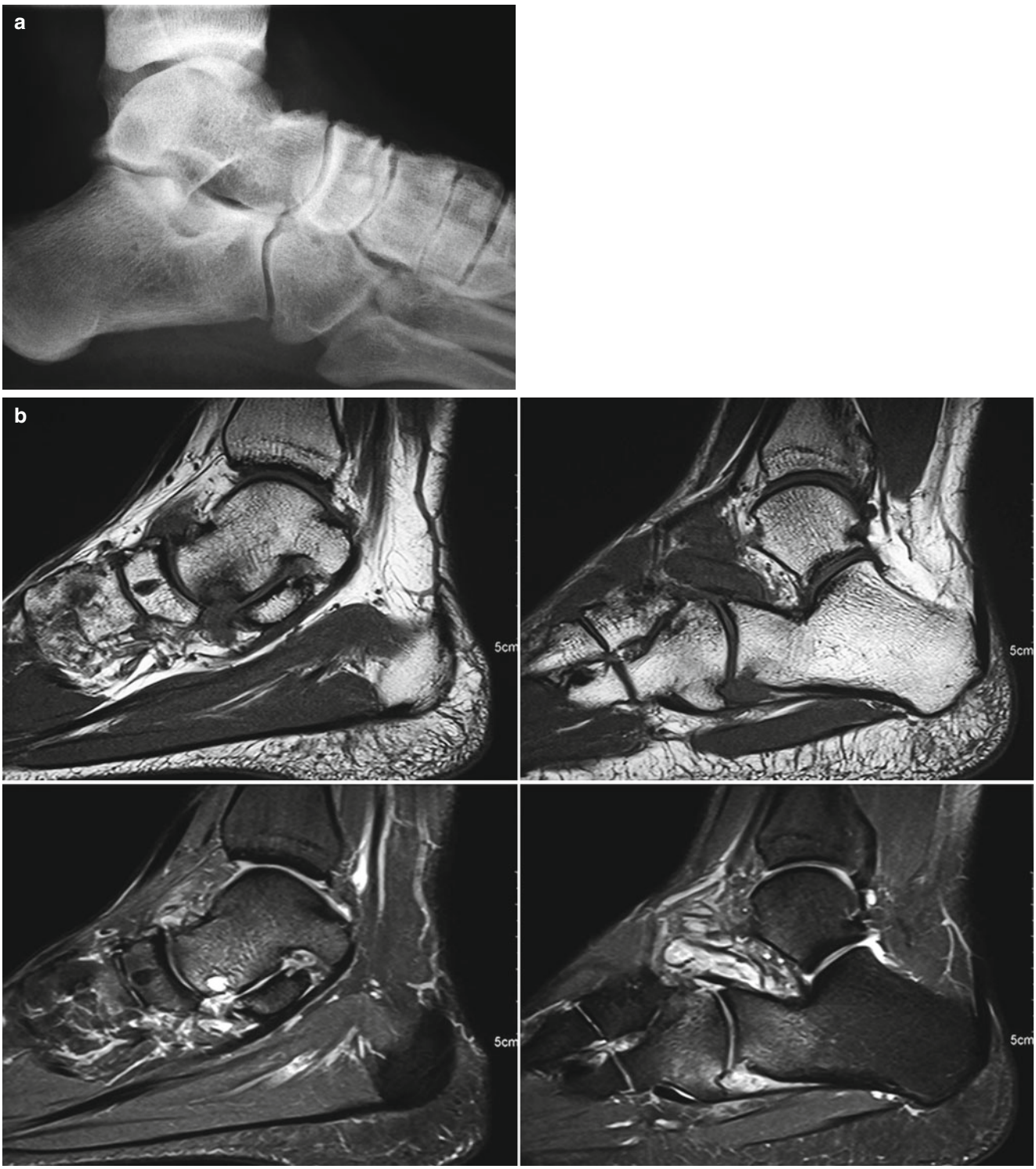

Fig. 4.1 An 18-year-old male with arthritis of the left midfoot and hindfoot since 3 years before. Lateral view (**a**) of the ankle demonstrates dorsal enthesophytosis in the midfoot and subcortical lucencies in the lowermost portion of the cuboid bone. In (**b**), sagittal T1-WI (*upper row*) and fat sat PD-WI (*lower row*) of the same ankle reveal arthritic changes, with joint effusion, synovial thickening, and bone marrow edema, as well as erosions in the talus, in the calcaneus, and in the cuboid. Post-gadolinium images (**c**) disclose enhancement of the thickened synovium. Tarsitis is a peculiar manifestation of juvenile spondyloarthritides, representing a combination of inflammation and bone proliferation that often leads to ankylosis

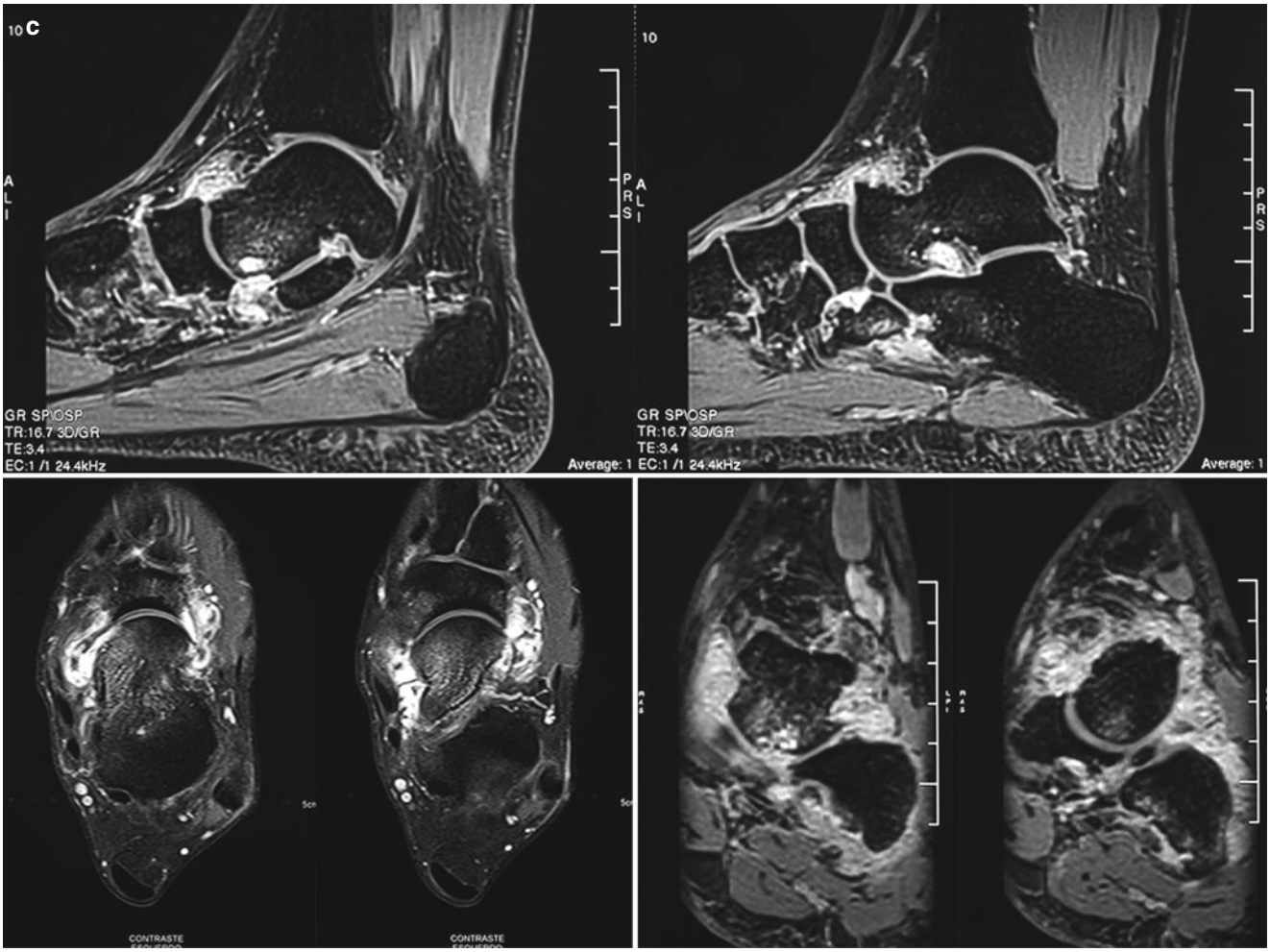

Fig. 4.1 (continued)

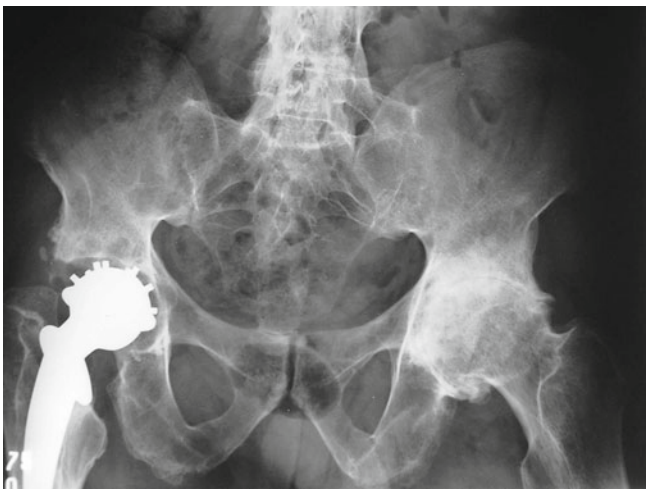

Fig. 4.2 Pelvic radiograph of a 27-year-old patient with JAS since late adolescence. There is severe osteoarthritis of the left hip (secondary to chronic arthritis) and right-sided sacroiliitis with pseudo-widening of the joint space, as well as ankylosis of the left sacroiliac joint and of the lower lumbar facet joints. Total replacement of the right hip joint is also seen, with a wide lucent zone surrounding the acetabular component of the prosthesis, indicative of loosening

Cortical erosions and bone marrow edema pattern are also present, as well as soft-tissue swelling and fluid distention of adjacent bursae.

Sacroiliitis in JAS is prototypical, very similar to that found in adult-type disease. When positive, radiographs show loss of definition of the articular surfaces, bone erosions, and subchondral sclerosis in the sacroiliac joints, which are most often bilateral. As the disease advances, there is gradual narrowing of the joint spaces, and ankylosis may be found in late-stage JAS. Pseudo-widening of the joint space is a peculiar finding, caused by confluence of subchondral erosions (Figs. 4.2 and 4.3). However, radiographs are insensitive for the assessment of the sacroiliac joints, largely because of their complex anatomy; furthermore, the classic radiographic findings are only found in advanced sacroiliitis (Fig. 4.2), and this imaging method is unable to distinguish active from inactive disease. In spite of the excellent bone assessment provided by computed tomography (CT) (Fig. 4.3), this imaging modality is also unable to yield accurate information about inflammation activity. MRI is the most suitable study for sacroiliac evaluation, as it is able to

detect subchondral areas of bone marrow edema that show post-gadolinium enhancement and are indicative of active disease (Fig. 4.4); these areas of osteitis are evident since the early stages of sacroiliitis, way before the development of erosions. Increased signal intensity on T2-weighted images (T2-WI) and post-gadolinium enhancement can also be seen inside the articular space in inflamed sacroiliac joints. Bone erosions are usually small, and large subchondral cysts are relatively rare (Fig. 4.5); subchondral sclerosis appears as areas of low signal intensity in all sequences (Fig. 4.5). Fatty replacement of bone marrow is a late finding, indicative of healing and typically found in chronic sacroiliitis. Despite the high sensitivity of bone scintigraphy, its usefulness is limited in the assessment of sacroiliitis in the juvenile spondyloarthropathies, mostly because of technical issues in the evaluation of the immature sacroiliac joints (see Chap. 1) and due to its inherently low specificity and spatial resolution (Fig. 4.6).

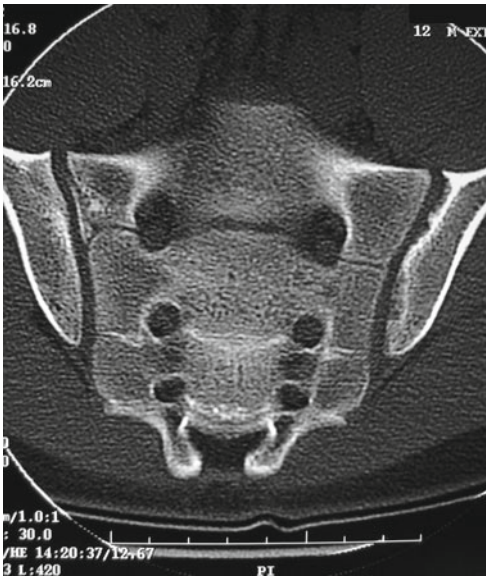

Fig. 4.3 A 12-year-old male with JAS. Coronal CT image shows confluent subchondral erosions in the iliac surface of the left sacroiliac joint, with subtle sclerosis of the adjacent bone. This confluence leads to pseudo-widening of the sacroiliac joint space, similar to that seen in the right sacroiliac joint in the patient of Fig. 4.2

Spondylitis usually occurs in late-stage JAS and is rarely found in children, affecting most often the thoracolumbar spine of adults with long-standing disease (Fig. 4.2); sacroiliitis almost always precede vertebral involvement. Involvement of the cervical spine is rare and late, presenting a more benign course if compared to that seen in juvenile idiopathic arthritis. Classic radiographic findings (infrequently seen in skeletally immature patients) include sclerosis of vertebral corners, squaring of the vertebral bodies, syndesmophytosis, and ankylosis of the facet joints.

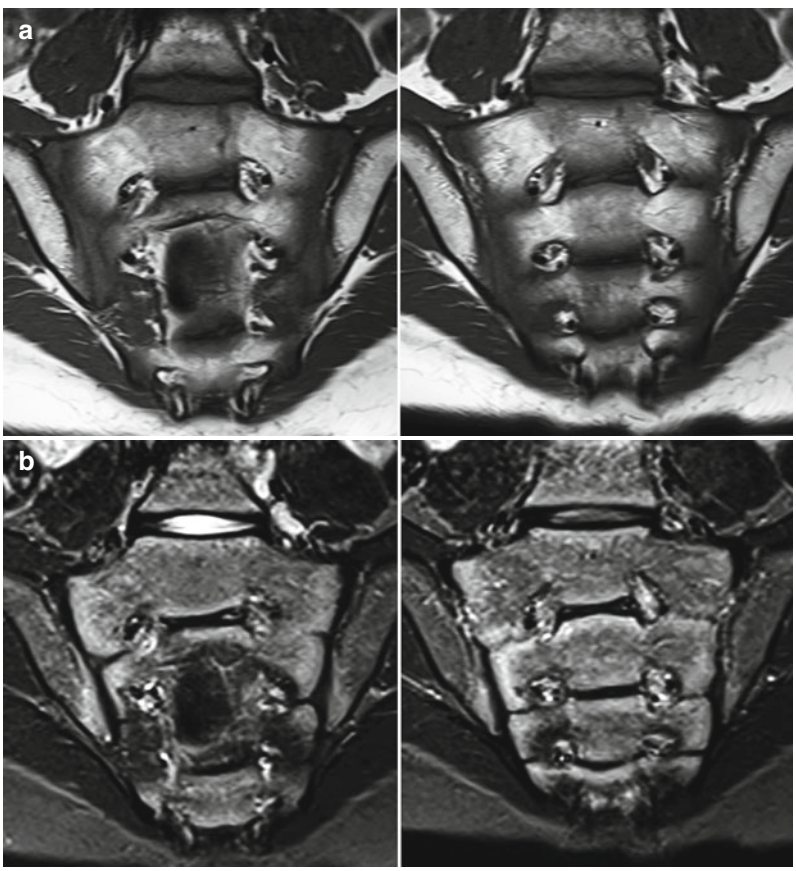

Fig. 4.4 Coronal T1-WI (**a**), STIR image (**b**), and post-gadolinium fat sat T1-WI (**c**) of a 13-year-old child with JAS and pre-erosive sacroiliitis. There is subchondral bone marrow edema pattern along the sacral surfaces and in the lowermost portions of the iliac surfaces of both sacroiliac joints, more prominent at right, with post-contrast enhancement. Joint spaces are preserved and there are no erosions. Similar findings are seen in (**d**) in a 9-year-old male with undifferentiated spondyloarthropathy (*upper row*, T1-WI; *lower row*, fat sat T2-WI)

Fig. 4.4 (continued)

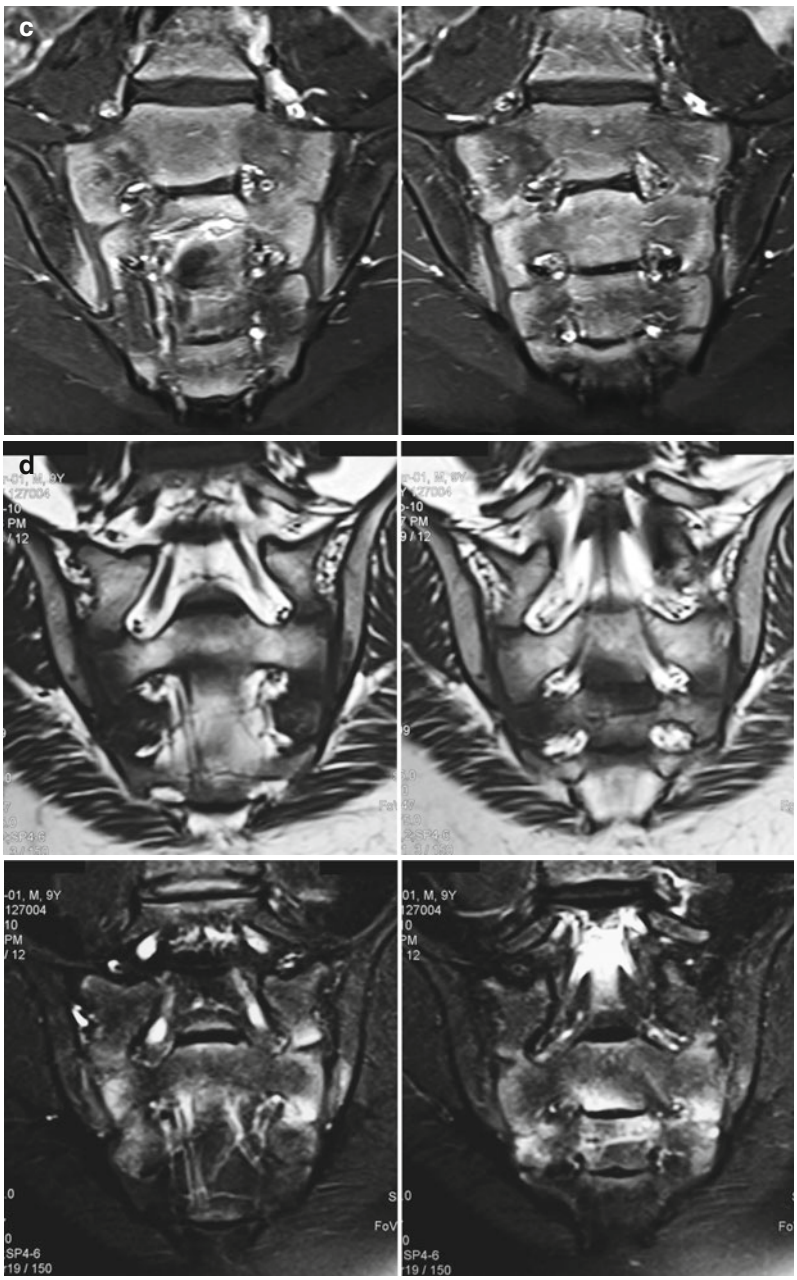

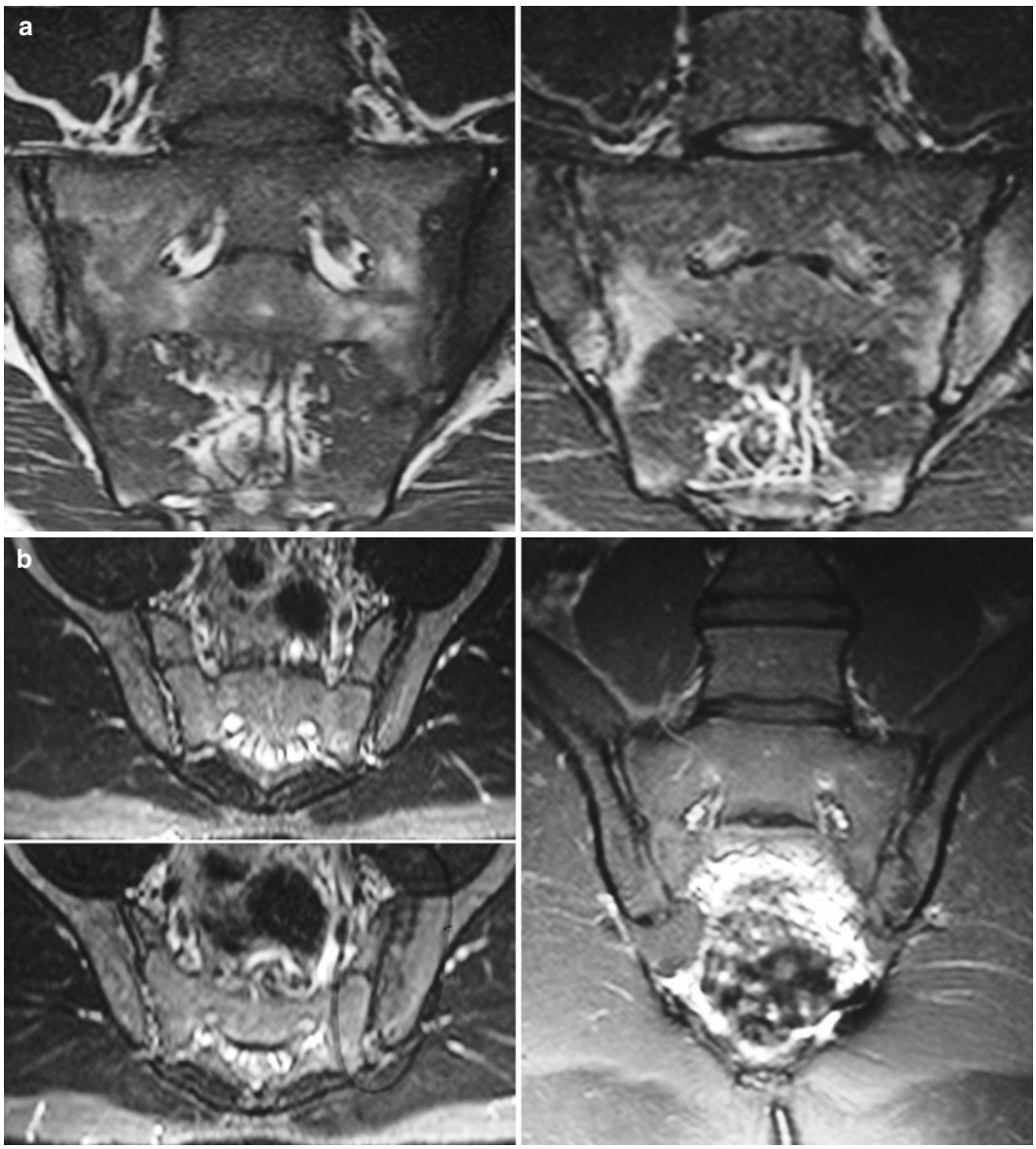

Fig. 4.5 MRI of the sacroiliac joints of two different patients. In (**a**), in a 19-year-old male with JAS since age 15, there is bilateral subchondral osteitis, which appears as areas of low signal intensity on T1-WI (*left image*) and high signal intensity on STIR (*right image*). There is narrowing of the joint spaces and irregularity of the articular surfaces due to micro-erosions; one dominant bone erosion is seen in the upper half of the left sacral surface. In (**b**), MRI of a 14-year-old male with JAS and good clinical control shows narrowing of the left sacroiliac joint space and subchondral sclerosis, which appears as hypointense areas on transverse T2-WI (*left images*) and coronal post-gadolinium fat sat T1-WI (*right image*). Absence of bone marrow edema or abnormal post-contrast enhancement is indicative of inactive disease

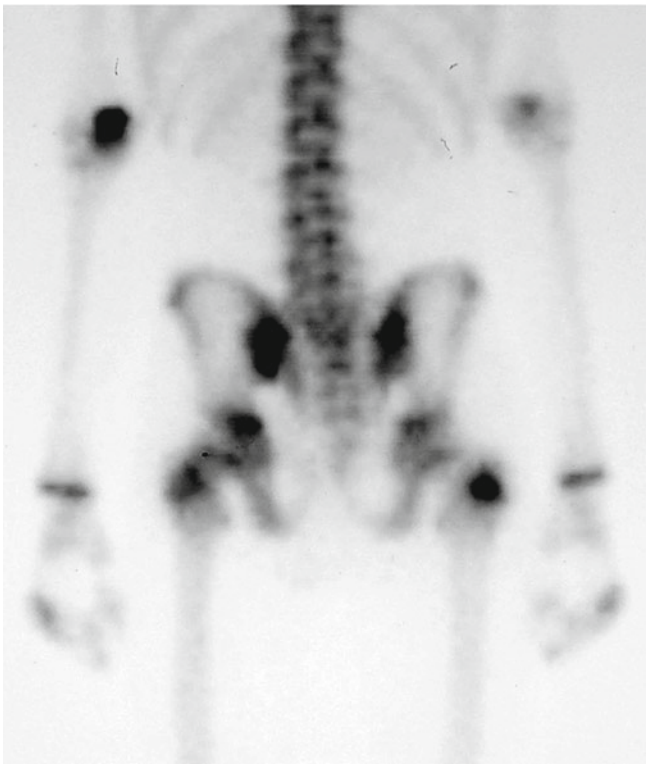

Fig. 4.6 Bone scintigraphy of the same patient of Fig. 4.3, posterior view. There is increased uptake in the lowermost portion of the left sacroiliac joint, indicative of active inflammation. Radiographs and CT are insensitive for assessment of disease activity

4.2.2 Juvenile Psoriatic Arthritis

Juvenile psoriatic arthritis (JPA) is a form of seronegative arthritis associated with psoriasis, much less common and more subtle than the adult form of the disease. The typical cutaneous rash is absent in up to half of the patients. This is the only spondyloarthropathy in which females are more frequently affected (up to 2.5:1), with an incidence peak at 11–12 years of age. Diagnosis is based on clinical features, a compatible family history, laboratory tests, and imaging findings.

Arthritis is usually oligoarticular and asymmetric, affecting most often the knees and the small joints of the hands and feet. Radiographs are insensitive for early-stage JPA; the association of periostitis, bone erosions, and enthesitis is very characteristic of JPA, but these are late findings, as well as sacroiliitis/spondylitis. The hands are affected most often and more severely than the feet, and arthritis of the distal interphalangeal joints is typical (Fig. 4.7). Peripheral erosions may lead to the classic "mouse ear" appearance (Fig. 4.8).

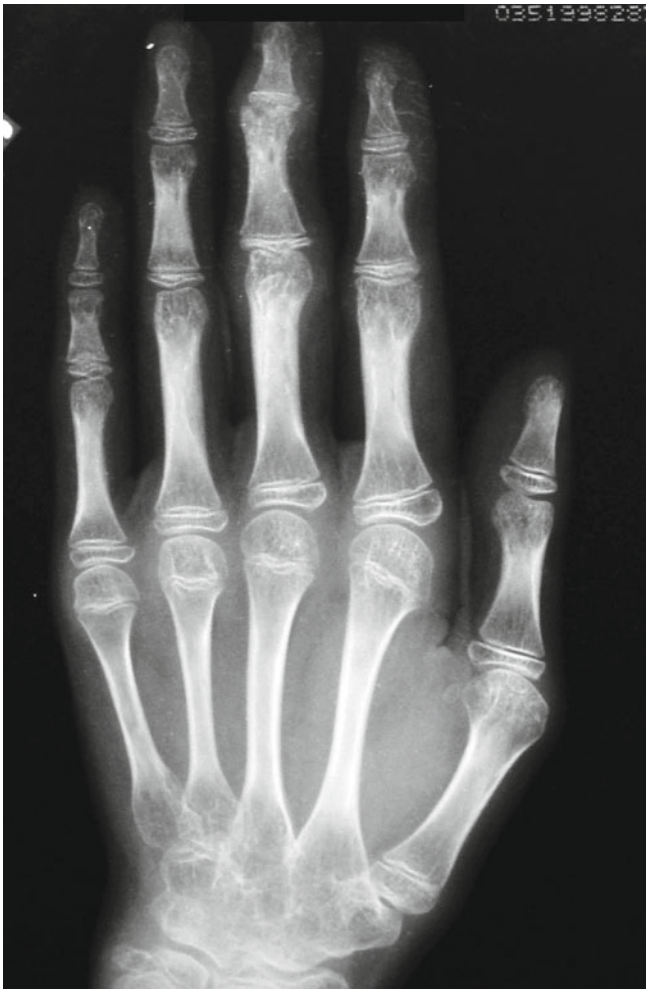

Fig. 4.7 A 12-year-old female with severe JPA. Erosive arthritis can be seen in the interphalangeal joints of the third finger, mainly distal. Solid periosteal reaction along the diaphyses of the proximal phalanges is also present, from the second to the fourth digits. Extensive carpal ankylosis is evident

Arthritis mutilans is a rare and severe form of JPA, presenting imaging findings similar to those of juvenile idiopathic arthritis (Figs. 4.9 and 4.10). Abnormalities commonly found in the adult-type form of the disease, such as acro-osteolysis (resorption of the distal phalanges), whiskering (proliferative bone neoformation in the entheses), and periostitis tend to be less aggressive in JPA. If compared to JAS, there is more extensive involvement of the small joints and less enthesopathy in JPA, features that help to narrow the differential diagnosis. The so-called "pencil-in-cup" deformity, a classic finding of psoriatic arthritis in adults, is uncommonly seen in children (Figs. 4.8 and 4.11).

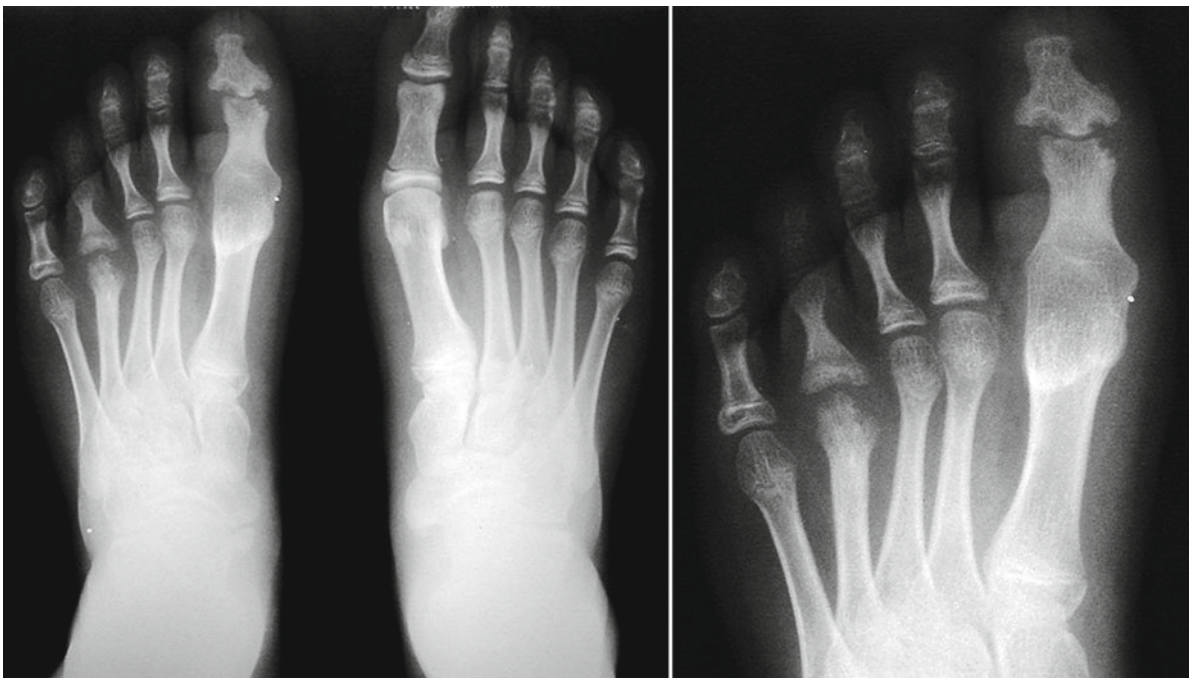

Fig. 4.8 Radiograph of the feet of a child with JPA (magnification of the right forefoot in the *right image*). Erosive arthritis is seen in the interphalangeal joint of the right hallux ("mouse ear" appearance), as well as ankylosis of the corresponding metatarsophalangeal joint. Arthritis of the metatarsophalangeal joint of the fourth toe is also evident, with the classic "pencil-in-cup" configuration, characterized by bone remodeling and a saucerlike appearance of the joint surface of the proximal phalanx, on which the severely eroded metatarsal head articulates. Periostitis is seen along the proximal phalanx of the fifth toe at right and along the diaphysis of the fourth metatarsal bone

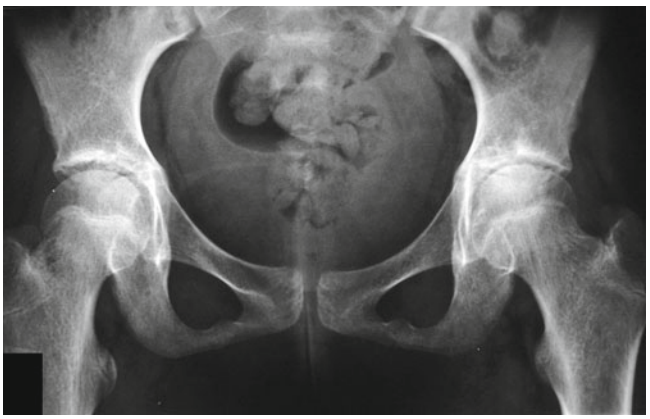

Fig. 4.9 Bilateral hip arthritis in a preadolescent girl with JPA, more important at left, with narrowing of the joint spaces and erosions of the articular surfaces

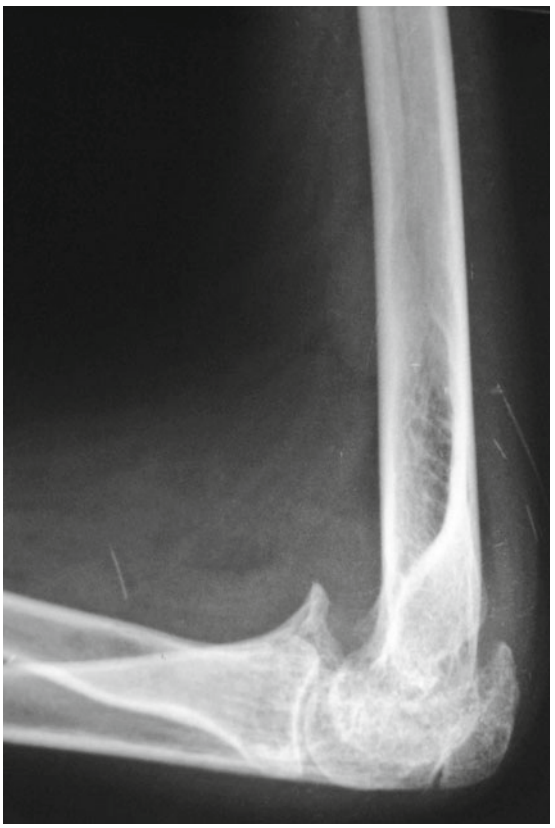

Fig. 4.10 Deforming arthritis of the right elbow of a child with psoriasis. There is marked remodeling of the joint surfaces, with widening of the trochlear notch. Bone erosions are present in the distal humerus

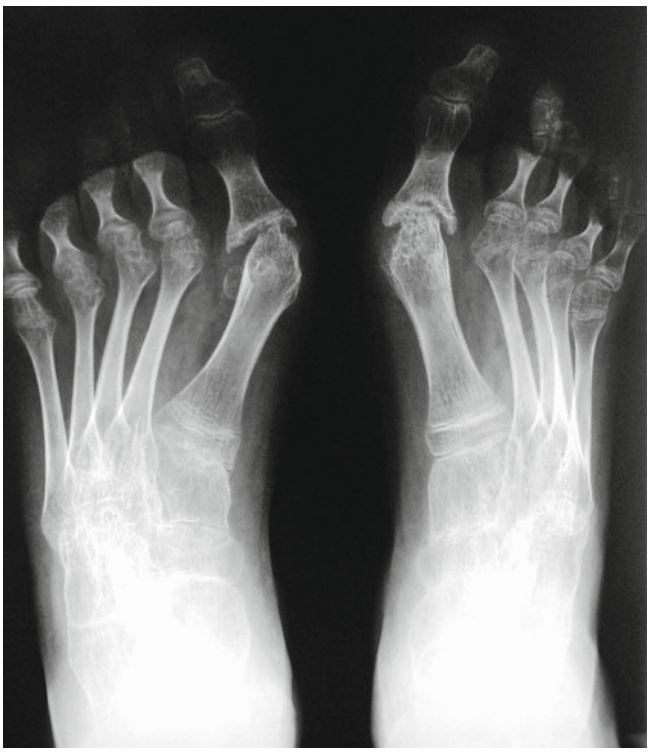

Fig. 4.11 Symmetric and bilateral erosive arthritis of the metatarsophalangeal joints can be seen in the feet of this female patient with JPA. Note the typical "pencil-in-cup" deformity and lateral deviation of the toes, as well as marked osteoporosis

Contrast-enhanced MRI is the most useful imaging method for assessing the extent of the disease and the activity of the inflammation in early-stage JPA. Joint effusion, synovitis, and subchondral areas of bone marrow edema (osteitis) are present long before the appearance of bone erosions. The so-called sausage finger (dactylitis) results from a combination of soft-tissue inflammation, tenosynovitis, arthritis, and periostitis, which is very suggestive of JPA, especially when found in a toe. The inflamed synovium and the edematous areas in the bone and in the soft tissues show post-gadolinium enhancement.

4.2.3 Arthritis Associated with Inflammatory Bowel Disease in Children

Arthritis is found in nearly 10 % of the children with inflammatory bowel disease. It may either precede or follow the clinical onset of the subjacent enteropathy, more frequently associated with ulcerative colitis than with Crohn's disease. Two distinct types of articular disease may occur: one of them with predominance of peripheral arthritis, without sex predilection, and another one with predominance of spondylitis and sacroiliitis, more common in males. Oligoarticular arthritis is the most common pattern, whose activity parallels that of the intestinal disease. Knees, ankles, and wrists are affected most often, followed by hands and shoulders. Axial involvement is less common, indistinguishable from that found in JAS, and both sacroiliitis and spondylitis may progress regardless of the control of the intestinal disease. Osteoporosis, periostitis, and digital clubbing may also be present.

4.2.4 Reactive Arthritis

Reactive arthritis occurs after an intestinal infection (mainly caused by *Yersinia*, *Shigella*, *Salmonella*, or *Campylobacter*) or an infection of the urogenital tract (most frequently caused by *Chlamydia*). Nonetheless, this is not a septic arthritis, as there are no viable microorganisms in the synovial fluid aspirated from affected joints. The classic clinical triad – arthritis, urethritis, and conjunctivitis – is only found in a minority of the patients. The disease usually affects males between 15 and 35 years of age, being rarely found in younger children. Arthritis is most often monoarticular or oligoarticular, characteristically affecting the joints of the lower limbs (Fig. 4.12); involvement of the first interphalangeal joint is typical. Tenosynovitis and synovial cysts may also be present. It is most commonly a self-limited condition, and erosive arthropathy is only occasionally found (Fig. 4.12). Sacroiliitis and enthesitis are less common in skeletally immature patients than in adults (Figs. 4.13 and 4.14). Radiographs are most often normal or nonspecific in benign cases (Fig. 4.15).

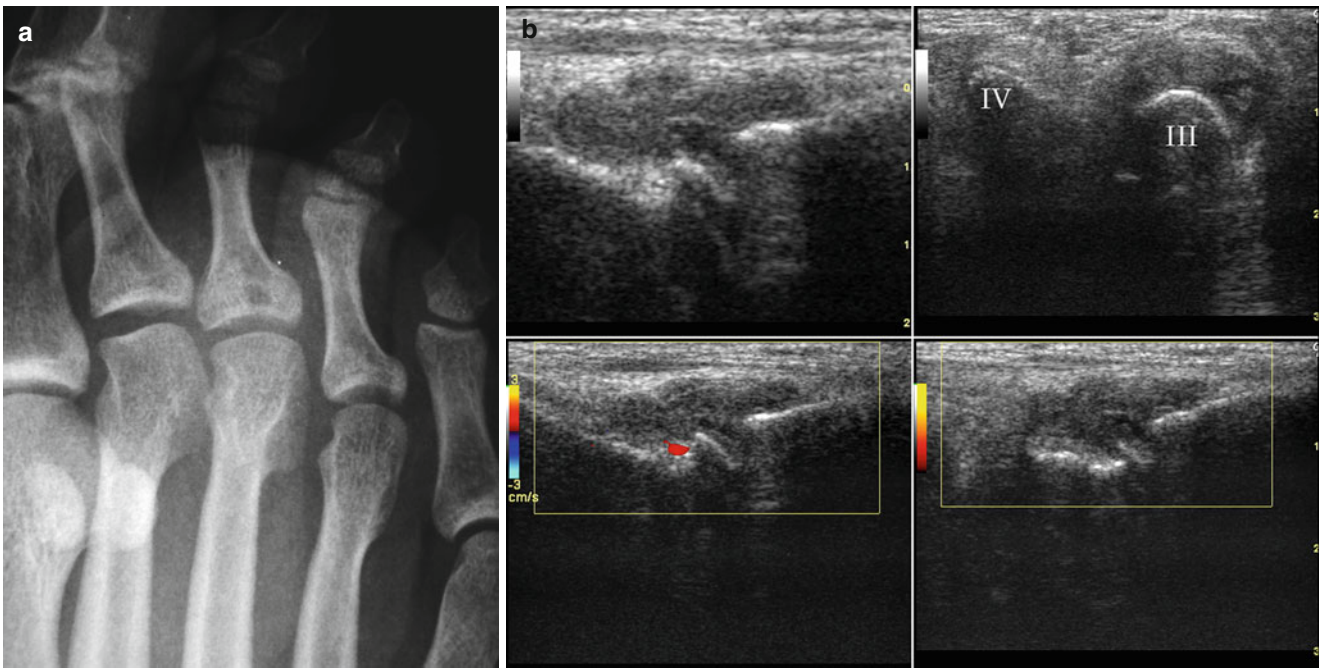

Fig. 4.12 Reactive arthritis with 6 months of evolution in a 15-year-old male adolescent (same patient of Fig. 1.14). Radiograph of the left foot (**a**) discloses a subchondral lucency in the proximal phalanx of the third toe and faint periosteal reaction along this bone. US of the third metatarsophalangeal joint (**b**) shows heterogeneous joint effusion and marked synovial thickening (*upper row*); in spite of the prominent synovial proliferation, Doppler US shows only mild hyperemia (*lower row*). T1-WI (**c**, *left*) reveals joint effusion, circumferential bone erosions in the head of the third metatarsal and synovitis, with adjacent bone marrow edema pattern on fat sat T2-WI (**c**, *right*), and intense enhancement of the inflamed tissues on post-gadolinium fat sat T1-WI (**d**). In addition to arthritis of the third metatarsophalangeal joint, bone scintigraphy (*left image*, **e**) also discloses increased uptake on both sacroiliac joints, indicative of active sacroiliitis (**e**, *right image*)

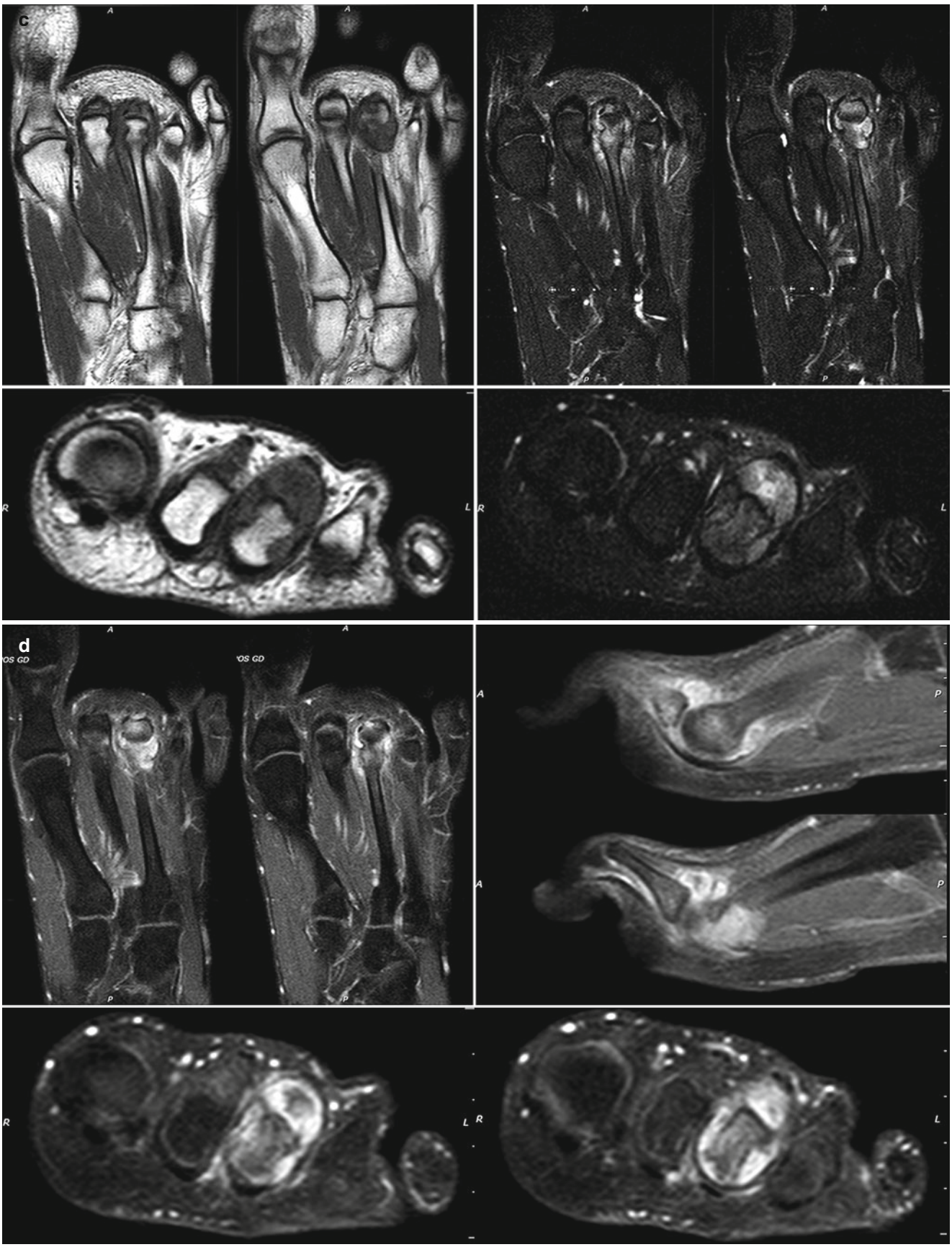

Fig. 4.12 (continued)

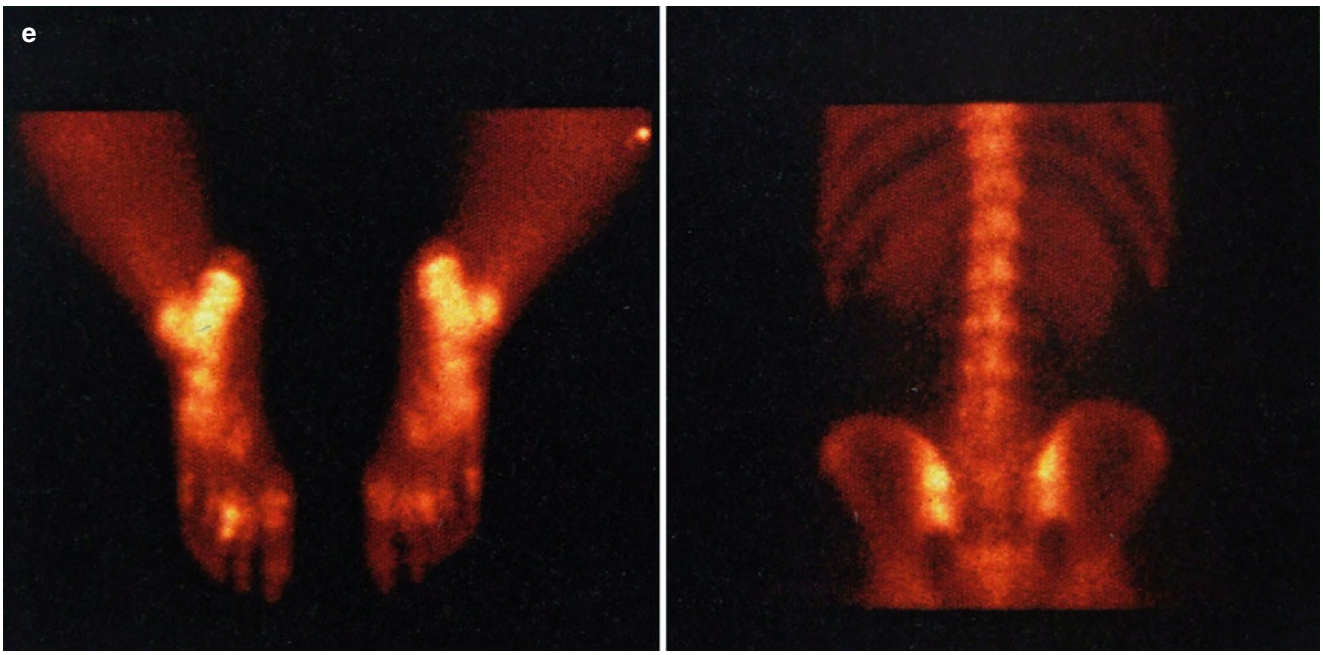

Fig. 4.12 (continued)

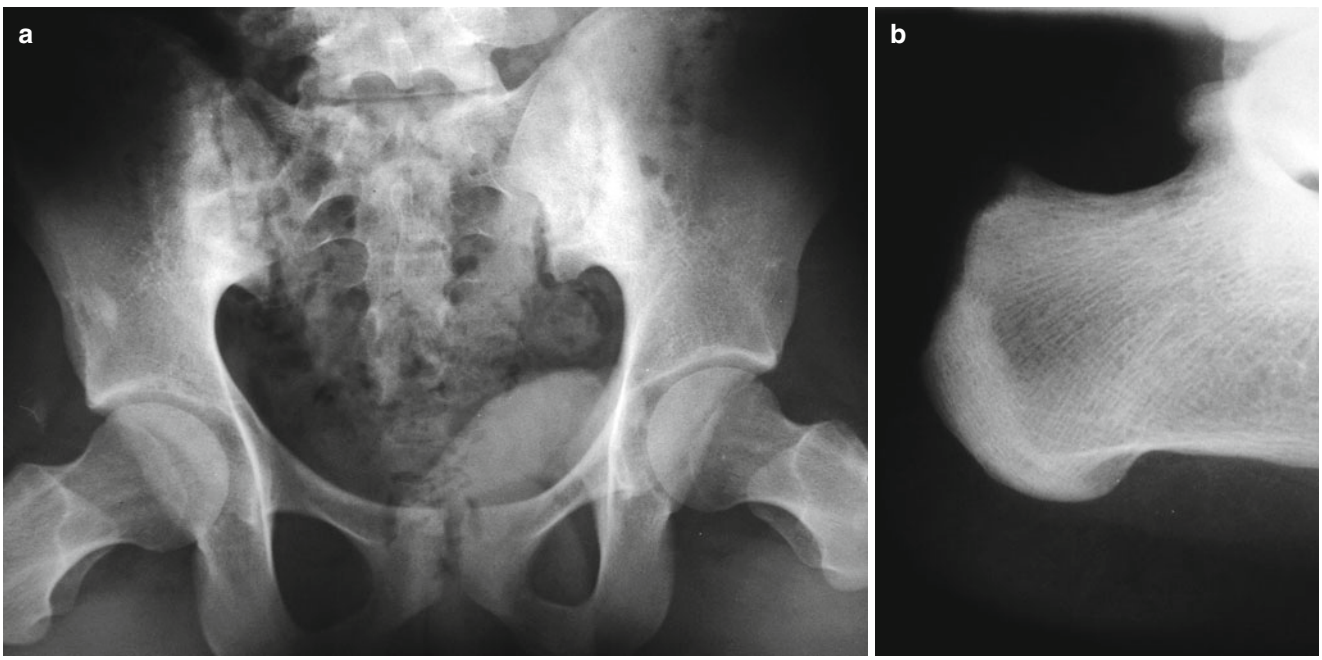

Fig. 4.13 A 19-year-old male with reactive arthritis since adolescence. Pelvic radiograph (**a**) shows bilateral sacroiliitis, with subchondral erosions and sclerosis. Lateral view of the left calcaneus (**b**) discloses signs of enthesopathy at the insertion of the Achilles tendon, with cortical irregularity, erosions, and bone neoformation

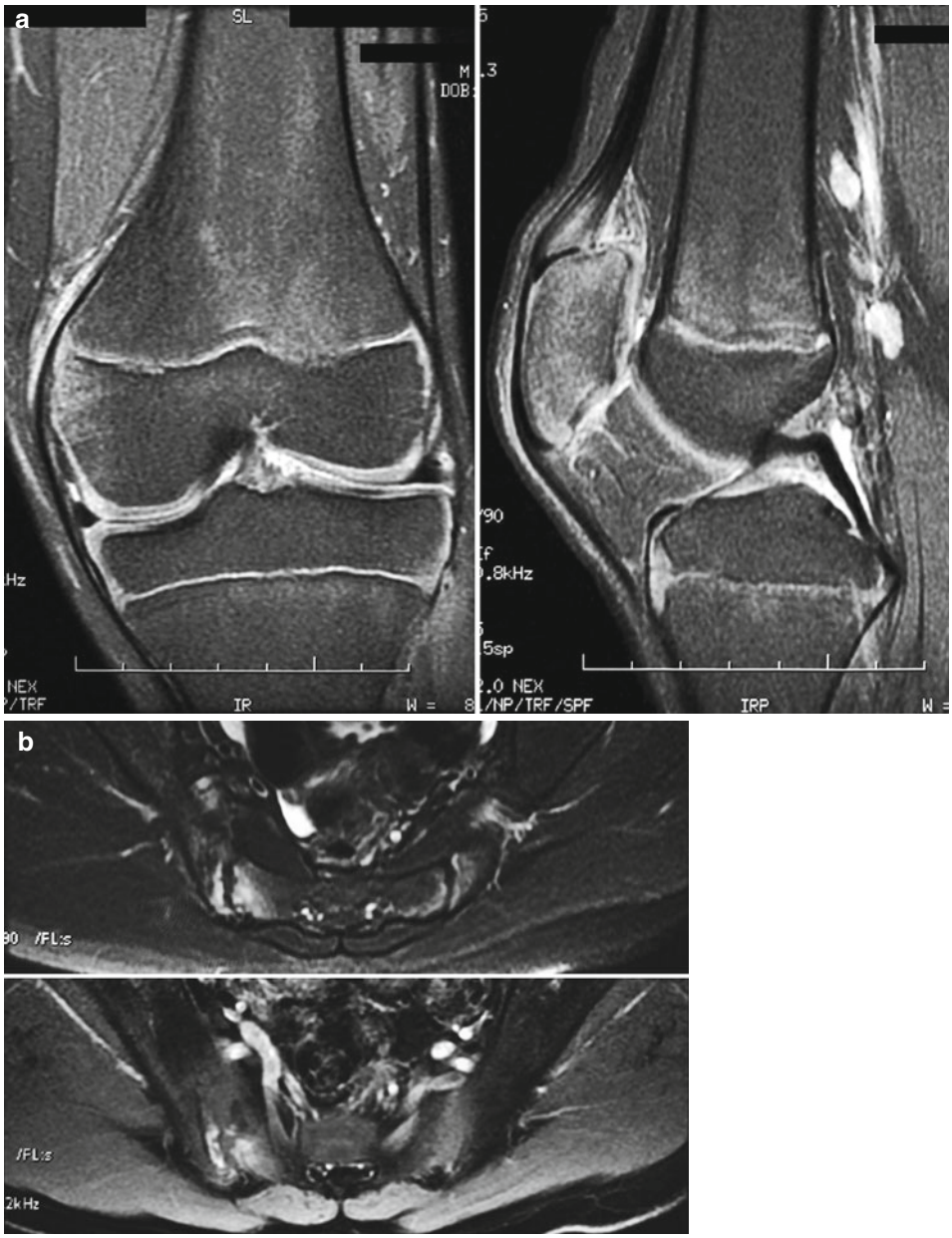

Fig. 4.14 A 14-year-old patient with reactive arthritis. In (**a**), fat sat PD-WI of the left knee in the coronal (*left*) and sagittal (*right*) planes show enthesopathy at the insertion of the quadriceps tendon (which is thickened and heterogeneous) and at the origin of the medial collateral ligament, with adjacent bone marrow edema pattern and soft-tissue swelling. Mild synovitis is also present, and enlarged lymph nodes can be seen in the popliteal fossa. Bilateral sacroiliitis is evident on a transverse STIR image (**b**, *upper image*), more important at right, with post-gadolinium enhancement on fat sat T1-WI (**b**, *lower image*)

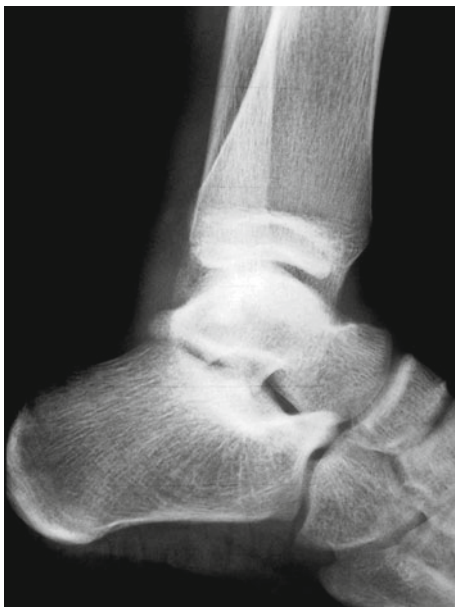

Fig. 4.15 A 12-year-old child with reactive arthritis in the left ankle and knee. Radiograph of the affected ankle shows only mild soft-tissue swelling, without further findings

4.3 Pediatric Collagen Vascular Disorders

4.3.1 Juvenile Dermatomyositis

Despite its rarity, juvenile dermatomyositis (JDM) is the most common of the noninfectious inflammatory myopathies of childhood, affecting mainly school-aged females around 6–7 years of age. Patients with JDM present proximal and symmetric muscle weakness and high serum levels of muscle enzymes; unlike adult-onset dermatomyositis, JDM is not associated with increased incidence of malignancies and prognosis is usually good.

Arthritis is typically transient, non-erosive, and nondeforming. Oligoarthritis occurs in two-thirds of the affected patients, and polyarthritis is found in the remaining; knees, wrists, elbows, and fingers are the most frequently involved joints, and marked osteoporosis may be present (Fig. 4.16). Dystrophic calcinosis is a characteristic feature of chronic JDM, occurring predominantly in superficial locations (mostly in the elbows and the knees). The calcific deposits are rarely present at onset, appearing later during the course of

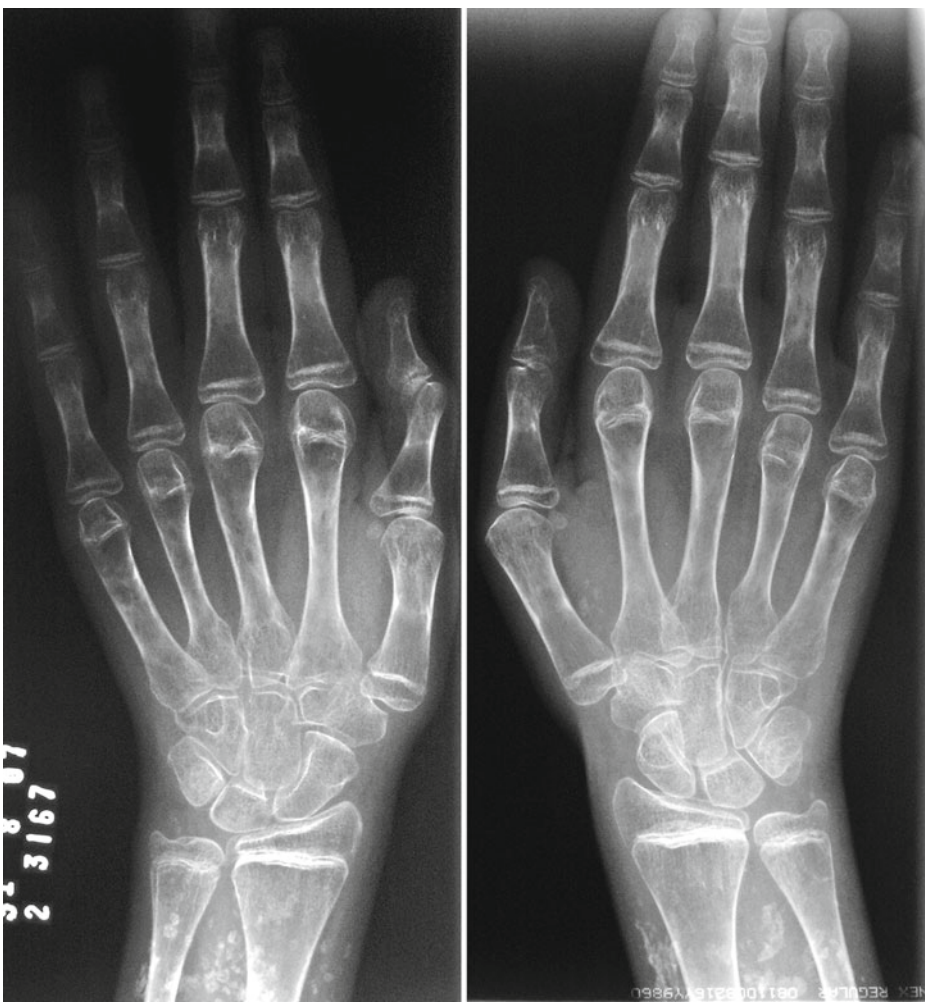

Fig. 4.16 Arthritis of hands and wrists in a child with JDM. In spite of subtle subluxation of the metacarpophalangeal joints of the thumbs, more evident at right, there are no signs of erosive arthritis. Soft-tissue swelling and generalized osteoporosis are also present, as well as symmetric and bilateral calcifications in the soft tissues of the forearms

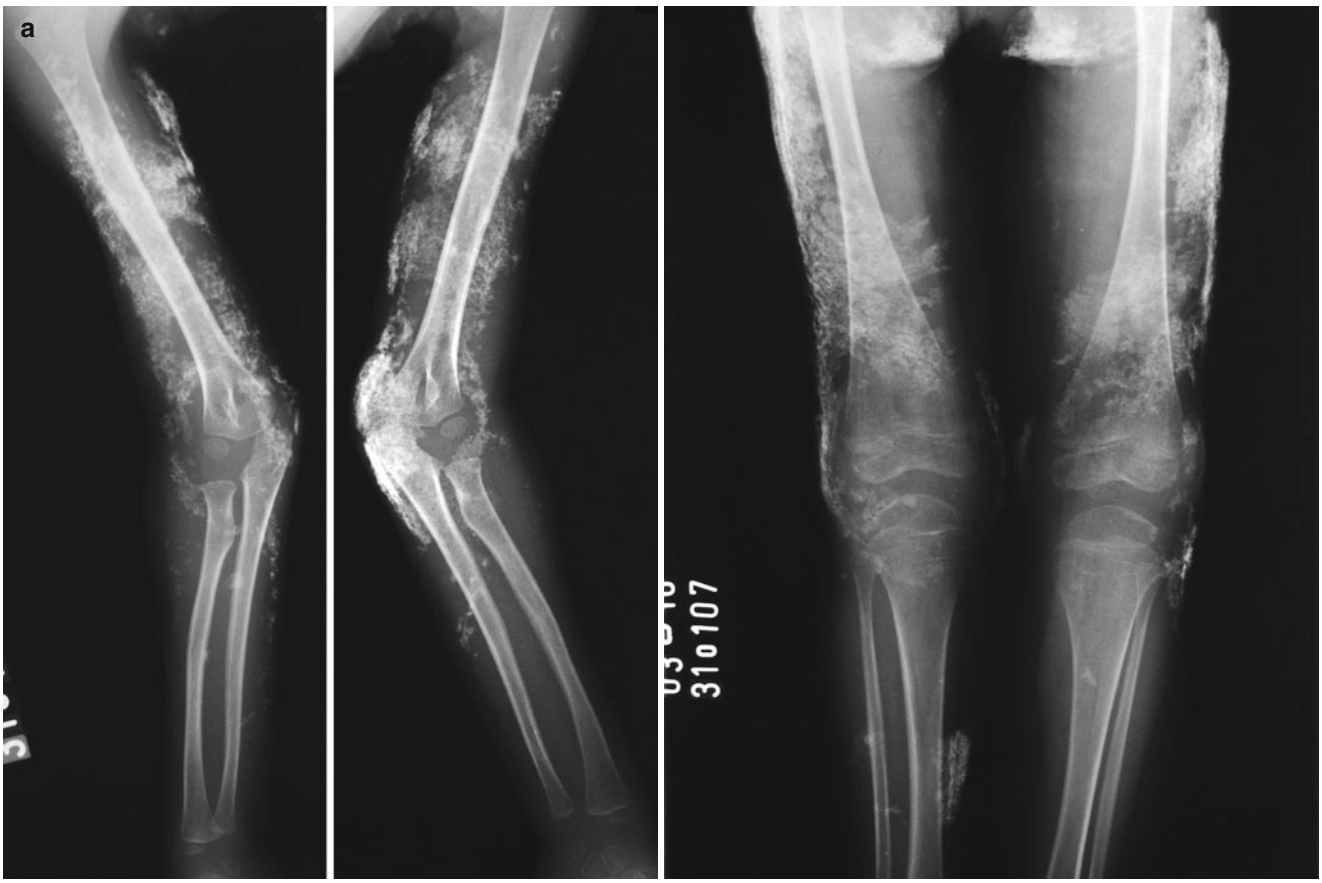

Fig. 4.17 A 3-year-old child with JDM. Radiographs show extensive, confluent plaques of calcification in the soft tissues of the upper limbs (**a**) and lower limbs (**b**), predominantly located in the elbows and in the proximal portions of the thighs and arms

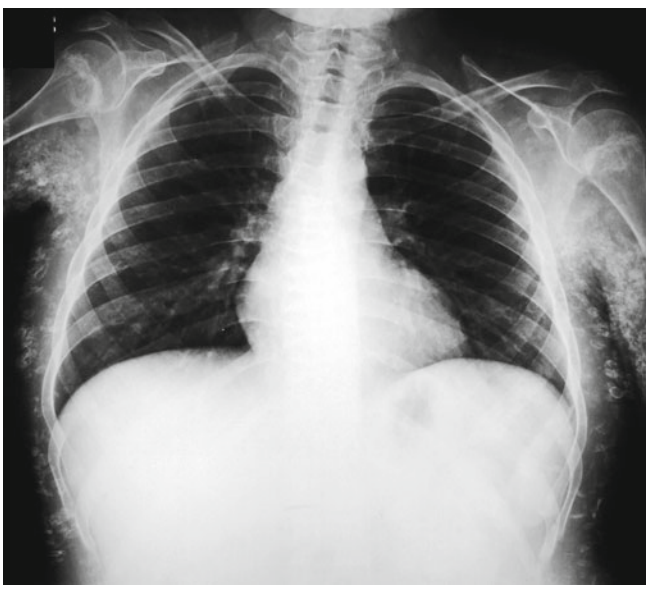

Fig. 4.18 Chest X-ray of an adolescent with long-standing JDM. There are multiple calcifications in the soft tissues of the chest wall and of the arms

the disease as superficial skin nodules, deeply seated deposits, and calcified plaques along fascial planes or in a widespread "exoskeleton" pattern (Figs. 4.16, 4.17, 4.18, 4.19, and 4.20).

Concerning myositis, radiographs are nonspecific and fairly insensitive for assessment of the acute phase. In long-standing JDM, radiographic findings include muscle atrophy, muscular calcifications (Fig. 4.19), and flexion deformities. US findings in the acute phase of myositis include increased volume and echogenicity of the affected muscles, while there is muscle atrophy in late-stage JDM; fibrosis/calcifications appear as hyperechogenic foci with posterior acoustic shadowing in the muscles and in the subcutaneous tissue (Fig. 4.20). CT is not useful for the assessment of active myositis, but it is the best imaging modality available to detect soft-tissue calcifications (Fig. 4.21). MRI is the preferred method to demonstrate edematous changes related to active inflammation (myositis, tenosynovitis, fasciitis, cellulitis) during the acute stage and the distribution of the disease; the adductor muscles of the thigh are affected more often. Moreover, it is a useful tool to monitor disease evolution and treatment response. Atrophy and fatty replacement of the affected muscles related to long-standing

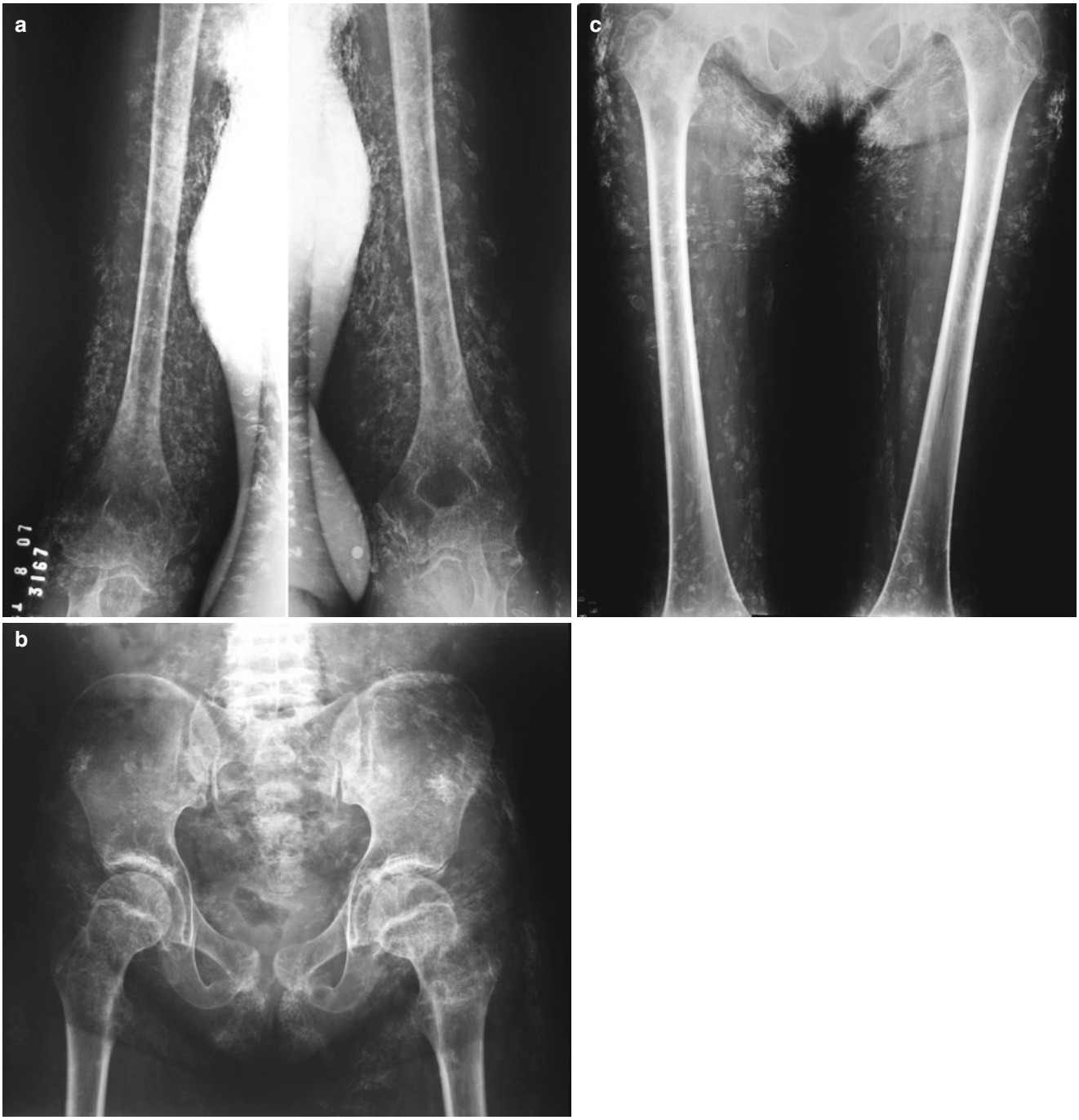

Fig. 4.19 Bizarre calcinosis (exoskeleton-like pattern) is seen on the radiographs of this adolescent with JDM, involving the soft tissues of the upper limbs (**a**), of the pelvis (**b**), and of the lower extremities (**c**). Diffuse osteoporosis is also evident

JDM are also evident on MRI, as well as foci of fibrosis/calcification, which appear hypointense in all sequences (Fig. 4.22). However, MRI is limited for the detection of calcifications, and even large plaques that would be easily seen on radiographs can be missed. Both US and MRI may be used to guide muscle biopsy, detecting areas in which active myositis is present; MRI is more sensitive, but US is less costly and more convenient in children, with no need for sedation.

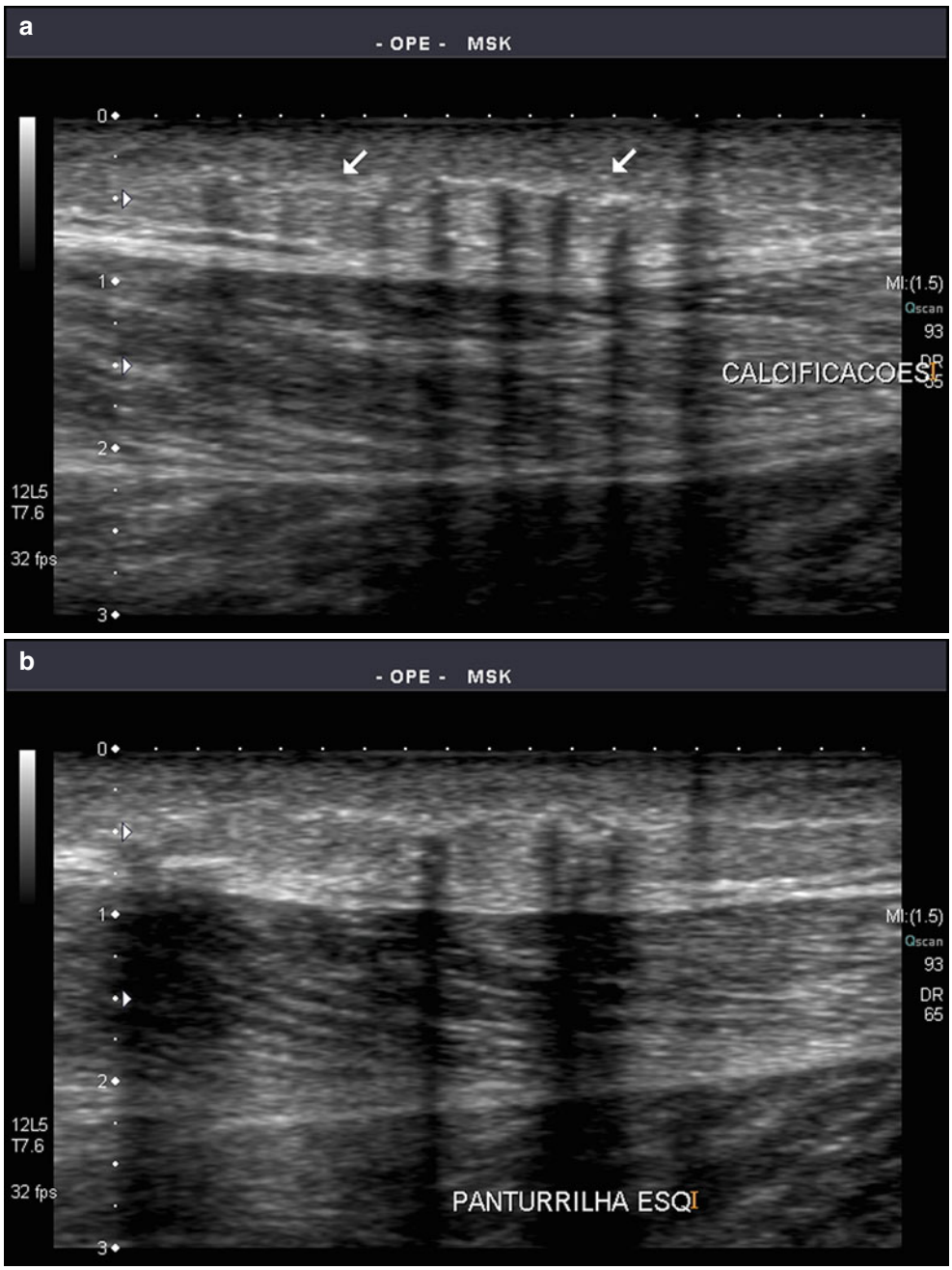

Fig. 4.20 On US, calcifications appear as hyperechogenic areas with variable posterior acoustic shadowing in the subcutaneous tissue (**a**–**c**), in the muscles or along the fascial planes (**d**), all of them seen in the left lower limb of the same patient. In this study, there are micronodular (**a** and **b**), nodular-clustered (**c**), and plaque-like (**d**) calcified deposits

Fig. 4.20 (continued)

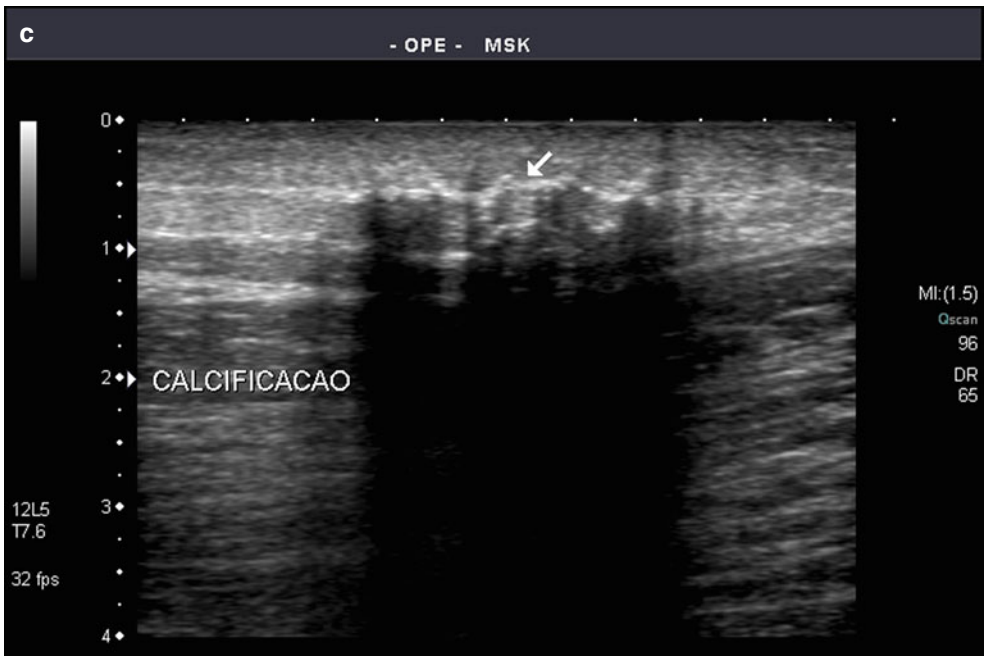

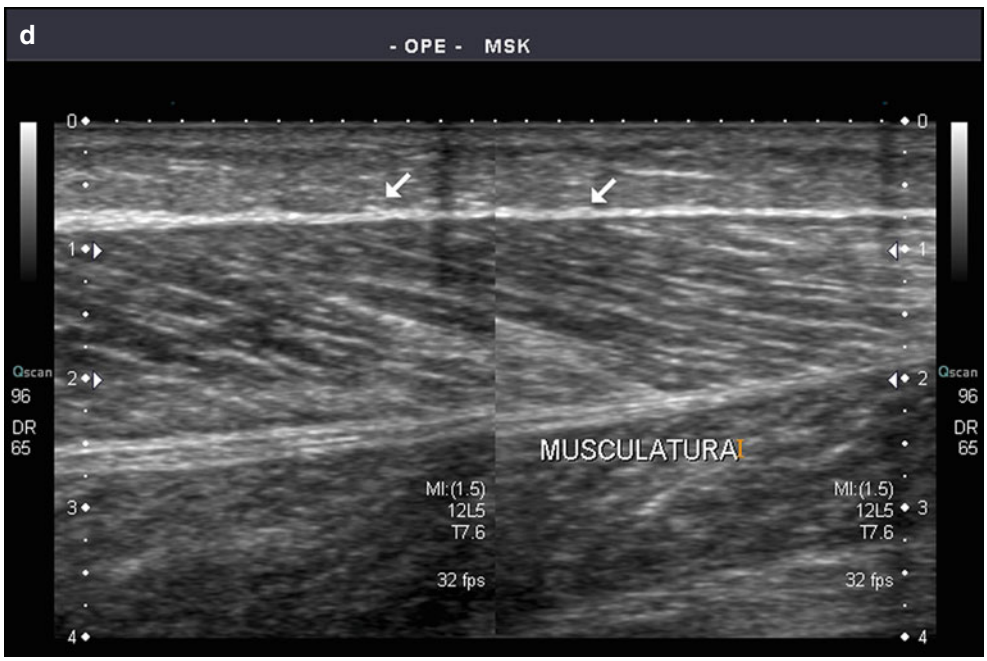

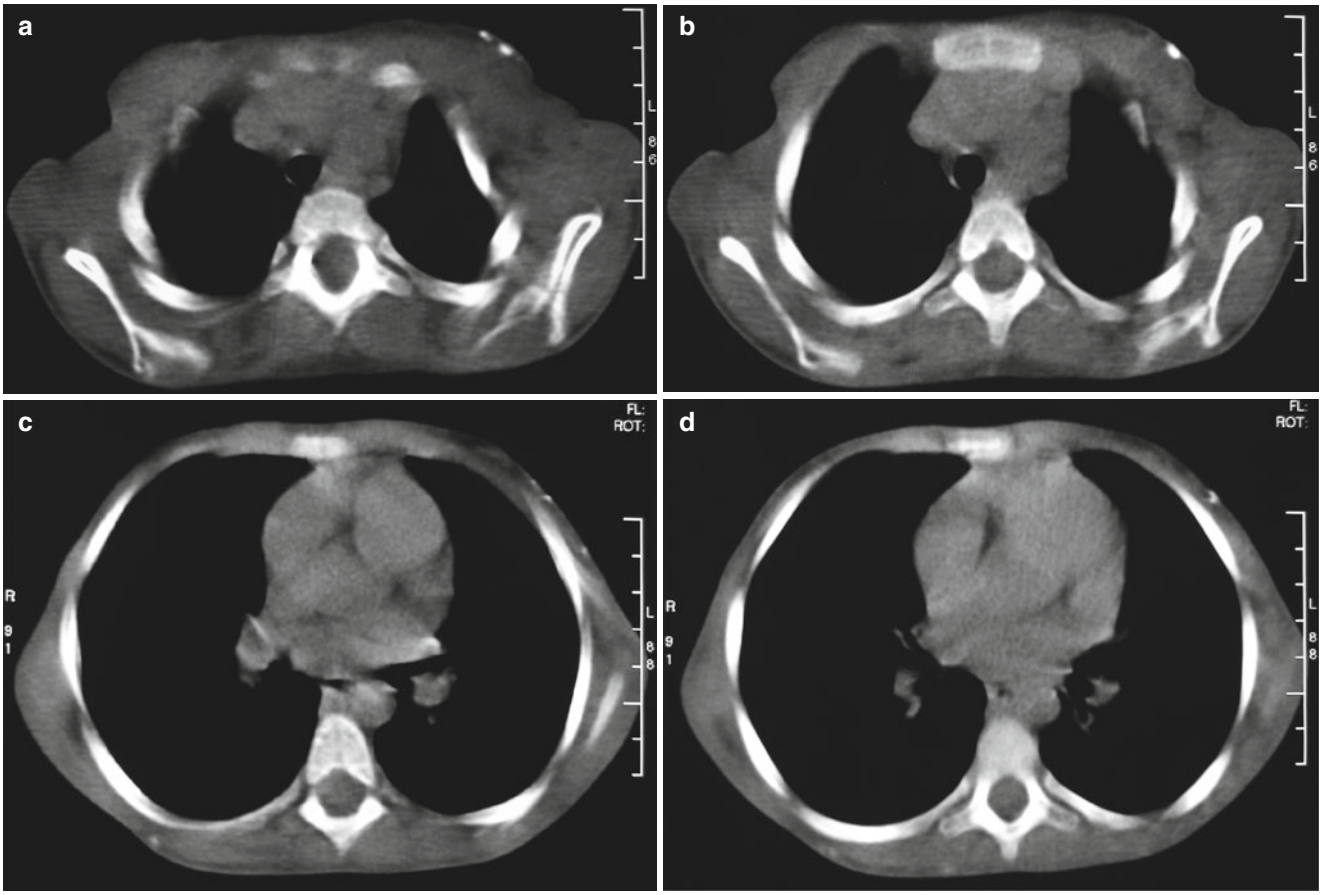

Fig. 4.21 CT of the chest of a child with JDM. Sequential images in the transverse plane with soft-tissue window settings demonstrate several superficial calcifications in the chest wall

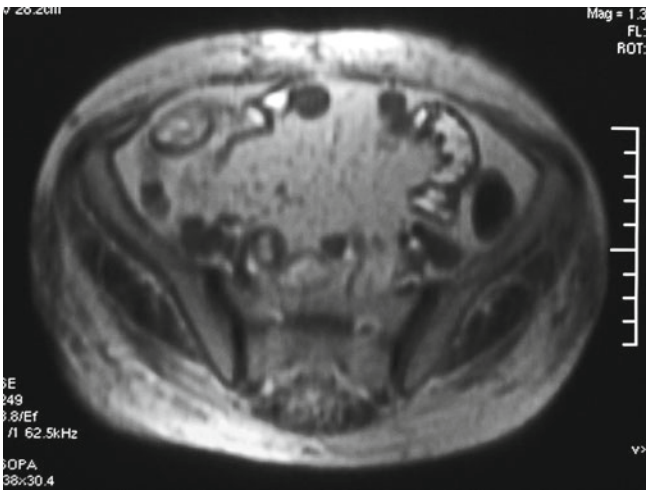

Fig. 4.22 Transverse T2-WI of the pelvis of a 16-year-old female with chronic JDM. There are striking atrophy and fatty replacement of the gluteal muscles, with hyperintense fat streaks permeating the muscle bellies. The anterior abdominal wall is markedly atrophic, with a strap-like appearance of the corresponding muscles. Subcutaneous calcinosis is also present, mainly in the buttocks, symmetric and bilateral, appearing as hypointense streaks across the gluteal fat

4.3.2 Pediatric Systemic Lupus Erythematosus

Pediatric systemic lupus erythematosus (PSLE) is the most common of the juvenile collagen vascular diseases. Approximately 20 % of all lupus patients are diagnosed before skeletal maturation, mostly females around age 12. The majority of these juvenile patients will present some kind of musculoskeletal involvement, being arthralgia/arthritis the most frequent manifestations. Affected children usually present bilateral and symmetric polyarthritis involving large and small joints; even though synovitis may be present, erosive articular disease is rare (Fig. 4.23). Other findings include periarticular osteoporosis, "swan neck" and "boutonniere" digital deformities (see Chap. 3), and ulnar deviation with volar subluxation of the metacarpophalangeal joints. Tenosynovitis is relatively frequent (Fig. 4.24), but myositis is rarely found. US is usually the first line of investigation for the assessment of arthritis and tenosynovitis in PSLE (Fig. 4.24), but MRI is more precise in determining the real extent of synovitis (Figs. 4.24, 4.25, and 4.26), allowing for early detection of erosions and osteochondral lesions (Fig. 4.26). One of the most feared complications of PSLE is avascular necrosis, which is more common in the femoral heads and in the tibial plateaus (Fig. 4.25).

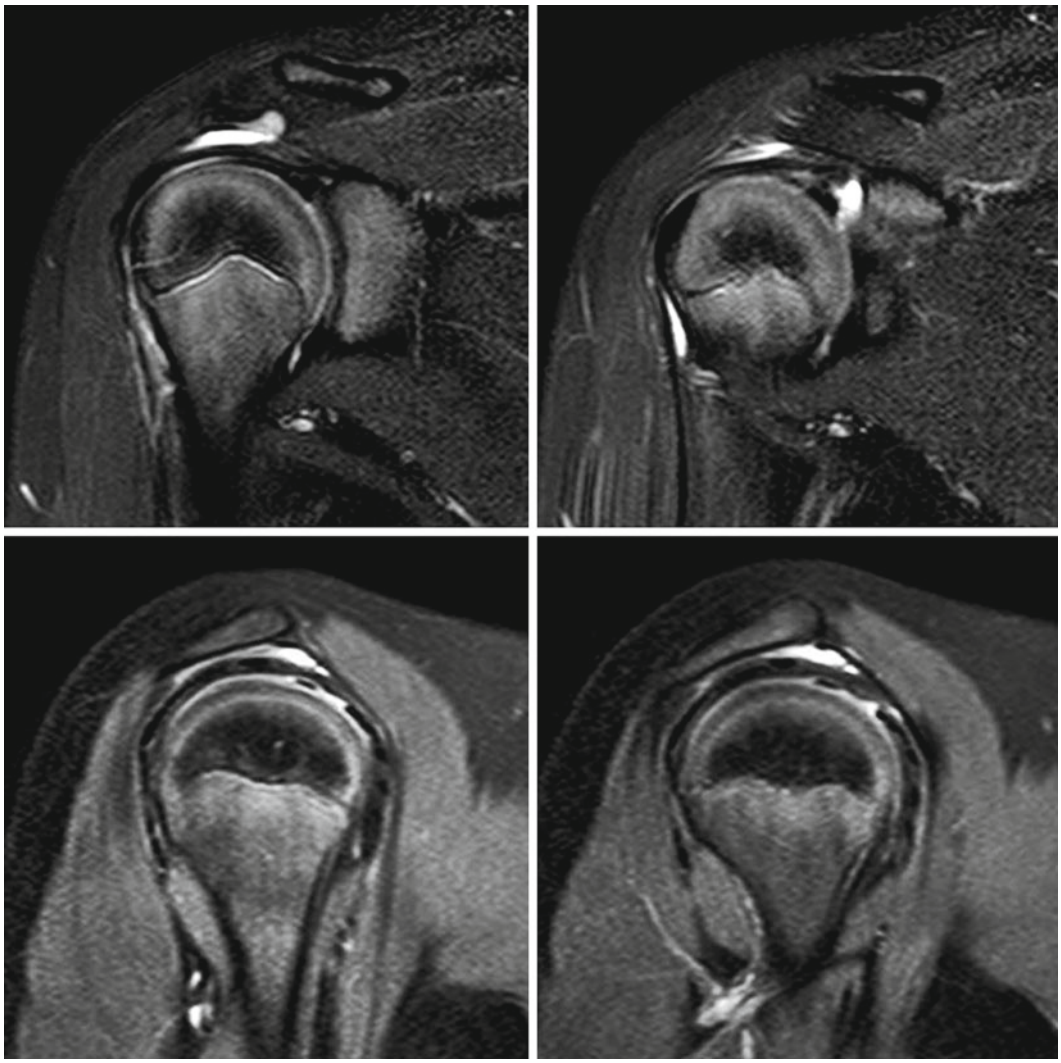

Fig. 4.23 A 14-year-old female with PSLE since age 8 complaining of right-sided shoulder pain. Coronal (*upper row*) and sagittal (*lower row*) fat sat PD-WI demonstrate fluid distension of the subacromial bursa, with no evidence of erosive arthropathy

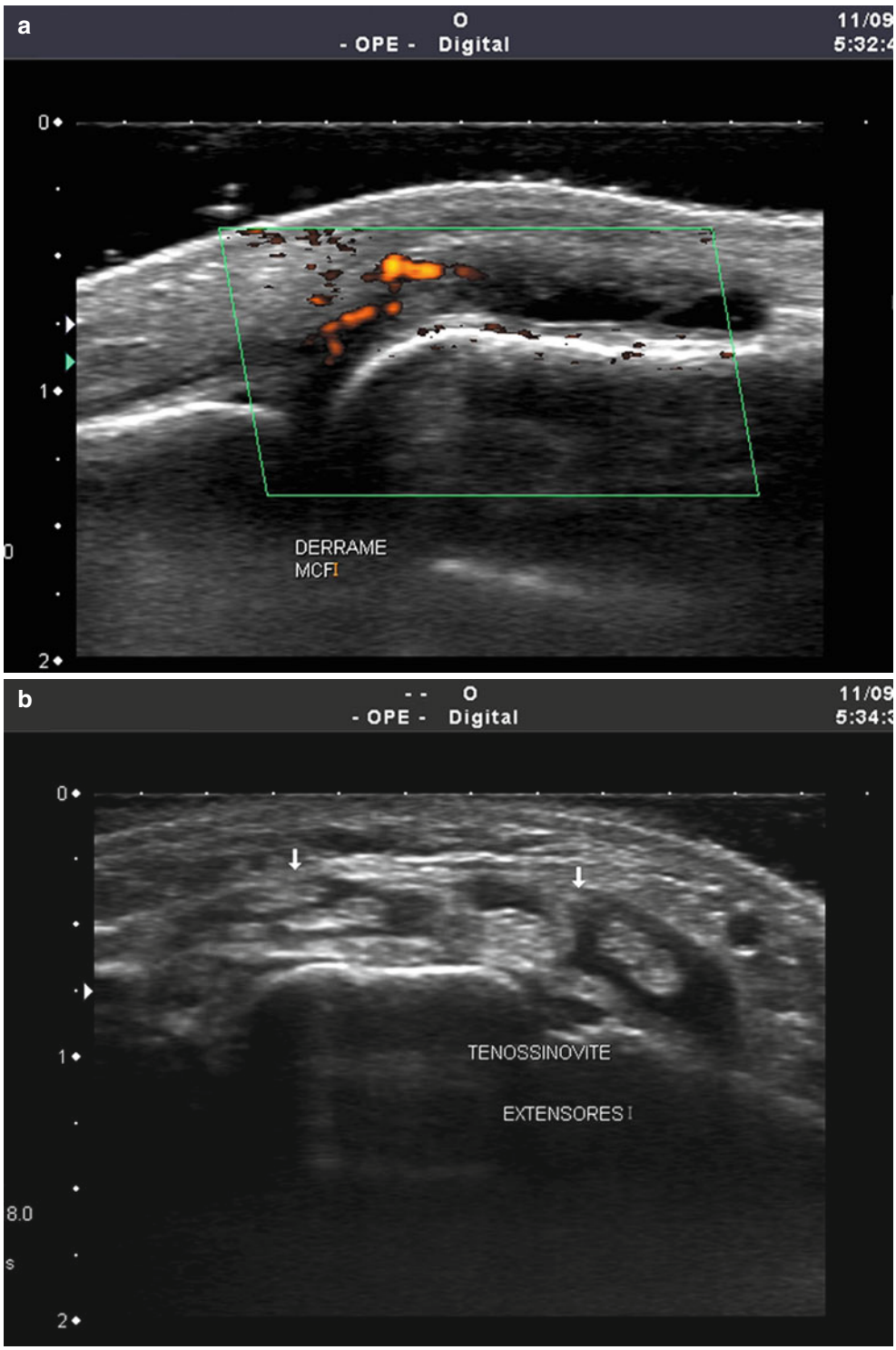

Fig. 4.24 A 15-year-old female with PSLE. In (**a**), Doppler US of the second metacarpophalangeal joint of the right hand reveals joint effusion, synovial thickening, and increased blood flow (*orange-colored* areas). In (**b**), the extensor tendons at the level of the wrist are surrounded by heterogeneous, hypoechogenic material, corresponding to fluid and thickened synovium. Coronal STIR image (**c**, *left*) and post-gadolinium fat sat T1-WI (**c**, *right*) reveal non-erosive arthritis of the proximal interphalangeal joints and, more importantly, of the metacarpophalangeal joints, much more evident on post-contrast T1-WI because of the enhancement of the inflamed synovium. In (**d**), in addition to metacarpophalangeal arthritis, transverse STIR images (*left*) and post-gadolinium fat sat T1-WI (*right*) also disclose flexor and extensor tenosynovitis. Fluid distension of the flexor tendon sheaths is quite evident, as well as ruptures of the radial sagittal bands of the extensor mechanisms from the second to the fourth digits, with ulnar subluxation of the central extensor tendons

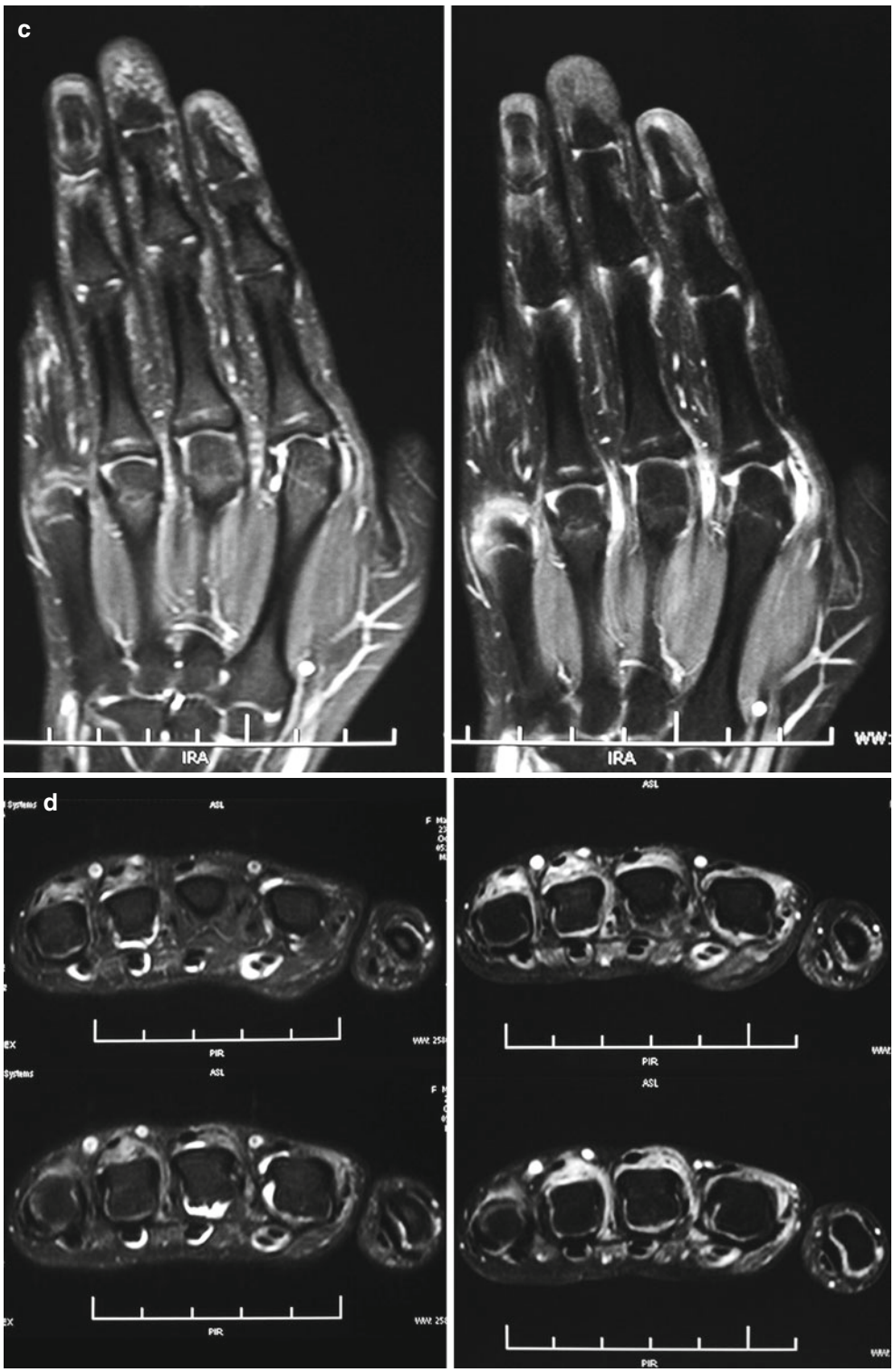

Fig. 4.24 (continued)

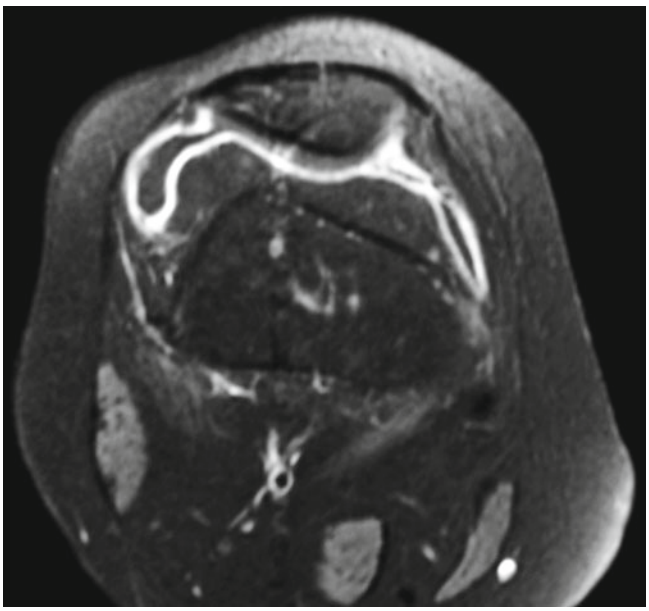

Fig. 4.25 Transverse post-gadolinium fat sat T1-WI of the left knee of an adolescent with PSLE displaying diffuse enhancement of the thickened synovium and erosions in the patellar cartilage. This patient had several areas of avascular necrosis in the proximal tibia and in the distal femur, the latter partially seen in this image as a geographic lesion in the medullary bone, displaying abnormal enhancement

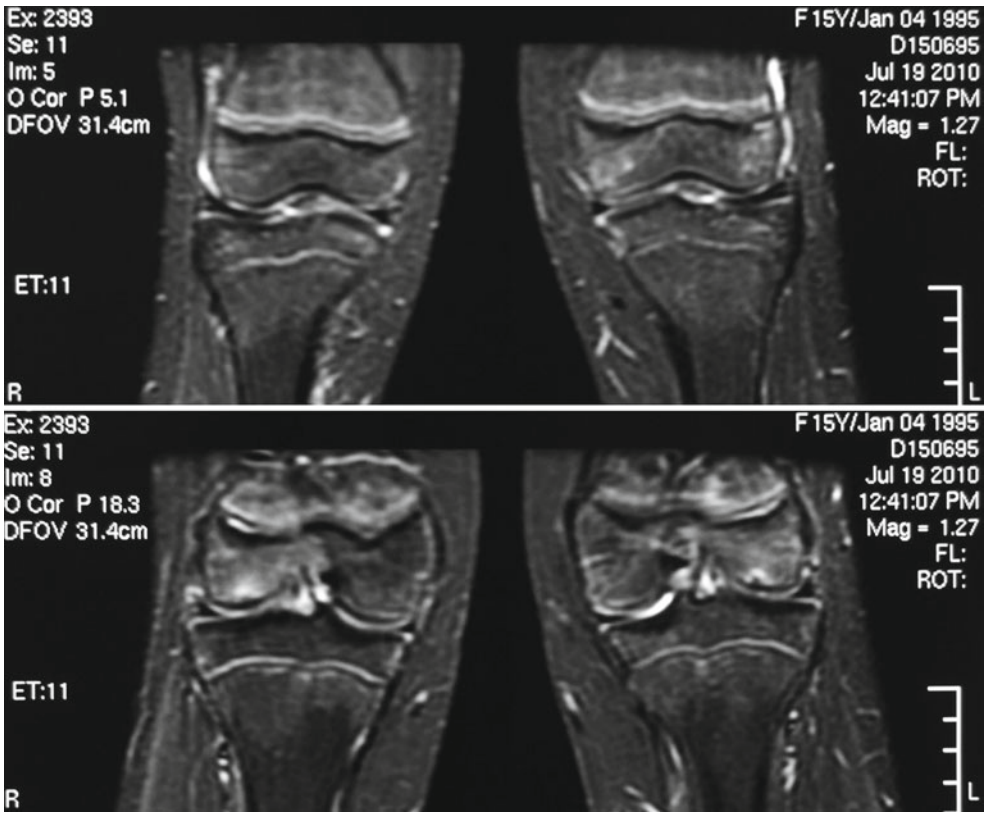

Fig. 4.26 Coronal STIR images of both knees of a 15-year-old female patient with PSLE and lupus arthropathy demonstrating osteochondral lesions in the joint surfaces of both lateral femoral condyles, surrounded by bone marrow edema pattern and associated with small joint effusion

4.3.3 Juvenile Systemic Sclerosis and Juvenile Localized Scleroderma

Scleroderma is a generic denomination applied to a group of connective tissue diseases characterized by excessive deposition of collagen, cutaneous fibrosis, and skin induration. There are two major subtypes, one of them characterized by cutaneous sclerosis and involvement of the internal organs, named systemic sclerosis, and the other predominantly limited to skin involvement, called localized scleroderma (or morphea). In any of these subtypes, juvenile scleroderma is defined by onset before age 16, being rarer than the classic adult form.

Juvenile systemic sclerosis (JSS) is the less frequent among the juvenile variants of scleroderma, affecting mainly females between 10 and 16 years of age. Arthritis (which is an early finding in JSS) and myositis are more prevalent than in adult-type disease. On the other hand, localized juvenile scleroderma (LJS) is ten times more frequent than JSS, more common in females, with disease onset usually occurring around age 7. The clinical spectrum of LJS varies from small plaques of cutaneous sclerosis to extensive dermatofibrosis, but the most common form is linear scleroderma, characterized by one or more band-like areas of skin induration that usually occur asymmetrically, in one of the limbs. When the face is involved, lesions are typical, varying from scleroderma "en coup de sabre" (asymmetric band-like lesion affecting the scalp and the supraorbital region – Fig. 4.27) to Parry-Romberg syndrome (a more diffuse condition in which there is progressive facial atrophy, affecting mostly the skin and the subcutaneous tissue – Fig. 4.28). US may show calcifications, sclerosis, and atrophy in the affected soft tissues. MRI is more accurate in demonstrating the real extent of the lesions and to monitor disease activity: if active inflammation is present, the dermis appears thickened, with edema of the subcutaneous tissue and post-gadolinium enhancement, while chronic lesions show skin atrophy, without inflammatory signs (Fig. 4.27). Articular involvement is the most common extracutaneous manifestation in LJS, affecting roughly 20 % of the patients. Arthritis is usually non-erosive and asymmetric, often associated with rapidly progressive disease in which there is predominance of osteoarticular abnormalities; early development of flexion deformities and tenosynovitis may also occur (Figs. 4.29 and 4.30). Reduced thickness of the soft tissues of the digital extremities, acro-osteolysis, and subcutaneous calcifications are late findings. There may be widening of the periodontal ligament space and edentulism (Fig. 4.31).

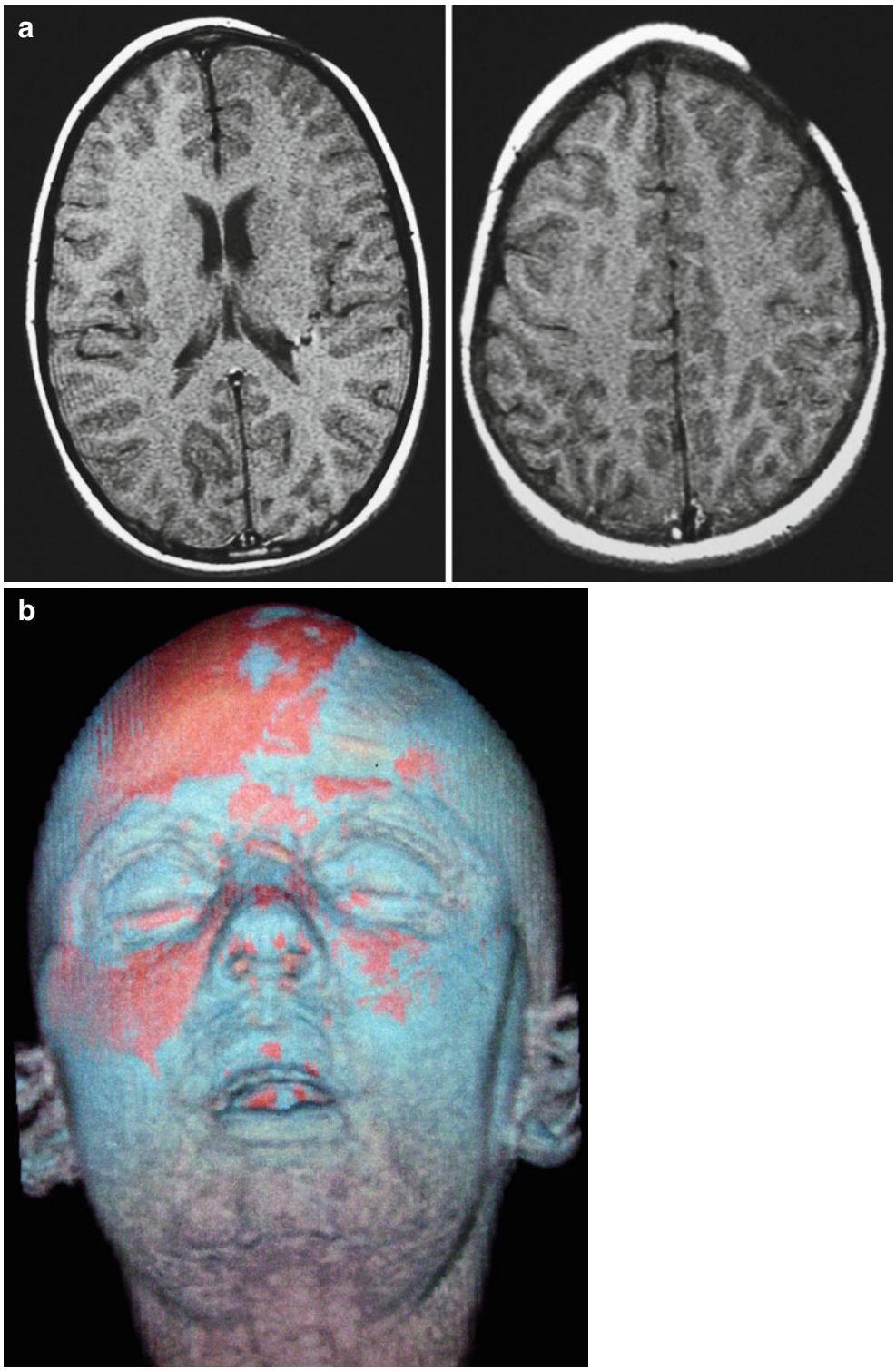

Fig. 4.27 Scleroderma "en coup de sabre" affecting the left hemiface of a 6-year-old male. In (**a**), transverse T1-WI demonstrates low signal intensity of the affected skin and subcutaneous tissue, with full-thickness atrophy of the soft tissues of the forehead and scalp. In (**b**), volume-rendered reconstruction of a volumetric 3D sequence displays the typical lesion of this type of scleroderma, with a band-like depression of the skin surface affecting the left supraorbital region and the scalp

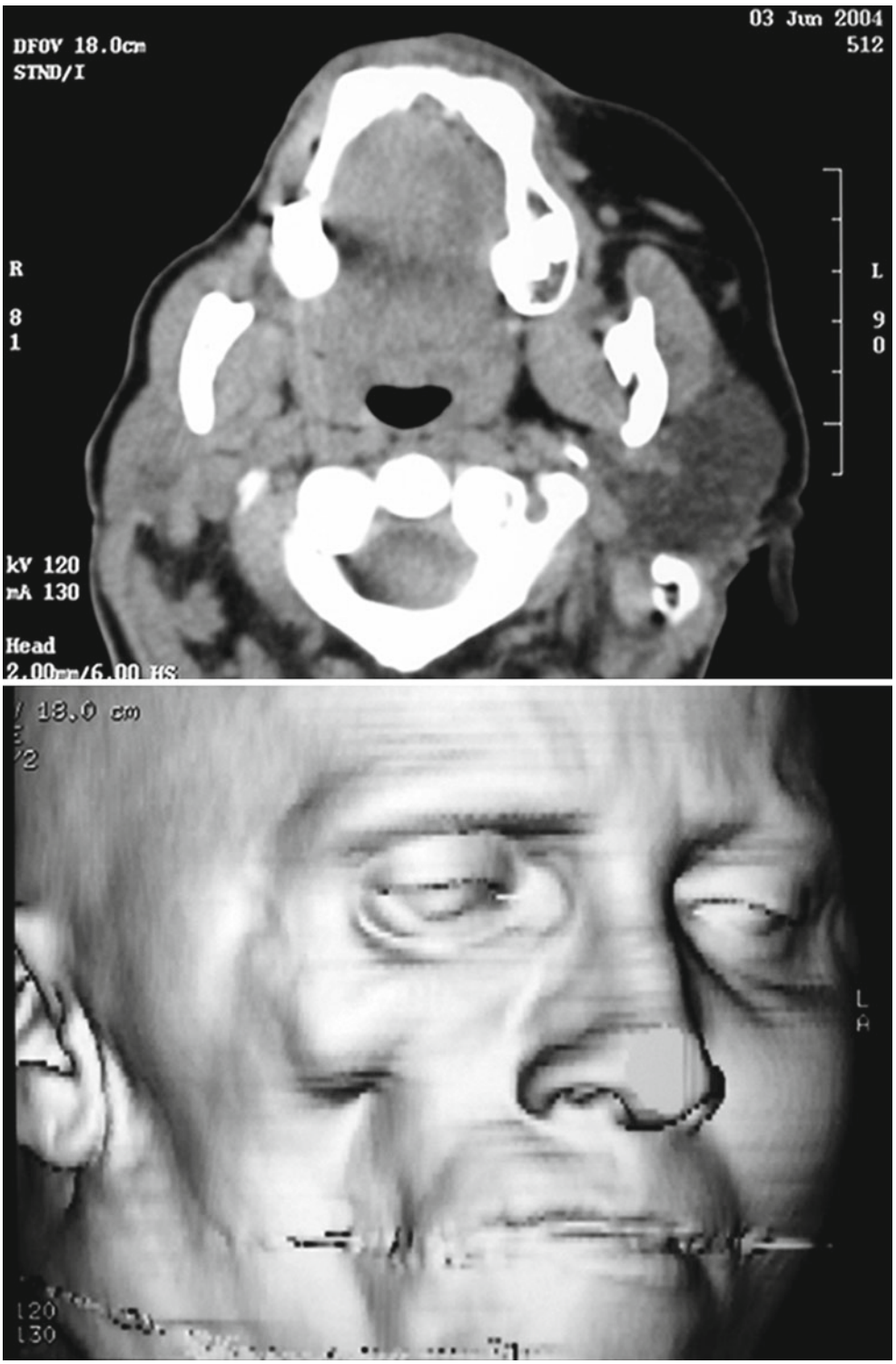

Fig. 4.28 Parry-Romberg syndrome in an adult patient, with 10 years of evolution. The *upper image* is a transverse CT section displaying marked atrophy of the right hemiface at the expense of skin and subcutaneous tissue. In the *lower image*, a volume-rendered reconstruction shows facial hemiatrophy with extensive wasting of the soft tissues and prominence of the zygomatic arch under the skin surface. These findings are similar to those seen in the juvenile form of the disease

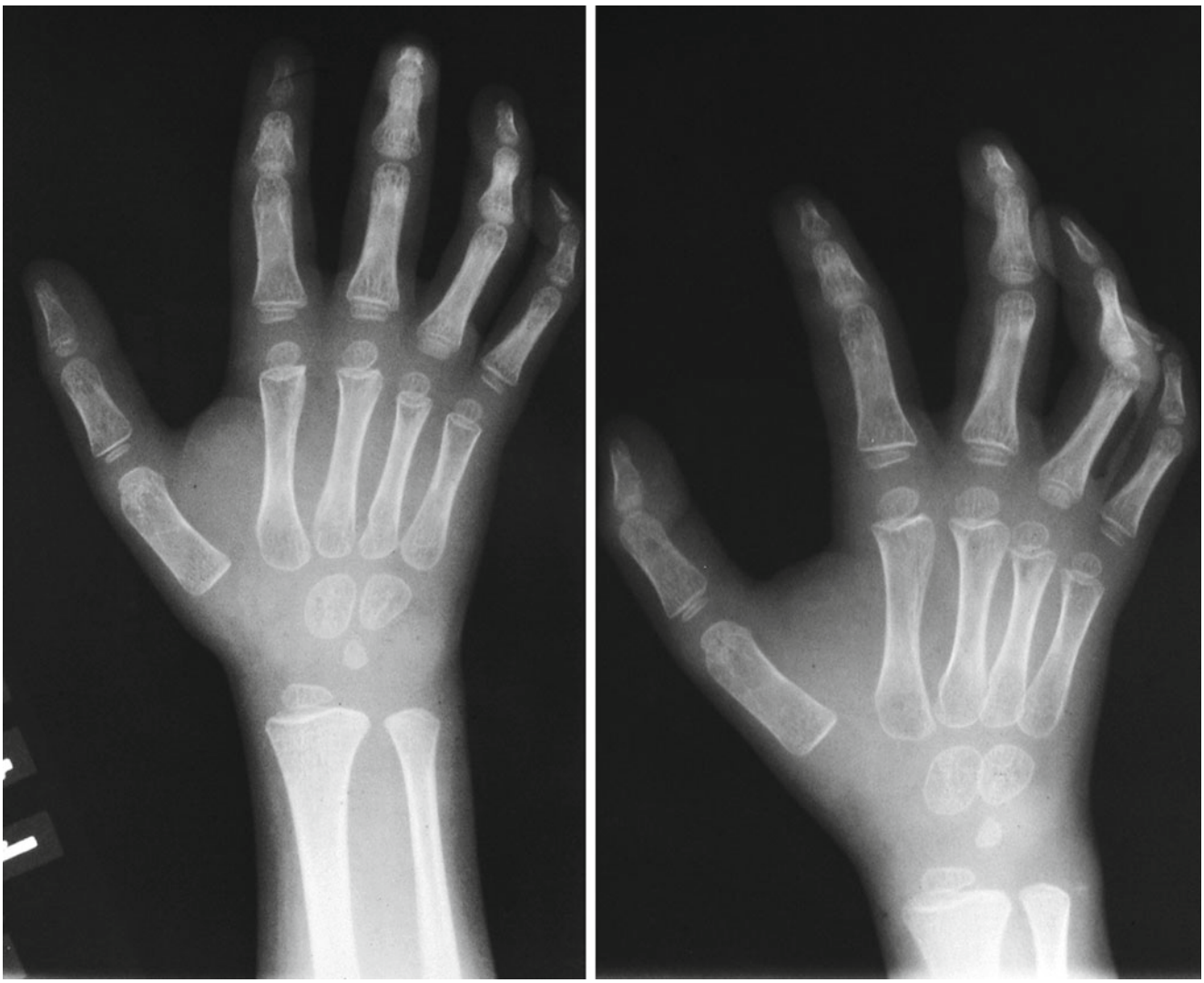

Fig. 4.29 Radiographs of the left hand of a 5-year-old boy with juvenile scleroderma and sclerodactyly. In spite of the absence of erosive arthropathy, flexion deformities are already present, affecting the proximal interphalangeal joints from the second to the fifth digits. Diffuse osteoporosis is also evident

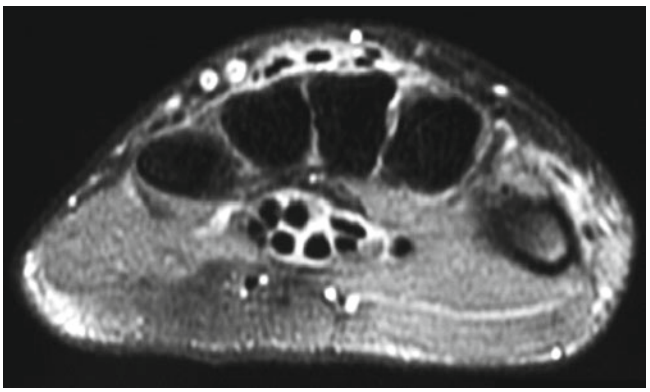

Fig. 4.30 Transverse fat sat T2-WI of the right wrist of a young female with scleroderma shows increased signal intensity in the soft tissues adjacent to the tendons, related to tenosynovitis. The tendons present normal appearance

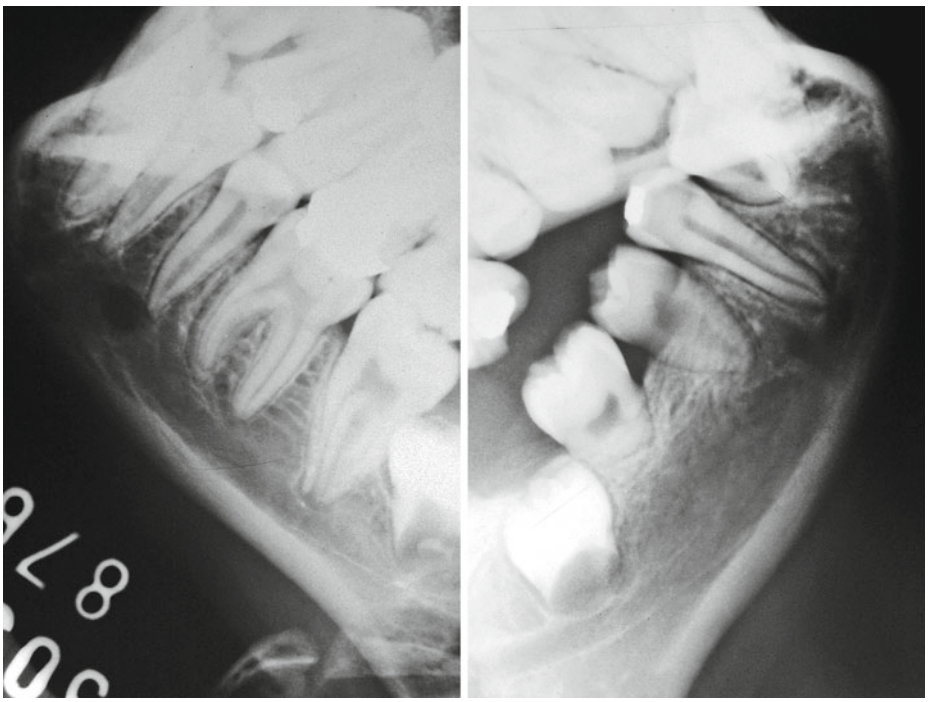

Fig. 4.31 Widening of the periodontal ligament space is seen in the jaw of a patient with juvenile scleroderma, with periapical lucencies in several teeth. Partial edentulism is already present, even prior to the eruption of the third molars

4.3.4 Mixed Connective Tissue Disease

Mixed connective tissue disease (MCTD) is a controversial condition, with protean clinical presentation and highly variable clinical course. Even though almost one-fourth of all described patients are children, pediatric MCTD is rare and presents a more benign course when compared to the adult type. Affected individuals typically present Raynaud phenomenon and positivity for anti-RNP antibody, usually developing into one of the major connective tissue diseases or into an overlap syndrome. Disease onset usually occurs between the end of childhood and the beginning of adolescence, and females are predominantly affected. Arthritis is common, of variable severity. Myositis may affect up to two-thirds of these patients, indistinguishable on imaging from that found in JDM. It has been described that dermatomyositis-related findings, commonly found at presentation, tend to involute during the course of the disease, while scleroderma-related abnormalities increase in frequency with time.

Key Points

- Unlike their adult counterparts, juvenile spondyloarthropathies present predominantly peripheral joint involvement at onset, while spondylitis/sacroiliitis are late findings. As radiographs are often normal, US and MRI – mainly the latter – are the most useful methods for the assessment of peripheral arthritis. MRI is the method of choice for evaluation of sacroiliitis.
- Distinctive features of JAS include asymmetric oligoarthritis and enthesitis. Sacroiliitis is prototypical, similar to that of the adult form of the disease.
- Periostitis is more prominent and there is less enthesopathy in JPA if compared to JAS. Patients usually present asymmetric oligoarthritis of the distal interphalangeal joints of the hands, and dactylitis is a typical finding.
- Arthritis associated with inflammatory bowel disease in children is most often an oligoarthritis that affects peripheral joints. Only a minority of these patients will present sacroiliitis/spondylitis.
- Reactive arthritis usually presents as a self-limited monoarthritis or oligoarthritis, involving most often the lower limbs. Erosive arthropathy, enthesitis, and sacroiliitis are occasionally found.
- Osteoarticular manifestations are not among the most prominent features of pediatric collagen vascular disorders. Nevertheless, from an imaging standpoint, there are some noteworthy features. Myositis and dystrophic calcinosis are typical of JDM, while cutaneous/subcutaneous areas of inflammation are characteristic of juvenile scleroderma, leading to skin atrophy and fibrosis. Non-erosive arthritis, tenosynovitis, and avascular necrosis are the most common findings in patients with PSLE. Arthritis and myositis are not uncommon in pediatric MCTD.

Recommended Reading

Babyn P, Doria AS (2007) Radiologic investigation of rheumatic diseases. Rheum Dis Clin North Am 33(3):403–440

Buchmann RF, Jaramillo D (2004) Imaging of articular disorders in children. Radiol Clin North Am 42(1):151–168

Burgos-Vargas R (2002) The juvenile-onset spondyloarthritides. Rheum Dis Clin North Am 28(3):531–560

Daldrup-Link HE, Steinbach L (2009) MR imaging of pediatric arthritis. Magn Reson Imaging Clin N Am 17(3):451–467

Eshed I, Bollow M, McGonagle DG, Tan AL, Althoff CE, Asbach P et al (2007) MRI of enthesitis of the appendicular skeleton in spondyloarthritis. Ann Rheum Dis 66(12):1553–1559

Hartman GH, Renaud DL, Sundaram M, Reed AM (2007) Spondyloarthropathy presenting at a young age: case report and review. Skeletal Radiol 36(2):161–164

Horger M, Fierlbeck G, Kuemmerle-Deschner J, Tzaribachev N, Wehrmann M, Claussen CD et al (2008) MRI findings in deep and generalized morphea (localized scleroderma). AJR Am J Roentgenol 190(1):32–39

Johnson K, Davis PJ, Foster JK, McDonagh JE, Ryder CA, Southwood TR (2006) Imaging of muscle disorders in children. Pediatr Radiol 36(10):1005–1018

Lalani TA, Kanne JP, Hatfield GA, Chen P (2004) Imaging findings in systemic lupus erythematosus. Radiographics 24(4):1069–1086

Lee EY, Sundel RP, Kim S, Zurakowski D, Kleinman PK (2008) MRI findings of juvenile psoriatic arthritis. Skeletal Radiol 37(11): 987–996

Mier RJ, Shishov M, Higgins GC, Rennebohm RM, Wortmann DW, Jerath R et al (2005) Pediatric-onset mixed connective tissue disease. Rheum Dis Clin North Am 31(3):483–496

Pruthi S, Thapa MM (2009) Infectious and inflammatory disorders. Magn Reson Imaging Clin N Am 17(3):423–438

Tomasová Studynková J, Charvát F, Jarosová K, Vencovsky J (2007) The role of MRI in the assessment of polymyositis and dermatomyositis. Rheumatology (Oxford) 46(7):1174–1179

Wagner-Weiner L (2008) Pediatric rheumatology for the adult rheumatologist. J Clin Rheumatol 14(2):109–119

Zulian F (2008) Systemic sclerosis and localized scleroderma in childhood. Rheum Dis Clin North Am 34(1):239–255

Infectious Arthropathies and Related Diseases

5

5.1 Introduction

Musculoskeletal infection in children often poses a diagnostic challenge, so much greater as the younger the patient is. Although joint aspiration remains indispensable for definitive diagnosis, imaging is a valuable tool in the workup. No matter the etiologic agent, early and accurate definition of the infectious origin of the arthritis is paramount in order to minimize structural damage and to avoid complications and long-term sequelae. This chapter will emphasize the articular component of musculoskeletal infections as well as related diseases that should be considered in the differential diagnosis, such as transient synovitis and chronic recurrent multifocal osteomyelitis. Spinal infection will be addressed in Chap. 11.

5.2 Pyogenic Arthritis

The term pyogenic arthritis (PA) is used to describe bacterial joint infection, which accounts for approximately 6 % of all childhood arthritides. PA is most often a monoarthritis, more frequent in males with less than 3 years of age. The joints of the lower extremities are involved in approximately 75 % of the patients, mostly the hips and the knees; ankles, elbows, and shoulders are other important sites of disease. Even though PA is usually secondary to hematogenous spread, in children younger than 18 months, the process may begin in a metaphyseal focus that disseminates via transphyseal vessels. These vessels involute in older children, in whom the growth plate acts as a barrier for dissemination. Less common ways of contamination include direct inoculation (open wounds, joint punctures, surgery) or dissemination from a contiguous focus in the adjacent soft tissues.

Time is a critical prognostic factor in PA, as delayed institution of treatment leads to irreversible joint destruction and permanent sequelae. The acute inflammatory response related to bacterial infection causes quick cartilaginous destruction, and increase in the intracapsular pressure – due to synovial hypertrophy and purulent effusion – may lead to joint dislocation and epiphyseal ischemia, mostly in septic hips. Definitive diagnosis relies on joint aspiration and analysis of the synovial fluid, which must be performed as soon as PA is suspected. Imaging plays a secondary role, given that none of the available methods is able to distinguish infectious from noninfectious arthritides and a normal imaging study does not rule out articular infection.

Radiographs must be obtained in all patients, even though this imaging modality is quite insensitive: irreversible joint damage is usually present by the time that radiographic abnormalities become evident (Fig. 5.1). Findings related to the early stages of articular infection are fairly nonspecific, including joint effusion, widening of the joint space, and soft-tissue swelling (Fig. 5.2). Narrowing of the joint space appears quickly, as well as epiphyseal osteopenia (less pronounced than that found in tuberculous arthritis) and peripheral erosions (Figs. 5.3 and 5.4). Despite the fact that the knee is the most affected joint, PA is usually more severe in the hips (Fig. 5.5). Polyarticular PA occurs in less than 10 % of all cases (Fig. 5.6).

Ultrasonography (US) is very useful for early detection of joint effusion and synovitis, being also very appropriate for image-guided joint aspiration. Common findings include joint effusion (often with suspended debris) and hyperemia of the inflamed synovium on Doppler studies, but they are not specific (Fig. 5.7). US is also able to demonstrate erosions (especially large ones) and dissemination of the infection to adjacent bursae and tendon sheaths.

Magnetic resonance imaging (MRI) is capable to identify the earliest changes related to PA, allowing for accurate assessment of disease extent and helping in preoperative planning. It is highly sensitive for joint effusion (which may be heterogeneous) and synovitis, mostly when intravenous contrast is administered, as there is enhancement of the synovium and of the inflamed tissues (Figs. 5.8, 5.9, 5.10, 5.11, 5.12, 5.13, and 5.14). Erosions and destructive changes of bone and cartilage are also clearly seen (Figs. 5.9, 5.10, 5.11, and 5.12), as well as dissemination of the infectious process to nearby bursae and tendon sheaths (Fig. 5.14). Subchondral bone marrow edema is common and not necessarily indicative

S.L. Viana et al., *Joint Imaging in Childhood and Adolescence*,
DOI 10.1007/978-3-642-35876-0_5, © Springer-Verlag Berlin Heidelberg 2013

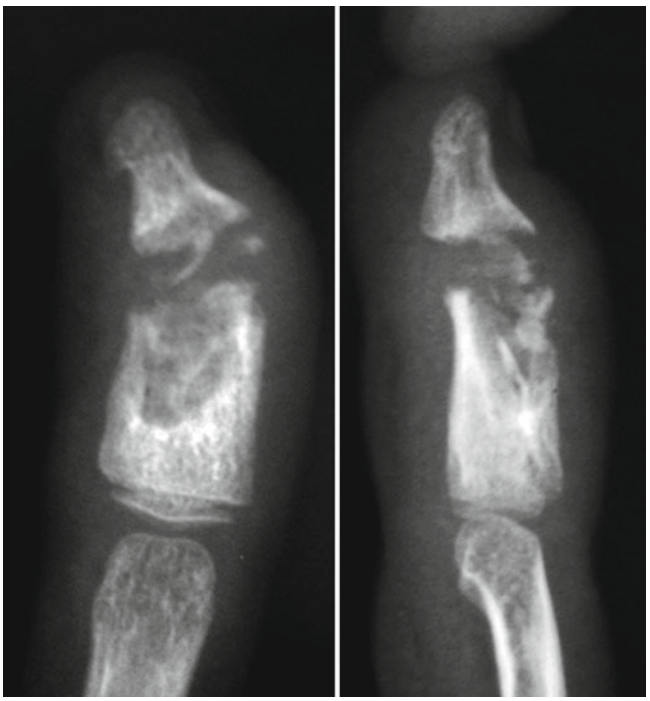

Fig. 5.1 Radiographs of the index finger of the right hand of a 6-year-old female who sustained an open fracture of the middle phalanx 6 months before, presenting spontaneous pus drainage from a fistulous tract and marked soft-tissue swelling. There are signs of chronic osteomyelitis of the middle phalanx, with extensive osteolysis and bone sequestra in the medullary cavity and in the distal interphalangeal joint. Destruction of corresponding joint surfaces due to PA is also evident, with deviation of the distal phalanx

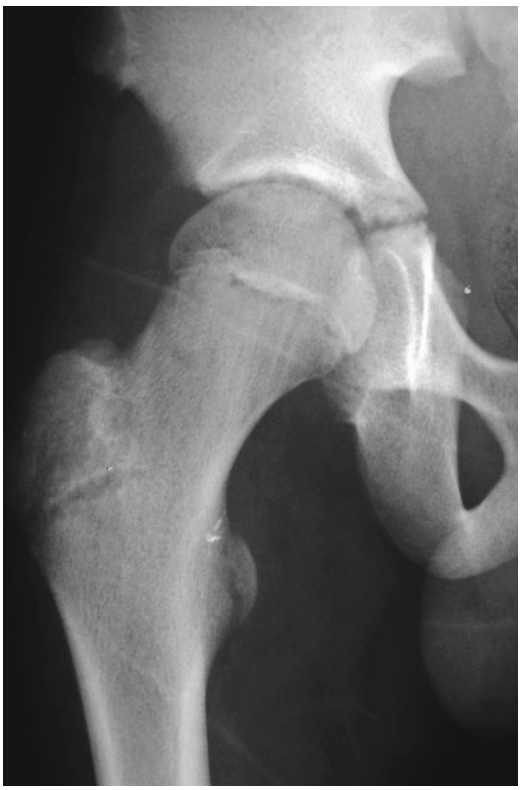

Fig. 5.3 Anteroposterior view of the right hip of a child with PA whose onset occurred less than 1 month earlier. There is osteoporosis of the proximal femur and narrowing of the coxofemoral joint space, as well as irregularity of the acetabulum. Such findings represent advanced cartilaginous destruction

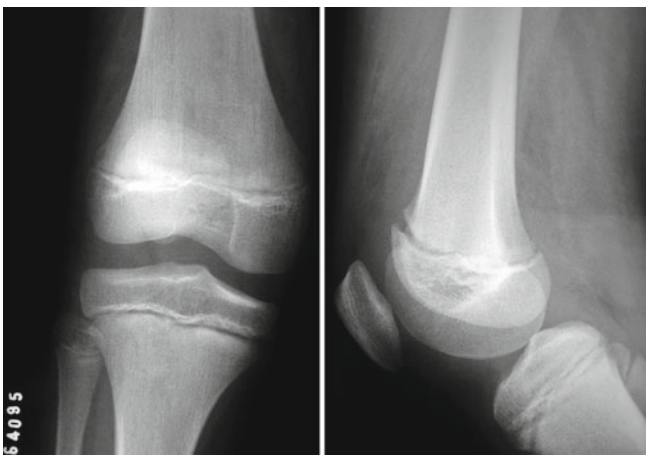

Fig. 5.2 A 9-year-old female with acute osteomyelitis of the right distal femur and secondary contamination of the joint cavity of the knee. There are no osseous abnormalities on radiographs, although swelling of periarticular soft tissues can be seen, mostly suprapatellar and more evident on the lateral view. There is also loss of definition of periarticular fat planes and subtle widening of the joint space. Nonetheless, these are nonspecific radiographic findings

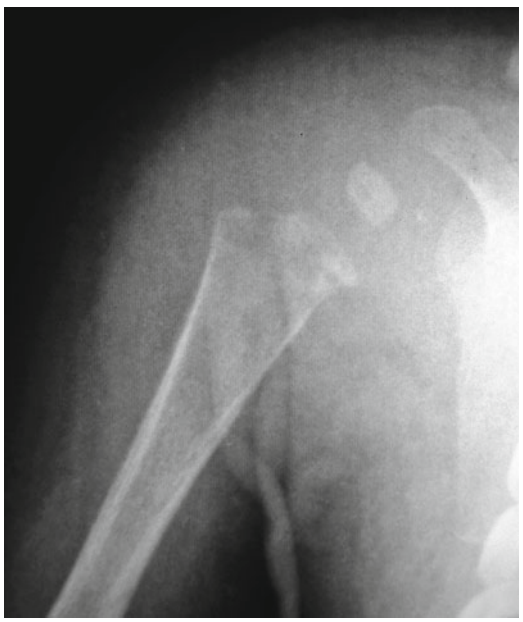

Fig. 5.4 Radiograph of the proximal portion of the right arm of a young child with bacterial osteomyelitis and secondary contamination of the shoulder joint. There are lytic lesions associated with cortical destruction in the proximal metaphysis, as well as marked swelling of periarticular soft tissues and widening of the proximal humeral physis

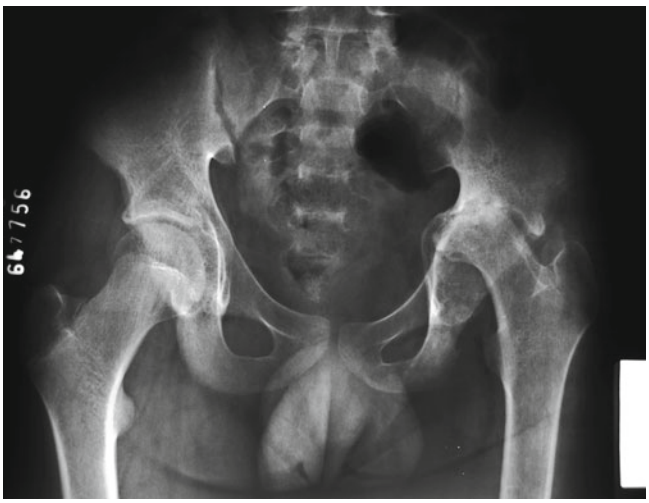

Fig. 5.5 Pyogenic arthritis of the left hip with poor evolution. There is marked bone destruction, with almost complete resorption of the left proximal femoral epiphysis and bone remodeling of the corresponding acetabulum; acetabular protrusion is also evident, with striking acetabular incongruity

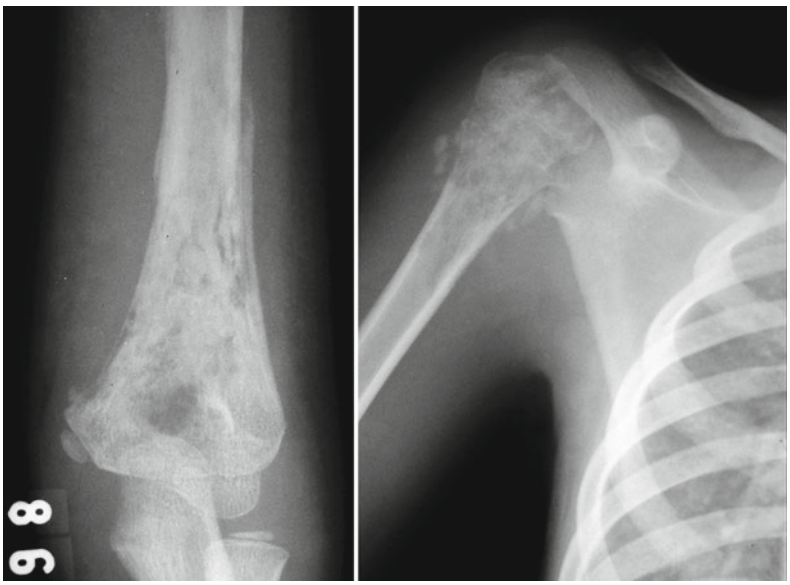

Fig. 5.6 Radiographs of the left elbow (*first image*) and of the right shoulder (*second image*) of a child with multifocal bacterial osteomyelitis and secondary articular contamination. There is metaphyseal osteomyelitis in the left distal and in the right proximal humeri, with permeative osteolysis, periosteal reaction, soft-tissue swelling, and epiphyseal involvement, the latter more evident in the shoulder. Osteomyelitis of the right femur and pyogenic arthritis of the homolateral hip were also present (not shown)

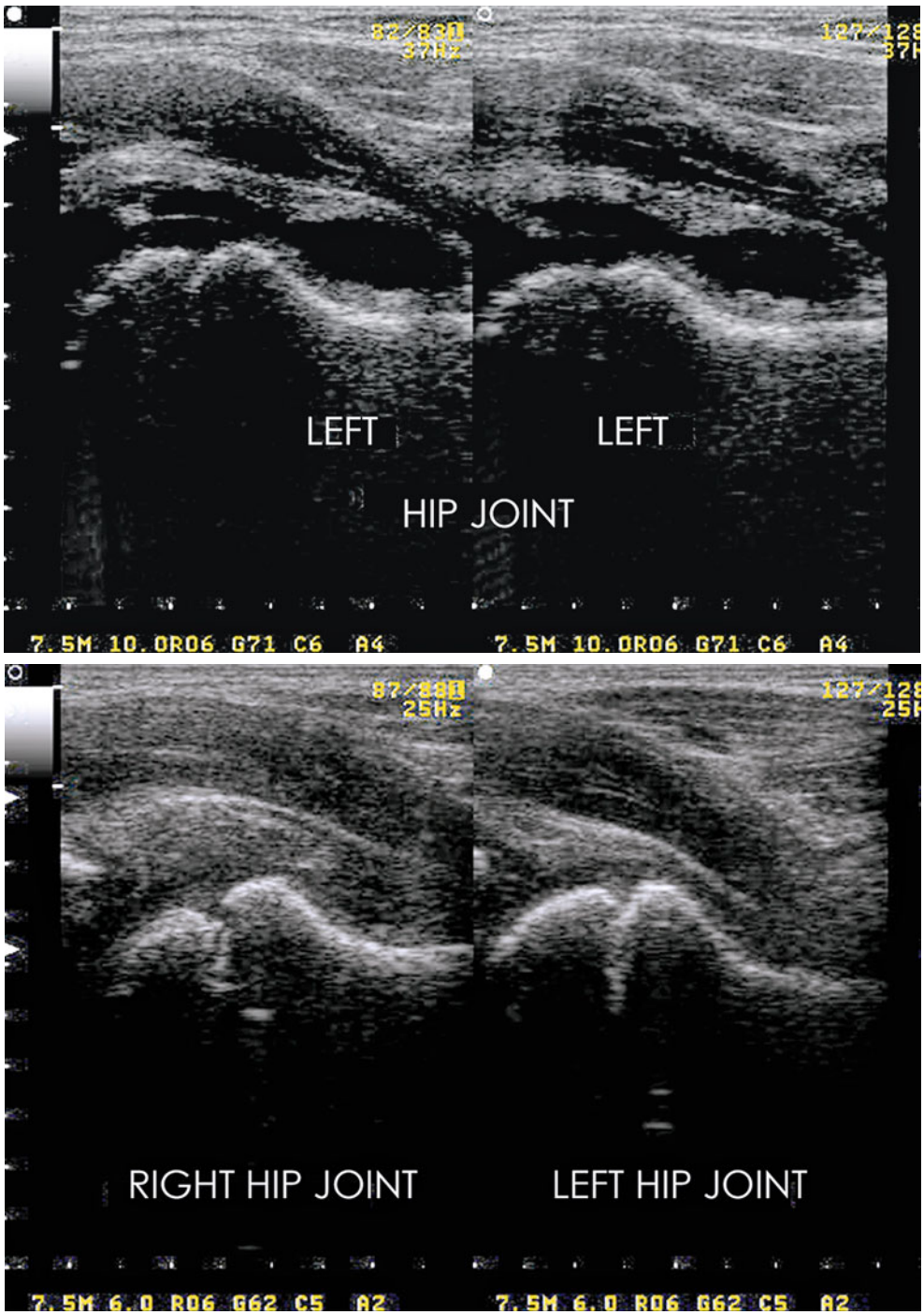

Fig. 5.7 US of the hips of two distinct children, both with pyogenic arthritis. The *upper images* show longitudinal scans of the left hip joint demonstrating joint effusion associated with irregular synovial thickening. In the *lower row*, there is a heterogeneous material filling the joint cavity of the right hip, representing synovial thickening and joint effusion with suspended debris. The proximal epiphysis of the right femur is irregular and of reduced size, notably if compared to the contralateral one (Courtesy of Dr. Telma Sakuno, Hospital Universitario da UFSC, Florianopolis, Brazil)

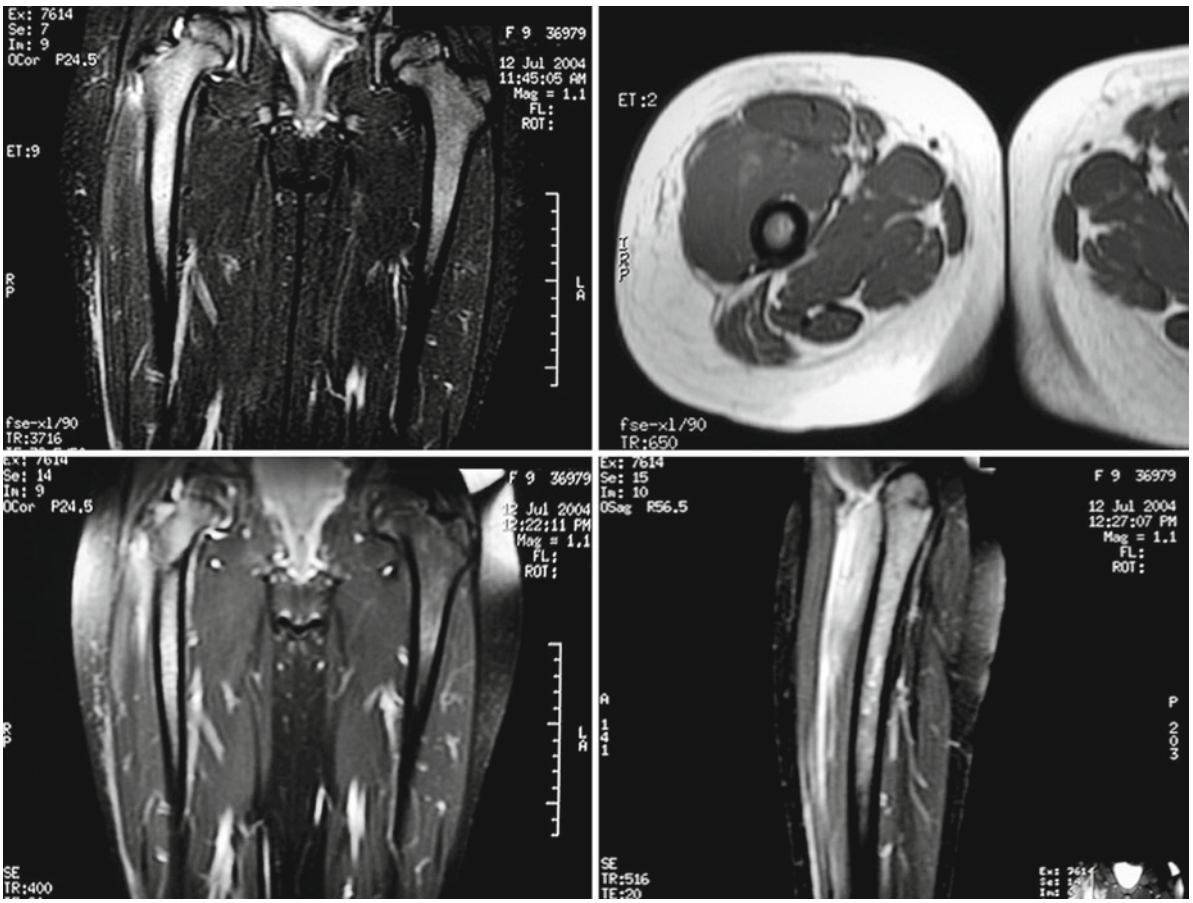

Fig. 5.8 Coronal STIR image (*upper-left image*), transverse T1-WI (*upper-right image*), and post-contrast fat sat T1-WI in the coronal and sagittal planes (*lower images*) of the hips and thighs of a 9-year-old female with right-sided septic coxofemoral arthritis. MRI is very suitable to demonstrate joint effusion in the right hip and bone marrow edema pattern in the ipsilateral femur, which extends far beyond the subchondral bone, reaching the mid-diaphysis, indicative of associated osteomyelitis. There is post-gadolinium enhancement of the edematous bone and of the proximal quadriceps

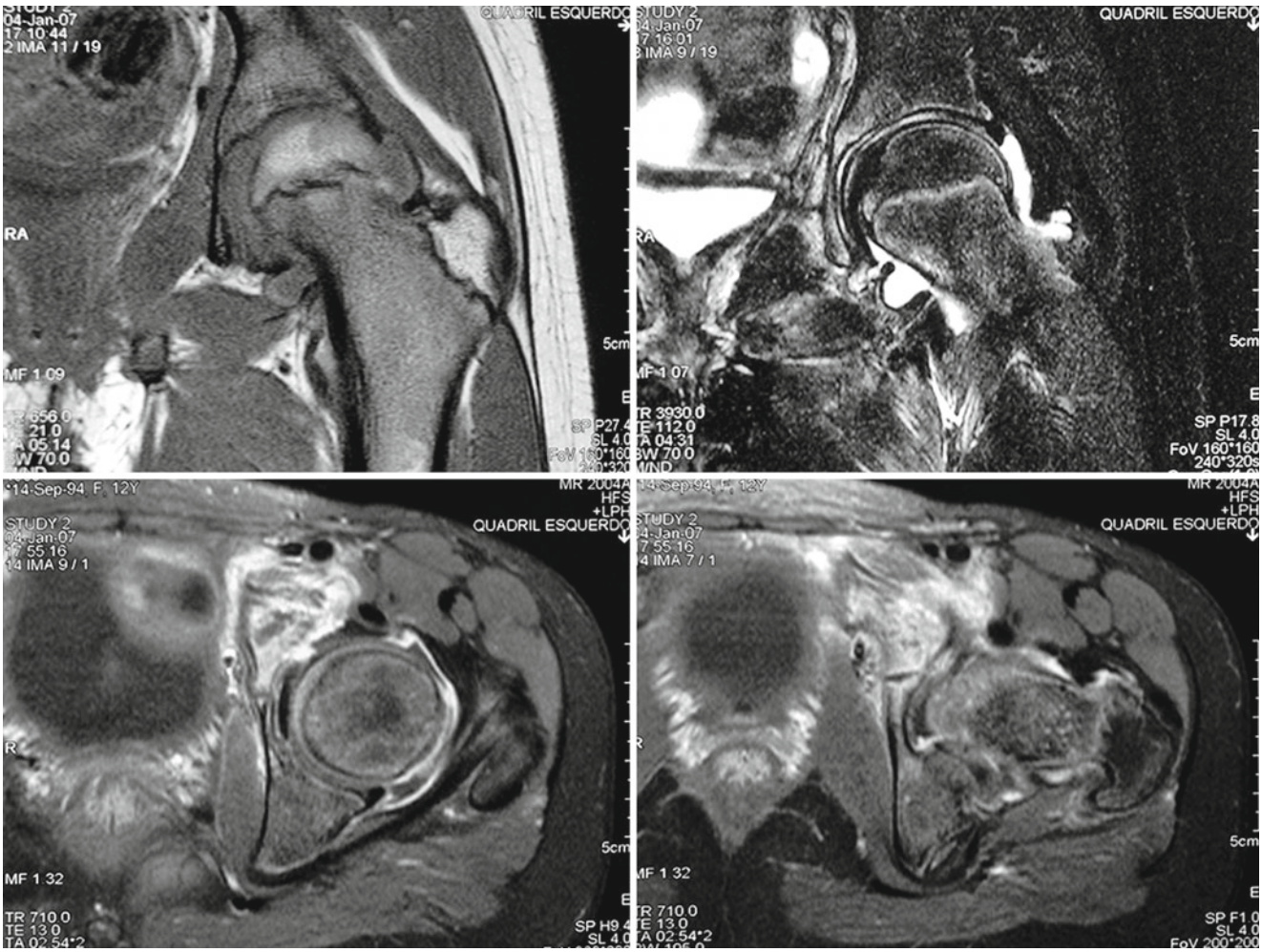

Fig. 5.9 Coronal T1-WI and fat sat T2-WI (*upper row*) of the left hip of a 12-year-old adolescent with PA reveal joint effusion and cartilaginous thinning, as well as edematous changes of the soft tissues of the proximal thigh and of the subchondral bone marrow of the acetabulum. Transverse post-contrast fat sat T1-WI (*lower row*) disclose intense enhancement of the thickened synovium and extensive destruction of the anterosuperior acetabulum, with cortical discontinuity and infiltration of the adjacent soft tissues; contrast enhancement is also seen in the edematous tissues. This appearance may resemble those seen in aggressive bone tumors, like Ewing's sarcoma

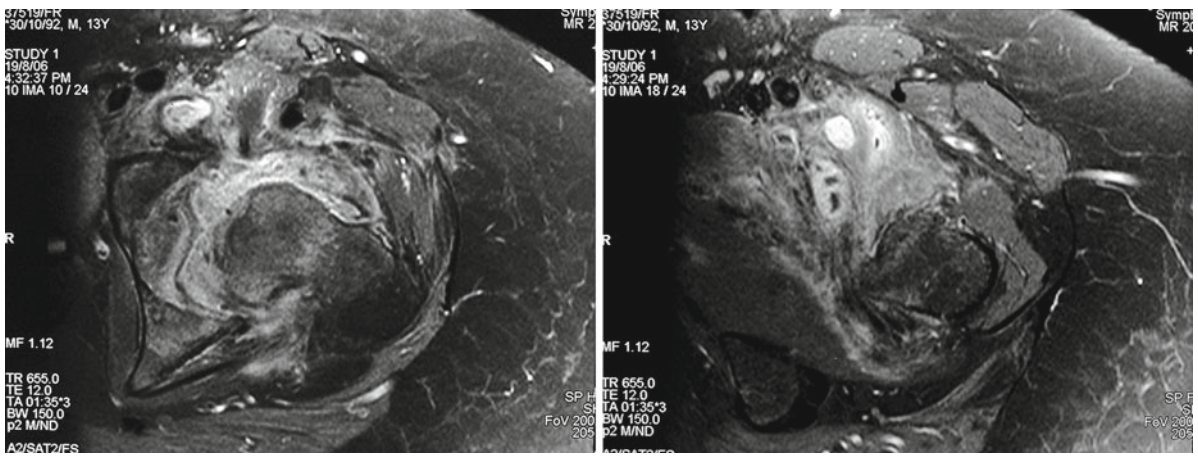

Fig. 5.10 Transverse post-gadolinium fat sat T1-WI of the left hip of a 13-year-old male with PA. Heterogeneous joint effusion, marked synovial thickening, and infected collections in the soft tissues of the proximal thigh can be seen, with post-contrast enhancement. The femoral head is deformed, and its appearance is suggestive of slippage of the proximal femoral epiphysis as a complication of septic arthritis

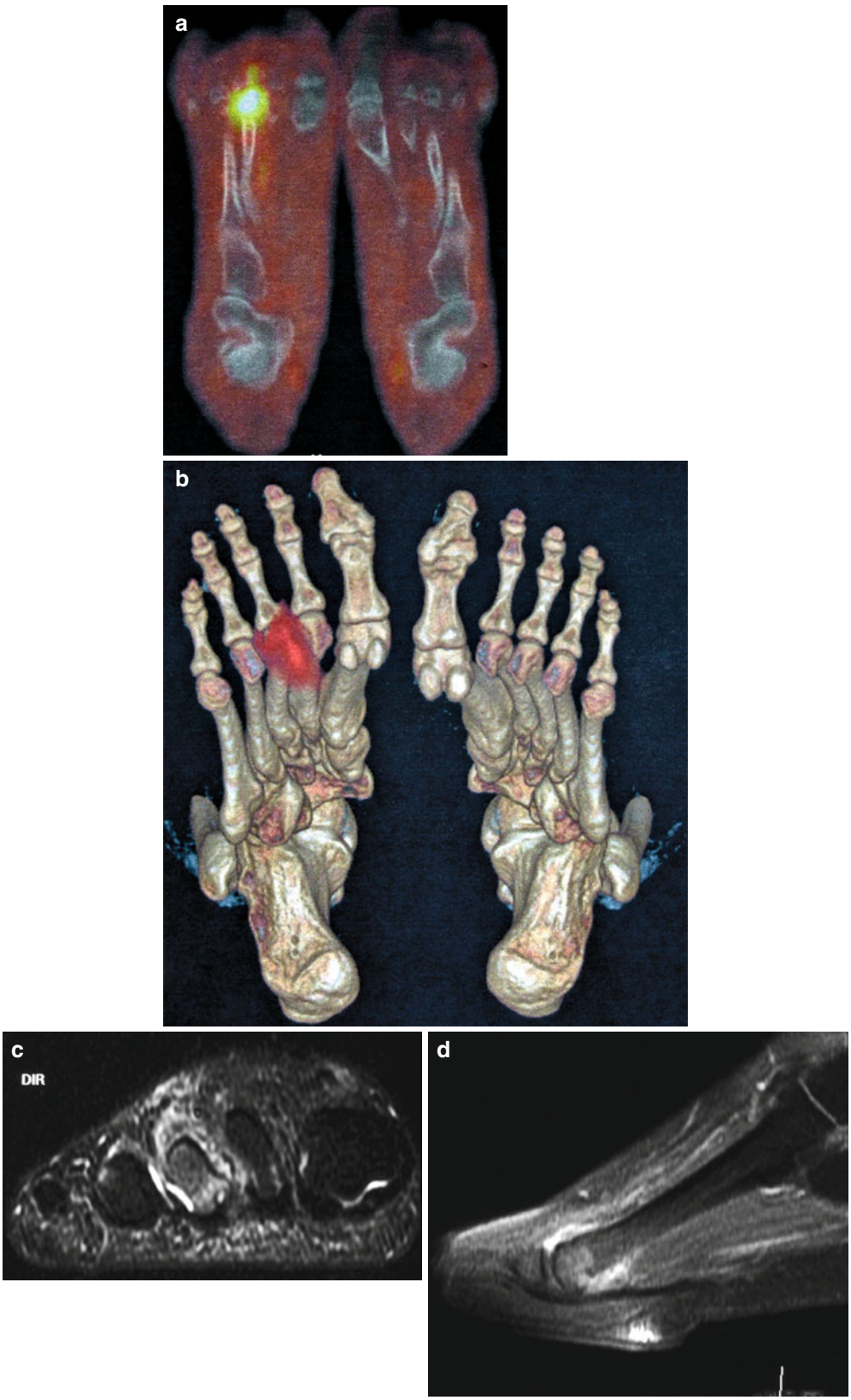

Fig. 5.11 Female adolescent with chronic, low-grade infection in the right forefoot. In (**a**) and (**b**), PET-CT demonstrates intense enhancement adjacent to the third metatarsophalangeal joint, initially interpreted as an infection of the periarticular soft tissues with secondary involvement of the contiguous bone. MRI performed 3 months later (coronal STIR image **c** and sagittal post-gadolinium fat sat T1-WI **d**) demonstrates that the infection was primarily articular, with joint effusion, synovitis, and erosions in the head of the third metatarsal, as well as edematous changes of the bone and of the adjacent soft tissues

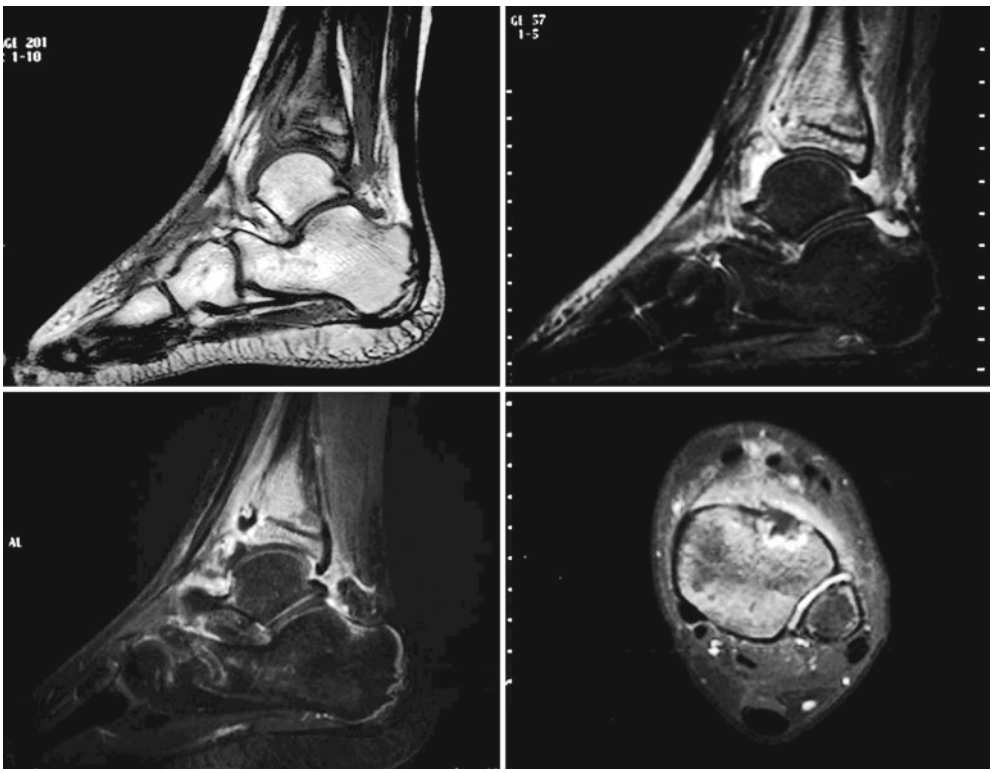

Fig. 5.12 MRI of the left ankle of a 12-year-old male with PA. T1-WI (*upper-left image*) and STIR image (*upper-right image*) evidence tibiotalar joint effusion, metaphyseal osteomyelitis of the distal tibia, and a small juxtaphyseal intraosseous abscess, anteriorly situated. Post-gadolinium fat sat T1-WI (*lower images*) demonstrate the intraosseous abscess with its hypointense content and peripheral enhancement draining to the joint cavity through a cortical break. Synovial enhancement is also present, distinguishing the thickened synovium from the joint effusion

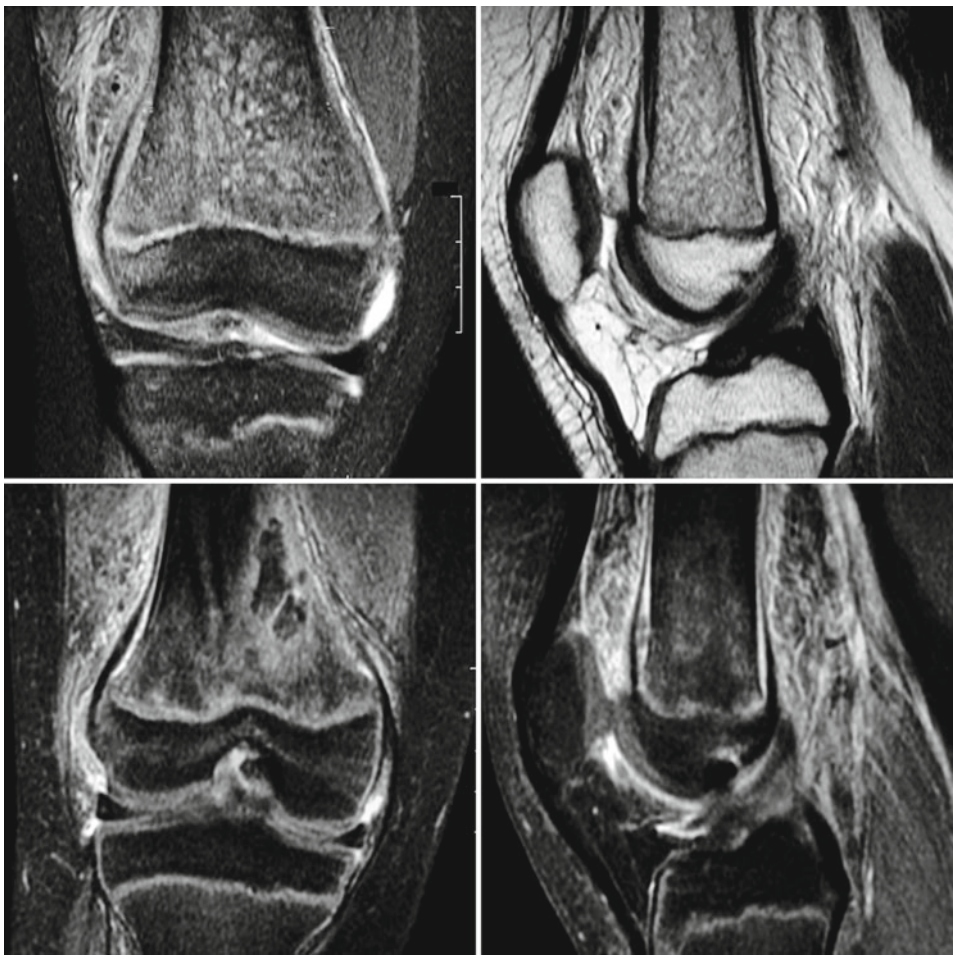

Fig. 5.13 MRI of the same patient of Fig. 5.2, performed on the same day (*upper row*, coronal fat sat T2-WI and sagittal T2-WI; *lower row*, coronal and sagittal post-gadolinium fat sat T1-WI). There is diffuse infiltration of the bone marrow of the distal femur, with post-gadolinium enhancement, as well as subperiosteal abscesses, extensive edema of the periarticular soft tissues, and contamination of the joint cavity, with joint effusion and synovitis

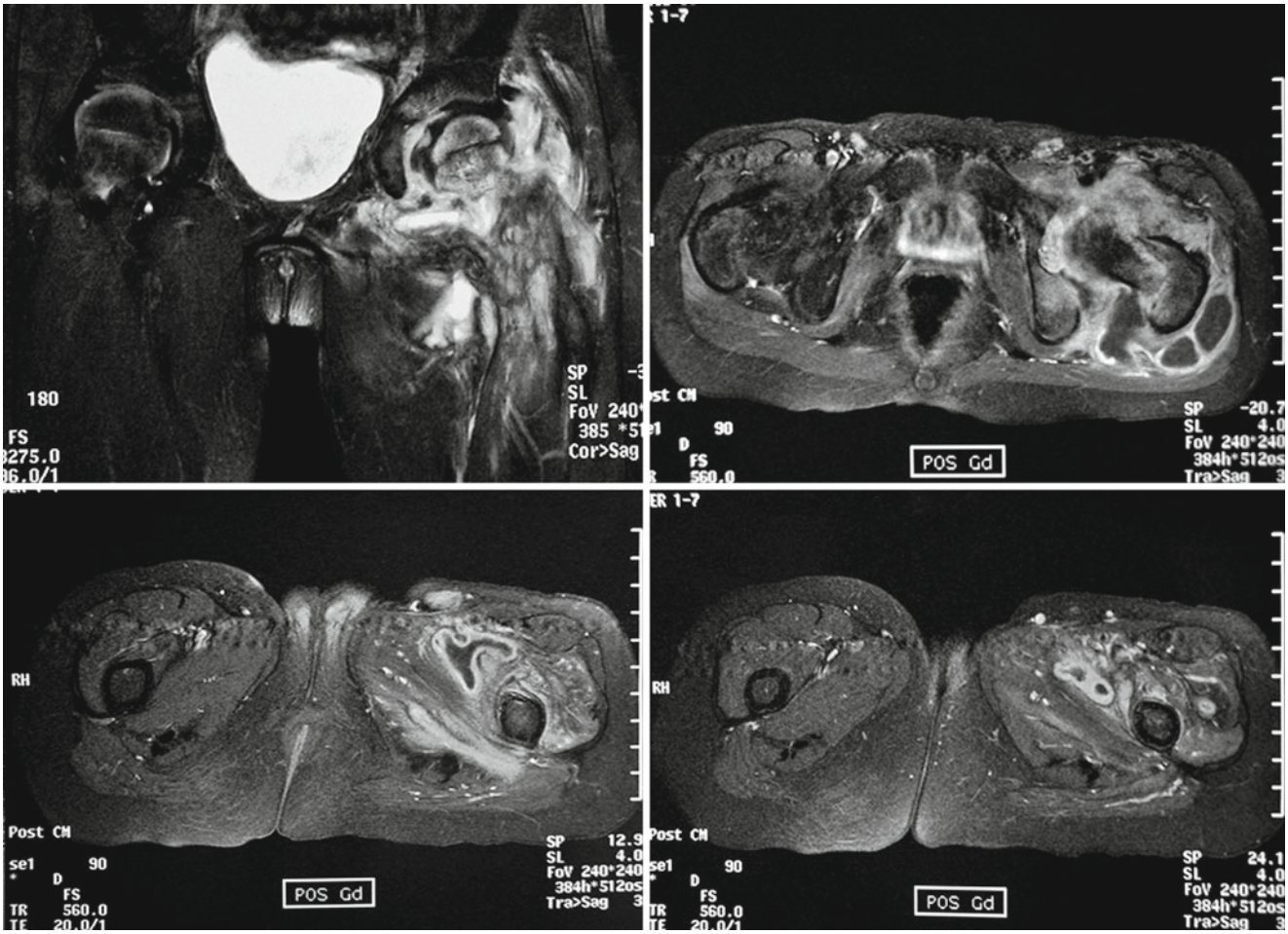

Fig. 5.14 MRI of the left hip of a child with PA (*upper-left image*, coronal fat sat T2-WI; remaining images, transverse post-gadolinium fat sat T1-WI). There is a large and heterogeneous joint effusion on fat sat T2-WI, with extensive bone marrow edema pattern in the proximal femur and acetabulum and edematous changes in the adjacent soft tissues. Post-gadolinium images display a large, complex soft-tissue abscess surrounding the hip and extending to nearby bursae, with thick and irregular enhancement, as well as adjacent myositis

of osteomyelitis, as it may be merely related to reactive (non-infectious) osteitis. Osteomyelitis is more likely if the edematous areas extend far beyond the subchondral bone, notably if there is prominent low signal intensity on T1-weighted images (T1-WI) (Figs. 5.8, 5.12, 5.13, and 5.14). Cortical discontinuity, periosteal reaction, intraosseous abscesses, and soft-tissue collections are typical of osteomyelitis (Figs. 5.9, 5.12, 5.13, and 5.14).

Computed tomography (CT) has restricted usefulness in the assessment of PA in pediatric patients (see Chap. 1). It is usually reserved for selected cases, most commonly used as an alternative (or an adjunct) to MRI for osseous assessment or to evaluate anatomically complex joints (Figs. 5.15, 5.16, 5.17, 5.18, and 5.19); the use of intravenous contrast is formally recommended. If there is associated osteomyelitis, CT is very helpful to demonstrate bone destruction and the presence of sequestra (Figs. 5.16, 5.17, and 5.19). Post-contrast enhancement is more evident in the thickened synovium (Fig. 5.19). CT is the best imaging method to detect gas bubbles in the infected tissues, which are indicative of the bacterial nature of the infection (Fig. 5.15).

Despite its high sensitivity, bone scintigraphy also plays a limited role in the assessment of articular infection (see Chap. 1). Nevertheless, because of its ability to assess the whole body in a single study, bone scintigraphy may be useful to detect "occult" sites of infection in multifocal PA. Increased uptake is generally present in the affected joint, although decreased uptake may be seen in the epiphysis if avascular necrosis ensues (which is more frequently seen in the hip). The role of PET-CT is not yet established (Fig. 5.11).

Long-term sequelae are found in up to 40 % of children with PA. Abnormal joint alignment/joint deformities (Figs. 5.20 and 5.21), premature physeal closure (Figs. 5.22 and 5.23), limb-length discrepancy (Fig. 5.23), early-onset osteoarthritis, avascular necrosis (Figs. 5.23 and 5.24), and, in advanced cases, bony ankylosis (in opposition to the fibrous ankylosis seen in tuberculous arthritis – Fig. 5.25) are among the most important complications.

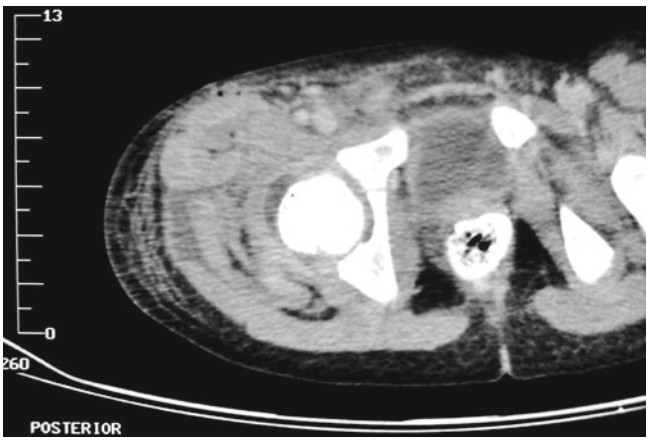

Fig. 5.15 A 9-year-old male with PA of the right hip and septicemia. CT scan reveals joint effusion, marked swelling of periarticular soft tissues, densification of the subcutaneous fat, and juxta-articular abscesses. Gas bubbles can be seen in the collections, indicative of the bacterial nature of the infection (Courtesy of Dr. Arthemizio Rocha, Hospital Santa Marta, Taguatinga, Brazil)

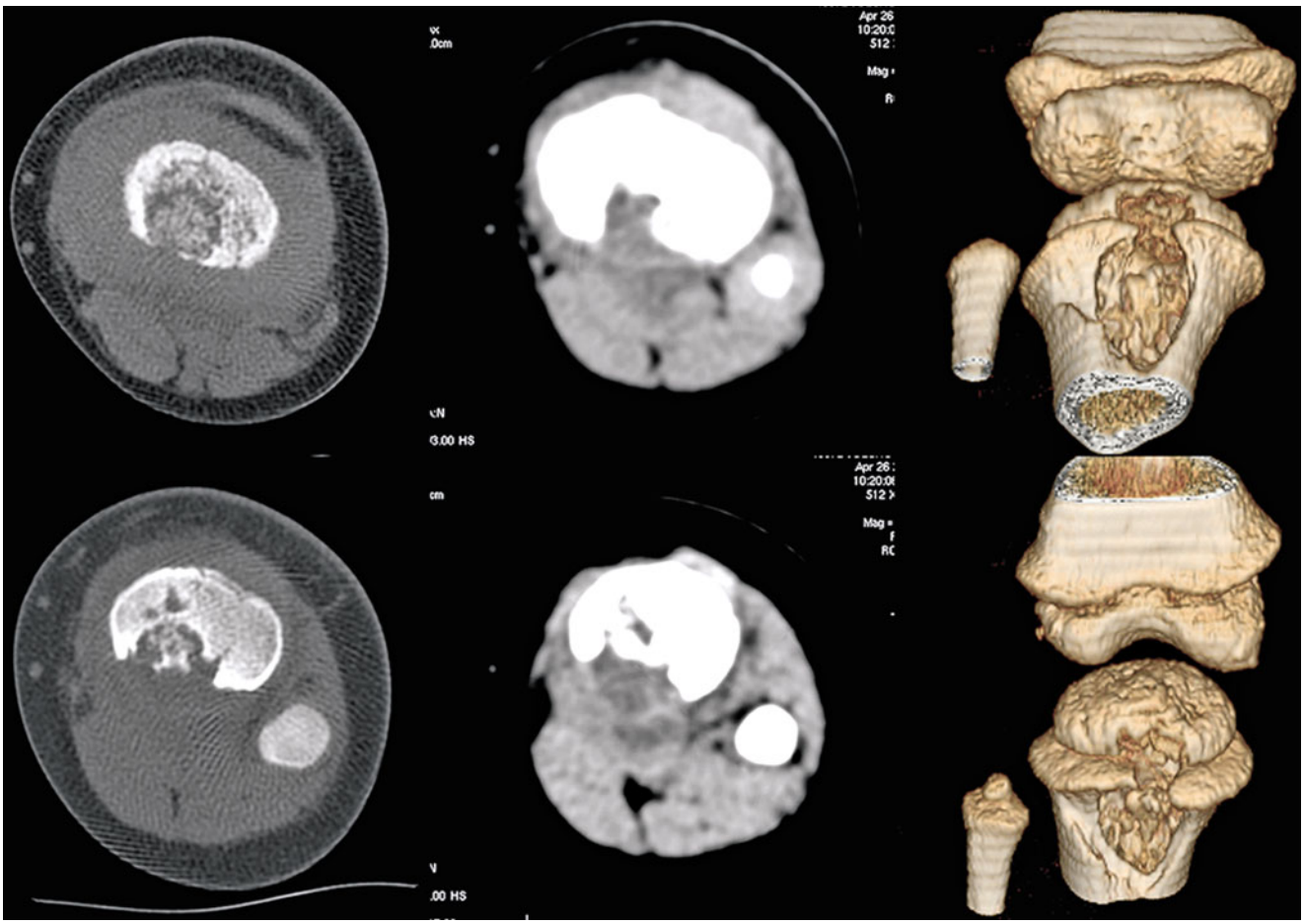

Fig. 5.16 CT scan of the left knee of a 2-year-old child with PA. Transverse images with bone window (*left images*) and soft-tissue window (*central images*) and volume-rendered reconstructions (*right images*) reveal an extensive lytic lesion of the proximal metadiaphysis of the tibia, which extends across the growth plate to the proximal epiphysis. There is a wide area of discontinuity of the posterior cortex, with bone sequestra in the medullary cavity, joint effusion, and a complex abscess in the posterior soft tissues of the proximal leg

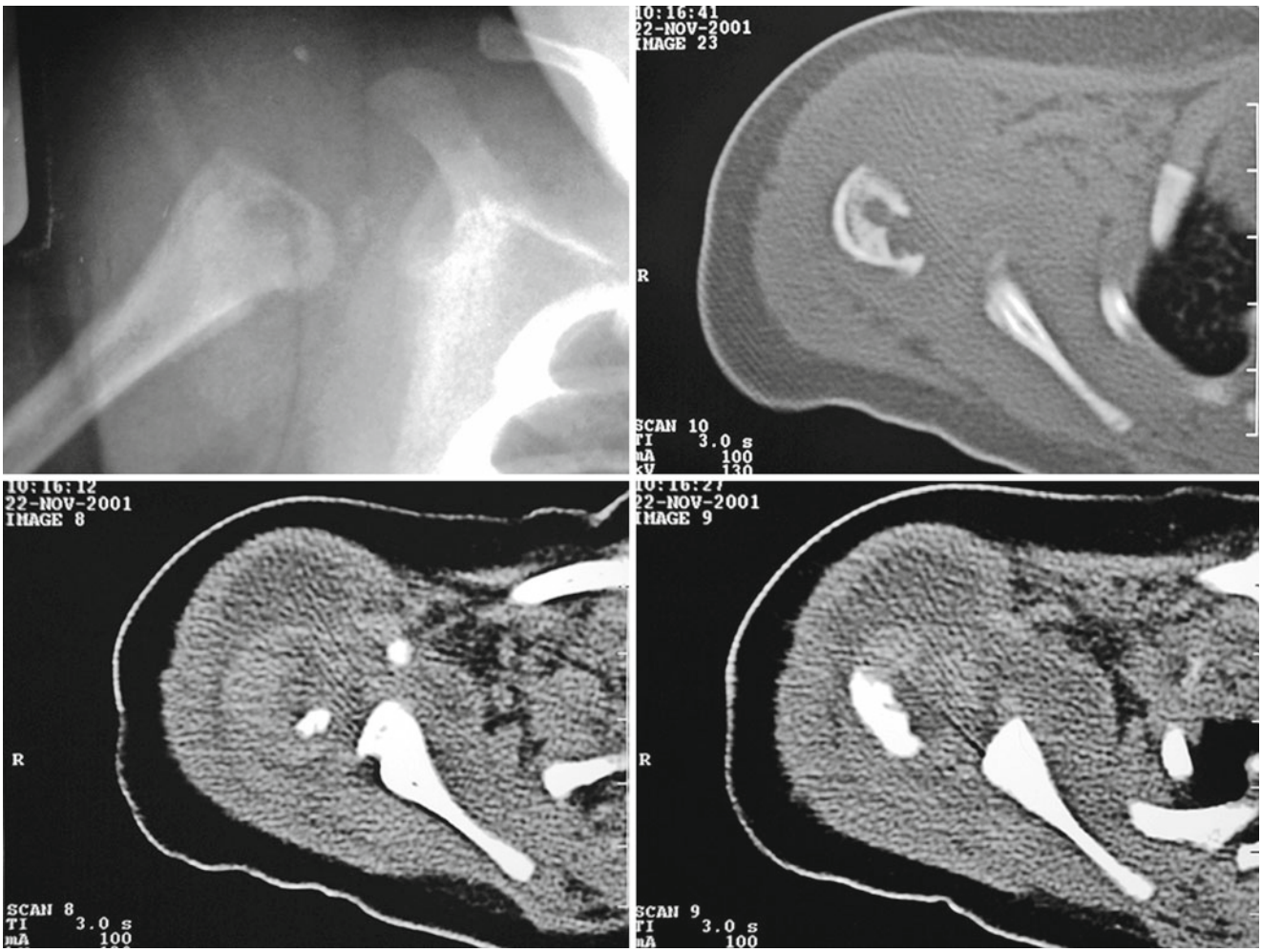

Fig. 5.17 Neonatal septic arthritis of the right shoulder. In the *first image*, radiograph of the affected joint reveals metaphyseal osteomyelitis of the proximal humerus, with a large intraosseous abscess and extensive periosteal reaction. In the following images, transverse CT sections corroborate the above-described findings, disclosing bone destruction and cortical rupture. There is contamination of the joint cavity, with a large joint effusion and abscesses in the adjacent soft tissues (Courtesy of Dr. Arthemizio Rocha, Hospital Santa Marta, Taguatinga, Brazil)

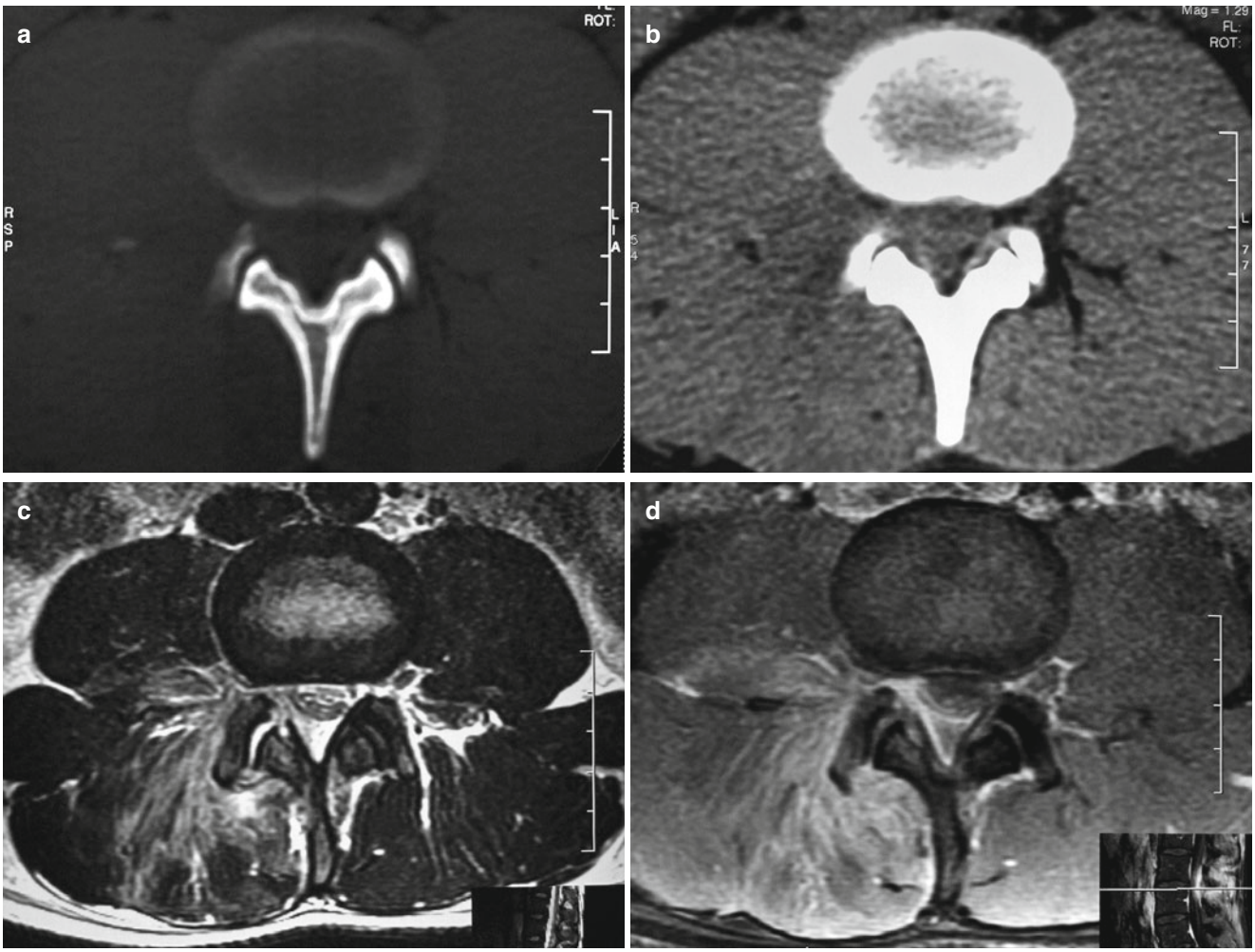

Fig. 5.18 A 17-year-old patient with PA of the right facet joint of L3-L4. In (**a** and **b**), transverse CT images evidence blurring and hypodensity of the soft tissues adjacent to the infected joint, without evidence of bone erosions. Transverse T2-WI (**c**) and post-gadolinium fat sat T1-WI (**d**) show fluid in the joint space extending deep to the homolateral ligamentum flavum, with discontinuity of the latter. Edema of the paravertebral soft tissues is also seen, as well as an epidural phlegmon at right, with contralateral displacement of the thecal sac. The inflamed tissues exhibit diffuse post-contrast enhancement

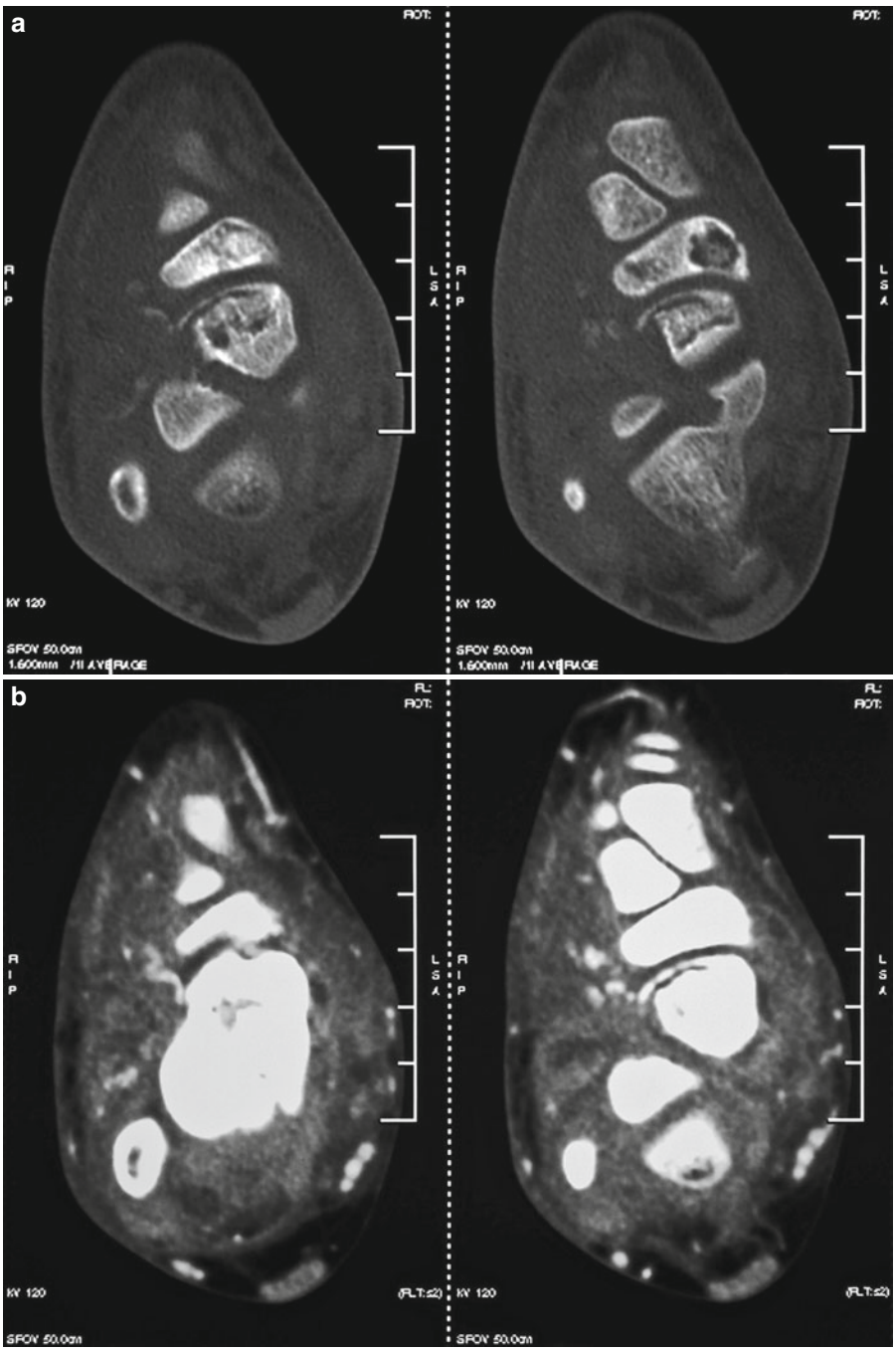

Fig. 5.19 Transverse CT images (**a** and **b**) and sagittal reformatted images (**c**) of the right ankle of a 7-year-old female. There are destructive lesions in the talus and in the navicular in the image with bone window settings (**a**), with sequestra in the affected bones and in the adjacent soft tissues. Diffuse edema of the periarticular soft tissues is evident in the images with soft-tissue window settings (**b** and **c**), as well as a large tibiotalar effusion. Post-contrast enhancement is seen in the thickened synovium and in the inflamed soft tissues

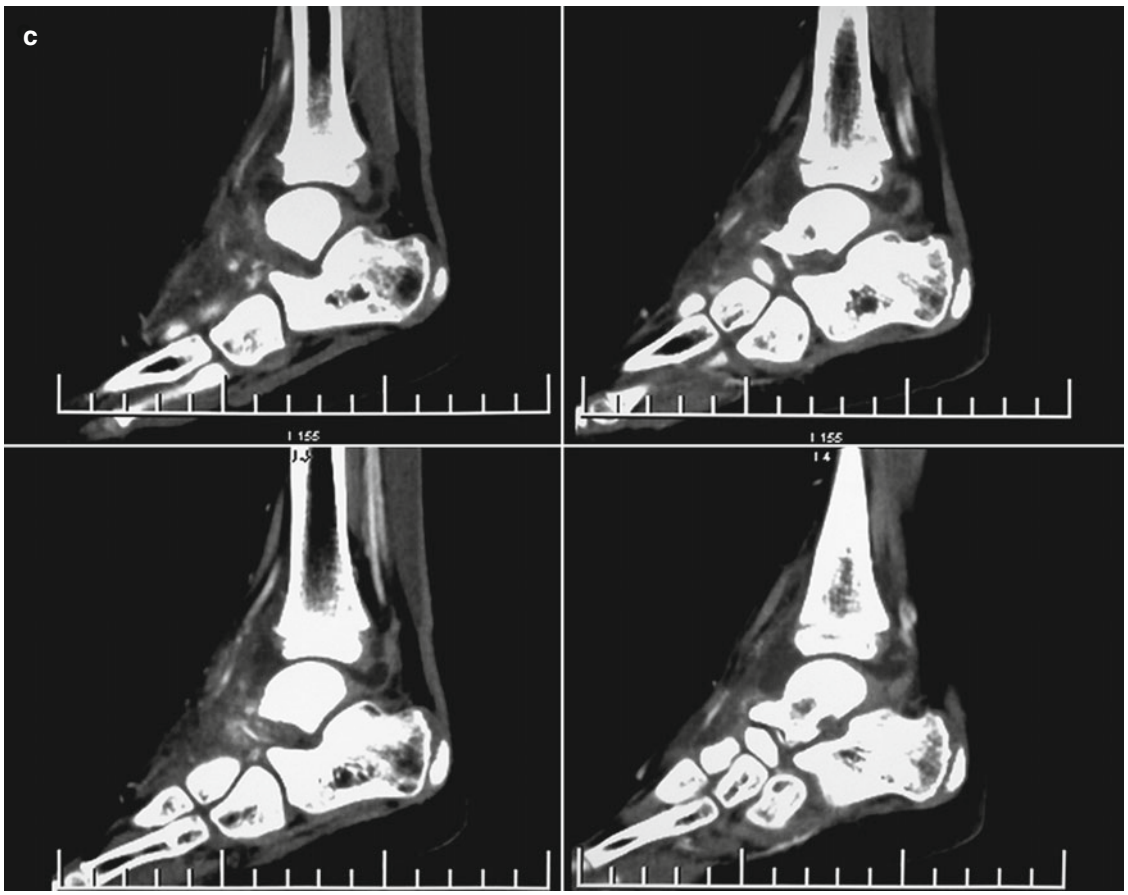

Fig. 5.19 (continued)

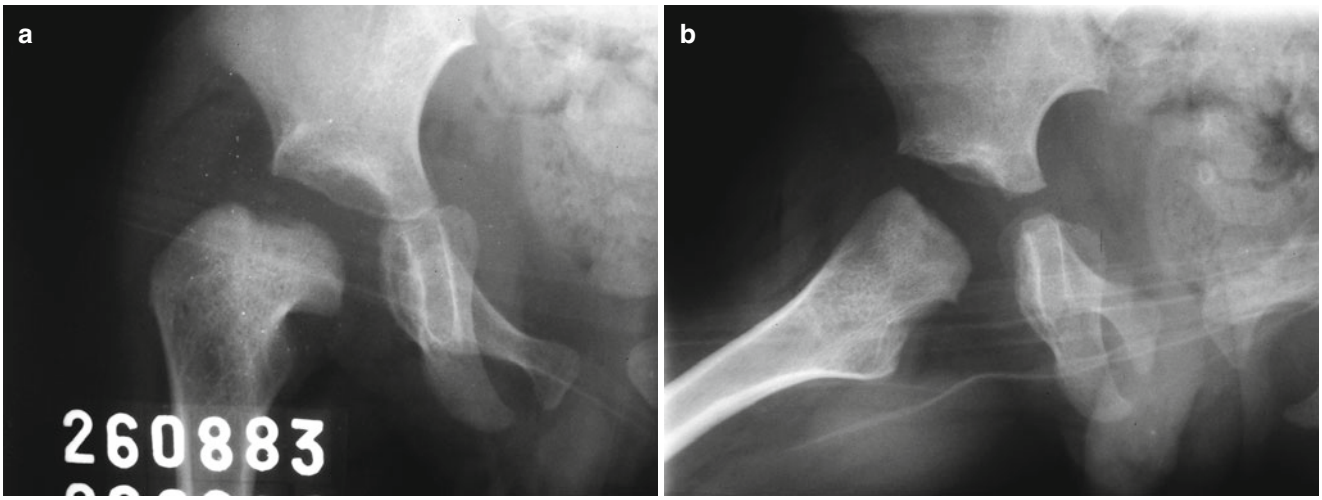

Fig. 5.20 Late-stage sequelae of neonatal PA of the right hip. Radiographs show deformity of the proximal femur, delayed epiphyseal ossification, and remodeling of the acetabulum

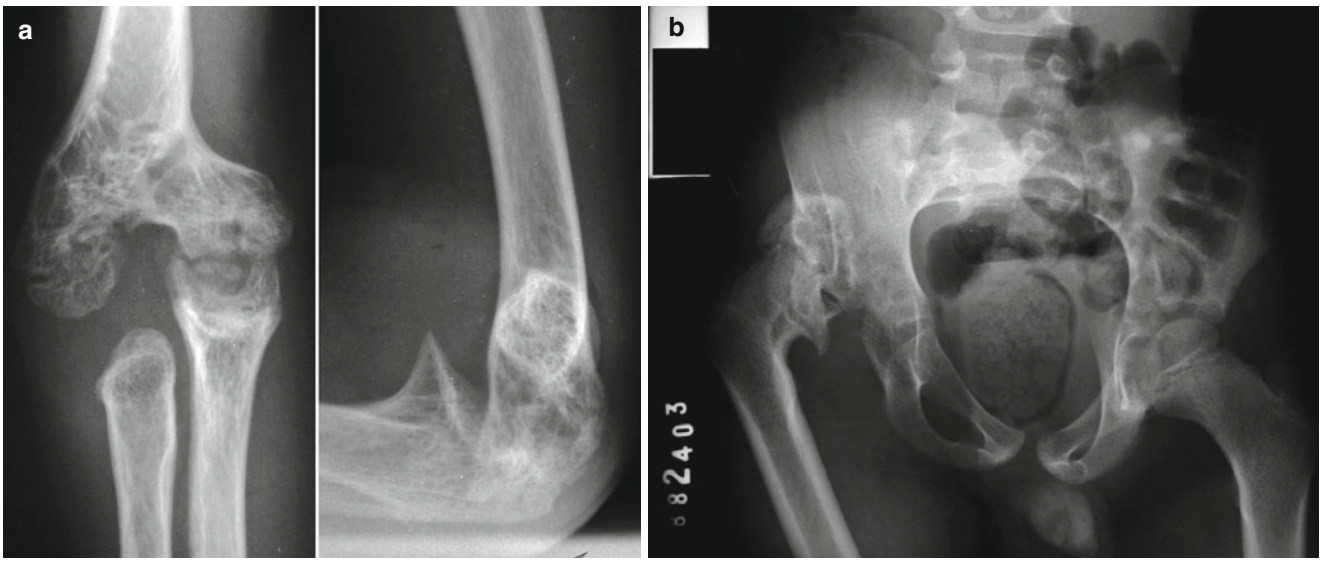

Fig. 5.21 Radiographs of the right elbow of a 7-year-old male with late-stage sequelae of PA (**a**). Joint deformity, bone remodeling, and articular incongruity can be seen, with radial shortening due to premature physeal closure. In (**b**), pelvic radiograph of a patient with late-stage sequelae of PA of the right hip shows coxofemoral dislocation and superior migration of the homolateral femur. The femoral head is articulated with the iliac bone and the homolateral acetabulum is poorly developed, indicators of a disease of long evolution

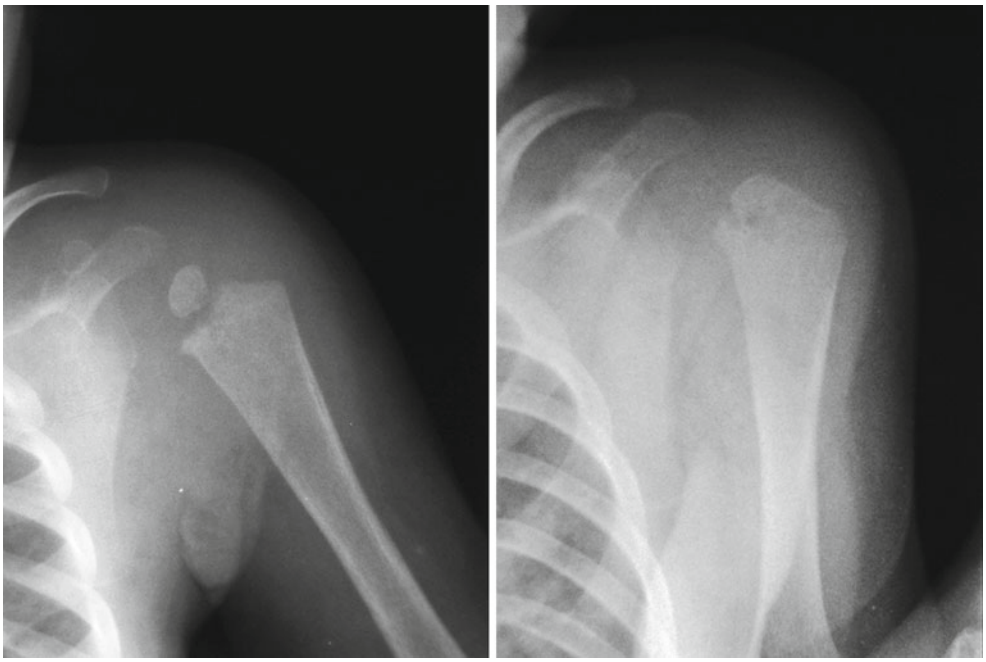

Fig. 5.22 Radiographs of the left shoulder of a young child with PA. The image at left, taken during the active stage, shows metaphyseal lucencies and cortical irregularity due to osteomyelitis. The radiograph at right, taken after healing has occurred, reveals early closure of the proximal humeral physis and residual deformity

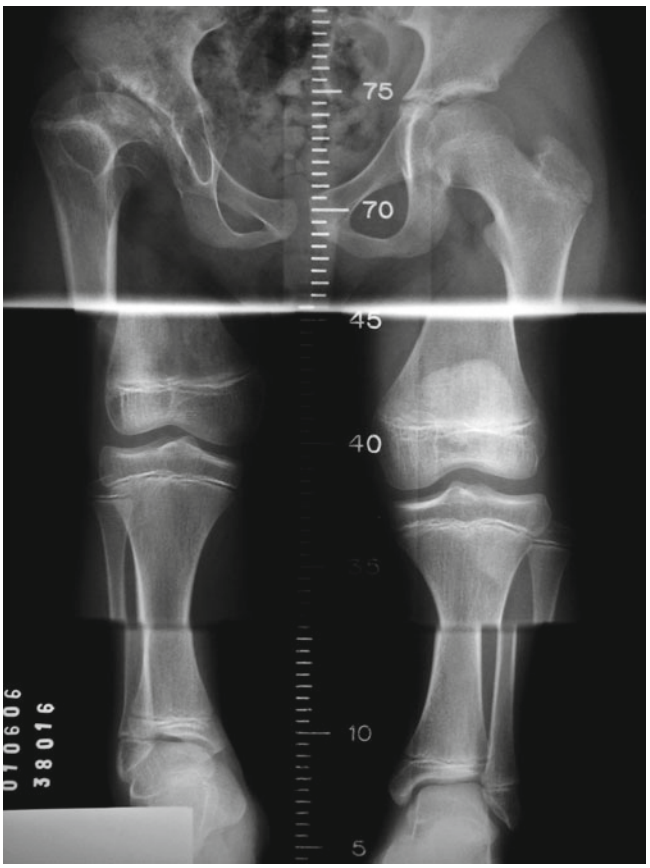

Fig. 5.23 Late-stage sequelae of PA of the right hip, probably complicated with avascular necrosis. Scanogram demonstrates shortening of the right lower limb due to deformity of the homolateral hip, characterized by a mushroom-shaped femoral head, a shortened and broadened femoral neck, flattening of the acetabulum, and early closure of the growth plates, with joint incongruity

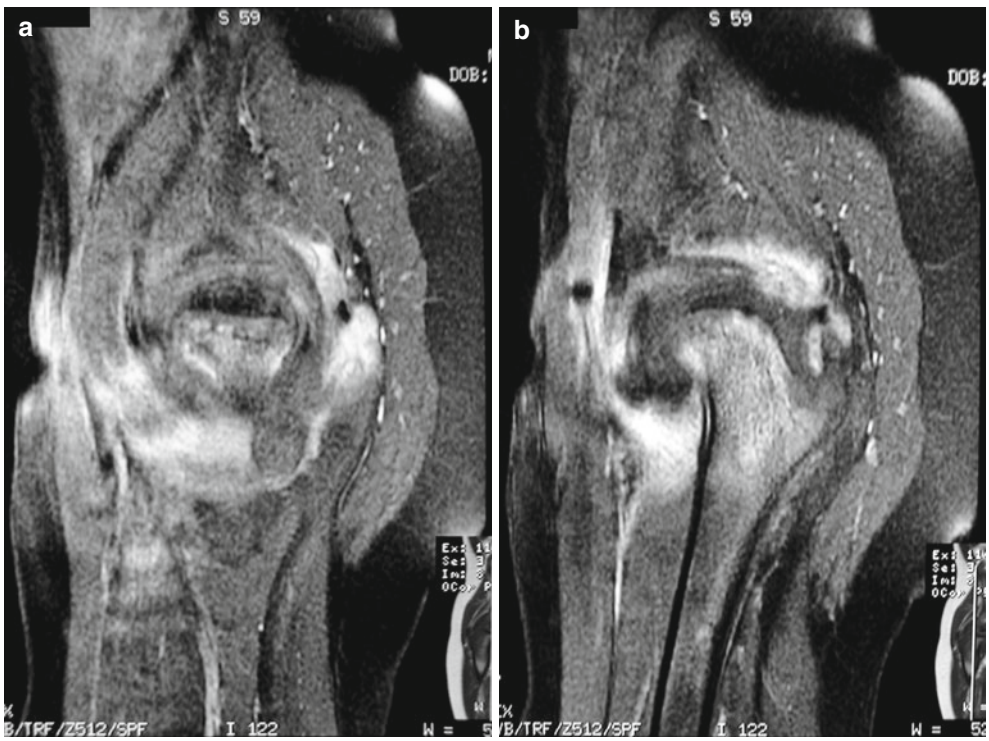

Fig. 5.24 Sagittal post-gadolinium fat sat T1-WI of the right hip of a 3-year-old child with PA. In addition to the abnormalities usually found in septic joints, there is marked decrease in the enhancement of the proximal femoral epiphysis, as well as subtle loss of its sphericity, related to avascular necrosis

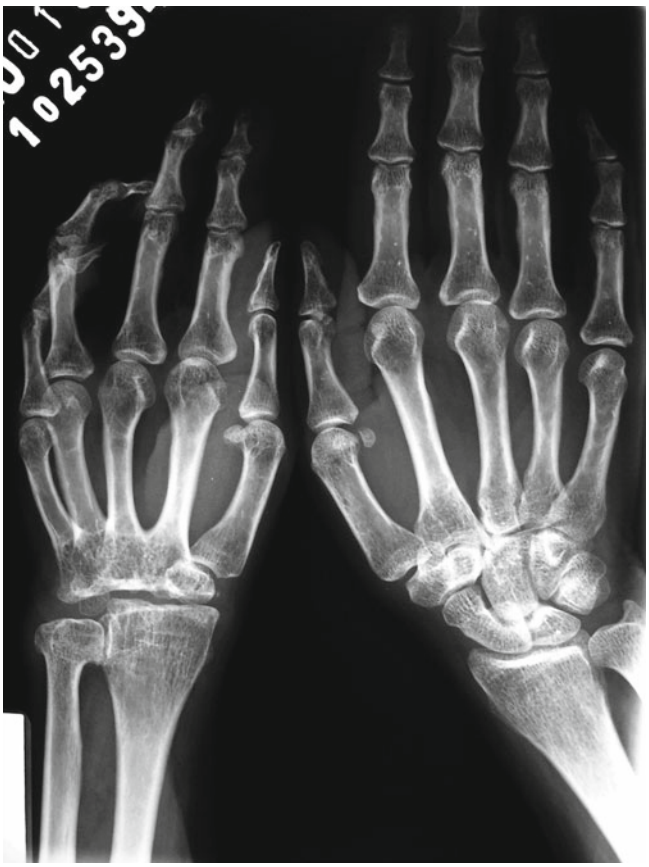

Fig. 5.25 Late-stage sequelae of PA of the right wrist. There is evidence of proximal row carpectomy at right, with fusion of the bones of the distal row and the adjacent metacarpals, as well as residual deformity and atrophy of the homolateral bones

5.3 Tuberculous Arthritis

Tuberculosis (TB) is an infectious condition known since ancient times. Even though several strains of mycobacteria may cause TB, *Mycobacterium tuberculosis* is the most important of them all. There has been a global increase in the incidence of TB in recent times, related mainly to the HIV/AIDS pandemic. Osteoarticular disease may account for up to 35 % of all cases of extrapulmonary TB, and it is noteworthy that less than half of these patients have concomitant pulmonary disease. Musculoskeletal TB is more common in children than in adults, notably in Asia and Africa, occurring in children younger than 10 years of age in up to 50 % of the cases. Tuberculous arthritis is typically monoarticular, though multifocal involvement is found in approximately 10 % of patients. Affected individuals typically present a slowly progressive monoarthritis that affects weight-bearing joints, such as the knees and the hips, even though any joint can be involved. In extraspinal TB, osteoarticular involvement is more frequent than isolated osteomyelitis, and infection of the joint cavity is usually due to transphyseal dissemination of an active tuberculous focus in the metaphysis of a long bone. This is characteristic of osteoarticular TB and uncommon in pyogenic arthritis, highlighting the importance of being acquainted with tuberculous osteomyelitis to better understand the findings of tuberculous arthritis. Only the involvement of the peripheral joints will be discussed in the following paragraphs, as spinal involvement, the most common presentation of musculoskeletal TB, will be the studied in Chap. 9.

Early-stage radiographic findings are nonspecific and include widening of the joint space and soft-tissue swelling. The classic Phemister triad of tuberculous arthritis refers to a combination of periarticular osteoporosis, peripheral bone erosions, and relative preservation of the joint space (Figs. 5.26 and 5.27). Periosteal reaction, cortical irregularity, and lytic lesions may also be present (Figs. 5.26, 5.28, 5.29, and 5.30), with minimal bone sclerosis. Chronic granulomatous synovitis leads to joint effusion, synovial thickening, and pressure erosions; nevertheless, as tuberculous arthritis lacks the proteolytic enzymes found in pyogenic arthritis, progression of joint space narrowing is slower in the former. Hyperemia is the cause of marked juxtaarticular osteoporosis, epiphyseal overgrowth (Figs. 5.7, 5.31, and 5.32), accelerated bone maturation with early/asymmetric physeal closure (Fig. 5.33), and widening of the intercondylar notch of the knees (Fig. 5.32). There is progressive destruction of the subchondral bone and extensive osteochondral damage (Figs. 5.33, 5.34, and 5.35), which may eventually lead to fibrous ankylosis. Subluxation of the femoral head is occasionally seen in tuberculous arthritis of the hip joint, just like in PA. The metaphyses of long bones (mainly the femora and the tibiae) are the most frequently affected sites in tuberculous osteomyelitis (Figs. 5.26, 5.28, and 5.29), but involvement of other sites (such as the ribs, patella, sternum, and skull) is not rare (Fig. 5.36). In children, there may be eccentric, well-delimited round, or ovoid lytic lesions, which are frequently multifocal and usually lack sclerotic borders, presenting metaphyseal expansion and periosteal reaction (Fig. 5.37); the term cystic TB (also known as osteitis cystica tuberculosa multiplex or multifocal tuberculous osteomyelitis) is often used to describe these multiple expansile metaphyseal lesions. As mentioned above, transphyseal dissemination is much more common in TB than in bacterial infections (Figs. 5.26 and 5.28); a cortical break may be present, disseminating the infection directly into the joint cavity, and sequestra are occasionally found. The term *spina ventosa* is used to describe a peculiar form of tuberculous osteomyelitis that is more common in children and usually affects the small bones of hands and feet (tuberculous dactylitis), characterized by osseous destruction, thickening of the overlying periosteum, and fusiform appearance of the bone. These lesions appear as cyst-like cavities on radiographs, leading to diaphyseal widening and swelling of the surrounding soft tissues.

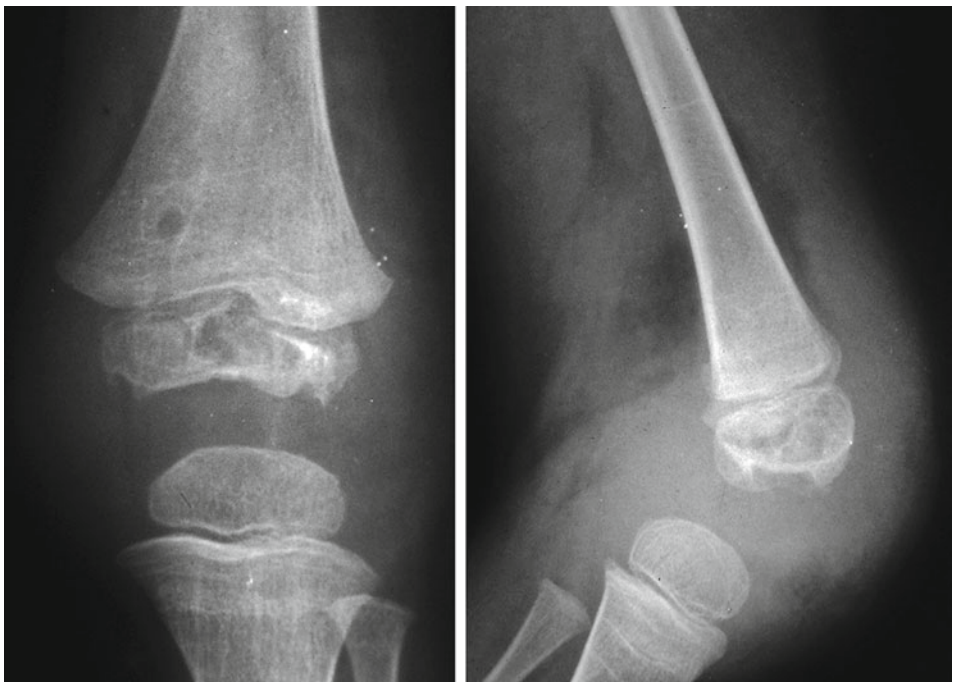

Fig. 5.26 Tuberculous arthritis of the left knee in a child. Phemister triad is present, with periarticular osteoporosis, predominantly peripheral erosions, and relative preservation of the joint space. Metaphyseal and epiphyseal lytic lesions are seen in the distal femur, representing active osteomyelitis (transphyseal spread)

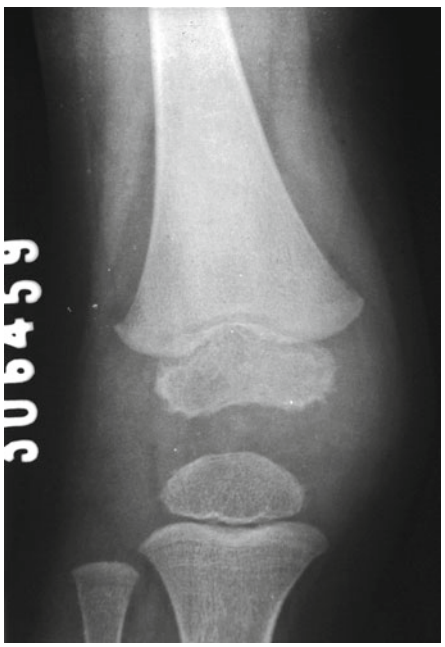

Fig. 5.27 Increased size and osteoporosis of the epiphyses are seen in this anteroposterior view of the right knee of a child with tuberculous arthritis, with preservation of the joint space and swelling of the periarticular soft tissues

MRI is the optimal imaging method for early demonstration of osteoarticular tuberculosis, revealing bone marrow edema adjacent to the affected joint, joint effusion (which is often heterogeneous), synovial thickening, cartilaginous damage, and bone erosions (Fig. 5.38). Administration of intravenous contrast is formally recommended, just like in pyogenic arthritis. Synovial proliferation may be hypointense or hyperintense on T2-weighted images (T2-WI), showing moderate to intense post-contrast enhancement when acutely inflamed (Fig. 5.38); nonetheless, chronically inflamed synovium may exhibit little enhancement or no enhancement at all. If compared to pyogenic arthritis, the erosive component is more prominent in tuberculous arthritis, with relatively less subchondral edema. When present, tuberculous abscesses usually display thin and smooth walls, while the walls of bacterial abscesses are most often thick and irregular; peripheral post-gadolinium enhancement is seen in both conditions. Intraosseous abscesses in TB are most often hypointense on T1-WI and hyperintense on T2-WI, also presenting post-gadolinium enhancement; the presence of hypointense areas on T2-WI usually indicates caseous transformation and is very suggestive of tuberculous osteomyelitis. CT is very useful to demonstrate bone sequestra (Fig. 5.39) and soft-tissue calcifications, the latter being typical of chronic osteoarticular TB; its advantages and drawbacks in the

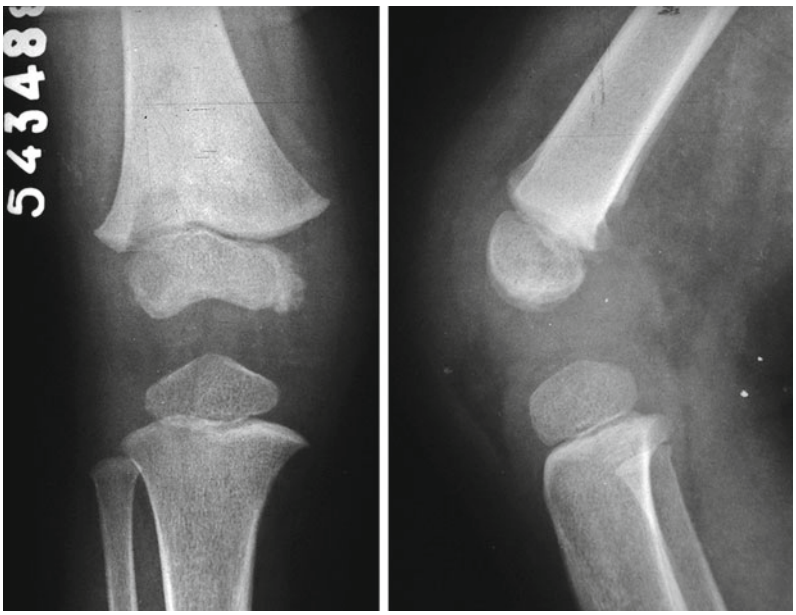

Fig. 5.28 Radiographs of the right knee disclosing posterolateral lytic lesions involving the metaphysis and the epiphysis of the distal femur, representing transphyseal dissemination of tuberculous osteomyelitis and concomitant tuberculous arthritis. There is discontinuity of the posterior cortex and diffuse swelling of the periarticular soft tissues

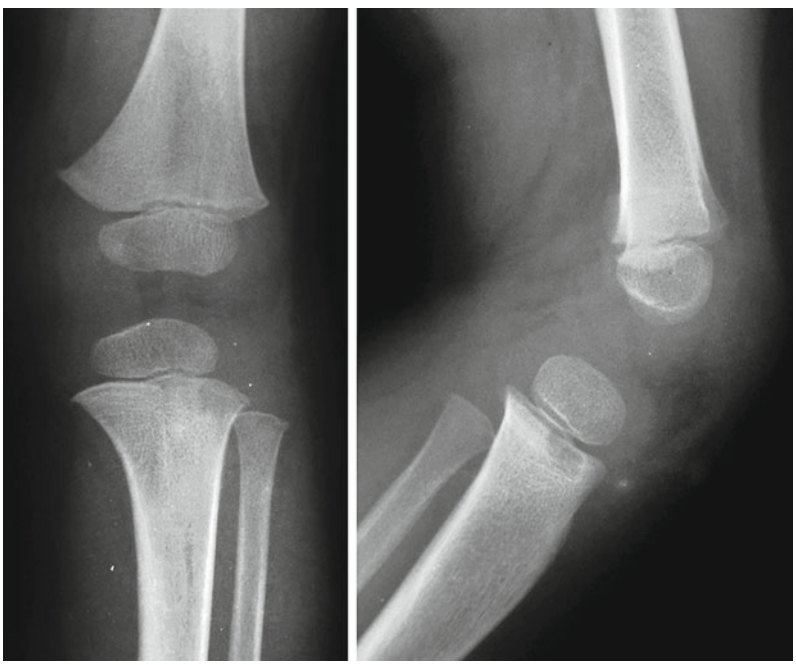

Fig. 5.29 Radiographs of the left knee of a 2-year-old child. There is a well-delimited lytic lesion adjacent to the anterolateral physis in the proximal tibial metaphysis. Tuberculous osteomyelitis

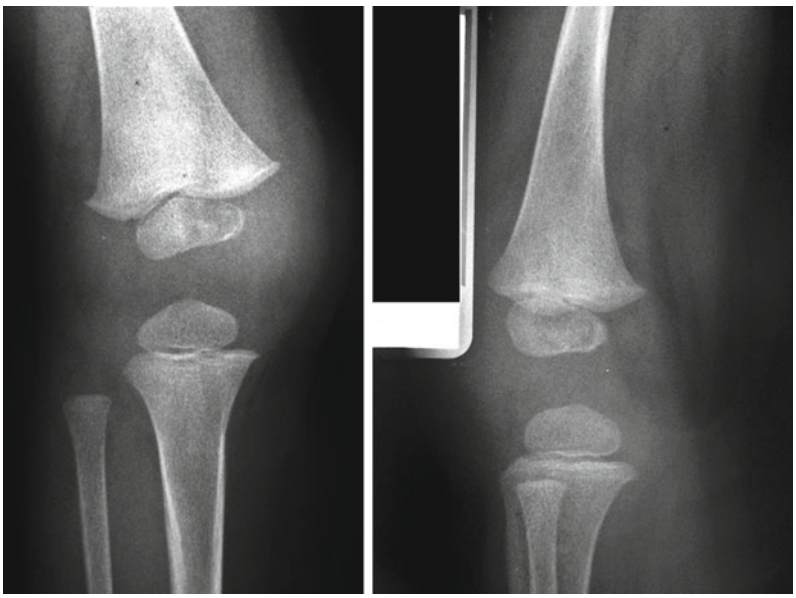

Fig. 5.30 Lytic lesion in the medial portion of the distal epiphysis of the right femur, ill-defined, associated with diffuse swelling of periarticular soft tissues, representing tuberculous osteomyelitis and concomitant arthritis

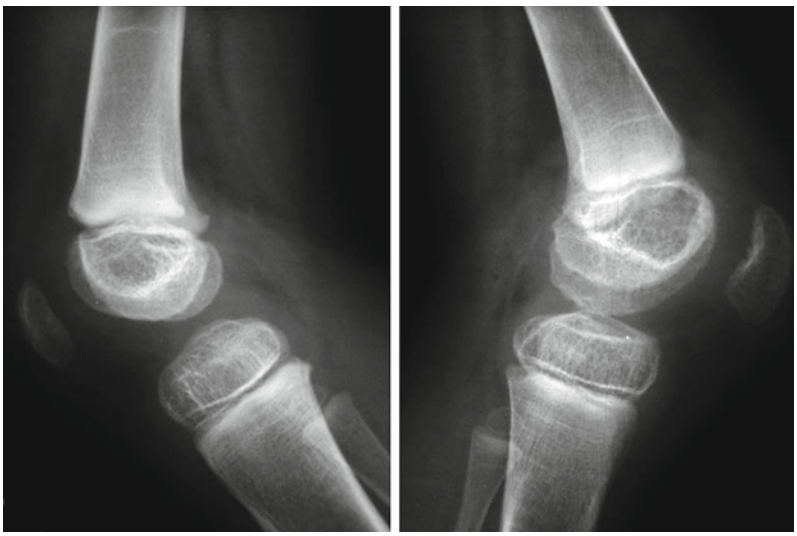

Fig. 5.31 Lateral views of both knees of a 5-year-old child with left-sided tuberculous arthritis. The left epiphyses are osteopenic and show increased size when compared to the contralateral ones; ipsilateral soft-tissue swelling is also evident

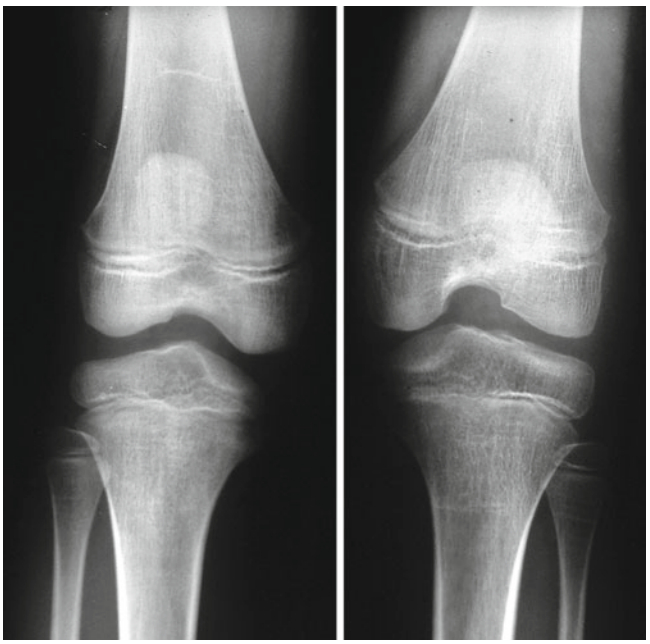

Fig. 5.32 Tuberculous arthritis of the left knee. There is increased size of the epiphyses and periarticular osteoporosis in the affected knee, with widening of the intercondylar notch, similar to those found in hemophiliac patients. Subtle narrowing of the joint space is already present

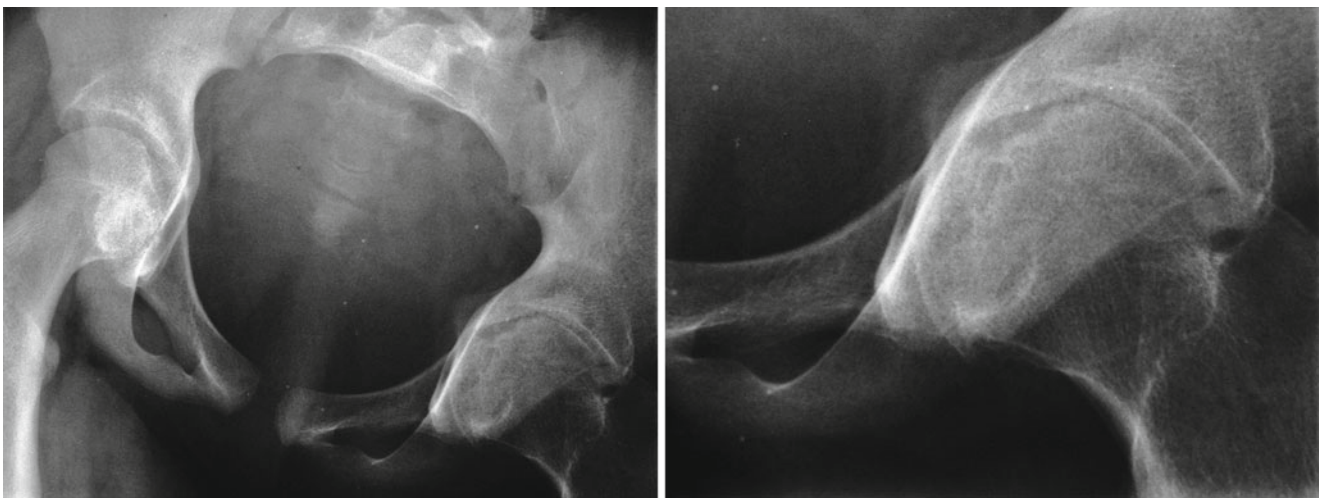

Fig. 5.33 Radiograph of the hips of a 15-year-old female with left-sided tuberculous arthritis. There is narrowing of the left joint space, with irregular joint surfaces and regional osteoporosis, as well as premature physeal closure in the ipsilateral femur

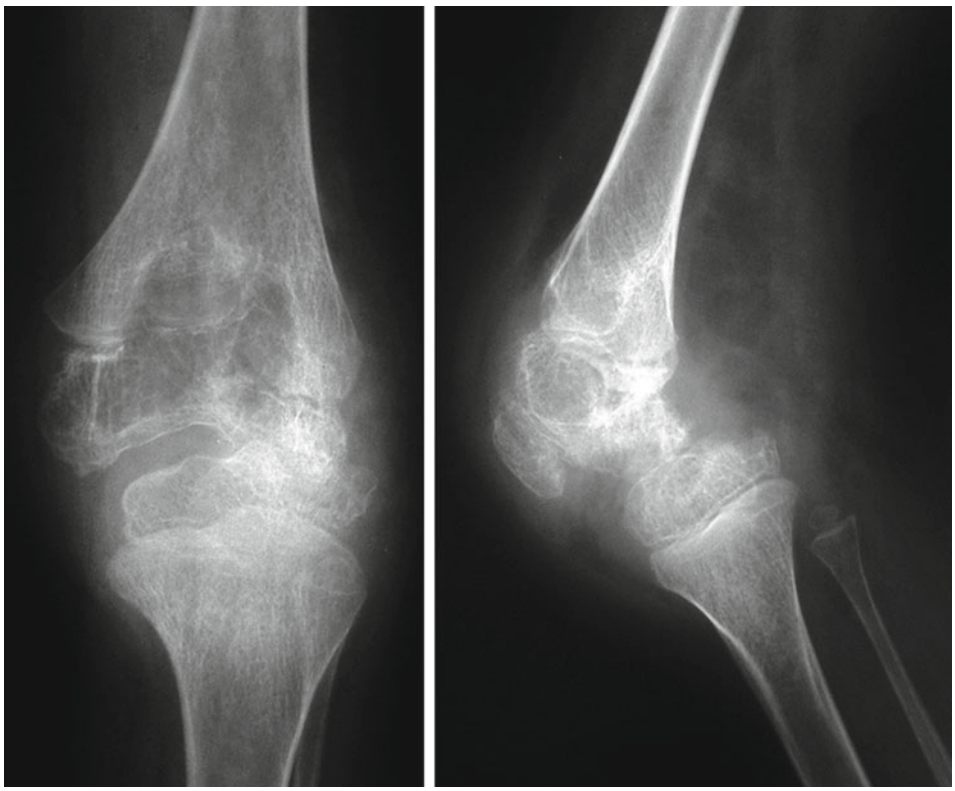

Fig. 5.34 A 6-year-old male with chronic arthritis in the left knee and a skin fistula. Radiographs disclose advanced destructive arthritis, marked osteoporosis, altered shape of the epiphyses, large bone erosions (mainly posterior, along the distal femur and the proximal tibia), and swelling of the regional soft tissues. Osteoarticular tuberculosis

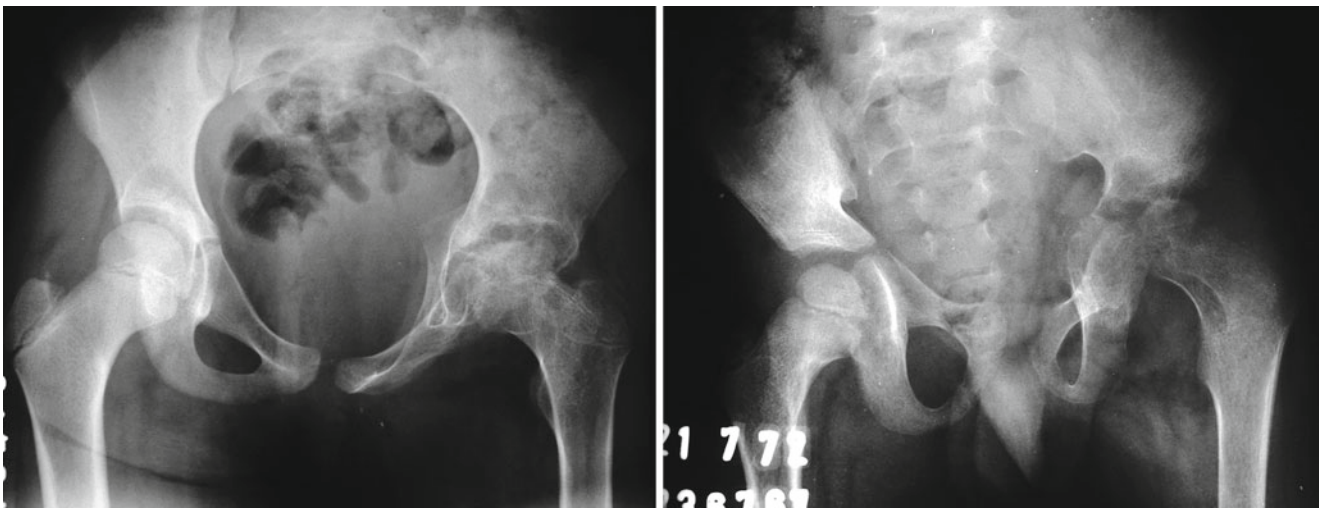

Fig. 5.35 Pelvic radiographs of two distinct children, both with advanced tuberculous arthritis of the left hip joints. Bone destruction with marked periarticular osteoporosis and irregularity of the joint surfaces can be seen, as well as hypoplasia of the left iliac bones and of the left proximal femora

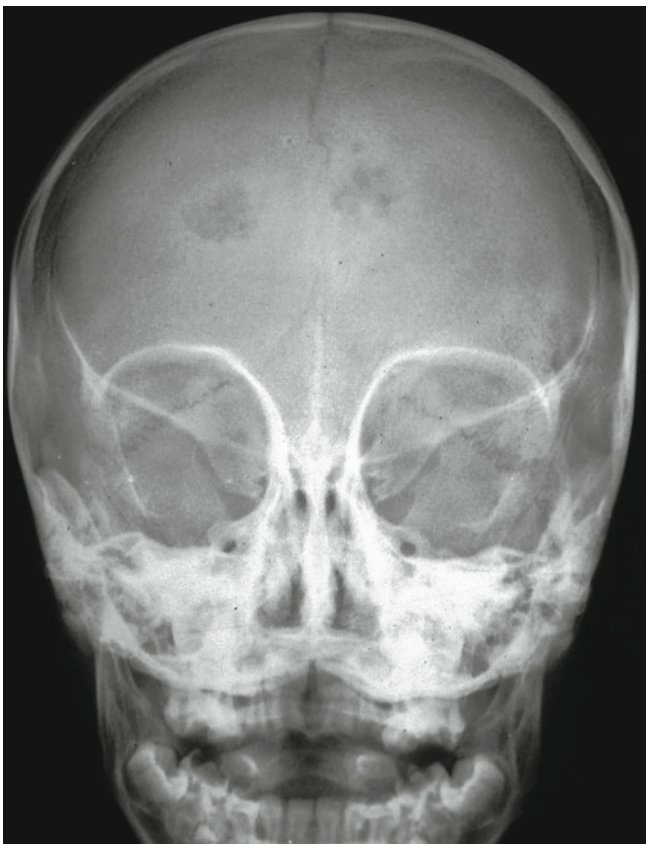

Fig. 5.36 A 3-year-old child with severe malnutrition and palpable nodules in the frontal region. Anteroposterior skull radiograph shows two paramedian lytic lesions in the frontal bone. A small button sequestrum is seen in the left-sided lesion. Tuberculous osteomyelitis

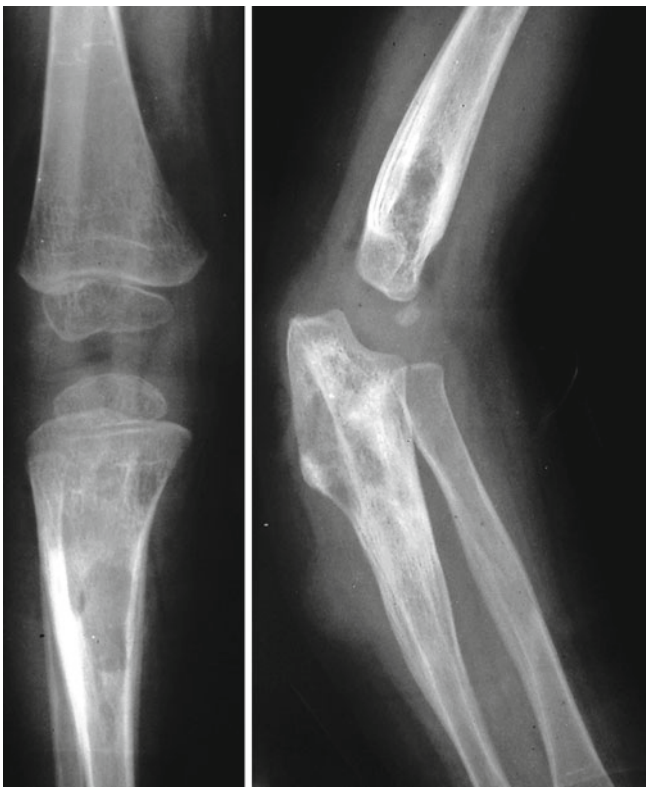

Fig. 5.37 Multifocal tuberculous osteomyelitis affecting the right knee and the left elbow. There is lamellar periosteal reaction in the humerus and solid periosteal apposition in the tibia and in the bones of the forearm, with mild bone expansion. Periarticular osteoporosis is also present, with lucent lesions in the distal humerus and in the proximal radius and tibia, as well as nodules in the dorsal soft tissues of the forearm

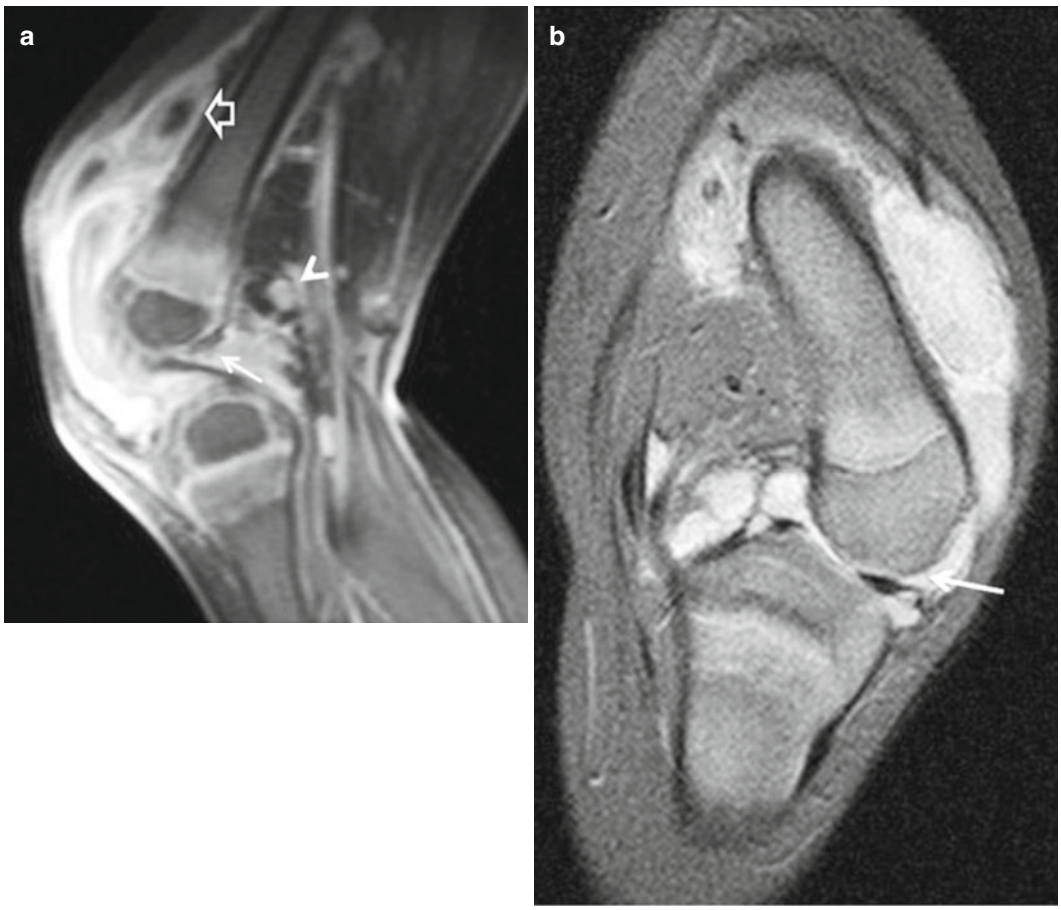

Fig. 5.38 Sagittal post-gadolinium T1-WI (**a**) and coronal STIR image (**b**) reveal cartilaginous loss (*arrow* in **a**), suprapatellar bursitis (*open arrow* in **a**), enlarged popliteal lymph nodes (*arrowhead* in **a**), and anatomical disorganization (*arrow* in **b**) in a 3-year-old boy with knee tuberculosis (Reprinted with permission from Prasad et al. (2012))

assessment of tuberculous arthritis are similar to those above described for pyogenic arthritis.

US is helpful in the assessment of tuberculous arthritis in children, being also able to guide joint aspirations. Just like in PA, common findings include joint effusion (which may be heterogeneous), synovial thickening/hyperemia, and soft-tissue swelling (Fig. 5.40); superficially located erosions may be seen. Soft-tissue abscesses appear as rounded/oval masses with variable echogenicity, depending on their content, presenting peripheral hyperemia on Doppler studies and posterior acoustic enhancement (Fig. 5.40).

5.4 Transient Synovitis of the Hip

Transient synovitis of the hip (TSH), also referred to as toxic synovitis, is an acute condition characterized by joint effusion and nonspecific synovial proliferation in the hip joint. It is one of the main differential diagnoses of the infectious arthritides and the most frequent cause of acute hip pain in children from 3 to 10 years of age, occurring bilaterally in up to 25 % of the patients. Its etiology is unknown and it is a diagnosis of exclusion. In most cases, prognosis is good and affected children will have complete recovery with conservative treatment. The main diagnostic

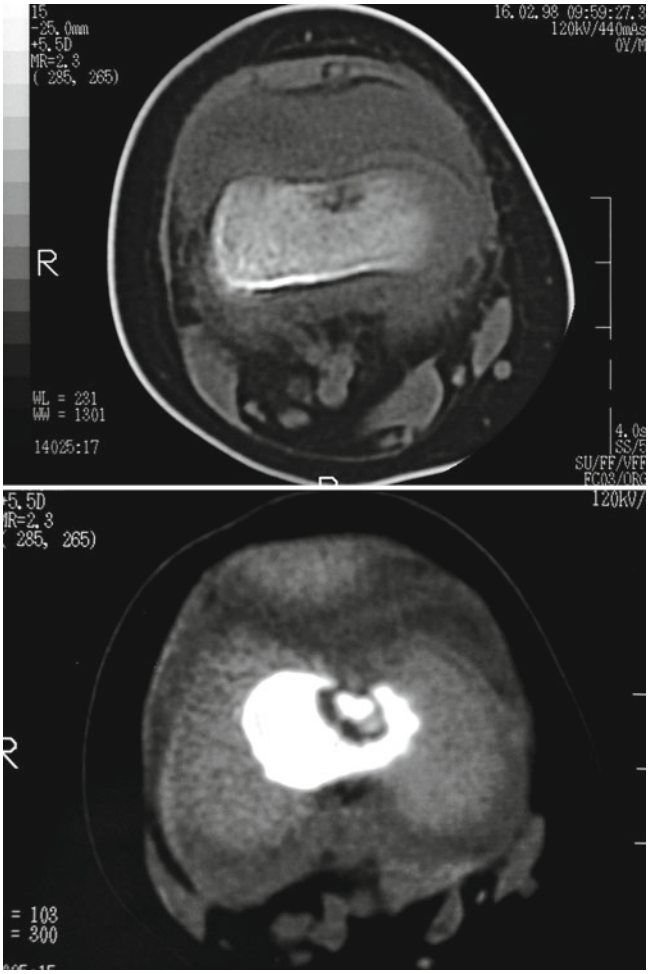

Fig. 5.39 Transverse CT images of the right knee of a child with tuberculous arthritis. Synovial thickening and a large joint effusion are present, as well as a lytic lesion containing a bone sequestrum in the distal femur

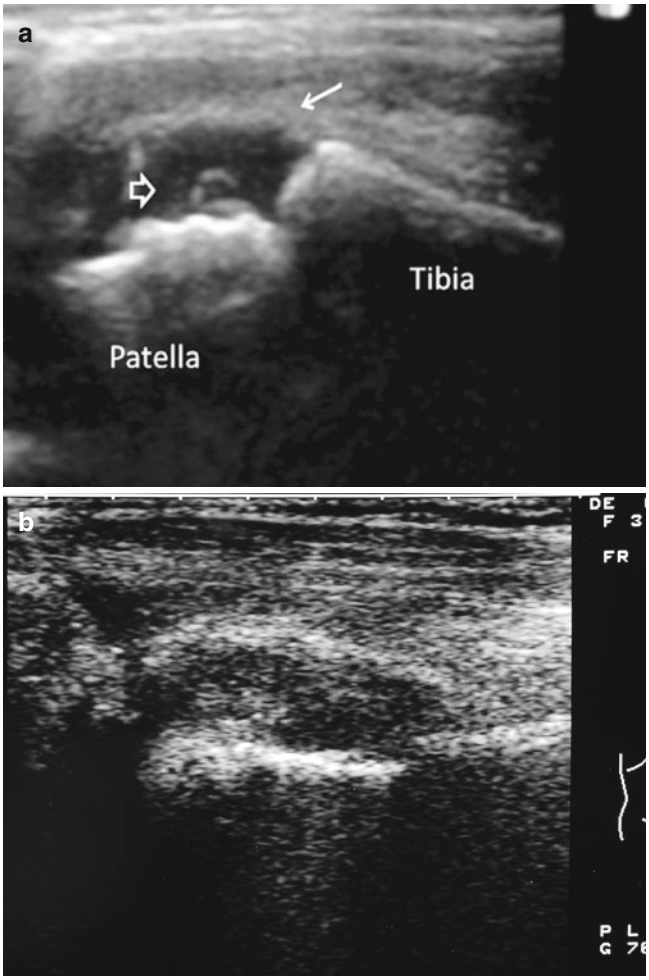

Fig. 5.40 In (**a**), US of the left knee in the sagittal plane shows synovial hypertrophy (*arrow*) and joint effusion (*open arrow*) in a 10-year-old boy with tuberculous arthritis (Reprinted with permission from Prasad et al. (2012)). In (**b**), a longitudinal US scan of the left hip of a patient with tuberculous arthritis reveals a deeply seated, well-delimited heterogeneous abscess adjacent to the femoral cortex, with posterior acoustic enhancement

challenge in TSH consists in distinguishing it from infectious arthritides, as the clinical picture and the imaging findings may be similar, but symptoms are usually more acute and severe in the latter. If left untreated, septic arthritis follows a relentless course, with abnormal laboratory tests; conversely, fever in children with TSH is usually low or absent, and there will be no clinical or laboratory evidence of systemic disease.

In TSH, radiographs are normal or show nonspecific findings, such as mild osteoporosis of the proximal femur, widening of the joint space, and obliteration of fat planes around the hip. Radiographs are especially recommended for children with less than 1 year of age and for those older than 8 years old because TSH is uncommon in these age groups, in which septic arthritis and child abuse (younger children) and slipped femoral capital epiphysis (older children) predominate. US is the first line of investigation for patients with TSH, as synovial thickening and even small joint effusions can be detected (Fig. 5.41) and image-guided joint aspiration may be performed in the same session. MRI is a second-line study in TSH, showing joint effusion and mild synovitis without significant bone marrow edema or erosive arthritis (Fig. 5.42). Other imaging studies are rarely used in patients with TSH.

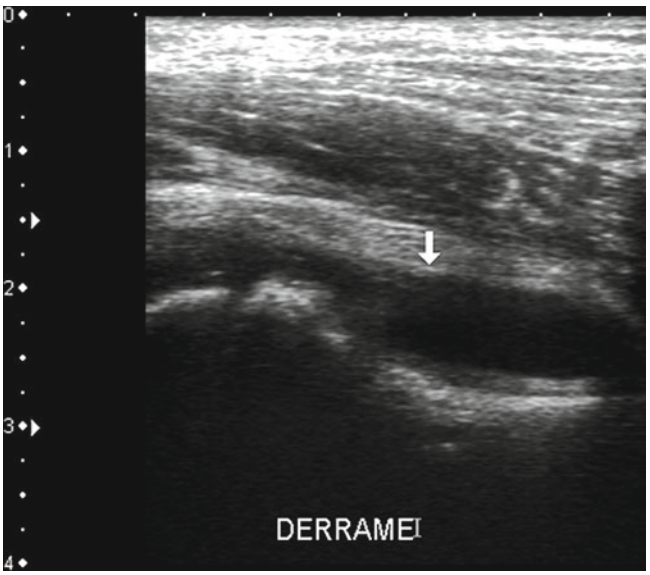

Fig. 5.41 US of the right hip of a child with TSH. Joint effusion is quite evident as well as synovial thickening. Nevertheless, these are nonspecific findings and do not allow to infer the real nature of the arthritis. Laboratory analysis of the synovial fluid was negative for infection and arthritis subsided with conservative treatment

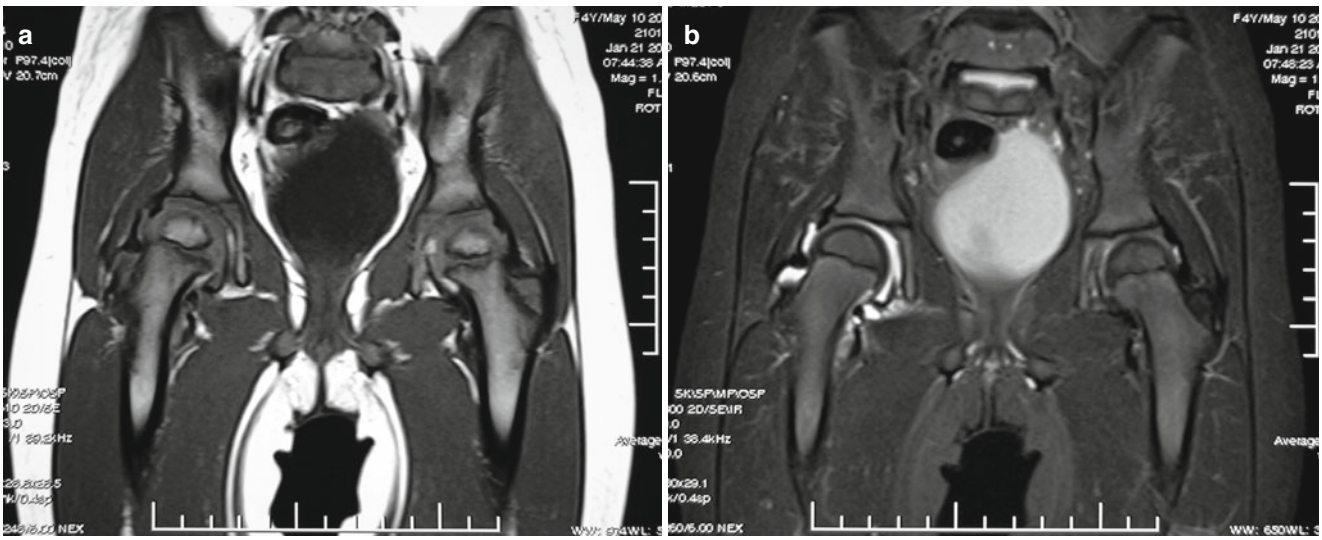

Fig. 5.42 T1-WI (**a**), STIR image (**b**), and post-gadolinium fat sat T1-WI (**c**) of a 4-year-old child with right-sided TSH. There is moderate joint effusion and synovial thickening presenting post-contrast enhancement. Erosions and bone marrow edema are notably absent. Complete recovery was achieved with conservative measures

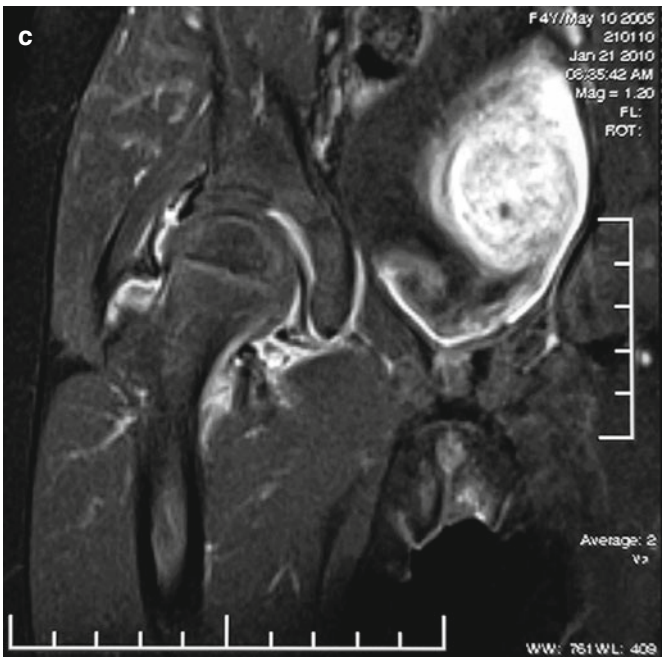

Fig. 5.42 (continued)

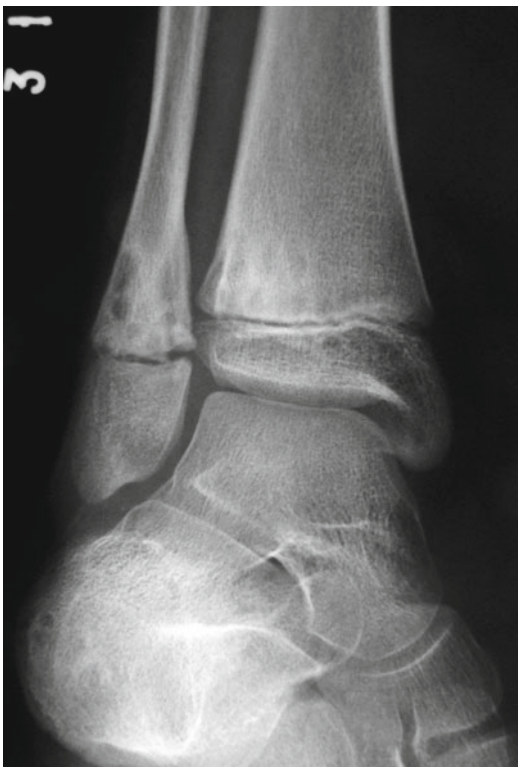

Fig. 5.43 Oblique view of the right ankle of a 12-year-old male with CRMO. Several well-delimited lytic lesions are seen in the distal metaphyses of the tibia and fibula, adjacent to the growth plates, surrounded by sclerosis and not associated with cortical rupture or periosteal reaction. Similar lytic lesions are also identified in the posterior portion of the calcaneus

5.5 Chronic Recurrent Multifocal Osteomyelitis

Chronic recurrent multifocal osteomyelitis (CRMO) is an idiopathic inflammatory disease of the bones that affects most often females from 9 to 14 years of age. CRMO is characterized by (1) multifocal and non-pyogenic bone lesions; (2) undulating course, with exacerbations and remissions; and (3) association with other inflammatory diseases. These patients present recurrent episodes of osteitis, with swelling and tenderness in the affected sites. Histological findings are compatible with chronic osteomyelitis, but there are no viable microorganisms in samples of the affected tissues, laboratory tests are nonspecific, and cultures are negative. CRMO is a diagnosis of exclusion, based on clinical data, histopathological findings, and imaging. Prognosis is usually good.

Radiographs are the first imaging study ordered for most patients. CRMO typically presents with one or more lytic, eccentrically located metaphyseal lesions surrounded by sclerosis, abutting the growth plate (Fig. 5.43). There is a distinct predilection for the long bones, and the distal metaphysis of the tibia is the most commonly involved site. The clavicles are also often affected, mainly in its medial portions, sparing the sternoclavicular joint. Pathologic fractures occur mainly in the thoracic vertebrae and may lead to scoliosis of acute onset. Recurrent episodes of osteitis lead to bone sclerosis, cortical thickening, and diaphyseal involvement (Fig. 5.44), with abnormal bone modeling and metaphyseal widening in long-standing disease. MRI may be helpful if radiographs are negative or inconclusive: active lesions are typically associated with bone marrow edema pattern, while inactive, chronic lesions exhibit predominance of sclerosis, with low signal intensity in all sequences (Fig. 5.45). Mild inflammation of the surrounding soft tissues may also be found, but abscesses are absent. Investigation of multifocal CRMO is usually performed with bone scintigraphy or whole-body MRI, aiming to detect "occult" sites of involvement.

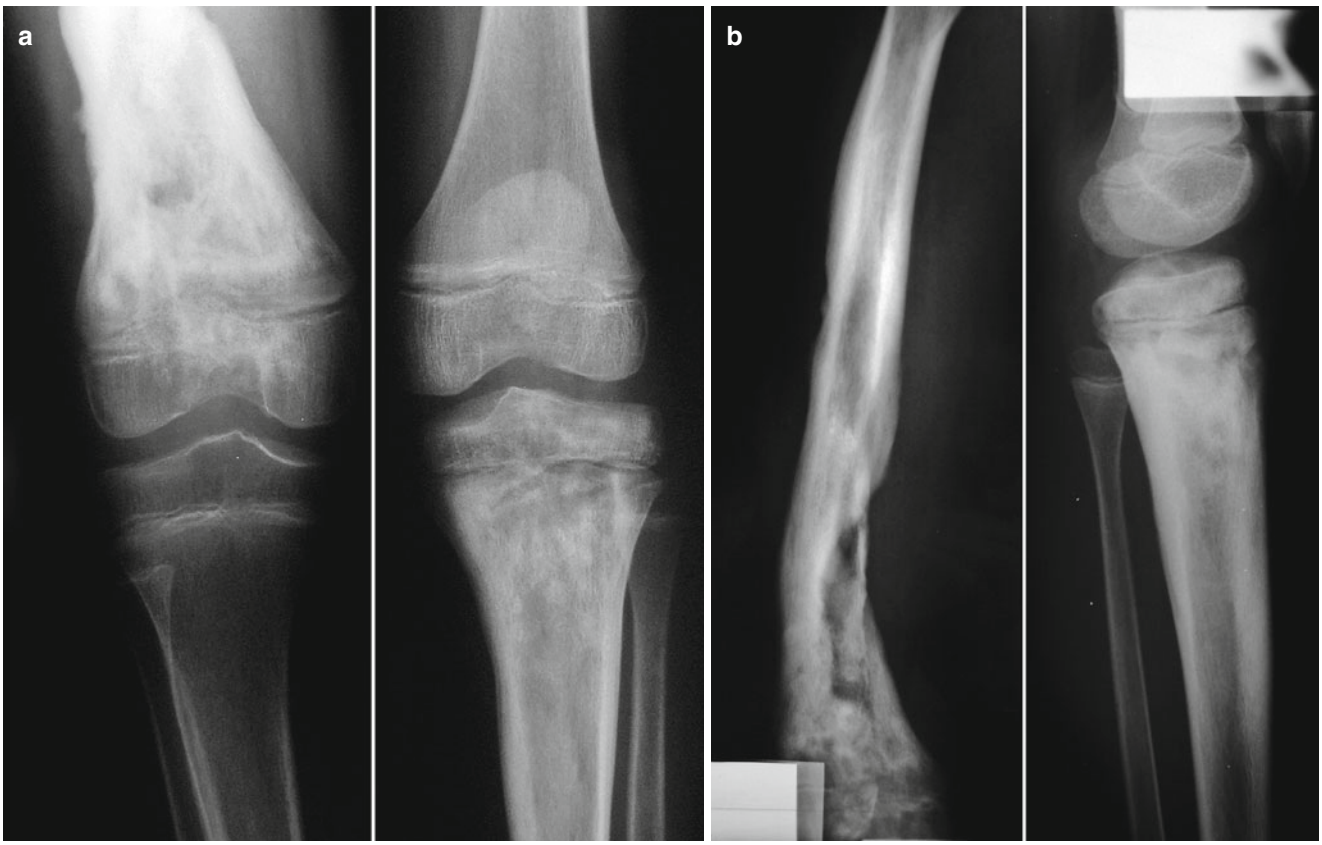

Fig. 5.44 Anteroposterior view of the knees (**a**) and lateral views of the right femur and of the left tibia (**b**) of an adolescent with CRMO of long evolution. The affected bones are widened, showing cortical thickening and heterogeneous density, intertwining sclerotic and lucent zones, which are mostly metaphyseal and diaphyseal. The posterior cortex of the femur is markedly irregular. These findings are quite similar to those found in chronic infectious osteomyelitis

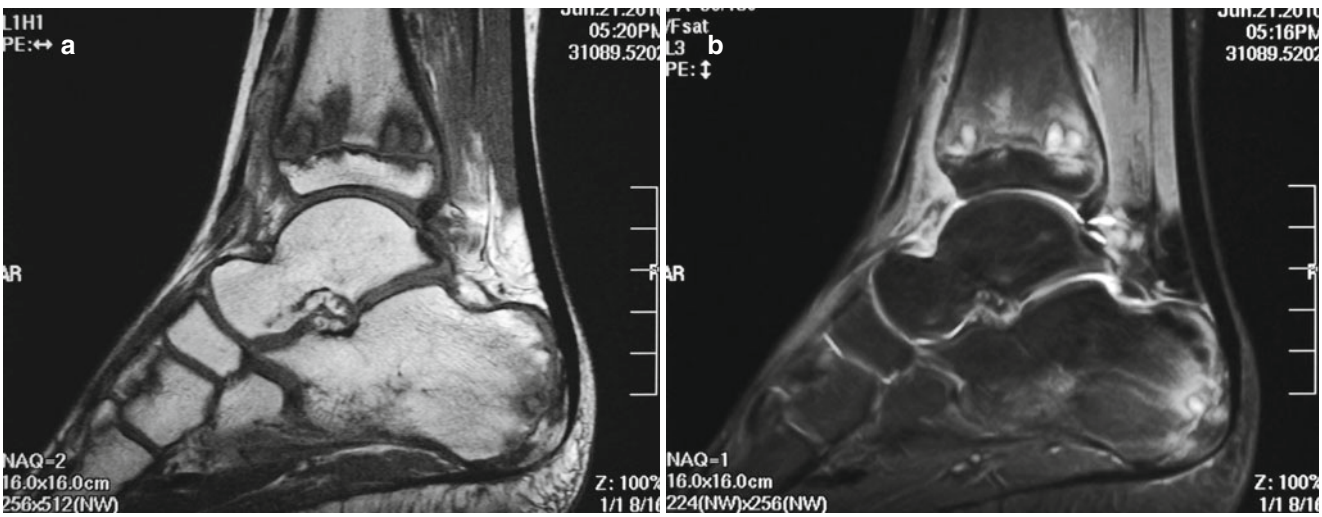

Fig. 5.45 Sagittal T1-WI (**a**) and fat sat T2-WI (**b**) and coronal fat sat T2-WI (**c**) of the right ankle of the same patient of Fig. 5.43. The lytic lesions seen on radiographs display low signal intensity on T1-WI and high signal intensity on T2-WI, with surrounding bone marrow edema and sclerotic borders. Edema of the periarticular soft tissues is also present

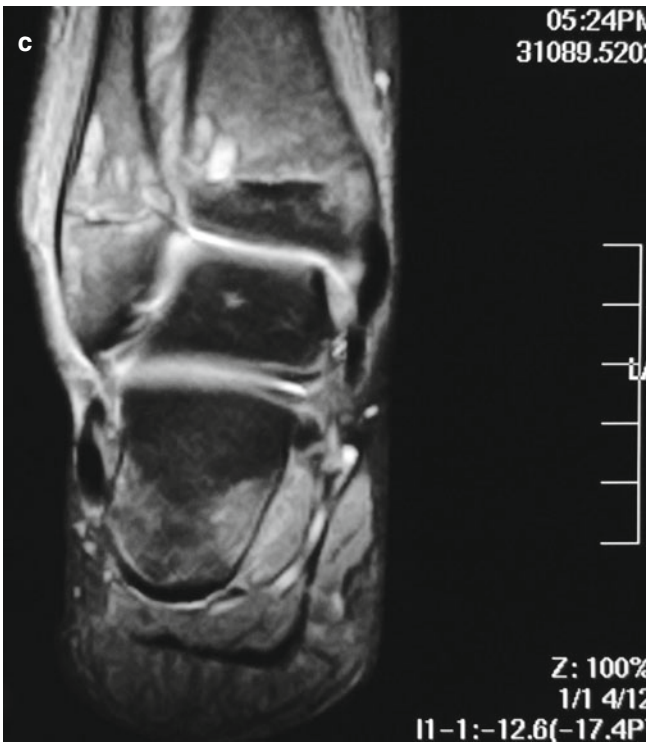

Fig. 5.45 (continued)

Key Points

- PA is a rapidly evolving disease that leads to accelerated joint destruction. Radiographs are insensitive, and radiographic findings appear late in the course of the disease. Early-stage abnormalities include synovitis and joint effusion: MRI is the most sensitive imaging method, being also able to demonstrate bone marrow edema, while US is also fairly sensitive for soft-tissue abnormalities, but insensitive for bone assessment. CT and bone scintigraphy have limited usefulness.
- Radiographic findings typical of tuberculous arthritis include marked periarticular osteoporosis, indolent course, and relative preservation of the joint space. Findings similar to those found in other hyperemic arthropathies can be found, such as epiphyseal overgrowth and early closure of the growth plates. The role of the imaging methods is similar in PA and in tuberculous arthritis.
- TSH is a self-limited and nondestructive arthritis that affects the hip of children. Joint effusion and synovitis are common, while bone erosions and significant bone marrow edema are notably absent. Radiographs and US are the first line of investigation, while MRI is reserved for selected cases.
- CRMO presents lytic lesions eccentrically located in the metaphyses of tubular bones, which may be associated with abnormal bone modeling and sclerosis of the medullary bone in long-standing disease. The main role of MRI is to distinguish active from inactive lesions. Bone scintigraphy and whole-body MRI are useful to demonstrate "occult" sites of involvement, considering the multifocal nature of CRMO.

Recommended Reading

Bancroft LW (2007) MR imaging of infectious processes of the knee. Radiol Clin North Am 45(6):931–941
Buchmann RF, Jaramillo D (2004) Imaging of articular disorders in children. Radiol Clin North Am 42(1):151–168
Daldrup-Link HE, Steinbach L (2009) MR imaging of pediatric arthritis. Magn Reson Imaging Clin N Am 17(3):451–467
Dwek JR (2009) The hip: MR imaging of uniquely pediatric disorders. Magn Reson Imaging Clin N Am 17(3):509–520
Fabry G (2010) Clinical practice: the hip from birth to adolescence. Eur J Pediatr 169(2):143–148
Frank G, Mahoney HM, Eppes SC (2005) Musculoskeletal infections in children. Pediatr Clin North Am 52(4):1083–1106
Gutierrez K (2005) Bone and joint infections in children. Pediatr Clin N Am 52(3):779–794
Khanna G, Sato TS, Ferguson P (2009) Imaging of chronic recurrent multifocal osteomyelitis. Radiographics 29(4):1159–1177
Koplas MC, Simonelli PS, Bauer TW, Joyce MJ, Sundaram M (2010) Your diagnosis? Chronic recurrent multifocal osteomyelitis. Orthopedics 33(4):218
Laine JC, Kaiser SP, Diab M (2010) High-risk pediatric orthopedic pitfalls. Emerg Med Clin North Am 28(1):85–102
McCarthy JJ, Noonan KJ (2008) Toxic synovitis. Skeletal Radiol 37(11):963–965
Prasad A, Manchanda S, Sachdev N, Baruah BP, Manchanda V (2012) Imaging features of pediatric musculoskeletal tuberculosis. Pediatr Radiol 42(10):1235–1249
Pruthi S, Thapa MM (2009) Infectious and inflammatory disorders. Magn Reson Imaging Clin N Am 17(3):423–438
Ranson M (2009) Imaging of pediatric musculoskeletal infection. Semin Musculoskelet Radiol 13(3):277–299
Teo HE, Peh WC (2004) Skeletal tuberculosis in children. Pediatr Radiol 34(11):853–860

Articular and Periarticular Tumors and Pseudotumors

6

6.1 Introduction

Even though tumors and pseudotumors are not rheumatic conditions per se, their clinical and/or imaging presentation often resemble those of articular diseases, especially when located within the joints or in nearby areas. Histopathological analysis remains indispensable for the definitive diagnosis, but imaging studies play a fundamental role in the assessment of these lesions. Many musculoskeletal tumors/pseudotumors have a typical appearance on imaging, thus allowing for a presumptive diagnosis with a reasonable degree of accuracy. In addition, surgical planning relies on adequate preoperative staging, which can be safely achieved with imaging. Only selected lesions more prone to simulate rheumatic conditions in the pediatric age group – either from a clinical standpoint or on imaging – will be included in this chapter.

6.2 Bone Lesions

Two primary bone tumors of the childhood will deserve special attention in this topic: osteoid osteoma (OO) and chondroblastoma. OO is the most common of the benign bone tumors, usually found in males in the second decade of life. It is a small (<1.5 cm), hypervascular osteogenic lesion, found most often in the lower limbs. Intra-articular lesions comprise roughly 13 % of all OO and are more common in the hips, in the tarsal and carpal bones, and in the spine. Classic OO is a cortical tumor of the diaphyses of the long bones, which usually does not pose an important diagnostic challenge (Fig. 1.17). However, juxta-articular/intra-articular lesions may be difficult to diagnose because they are often subperiosteal or centrally located, not infrequently found in anatomically complex regions. Patients complain of local pain (which typically gets worse at night and is relieved by salicylates), inflammatory signs, and limited range of motion that may simulate primary monoarthritis. Typical radiographic findings include a radiolucent nidus with central calcification, periosteal reaction, and peripheral sclerosis (Fig. 6.1); however, detection of articular/periarticular OO may be particularly tricky due to superimposition of osseous structures, especially in complex joints (Fig. 6.2). In addition, the real size of the tumoral nidus is often underestimated, as reactive sclerosis and periosteal reaction are frequently mild or even absent in intra-articular lesions. Regional osteoporosis and widening of the joint space (due to joint effusion/synovitis) are also found, as well as premature osteoarthritis (Fig. 6.1). Computed tomography (CT) is the most sensitive imaging method to demonstrate the hypodense nidus, the internal calcifications, and the peripheral bone sclerosis, being especially useful in the assessment of intra-articular OO (Figs. 6.2 and 6.3). On magnetic resonance imaging (MRI), the nidus show low to intermediate signal intensity on T1-weighted images (T1-WI) and variable signal on T2-weighted images (T2-WI), with post-gadolinium enhancement in most cases (Figs. 6.1 and 6.2); calcifications appear as areas of low signal intensity in all sequences. MRI is the best imaging method to demonstrate the inflammatory component associated with OO, represented by bone marrow edema pattern (which may be very intense, up to the point of masking the tumor itself) and edematous changes of the surrounding soft tissues (Figs. 6.1 and 6.2). Although insensitive for tumor detection, US is useful to demonstrate synovitis and hyperemia. Scintigraphies are not particularly valuable for the diagnosis of intra-articular OO, usually showing diffuse and nonspecific uptake (Fig. 6.4).

The second bone tumor to be addressed in this topic is chondroblastoma, a rare and benign neoplasm that originates from cartilage germ cells in the epiphyses of the long bones of skeletally immature patients. It is more prevalent in males in their second or third decades of life, and typical locations include the proximal epiphyses of the humerus and of the tibia and the distal epiphysis of the femur. In most cases, chondroblastomas are small lesions (<4 cm), but as much as 60 % of these tumors may cross the growth plate and extend to the metaphysis; cortical rupture and intra-articular dissemination may also occur. On radiographs, they appear as lytic, geographic expansile lesions,

S.L. Viana et al., *Joint Imaging in Childhood and Adolescence*,
DOI 10.1007/978-3-642-35876-0_6, © Springer-Verlag Berlin Heidelberg 2013

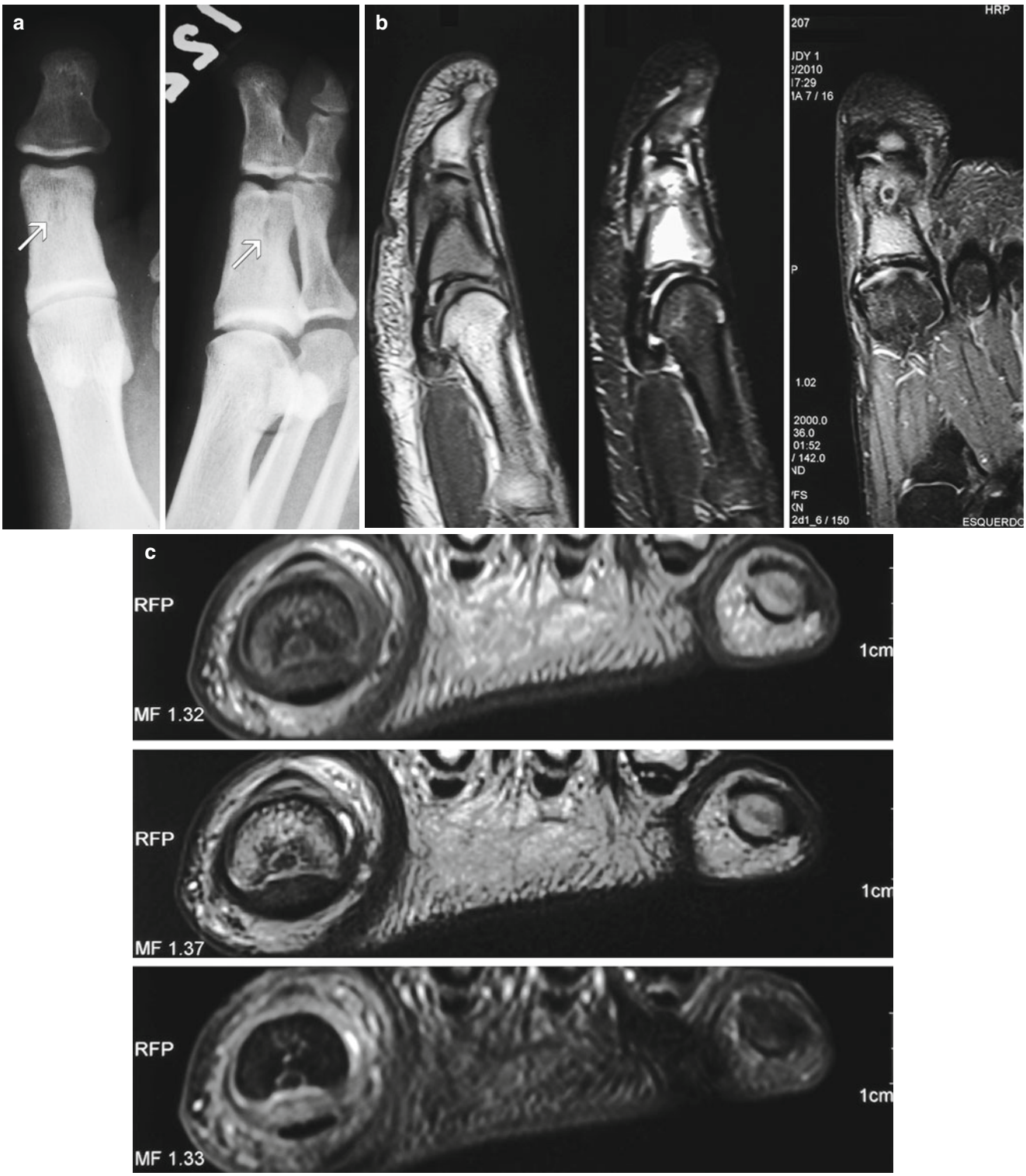

Fig. 6.1 Female adolescent complaining of painful swelling of her left hallux. Radiographs (**a**) reveal widening of the mid-diaphysis of the proximal phalanx of the hallux, as well as solid periosteal reaction and premature osteoarthritis of the metatarsophalangeal joint. There is an ill-defined lucency in the distal diaphysis (*arrows*), with a central area of increased density. In (**b**), T1-WI (*left*) and STIR images (*center* and *right*) demonstrate a subperiosteal OO adjacent to the plantar cortex of the proximal phalanx, with low signal intensity in all sequences in its inner portion due to calcification of the nidus. Extensive bone marrow edema pattern and edema of the adjacent soft tissues are evident, as well as metatarsophalangeal arthritis. In (**c**), coronal gradient-echo image (*upper image*), T2-WI (*central image*), and post-gadolinium fat sat T1-WI (*lower image*) corroborate the above-mentioned findings and reveal enhancement of the non-mineralized portion of the nidus and of the inflamed tissues

with lobulated borders. A thin peripheral rim of sclerosis may be present, as well as punctate calcifications in the tumor matrix, which are even more evident on CT (Fig. 6.5). Roughly half of the patients present solid periosteal reaction along the diaphysis of the affected bone. On MRI, the lesion is predominantly hypointense on T1-WI and heterogeneous on T2-WI, varying from hypointense to hyperintense depending on the degree of mineralization of the tumor matrix. Calcifications are hypointense in all sequences, while cartilaginous islets are hypointense on T1-WI and hyperintense on T2-WI. Extensive bone marrow edema pattern (which is often disproportionate to the size of the tumor), joint effusion, and edema of the soft tissues can also be seen on MRI, as well as post-contrast enhance-

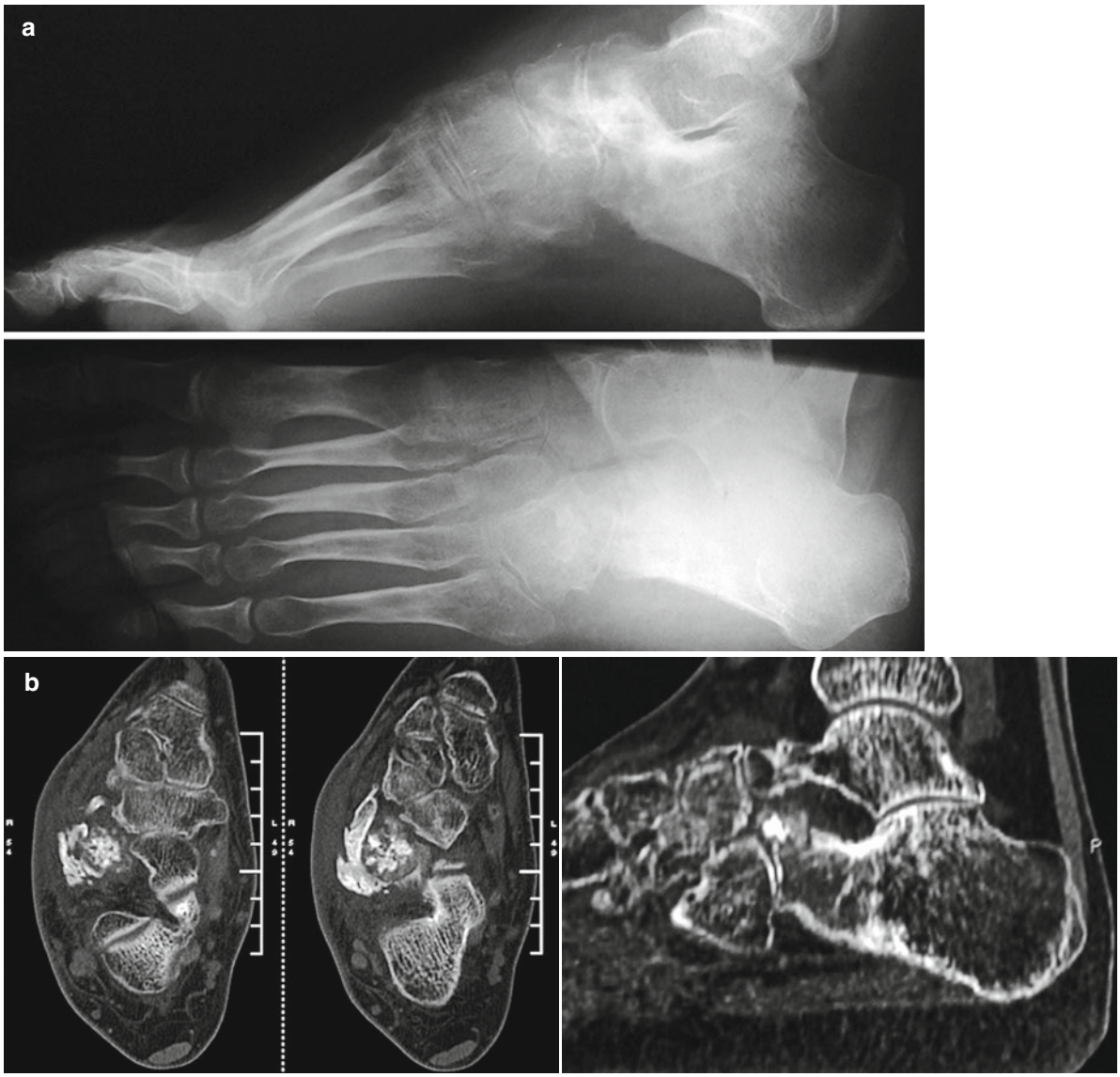

Fig. 6.2 An 18-year-old patient complaining of chronic arthritis of the right ankle, with onset 3 years earlier; two biopsies of the calcaneus were inconclusive. Radiographs (**a**) reveal marked osteoporosis and osteoarthritis of the midfoot and of the hindfoot, with sclerosis of the anterior portion of the calcaneus. In (**b**), transverse CT images (*left*) and sagittal reformatted images (*right*) demonstrate, in addition to the above-mentioned findings, the grossly calcified nidus of an OO in the anterior calcaneal process. There is reactive sclerosis and exuberant bone neoformation. In (**c**), sagittal T1-WI (*upper-left image*) and STIR image (*upper-right image*) demonstrate that the nidus is predominantly hypointense in all sequences, with surrounding bone marrow edema and edema of the adjacent soft tissues. In the *lower row*, STIR images in the transverse (*left*) and coronal (*right*) planes are very helpful to demonstrate the edematous changes and the arthritic component in the ankle, with joint effusion and synovitis

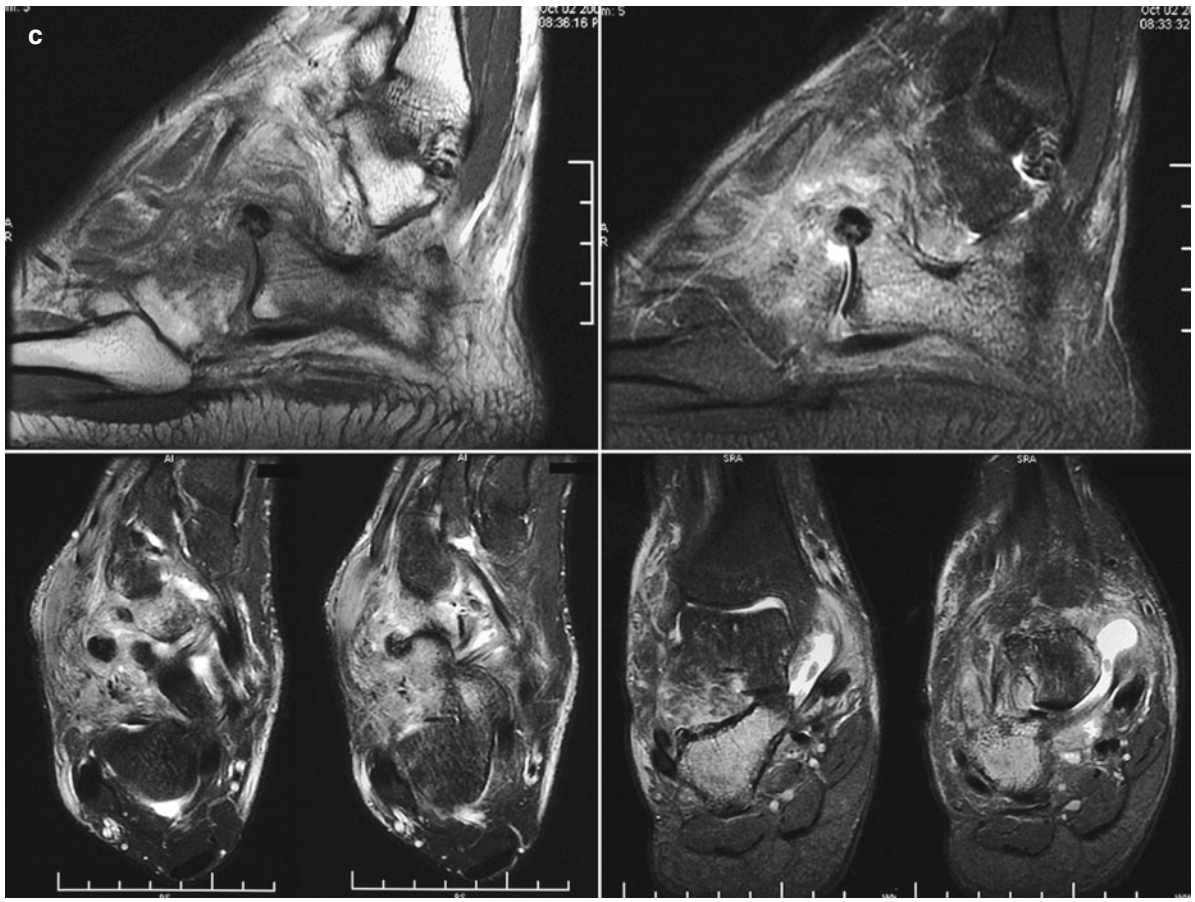

Fig. 6.2 (continued)

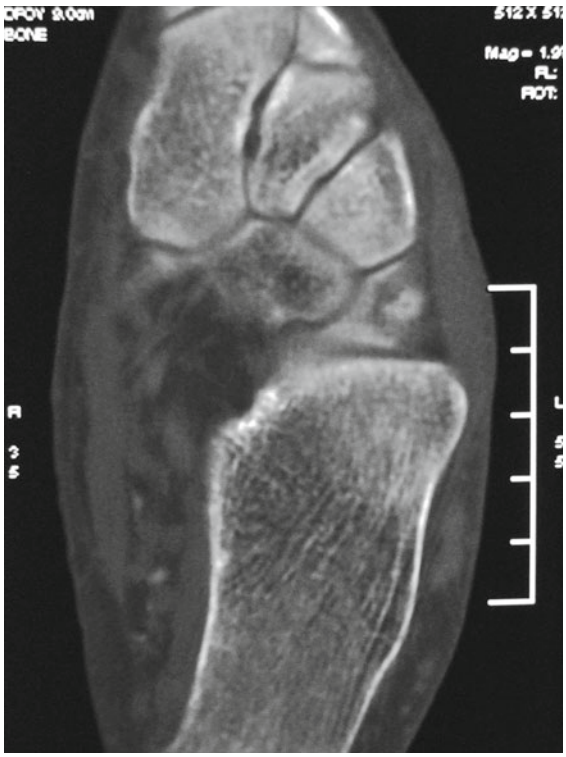

Fig. 6.3 Transverse CT image of the left midfoot demonstrates a nidus of OO in the superolateral portion of the cuboid, with peripheral hypodensity and a calcified central component

ment of the tumor itself and of the above-described edematous changes. Fluid levels may indicate coexistence of an aneurysmal bone cyst.

Other conditions may simulate bone tumors and must be included in the differential diagnosis of true neoplasms. Cortical desmoids are common lesions, more frequently found in the posterior cortex of the medial femoral condyle of preadolescent and adolescent males, a few centimeters above the growth plate. They are benign, self-limited fibro-osseous lesions that may represent a developmental variant or a response to chronic traction in the insertion of the aponeurosis of the adductor magnus or at the origin of the medial gastrocnemius. On radiographs and CT, they vary from a subtle focal irregularity (Fig. 6.6a, b) to a bone defect (Fig. 6.6c–f) along the posterior cortex of the femur, which sometimes may be ill-defined, simulating an aggressive condition, especially if associated with bone overgrowth or periostitis. On MRI, cortical desmoids are hypointense on T1-WI and hyperintense on T2-WI (Fig. 6.6b), and a rim of low signal intensity in all sequences may be present; bone marrow edema pattern and edema of the adjacent soft tissues are also sometimes found. Although the bone defect itself may present some degree of post-gadolinium enhancement, there is no soft-tissue mass.

At least two dysplastic lesions that may simulate tumors also deserve mention here: focal fibrocartilaginous dysplasia

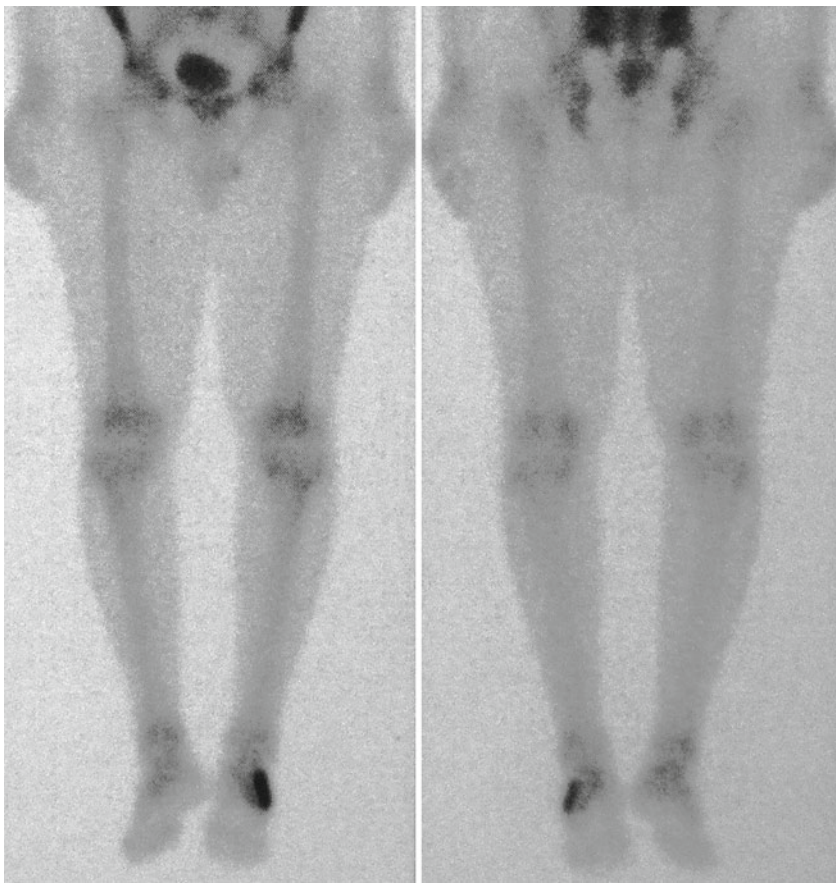

Fig. 6.4 Bone scintigraphy of the same patient of Fig. 6.3. There is increased uptake in the lateral portion of the left midfoot, which is completely nonspecific. In cases like this, other imaging studies should be requested in order to clarify the real nature of the abnormal finding

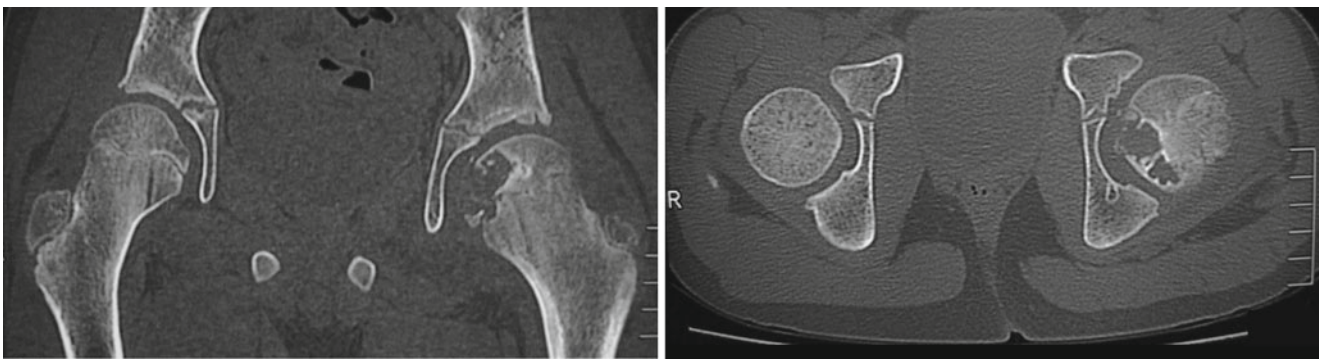

Fig. 6.5 CT of the hips of an adolescent with chondroblastoma of the left proximal femur. Coronal reformatted image (*left image*) and transverse section (*right image*) demonstrate a well-delimited lytic lesion in the left femoral head, surrounded by a thin sclerotic rim, with delicate foci of calcification in the tumor matrix. In spite of the circumscribed appearance of the lesion, there is cortical discontinuity with dissemination to the joint cavity

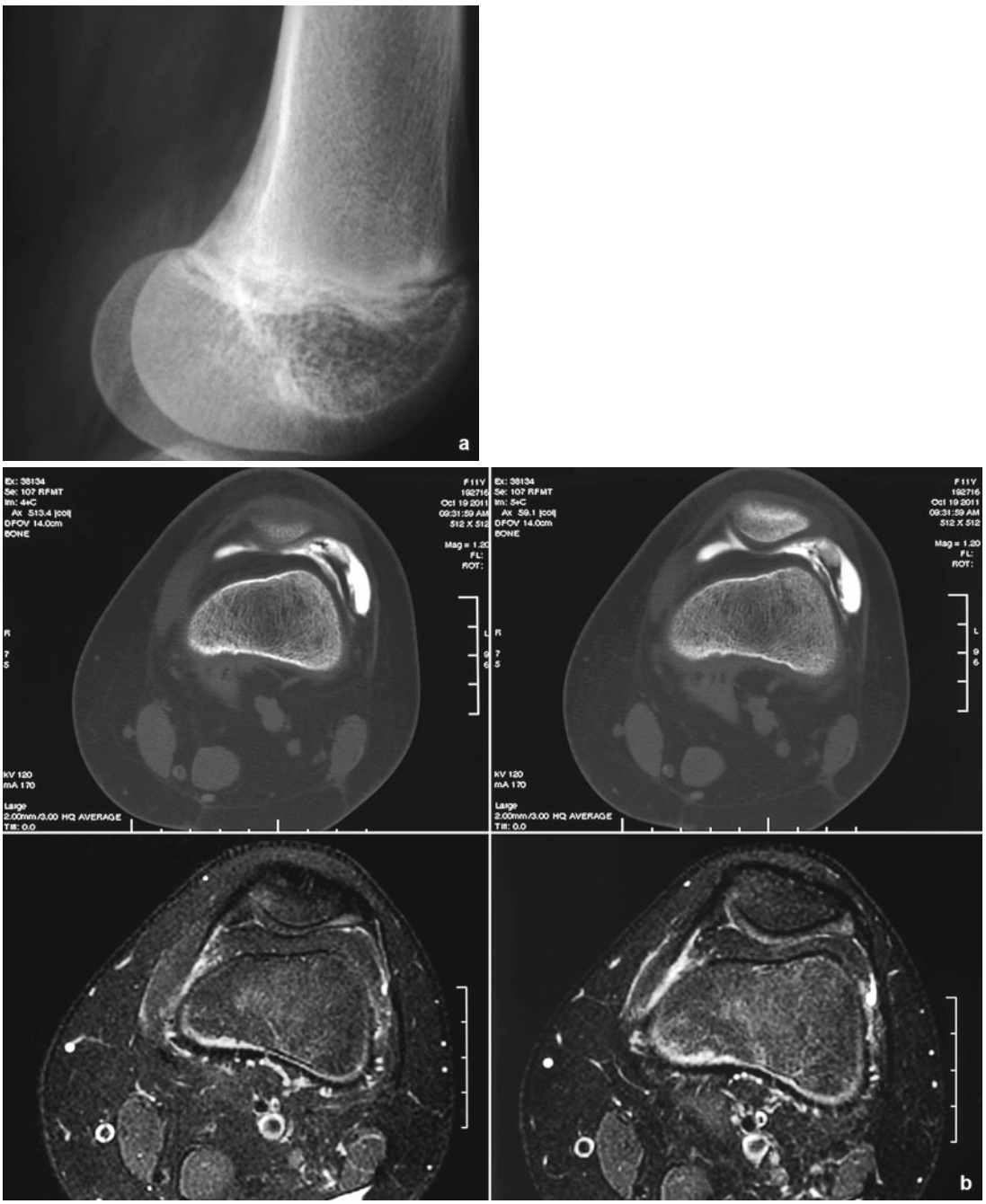

Fig. 6.6 In (**a**), lateral view of the left knee of an 11-year-old female with joint pain shows irregularity of the posterior cortex of the medial femoral condyle, immediately above the growth plate. In (**b**), transverse images of a CT-arthrography (*upper row*) demonstrate that the irregular cortex is adjacent to the origin of the medial gastrocnemius, with subtle subcortical sclerosis. This cortical desmoid is hyperintense on transverse fat sat T2-WI (**b**, *lower row*). In (**c**–**f**), a large bone defect is seen in a similar location in a 13-year-old male, clearly associated with the origin of the medial gastrocnemius, which is more evident on reformatted and volume-rendered images

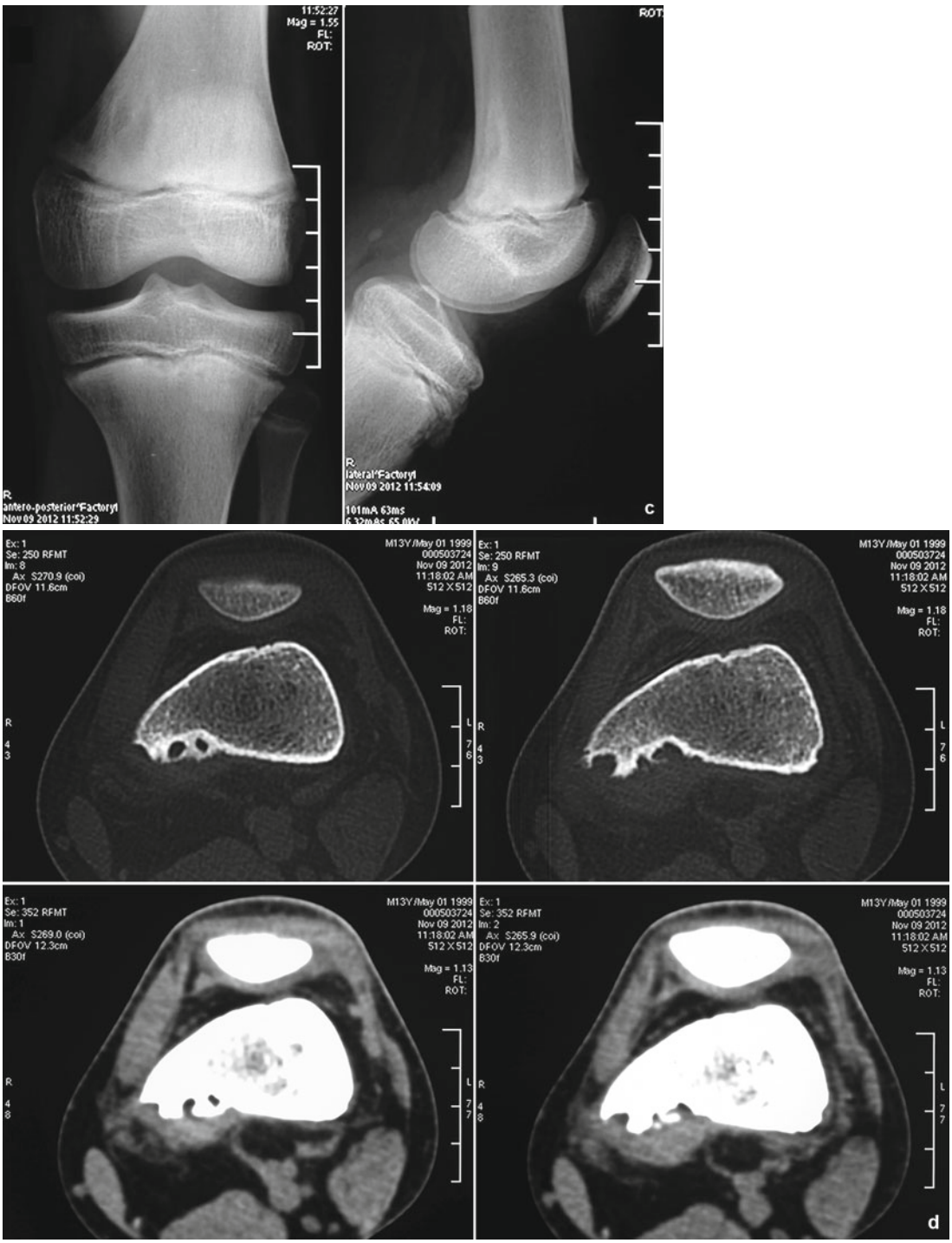

Fig. 6.6 (continued)

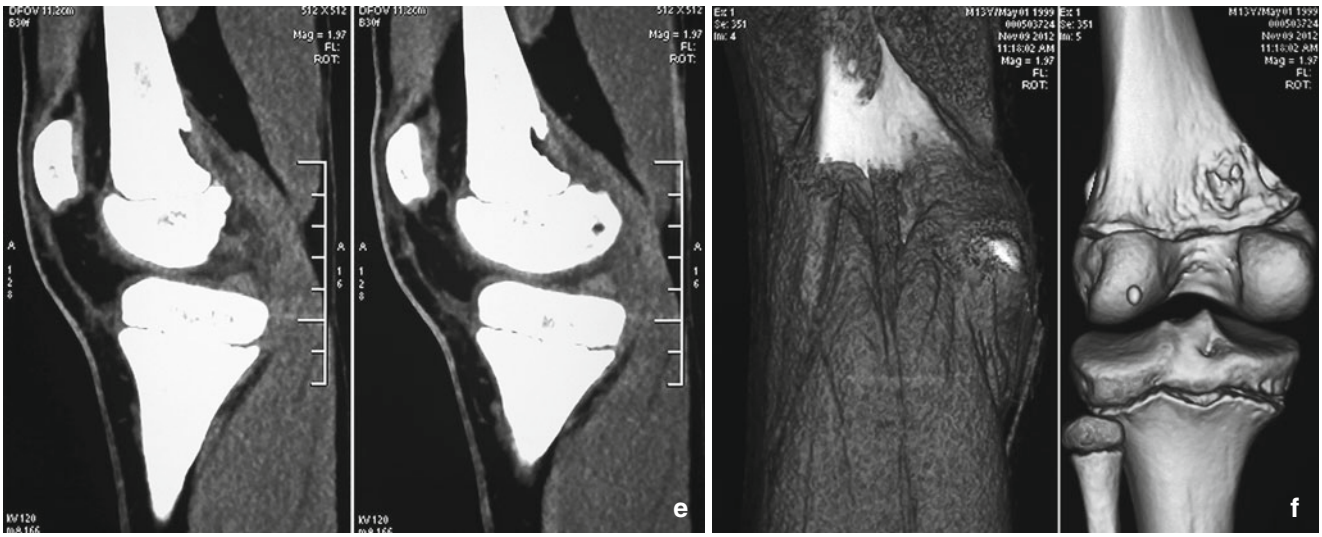

Fig. 6.6 (continued)

(FFD) and dysplasia epiphysealis hemimelica (DEH). FFD is a rare entity, probably related to abnormal development of the mesenchymal anlage at the insertion of the pes anserinus. It is usually diagnosed during the second year of life, after the child begins to walk. Affected patients present pain, limping, and, occasionally, refusal to walk, often associated with progressive tibia vara. Radiographic and CT findings are typical, demonstrating a well-delimited cortical lucency with sclerotic borders in the anteromedial portion of the proximal tibial metaphysis, extending to the diaphysis (Fig. 6.7). On MRI, the lesion presents low signal intensity in all sequences due to the presence of dense fibrous connective tissue. FFD usually follows a benign course, with spontaneous correction of the deformity and resolution of the lesion within a few years, although surgical correction may be occasionally required.

Dysplasia epiphysealis hemimelica (DEH, also referred to as Trevor's disease) is a rare skeletal abnormality of unknown etiology characterized by unilateral overgrowth of the epiphyseal cartilage. It usually affects joints of the lower limbs of males before age 15, being considered by many as an intra-articular variant of osteochondroma. Involvement of the medial portions of the epiphyses is twice as common as lateral involvement. The distal femur and the talus are the preferred sites, followed by the proximal and the distal tibia and the tarsal bones. There is a mass in the affected area (which may be painful) that frequently leads to restricted joint mobility, limb-length discrepancy, and joint deformity. DEH may affect one or more epiphyses in the same limb and, in some cases, the whole extremity is involved. Imaging findings are characteristic and biopsy is not necessary in most cases. Radiographs and CT reveal a variably calcified/ossified lobulated mass in one of the halves of the epiphysis of a long bone, in an apophysis, or in the tarsal bones (Figs. 6.8 and 6.9). As bone maturation occurs, the lesion tends to be incorporated into the adjacent bone. Nevertheless, some lesions remain separated from the host bone and may resemble loose bodies on radiographs. On MRI, DEH usually displays intermediate signal intensity on T1-WI and high signal intensity on T2-WI; scattered hypointense foci in all sequences are related to the presence of calcifications. Ossified lesions have signal intensity similar to that of the host bone (Fig. 6.8). Post-contrast

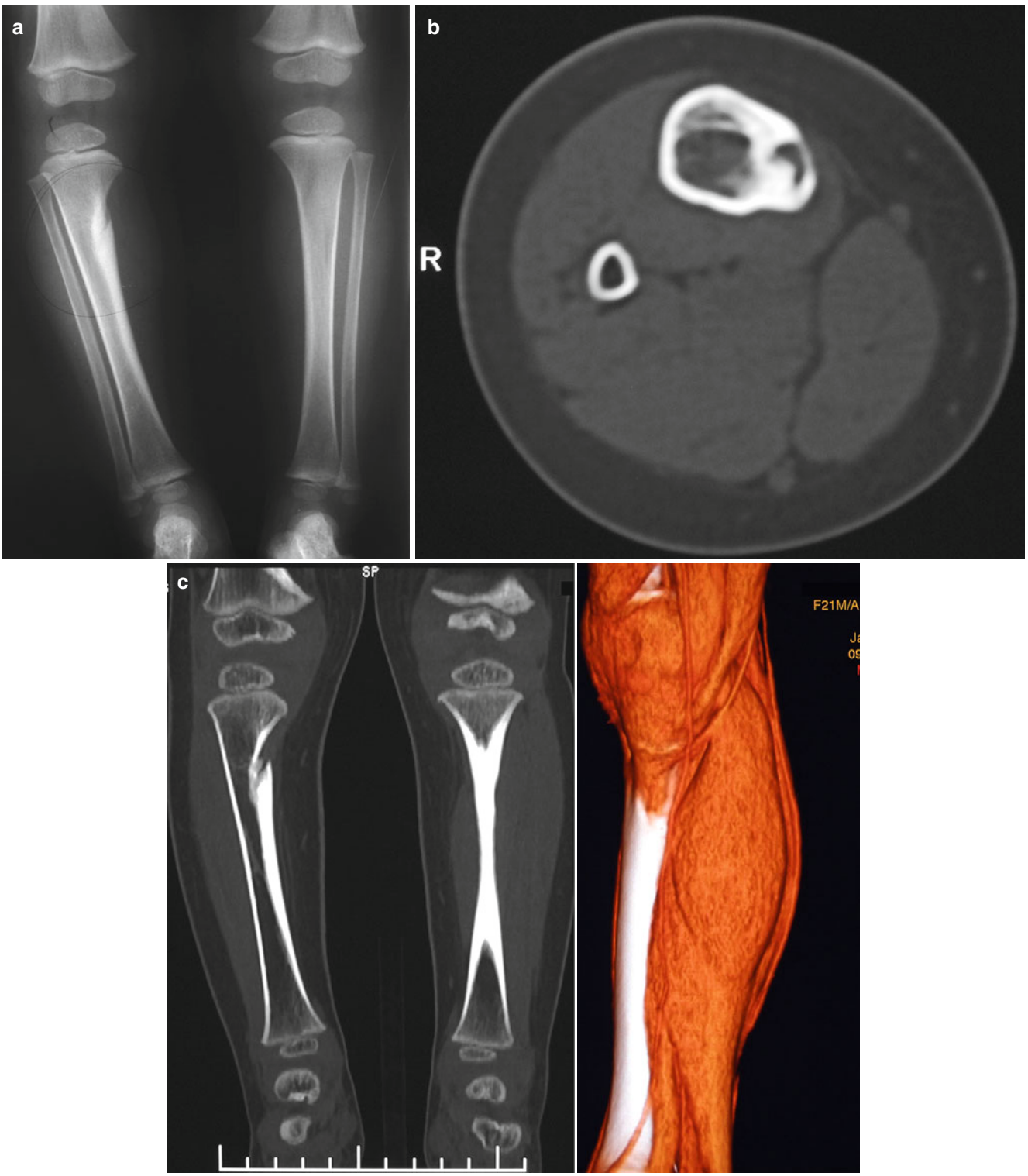

Fig. 6.7 A 21-month-old female with painful limp, progressive deformity of the right leg, and refusal to walk. Radiographs of the legs (**a**) demonstrate a lucent lesion extending obliquely downward in the medial cortex of the proximal portion of the right tibia. Varus deformity and marked peripheral sclerosis are also present, making this radiographic picture typical of FFD. Transverse CT image at the level of the lesion (**b**) also shows a well-delimited lytic cortical lesion and prominent perilesional sclerosis. In (**c**), coronal reformatted image (*left*) and volume-rendered reconstruction (*right*) demonstrate close relation of the lesion with the insertion of the pes anserinus tendons

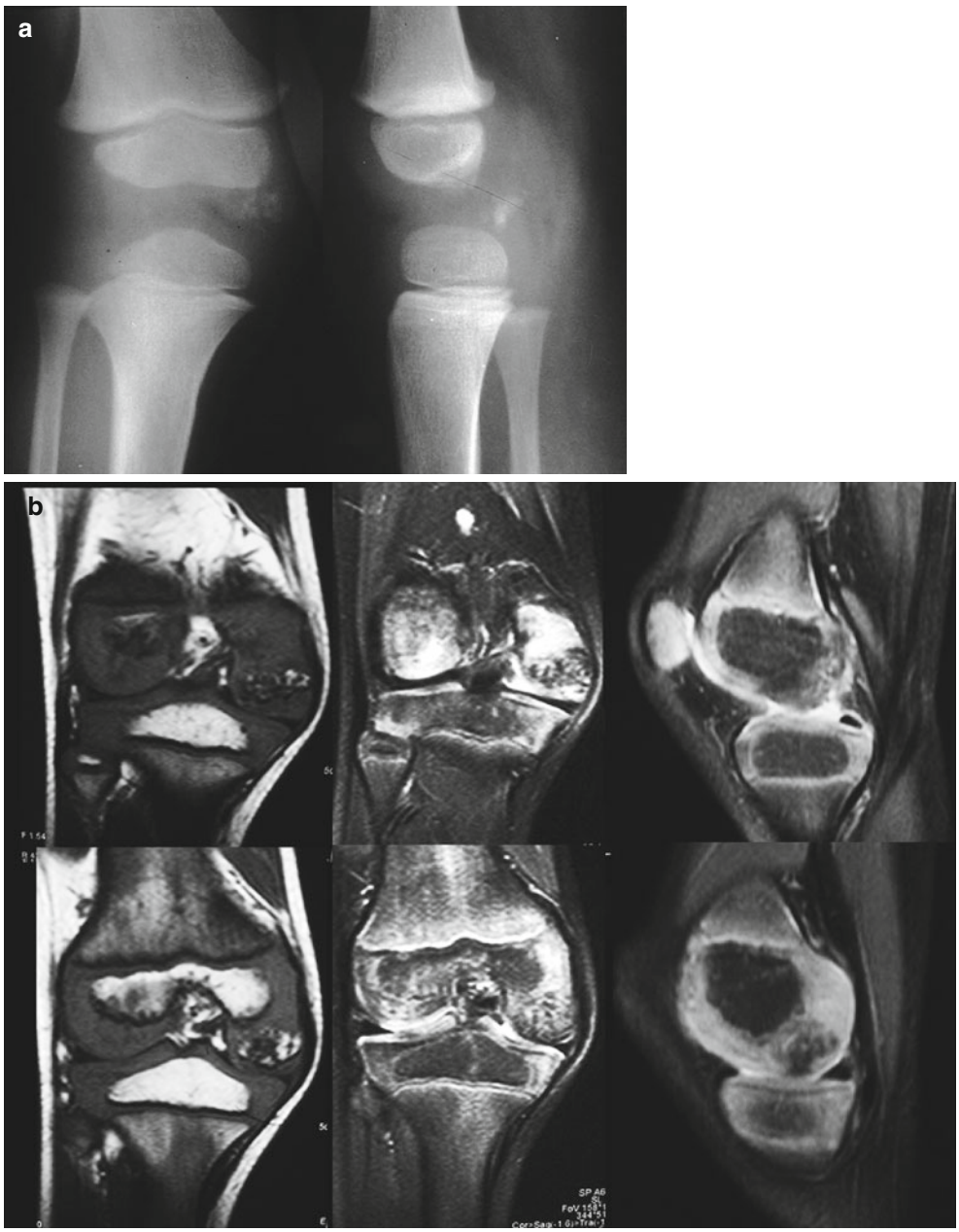

Fig. 6.8 Radiographs of the right knee of a skeletally immature patient (**a**) demonstrate a partially calcified soft-tissue mass in the posteromedial portion of the distal femoral epiphysis, projected over the non-ossified epiphyseal cartilage. MRI performed some months later (**b**, coronal T1-WI (*left*) and fat sat PD-WI (*center*) and sagittal post-gadolinium fat sat T1-WI (*right*)) discloses an epiphyseal mass containing areas of ossification, which are predominantly isointense with the ossified portion of the adjacent secondary ossification center. There is focal bulging of the epiphyseal cartilage, without abnormal enhancement on post-contrast images. These findings are typical for DEH

enhancement is variably found, but edematous changes of the bone marrow and of the soft tissues are absent. MRI is the method of choice to evaluate the relation between the mass and the subjacent bone and to demonstrate the real extent of the lesion, mostly in small children, because of its ability to assess both calcified and non-calcified components (Fig. 6.8).

6.3 Soft-Tissue Lesions

Pigmented villonodular synovitis (PVNS) is a rare condition of unknown etiology, considered a benign neoplasm. It is characterized by thickening of the synovium secondary to recurrent bleeding, mostly found in large joints and frequently extending to adjacent bursae and tendon sheaths.

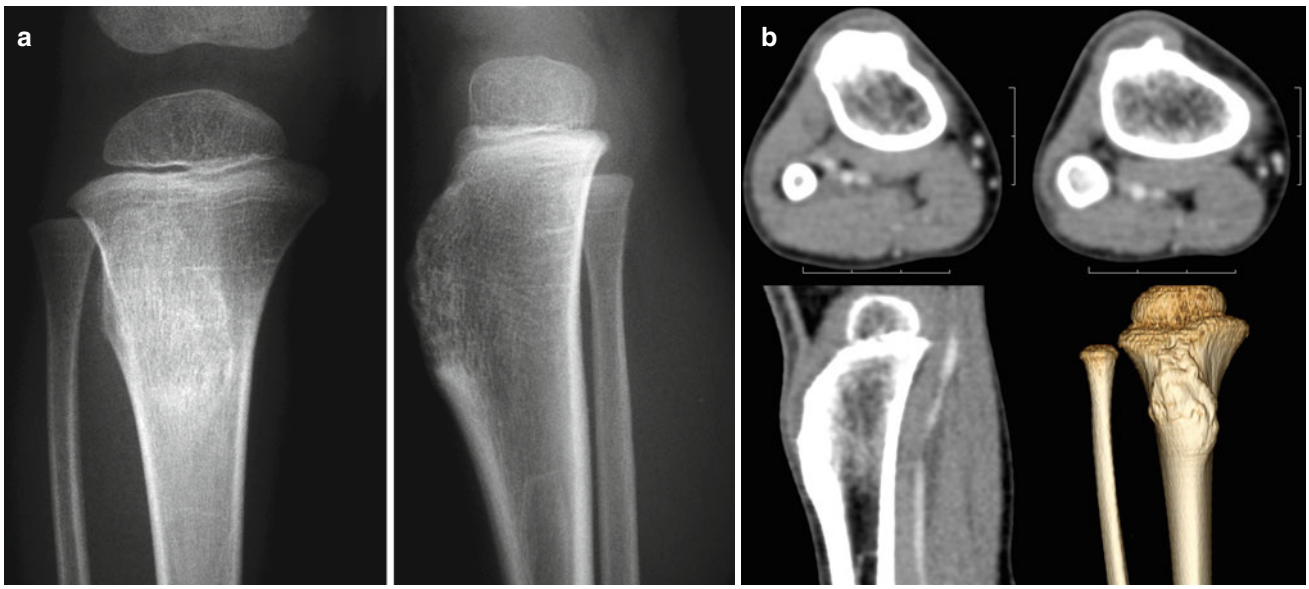

Fig. 6.9 A 3-year-old male with DEH of the right tibial tubercle. Radiographs (**a**) reveal increased size of the tibial tubercle, with continuity between the cortical and the cancellous bone of the mass and those of the tibia. In (**b**), transverse sections (*upper images*), sagittal reformatted image (*lower-left image*), and volume-rendered reconstruction (*lower-right image*) of a contrast-enhanced CT scan corroborate the radiographic findings, demonstrating a cartilaginous cap of normal appearance and absence of periosteal reaction, cortical discontinuity, soft-tissue mass, or abnormal post-contrast enhancement

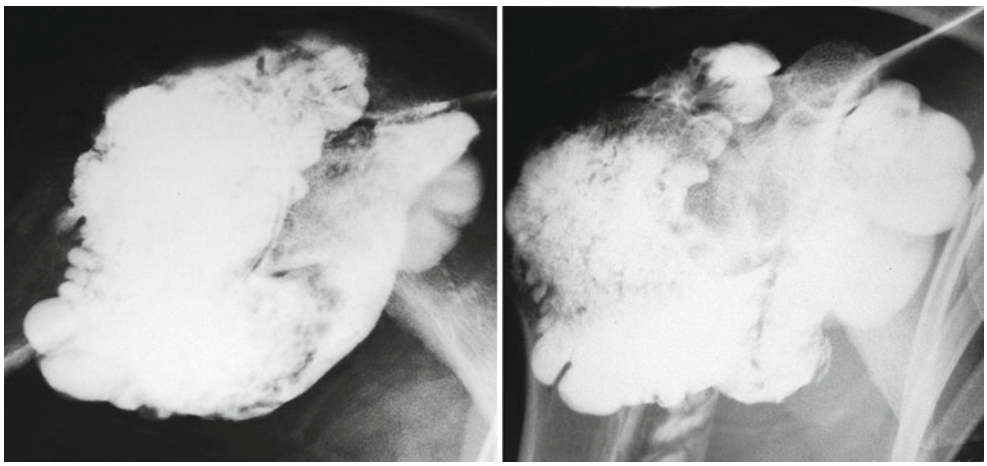

Fig. 6.10 Conventional arthrogram of the right shoulder. The contrast agent inside the joint cavity delineates an intra-articular mass with irregular and lobulated contours related to villous synovial thickening in this patient with PVNS. Even though this image is very illustrative of the macroscopic appearance of the synovial proliferation, its value is essentially pictorial and historical, as conventional arthrograms are no longer used and became obsolete after the advent of modern imaging methods

Patients present with recurrent hemarthroses that lead to chronic monoarthritis and progressive joint swelling. The knee and the hip are the most affected joints, and disease onset usually occurs between the second and the fourth decades of life. Nodular and diffuse forms of PVNS may occur, the latter being more common; approximately 80 % of the patients with diffuse PVNS present involvement of the knee, which is more frequent in the suprapatellar pouch, in the infrapatellar fat pad, and posterior to the cruciate ligaments. Radiographs may show soft-tissue swelling and joint effusion of high density, due to the presence of hemosiderin (Figs. 6.10 and 6.11), as well as pressure erosions and bone remodeling (Figs. 6.11 and 6.12), the latter being more frequently found in joints with a tight capsule, such as the hips. Late findings include osteoporosis and joint space narrowing. MRI discloses joint effusion and a frondlike synovial

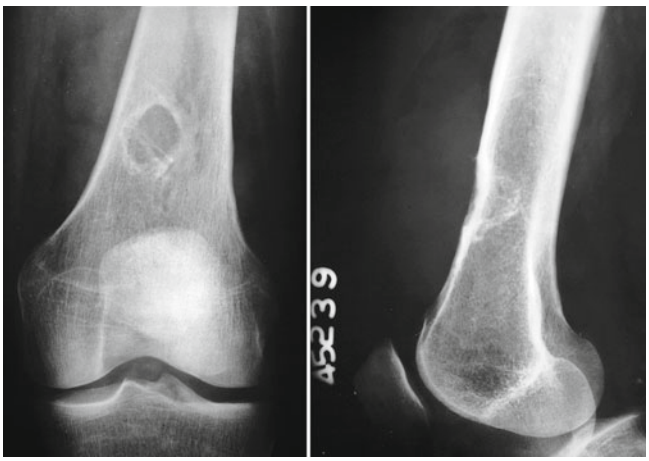

Fig. 6.11 Radiographs of the left knee of a patient with PVNS. There is a lobulated suprapatellar mass in the anteromedial soft tissues, whose density is higher than that of the adjacent soft-tissue planes. Pressure erosions in the anterior cortex of the distal femur are also present, well-defined, and presenting sclerotic borders, which are indicative of long evolution and low aggressiveness

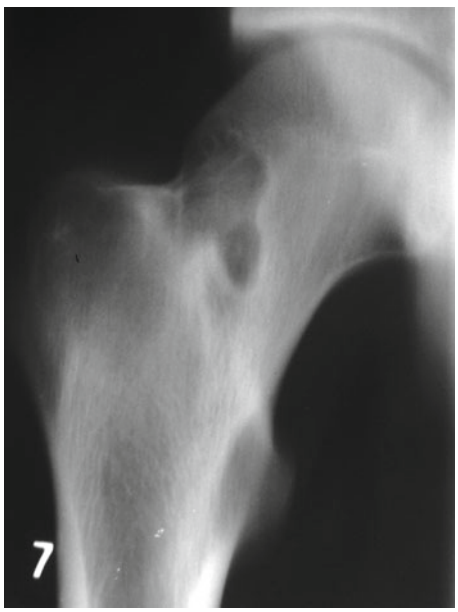

Fig. 6.12 Planigraphy of the right hip of a patient with PVNS disclosing an extensive lucent lesion in the superior cortex of the femoral neck, surrounded by a sclerotic rim (pressure erosion)

proliferation, which may be associated with intra-articular masses; the most typical finding, however, is the presence of extensive areas of low signal intensity in all sequences related to hemosiderin impregnation, with blooming artifacts more evident on gradient-echo images (Figs. 6.13 and 6.14). This widespread abnormal signal intensity can be seen inside the joint and in nearby bursae and/or tendon sheaths, with diffuse post-gadolinium enhancement in the inflamed tissues. The signal intensity of the synovium and of the soft tissues is often markedly heterogeneous, including hyperintensity on fluid-sensitive sequences. Additional findings include bone erosions, subchondral cysts, and bone marrow edema pattern; it is important to keep in mind that other conditions also associated with recurrent intra-articular bleeding (such as vascular malformations and hemophilia) may closely resemble PVNS (Fig. 6.14). MRI is valuable for staging, preoperative planning, and follow-up, as it is able to detect PVNS even in sites of difficult arthroscopic visualization, such as the popliteal hiatus or Baker's cysts.

The nodular form of PVNS (localized nodular synovitis) consists in a small intra-articular mass that is almost always located in the knee, mainly in the infrapatellar fat pad, protruding to the joint cavity. Although similar to classic PVNS in many aspects, localized nodular synovitis has a distinct imaging appearance. On MRI, there is a well-delimited, ovoid/rounded lesion that is predominantly hypointense on T1-WI and T2-WI; there is proportionally less hemosiderin impregnation if compared to the diffuse form of PVNS, with heterogeneous post-gadolinium enhancement (Fig. 6.15). Another related condition is the giant cell tumor of the tendon sheath (GCTTS), the tenosynovial counterpart of PVNS. Affected patients present a painless soft-tissue mass that is more commonly found in the fingers, although involvement of feet, wrists, and ankles is not unusual. Radiographic findings are most often nonspecific, including soft-tissue swelling and, occasionally, pressure erosions of the adjacent bone (Fig. 6.16). This lesion appears on MRI as a well-delimited mass attached to a tendon sheath, which tends to grow and envelop the corresponding tendon, preserving the structure of the latter. Signal intensity of GCTTS is similar to that above described for PVNS, and post-gadolinium enhancement is usual (Fig. 6.17).

Lipoma arborescens (LA) is an intra-articular mass of villous appearance characterized by synovial proliferation and replacement of the subsynovial tissue by mature adipose cells. It is usually monoarticular, affecting mainly males in their fifth or sixth decades of life; nonetheless, children may be occasionally affected too. The knee is the most commonly involved joint, notably in the suprapatellar pouch. Radiographs display nonspecific soft-tissue swelling, and osteoarthritis – which is frequently found in adult patients – is typically absent in children with LA. Areas of low density suggestive of fatty tissue may be present, but this is an inconstant and unreliable finding. CT images reveal an intra-articular expansile lesion of fatty density and villous appearance, while US demonstrates a villous hyperechogenic mass that waves as the transducer moves. On MRI, LA classically appears as a frondlike synovial proliferation that is predominantly isointense to fat in all sequences, with signal drop on STIR or fat sat images (Fig. 6.18). Large joint effusions and synovitis are common,

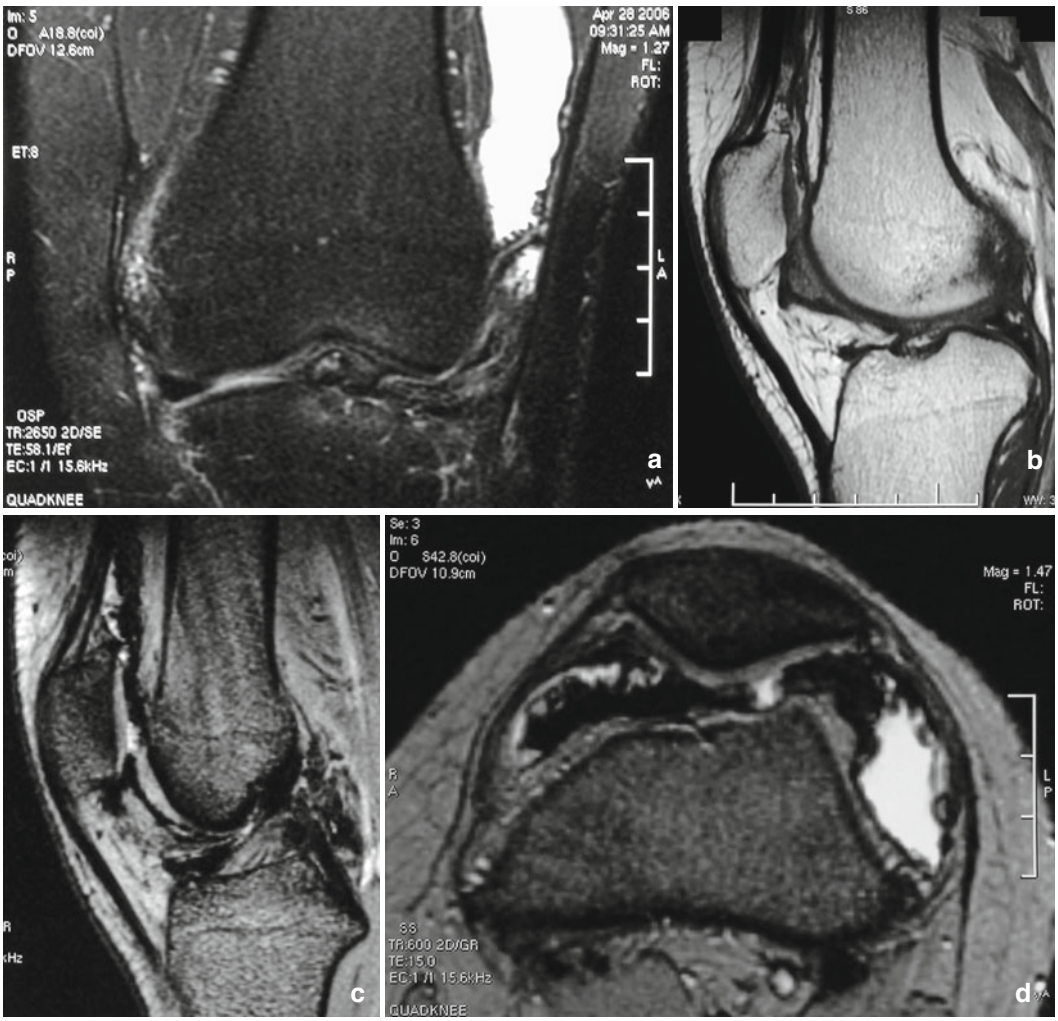

Fig. 6.13 MRI of the left knee of a female adolescent with PVNS (3 years of evolution). Coronal fat sat T2-WI (**a**), sagittal T1-WI (**b**) and gradient-echo image (**c**), and transverse gradient-echo image (**d**) disclose nodular thickening of the synovium, which has a villous appearance and displays low signal intensity in all sequences, mostly gradient-echo images, related to hemosiderin buildup. This is more prominent in the suprapatellar pouch, posterior to the cruciate ligaments and in the infrapatellar fat pad

as well as post-gadolinium enhancement, and chemical shift artifacts may occasionally be present at the fluid/fat interface. The most important condition to consider in the differential diagnosis is true synovial lipoma; however, unlike LA, it is a round or oval adipose lesion of smooth contours, well-delimited, and not associated with synovitis.

Primary synovial osteochondromatosis (PSO) is a benign disease of unknown etiology characterized by metaplasia, inflammation, and development of cartilaginous nodules in the synovium. These metaplastic nodules may contain non-calcified cartilage only (synovial chondromatosis) or calcified cartilage/mature bone (synovial osteochondromatosis). The nodules may eventually detach and migrate to the joint cavity, with development of loose bodies. PSO occurs predominantly in males between the third and the fifth decades of life, presenting as a monoarticular condition that affects large joints, such as the knees, hips, and elbows. Radiographs are diagnostic if the metaplastic nodules are calcified or ossified, showing several intra-articular mineralized nodules that are relatively uniform in size (Fig. 6.19). However, non-mineralized nodules are difficult to demonstrate on radiographs and may occasionally resemble aggressive lesions. Peripheral erosions and early osteoarthritis are not uncommon, mainly found in joints with a tight capsule, such as the hips and the wrists. In skeletally immature patients, the hyperemic state associated with PSO may lead to regional osteoporosis, increased epiphyseal size, and premature closure of the growth plates, simulating primary chronic arthritides of the childhood (Fig. 6.19). The appearance of the nodules on CT and MRI varies depending on the degree of calcification. Non-calcified nodules may form clusters of low to intermediate density on CT, which are isointense to the skeletal muscle on T1-WI and hyperintense on T2-WI, hardly distinguishable

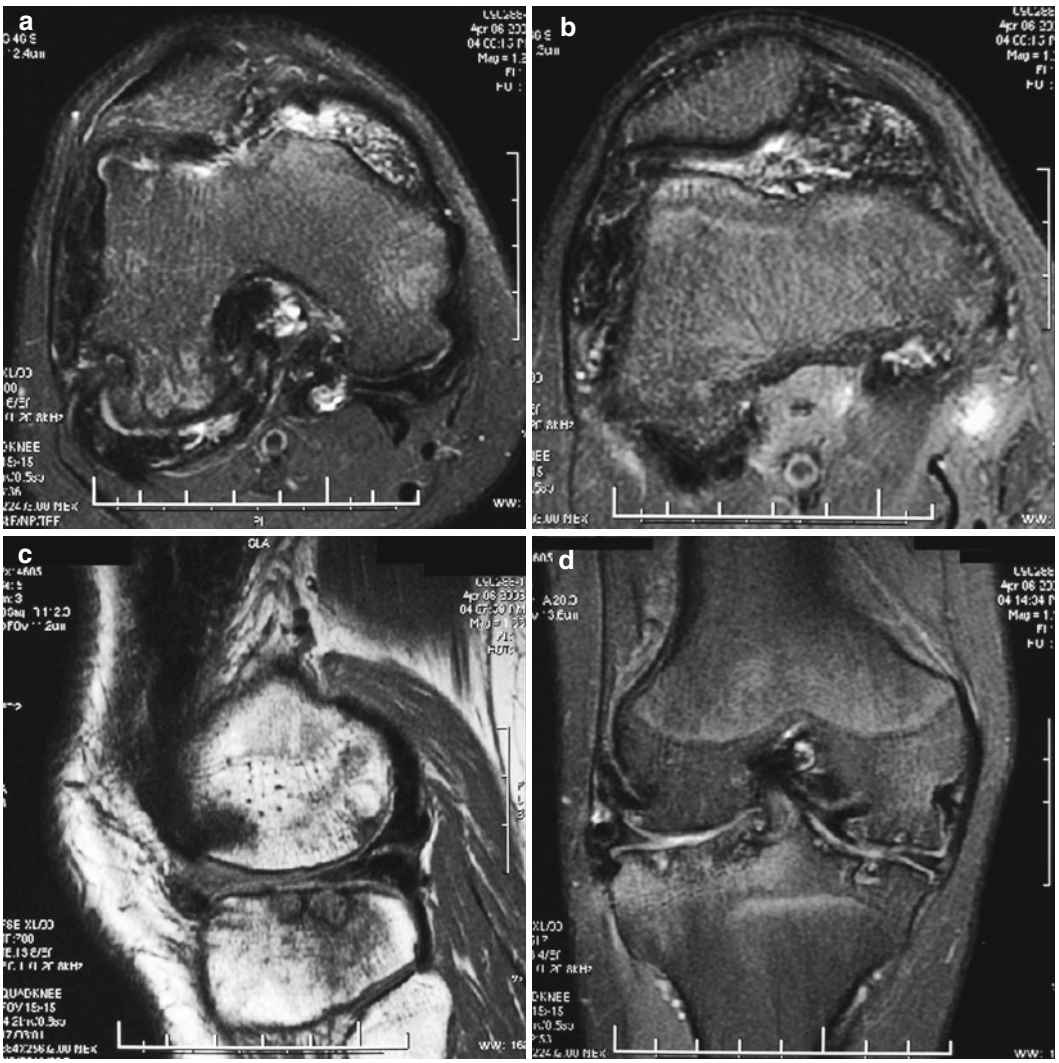

Fig. 6.14 Transverse fat sat PD-WI (**a** and **b**), sagittal T1-WI (**c**), and coronal fat sat PD-WI (**d**) of the right knee of an adolescent with long-standing PVNS. In addition to hypointense synovial thickening and intra-articular buildup of hemosiderin, there is a destructive arthropathy similar to that found in hemophilia, with diffuse cartilaginous thinning, cortical erosions, and osteochondral lesions. Overgrowth of the medial femoral condyle is also evident

from the synovial fluid. Post-gadolinium images will show enhancement of these cartilaginous masses long before calcifications become evident on radiographs. Calcifications are obvious on CT images and display low signal intensity in all MRI sequences. If mature bone is present, the nodules will exhibit a peripheral rim of cortical bone and an inner core of cancellous bone. PSO must be distinguished from secondary synovial osteochondromatosis, which is related to an underlying joint disease (e.g., osteoarthritis, trauma, or osteochondritis dissecans) that leads to the development of loose bodies through detachment of fragments of the articular cartilage, which are nourished by the synovial fluid. The loose bodies of the secondary form typically have varied sizes and shapes, and the underlying articular disease is usually obvious.

The most common intra-articular vascular anomaly is the synovial venous malformation (SVM), widely referred to as cavernous hemangioma. The SVM is a rare condition that affects mainly children and young adults, more frequent in the knees. Patients present joint pain, soft-tissue swelling, restricted range of motion, and recurrent hemarthroses. Radiographs are most often normal or show nonspecific findings in the early stages. Phleboliths, which are indicative of the vascular nature of the mass, are rare in SVM if compared to other venous malformations of the soft tissues, except if an extraarticular component is present. Long-standing lesions are associated with osteoporosis, epiphyseal overgrowth, limb-length discrepancy, periosteal reaction, and destructive joint disease similar to hemophilic arthropathy, related to recurrent intra-articular

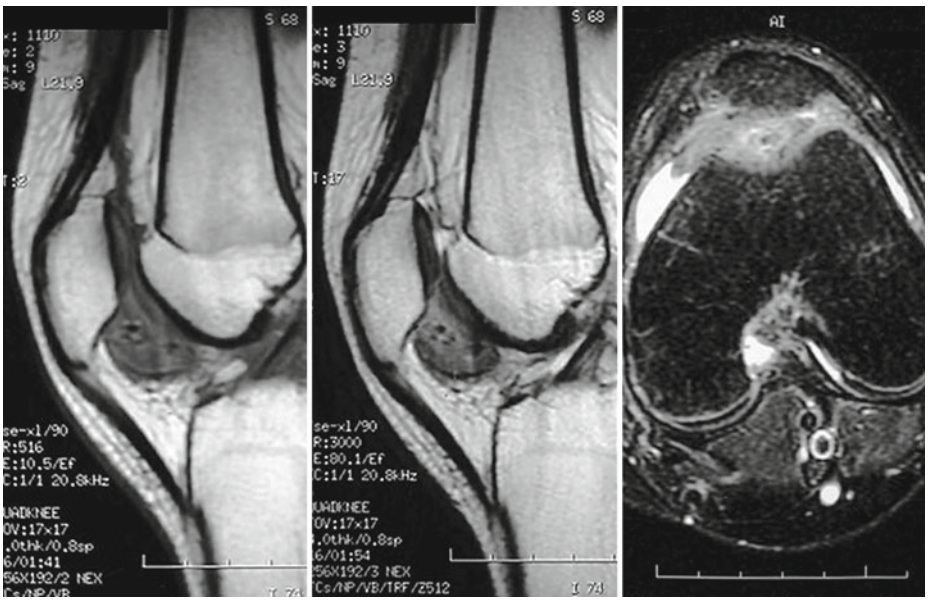

Fig. 6.15 Nodular synovitis of the left knee in a 15-year-old patient. There is a well-delimited mass of low to intermediate signal intensity on T1-WI (*left*) and T2-WI (*center*) in the Hoffa fat pad, with high signal intensity on fat sat PD-WI (*right*). Magnetic susceptibility artifacts can be seen inside the lesion. Nevertheless, hemosiderin impregnation is less prominent than that usually present in the diffuse form of PVNS

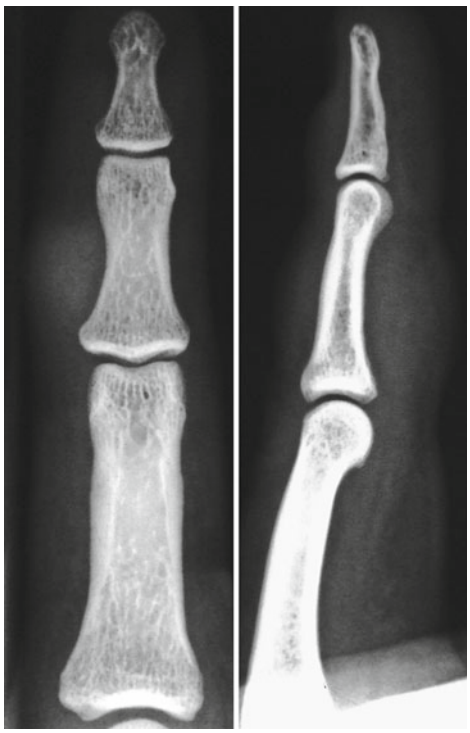

Fig. 6.16 Radiographs of the index finger of a 15-year-old patient with GCTTS revealing nodular soft-tissue swelling that is volar and medial relative to the middle phalanx, with subtle remodeling of the adjacent cortex

bleeding. Pressure erosions and bone remodeling may be occasionally found, due to associated mass effect. On US, the lesion displays compressible venous lakes and channels with low blood flow; hyperechogenic intravascular thrombi and phleboliths are occasionally seen. MRI is the best imaging method to evaluate venous malformations, showing a spongiform mass that contains dilated vascular structures, without significant mass effect in most cases. These structures are hypointense/isointense on T1-WI and markedly hyperintense on T2-WI (even more on fluid-sensitive sequences), features related to blood pooling in the vascular spaces (Fig. 6.20); flow voids indicative of high-speed flow are characteristically absent in synovial venous malformations. Fluid-fluid levels are occasionally found, related to previous hemorrhage. Post-gadolinium enhancement is intense and usually heterogeneous (Figs. 6.20 and 6.21). As mentioned above, recurrent hemarthroses may lead to the development of an osteoarthropathy similar to that found in hemophilia (see Chap. 8 – Fig. 6.21). Given the paramagnetic properties of hemosiderin, low signal intensity in all sequences and susceptibility artifacts are often found in the impregnated tissue (Fig. 6.20).

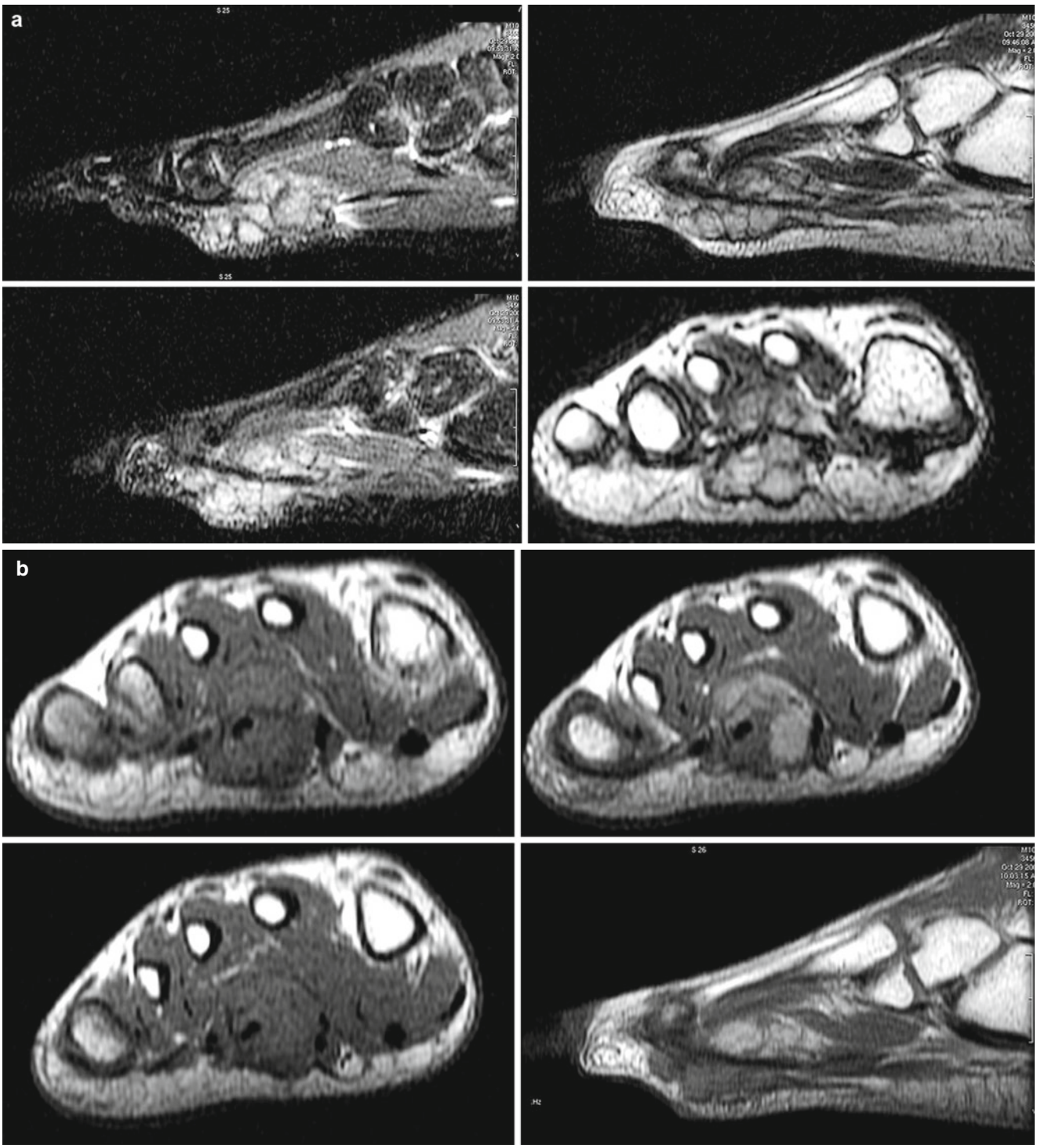

Fig. 6.17 GCTTS of the flexor tendons of the third toe in the right foot of a 10-year-old male. Figure (**a**) shows sagittal STIR images (*left*) and T2-WI in the sagittal and coronal planes (*right*), while (**b**) displays pre-contrast coronal T1-WI (*left*) and post-contrast sagittal and coronal T1-WI (*right*). The mass is heterogeneous, containing thin septa, with low to intermediate signal intensity on T1-WI and T2-WI and high signal intensity on STIR images. The tumor envelops the flexor tendons of the third toe, displacing the flexor tendons of the second and of the fourth toes. Irregular enhancement is seen on post-gadolinium images

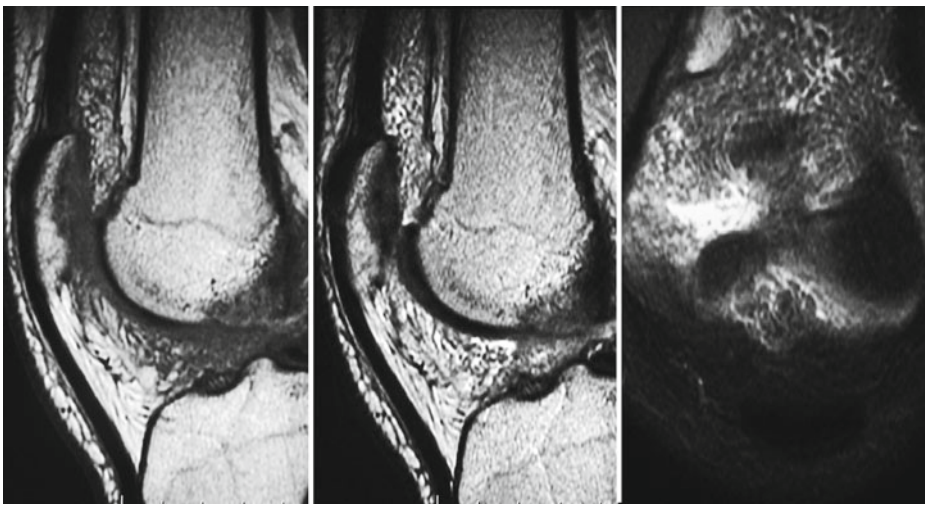

Fig. 6.18 Lipoma arborescens of the right knee. There is a mass of villous appearance in the suprapatellar pouch and in the Hoffa fat pad, whose signal intensity is similar to that of the subcutaneous fat on T1-WI (*left*) and on T2-WI (*center*), showing signal drop on fat sat T2-WI (*right*). Joint effusion is also evident

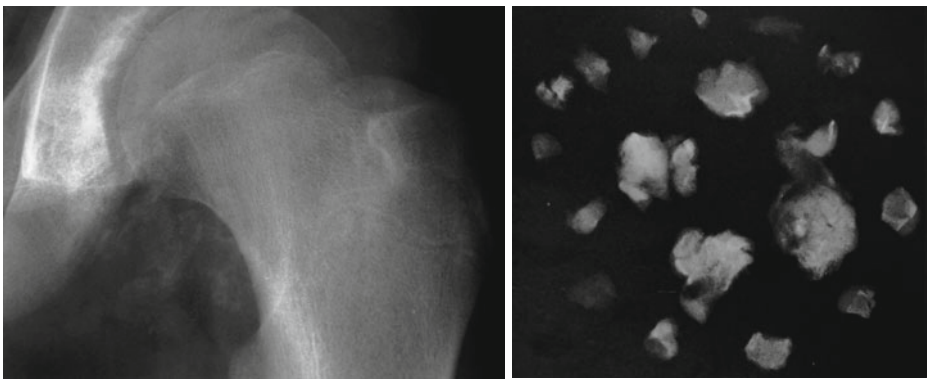

Fig. 6.19 PSO of the left hip joint in a skeletally immature patient. Anteroposterior radiograph (*left image*) discloses several mineralized nodules medial to the femoral neck, as well as osteoporosis of the proximal femur. The *right image* is a radiograph of the surgical specimen (post-synovectomy) revealing that most nodules have a rim of cortical bone and an inner core of cancellous bone. Even though there are at least four dominant nodules, most of the remaining are small and relatively uniform in size

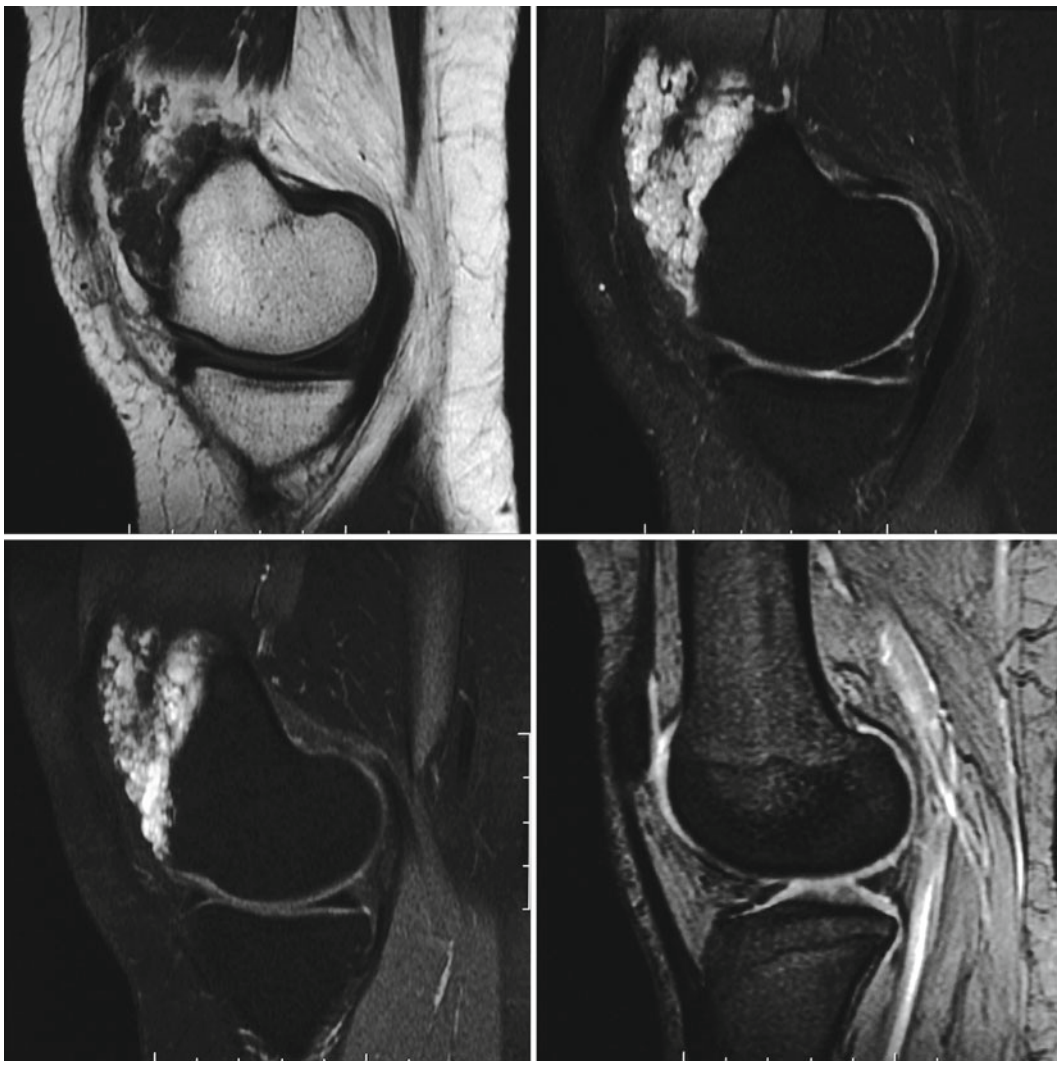

Fig. 6.20 SVM of the medial recess of the suprapatellar pouch. The mass is composed of serpiginous vessels that show low signal intensity on T1-WI (*upper-left image*), high signal intensity on STIR (*upper-right image*), and marked enhancement on post-gadolinium fat sat T1-WI (*lower-left image*). Gradient-echo image (*lower-right image*) is useful to demonstrate low signal intensity in the joint surfaces and in the infrapatellar fat pad, related to hemosiderin buildup due to recurrent hemarthroses

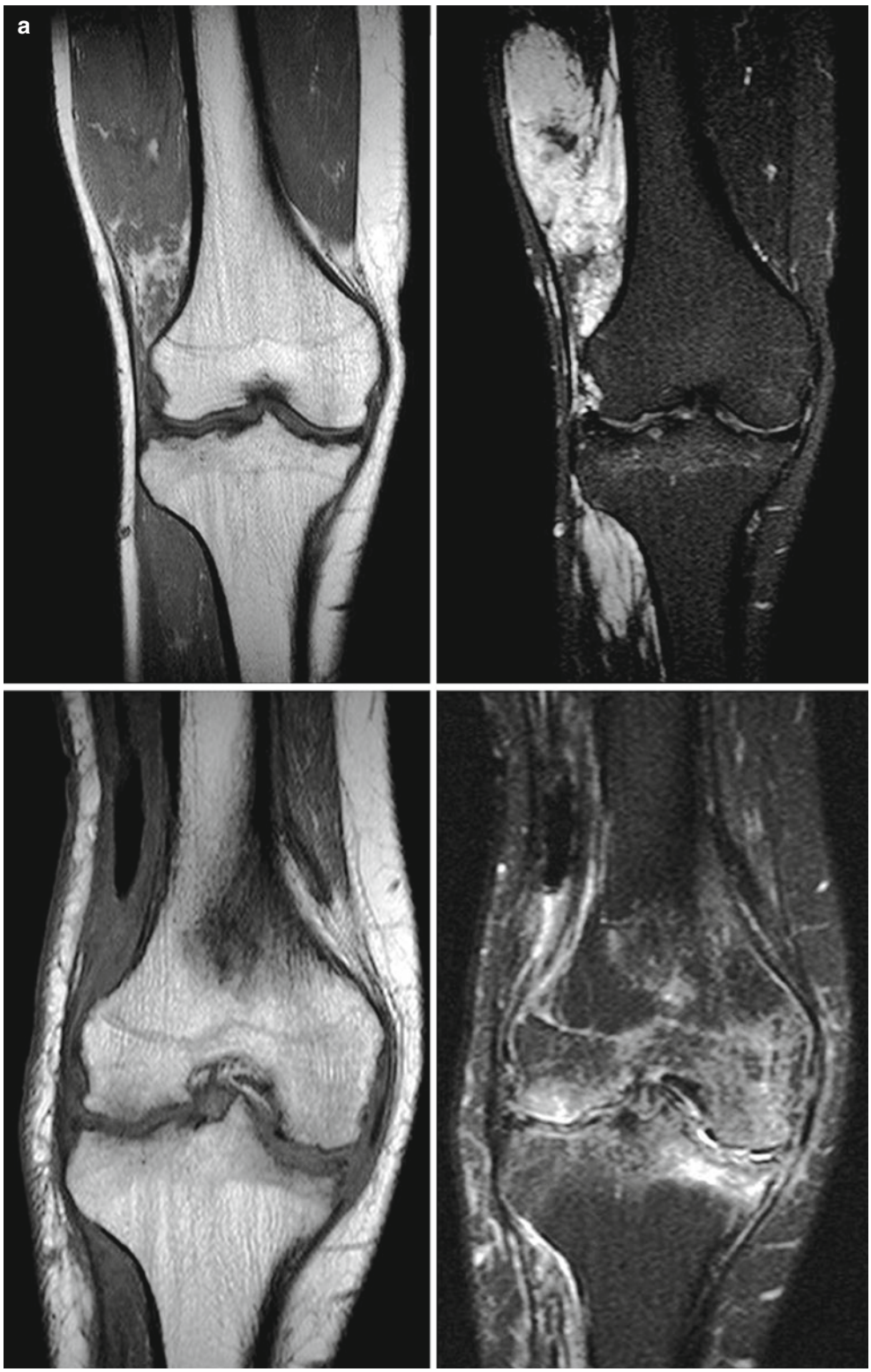

Fig. 6.21 Imaging studies demonstrating the evolution of the arthropathy in a patient with SVM. In (**a**), the images in the upper row (coronal T1-WI (*left*) and fat sat T2-WI (*right*)) reveal a large venous malformation with intra-articular and extraarticular components, which presents intermediate signal intensity on T1-WI and is hyperintense on T2-WI, involving the lateral portions of the distal thigh, of the knee, and of the proximal leg. Osteoarthropathy is already present, with thinning of the articular cartilages, irregularity of the joint surfaces, and subtle edema of the subchondral bone marrow. The images in the lower row, taken 6 months later (after percutaneous treatment), disclose marked decrease of the size of the malformation. However, there is worsening of the osteoarthropathy, with progression of the aforementioned findings and development of significant muscle atrophy. In (**b**), post-gadolinium fat sat T1-WI acquired prior to treatment demonstrate marked enhancement of the anomalous vascular structures, highlighting the usefulness of contrast-enhanced MRI for accurate staging of SVM

Fig. 6.21 (continued)

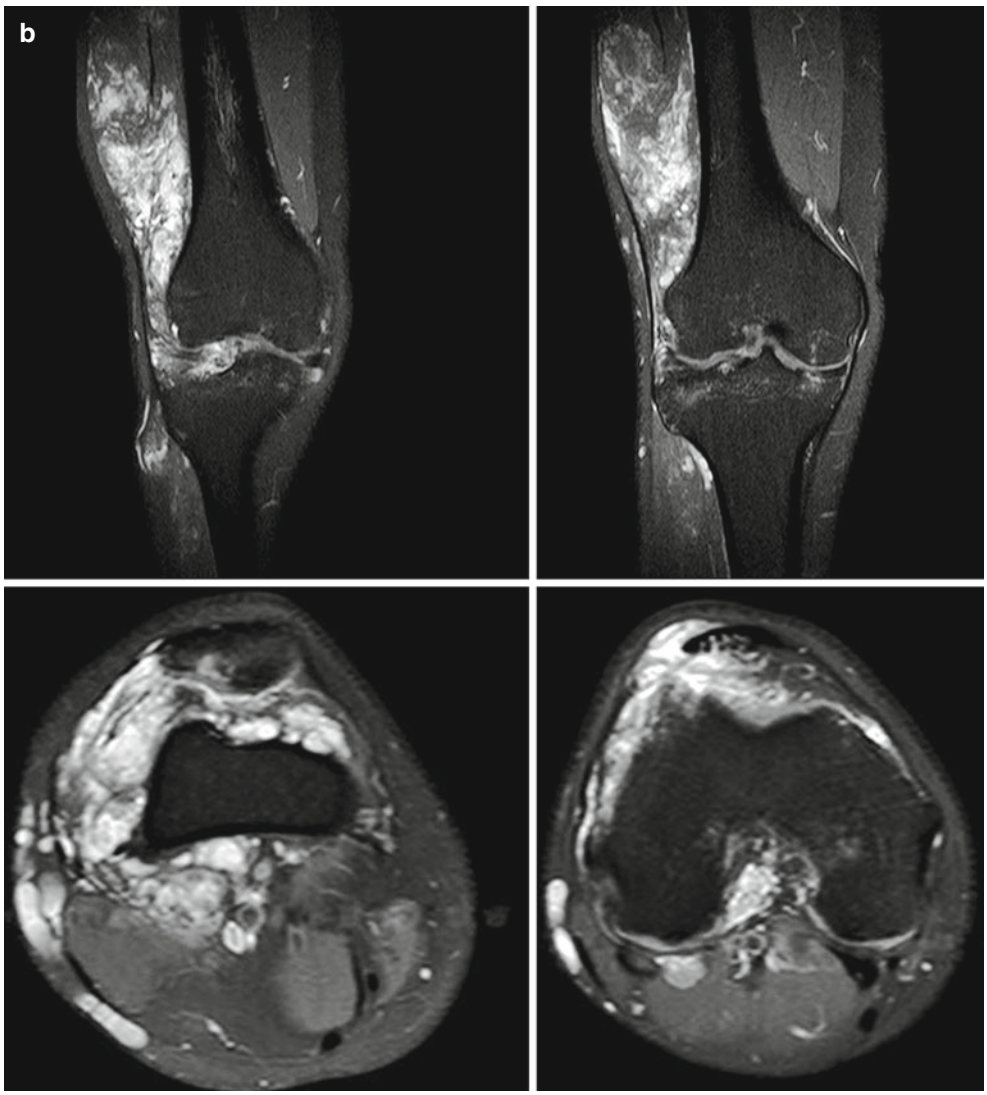

Key Points

- Intra-articular OO are more difficult to detect than classic diaphyseal lesions, mostly because reactive sclerosis and periosteal reaction are often mild or even absent in the former. They may simulate monoarthritis and lead to premature osteoarthritis. CT is particularly useful to diagnose intra-articular lesions. The nidus displays variable signal intensity on MRI, often associated with inflammatory changes and post-contrast enhancement.
- Chondroblastomas are lytic epiphyseal lesions whose matrix appears variably calcified on imaging, usually surrounded by a thin sclerotic rim. The signal intensity of the lesion varies, depending on the extent of calcifications; bone marrow edema and post-gadolinium enhancement are common.
- FFD is a cause of infantile tibia vara characterized by a cortical lucency with sclerotic borders at the insertion of the pes anserinus. On MRI, FFD displays low signal intensity in all sequences.
- DEH is an eccentric cartilaginous mass most often found in the epiphyses of the long bones of the lower limbs, presenting variable degrees of calcification/ossification. MRI is the best imaging method, as it is able to assess both the mineralized and the non-mineralized components of the mass.
- PVNS is a frondlike synovial proliferation related to recurrent bleeding episodes that presents diffuse impregnation by hemosiderin, as evidenced by MRI. Localized forms may be also seen, either inside the joint cavity (nodular synovitis) or adjacent to tendons (giant cell tumor of tendon sheath).

- Lipoma arborescens is a benign villous synovial proliferation that typically displays adipose content on imaging studies, commonly associated with joint effusion and synovitis.
- PSO is characterized by the presence of metaplastic cartilaginous nodules in the synovium, which typically have uniform size and show calcification/ossification in varied degrees; thus, their appearance on imaging depends on the extent of mineralization. Signs of joint hyperemia may be present in children.
- SVM are better assessed with MRI, which demonstrates a spongiform mass containing anomalous vessels, with low to intermediate signal intensity on T1-WI, high signal intensity on T2-WI, and post-gadolinium enhancement. Recurrent hemarthroses may lead to the development of an osteoarthropathy similar to that seen in hemophiliac patients, with diffuse impregnation by hemosiderin.

Recommended Reading

Bahk WJ, Lee HY, Kang YK, Park JM, Chun KA, Chung YG (2010) Dysplasia epiphysealis hemimelica: radiographic and magnetic resonance imaging features and clinical outcome of complete and incomplete resection. Skeletal Radiol 39(1):85–90

Bancroft LW, Peterson JJ, Kransdorf MJ (2005) MR imaging of tumors and tumor-like lesions of the hip. Magn Reson Imaging Clin N Am 13(4):757–774

Chung CB, Boucher R, Resnick D (2009) MR imaging of synovial disorders of the knee. Semin Musculoskelet Radiol 13(4):303–325

Ebrahim FS, Jacobson JA, Lin J, Housner JA, Hayes CW, Resnick D (2001) Intraarticular osteoid osteoma: sonographic findings in three patients with radiographic, CT, and MR imaging correlation. AJR Am J Roentgenol 177(6):1391–1395

Eckhardt BP, Hernandez RJ (2004) Pigmented villonodular synovitis: MR imaging in pediatric patients. Pediatr Radiol 34(12): 943–947

Frick MA, Wenger DE, Adkins M (2007) MR imaging of the synovial disorders of the knee: an update. Radiol Clin North Am 45(6): 1017–1031

Lobo-Mueller E, Amaral JG, Babyn PS, John P (2009) Extremity vascular anomalies in children: introduction, classification, and imaging. Semin Musculoskelet Radiol 13(3):210–235

Navarro OM, Laffan EE, Ngan BY (2009) Pediatric soft-tissue tumors and pseudo-tumors: MR imaging features with pathologic correlation: part 1. Imaging approach, pseudotumors, vascular lesions, and adipocytic tumors. Radiographics 29(3):887–906

Papaioannou G, Sebire NJ, McHugh K (2009) Imaging of the unusual pediatric 'blastomas'. Cancer Imaging 9:1–11

Sanchez R, Strouse PJ (2009) The knee: MR imaging of uniquely pediatric disorders. Magn Reson Imaging Clin N Am 17(3): 521–537

Sheldon PJ, Forrester DM, Learch TJ (2005) Imaging of intraarticular masses. Radiographics 25(1):105–119

Stacy GS, Heck RK, Peabody TD, Dixon LB (2002) Neoplastic and tumorlike lesions detected on MR imaging of the knee in patients with suspected internal derangement: part I, intraosseous entities. AJR Am J Roentgenol 178(3):589–594

Stein-Wexler R (2009) MR imaging of soft tissue masses in children. Magn Reson Imaging Clin N Am 17(3):489–507

Vanhoenacker FM, Gielen JL, Vandervliet E, Van Dyck P (2008) Focal fibrocartilaginous dysplasia. JBR-BTR 91(2):67

Wootton-Gorges SL (2009) MR imaging of primary bone tumors and tumor-like conditions in children. Magn Reson Imaging Clin N Am 17(3):469–487

Legg-Calvé-Perthes Disease

7

7.1 Introduction

Legg-Calvé-Perthes disease (LCPD) is an idiopathic form of avascular necrosis of the immature proximal femoral epiphysis. As it occurs in the growing skeleton, there are peculiarities that distinguish it from the adult type of avascular necrosis of the femoral head. It is important to keep in mind that this epiphysis bears a significant remodeling potential in skeletally immature patients, which can correct architectural changes caused by ischemia; the younger the patient, the greater is this ability. Nevertheless, abnormal epiphyseal development and deformation of the femoral head do occur in cases of poor evolution. The cascade of phenomena that follows bone necrosis is paralleled by the evolution of imaging findings. This chapter will provide an overview of the role of imaging in the assessment of LCPD.

7.2 Clinical Aspects

LCPD is more common in white males, with an incidence peak around 4–8 years, and the disease is bilateral in 10–20 % of the patients. Symptomatic children present insidious hip pain and intermittent limp, which are exacerbated by physical activity, as well as limited abduction and internal rotation of the affected hip. In general, the younger the patient and the smaller the extent of the epiphyseal necrosis, the better is the prognosis. Similarly, prognosis for older children and/or patients with large necrotic areas tends to be poor. As the prognosis is better in the most affected age group, the majority of the patients have good evolution.

Considering its idiopathic nature, LCPD is a diagnosis of exclusion. Thus, potential causes of avascular necrosis must be ruled out, such as systemic diseases, complications of drug therapy (mostly systemic corticosteroids), and other causes of impaired epiphyseal blood supply (e.g., vasculitis, radiation therapy and surgery). Infectious and noninfectious arthritides, slipped capital femoral epiphysis, traumatic injuries, and transient synovitis must be considered in the differential diagnosis. Even though epiphyseal dysplasias can closely resemble LCPD on imaging, dysplastic abnormalities are usually bilateral, simultaneous, and symmetric, with flattening/fragmentation of the femoral heads (and other epiphyses as well) and delayed maturation of the secondary ossification centers (see Chap. 12).

7.3 Imaging

7.3.1 Radiographs

Imaging investigation usually starts with radiographs of both hips (anteroposterior and lateral views). Radiographs are most often normal during the initial phase of LCPD, though subtle epiphyseal osteoporosis may be occasionally present. During the condensation phase, there is an increase in the epiphyseal density due to bone apposition and thickening of the trabeculae (Fig. 7.1). The classic subchondral fracture – Caffey's sign or "crescent sign" – appears as a linear lucency parallel to the articular surface of the femoral head, often associated with epiphyseal flattening (Figs. 7.1, 7.2, and 7.3). Widening of the joint space may also be found, related to cartilaginous thickening, as the superficial cartilage is nourished via diffusion from the synovial fluid and does not suffer from ischemia at this stage. The so-called metaphyseal reaction, characterized by the appearance of round lucencies (commonly referred to as "cysts") along the physis, also begins in the condensation phase (Figs. 7.3, 7.4, and 7.5), as well as bone remodeling of the femoral neck, which becomes progressively shortened and broadened; the growth plate may appear wavy or cupped. In the following stage, referred to as the fragmentation phase, the ossified portion of the epiphysis becomes fragmented and heterogeneous, occasionally exhibiting a central sequestrum (Fig. 7.6). There is also progression of the metaphyseal reaction and of the bone remodeling of the femoral neck (Figs. 7.6, 7.7, and 7.8). Widening of the joint space becomes even more marked, and acetabular deformity may occur, with lateral protrusion of the femoral

S.L. Viana et al., *Joint Imaging in Childhood and Adolescence*,
DOI 10.1007/978-3-642-35876-0_7, © Springer-Verlag Berlin Heidelberg 2013

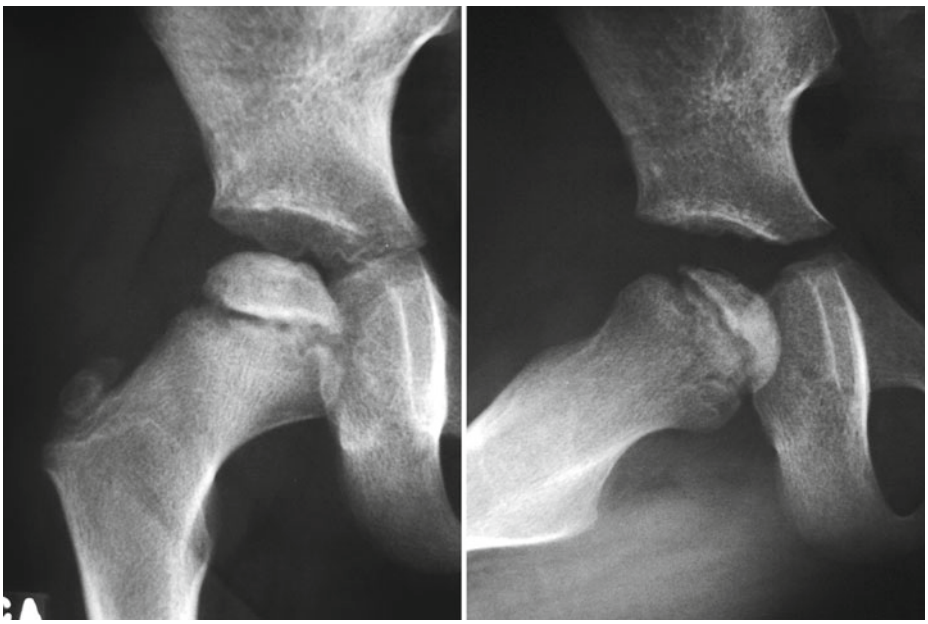

Fig. 7.1 Radiographs of the right hip of a child with LCPD show diffuse sclerosis and reduced height of the femoral epiphysis, as well as a subchondral fracture, more evident on the lateral view (*right image*). Widening of the joint space is also present

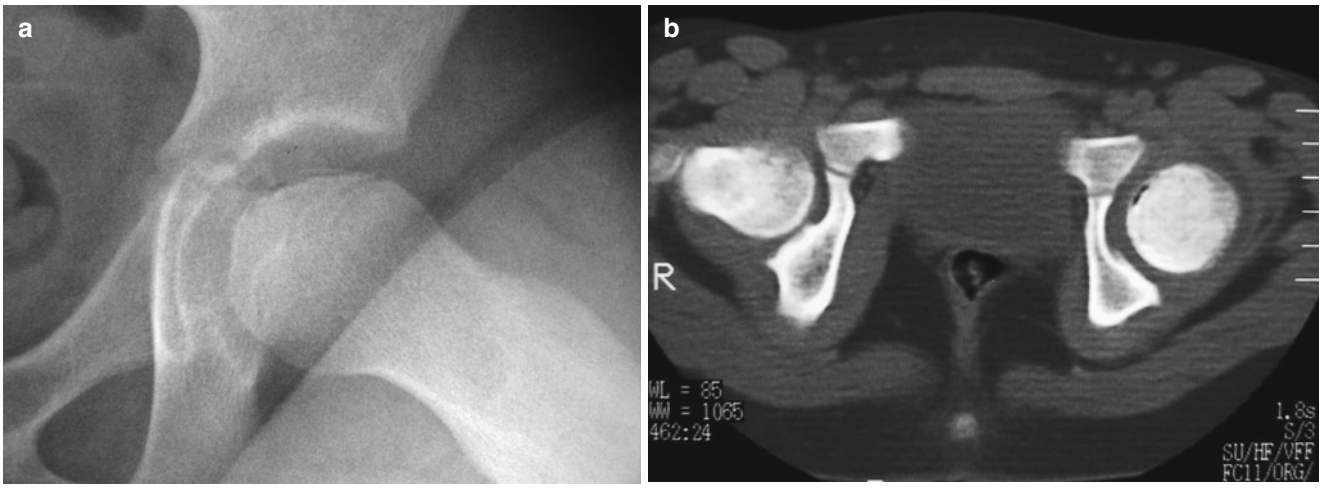

Fig. 7.2 Lateral view of the left hip (**a**) of a patient with LCPD displaying reduced height of the femoral epiphysis and a crescent-shaped subcortical lucency (subchondral fracture). Transverse CT image (**b**) of the same patient demonstrates gas in the fracture site and epiphyseal sclerosis

head (Figs. 7.6 and 7.8). Progressive restoration of bone density and reossification of the ischemic epiphysis occurs with healing, during the reparative phase (Fig. 7.9). Definitive deformation and loss of the spherical shape of the epiphysis are found in cases of poor evolution, as well as varus deformity of the femoral neck, with eventual onset of secondary osteoarthritis (Fig. 7.10). As stated above, epiphyseal dysplasias are usually bilateral and symmetric, with simultaneous involvement of other joints, features that allow them to be distinguished from LCPD (Fig. 7.11).

Several radiographic classifications have been used for staging of LCPD. Catterall's system, which was the standard for many decades, proposed four categories based on the extent of the involvement of the femoral head, complemented with the classic "head-at-risk" signs (lateral subluxation of the femoral head, horizontal physis, calcification lateral to the epiphysis, Gage's sign [V-shaped osteoporotic area in the lateral portion of the epiphysis and/or the metaphysis], and metaphyseal cysts). However, as correlation with the clinical evolution and the prognosis is limited with this classification, other staging systems were devised. Herring proposed a new classification based on the height of the lateral pillar of the femoral head as seen on the anteroposterior view during early fragmentation phase (Fig. 7.12): as an intact lateral pillar is considered a weight-bearing support which protects the central avascular

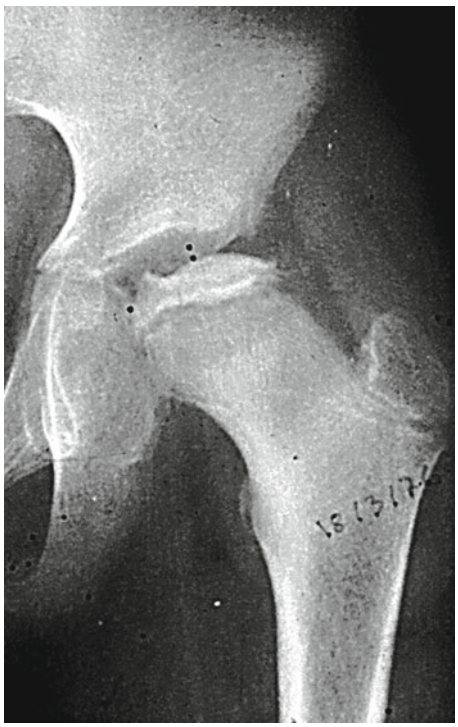

Fig. 7.3 Marked epiphyseal sclerosis is seen in this anteroposterior view of the left hip, with flattening of the articular surface and collapse of the lateral two-thirds of the ossified portion of the femoral head. There is also mild lateral subluxation of this epiphysis

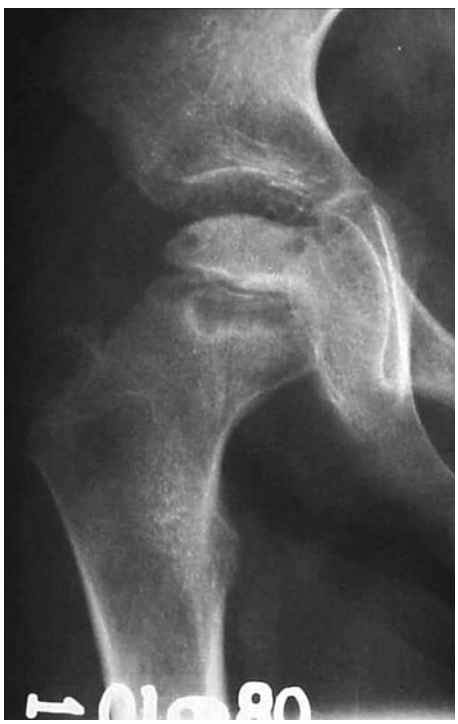

Fig. 7.4 Metaphyseal reaction in the right hip of a patient with LCPD. There are multiple well-delimited, confluent lucencies adjacent to the physis, with broadening of the femoral neck. The femoral head is dense, with focal lucencies permeating the sclerotic bone

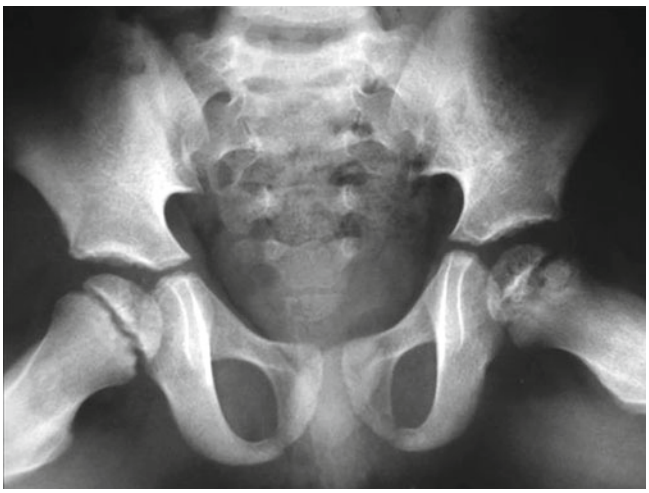

Fig. 7.5 The left proximal femoral epiphysis shows decreased density and size when compared with the contralateral one in this radiograph, findings related to LCPD. Metaphyseal reaction is evident, as well as slight widening of the joint space

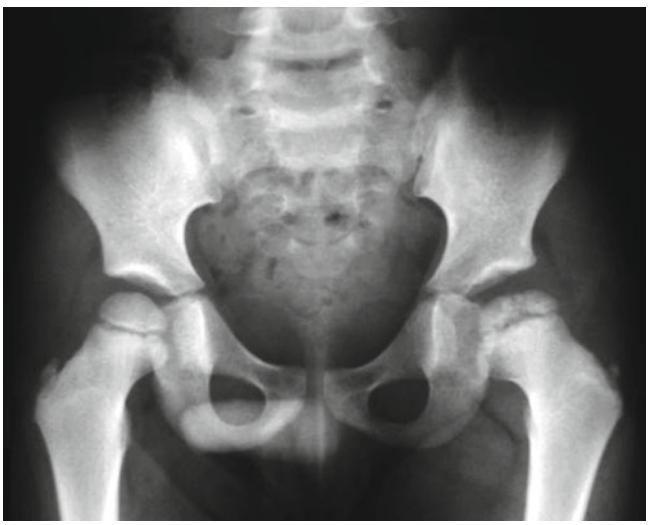

Fig. 7.6 The left proximal femoral epiphysis is flattened and fragmented due to ischemia, with a centrally located sequestrum. There is remodeling of the femoral neck, which is broadened and shortened, in addition to obvious widening of the joint space and extrusion of the lateral portion of the femoral epiphysis

portion of the epiphysis, limiting its collapse, Herring's classification is widely used to assess the severity of the disease and to estimate the prognosis. Children with LCPD Herring type A have an intact lateral pillar, while those with type B present involvement of this pillar, affecting less than 50 % of its height. Patients with LCPD Herring type C have preservation of less than 50 % of the height of lateral pillar, which is an indicator of poor prognosis.

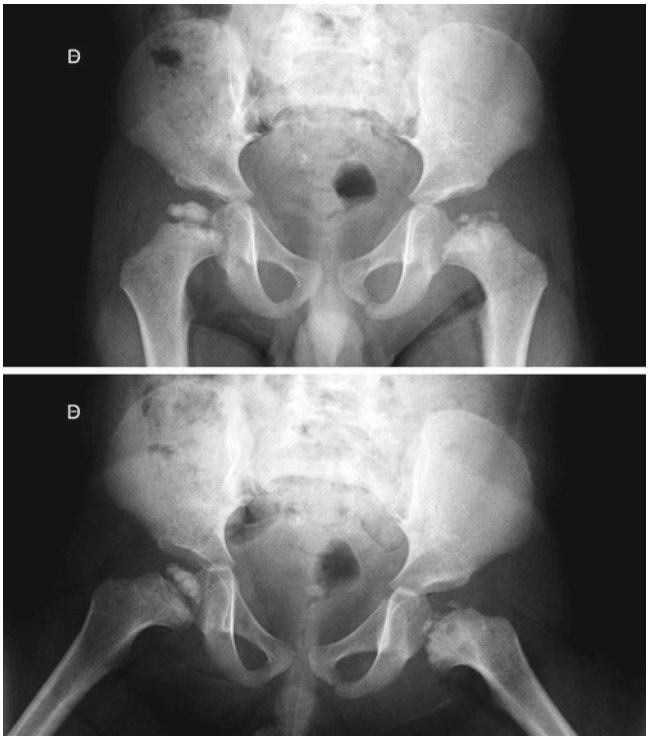

Fig. 7.7 Radiographs of the hips of a patient with bilateral LCPD displaying fragmentation and reduced size of the left proximal femoral epiphysis, with ipsilateral metaphyseal reaction and broadening of the femoral neck. The right femoral head is also flattened, sclerotic, and irregular

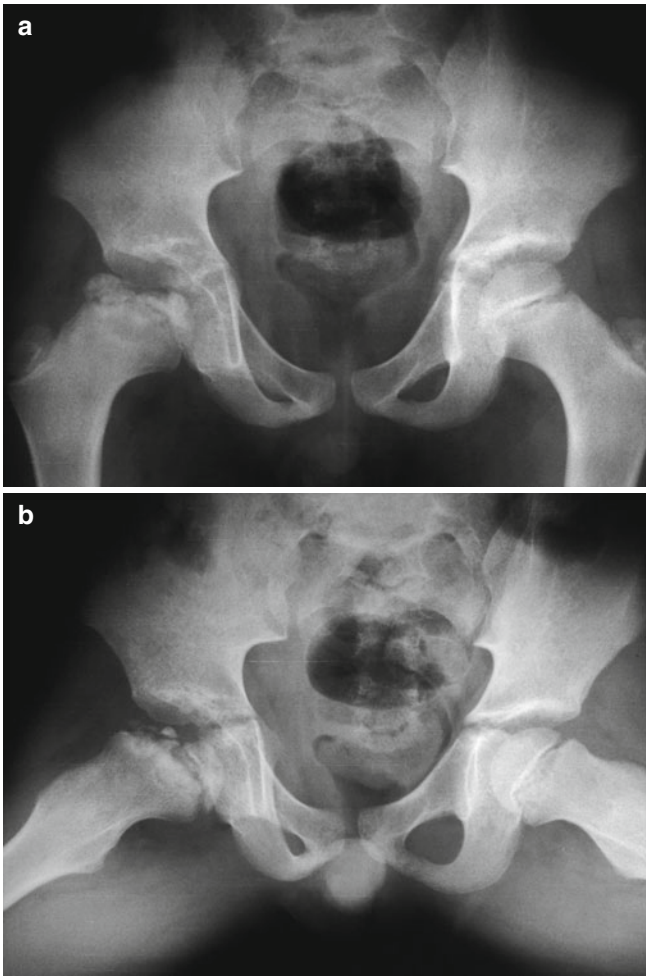

Fig. 7.8 Radiographs of both hips showing flattening and fragmentation of the right proximal femoral epiphysis, affecting mainly its lateral two-thirds, with evident metaphyseal reaction. There is partial extrusion of the right femoral head and remodeling of the acetabular cavity, which is widened and shallow. The right femoral neck is short and broad

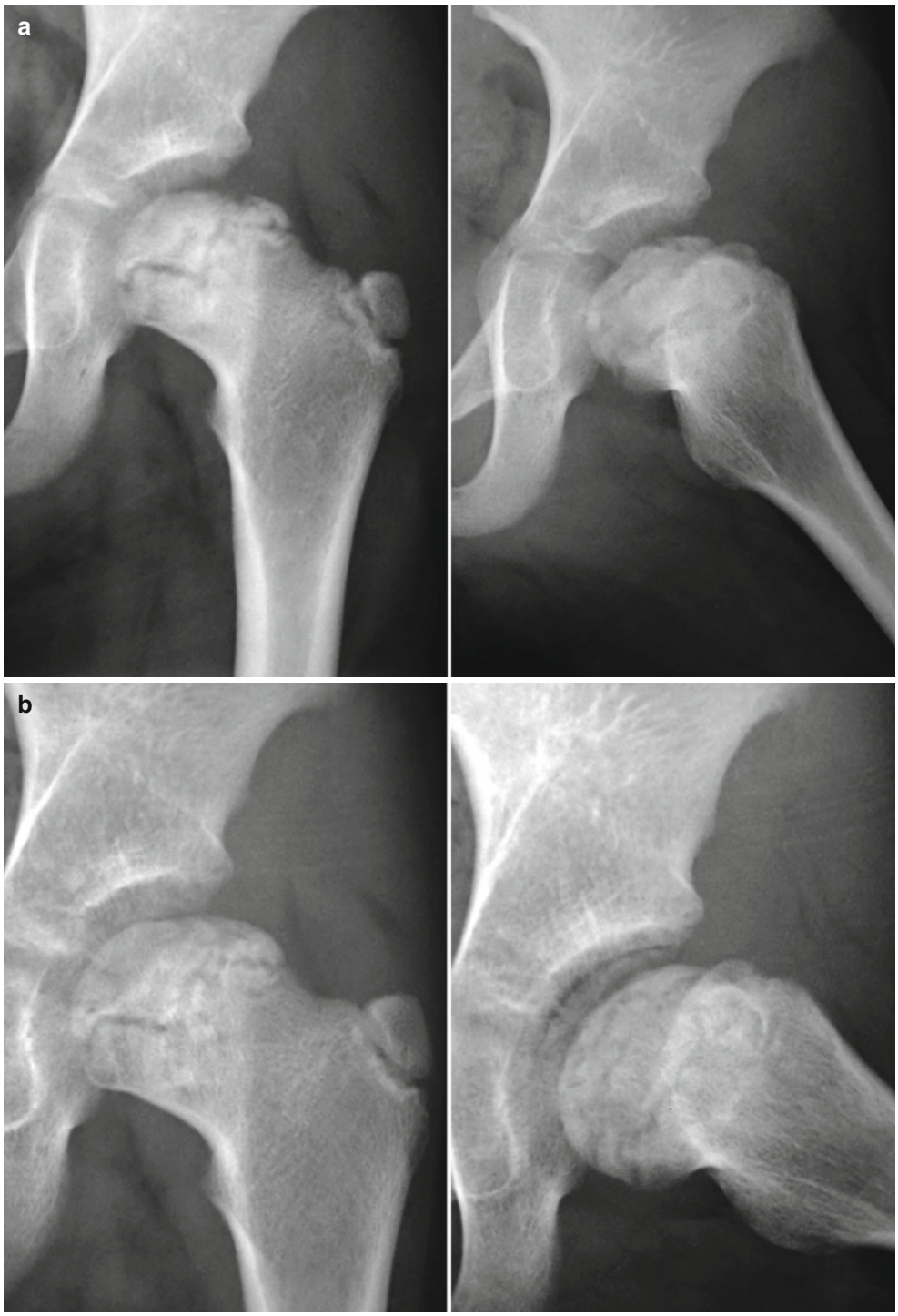

Fig. 7.9 In (**a**), radiographs of the left hip of a child with LCPD display flattening and fragmentation of the proximal femoral epiphysis affecting mainly its lateral third, with a wavy, M-shaped growth plate. The femoral neck is broadened and shortened, with sclerosis of the medial cortex, representing a response to anomalous overload. In (**b**), radiographs taken 9 months later demonstrate coalescence of bone fragments, with reossification of the lateral pillar and partial restoration of the convexity of the articular surface. Nonetheless, the epiphysis is deformed and partially extruded

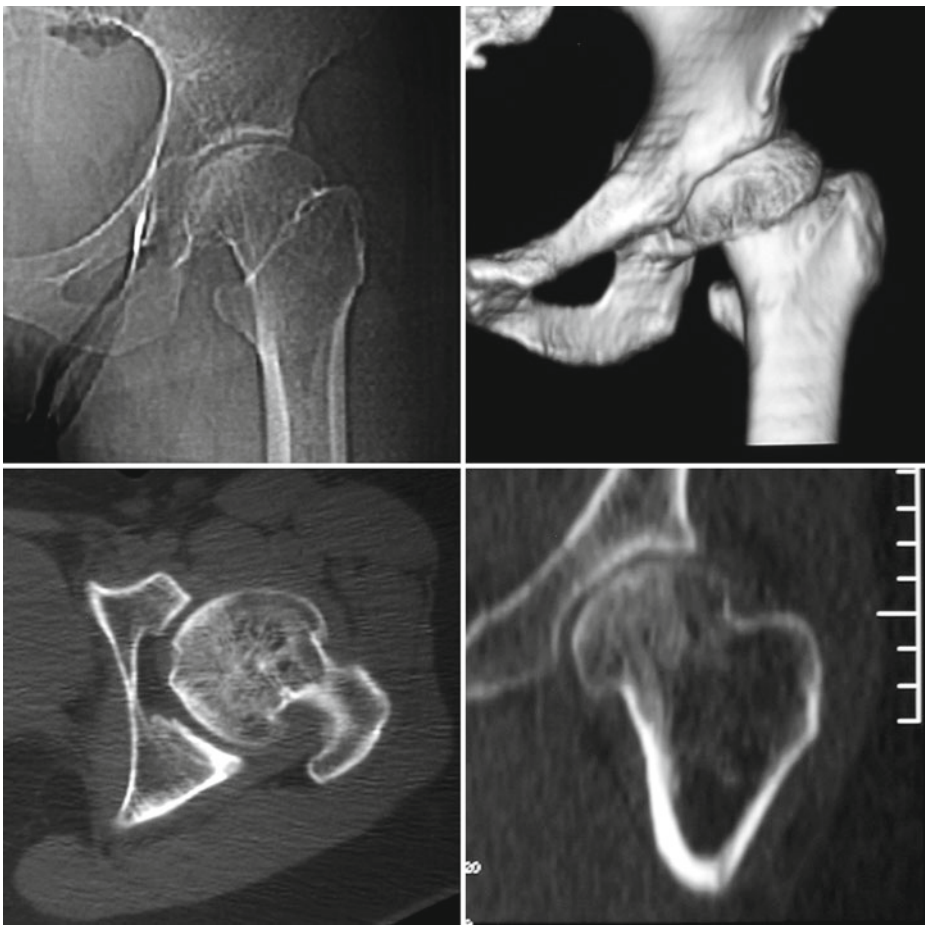

Fig. 7.10 Late-stage sequelae of LCPD in a young adult. Radiograph (*upper-left image*), volume-rendered reconstruction (*upper-right image*), transverse CT section (*lower-left image*), and reformatted coronal image (*lower-right image*) demonstrate morphologic abnormalities of the left femoral head (flattening and loss of its spherical shape, lateral subluxation, and joint incongruity) and femoral neck (shortening and broadening), with secondary osteoarthritis

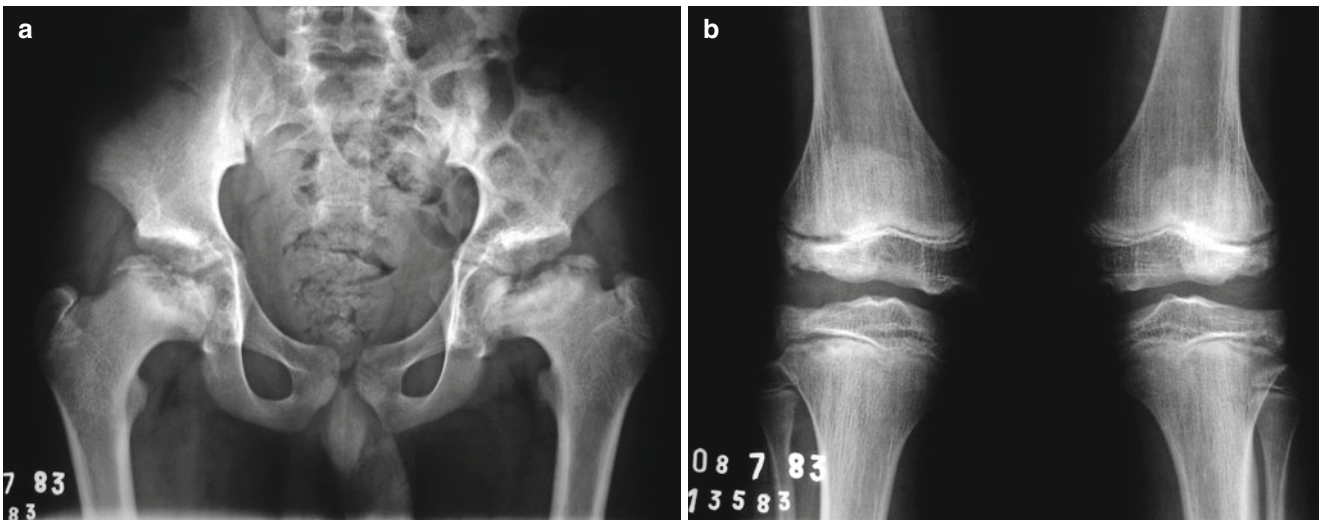

Fig. 7.11 Radiographs of the pelvis (**a**) and of the knees (**b**) of a child with multiple epiphyseal dysplasia. Radiographic findings in the hips resemble those found during the fragmentation phase of LCPD. However, as these findings are bilateral and symmetric and considering that concomitant morphologic epiphyseal abnormalities are also found in the distal femora and proximal tibiae, these features are indicative of their dysplastic nature

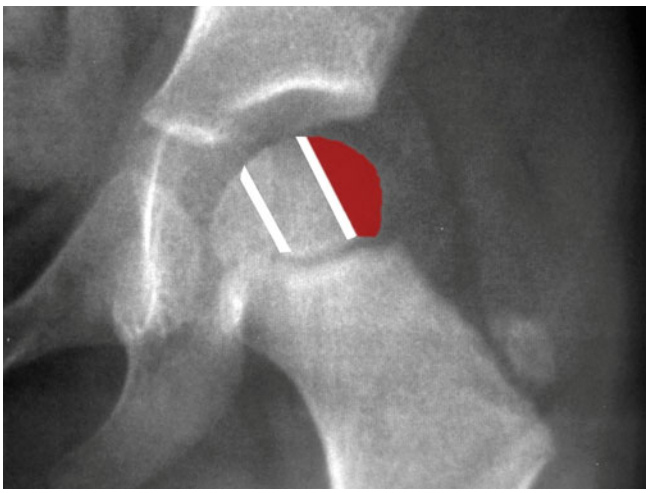

Fig. 7.12 Schematic representation of the three pillars of the proximal femoral epiphysis, with the lateral pillar highlighted in *red*. Lack of involvement of this pillar in the early fragmentation phase of LCPD corresponds to Herring type A. When this pillar is involved and there is less than 50 % of reduction of its height, the patient is Herring type B. In patients Herring type C, more than 50 % of this pillar is collapsed

7.3.2 Magnetic Resonance Imaging

Magnetic resonance imaging (MRI) is able to detect ischemic changes in the bone long before radiographic abnormalities appear, also allowing for accurate staging and demonstrating the progress of the revascularization process. Intravenous contrast is indicated in children with LCPD, as well as inclusion of the contralateral hip in the field of view and digital subtraction of post-contrast images, aiming to maximize detection of decreased bone perfusion. Post-contrast images must be acquired as early as possible, as the enhancement of the early vascular phase fades out from 2 to 5 min after the injection, rendering the differentiation between the normal and the affected hip less evident. Coronal sections are the most suitable for comparative analysis of the hips, while sagittal images are helpful in estimating the severity of the collapse of the femoral head and the real extent of bone necrosis.

Small to moderate joint effusion and reactive synovitis are common findings. One of the earliest osseous abnormalities on non-enhanced MRI is nonspecific bone marrow edema pattern affecting the ischemic epiphysis (Fig. 7.13), though hypointense signal may be present on T2-WI as well. Once necrosis is established, the affected bone usually displays low to intermediate signal intensity on T1-weighted images (T1-WI) and variable signal intensity in fluid-sensitive sequences; low signal intensity of the bone marrow in all sequences is indicative of advanced necrosis (Figs. 7.14, 7.15, 7.16, 7.17, and 7.18). The subchondral fracture appears as a curvilinear area in the anteroposterior portion of the femoral head, with low signal intensity on T1-WI and variable signal intensity (usually hyperintense) on T2-WI. Contrast-enhanced MRI show decreased perfusion of the ischemic epiphysis even before the appearance of edematous changes in the affected bone marrow. Absent enhancement of the epiphyseal bone marrow is strongly suggestive of ischemia (Fig. 7.17), being the anterior portion of the epiphysis involved earlier and more severely. However, it is not possible to differentiate reversible ischemia from established necrosis with the standard protocols in current use, and signs of bone ischemia should be interpreted prudently; diffusion-weighted sequences hold promise in this field, but studies are yet at an embryonic stage. It is important to remember that most patients will have good evolution and that epiphyseal hypoperfusion will not necessarily develop into the classic form of LCPD. Areas of reossification and reperfusion present heterogeneous signal intensity, with persistent post-gadolinium enhancement, which is more intense than that observed in non-ischemic bone (Fig. 7.19). MRI allows for noninvasive demonstration of morphological abnormalities of the femoral head typical of advanced disease, which may eventually lead to bone collapse and loss of epiphyseal sphericity, with joint incongruity (Figs. 7.15, 7.17, 7.18, and 7.20). The so-called hinge abduction is an abnormal movement of the hip that occurs when a deformed femoral head fails to move medially and slide within the acetabulum, hinging on the lateral acetabular margin and leading to impingement, with widening of the medial joint space and epiphyseal subluxation/extrusion. This abnormality – which once was demonstrated with conventional arthrograms – is indicative of joint incongruity and increased risk of premature osteoarthritis and can be diagnosed on dynamic MRI studies. The metaphyseal reaction seen on radiographs probably corresponds to invagination/ectopy of the growth cartilage or focal bone resorption (Fig. 7.17), and it is often associated with post-gadolinium enhancement. With healing, epiphyseal height is gradually restored and the bone fragments tend to coalesce, but several years may elapse before bone marrow reverts back to its normal signal intensity (Fig. 7.21). Broadening and shortening of the femoral neck and secondary osteoarthritis can also be demonstrated with MRI (Figs. 7.21 and 7.22).

Indicators of poor prognosis on MRI include hinge abduction, severe involvement and/or absent enhancement of the lateral pillar of the femoral head, and extensive necrosis of the epiphyseal bone marrow. Transphyseal bone bridges may lead to premature physeal closure and arrested/asymmetric growth. On the other hand, early enhancement of the lateral pillar is considered a sign of good prognosis, representing adequate revascularization, osseous viability, and stopped loss of height.

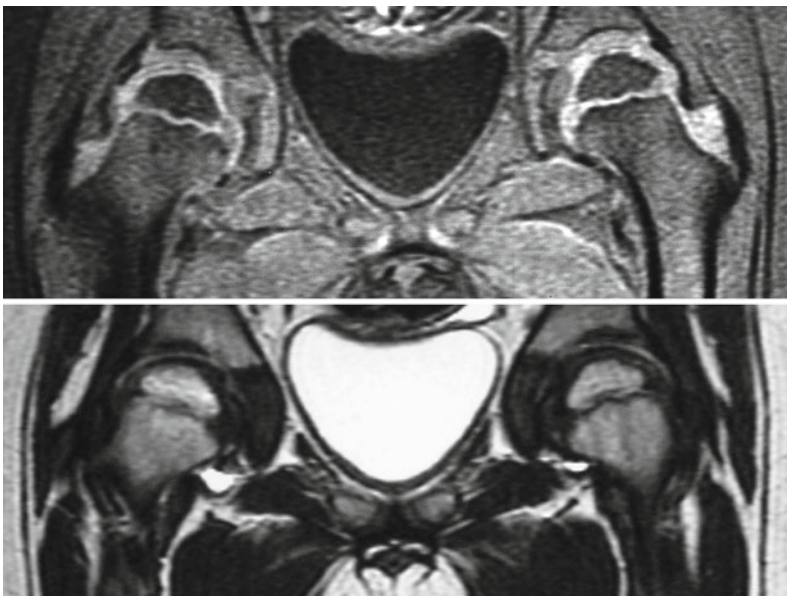

Fig. 7.13 MRI of the hips of a child with right-sided LCPD. A coronal fat sat T1-WI (*upper image*) displays low signal intensity in the right proximal femoral epiphysis if compared to the contralateral one, with increased signal intensity in the same epiphysis on a coronal T2-WI (*lower image*), representing bone marrow edema. Reduced epiphyseal size, bone fragmentation, and epiphyseal collapse are notably absent, but decreased epiphyseal perfusion was present in post-contrast images (not shown)

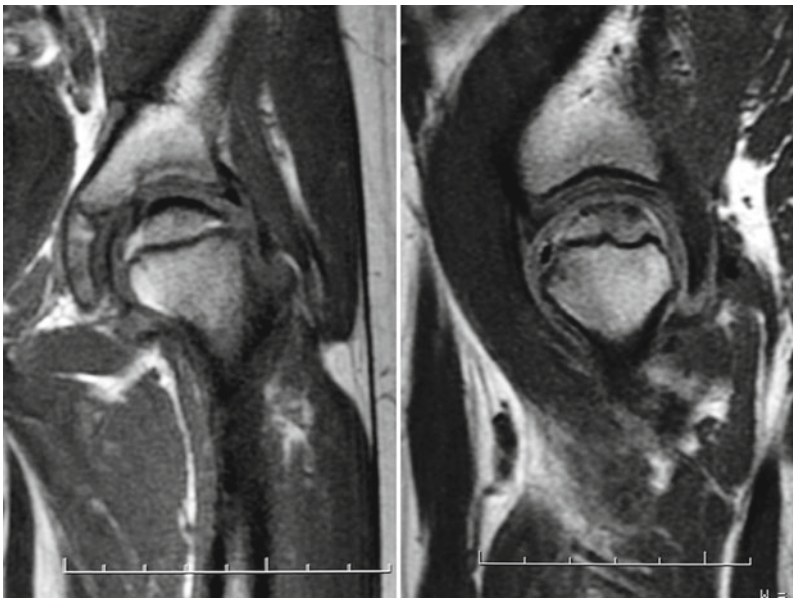

Fig. 7.14 Coronal T1-WI (*left*) and sagittal T2-WI (*right*) of the left hip of a child with LCPD reveal low signal intensity in all sequences in the subchondral bone of the weight-bearing zone of the femoral epiphysis

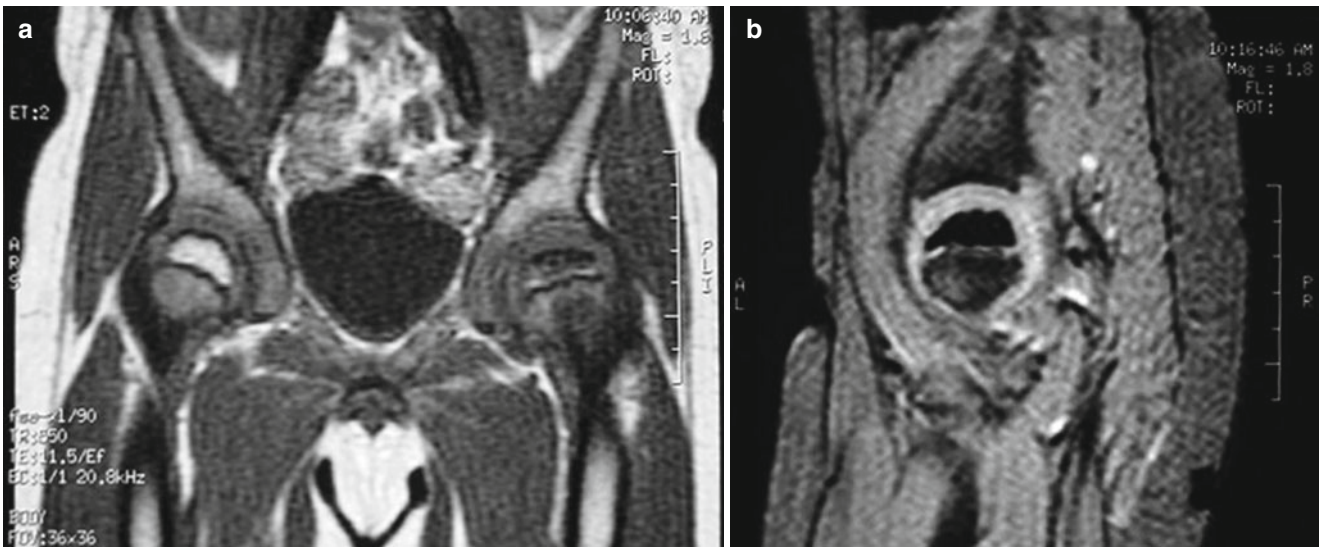

Fig. 7.15 Coronal T1-WI (**a**) and sagittal gradient-echo image (**b**) demonstrate reduced size and abnormal shape of the left proximal femoral epiphysis, with low signal intensity of the epiphyseal bone marrow in both sequences. There is thickening of the femoral cartilage, more evident in (**a**)

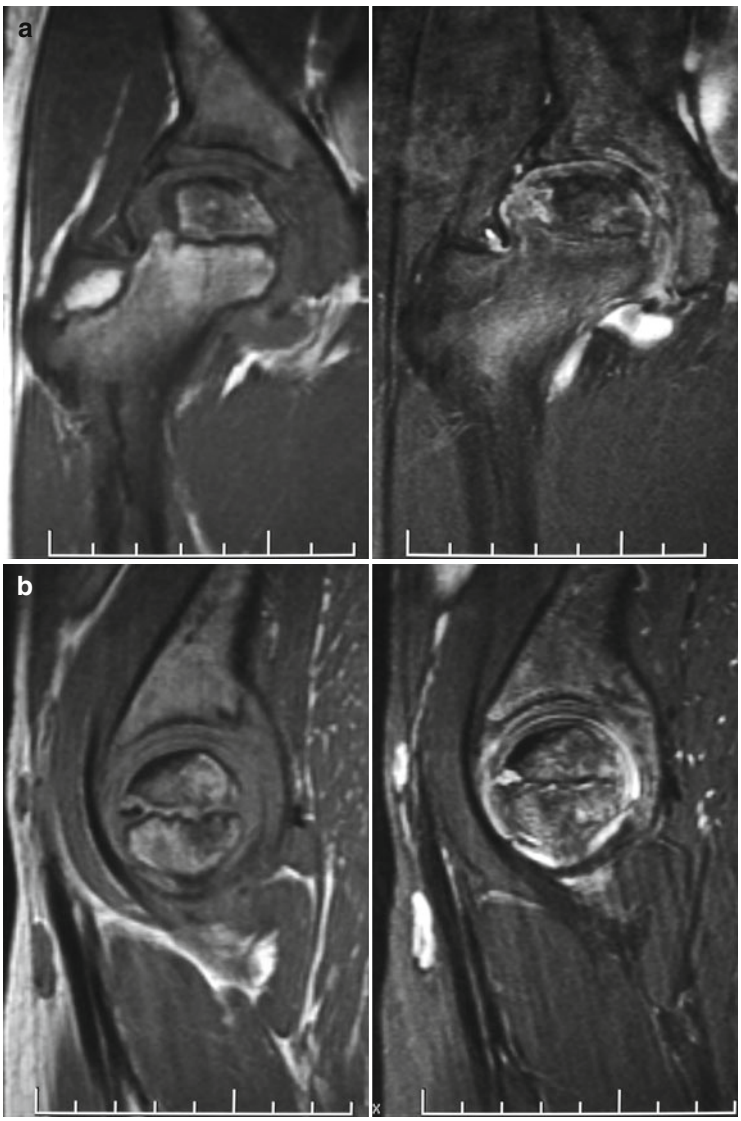

Fig. 7.16 MRI of the right hip of a 9-year-old male with LCPD. T1-WI (**a** and **b**, *left images*) and fat sat T2-WI (**a** and **b**, *right images*) in the coronal and sagittal planes demonstrate bone marrow edema in the lateral pillar of the proximal femoral epiphysis and low signal intensity in all sequences in the subchondral bone of its central portion, being the latter indicative of sclerosis. Joint effusion is also present, as well as bone marrow edema in the femoral neck

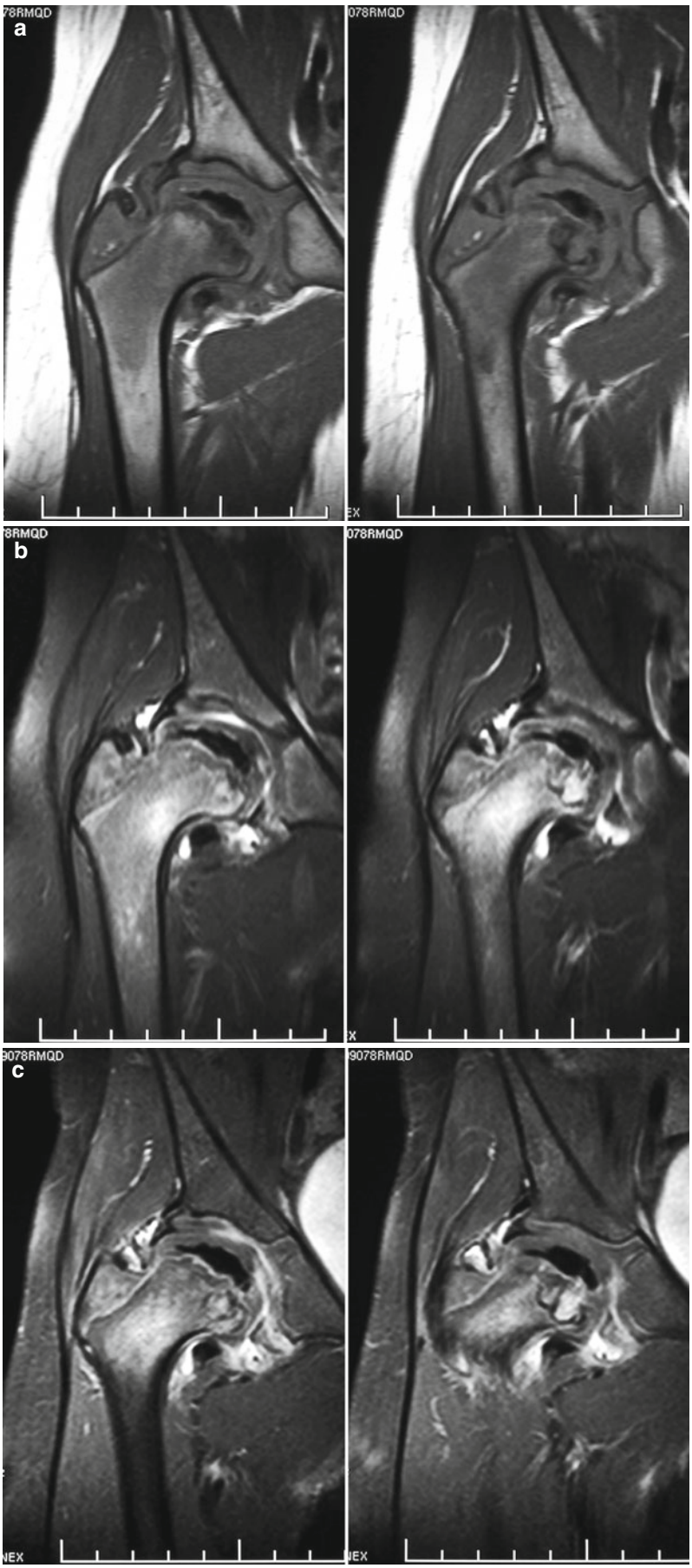

Fig. 7.17 Coronal T1-WI (**a**), fat sat T2-WI (**b**), and post-gadolinium fat sat T1-WI (**c**) of the right hip of a 4-year-old male with LCPD. The proximal femoral epiphysis is irregular, presenting reduced size and markedly decreased signal intensity in all sequences. There is also joint effusion, bone marrow edema pattern in the femoral neck, and metaphyseal reaction. Post-contrast images demonstrate absent enhancement in the ischemic epiphysis, while the edematous areas, the inflamed synovium, and the metaphyseal reaction display obvious enhancement

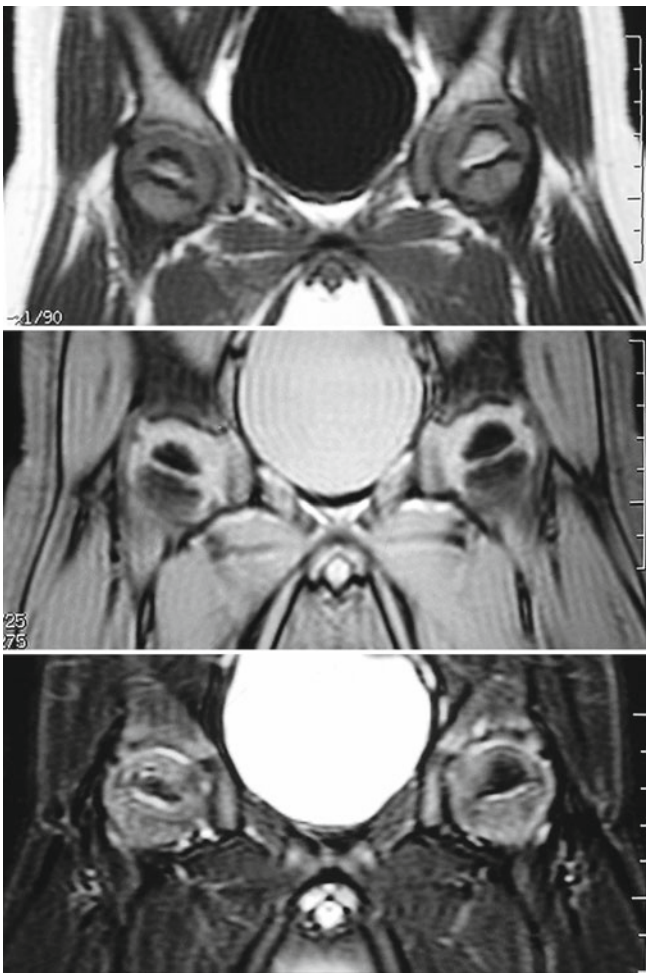

Fig. 7.18 MRI of the hips of a young child with right-sided LCPD, coronal T1-WI (*upper image*), gradient-echo image (*central image*), and post-contrast fat sat T1-WI (*lower image*). The affected epiphysis is reduced in size, presenting low signal intensity of the subchondral bone and ipsilateral cartilaginous thickening

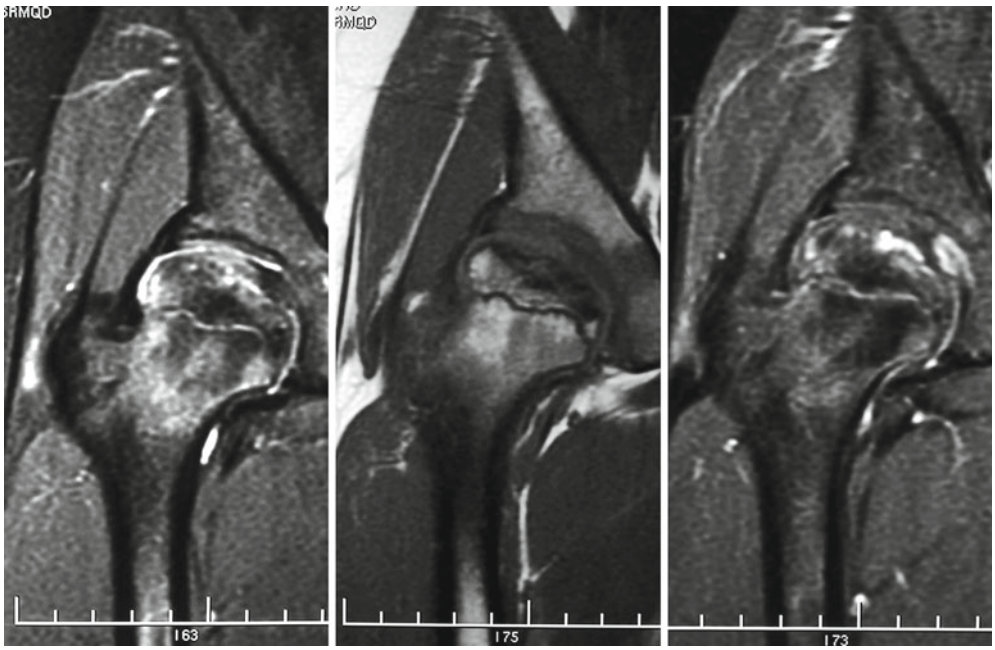

Fig. 7.19 A 8-year-old male with right-sided LCPD, coronal fat sat T2-WI (*left*), T1-WI (*center*), and post-gadolinium fat sat T1-WI (*right*). There is ischemic involvement of the proximal femoral epiphysis, more evident in the central and medial pillars, characterized by a geographic area of heterogeneously high signal intensity on T2-WI and low signal intensity on T1-WI. Mildly abnormal signal intensity is also seen in the lateral pillar. Post-gadolinium images show areas of persistent enhancement permeating the ischemic area and the lateral pillar, representing ongoing bone repair and revascularization. The femoral neck is shortened and broadened

Fig. 7.20 LCPD of the left hip, late fragmentation phase. Coronal T1-WI (*upper image*) and post-gadolinium fat sat T1-WI (*lower image*) demonstrate extensive epiphyseal collapse, with fragmentation, heterogeneous enhancement of the necrotic areas, and remodeling of the metaphysis and of the acetabulum. A large joint effusion is also present

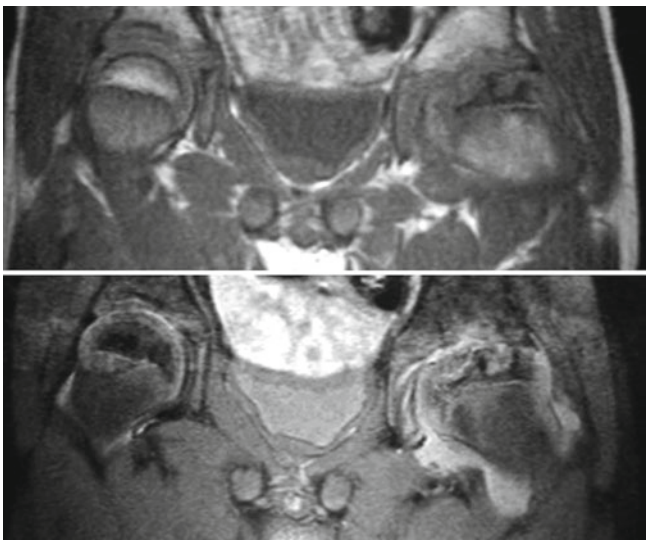

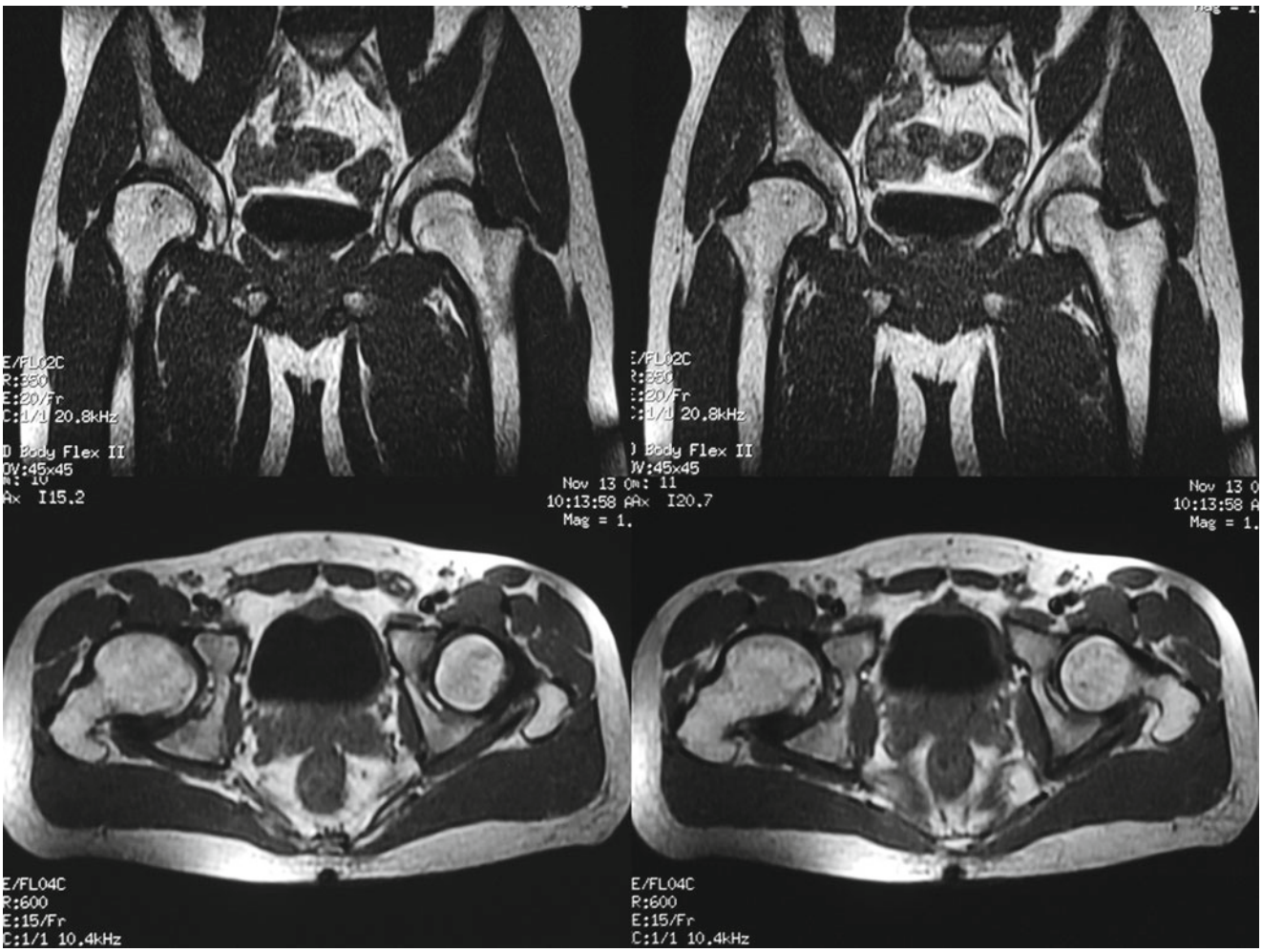

Fig. 7.21 MRI of a young adult with late-stage sequelae of right-sided LCPD. T1-WI in the coronal (*upper images*) and transverse (*lower images*) planes demonstrate complete restoration of the normal signal intensity of the femoral head. Nonetheless, the epiphysis is deformed and flattened, with acetabular remodeling, joint incongruity, and lateral subluxation

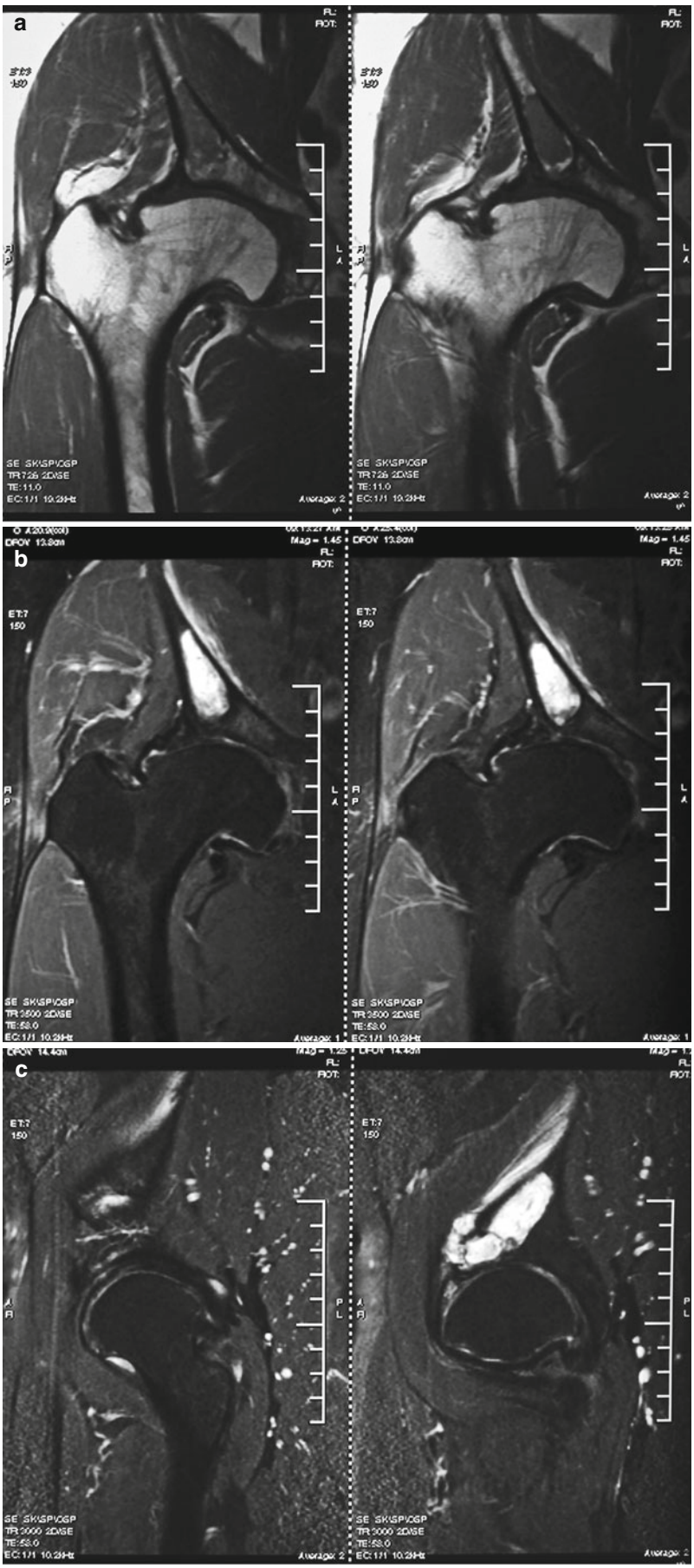

Fig. 7.22 A 47-year-old patient with late-stage sequelae of right-sided LCPD. Coronal T1-WI (**a**) and fat sat T2-WI (**b**) and sagittal fat sat T2-WI (**c**) reveal a femoral head whose shape is markedly abnormal, with severe secondary osteoarthritis. A large degenerative subchondral cyst can be seen in the acetabular roof, breaking the cortex of the iliac bone and presenting an intrapelvic component

7.3.3 Other Imaging Methods

As the shape of the secondary ossification center seen on radiographs does not allow for an accurate prediction of the morphology of the non-mineralized epiphyseal cartilage, conventional arthrograms (see Chap. 1) were used for the assessment of hip congruity during several decades. Even though only the contours of the articular surfaces were analyzed with arthrograms, fluoroscopy provided a dynamic way to assess joint mobility. They are no longer used, being mentioned only because of its historical relevance. MRI took the place of conventional arthrograms because it is noninvasive and nonionizing, providing images with unsurpassable anatomic detail and similar diagnostic accuracy. Scintigraphy, which once was the standard for assessment of epiphyseal revascularization in LCPD, is rarely used for such purpose nowadays, as it was gradually abandoned in favor of MRI. In spite of its excellence for bone assessment, computed tomography (CT) is seldom used in patients with LCPD, mostly due to its limitations in the evaluation of the soft tissues and because it is unable to assess bone revascularization (Figs. 7.2 and 7.23). Nevertheless, CT is useful in the characterization of late-stage sequelae, such as residual bone deformities (Figs. 7.10 and 7.24). Although ultrasonography is not particularly useful for the diagnosis of LCPD, it is often used in the assessment of children with hip pain because of its high sensitivity in the detection of joint effusion and synovitis.

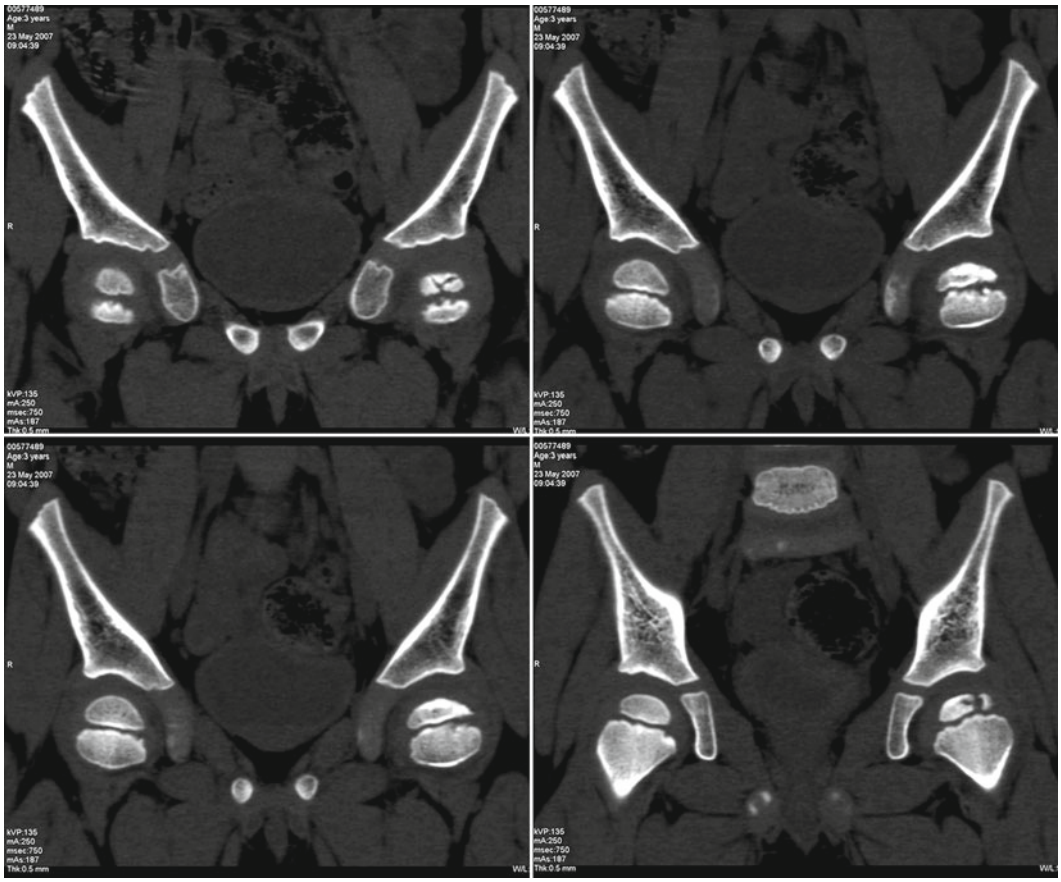

Fig. 7.23 CT of the hips of a 3-year-old male. Coronal reformatted images show sclerosis, fragmentation, and reduced size of the ossified portion of the proximal femoral epiphysis at left. Even though the diagnosis of LCPD in early fragmentation stage is quite obvious, CT is unable to detect bone marrow edema or to assess the pattern of revascularization, being also limited in the evaluation of the soft tissues (Courtesy of Dr. Pablo Picasso Coimbra, Clinica Boghos Boyadjian, Fortaleza, Brazil)

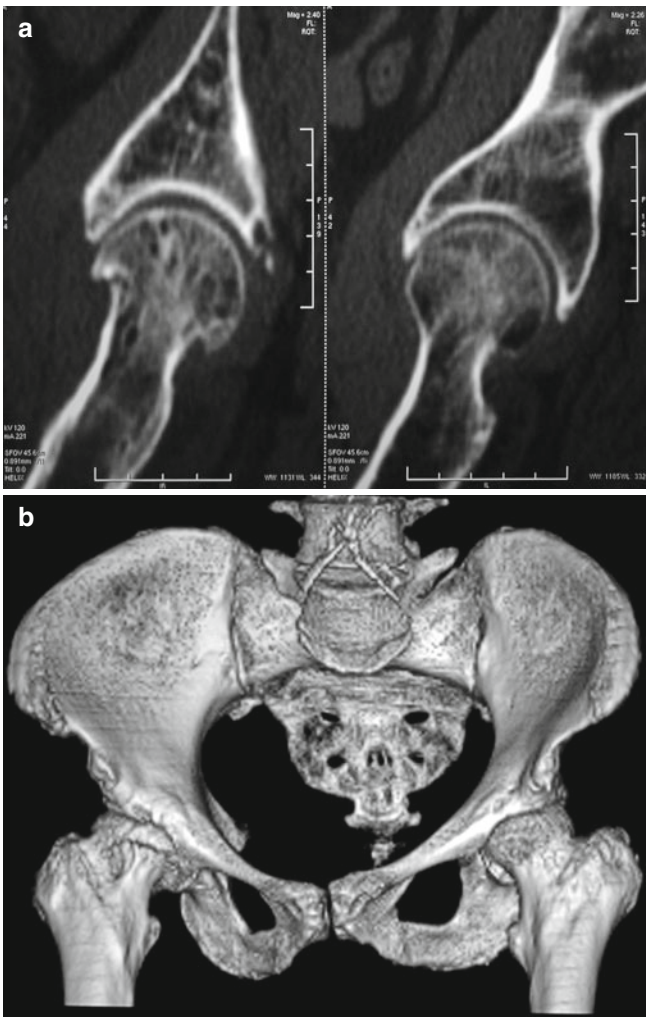

Fig. 7.24 Oblique reformatted CT images (**a**) and volume-rendered reconstruction (**b**) of a 62-year-old patient with late-stage sequelae of right-sided LCPD. There is loss of the spherical shape of the femoral head, which presents a "mushroom" appearance, in addition to broadening and shortening of the femoral neck. Acetabular remodeling and secondary osteoarthritis are also evident

Key Points

- LCPD is a diagnosis of exclusion, consisting in an idiopathic form of avascular necrosis of the immature femoral head. The younger the patient and the lesser the extent of epiphyseal necrosis, the better the prognosis (and vice versa).
- Typical radiographic findings include epiphyseal sclerosis, subchondral fracture ("crescent sign") and the so-called metaphyseal reaction, with eventual development of bone fragmentation and epiphyseal collapse. However, these are late-stage findings, not useful for early diagnosis.
- Contrast-enhanced MRI allows for early diagnosis of bone ischemia. MRI is also able to follow the cascade of phenomena that occur after bone necrosis and, even more, to obtain information about the pattern of revascularization. Joint deformities can be safely demonstrated in a noninvasive way.
- Involvement of the lateral pillar of the femoral epiphysis is one of the most important prognostic factors in LCPD: the more extensive is the involvement, the worse the prognosis.
- Radiographs and MRI aside, other imaging studies have only a complementary role or are used in exceptional circumstances in LCPD.

Recommended Reading

Dillman JR, Hernandez RJ (2009) MRI of Legg-Calve-Perthes disease. AJR Am J Roentgenol 193(5):1394–1407

Dillon JE, Connolly SA, Connolly LP, Kim YJ, Jaramillo D (2005) MR imaging of congenital/developmental and acquired disorders of the pediatric hip and pelvis. Magn Reson Imaging Clin N Am 13(4): 783–797

Doria AS, Cunha FG, Modena M, Maciel R, Molnar LJ, Luzo C et al (2008) Legg-Calvé-Perthes disease: multipositional power Doppler sonography of the proximal femoral vascularity. Pediatr Radiol 38(4):392–402

Dwek JR (2009) The hip: MR imaging of uniquely pediatric disorders. Magn Reson Imaging Clin N Am 17(3):509–520

Fabry G (2010) Clinical practice: the hip from birth to adolescence. Eur J Pediatr 169(2):143–148

Frick SL (2006) Evaluation of the child who has hip pain. Orthop Clin North Am 37(2):133–140

Herring JA, Kim HT, Browne R (2004) Legg-Calve-Perthes disease. Part I: classification of radiographs with use of the modified lateral pillar and Stulberg classifications. J Bone Joint Surg Am 86-A(10): 2103–2120

Jaramillo D (2009) What is the optimal imaging of osteonecrosis, Perthes, and bone infarcts? Pediatr Radiol 39(Suppl 2):S216–S219

Kocher MS, Tucker R (2006) Pediatric athlete hip disorders. Clin Sports Med 25(2):241–253

Lamer S, Dorgeret S, Khairouni A, Mazda K, Brillet PY, Bacheville E et al (2002) Femoral head vascularisation in Legg-Calvé-Perthes disease: comparison of dynamic gadolinium-enhanced subtraction MRI with bone scintigraphy. Pediatr Radiol 32(8):580–585

Merlini L, Combescure C, De Rosa V, Anooshiravani M, Hanquinet S (2010) Diffusion-weighted imaging findings in Perthes disease with dynamic gadolinium-enhanced subtracted (DGS) MR correlation. Pediatr Radiol 40(3):318–325

Nelitz M, Lippacher S, Krauspe R, Reichel H (2009) Perthes disease: current principles of diagnosis and treatment. Dtsch Arztebl Int 106(31–32):517–523

Sheikh A, Koujok K, Sampaio ML, Schweitzer ME (2013) MR imaging of osseous lesions of the hip. Magn Reson Imaging Clin N Am 21(1):111–125

Weishaupt D, Exner GU, Hilfiker PR, Hodler J (2000) Dynamic MR imaging of the hip in Legg-Calvé-Perthes disease: comparison with arthrography. AJR Am J Roentgenol 174(6):1635–1637

Yazici M, Aydingöz U, Aksoy MC, Akgün RC (2002) Bipositional MR imaging vs arthrography for the evaluation of femoral head sphericity and containment in Legg-Calvé-Perthes disease. Clin Imaging 26(5):342–346

Musculoskeletal Disorders Related to Pediatric Hematologic Diseases

8

8.1 Introduction

The vast majority of hematologic diseases (hemoglobinopathies, coagulopathies, or malignancies) lead to some kind of osteoarticular involvement. Such involvement is often responsible either for the clinical presentation or for some of the most disabling features of these conditions. It is not uncommon for the radiologist to be the one who first suggests the diagnosis. Awareness of the imaging appearance of the main pediatric hematologic diseases is essential in order to avoid diagnostic errors and allow timely institution of treatment.

8.2 Hemoglobinopathies

The hemoglobinopathies encompass a heterogeneous group of diseases in which there is some abnormality of the hemoglobin molecule, frequently associated with hemolytic anemia. The most prevalent of them is sickle-cell disease (SCD), an autosomal recessive condition that predominates in Afro-descendants. In SCD, there is an abnormal form of hemoglobin with a mutant beta globin chain, named hemoglobin S; it predominates over hemoglobin A, which is the dominant form in healthy individuals. Upon deoxygenation, erythrocytes with hemoglobin S lose their malleability and undergo irreversible deformation (sickling), being removed from circulation by the reticuloendothelial system. Thalassemia is the most frequent hemoglobinopathy in individuals with Mediterranean, Arab, or Asian ancestry, characterized by defective formation of alpha or beta chains of the hemoglobin molecule, being the latter (beta-thalassemia) the most common form. Because of its prevalence, SCD will be used as the prototype to describe the imaging findings of hemoglobinopathies unless otherwise specified.

Chronic anemia related to SCD leads to persistence and hyperplasia of the hematopoietic red marrow (see Chap. 2 – Fig. 8.1), with osteoporosis, widening of the medullary cavities, coarse appearance of bone trabeculae, and thinning of the cortex (Fig. 8.2). Classic radiographic findings in the calvaria include widening of the diploic space, thickening of the inner table, thinning of the outer table, and prominent trabeculae (hair-on-end sign) (Fig. 8.3). Spinal involvement is characterized by biconcave "fish" (or "fish mouth") vertebrae, cortical thinning, and weakening of the medullary bone, all related to osteoporosis, with vertebral wedging/collapse in advanced cases (Figs. 8.4 and 8.5).

Abnormalities of bone development are also common in children with SCD, mostly related to ischemia of the growth cartilages (vasoocclusion due to trapping of the abnormally shaped erythrocytes). In the ankles, ischemic changes typically occur in the lateral portion of the distal tibia, leading to medial inclination of the tibiotalar joint surfaces (tibiotalar slant – Fig. 8.6). Sharply delimited depressions of the vertebral endplates ("H-shaped" vertebra) are related to centrally located infarctions and abnormal endochondral bone formation (Figs. 8.4 and 8.7). Protrusio acetabuli is found in up to 20 % of the patients, secondary to ischemic involvement of the triradiate cartilage.

The so-called hand-foot syndrome (sickle-cell dactylitis) is characterized by recurrent episodes of pain and swelling of hands and feet related to infarction of the diaphyses of the small tubular bones. It is typical of small children (before age 2), consisting in one of the earliest manifestations of SCD. Radiographs are insensitive during the early stages, and characteristic radiographic findings (which include mottled osteoporosis, periosteal reaction, bone neoformation, and cortical thickening) may take some weeks to become apparent (Fig. 8.8). Moth-eaten lesions may be seen in more severe cases, and in long-standing disease, there is squaring and widening of the small tubular bones of hands and feet (Figs. 8.2 and 8.9).

Painful episodes of vasoocclusion leading to acute bone infarction are the most frequent musculoskeletal complication of SCD after the second year of life, affecting mainly the long bones, vertebrae, and ribs. Even though radiographs are often normal in the early stages, lucent areas appear as bone destruction advances (Fig. 8.10). Chronic bone infarcts in the long bones appear as centrally located metadiaphyseal/

S.L. Viana et al., *Joint Imaging in Childhood and Adolescence*,
DOI 10.1007/978-3-642-35876-0_8, © Springer-Verlag Berlin Heidelberg 2013

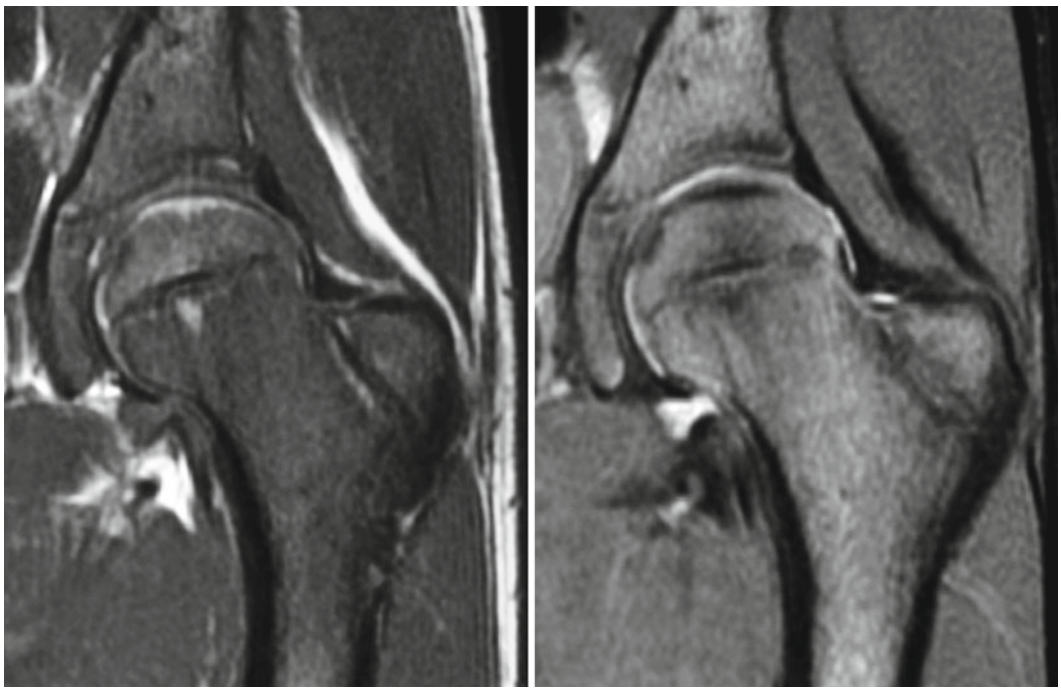

Fig. 8.1 Coronal T1-WI (*left*) and fat sat T2-WI (*right*) of the left hip of a child with SCD. There is diffuse alteration of the signal intensity of the bone marrow, which presents low/intermediate signal intensity on T1-WI and hyperintense on fat sat T2-WI, representing hyperplasia of the red marrow related to chronic anemia

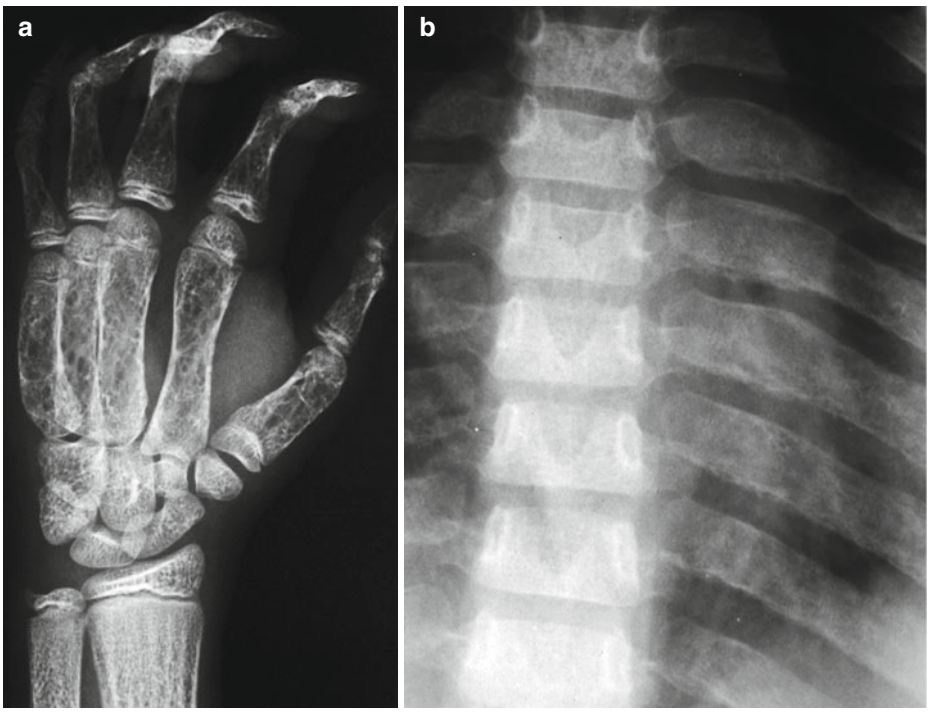

Fig. 8.2 Radiographic abnormalities related to marrow hyperplasia in SCD. In (**a**), there is enlargement of the tubular bones of the right hand and coarse appearance of the trabeculae. In (**b**), the ribs are widened due to enlargement of the medullary cavities, with irregular periosteal reaction in several of them at left

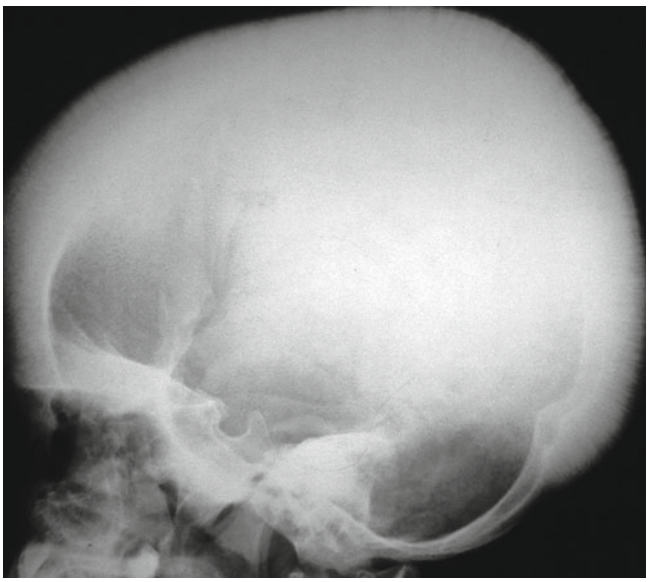

Fig. 8.3 Lateral radiograph of the skull of a 7-year-old child with SCD. Widening of the diploic space is evident, with prominence of bone trabeculae, thickening of the inner table, and thinning of the outer table. The occipital squama is spared

diaphyseal lesions that exhibit a serpiginous calcified rim (Figs. 8.11 and 8.12), while marked sclerosis is found in chronic infarcts of the pelvic bones and of the vertebrae (Fig. 8.13). Additional findings that may be related to chronic infarcts include cortical thickening, layered periosteal reaction, and a "bone-within-bone" appearance (Figs. 8.11, 8.12, 8.13, and 8.14). Bone infarcts usually display normal or decreased uptake on bone scintigraphy in the first few days after the ischemic insult, showing increased uptake after the onset of revascularization; necrotic areas will remain "cold," while ischemic bone with adequate revascularization will return to its normal appearance within a few months. On MRI, acute infarctions are ill-defined and may present a non-specific edematous appearance; in time, however, hemoglobin degradation products eventually appear (showing high signal intensity on T1-WI and T2-WI), and heterogeneous post-gadolinium enhancement is often present ("ink stain" pattern), with surrounding bone marrow edema (Figs. 8.13, 8.15, and 8.16). On the other hand, chronic bone infarcts are geographic and well defined, presenting a hypointense rim on T1-WI and T2-WI and variable signal intensity in the

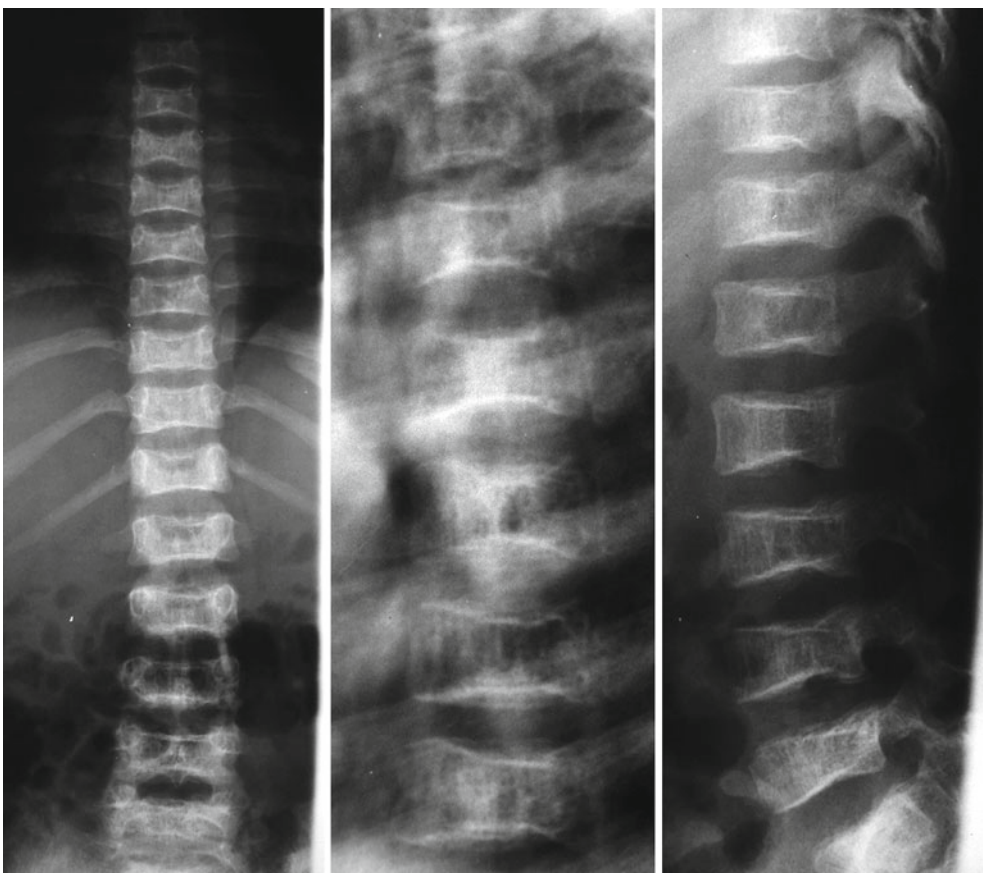

Fig. 8.4 Radiographic abnormalities of the spine of a child with SCD. There is diffuse osteoporosis and thickening of the trabeculae. Several vertebrae present mildly reduced height and biconcave appearance, notably in the dorsal spine, related to hyperplasia of red marrow. "H-shaped" vertebrae are also present in the lumbar spine

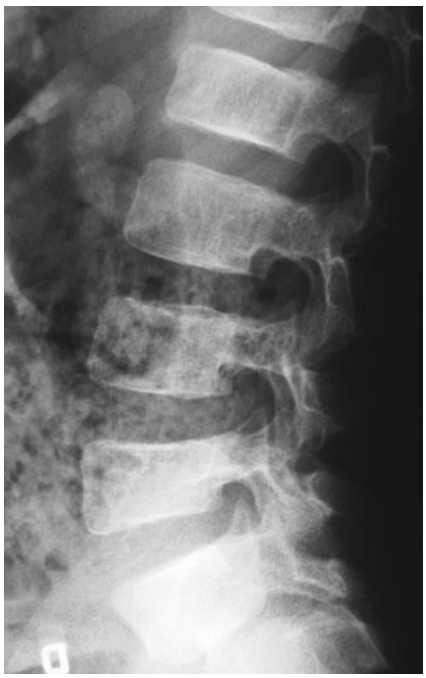

Fig. 8.5 Lateral view of the lumbar spine of a child with SCD revealing diffuse osteoporosis and reduction of the height of L2 and L5, as well as subtle posterior wedging of the latter

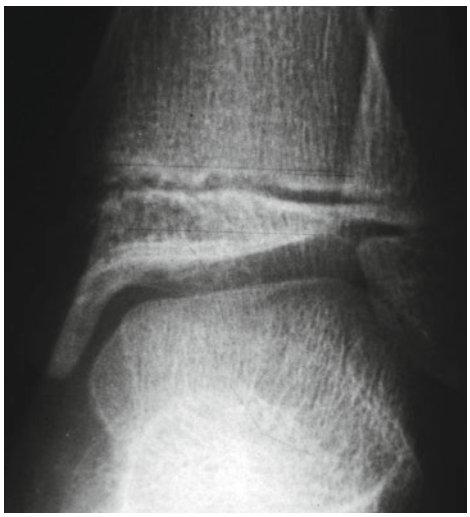

Fig. 8.6 Radiograph of the left ankle of a 15-year-old boy with SCD and tibiotalar slant. Even though this is a classic radiographic finding, other diseases, such as hemophilia and juvenile idiopathic arthritis, may present a similar appearance

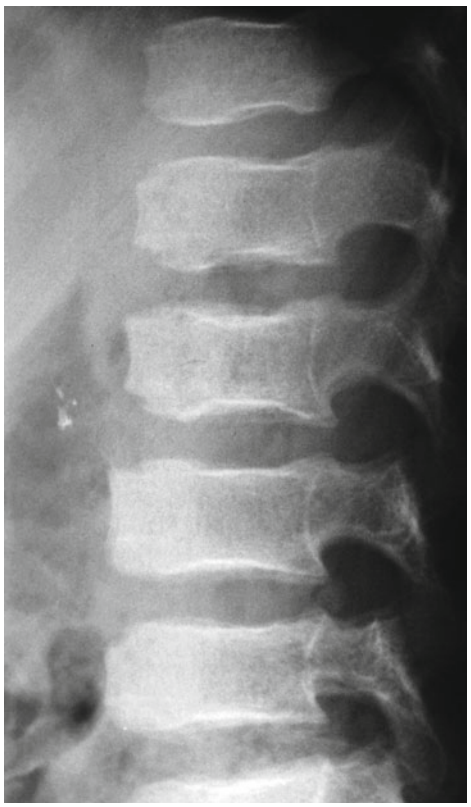

Fig. 8.7 Lateral view of the thoracolumbar spine of a child with SCD showing the typical "H-shaped" vertebrae. There are focal depressions of the affected endplates, whose appearance differs from that of the biconcave vertebrae weakened by hyperplasia of the red marrow

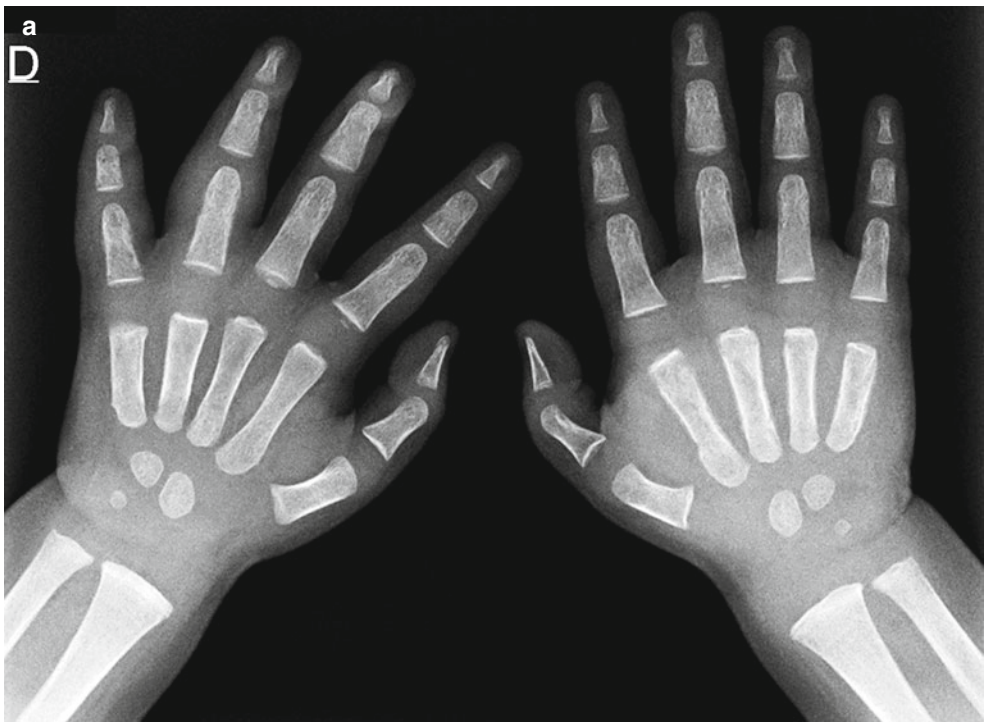

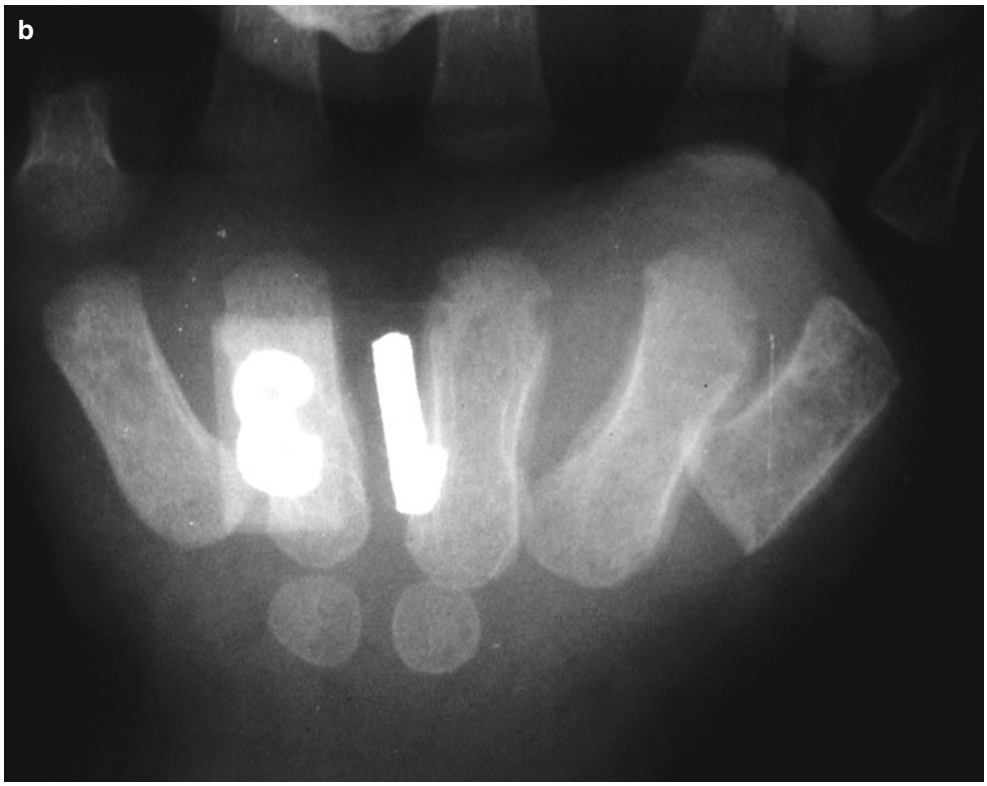

Fig. 8.8 In (**a**), radiograph of hands and wrists of a child with sickle-cell dactylitis demonstrates soft-tissue swelling and irregular periosteal reaction in the left metacarpals (from the second to the fifth) and in the right proximal phalanges of the fourth and fifth digits. There is also symmetric, diffuse, and bilateral enlargement of the phalanges, which show prominent bone trabeculae and solid periosteal reaction in some diaphyses. In (**b**), radiograph of the right hand of an 11-month-old male with acute dactylitis shows periosteal reaction in several metacarpals and cortical erosions, mainly in the third one; mottled osteoporosis is also present

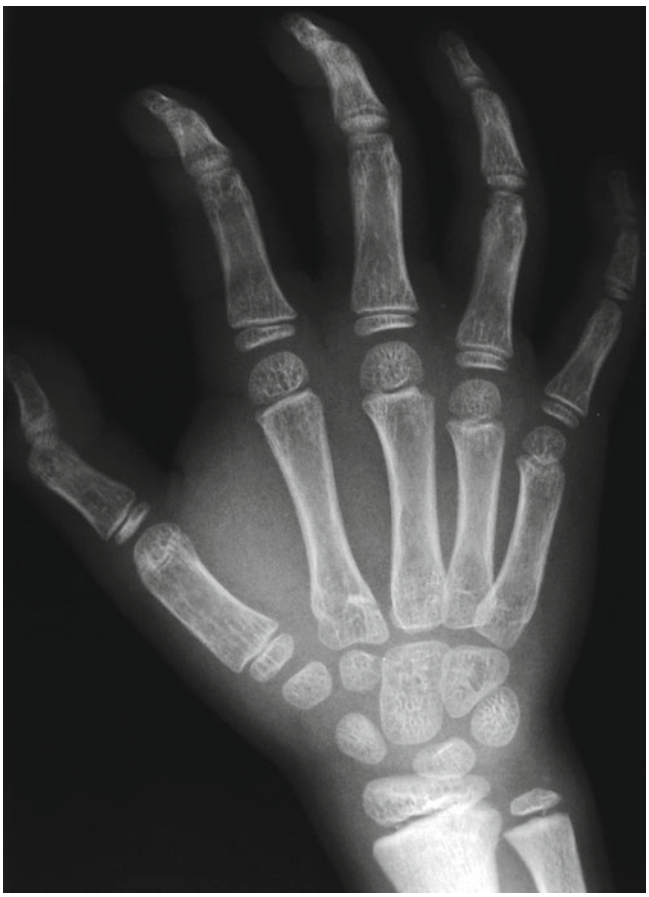

Fig. 8.9 There is diaphyseal widening of the first metacarpal (which displays a cylindrical appearance in this child with SCD) due to expansion of the medullary cavity. Bone trabeculae are prominent and coarse, with a striated pattern. Solid periosteal reaction is seen in the proximal phalanges, mainly in the fourth finger

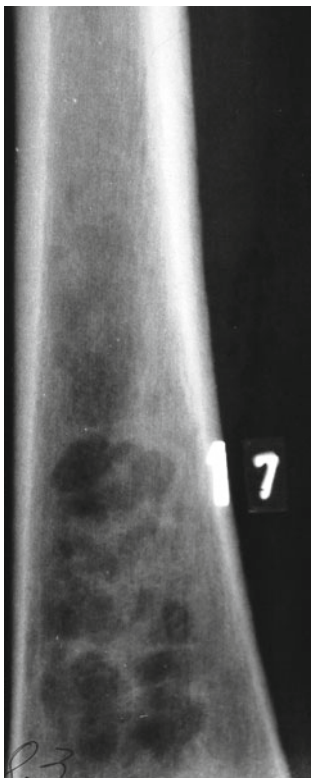

Fig. 8.10 Bone infarct of the right femur of a male adolescent with SCD. An extensive lucency with lobulated borders can be seen in the medullary cavity of the distal diaphysis, without associated calcifications. The distal portion of the lesion is reasonably well delimited, while the proximal portion is ill-defined

central portion (Fig. 8.16). Avascular necrosis (epiphyseal infarct) in SCD is more common in adults than in children. The epiphyses of the proximal femur and of the proximal humerus are the preferential sites, with imaging findings similar to those of Legg-Calvé-Perthes disease, discussed in Chap. 7; lesions are usually larger and more frequently bilateral in SCD if compared to other causes of avascular necrosis (Figs. 8.13, 8.17, and 8.18). Subperiosteal fluid collections and hematomas are occasionally found in the limbs (Fig. 8.19), although they are more common in the orbits, associated with bone infarcts.

Patients with SCD are more susceptible to infections, caused mainly by gram-negative bacteria. Osteomyelitis is more frequently caused by *Salmonella* (in opposition to the predominance of *S. aureus* in the general population), being often diaphyseal, extensive, and multifocal (Figs. 8.20 and 8.21). Differentiation between osteomyelitis and acute bone infarcts in SCD may be difficult, given that osteomyelitis is frequently preceded or accompanied by bone infarcts (Figs. 8.15 and 8.22). In both conditions, radiographs are usually normal or nonspecific in the initial stages. Radiographic findings typical of chronic osteomyelitis – such as bone sequestra, involucrum, sinus tracts, or soft-tissue abscesses (Figs. 8.20 and 8.21) – aid in the differential diagnosis, but these are late findings. Ultrasonography (US) is valuable to guide invasive procedures and to demonstrate subperiosteal and soft-tissue collections, even though it is not able to determine if the latter are related to hematomas or abscesses. Magnetic resonance imaging (MRI) is useful in this setting, as the lack of hemoglobin degradation products in the medullary bone and the presence of intraosseous, subperiosteal, or soft-tissue collections with peripheral post-contrast enhancement favor musculoskeletal infection over bone infarct (Figs. 8.15 and 8.22).

Arthritis in SCD – which may present as monoarthritis, oligoarthritis, or polyarthritis – is typically transient, self-limited, and nondestructive, affecting primarily the knees,

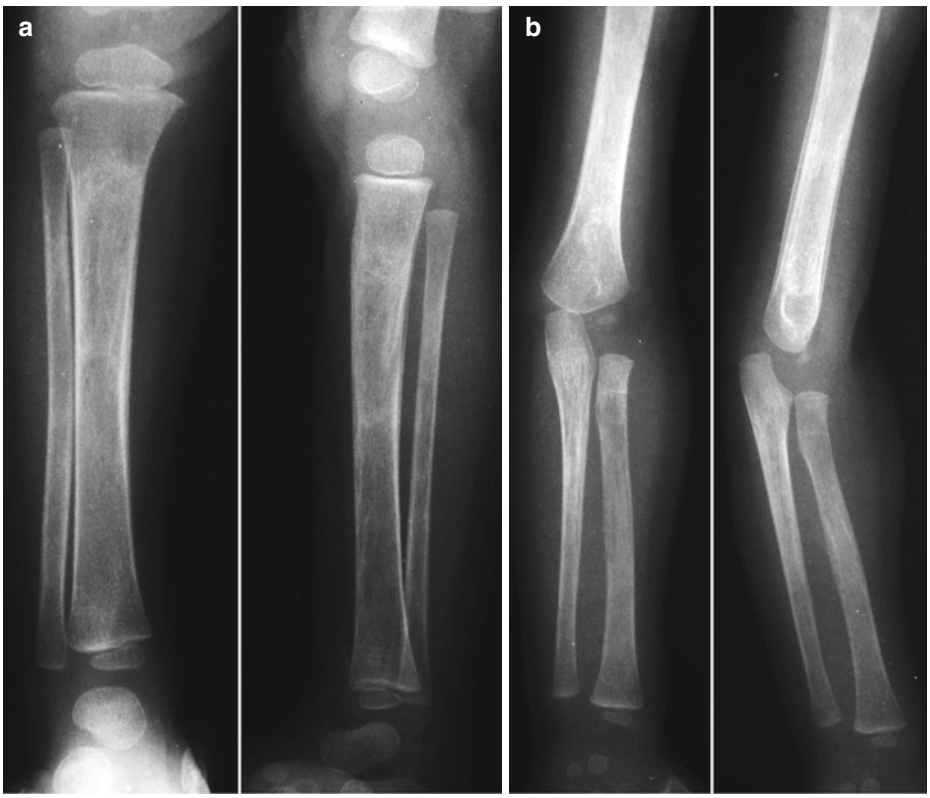

Fig. 8.11 Bone infarcts in a child with SCD (1 year and 6 months old). Radiographs of the right leg (**a**) and of the left upper limb (**b**) reveal diffuse osteoporosis, areas of bone sclerosis, and solid periosteal reaction in the long bones

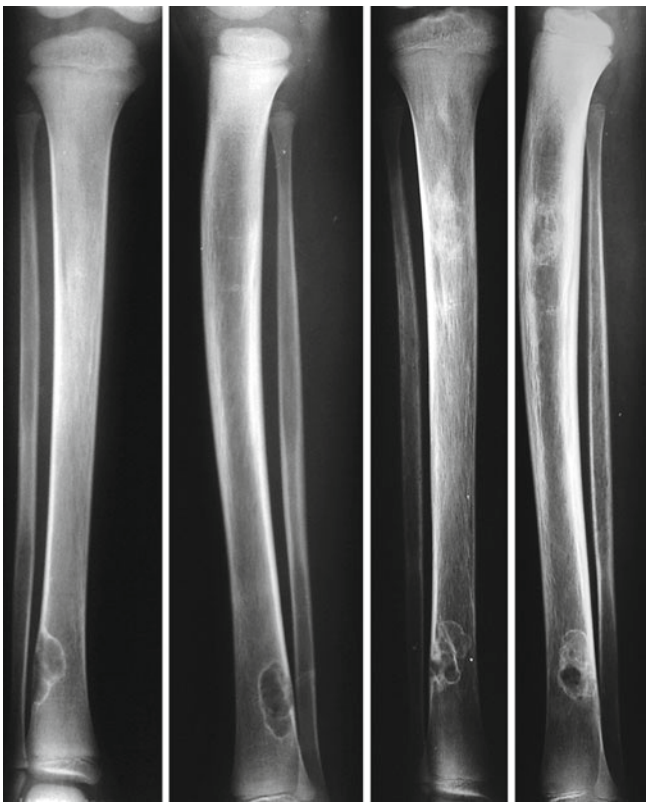

Fig. 8.12 Anteroposterior and lateral views of the left leg of the same child, taken 3 years apart, demonstrating the low sensitivity of this method for the assessment of acute infarcts in SCD. At left, radiographs obtained during an acute painful crisis do not reveal abnormal findings, except for a non-ossifying fibroma in the distal tibia. The *right images* disclose sclerotic areas in the medullary cavity of the proximal tibia, with periosteal reaction and cortical thickening, representing chronic bone infarcts

elbows, and hands. Despite the increased incidence of osteomyelitis in SCD, septic arthritis is relatively uncommon, affecting mostly children and often associated with vasoocclusion and osteonecrosis. Polyarticular involvement may occur in septic arthritis, and osteomyelitis is commonly associated. The knees, the hips, the ankles, and the shoulders are the most affected joints (Figs. 8.23 and 8.24). Imaging findings of joint infection were discussed in Chap. 6.

Many of the above-mentioned imaging findings of SCD are also found in thalassemia. In the same way as SCD, thalassemia leads to expansion of the hematopoietic marrow with widening of medullary and diploic spaces, deep osteoporosis, and coarse appearance of the trabeculae; extramedullary hematopoiesis may be present, more common than in SCD (Fig. 8.25). Prominence of the facial bones is common ("rodent" facies), with underdevelopment of the paranasal sinuses. Just like in SCD, there is increased predisposition to infections, but avascular necrosis is less frequently found. Thalassemia-related osteoarthropathy may result from the disease itself or may be attributed to its therapy, including hemosiderosis, gout, or calcium-crystal arthropathy. Therapy with deferoxamine may lead to metaphyseal and vertebral changes similar to that found in spondylometaphyseal dysplasia, while imaging findings of deferiprone-related arthropathy include patellar beaks, synovitis, irregular thickening of the epiphyseal and articular cartilage (with hyperintense lesions of the latter on T2-WI), and subchondral bone defects.

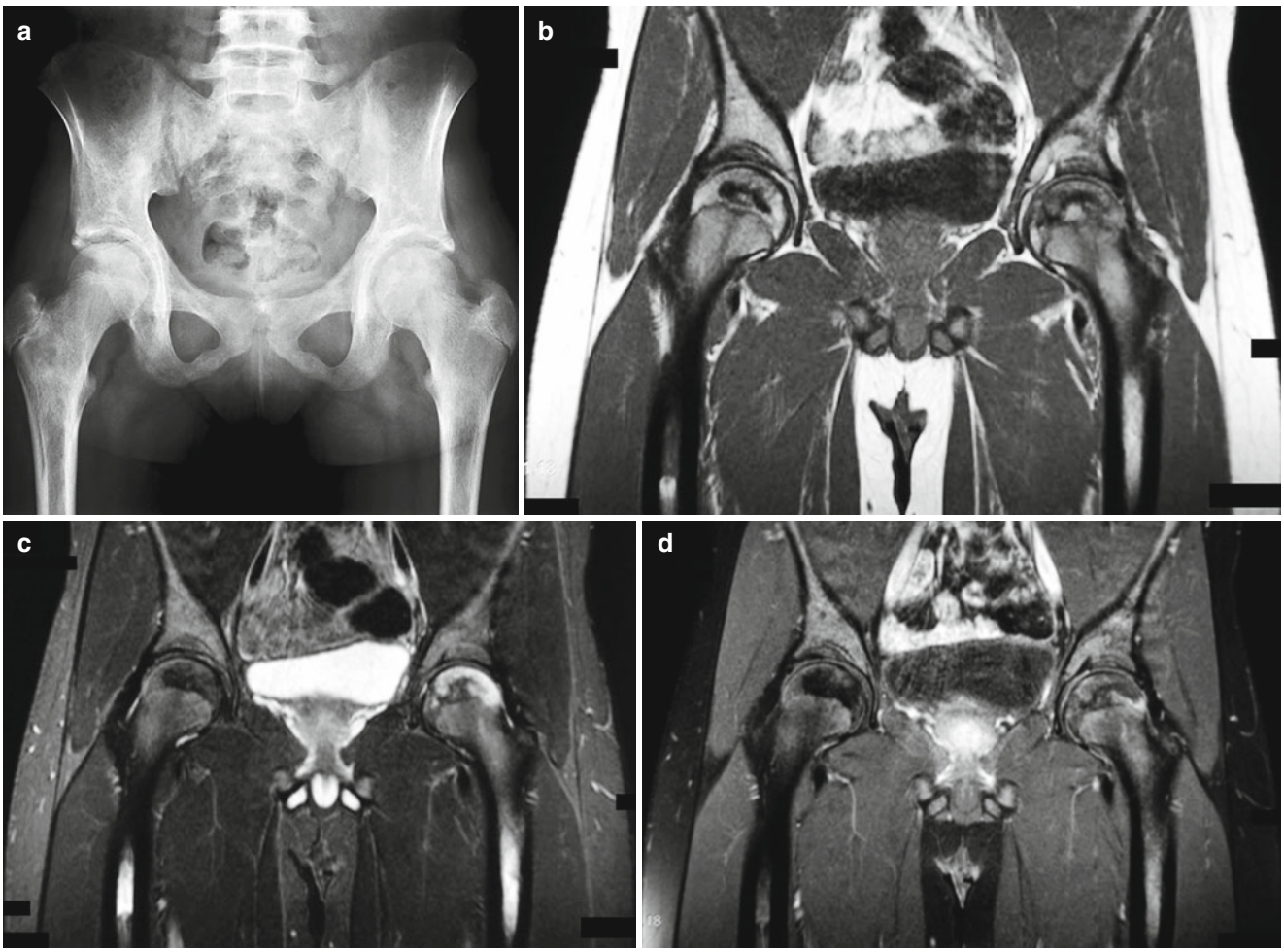

Fig. 8.13 A 16-year-old female with long-standing SCD. Pelvic radiograph (**a**) shows sclerotic areas in the medullary bone of the iliac bones and of the femora, with "bone-within-bone" appearance in the proximal femoral diaphyses. Even though it is clear that there are multiple chronic bone infarcts, this method is insensitive to detect acute ischemia. Coronal T1-WI (**b**), fat sat T2-WI (**c**), and post-gadolinium fat sat T1-WI (**d**) of the hips of the same patient reveal recent bone infarcts in the femoral diaphyses, with hyperintense areas on T1-WI and T2-WI and mild post-contrast enhancement. There is also extensive avascular necrosis of the left femoral head, with enhancement of the lateral pillar. A non-enhancing, serpiginous area of low signal intensity in all sequences in the right femoral head represents an old infarct, with bone sclerosis

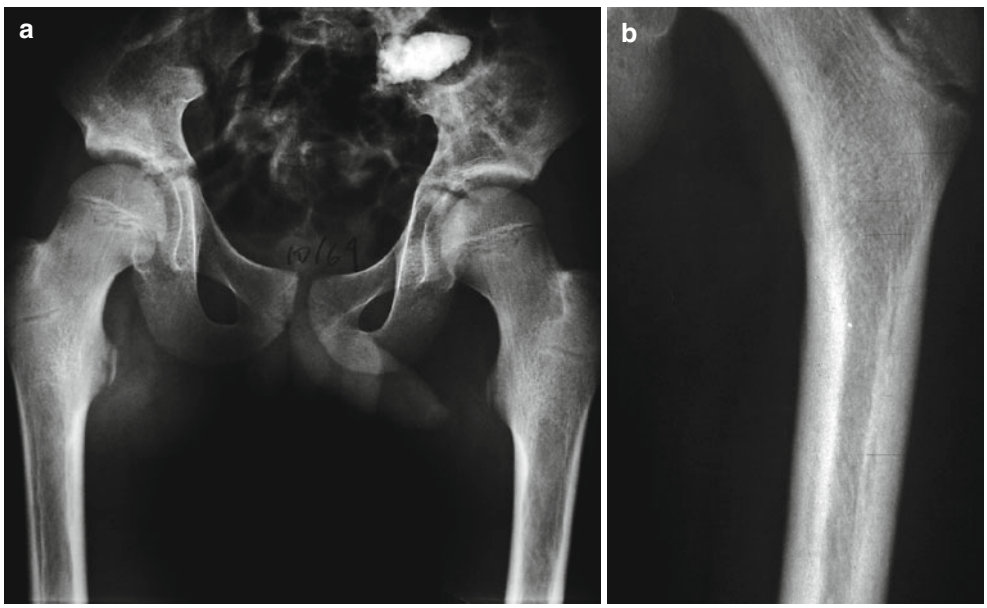

Fig. 8.14 In (**a** and **b**), radiographs of distinct patients demonstrate linear areas of sclerosis in the medullary cavities of the proximal femora, adjacent to the cortical bone ("bone-within-bone"). In SCD, this finding – which may be found in many other conditions – is related to osteonecrosis

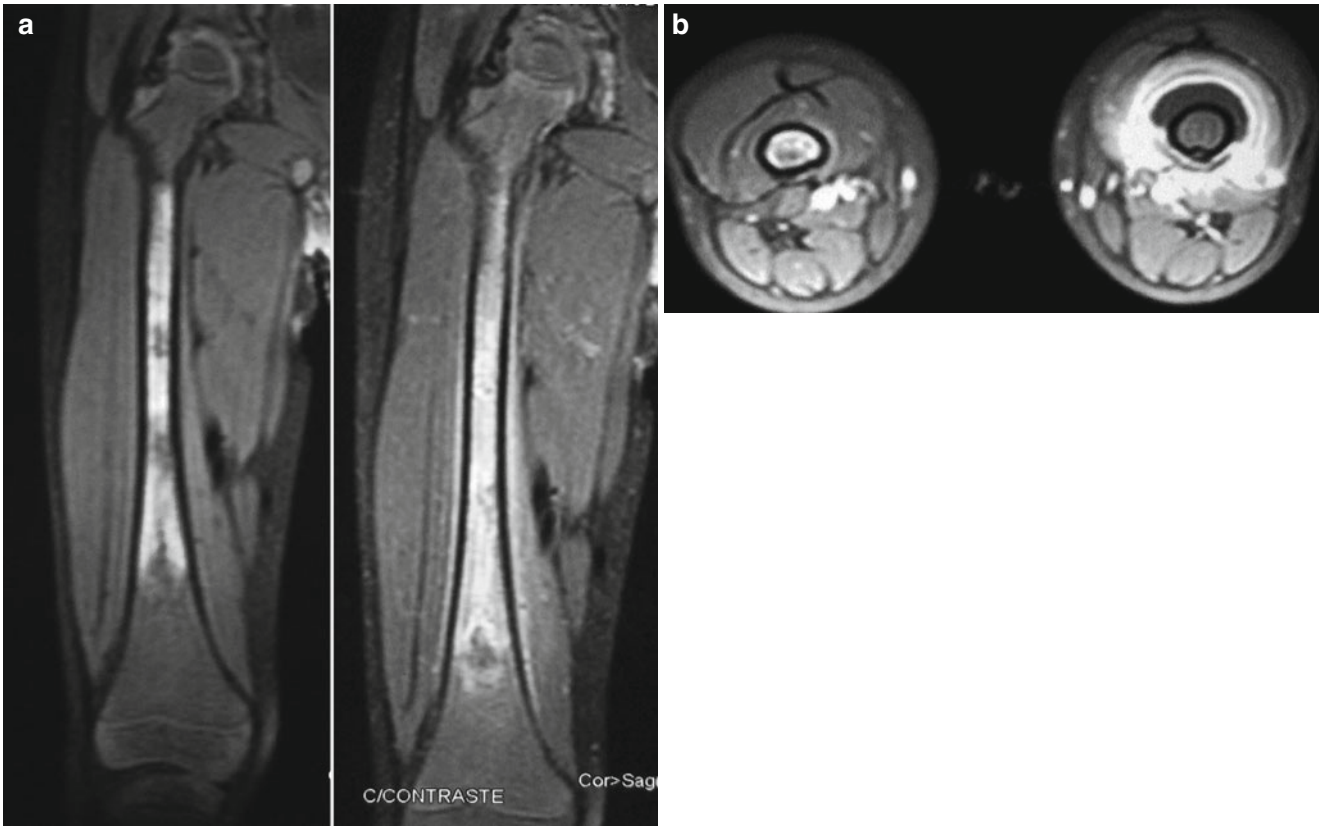

Fig. 8.15 An 8-year-old child with SCD and acute painful crisis in the right thigh. In (**a**), coronal fat sat T1-WI pre- (*left*) and post-gadolinium (*right*) reveal an extensive area of heterogeneous hyperintensity in the medullary cavity of the femur, representing bone infarct and the presence of hemoglobin degradation products. There is post-contrast enhancement of the ischemic bone and of the surrounding soft tissues. In (**b**) (transverse post-gadolinium fat sat T1-WI of the thighs taken 1 month later), the bone infarct of the right femur displays predominantly peripheral enhancement. Diaphyseal osteomyelitis in the contralateral femur is also present, with inflammation of the adjacent soft tissues, where diffuse and intense post-contrast enhancement can be seen. An intraosseous abscess is present in the left femur, appearing as an encapsulated fluid collection with subperiosteal extension and peripheral enhancement. Diaphyseal osteomyelitis of the left tibia was also present (not shown)

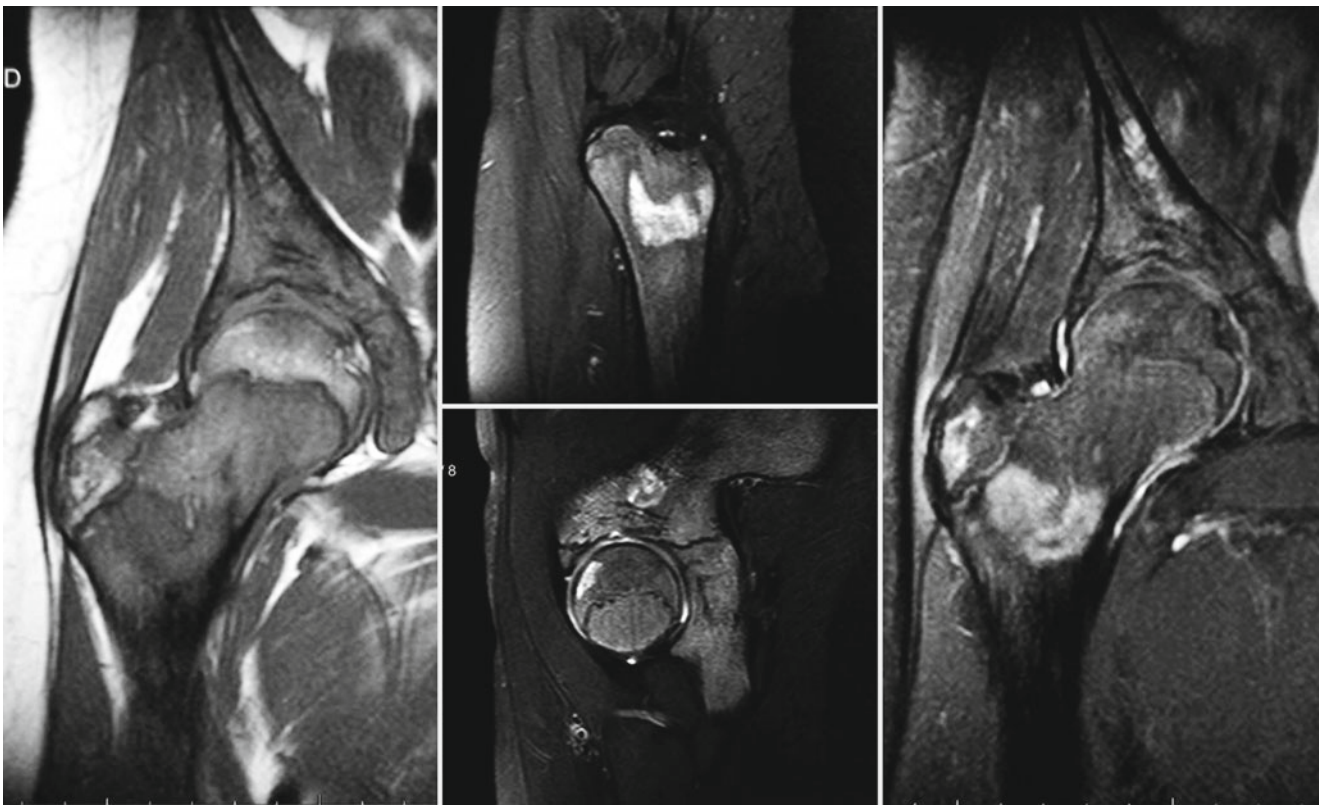

Fig. 8.16 T1-WI (*left*), fat sat T2-WI (*center*), and post-gadolinium fat sat T1-WI (*right*) of the right hip of a 15-year-old female with SCD. Geographic areas of abnormal signal intensity can be seen in the apophysis of the greater trochanter and in the supra-acetabular iliac bone, as well as in the femoral epiphysis and in the medullary cavity of the proximal diaphysis. The former two are heterogeneous lesions with fat in their central portion surrounded by a thin rim of low signal intensity in all sequences, while the latter two are ill-defined, presenting low signal intensity on T1-WI and high signal intensity on fat sat T2-WI; predominantly peripheral post-gadolinium enhancement is seen in all lesions. These are bone infarcts in different stages: the apophyseal and the iliac lesions are older, while the epiphyseal and diaphyseal ones show evidence of recent ischemia

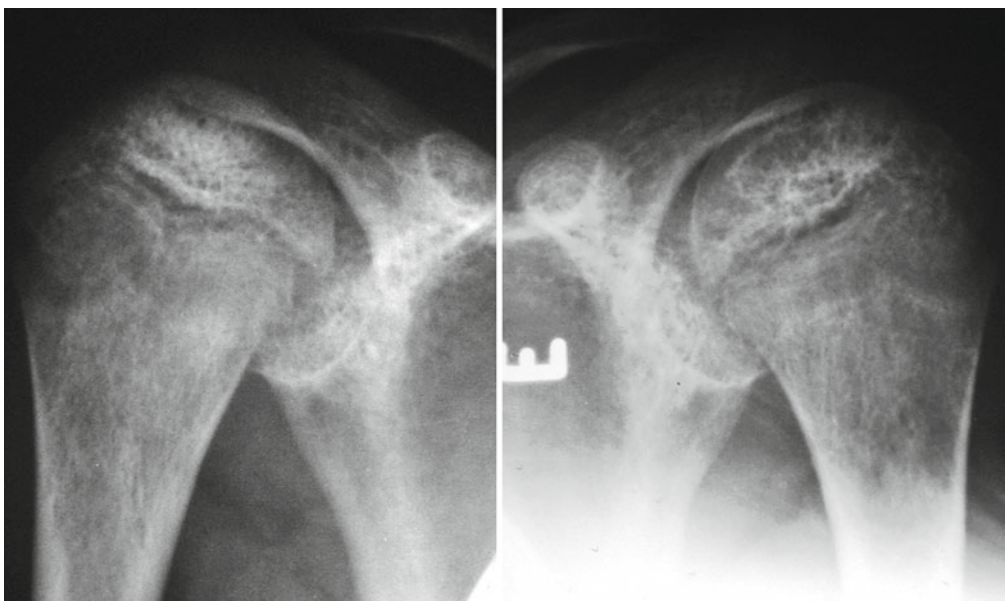

Fig. 8.17 Geographic areas of sclerosis are seen in the medullary bone of the proximal humeral epiphyses, symmetric and bilateral, also present in the proximal metadiaphyses of the same bones, mainly at right. These lesions represent chronic bone infarcts/avascular necrosis

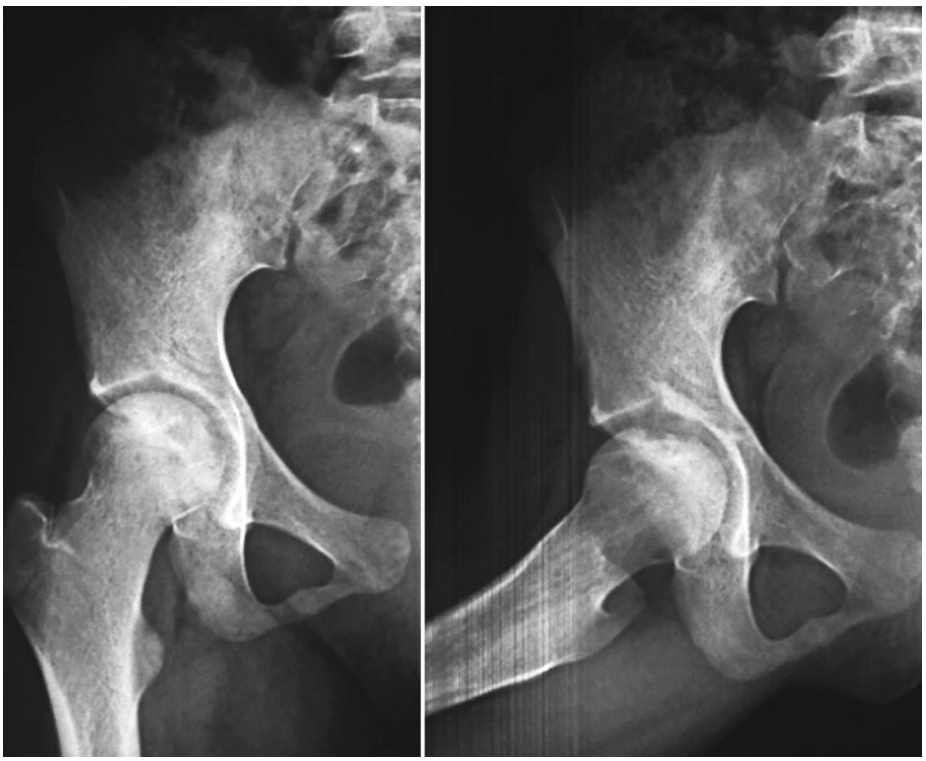

Fig. 8.18 Avascular necrosis of the right femoral head can be seen in this child with SCD. The femoral epiphysis presents heterogeneous density, with flattening and irregularity of the epiphyseal surface (the latter more evident in the lateral view)

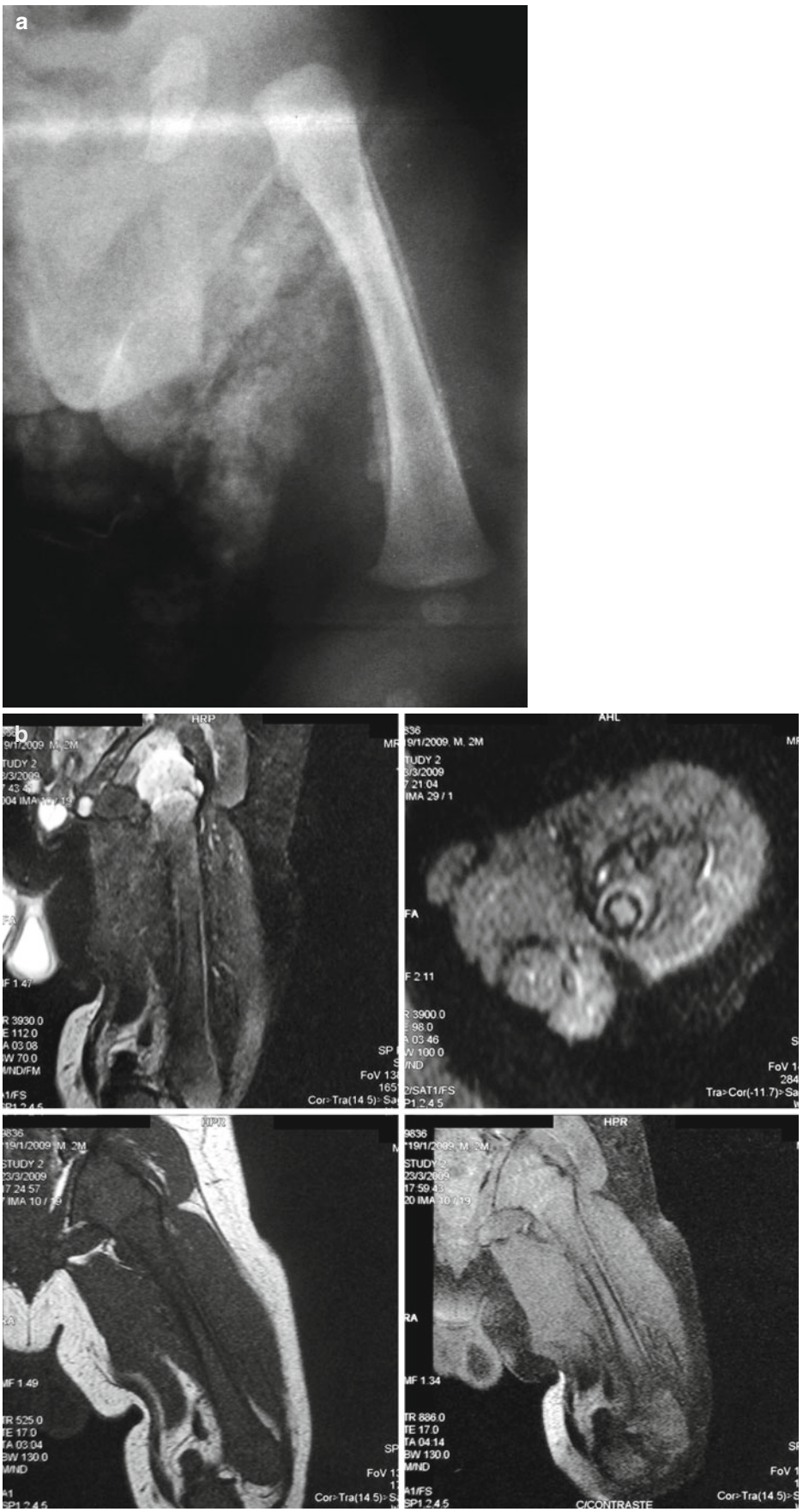

Fig. 8.19 Subperiosteal bleeding in a 2-month-old male with SCD and pain upon mobilization of the left lower limb. Radiograph of the left thigh (**a**) demonstrates solid periosteal reaction along the femoral diaphysis. Sagittal and transverse fat sat T2-WI of the same patient (**b**, *upper images*) disclose a hyperintense subperiosteal collection, which is hypointense on T1-WI (*lower-left image*) and presents minimal post-gadolinium enhancement (*lower-right image*); the adjacent bone is normal

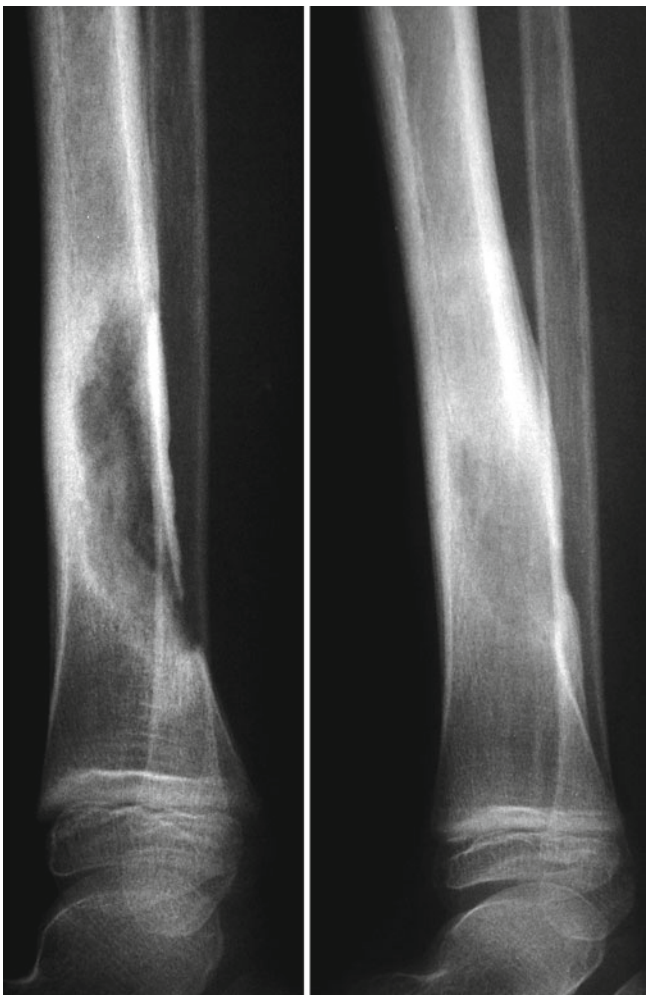

Fig. 8.20 An 8-year-old child with SCD and signs of infection in the left leg. Radiographs demonstrate chronic osteomyelitis in the distal diaphysis of the tibia, with extensive bone destruction, layered periosteal reaction ("onion skin" pattern), and a posterolateral cloaca in the lower portion of the lesion

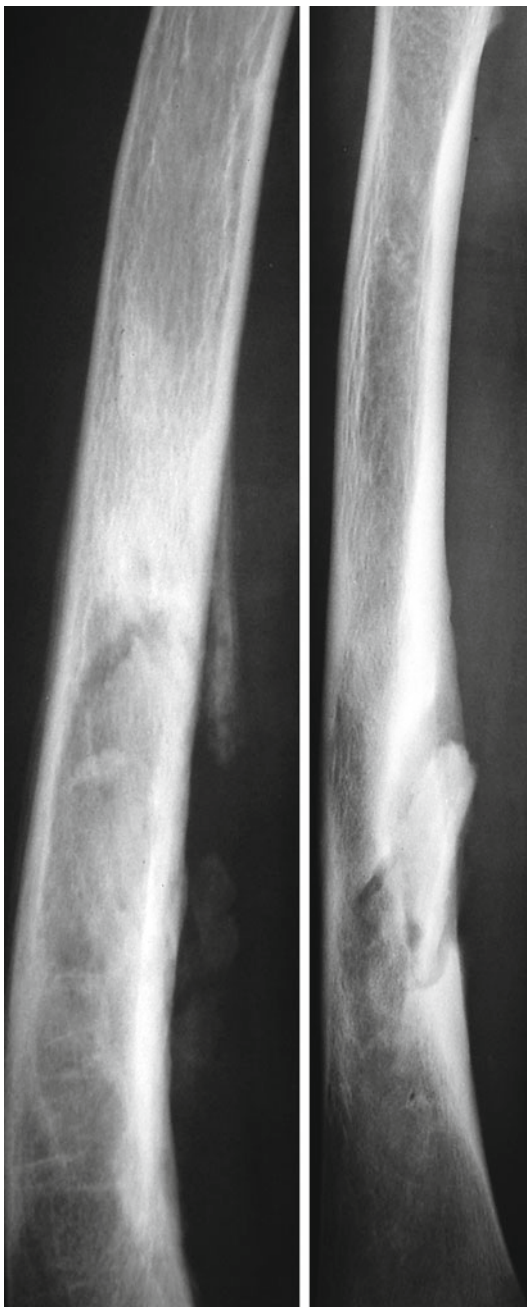

Fig. 8.21 Chronic osteomyelitis of the diaphysis of the right femur of a 5-year-old child with SCD. At left, lateral view reveals an extensive lucency in the medullary bone of the mid-diaphysis, with sclerosis of the surrounding bone and discontinuous periosteal reaction. There are some calcified/ossified nodules in the posterior soft tissues of the thigh, possibly representing bone sequestra contained by the periosteum. At right, lateral radiograph of the same site taken 11 months later reveals cavitation in the posterior portion of the femoral diaphysis, surrounded by a sclerotic rim and containing a large bone fragment. Periosteal reaction is solid and continuous

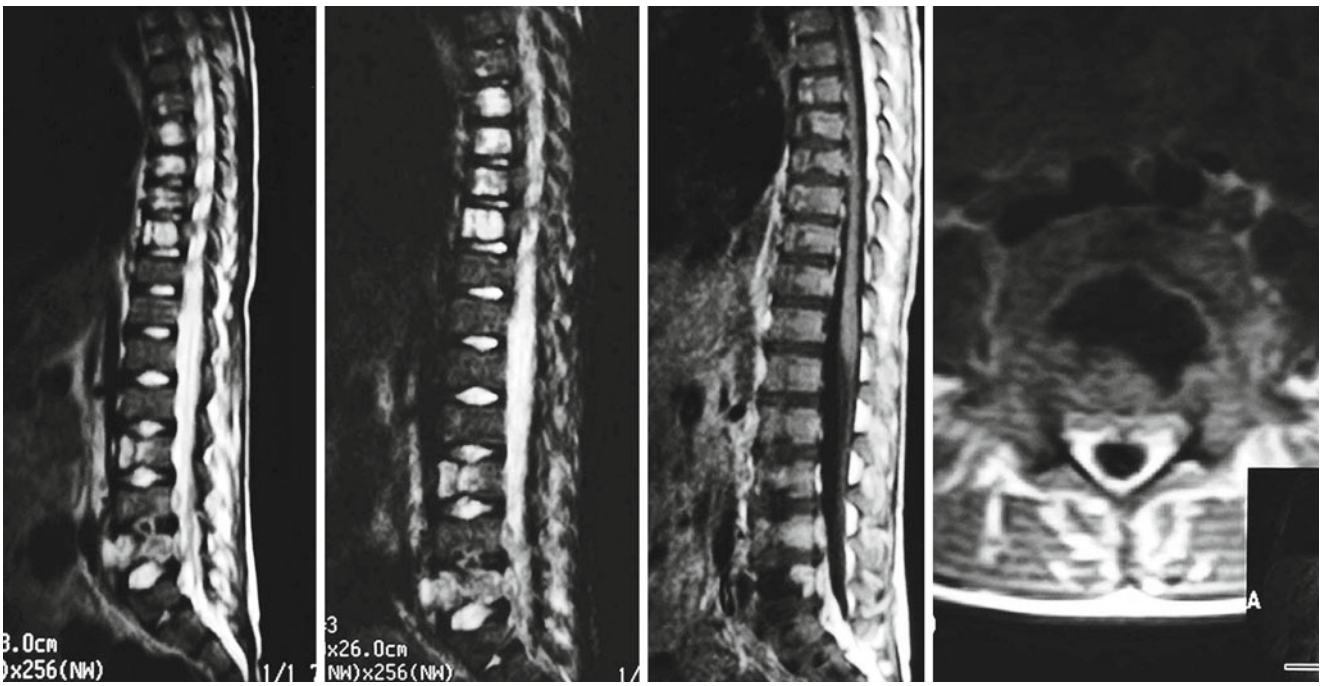

Fig. 8.22 Multiple vertebral infarcts and spondylodiscitis in an 8-year-old child with SCD. Sagittal T2-WI (*first image*) and STIR image (*second image*) reveal areas of increased signal intensity in several vertebral bodies (from T6 to T10 and in L3), related to bone infarction, with normal appearance of the adjacent intervertebral disks. In L4–L5, however, there is heterogeneous signal intensity of the disk and reduction of the disk height, as well as destruction of the adjacent endplates and bone marrow edema. An intraosseous abscess is seen in the anterior portion of L5, presenting cortical discontinuity and extension to the prevertebral space, contained by the anterior longitudinal ligament. An epidural phlegmon is also present, extending from L4 to S1. Post-gadolinium T1-WI in the sagittal (*third image*) and transverse (*fourth image*) planes disclose peripheral enhancement in the above-mentioned abscess and diffuse enhancement in the inflamed epidural tissue, as well as mild enhancement of the bone marrow of the ischemic vertebral bodies

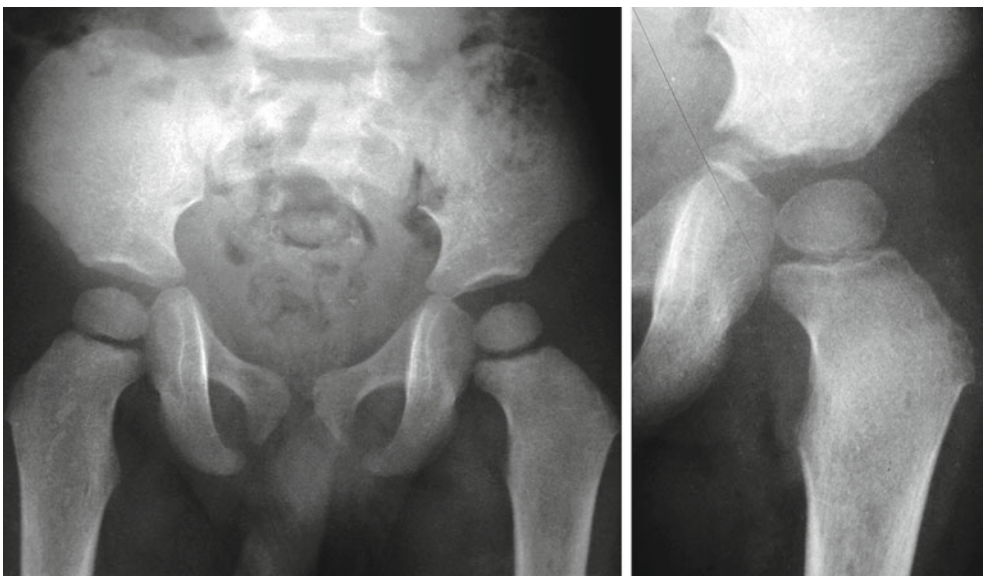

Fig. 8.23 Septic arthritis of the left hip in a child with SCD. At *left*, pelvic radiograph demonstrates subtle widening of the joint space of the left hip (purulent effusion and capsular distension) and reduced size of the ossified portion of the homolateral epiphysis. At *right*, radiograph of the affected hip taken 5 months later reveals diffuse osteoporosis of the proximal femur, narrowing of the uppermost portion of joint space (an indirect marker of cartilaginous damage) and widening of its medial portion, without significant bone destruction. The relatively slow progression of the radiographic findings is suggestive of low-virulence infection, given that classic pyogenic arthritis is rapidly destructive

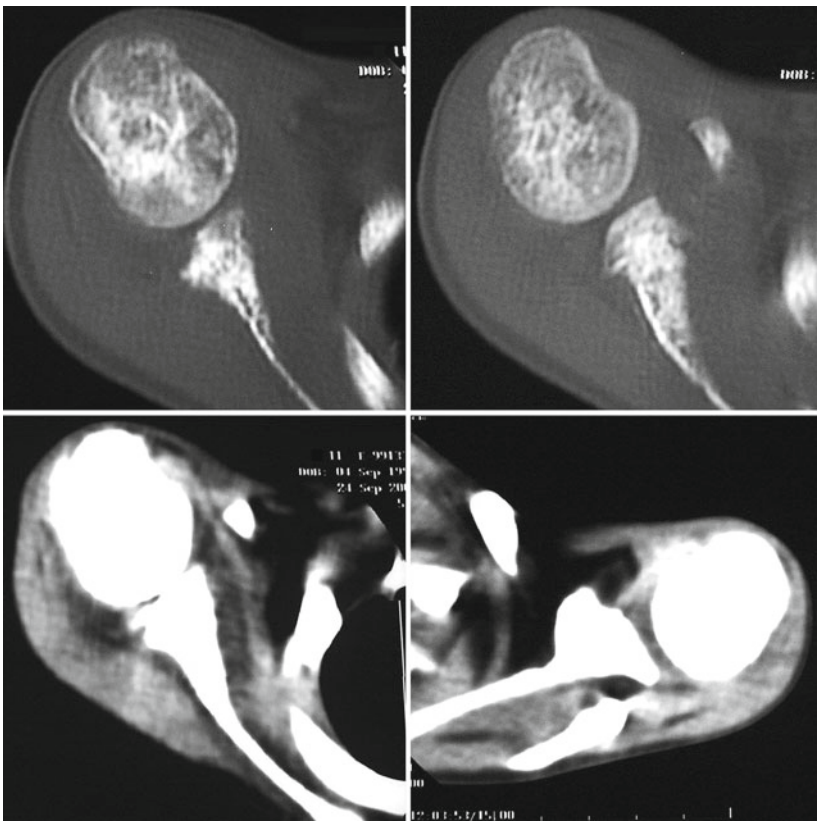

Fig. 8.24 Transverse CT images of the right shoulder of a child with SCD (*upper images* and *lower-left image*). There is heterogeneous sclerosis of the medullary bone of the proximal humerus and of the scapula, related to chronic bone infarcts, as well as a large joint effusion and erosions of the posteroinferior glenoid rim, the latter related to septic arthritis. Transverse image of the left shoulder (*lower-right image*) displays purulent effusion in this joint too

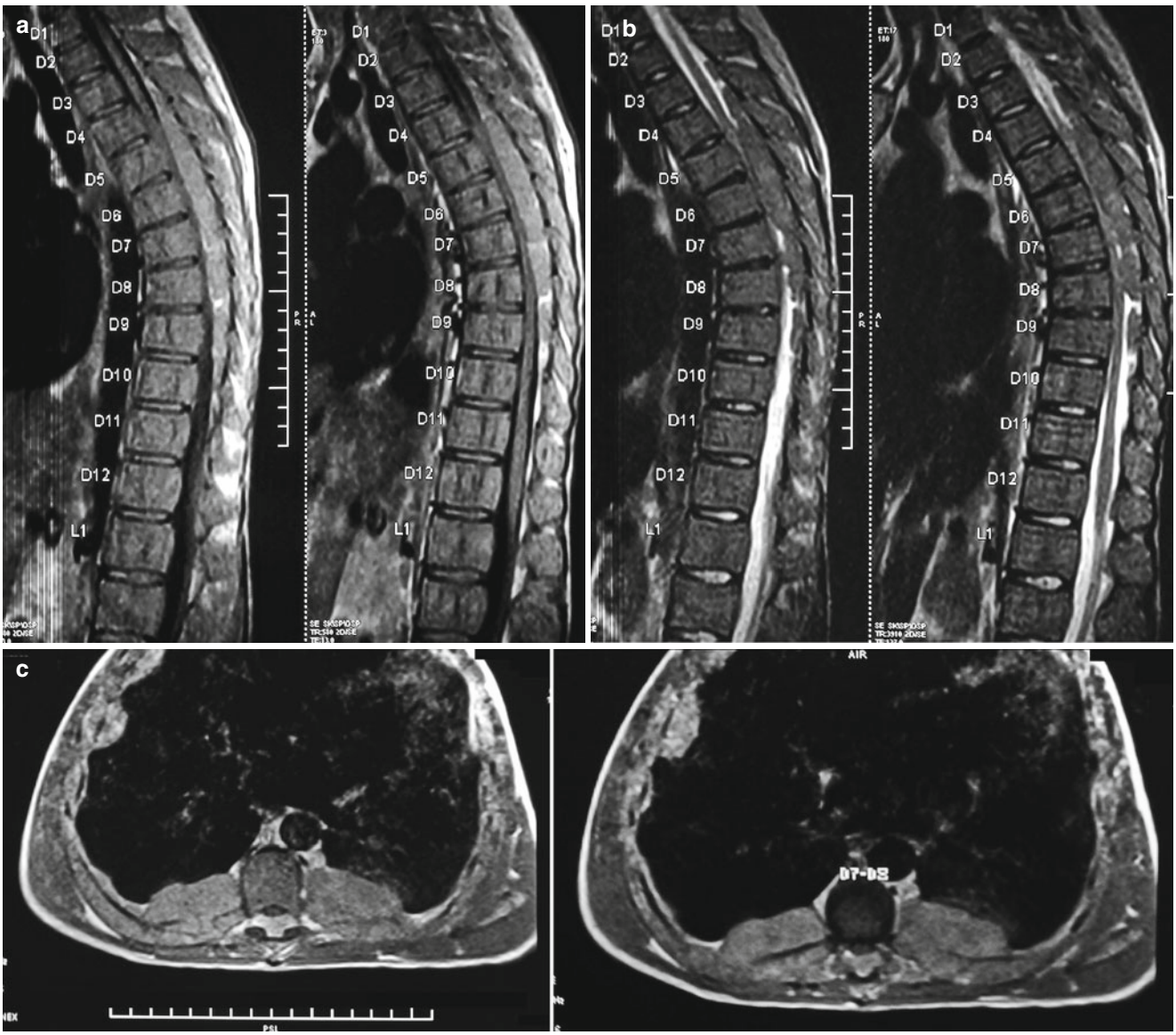

Fig. 8.25 A 13-year-old male with beta-thalassemia and exuberant extramedullary hematopoiesis. Sagittal T1-WI (**a**) and T2-WI (**b**) and transverse post-gadolinium T1-WI (**c**) of the thoracic spine demonstrate persistence of red marrow in all vertebral bodies, some of which are mildly enlarged. Expansion of the medullary cavity of the ribs is also present, bilaterally (**c**). Extramedullary hematopoiesis appears as paraspinal masses and multiple coalescent nodules in the posterior epidural space, presenting signal intensity slightly higher than that of the red marrow and mild post-gadolinium enhancement. The epidural component causes severe compression of the spinal cord, mostly from T5 to T8 (Courtesy of Dr. Aline Magnago, Bioscan Diagnostico por Imagem, Vitoria, Brazil)

8.3 Coagulation Disorders

Hemophilia is the most important coagulation disorder, accounting for approximately 80 % of the hereditary coagulopathies. It is an X-linked recessive disease virtually exclusive of males caused by deficiency of factor VIII (hemophilia A, the classic and most common form) or factor IX (hemophilia B, Christmas disease). The vast majority of the bleeding episodes involve the joints. The diagnosis is essentially clinical and based on laboratory tests, but imaging plays an important role in follow-up, being useful to evaluate the therapeutic response and to detect late complications. Early diagnosis of

hemophilic arthropathy and timely introduction of prophylactic therapeutic measures are critical to reduce the risk of disabling articular disease.

Articular disease is the main cause of morbidity and disability in hemophiliac patients, affecting mostly the knees, elbows, and ankles. The term hemophilic arthropathy is used to describe a form of progressive joint damage caused by recurrent hemarthroses, which is found mainly in patients with severe hemophilia. Bleeding leads to synovial inflammation/hypertrophy and intra-articular breakdown of hemoglobin, with degradation of articular cartilage and development of multiple subchondral cysts, being the latter the hallmark of hemophilic arthropathy. End-stage disease is characterized by destructive arthropathy and severe osteoarthritis, with collapse of joint surfaces, articular incongruity, flexion deformities, and occasional ankylosis.

Radiographs remain indispensable in the assessment of hemophilic arthropathy. However, their main role is to monitor the evolution of established articular damage in advanced disease and help surgical planning, as they are insensitive for early diagnosis. Joint effusion (which may occasionally display increased density because of its iron content – Fig. 8.26) and nonspecific soft-tissue edema are the earliest findings. Articular hyperemia may cause osteoporosis, epiphyseal overgrowth, and early closure of the growth plates. These findings are more evident in the knees, in which widening of the intercondylar notch and asymmetric development of the femoral condyles are also commonly found (Fig. 8.26). Squaring of the inferior pole of the patella is present in almost one-third of hemophiliac patients. In the elbow, early appearance of the ossification centers and overgrowth of the radial head (leading to valgus deformity) may be present, as well as pressure erosions in the radial notch of the ulna and widening of the articular fossae and incisurae (Fig. 8.27). Asymmetric growth of the distal tibial epiphysis leads to tibiotalar slant, similar to that above described for SCD. Bone erosions, subchondral cysts, and premature osteoarthritis are typical findings but appear late in the course of disease (Fig. 8.27).

MRI is the best imaging method for early diagnosis of hemophilic arthropathy (Figs. 8.28 and 8.29). Even though hemorrhagic and non-hemorrhagic joint effusions may be indistinguishable, subacute hemarthroses often appear hyperintense on T1-WI and T2-WI (Fig. 8.30), and fluid levels are also indicative of recent bleeding. The thickened synovium usually displays low signal intensity in all sequences (mostly on gradient-echo images) due to the paramagnetic properties of hemosiderin, which also impregnates the cartilages and the joint capsule (Figs. 1.20, 8.28, 8.29, 8.30, 8.31, and 8.32). Nonetheless, the synovium may appear heterogeneous, with hyperintense areas on T2-WI related to the presence of fluid/inflammation (Fig. 8.30). Post-gadolinium enhancement is seen during active synovitis, distinguishing the thickened synovium from the synovial fluid (Figs. 8.30 and 8.32). Osteocartilaginous damage is evident from its earliest stages (Fig. 8.33) to the extensive joint destruction typically found in advanced disease (Figs. 8.30, 8.31, and 8.32). Meniscal hypoplasia is a frequent finding, also encountered in other chronic hyperemic articular diseases (Figs. 8.28 and 8.29). Subchondral cysts are readily apparent on MRI, presenting variable signal intensity according to their content (e.g., fresh blood, fluid, fibrosis, hypertrophic synovium, hemosiderin – Figs. 8.31 and 8.32). Despite the advantages of US in pediatric patients (see Chap. 1) and its ability to demonstrate joint effusion and synovial thickening/hyperemia, MRI is superior in hemophilic osteoarthropathy because it can assess the joint as a whole and is very sensitive to the presence of hemosiderin. CT is only exceptionally employed in the articular evaluation of the hemophilic child, serving mostly as a diagnostic alternative for patients who cannot undergo MRI (Fig. 8.31). Scintigraphic studies have limited usefulness, showing nonspecific uptake in the affected joints (see Chap. 1).

Hemophilic pseudotumors are chronic, encapsulated hemorrhagic collections that grow slowly, fed by recurrent bleeding, affecting 1–2 % of all patients. They are more frequent in the soft tissues of the pelvic muscles and of the lower limbs, though intraosseous and subperiosteal pseudotumors can be found as well. These lesions are occasionally associated with mass effect and compression of the adjacent neurovascular structures, and their appearance on imaging may simulate aggressive tumors. On radiographs, soft-tissue pseudotumors appear as nonspecific masses that occasionally calcify and/or lead to pressure erosions in the adjacent bones. Intraosseous pseudotumors are lytic, expansile lesions of lobulated appearance, which are often associated with bone remodeling and pathologic factures (Fig. 8.34), while subperiosteal lesions lead to periosteal detachment and pressure erosions on the adjacent cortex, with bone neoformation and development of soft-tissue masses. US is valuable to estimate the real size of these lesions – which are most often heterogeneous, with internal echoes – and to monitor their evolution. CT is particularly useful for bone assessment and to evaluate deeply seated masses; the different densities found inside the mass are related to different stages of hemoglobin breakdown, and a thick, hyperdense, and enhancing capsule may be present. On MRI, pseudotumors appear as expansile and heterogeneous lesions (also due to different stages of hemoglobin degradation); a capsule is most often seen in soft-tissue masses, usually displaying low signal intensity in all sequences.

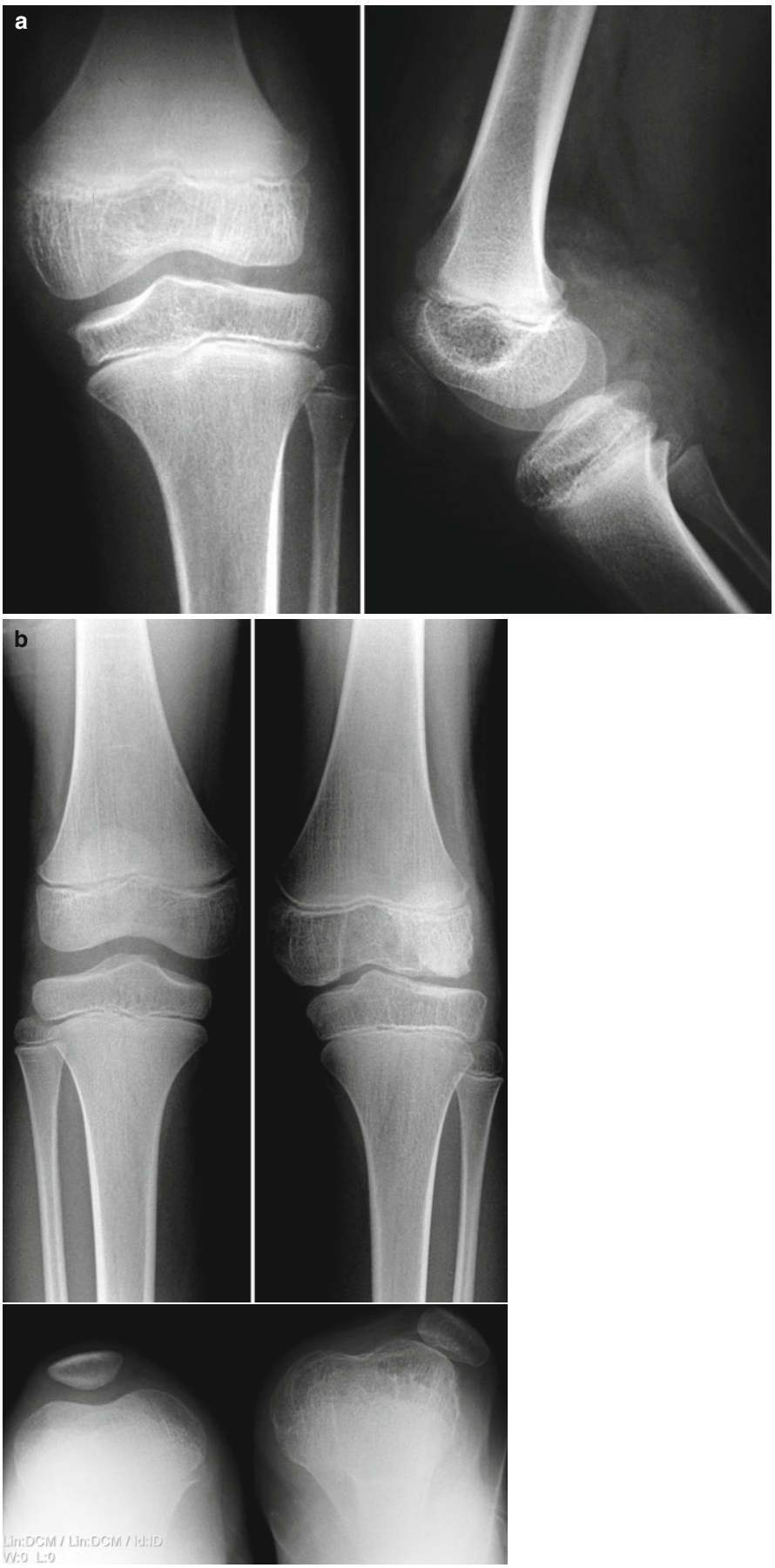

Fig. 8.26 In (**a**), radiographs of the left knee of an 8-year-old hemophiliac patient show epiphyseal osteoporosis and overgrowth of the medial femoral condyle, as well as a high-density effusion in the suprapatellar pouch and in the popliteal fossa. In (**b**), radiographs of the knees of a 6-year-old hemophiliac patient reveal soft-tissue swelling, regional osteoporosis, widening of the intercondylar notch, irregularity of the articular surfaces, and increased size of the epiphyses of the left knee; patellofemoral misalignment is also present, as well as abnormal patellar shape

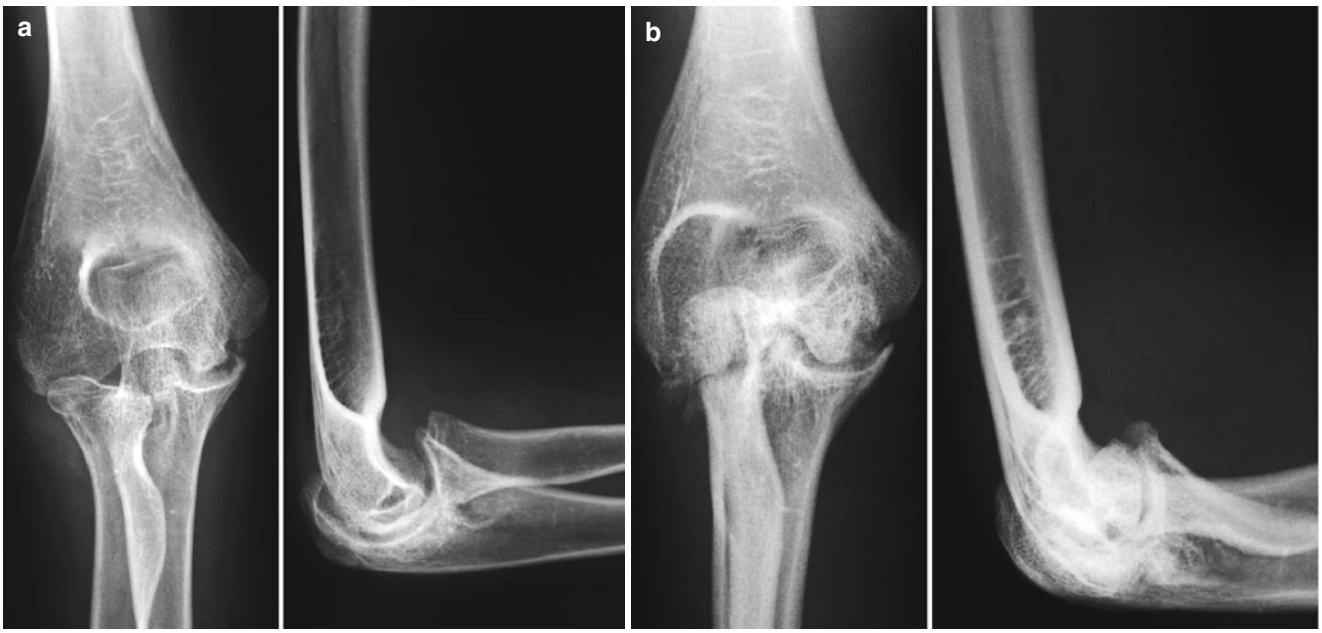

Fig. 8.27 Radiographic evolution of hemophilic arthropathy of the right elbow. In (**a**), radiographs taken when the patient was 13 years old show regional osteoporosis, early closure of the growth plates, moderately destructive arthropathy, and widening of the trochlear notch. In (**b**), radiographs of the same elbow taken at age 18 demonstrate advanced osteoarthritis and deformity of the joint surfaces, with prominence of the proximal radius and altered joint alignment leading to marked remodeling of the radial fossa of distal humerus

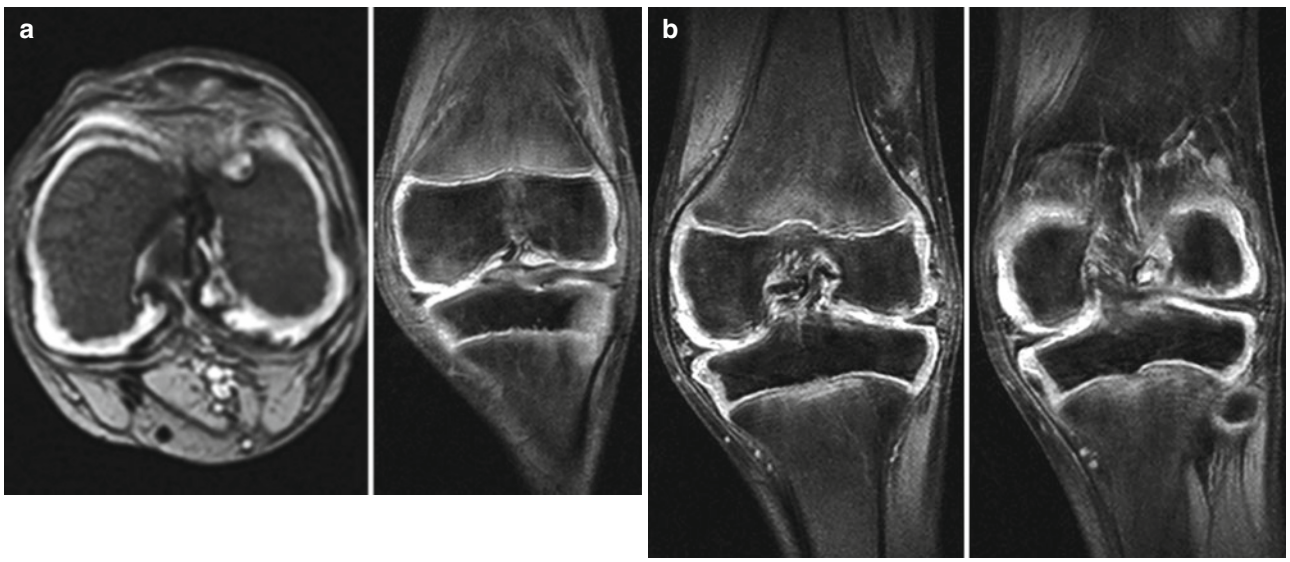

Fig. 8.28 Transverse gradient-echo image (*first image*) and coronal fat sat T2-WI (remaining images) of the left knee of an 11-year-old hemophiliac patient demonstrate small joint effusion, synovial thickening, and chondral/osteochondral lesions, mainly in the lateral femoral condyle, with bone marrow edema and erosive changes of the subchondral bone. The first image demonstrates mild hemosiderin impregnation – seen in the joint capsule, in the thickened synovium, and inside the erosion seen in the lateral femoral condyle – as areas of low signal intensity. Meniscal hypoplasia is also present, mostly medial

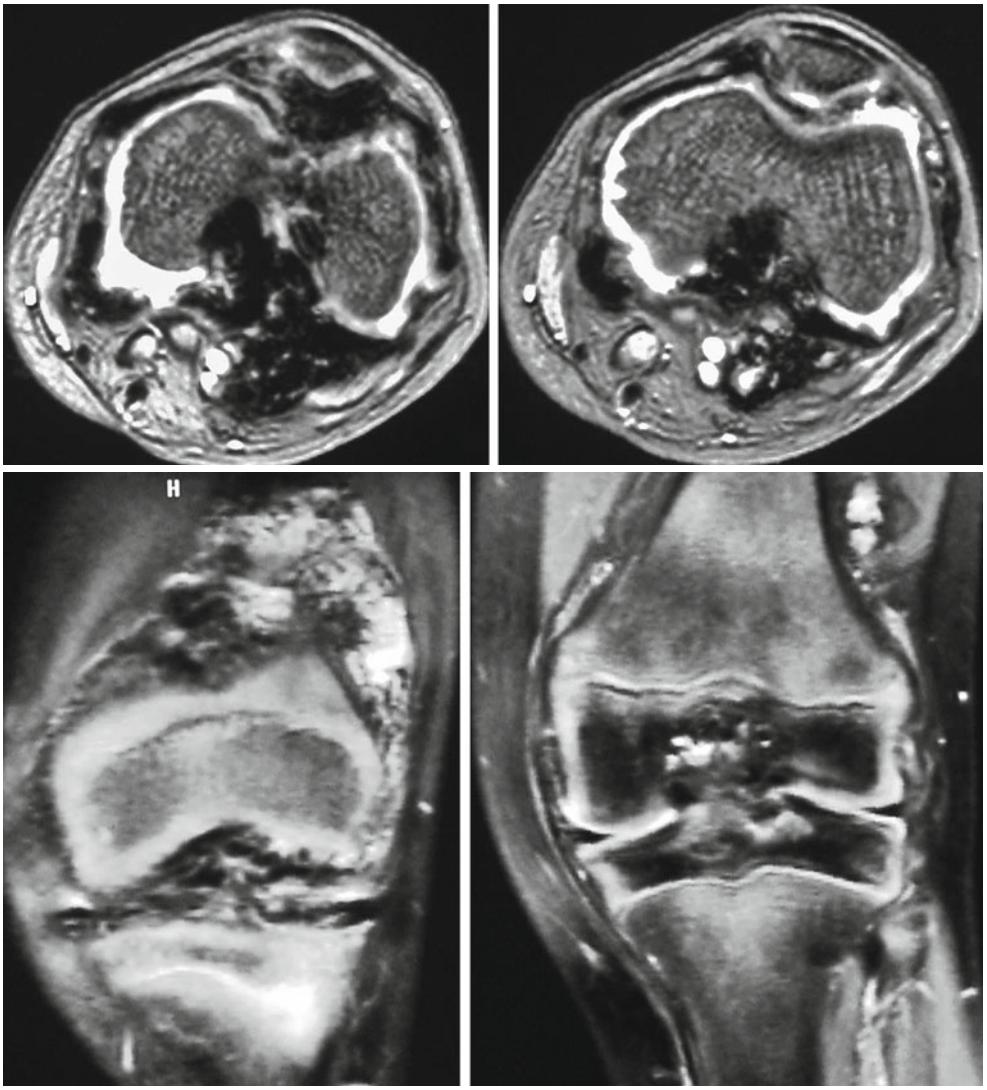

Fig. 8.29 Transverse (*upper row*) and coronal (*lower row*) gradient-echo images of the left knee of an 8-year-old hemophiliac patient. Synovitis and hemosiderin impregnation are more prominent in this child if compared to those seen in the patient of Fig. 8.28, and the cartilages are irregular. Meniscal hypoplasia is also evident

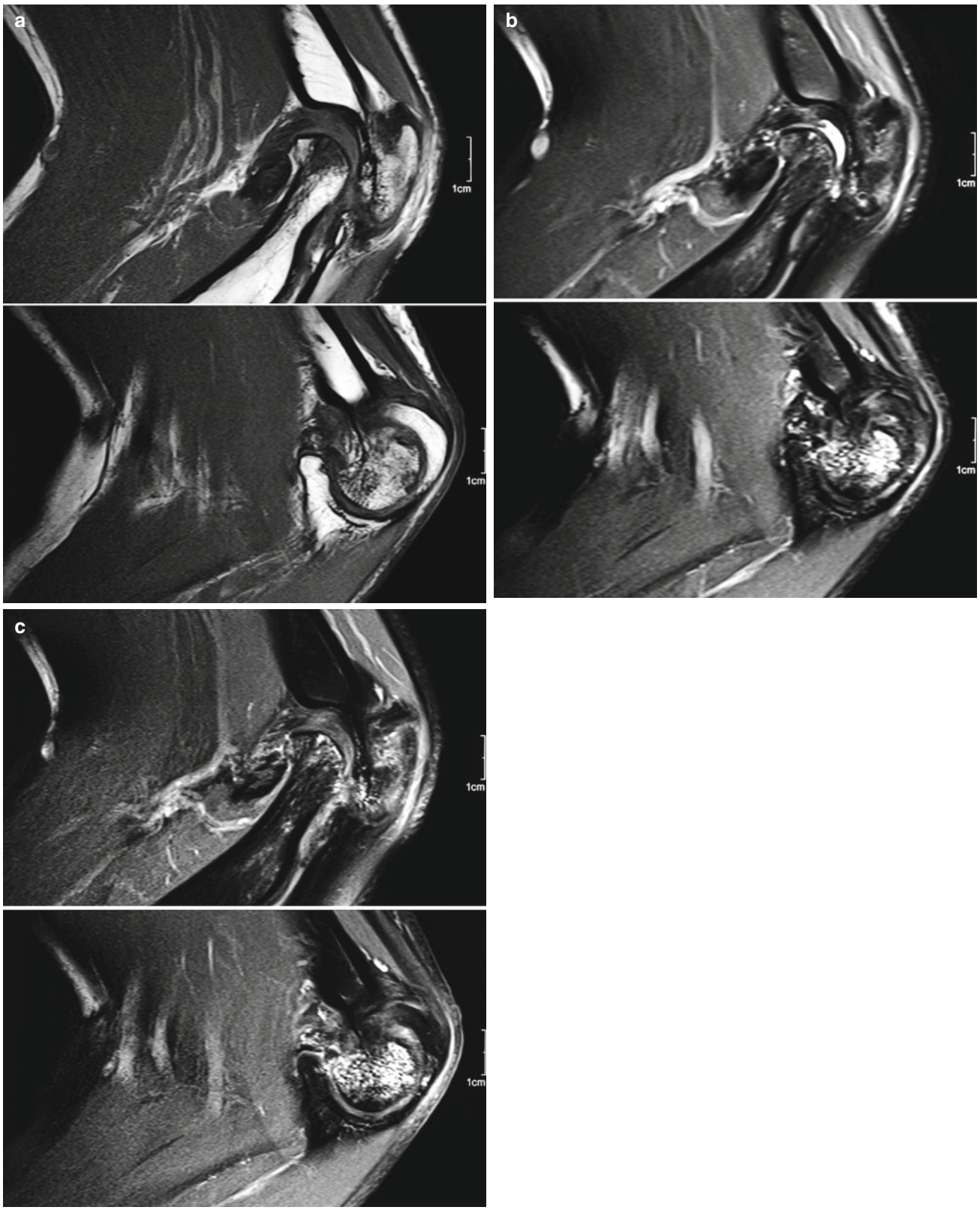

Fig. 8.30 MRI of the right elbow of the same patient of Fig. 8.27, sagittal T1-WI (**a**), fat sat T2-WI (**b**), post-gadolinium fat sat T1-WI (**c**), and gradient-echo image (**d**). In addition to the previously described radiographic findings, MRI shows joint effusion of intermediate signal intensity on T1-WI and high signal intensity on T2-WI (hemarthrosis with hemoglobin degradation products) and bone marrow edema associated with subchondral erosions, which enhance on post-contrast images. Markedly heterogeneous synovial thickening is also present, exhibiting post-gadolinium enhancement and low signal intensity on gradient-echo images (hemosiderin impregnation)

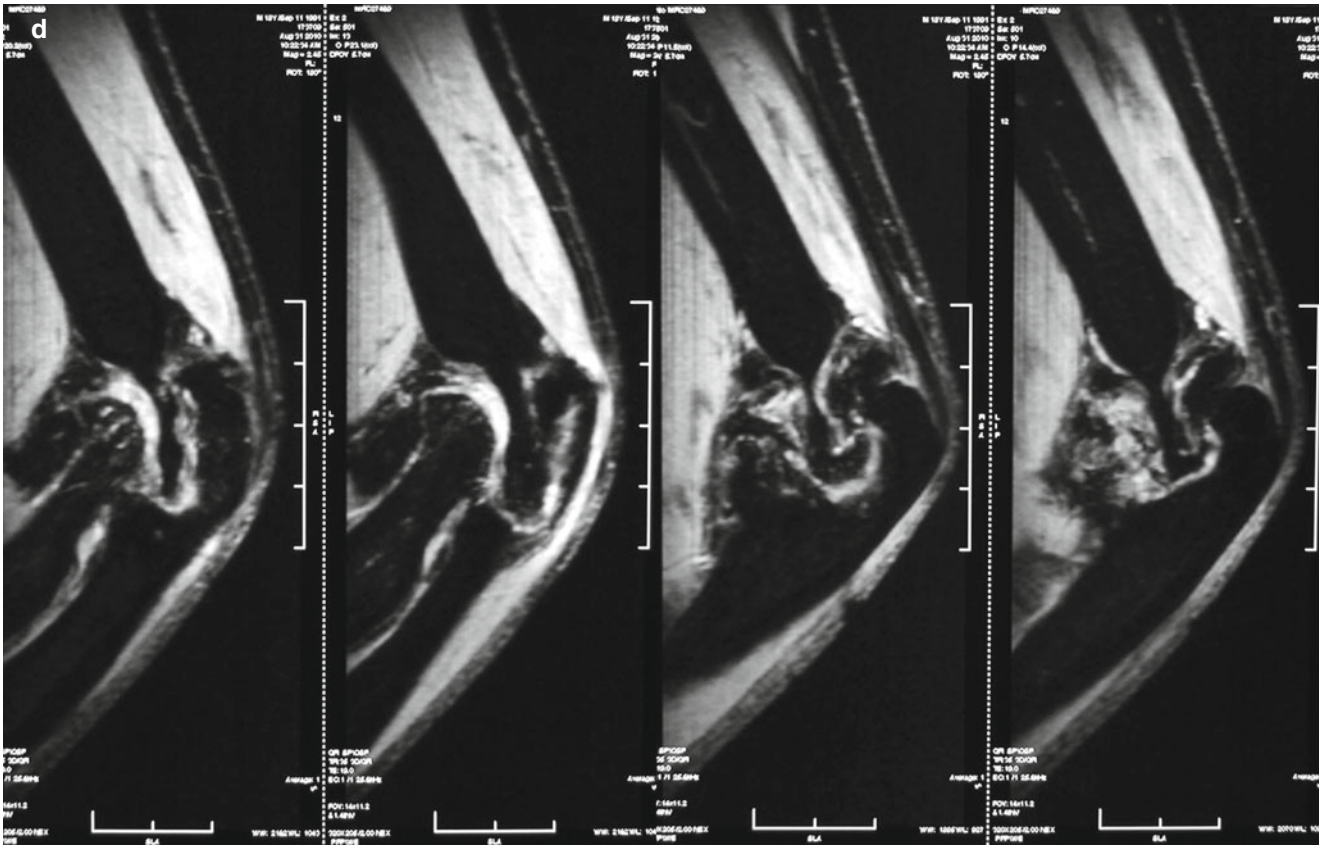

Fig. 8.30 (continued)

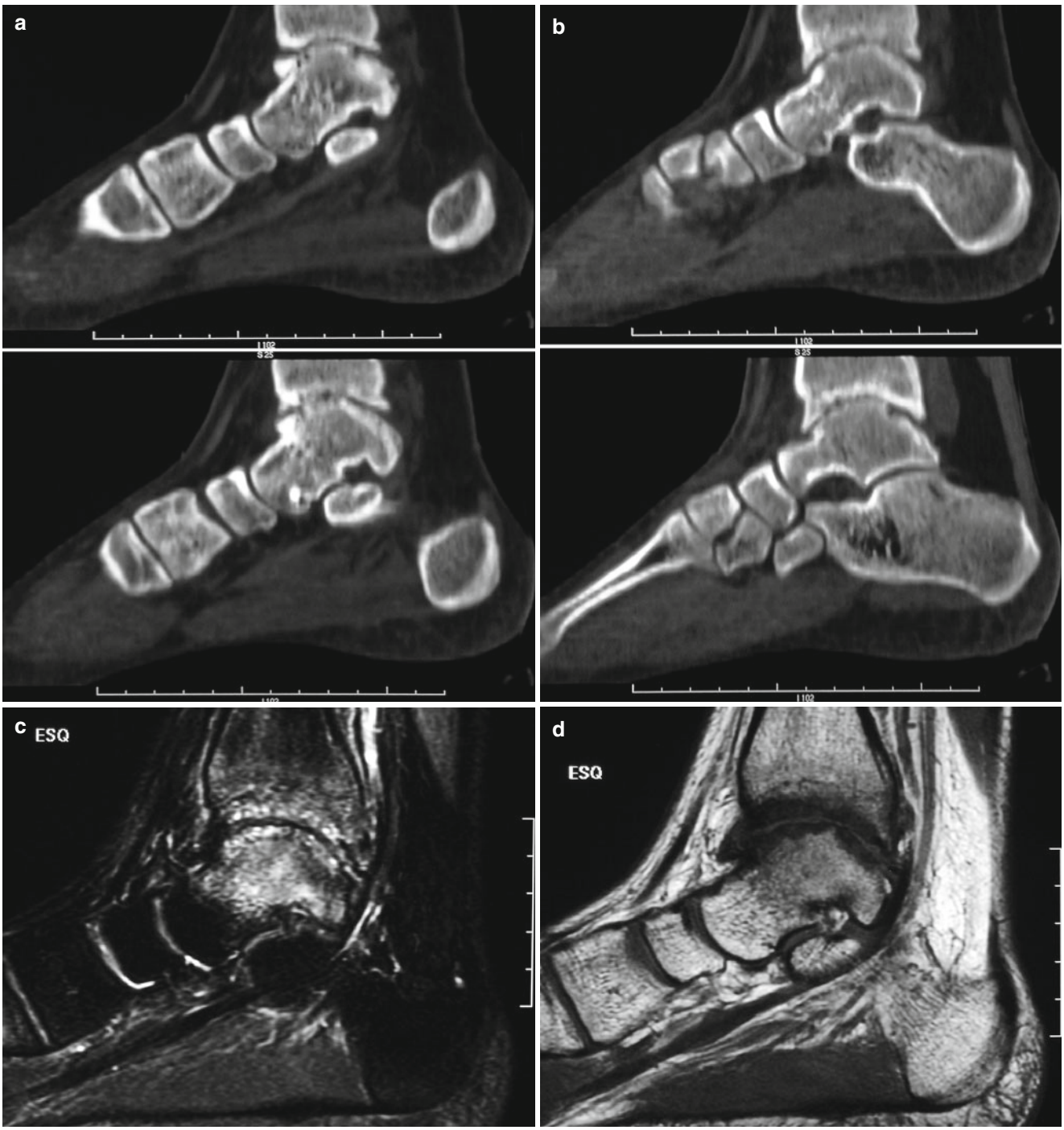

Fig. 8.31 Advanced hemophilic arthropathy in the left ankle of a 17-year-old patient. Sagittal reformatted CT images (**a** and **b**) demonstrate severe tibiotalar osteoarthritis, with large marginal osteophytes, marked narrowing of the joint space, and multiple subchondral cysts (the hallmark of hemophilic arthropathy). Sagittal fat sat T2-WI (**c**) and T1-WI (**d**) show destruction of the articular cartilages, with subchondral cysts and extensive bone marrow edema pattern, as well as hemosiderin impregnation in the anterior recess of the articular capsule, which is hypointense in all sequences

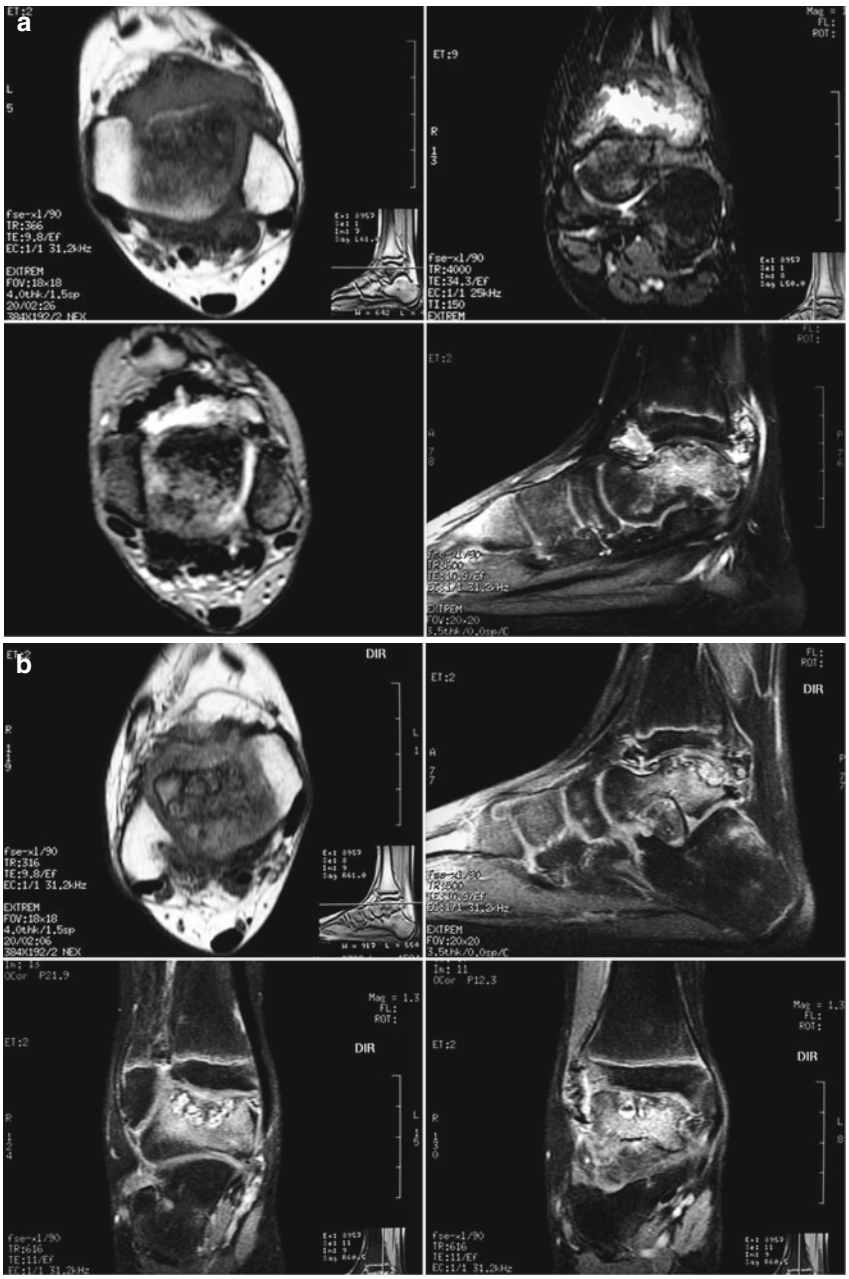

Fig. 8.32 MRI of the ankles of a 13-year-old male with bilateral hemophilic arthropathy. In (**a**), images obtained in several spatial planes with different sequences reveal destructive arthropathy of the left ankle, with joint effusion, marked synovitis, osteochondral lesions in the talar dome, and extensive hemosiderin impregnation, the latter more evident in the gradient-echo sequence (*lower-left image*). In (**b**), post-gadolinium T1-WI of the right ankle demonstrate enhancement of the thickened synovium, of the edematous bone marrow, and of the subchondral cysts. Arthropathy is more advanced at right, with multiple and coalescent subchondral cysts (some of them with mixed content) and secondary osteoarthritis

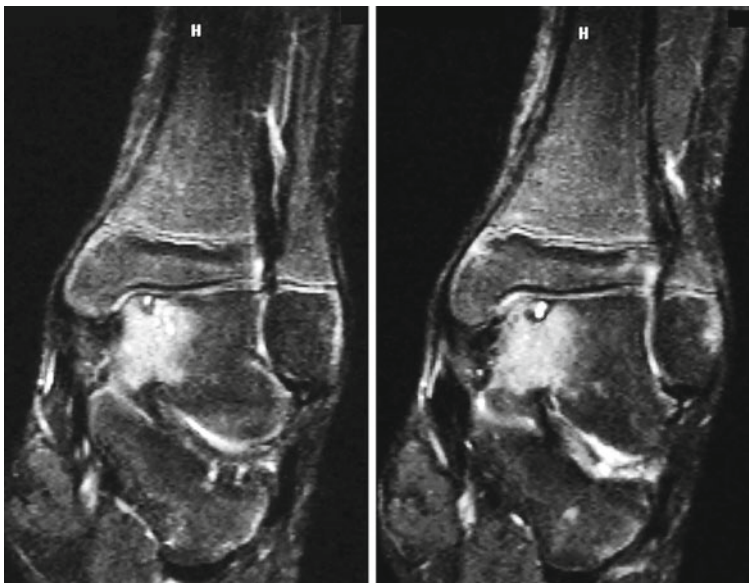

Fig. 8.33 A 7-year-old male with hemophilic arthropathy of the left ankle. Coronal fat sat T2-WI display a subchondral cyst surrounded by a rim of low signal intensity in the medial convexity of the talar dome, as well as extensive bone marrow edema pattern. Mild tibiotalar slant is also present

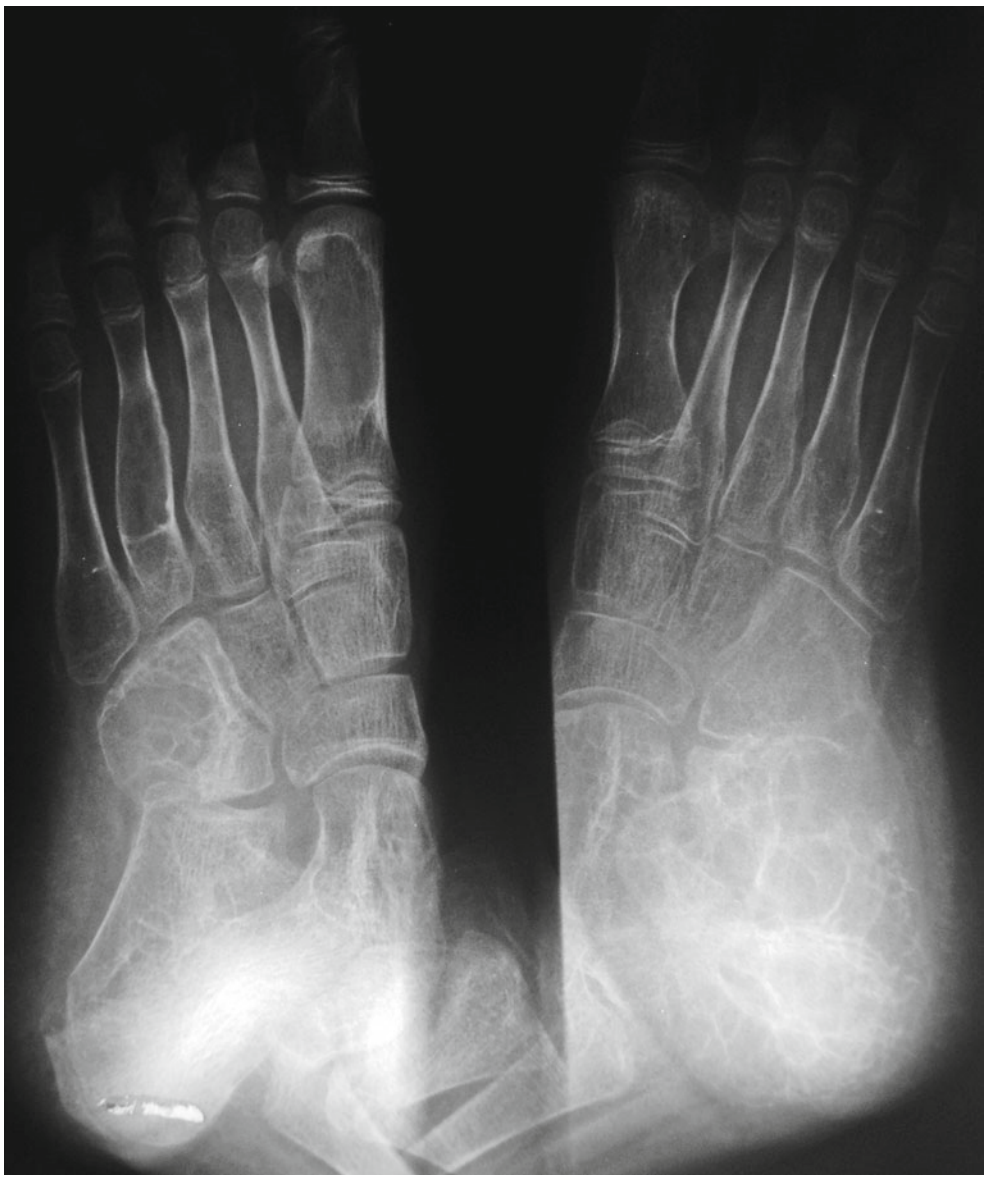

Fig. 8.34 Oblique radiographs of the feet of a hemophiliac patient with palpable masses in both heels caused by hemophilic pseudotumors. There is soft-tissue swelling in the hindfeet (notably in the left extremity) and diffuse osteoporosis. Expansile, multiloculated bone lesions are seen in the right cuboid and in the left calcaneus, the latter being larger, with ill-defined cortical edges. Coarse trabecular pattern is present in the anterior portion of the right talus, as well as a complete pathologic fracture in the homolateral calcaneus. Expansion of the medullary cavities of the diaphyses of the first and of the fourth metatarsals is also evident at right, with cortical thinning (Courtesy of Dr. Marcelo Ricardo Canuto Natal, Hospital de Base do Distrito Federal and Pasteur Medicina Diagnostica – Diagnosticos da America S.A., Brasilia, Brazil)

8.4 Hematologic Malignancies

Among the hematologic malignancies, the leukemias are particularly prone to involve the musculoskeletal system, notably acute lymphoblastic leukemia. Osseous and articular abnormalities may even precede other systemic manifestations, mimicking primary arthritis. The most common form of articular involvement in children is a transient and recurrent polyarthritis that affects mainly the knees and, less often, shoulders and ankles. Despite the increased risk of infections in leukemic children, osteomyelitis/septic arthritis are relatively uncommon. Bone pain in leukemia is multifactorial, occurring much more frequently in children than in adults. Lytic or sclerotic bone lesions may be found, in addition to joint effusion, osteoporosis, and subperiosteal bone neoformation; however, radiographs are often entirely normal. Metaphyseal lucent bands ("leukemic lines") are among the most frequent findings, even though they are nonspecific (Fig. 8.35). On MRI, neoplastic infiltration leads to abnormal signal intensity of the bone marrow, which is hypointense on T1-WI and hyperintense on T2-WI and presents post-gadolinium enhancement.

Up to 25 % of the patients with lymphoma eventually develop musculoskeletal symptoms, though arthritis is much less common. The latter may present as a monoarthritis or as a polyarthritis, either related to neoplastic infiltration of the synovium or arising out of a reactive process (nonneoplastic). Non-Hodgkin lymphomas respond for the majority of these manifestations in the pediatric group.

Avascular necrosis and bone infarcts are common in children undergoing treatment for hematologic malignancies. These ischemic areas are frequently multiple and asymptomatic, related to chemotherapy or radiation therapy. Imaging findings are similar to those of osteonecrosis found in other conditions.

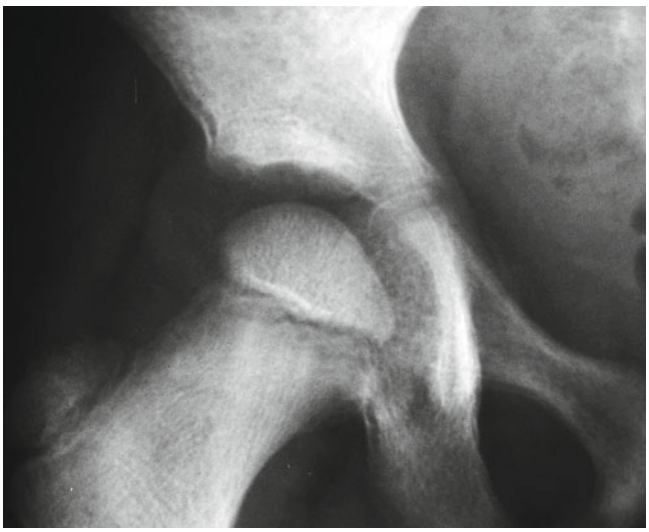

Fig. 8.35 Radiograph of the right hip of a child with acute lymphoblastic leukemia demonstrates regional osteoporosis, a lucent metaphyseal band in the proximal femur, and periosteal reaction along the femoral neck and in the homolateral iliac bone

Key Points

- Imaging findings in SCD are related mainly to hyperplasia of the hematopoietic red marrow and bone ischemia. There is increased risk of osteomyelitis, but septic arthritis is relatively uncommon. Arthritis is not a prominent feature in most cases. Imaging is most useful in distinguishing painful vasoocclusive crises from diaphyseal osteomyelitis. Osteoarthropathy in thalassemia may be attributed to the disease itself or to its therapy, with peculiar imaging findings related to the use of iron chelators.
- Hemophilic arthropathy, related to recurrent hemarthroses, is common and consists in one of the most important causes of morbidity in hemophiliac patients. Its appearance on imaging studies resembles an atypical and severe form of osteoarthritis. Impregnation of the affected joints by hemosiderin, seen on MRI, is the hallmark of the disease. Growth disturbances related to articular hyperemia are also frequent. Hemophilic pseudotumors may simulate aggressive neoplastic lesions, but the clinical background and the presence of hemoglobin degradation products inside the mass usually help in the differential diagnosis.
- Even though musculoskeletal manifestations are common in the hematologic malignancies of childhood, imaging studies are frequently normal or reveal nonspecific findings, such as osteoporosis, leukemic lines, and periosteal reaction. MRI is useful to detect neoplastic infiltration of the bone marrow and/or bone ischemia.

Recommended Reading

Abramson SJ, Price AP (2008) Imaging of pediatric lymphomas. Radiol Clin North Am 46(2):313–338

Aloui N, Nessib N, Jalel C, Ben Chehida F, Zidi A, Bellagha I et al (2005) Douleurs osseuses fébriles chez l'enfant drépanocytaire: apport de l'IRM. J Radiol 86(11):1693–1697

Babyn P, Doria AS (2007) Radiologic investigation of rheumatic diseases. Rheum Dis Clin North Am 33(3):403–440

Daldrup-Link HE, Steinbach L (2009) MR imaging of pediatric arthritis. Magn Reson Imaging Clin N Am 17(3):451–467

Doria AS (2010) State-of-the-art imaging techniques for the evaluation of haemophilic arthropathy: present and future. Haemophilia 16(Suppl 5):107–114

Ejindu VC, Hine AL, Mashayekhi M, Shorvon PJ, Misra RR (2007) Musculoskeletal manifestations of sickle cell disease. Radiographics 27(4):1005–1021

Frank G, Mahoney HM, Eppes SC (2005) Musculoskeletal infections in children. Pediatr Clin North Am 52(4):1083–1106

Karimova EJ, Rai SN, Ingle D, Ralph AC, Deng X, Neel MD et al (2006) MRI of knee osteonecrosis in children with leukemia and lymphoma: part 2, clinical and imaging patterns. AJR Am J Roentgenol 186(2):477–482

Kellenberger CJ, Schmugge M, Saurenmann T, Di Gennaro L, Eber SW, Willi UV et al (2004) Radiographic and MRI features of deferiprone-related arthropathy of the knees in patients with beta-thalassemia. AJR Am J Roentgenol 183(4):989–994

Kerr R (2003) Imaging of musculoskeletal with complications of hemophilia. Semin Musculoskelet Radiol 7(2):127–136

Maclachlan J, Gough-Palmer A, Hargunani R, Farrant J, Holloway B (2009) Haemophilia imaging: a review. Skeletal Radiol 38(10):949–957

Menon S, Isenberg DA (1995) Rheumatological manifestations of haematological diseases. Ann Rheum Dis 54(10):787–795

Ng WH, Chu WC, Shing MK, Lam WW, Chik KW, Li CK et al (2005) Role of imaging in management of hemophilic patients. AJR Am J Roentgenol 184(5):1619–1623

Patel CV (2009) The foot and ankle: MR imaging of uniquely pediatric disorders. Magn Reson Imaging Clin N Am 17(3):539–547

Pruthi S, Thapa MM (2009) Infectious and inflammatory disorders. Magn Reson Imaging Clin N Am 17(3):423–438

9 Accidental and Non-accidental Articular Injuries in the Skeletally Immature Patient

9.1 Introduction

The notion that children are not small adults is proverbial in medicine. This is also valid for osteoarticular trauma, as the immature musculoskeletal system responds to traumatic injuries differently from the adult organism. Lesions due to acute high-energy trauma, which are discussed in this chapter, differ from those caused by overuse/anomalous stress, such as the sports-related injuries studied in Chap. 10. Special emphasis will be put on articular injuries, although some extraarticular lesions typical of the pediatric age group are also described. In addition to accidental traumatic injuries, this chapter will also cover non-accidental trauma, given the importance of imaging as an objective evidence of child abuse. A concise approach will be used in the following topics, highlighting the imaging appearance of the most frequent lesions. Pediatric trauma is an extensive and complex issue and an in-depth study of it is beyond the scope of this brief review.

9.2 Peculiar Aspects of the Fractures of the Immature Skeleton

The most important difference between the immature skeleton and the adult organism is the presence of the physis, a specialized region located in the transition between the metaphysis and the epiphysis (see Chap. 2), which is most vulnerable in the provisional calcification zone. Because of its high collagen content, the immature bone is weaker than the adjacent ligaments and tendons, and traumatic lesions that would lead only to ligament injuries in adults may cause fractures in children. Nonetheless, the bones of children are more elastic than the undeformable bones of adults, so that pediatric fractures are less prone to propagation/comminution. As the periosteum is thicker, more active, and more resistant in children than in adults, there is speedy callus formation and prompt healing of fractures in the former.

Radiographs are indispensable in the initial assessment of a suspected fracture, and at least two orthogonal views are mandatory in order to describe the affected bone segments, the extent and the orientation of the fracture line, and the occasional presence of comminution, diastasis, angulation, or displacement (Figs. 9.1 and 9.2). The joints above and below the region of interest must be included in the radiographs, aiming to demonstrate physeal/intra-articular compromise or concomitant dislocation, which often go unnoticed. Indirect radiographic signs of fracture include displacement of periarticular fat planes (an indicator of joint effusion), irregularity of bone surfaces, abnormal alignment between the epiphysis, and the metaphysis and focal physeal widening (Fig. 9.3).

Computed tomography (CT), magnetic resonance imaging (MRI), and ultrasonography (US) are usually electively performed, as a second line of investigation. CT is very useful in diagnosing and staging fractures, especially in patients with inconclusive radiographs or in regions of complex anatomy, being also helpful in the assessment of late complications (Fig. 9.4). MRI is very suitable to evaluate soft-tissue structures and to evidence the presence of bone marrow edema pattern, a reliable marker of bone alterations that may herald "hidden" fractures (Figs. 9.5 and 9.6). Because of its appropriateness for the study of the non-ossified cartilage, MRI is also valuable in the evaluation of physeal fractures and in the assessment of joint dislocations in small children (Fig. 9.7). Bone scintigraphy has high sensitivity in the detection of fractures, being able to evaluate the whole skeleton in a single study; the latter feature is especially useful in the screening of fractures, such as those found in polytraumatized or physically abused children. However, because of its low specificity and limited spatial resolution, most areas of abnormal uptake demand additional investigation in order to determine their real nature. US is more adequate for the assessment of soft-tissue abnormalities associated with fractures, such as joint effusion, periosteal detachment, and periarticular fluid collections. In addition, fractures of the non-ossified portions of the ossification centers (which are undetectable on radiographs) may be diagnosed with US (Fig. 9.8).

S.L. Viana et al., *Joint Imaging in Childhood and Adolescence*,
DOI 10.1007/978-3-642-35876-0_9, © Springer-Verlag Berlin Heidelberg 2013

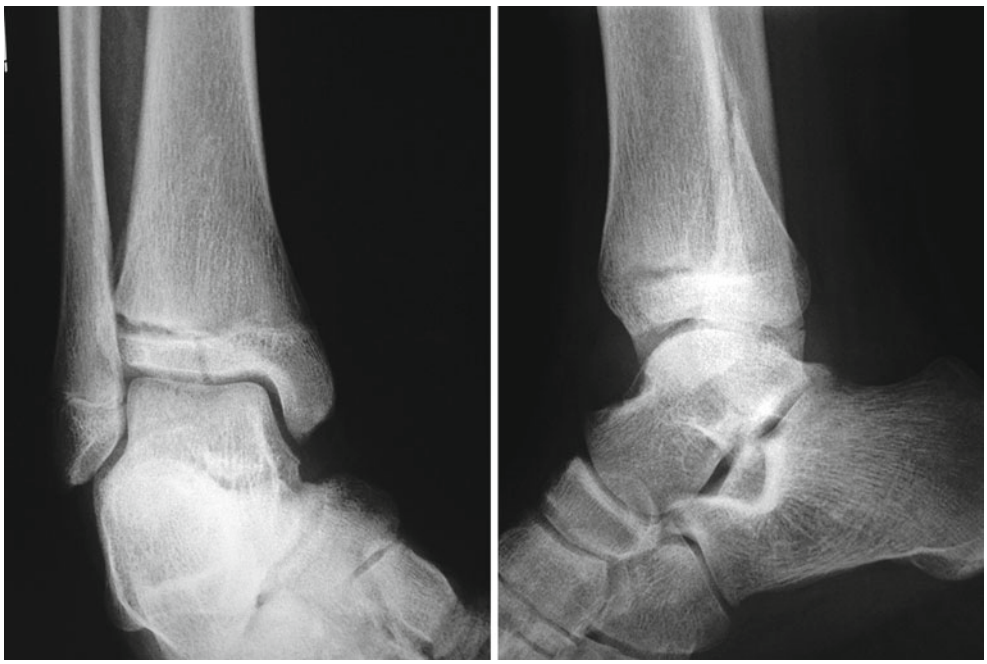

Fig. 9.1 Anteroposterior view (*left*) and lateral view (*right*) of the right ankle of a child with triplanar fracture. The *first image* shows a vertical fracture affecting the lateral portion of the distal epiphysis of the tibia and lateral physeal widening, which could be taken as a Salter-Harris fracture type III. Nonetheless, there is a bone fragment projected posterior and lateral to the distal metaphysis of the tibia, better seen in the lateral view, which demonstrates a coronal fracture of the metaphysis. Complex fractures like this one require CT for proper evaluation

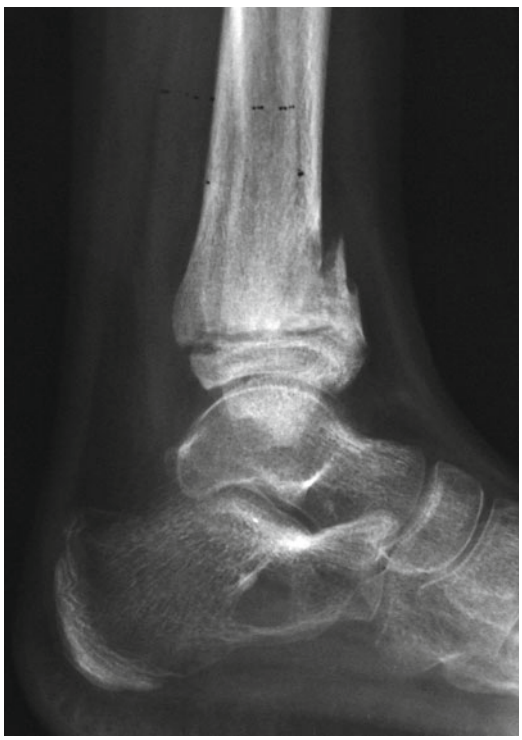

Fig. 9.2 Lateral view of the left ankle demonstrating a type II fracture of the distal tibia with anterior displacement of the epiphysis and of the metaphyseal fragment. Marked osteoporosis is also present

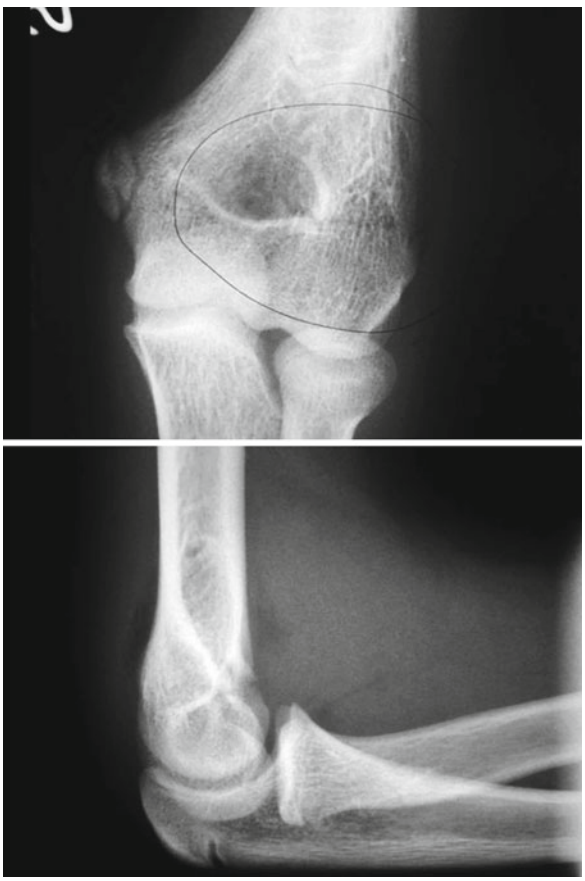

Fig. 9.3 Radiographs of the left elbow of a child with supracondylar fracture of the humerus. Although the fracture line is quite subtle in the anteroposterior view, additional markers seen on the lateral view include displacement of the anterior and posterior fat planes and absent intersection between the anterior humeral line and the central portion of the distal epiphysis

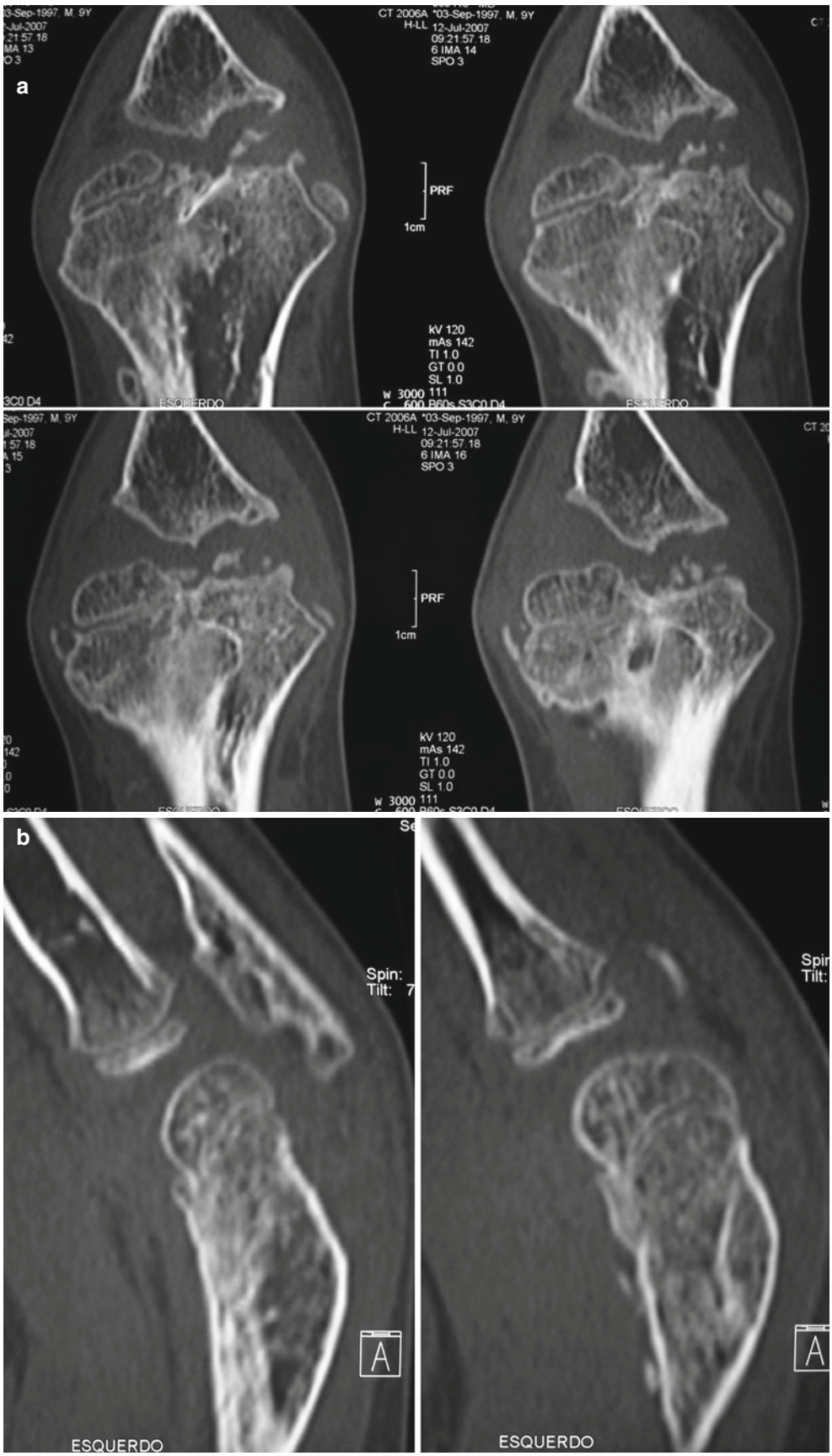

Fig. 9.4 Reformatted CT images in the coronal (**a**) and sagittal (**b**) planes of the distal humerus of a 9-year-old child show a healed transphyseal fracture (type IV) of the lateral condyle. There is a bony bridge between the humeral metaphysis and the anteromedial portion of the capitulum, more evident in (**b**). Premature osteoarthritis is also present

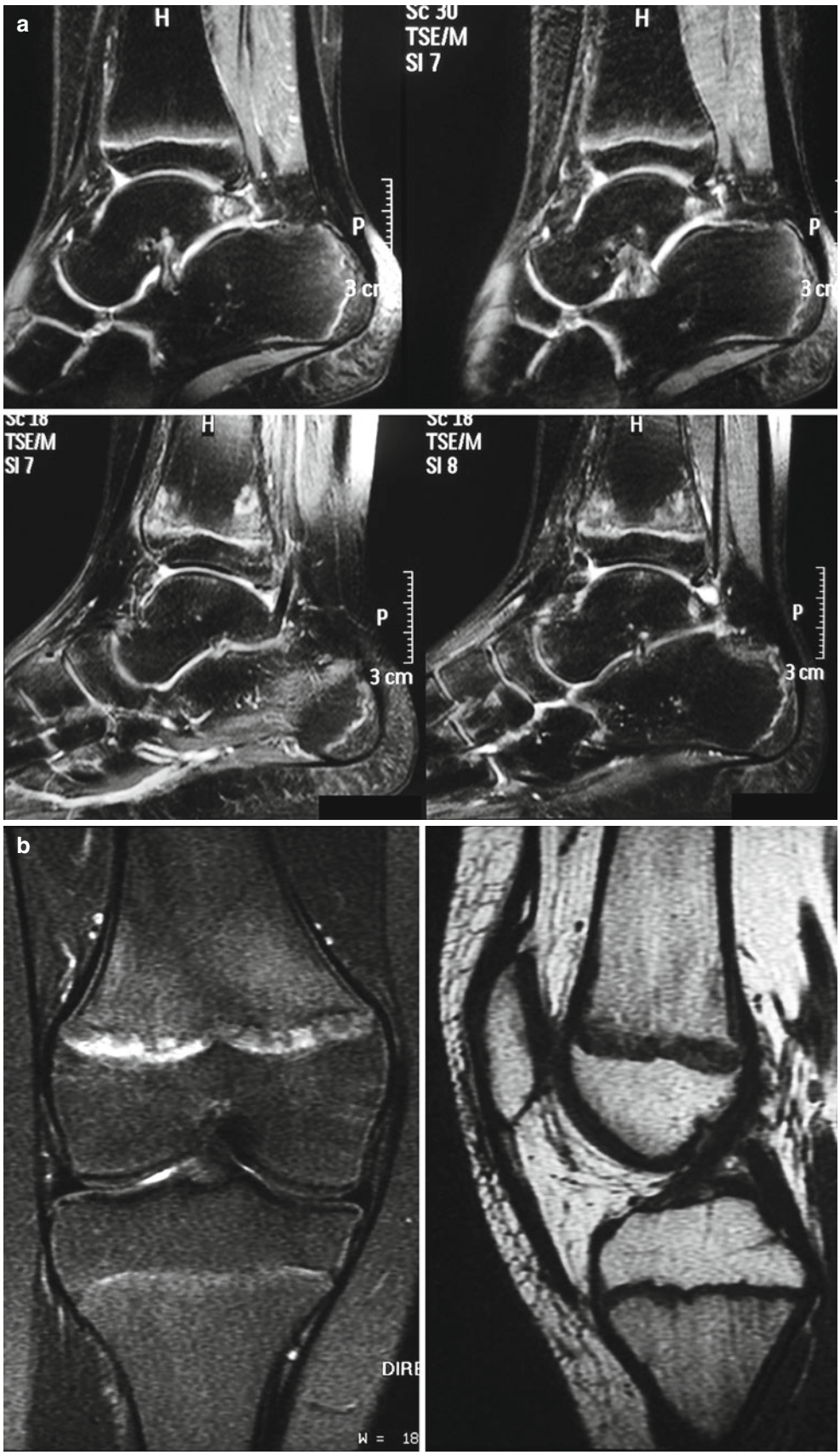

Fig. 9.5 In (**a**), sagittal fat sat T2-WI of the ankles (*right*, *upper row*; *left*, *lower row*) allows for clear demonstration of widening and increased signal intensity of the left tibial physis, as well as homolateral periphyseal edema. This acute, non-displaced Salter-Harris type I fracture would be difficult to detect with other imaging methods. Although similar findings are present in (**b**) (coronal fat sat PD-WI (*left*) and sagittal T1-WI (*right*) of the right knee of a 12-year-old child), bone marrow edema is less prominent and physeal widening is more evident, as this is a subacute lesion

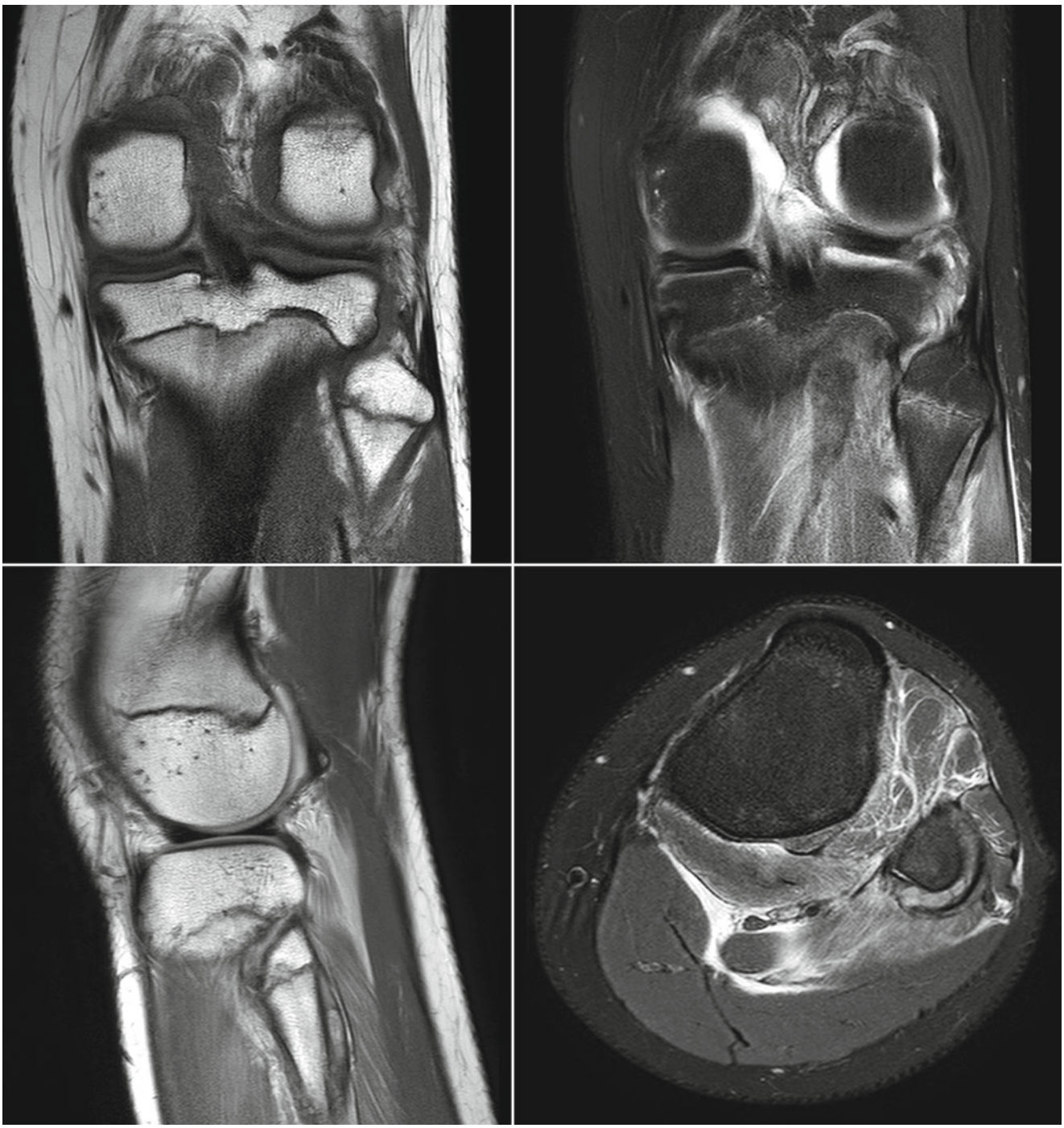

Fig. 9.6 T1-WI (*left*) and fat sat T2-WI (*right*) of the left knee show subtle lateral displacement of the proximal epiphysis of the fibula, more evident in the coronal images (Salter-Harris lesion type I), with bone marrow edema pattern centered at the physis. There is also extensive edema in the adjacent muscles and a subperiosteal hematoma along the proximal metadiaphysis of the fibula

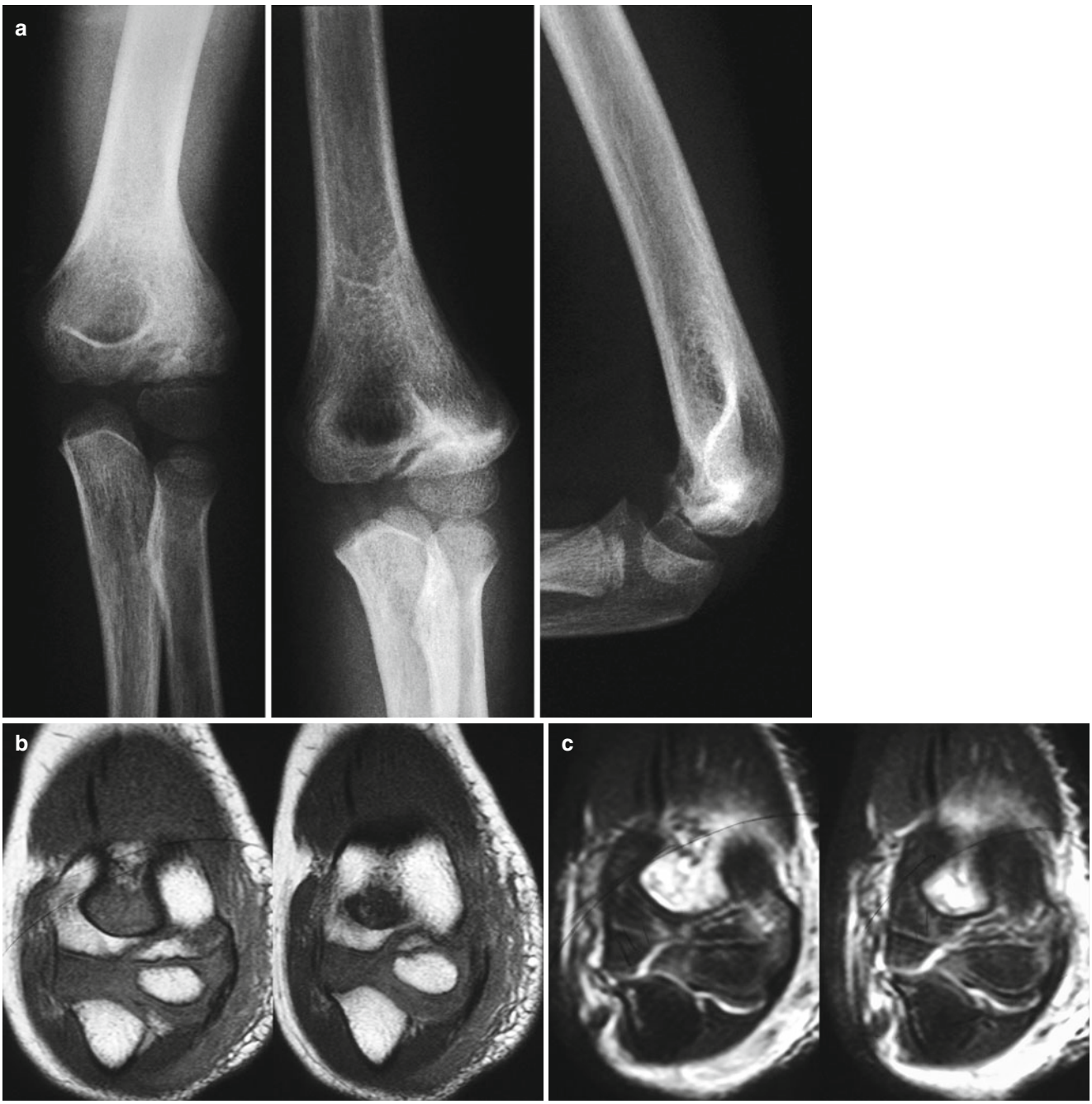

Fig. 9.7 In (**a**), radiographs of the left elbow demonstrate a fracture line involving the lateral condyle of the humerus, extending from the lateral cortex of the metaphysis to the physis, medial to the ossification center of the capitulum, which is already mineralized. Nonetheless, radiographs do not allow proper assessment of the extension of the fracture into the non-ossified portion of the epiphysis. Coronal T1-WI (**b**) is also limited to demonstrate the real extent of the fracture, which is clearly shown on fat sat PD-WI (**c**) (Salter-Harris fracture type IV). Joint effusion and marked edema of the periarticular soft tissues are also present

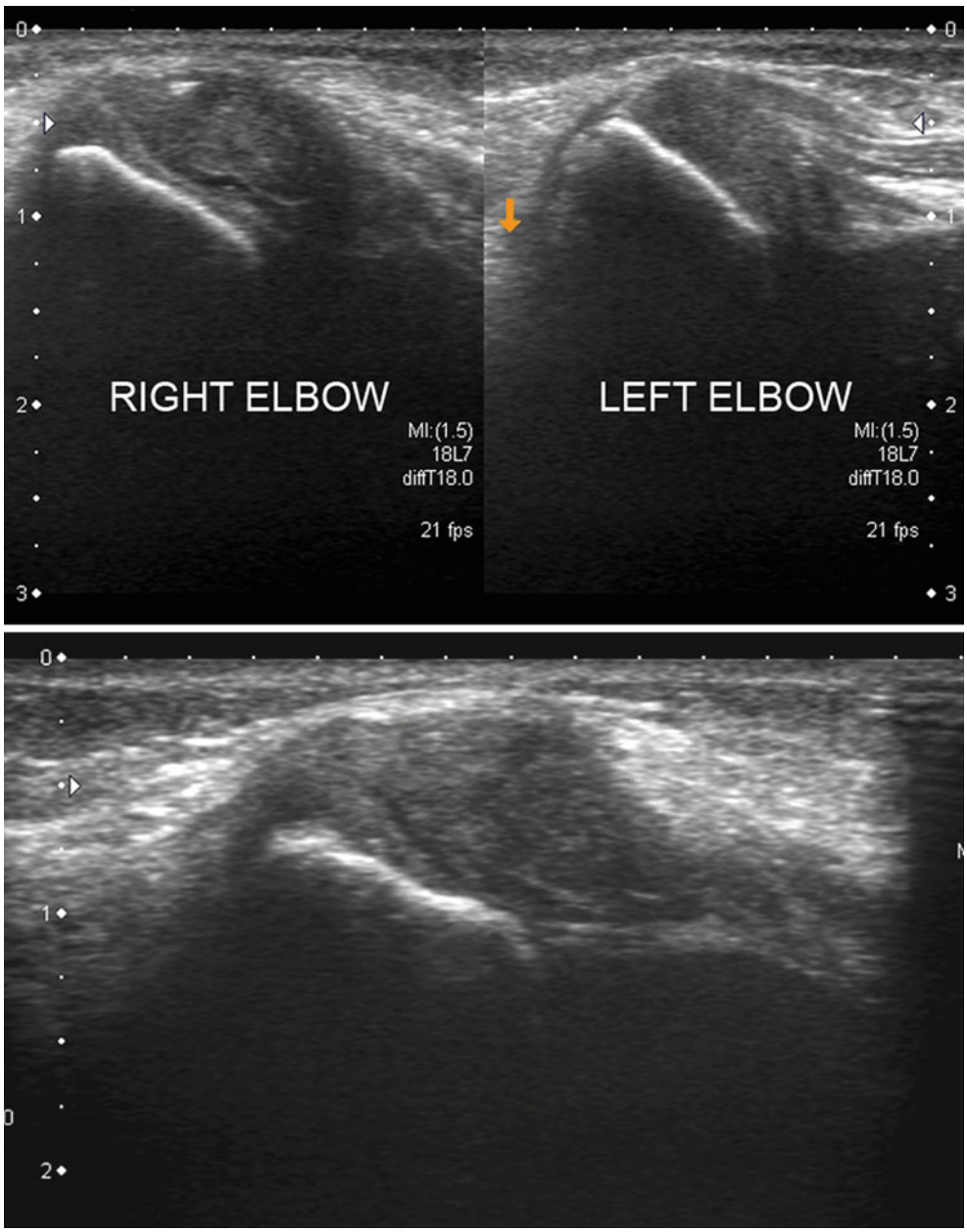

Fig. 9.8 US of a very young child with right-sided avulsion fracture of the non-ossified medial epicondyle of the humerus. The *upper image* shows caudal displacement of the avulsed epicondyle, with hypoechogenic fluid interposed between the fragment and the host cartilage (compare with the normal appearance of the left medial epicondyle). In addition to the above-described avulsion fracture, the *lower image* also discloses a subtle zigzag hypoechogenic fracture line coursing transversely through the cartilaginous fragment

Pediatric fractures may be divided in physeal and non-physeal. Physeal fractures, the main subject of this topic, only occur in the immature skeleton, accounting for 10–30 % of all fractures in children; they raise particular interest because of its potential to cause joint damage and abnormal bone growth. The Salter-Harris classification system is the most widely used, dividing the fractures into five groups according to their location and type of damage to the growth plate, each one of them with distinct prognostic and therapeutic implications (Fig. 9.9). Type I fractures course transversely through the growth cartilage, with no epiphyseal or metaphyseal extension, leading to physeal widening or epiphyseal dislocation (Figs. 9.5, 9.6, and 9.10). Type II fractures are the most common (75 % of all cases), involving the peripheral portion of the metaphysis and part of the growth plate, creating a bone fragment that includes the whole epiphysis and a portion of the metaphysis (Figs. 9.2 and 9.11). Type III lesions are intra-articular fractures that involve the epiphysis and the physis: the fracture line begins in the articular surface, crosses the epiphysis, and presents a transverse component coursing through the peripheral portion of the physis, creating an epiphyseal fragment without connection

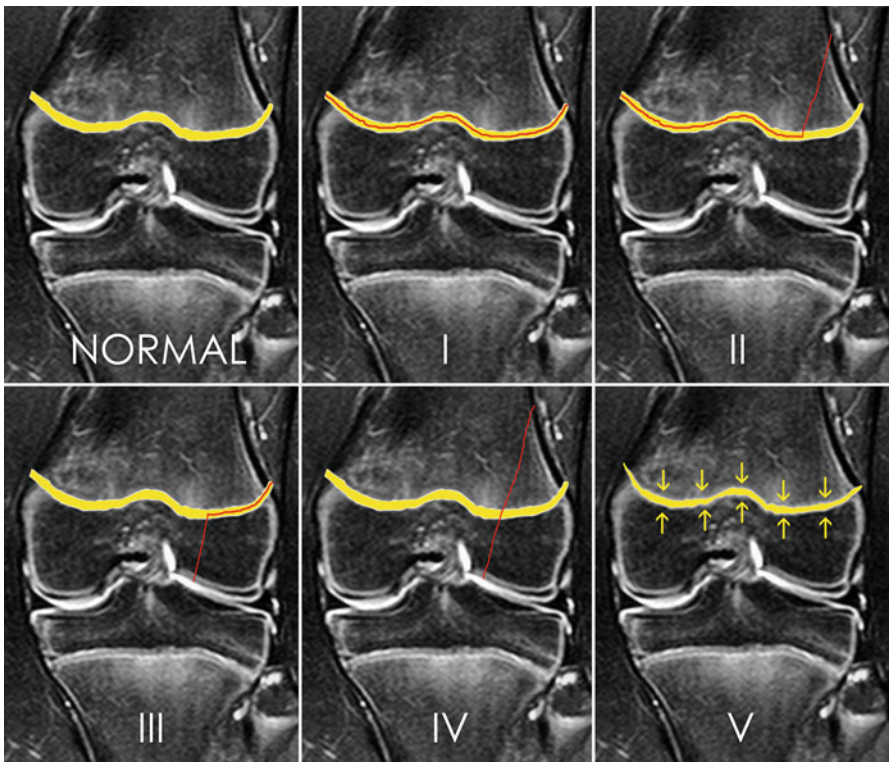

Fig. 9.9 Schematic representation of the Salter-Harris classification for physeal fractures. The physis is represented in yellow and the fracture lines appear in red. While types I and II are physeal and physeal/metaphyseal, respectively, types III and IV are associated with epiphyseal involvement and extend to the joint surface. Type V fracture is a compressive physeal lesion, resulting from the action of axial forces

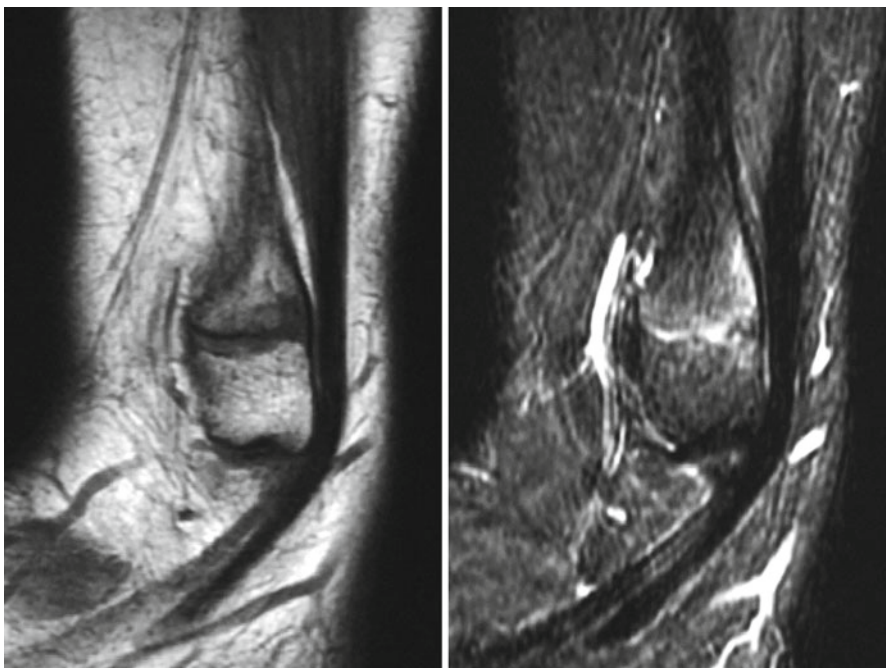

Fig. 9.10 Sagittal T1-WI (*left*) and fat sat T2-WI (*right*) of the right ankle. There is widening of the physis of the distal fibula, more evident on T1-WI, with edematous changes of the physis itself and of the adjacent bone marrow on fat sat T2-WI (Salter-Harris fracture type I)

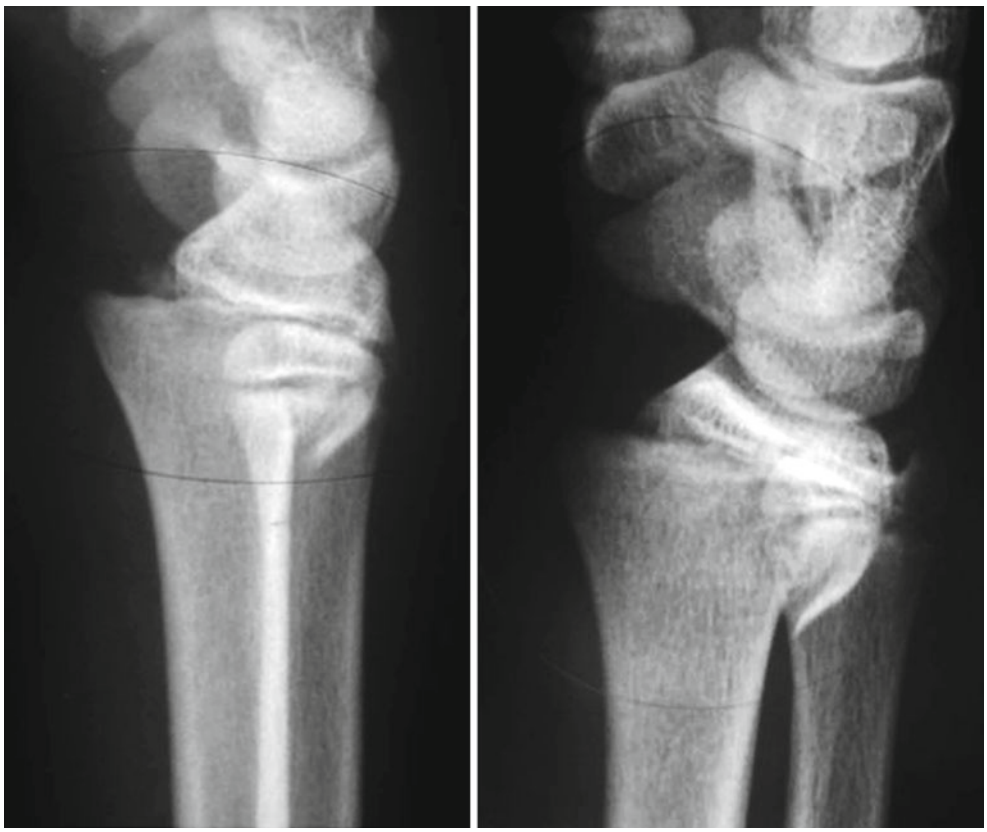

Fig. 9.11 Lateral (*left image*) and oblique (*right image*) views of the wrist disclosing a physeal/metaphyseal fracture of the distal radius, with dorsal angulation and displacement of the epiphysis and of the metaphyseal fragment

with the metaphysis (Figs. 9.12 and 9.13). Type IV lesions cross the metaphysis and the epiphysis, transecting the physis and the joint surface, therefore producing a bone fragment that includes epiphyseal and metaphyseal components (Fig. 9.7). Type V lesions are the rarest of all (approximately 1 %) and are difficult to diagnose, being caused by axial compressive forces that lead to crushing injury of the physis, without obvious epiphyseal or metaphyseal fractures; radiographs are usually normal or display subtle physeal narrowing. Diagnosis of type V lesions is most often late and retrospective, made after the appearance of complications, such as growth arrest. Generally speaking, type I and type II lesions present good evolution because they do not involve the joint surfaces (Fig. 9.14), while intra-articular lesions (types III and IV) have worse prognosis, with increased risk of secondary osteoarthritis and functional limitation (Figs. 9.4, 9.15, 9.16, and 9.17). Fractures that involve the physis may lead to development of transphyseal bone bridges and/or early physeal closure (Figs. 9.4, 9.16, 9.17, and 9.18). Both MRI and CT are useful in the demonstration of physeal bridges (Fig. 9.4): when centrally located, they tend to cause limb-length discrepancy, while peripheral bridges cause localized growth arrest and angular deformities. In addition to limb shortening, bone bridges may cause damage to the adjacent joints, as well as bowing of the forearm or of the leg if only one of the paired bones is affected (Fig. 9.16). Growth recovery lines that are angled or obliquely oriented – instead of parallel – relative to the physis are indicative of disturbed bone growth related to the presence of bone bars (Fig. 9.16).

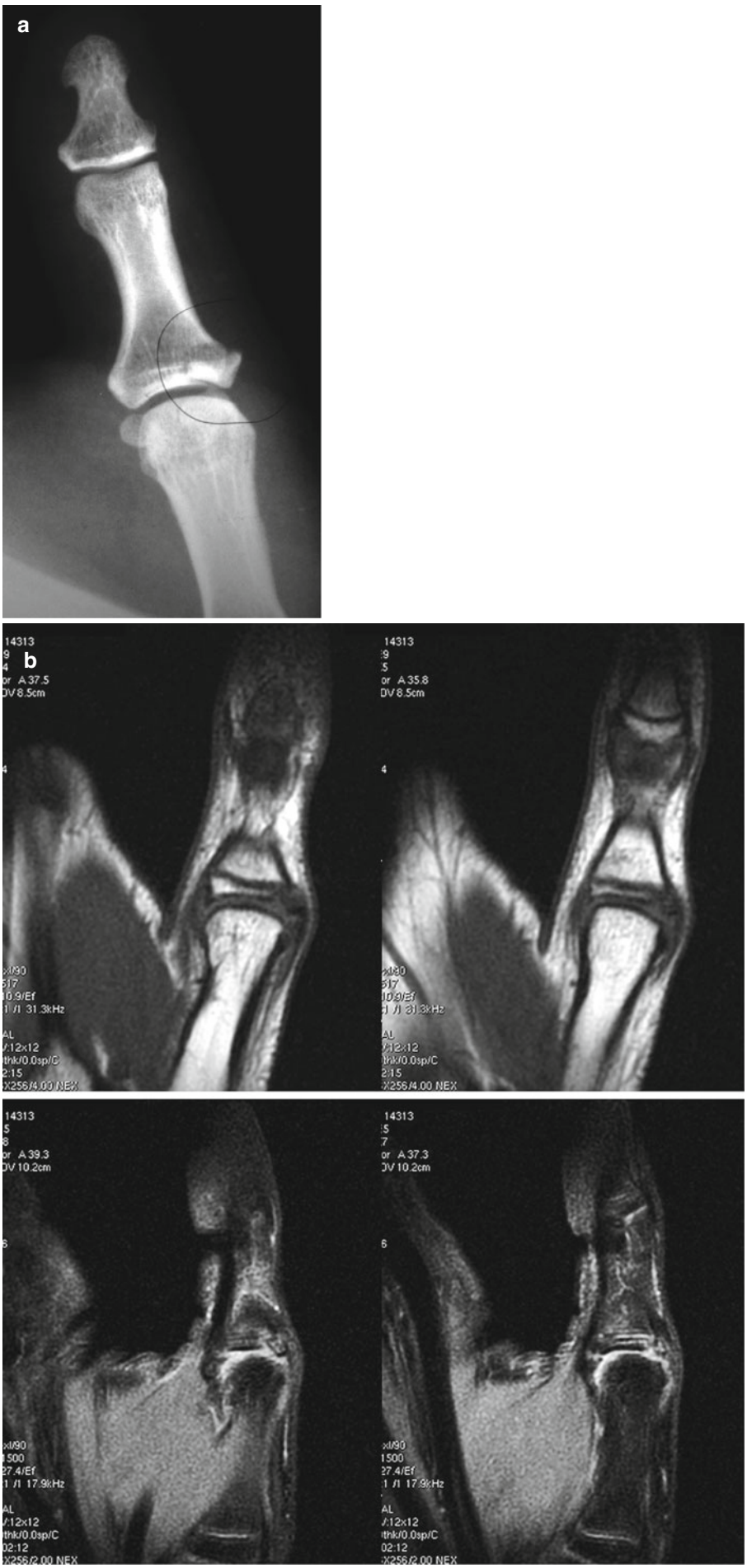

Fig. 9.12 Type III fracture of the base of the proximal phalanx of the thumb in a 14-year-old male. Radiograph (**a**), coronal T1-WI (**b**, *upper row*), and sagittal fat sat PD-WI (**b**, *lower row*) show a mildly displaced physeal/epiphyseal fracture leading to discontinuity of the joint surface

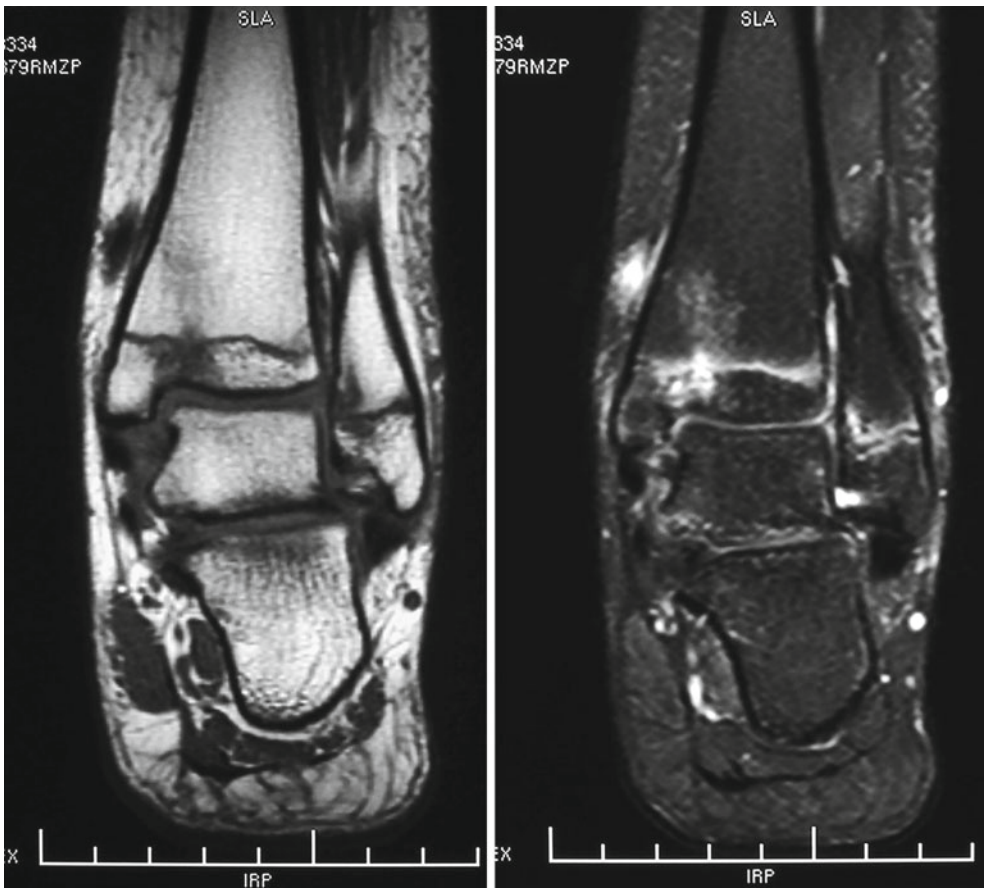

Fig. 9.13 Coronal T1-WI (*left*) and fat sat PD-WI (*right*) of the left ankle of a 12-year-old female demonstrate periphyseal bone marrow edema in the tibia and in the fibula, with a vertical fracture line extending to the joint surface in the medial portion of the tibial epiphysis, also surrounded by marrow edema. These findings are compatible with Salter-Harris fractures type III in the tibia and type I in the fibula

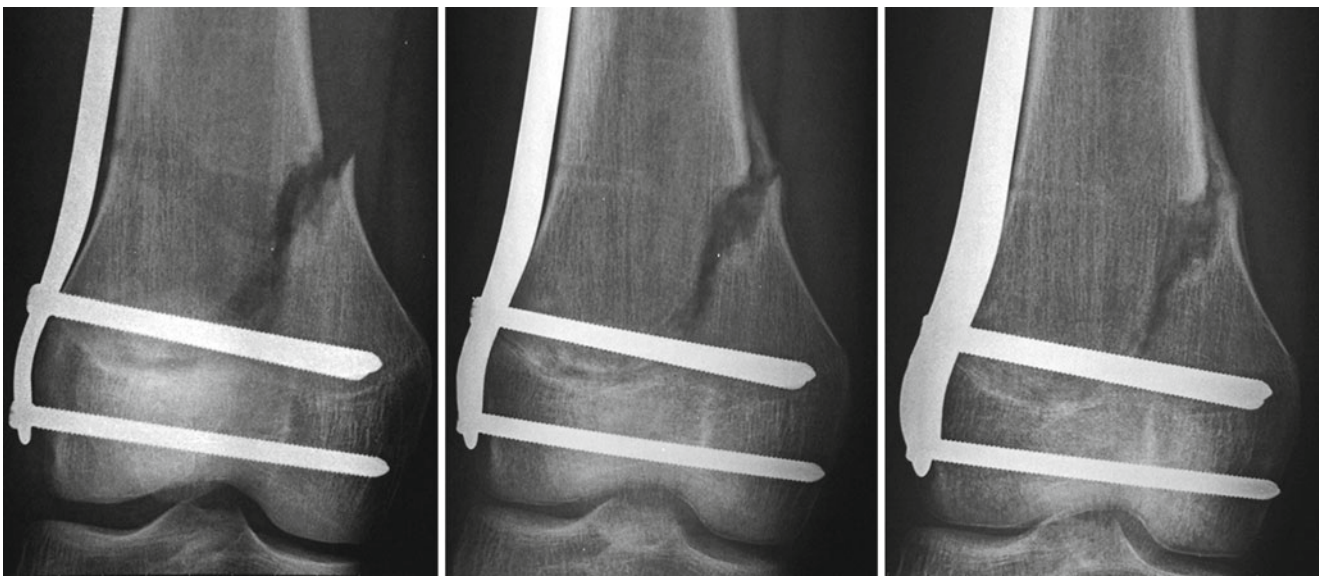

Fig. 9.14 Evolution a type II fracture of the distal femur treated with surgical fixation. Formation of bone callus and progressive healing of the fracture are evident in serial radiographs, with gradual onset of osteoporosis

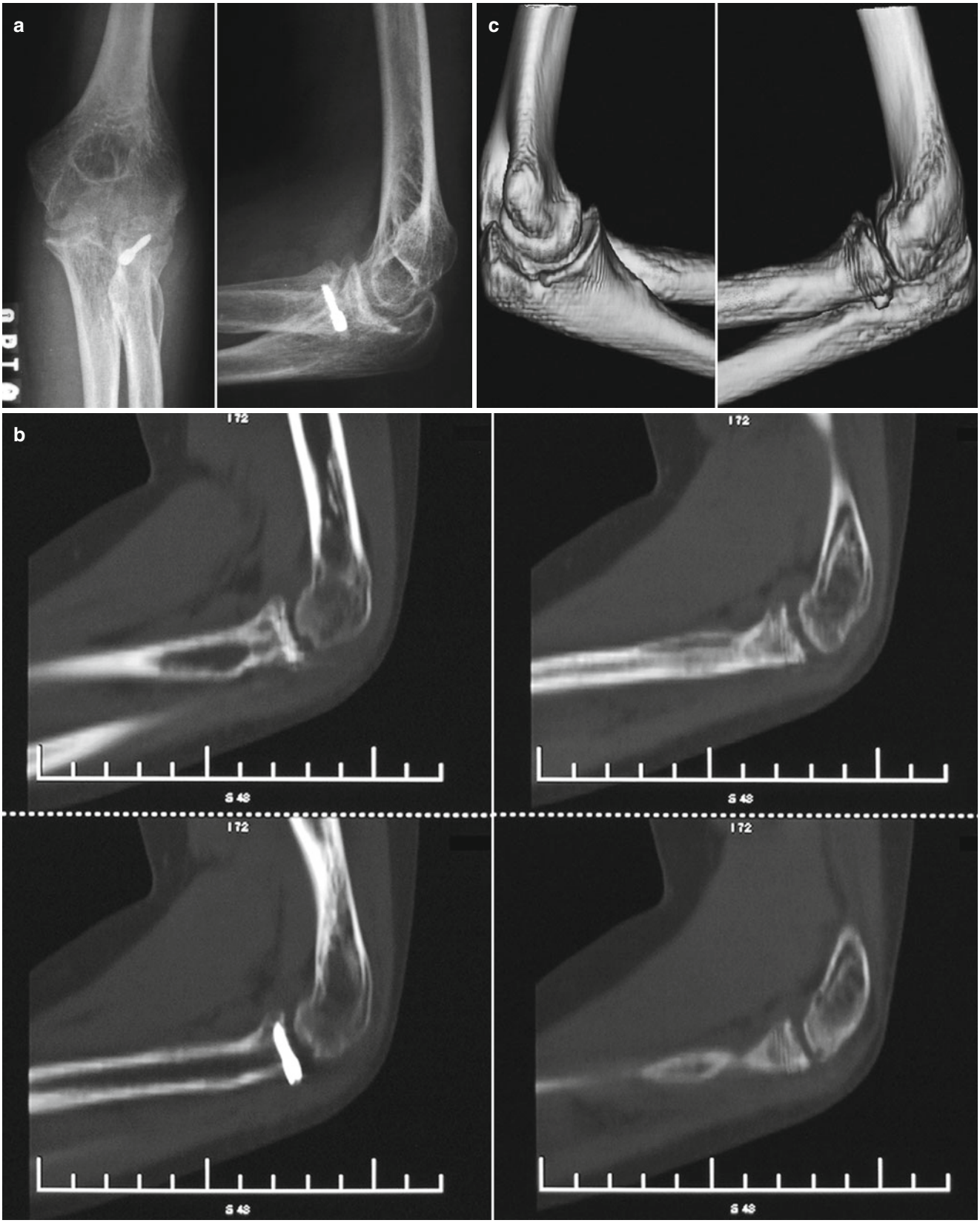

Fig. 9.15 Radiographs (**a**), sagittal reformatted CT images (**b**), and volume-rendered reconstructions (**c**) of an adolescent with sequelae of a surgically corrected elbow fracture. There is irregularity of the joint surfaces, with early-onset osteoarthritis and flexion deformity

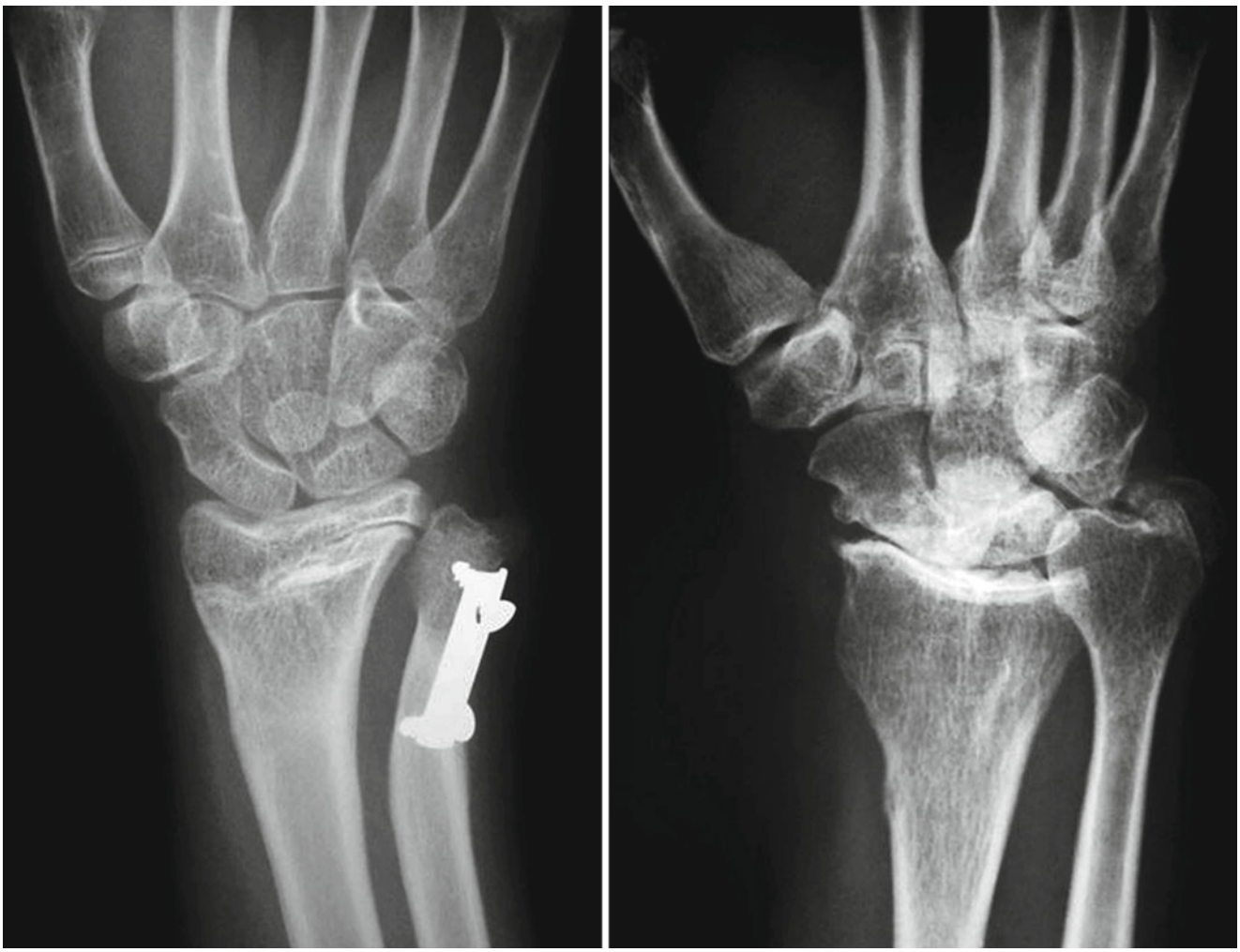

Fig. 9.16 In the *left image*, radiograph of the wrist and of the forearm of a skeletally immature patient demonstrates bowing and residual deformity of the radius and of the ulna, with orthopedic plate and screws in the distal ulna. A peripheral transphyseal bone bridge is seen in the distal radius (to which growth recovery lines converge), as well as incongruity of the radiocarpal joint. At *right*, radiograph of a young adult with sequelae from an old healed fracture of the distal forearm reveals radial shortening (growth arrest related to physeal injury) and premature osteoarthritis of the wrist, as well as deformity of the distal ulna

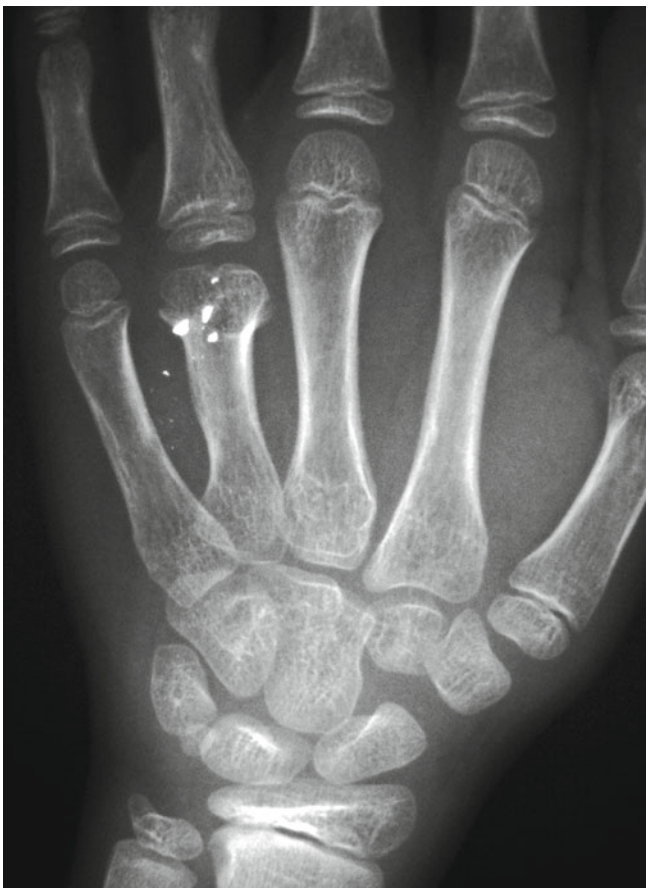

Fig. 9.17 Old gunshot injury in the head of the fourth metacarpal bone associated with physeal lesion. There is deformity of the metacarpal head and premature physeal closure leading to bone shortening

Some incomplete non-physeal fractures – more frequently found in the distal third of the forearm – will be briefly described as they are typical of the pediatric group. The greenstick fracture is characterized by an incomplete cortical break in the convex edge of the bone and cortical bowing in the concave border, with periosteal apposition that creates a hinge-like effect (Figs. 9.19 and 9.20). Almost one-third of the patients with greenstick fractures will present refractures (which may occur in other types of fracture as well) due to incomplete and/or asymmetric healing (Fig. 9.21). Buckle (torus) fractures present as a subtle cortical irregularity with bulging of the bone surface, typically located adjacent to the metaphyses (Fig. 9.22). The plastic deformation is just an accentuation of the physiological bowing of the affected bone, with no discernible fracture line on radiographs (Figs. 9.21 and 9.23); it is not infrequent for plastic deformation to be associated with other fractures (Fig. 9.21).

Complete diaphyseal fractures are less common in children than in adults (Fig. 9.24). Traumatic osteochondral lesions without fractures are rare in small children and more common in adolescents, usually associated with ligament injuries and joint dislocations, being more frequently found in the talar dome and in the femoral condyles (Figs. 9.25 and 9.26). MRI and CT-arthrography are the only imaging methods able to detect purely chondral lesions, but radiographs and regular non-contrast CT may occasionally disclose fragments of bone attached to displaced osteocartilaginous fragments.

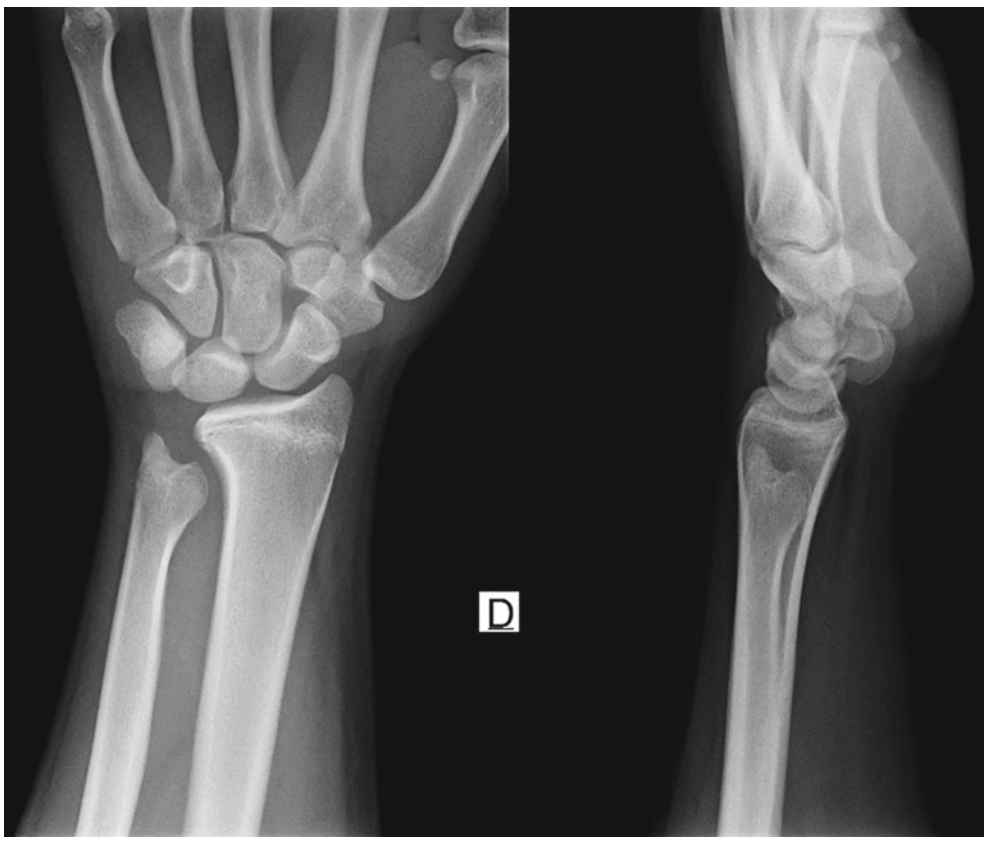

Fig. 9.18 Radiographs of the right wrist and distal forearm of a child with old healed fractures of the homolateral radius and ulna. There is discrepancy in the length of the forearm bones due to early closure of the ulnar physis and, as a consequence, ulnar shortening. Secondary deformity of the distal radius is also present

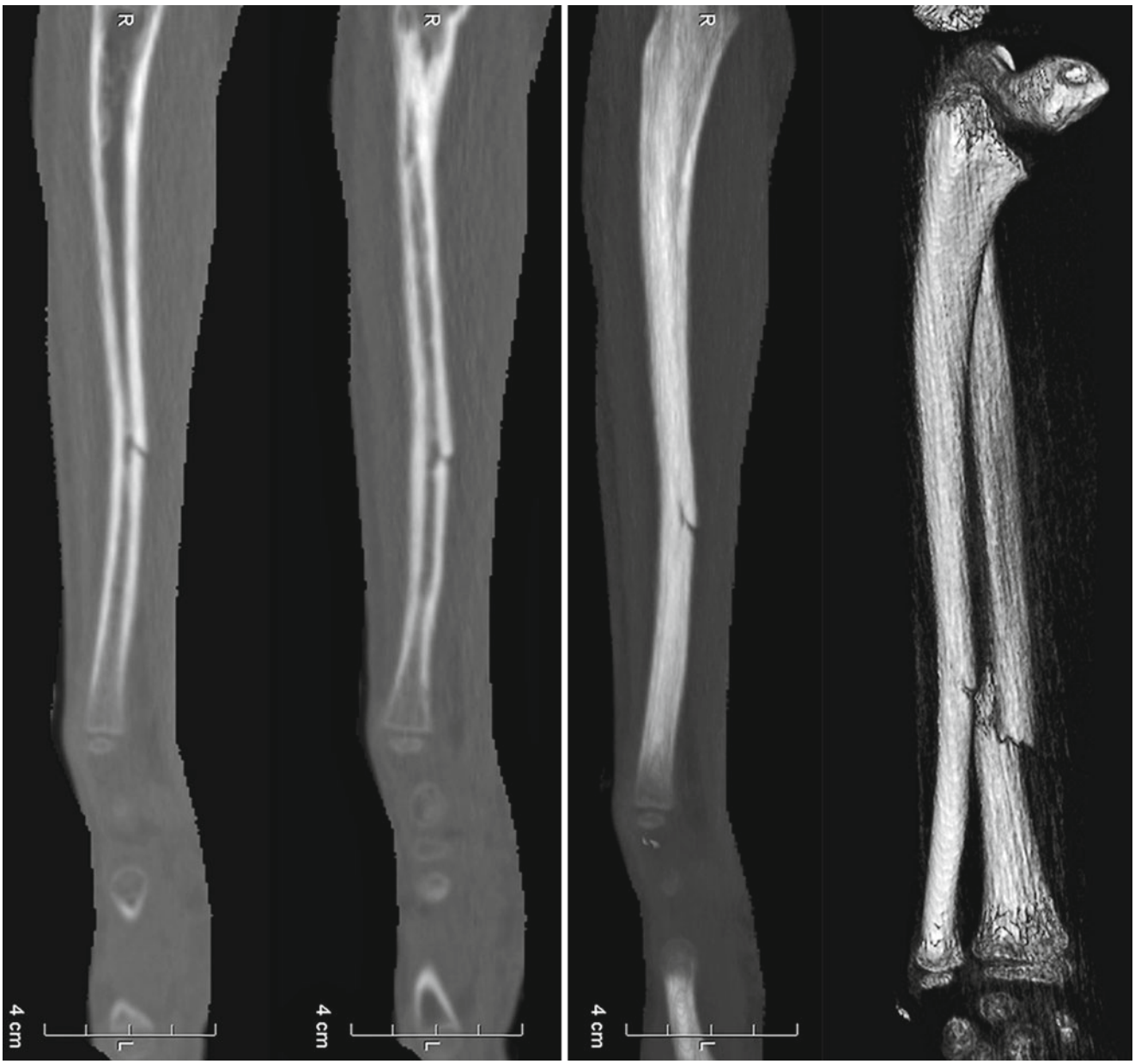

Fig. 9.19 Sagittal reformatted images (*left*) and volume-rendered reconstructions (*right*) of a CT scan of the forearm of a child demonstrating a greenstick fracture of the distal third of the ulna, with discontinuity of the volar cortex and bending of the opposite side. A complete diaphyseal fracture of the distal radius can be seen in the last image

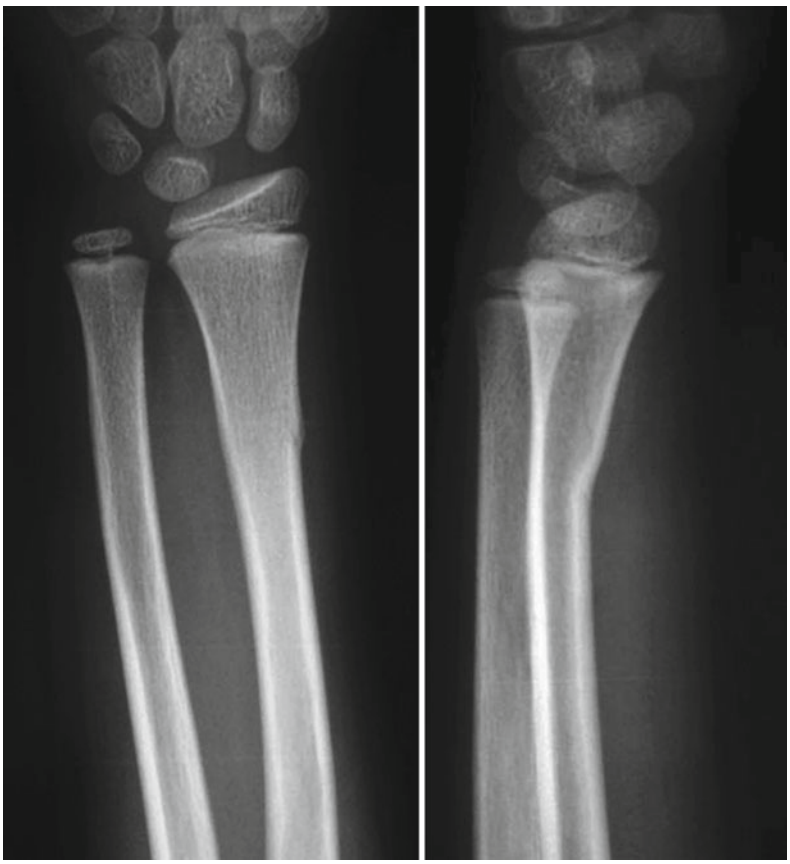

Fig. 9.20 Radiographs of the distal third of the right forearm of a child who fell on his outstretched hand reveal a subtle incomplete fracture in the lateral cortex of the radius without involvement of the opposite side, as well as mild volar bowing of this bone ("hinge" effect). Greenstick fracture

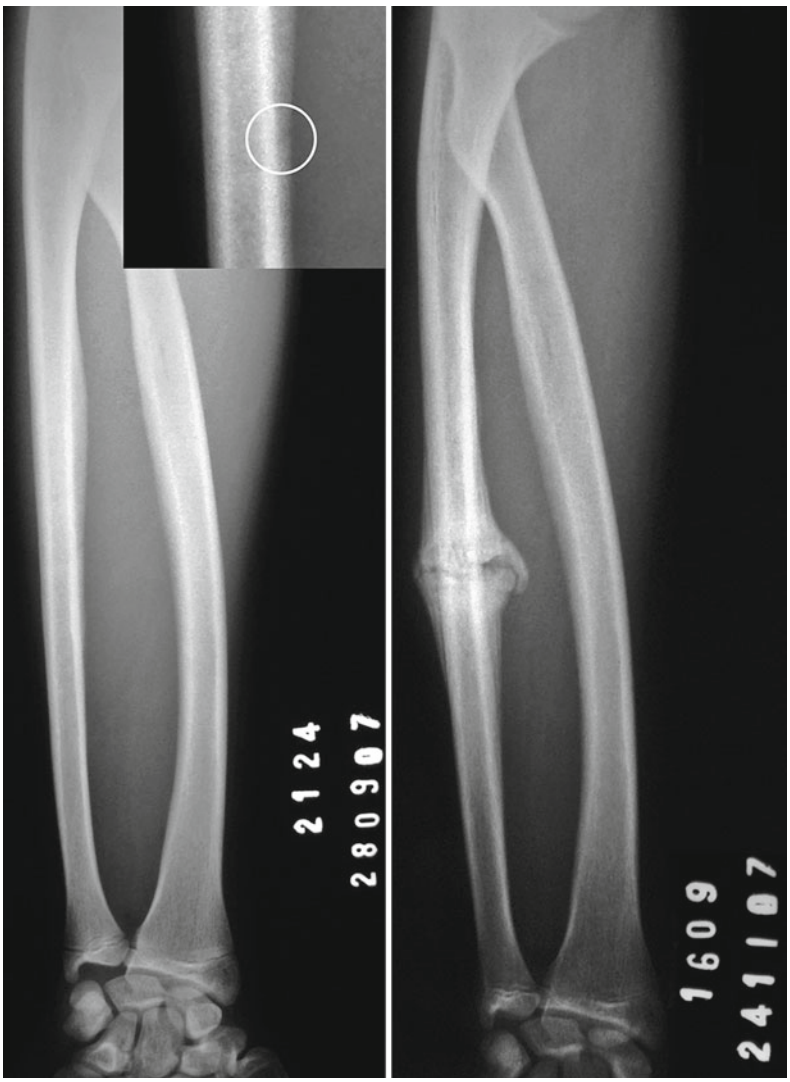

Fig. 9.21 Radiographs of the right forearm of the same child, taken some months apart. In the *left image*, the first radiograph reveals plastic deformation of the radial mid-diaphysis as well as a subtle incomplete fracture of the lateral cortex of the ulnar mid-diaphysis (more evident in the magnified image) associated with solid periosteal reaction. The follow-up radiograph discloses refracture of the ulna in the same level of the previously described lesion; the fracture complete in the second radiograph, with exuberant bone callus and extensive periosteal reaction. The plastic deformation of the radius remains unchanged

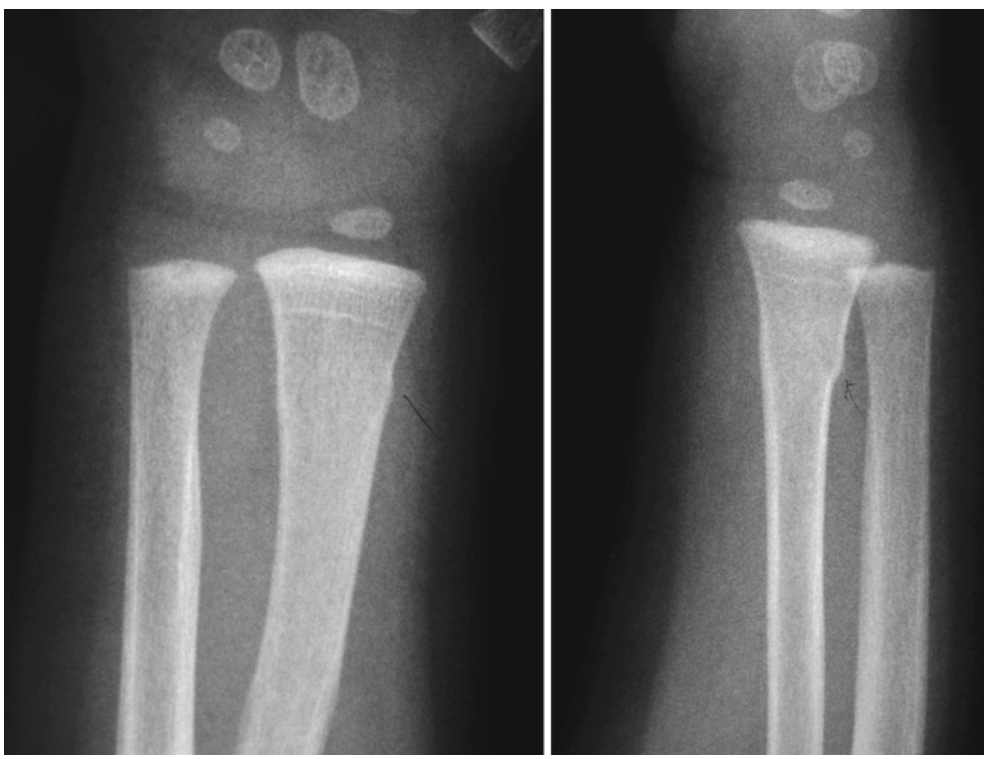

Fig. 9.22 Radiographs of the distal forearm of a young child demonstrate focal bulging in the anterolateral cortex of the distal diaphysis of the radius, typical of a buckle fracture

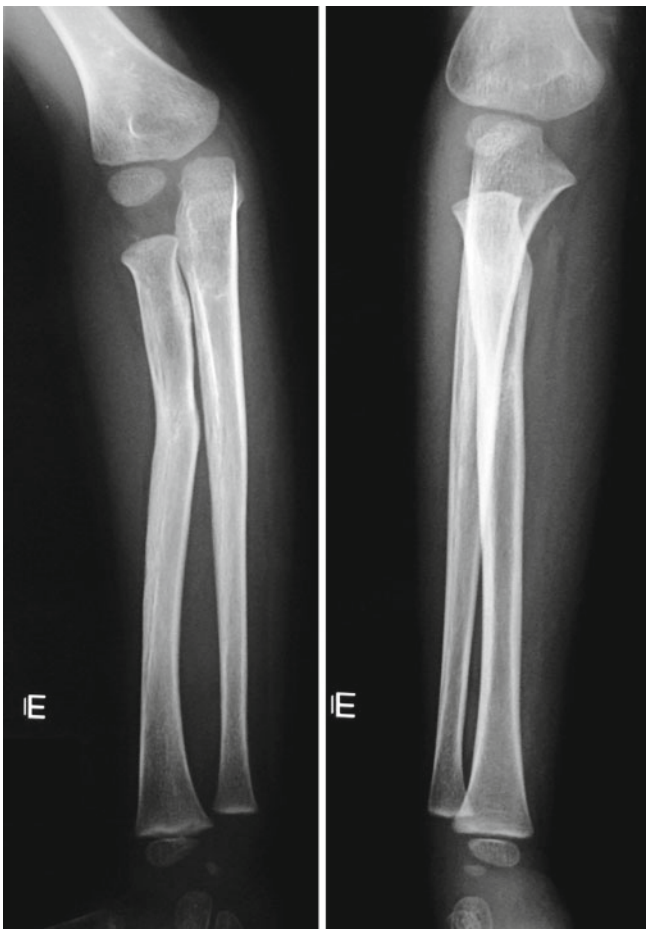

Fig. 9.23 Radiographs of the forearm displaying plastic deformation of the proximal third of the radius, with diaphyseal bowing and absence of cortical discontinuity

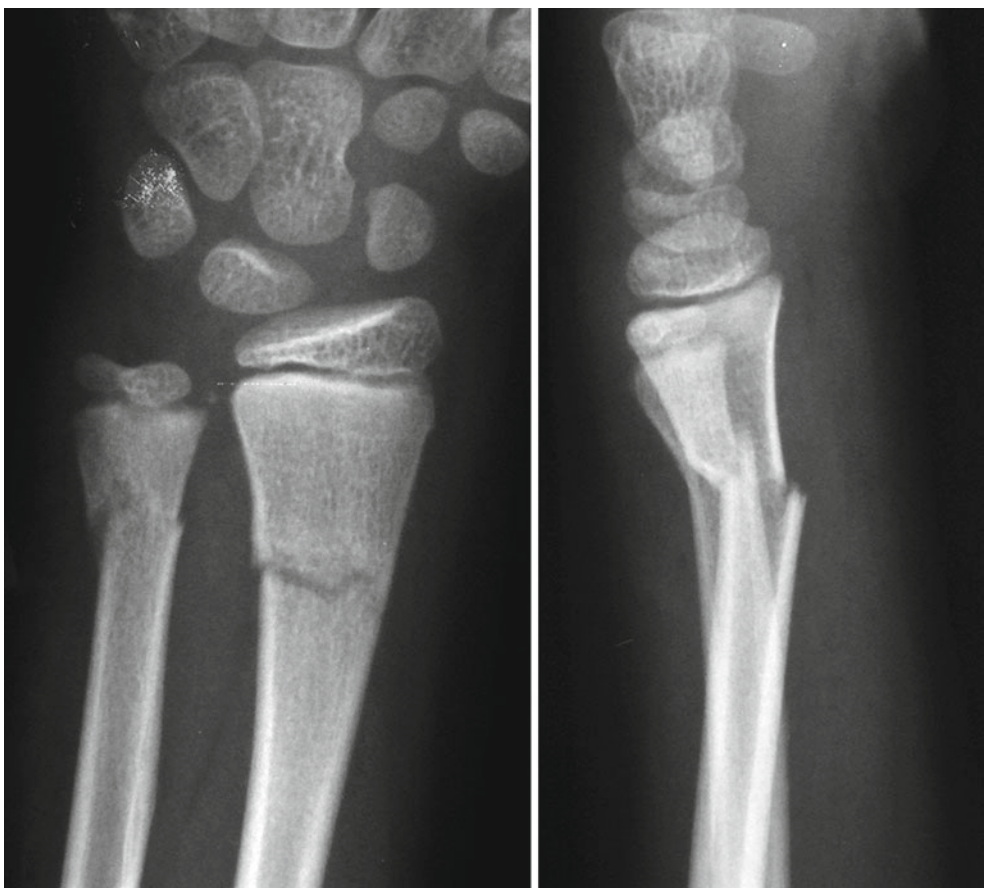

Fig. 9.24 Anteroposterior (*left*) and lateral (*right*) views of the right distal forearm of a child display complete fractures of the distal diaphyses of the radius and of the ulna, with dorsal displacement and angulation of the fragments, leading to the classic "bayonet" deformity. The lateral view is more adequate in estimating the real extent of displacement

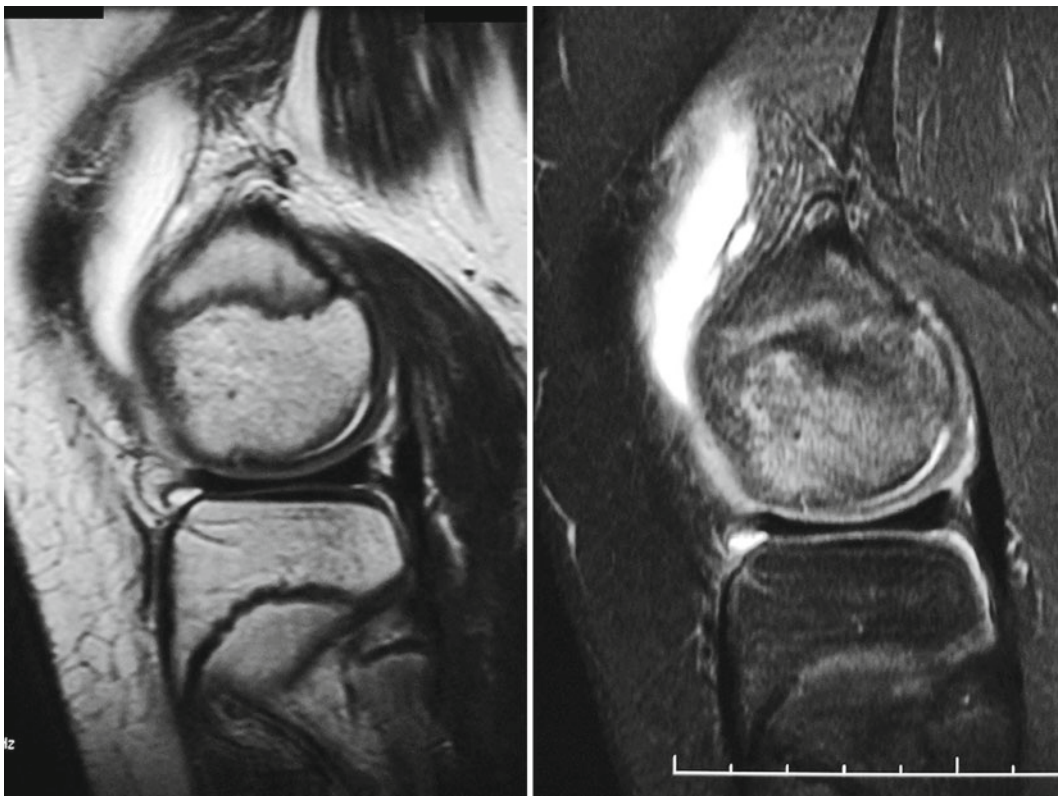

Fig. 9.25 Sagittal T2-WI (*left*) and fat sat PD-WI (*right*) of the left knee of a 13-year-old child at the level of the lateral femoral condyle. There is extensive strip off of the articular cartilage, with fluid in the interface with the subchondral bone, not associated with detachment of cartilaginous fragments. Extensive bone marrow edema pattern is also seen, as well as large joint effusion

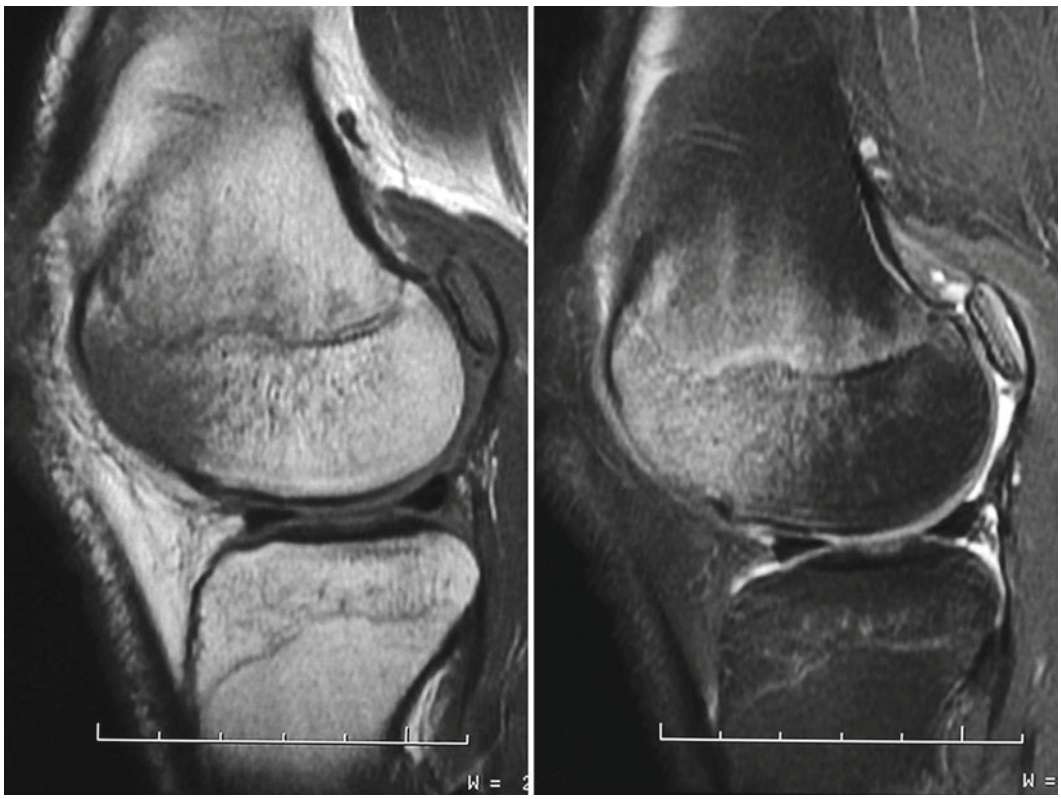

Fig. 9.26 Sagittal T1-WI (*left*) and fat sat PD-WI (*right*) of the right knee of a 17-year-old male with recent trauma evidence detachment of a large cartilaginous fragment from the anterior portion of the medial femoral condyle, with exposure of the subchondral bone and extensive bone marrow edema pattern. The cartilaginous fragment is posterior to the affected condyle and presents signal intensity similar to that of the normal articular cartilage in all sequences

9.3 Pediatric Fractures of the Upper Extremity

The most fractured bone in the shoulder (and in body) is the clavicle, mainly in its middle third (Fig. 9.27). Physeal fractures of the proximal humerus are not common in the pediatric age group, and for the most part are Salter-Harris lesions types I or II. Glenohumeral instability is rare in small children and more frequent in adolescents, presenting as anterior dislocations in more than 90 % of the cases. Classic findings include Hill-Sachs lesion (cortical depression in the posterolateral portion of the humeral head) and Bankart lesion (lesion of the anteroinferior labroligamentous complex, occasionally accompanied by fracture of the adjacent glenoid rim and/or periosteal stripping). MR-arthrography is the preferred imaging method to demonstrate these abnormalities (Fig. 9.28).

The supracondylar fractures and the fractures of the lateral condyle fractures are lesions of the distal humerus that deserve special attention in the pediatric age group. Supracondylar fractures correspond to approximately one-third of the fractures of the extremities in pediatric patients, usually occurring between 5 and 7 years of age. The lateral view is the most important to determine if there is angulation and/or displacement: a line drawn along the anterior cortex of the humerus should intersect the middle third of the capitulum in a normal elbow, but this relation is lost if there is shift – most often posteromedial or posterolateral – of the distal condylar complex (Figs. 9.3 and 9.29). Fractures of the lateral condyle correspond to approximately 20 % of all of fractures of the elbow, occurring more frequently around 4–5 years of life; most lesions are Salter-Harris type IV, following an inferomedial course (Figs. 9.4, 9.7 and 9.30). It may be difficult to distinguish these fractures from joint

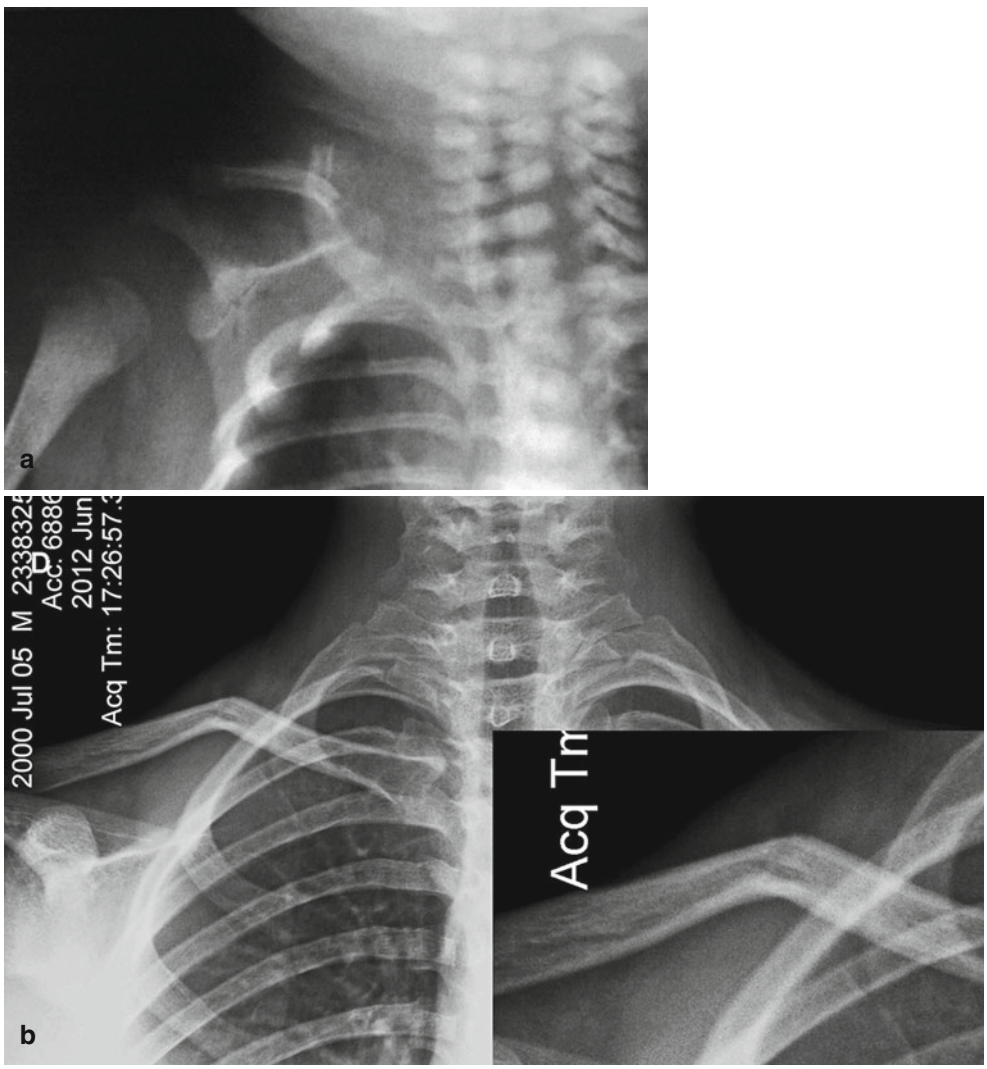

Fig. 9.27 In (**a**), radiograph of a newborn demonstrates complete fracture of the middle third of the right clavicle, with displacement, angulation, and rotation of the medial portion of this bone (birth trauma). In (**b**), radiograph of an 11-year-old child discloses a greenstick fracture of the clavicle, with incomplete cortical disruption in the upper (convex) border and bending of the concave side

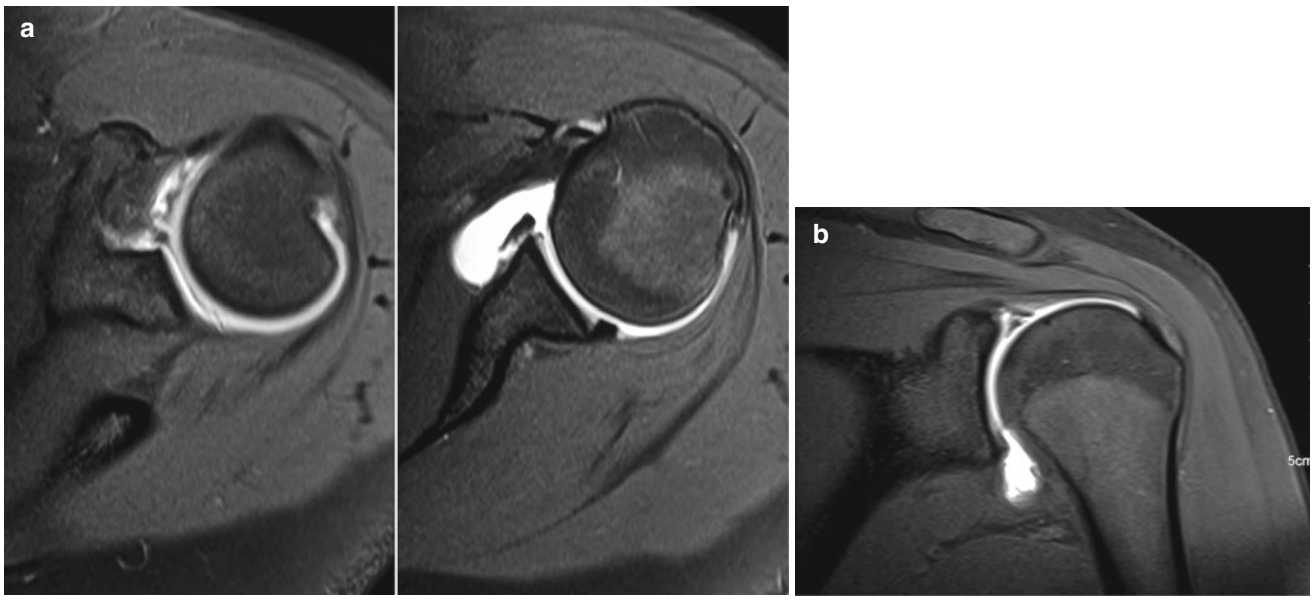

Fig. 9.28 MR-arthrography of the left shoulder of a 16-year-old handball player, performed after an episode of anterior glenohumeral dislocation. Transverse (**a**) and coronal (**b**) fat sat T1-WI demonstrate classic signs of anterior instability, with posterolateral cortical depression of the humeral head (Hill-Sachs lesion) and extensive rupture of the anterior/anterosuperior labrum, as well as avulsion of the adjacent periosteum

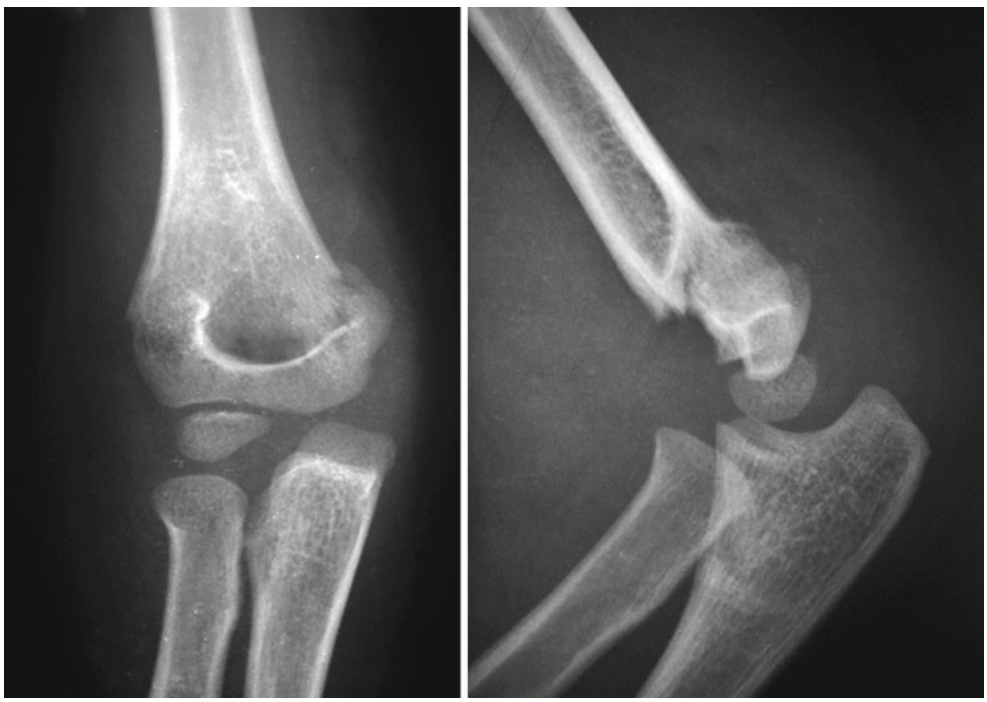

Fig. 9.29 Supracondylar fracture of the humerus. A fracture line is clearly seen in the anteroposterior view, with gross posterior displacement of the distal humerus in the lateral view

dislocations, but in the latter there is loss of the normal relationship between the radial head and the capitulum, which is preserved in fractures. Nonetheless, in small children the capitulum is not yet ossified and radiographic assessment is not feasible, so that MRI and US are useful diagnostic adjuncts in this scenario.

Avulsion of the medial epicondyle is the most important of the avulsion fractures of the ossification centers of the elbow, more prevalent between 7 and 15 years of age; elbow dislocation is associated in up to half of the cases (Figs. 9.8, 9.31, 9.32, and 9.33). The avulsed medial epicondyle may become entrapped within the joint space,

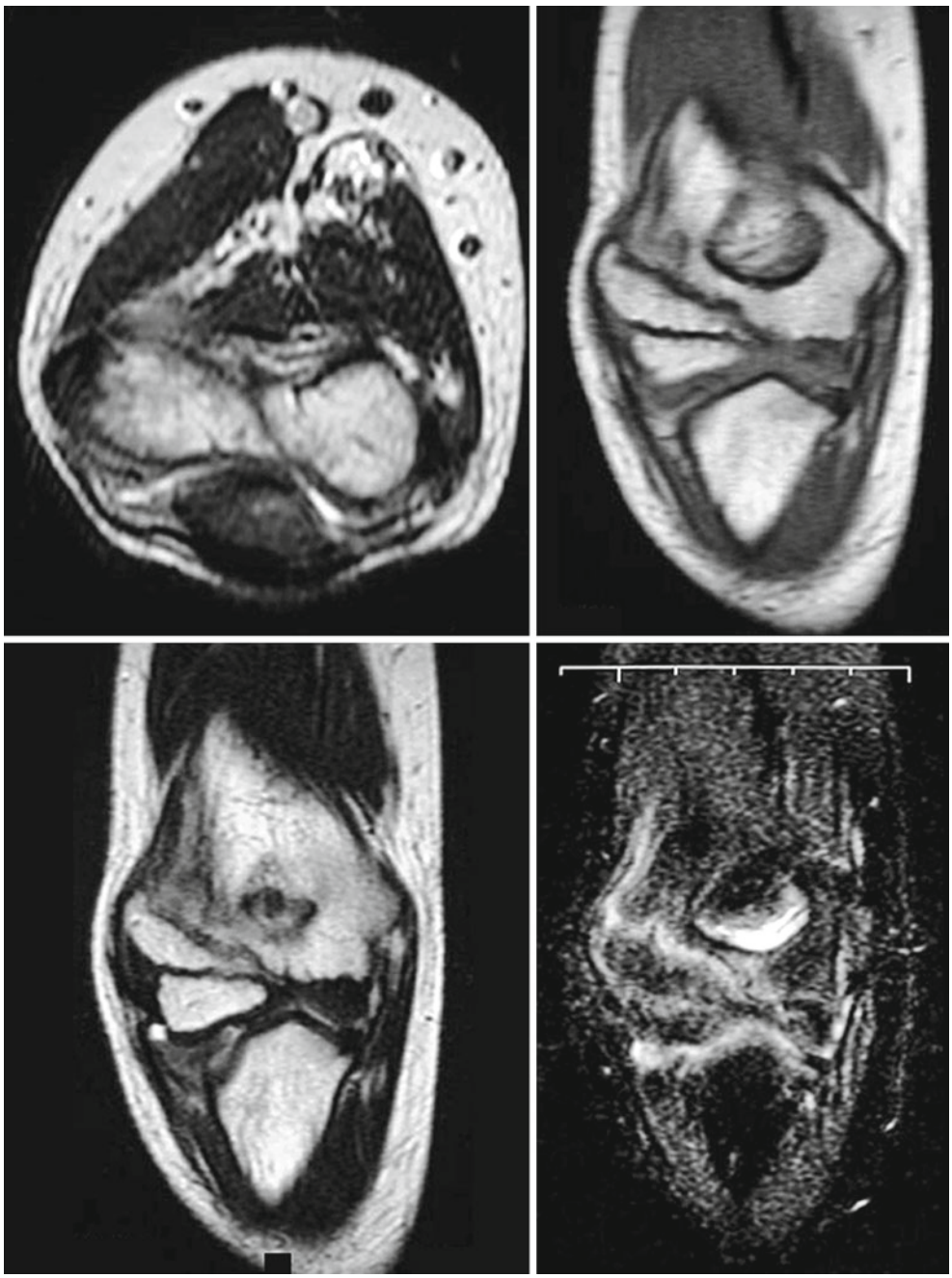

Fig. 9.30 Transverse T2-WI (*upper-left image*) and coronal T1-WI (*upper-right image*), T2-WI (*lower-left image*), and STIR image (*lower-right image*) of the right elbow of a child with a type IV fracture of the lateral condyle of the distal humerus. The fracture line, which is non-displaced and surrounded by bone marrow edema pattern, begins in the lateral cortex of the distal humerus and follows an inferior course, crossing the physis and the non-ossified epiphyseal cartilage

especially if joint dislocation is also present (Fig. 9.32). In small children (under age 6), in whom the ossification center is not yet ossified, radiographs have limited usefulness and intra-articular fragments may appear simply as widening of the medial joint space. US and MRI are often required for proper assessment (Fig. 9.8).

Considering the paired nature of the forearm bones, fracture of one of them is commonly associated with fracture and/or dislocation of the other. Monteggia's fracture, for instance, consists in an association of a fracture of the proximal third of the ulna with dislocation of the radial head (most commonly posterior, which often goes unnoticed), leading to injury of the collateral ligaments of the elbow and of the proximal radioulnar joint (Fig. 9.34). The Galeazzi fracture is a fracture of the distal radius associated with lesion of the distal radioulnar joint. Angulation and displacement are commonly present, leading to radial shortening. In children, there may be separation of the distal ulnar physis instead of injury of the radioulnar joint, a lesion referred to as Galeazzi equivalent.

Fractures of the distal radius are the most common in the pediatric wrist, whether physeal or non-physeal. MRI

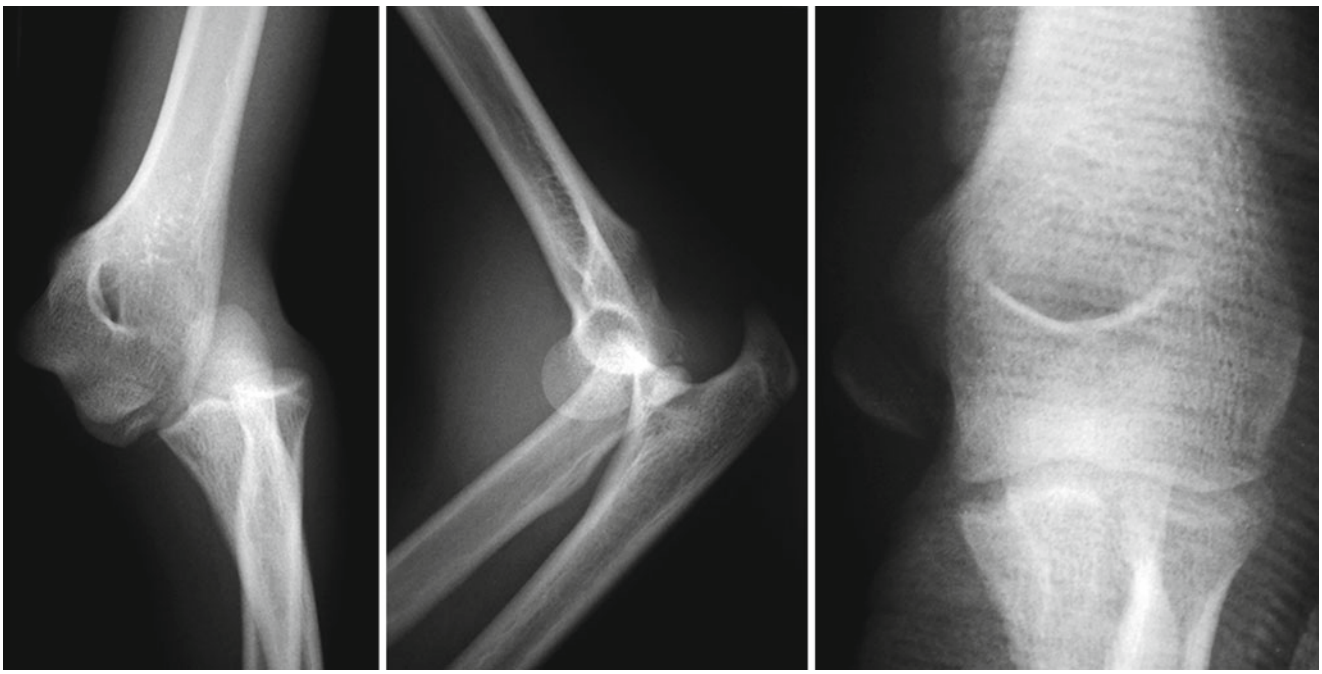

Fig. 9.31 Oblique and lateral radiographs of the left elbow of an adolescent (*left images*) reveal joint dislocation and avulsion of the ossification center of the medial epicondyle, which overlaps the lateral condyle in the *first image* and the coronoid process in the *second one*. The *right image* is an anteroposterior view obtained after reduction that demonstrates the ossification center in its usual position, with obvious physeal widening and subtle bone fragmentation

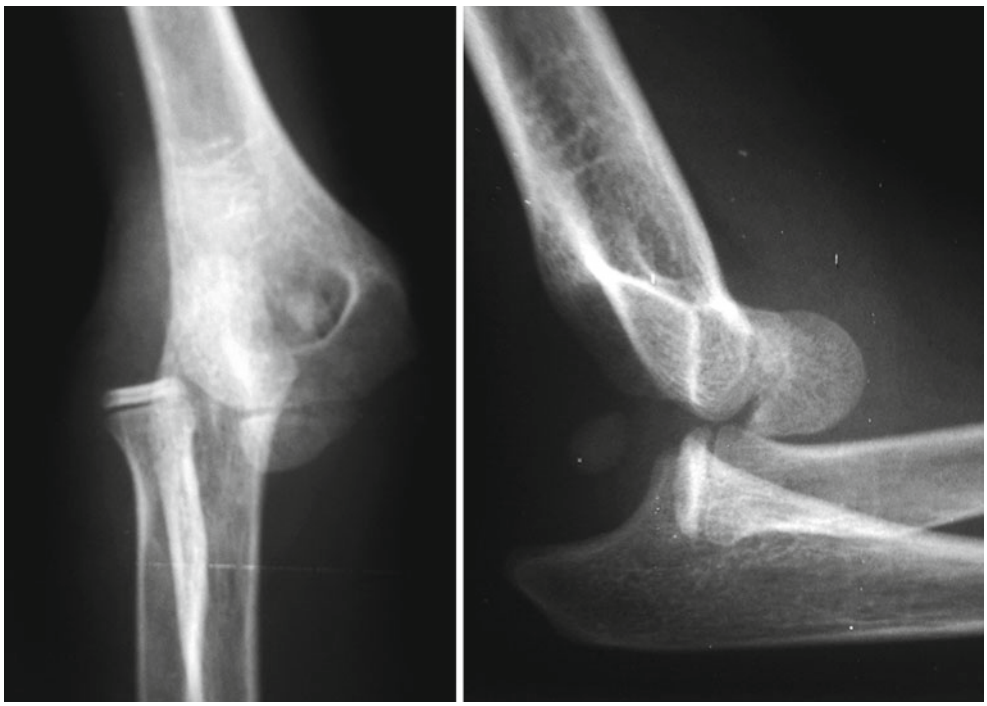

Fig. 9.32 Anteroposterior and lateral radiographs of a child with fracture-dislocation of the right elbow and avulsion of the medial epicondyle. The bone fragment overlies the olecranon fossa in the anteroposterior view, while the lateral view confirms its intra-articular location

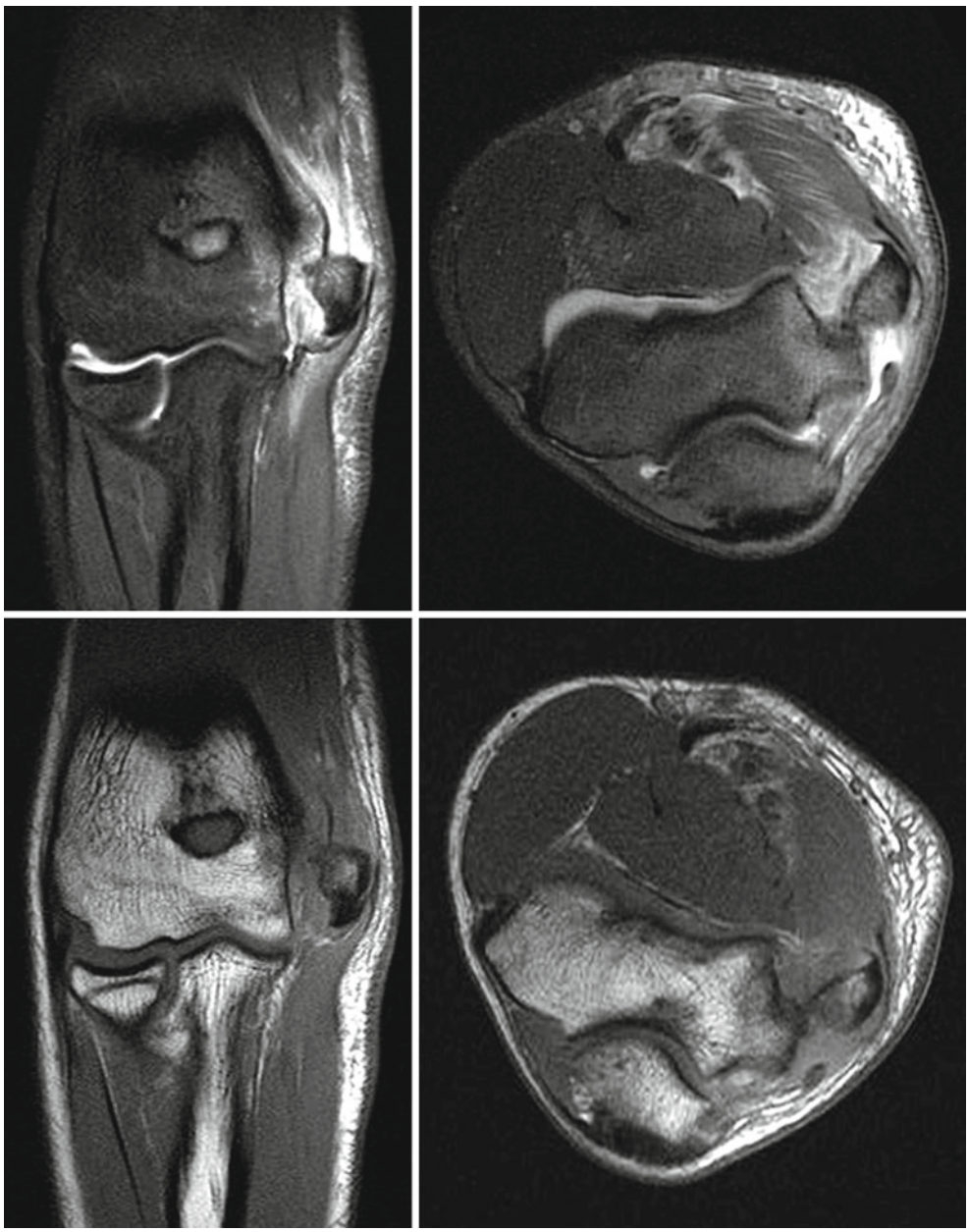

Fig. 9.33 MRI of the right elbow of a child with avulsion of the medial epicondyle, coronal and transverse fat sat T2-WI (*upper row*) and T1-WI (*lower row*). The avulsed ossification center, which presents medial displacement and anterior rotation, is attached to the medial collateral ligament, with edematous changes of the bone marrow and of the soft tissues

is especially valuable to diagnose type I fractures (Fig. 9.35) or to detect associated lesions involving soft-tissue structures, such as the triangular fibrocartilage complex or the intrinsic carpal ligaments. Carpal fractures in skeletally immature patients are relatively rare and difficult to diagnose due to the large cartilaginous component of the carpal bones. The scaphoid is the more vulnerable of them, and fractures of this bone are more frequently non-displaced lesions through the distal third, which affect mostly adolescents between the ages of 12 and 15 years (Fig. 9.36). These fractures are frequently undetectable on radiographs; thus, CT and MRI may be useful in difficult cases and the latter is also valuable to detect complications, such as avascular necrosis.

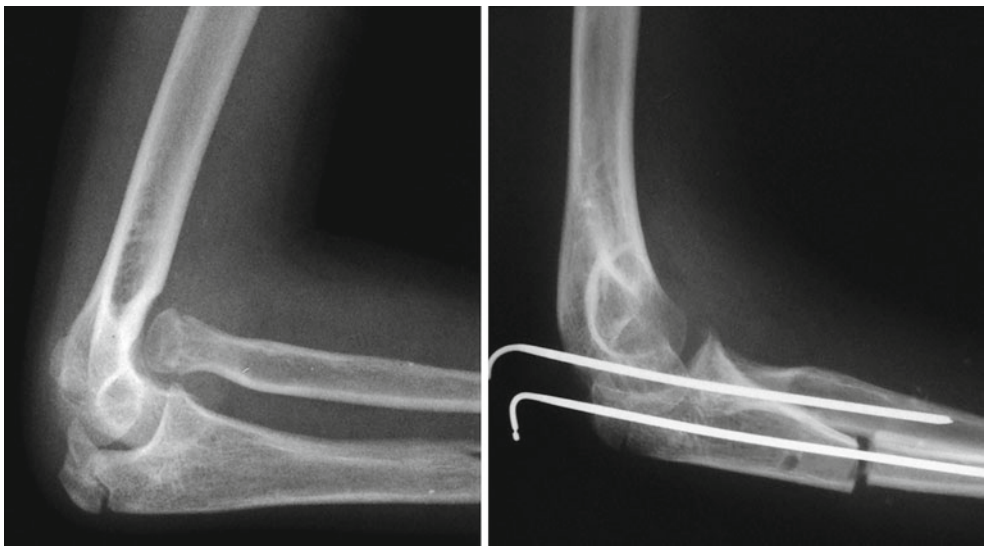

Fig. 9.34 Radiographs of the left elbow and proximal forearm of a patient with Monteggia's fracture performed before (*left*) and after (*right*) surgical correction. It is important to emphasize that the radiograph at left was taken several years after the traumatic event: only the ulnar fracture was diagnosed in the emergency unit and the radial dislocation went unnoticed. There is dislocation of the radial head in the first image, as well as pressure erosion in the anterior cortex of the adjacent humerus, with restoration of its normal relationship with the capitulum in the second image. The fracture of the ulnar diaphysis is partially seen in the first image

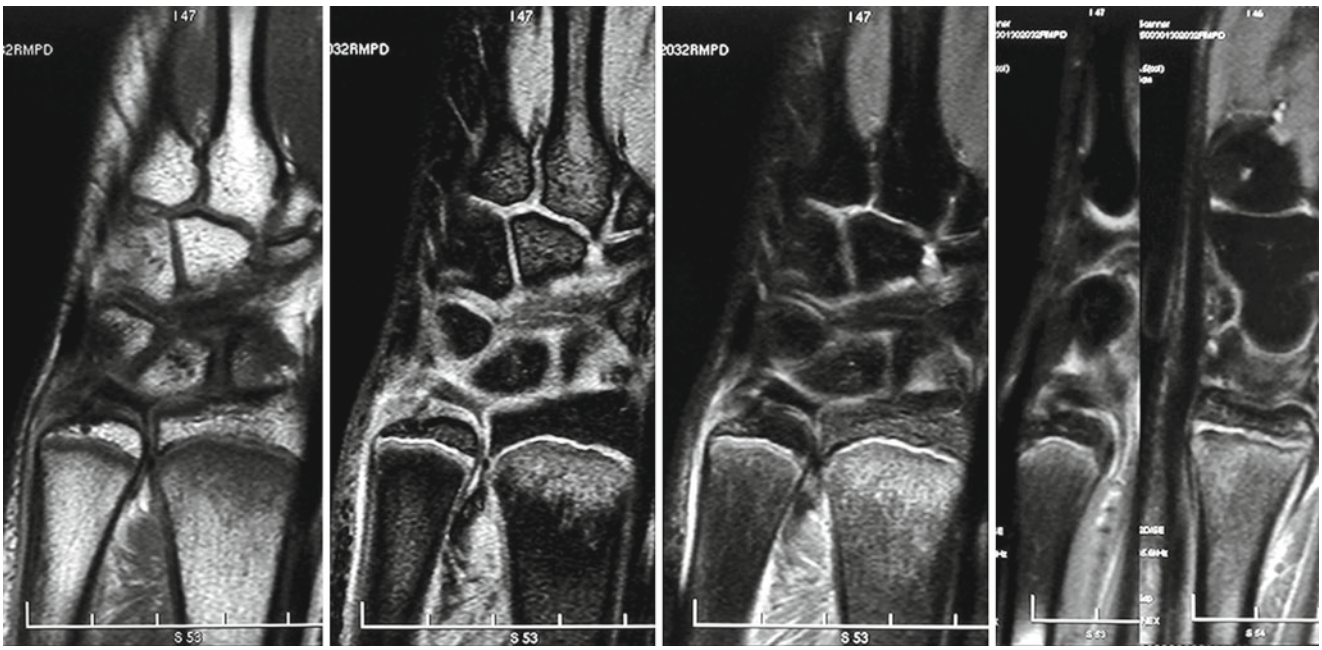

Fig. 9.35 Salter-Harris type I fractures. In the *first two images*, coronal T1-WI and gradient-echo image of the wrist of a 13-year-old patient reveal metaphyseal bone marrow edema of the radius and of the ulna, as well as increased signal intensity in the corresponding physes in the second image. Post-gadolinium fat sat T1-WI in the coronal (*third image*) and sagittal (*fourth image*) planes disclose enhancement of the physes and of the edematous bone marrow. Physeal widening is more evident in the dorsal portion of the radius

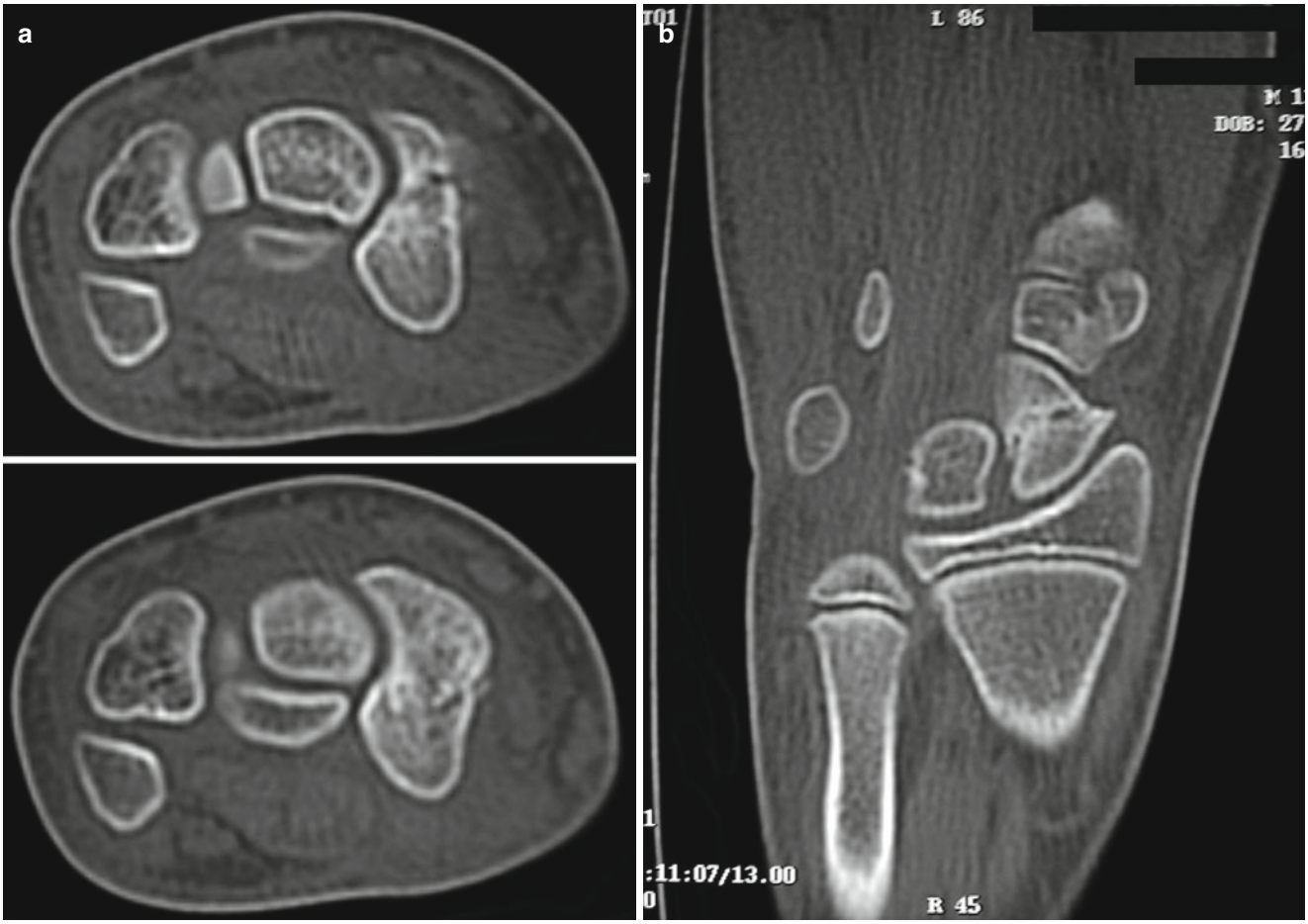

Fig. 9.36 Transverse (**a**) and coronal (**b**) CT images of the right wrist of a 13-year-old male demonstrate a complete fracture of the scaphoid, with subtle proximal migration of the distal fragment, which is partially interposed between the proximal portion of the scaphoid and the lunate bone, more evident in the coronal plane

9.4 Pediatric Fractures of the Lower Extremity

Hip fractures in children are rare, occurring most frequently in the proximal femur (Fig. 9.37). Posterior hip dislocation and acetabular fractures may be associated, and avascular necrosis of the femoral head is a potential complication. Physeal fractures are relatively uncommon in the knees, which for the most part are Salter-Harris type II lesions (Figs. 9.14 and 9.38); nevertheless, depending on the intensity of the traumatic event, any type of physeal fractures may be found (Figs. 9.5, 9.39, and 9.40).

The most frequent physeal fractures of the ankle are Salter-Harris lesions type I or II of the distal fibula, often associated with partial disruption of the lateral ligaments (Figs. 9.10, 9.13, 9.41, and 9.42). Types II and III lesions of the distal tibia are also relatively frequent (Fig. 9.13). Type IV fractures of the ankle are usually complex, resulting from severe traumatic injuries and more common in the tibia (Fig. 9.43). The triplanar fracture of the distal tibia is a lesion with three components, a sagittal one (coursing through the epiphysis), a horizontal one (through the physis), and a coronal one (through the metaphysis) (Fig. 9.1); CT is especially useful for accurate assessment of complex fractures like this one.

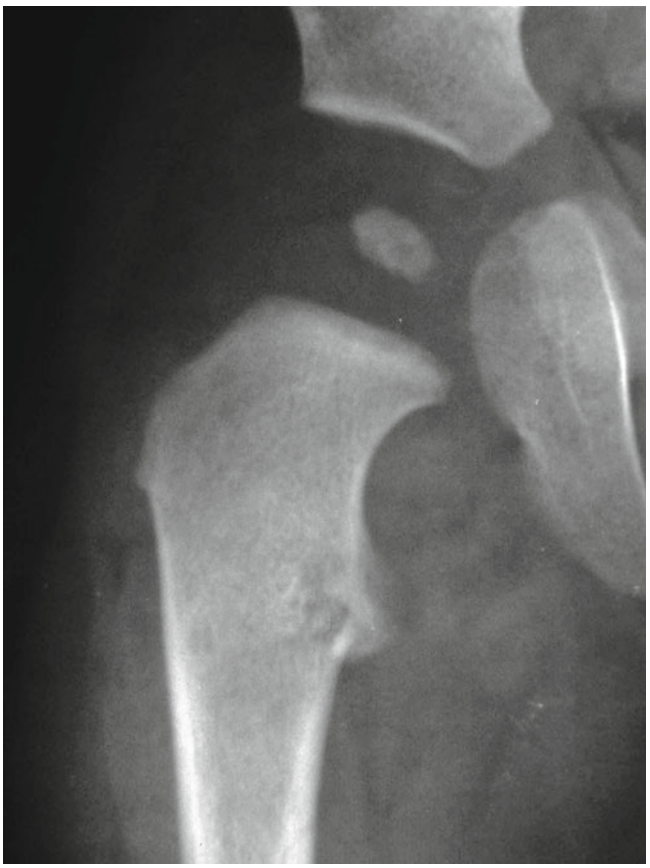

Fig. 9.37 Anteroposterior view of the right hip of a child with a trochanteric fracture of the femur. Pediatric fractures of the proximal femur are rare and usually evident on radiographs.

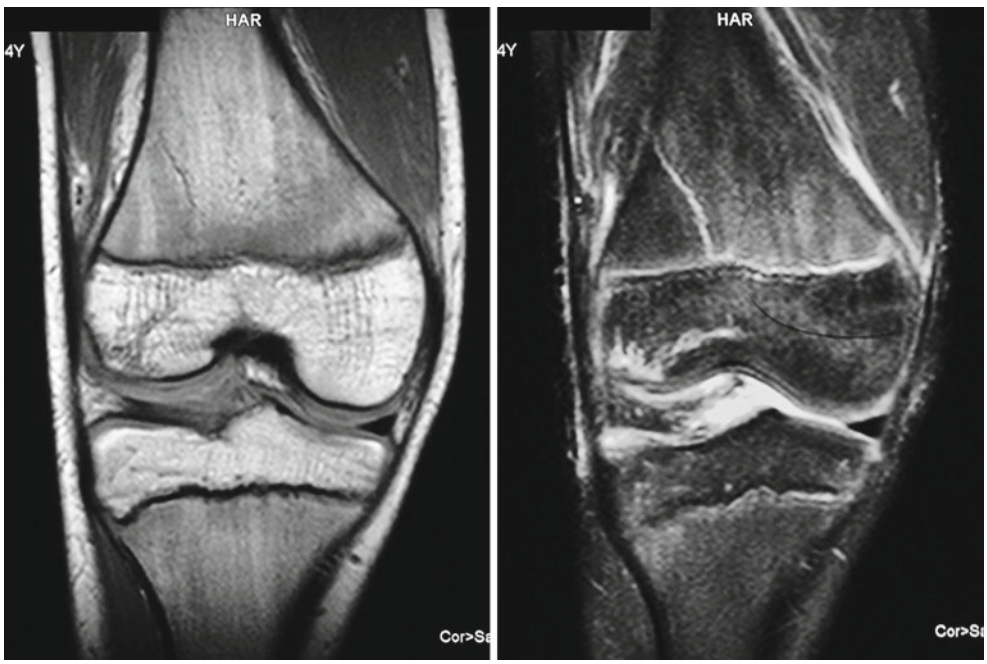

Fig. 9.38 MRI of the left knee of a 14-year-old patient with a Salter-Harris type II fracture of the distal femur. Coronal T1-WI (*left*) and fat sat T2-WI (*right*) disclose an oblique fracture line across the femoral metaphysis, extending from the lateral cortex to the physis. There is obvious physeal widening, medial to the metaphyseal fracture line, representing the horizontal component of the lesion. A subchondral bone bruise is seen on the lateral femoral condyle

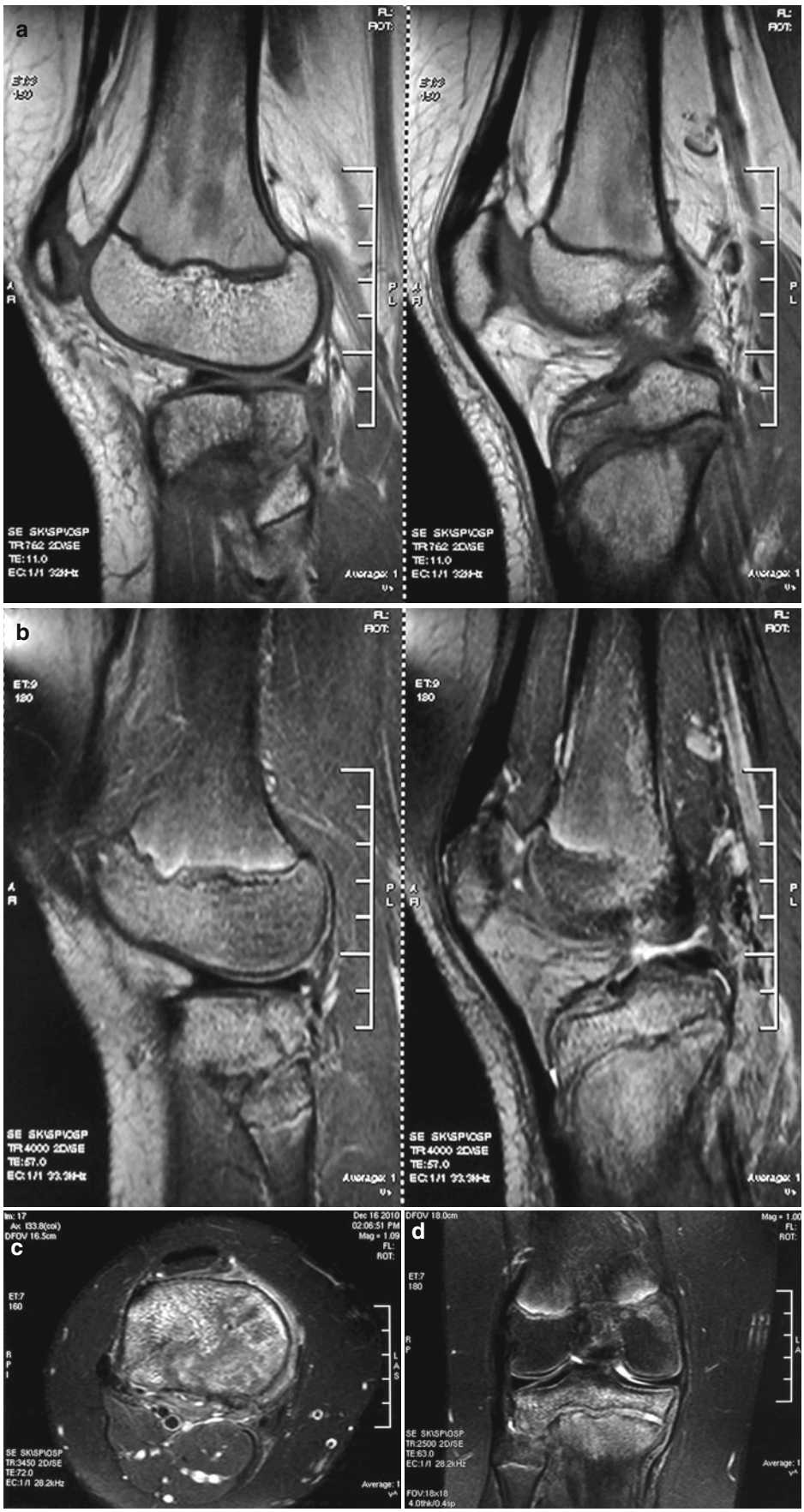

Fig. 9.39 Salter-Harris fracture type III of the proximal tibia. Sagittal T1-WI (**a**) and fat sat T2-WI in the sagittal (**b**), transverse (**c**), and coronal (**d**) planes demonstrate physeal widening associated with a vertical fracture of the tibial epiphysis, in its lateral portion. There is extensive bone marrow edema pattern in the tibial epiphysis and in the metaphysis

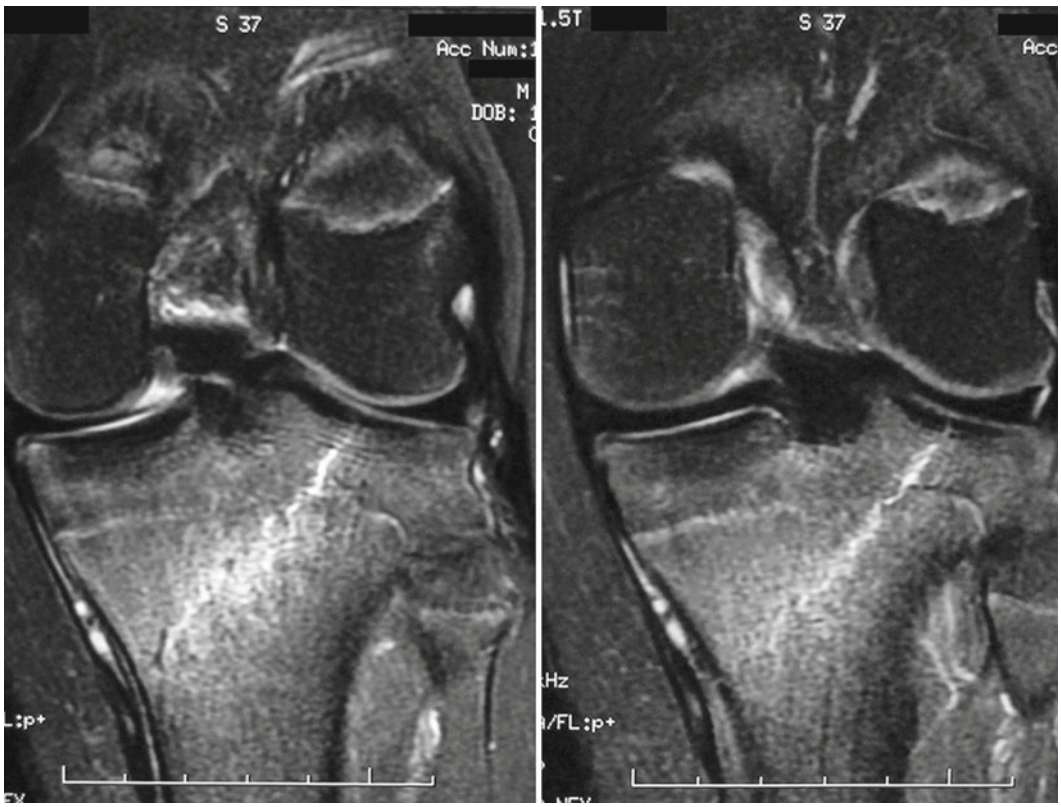

Fig. 9.40 Coronal fat sat T2-WI of the left knee disclose a Salter-Harris fracture type IV of the proximal tibia involving the physis and the epiphysis, extending from the proximal metadiaphysis to the articular surface of the lateral plateau. The fracture line is hyperintense, surrounded by bone marrow edema

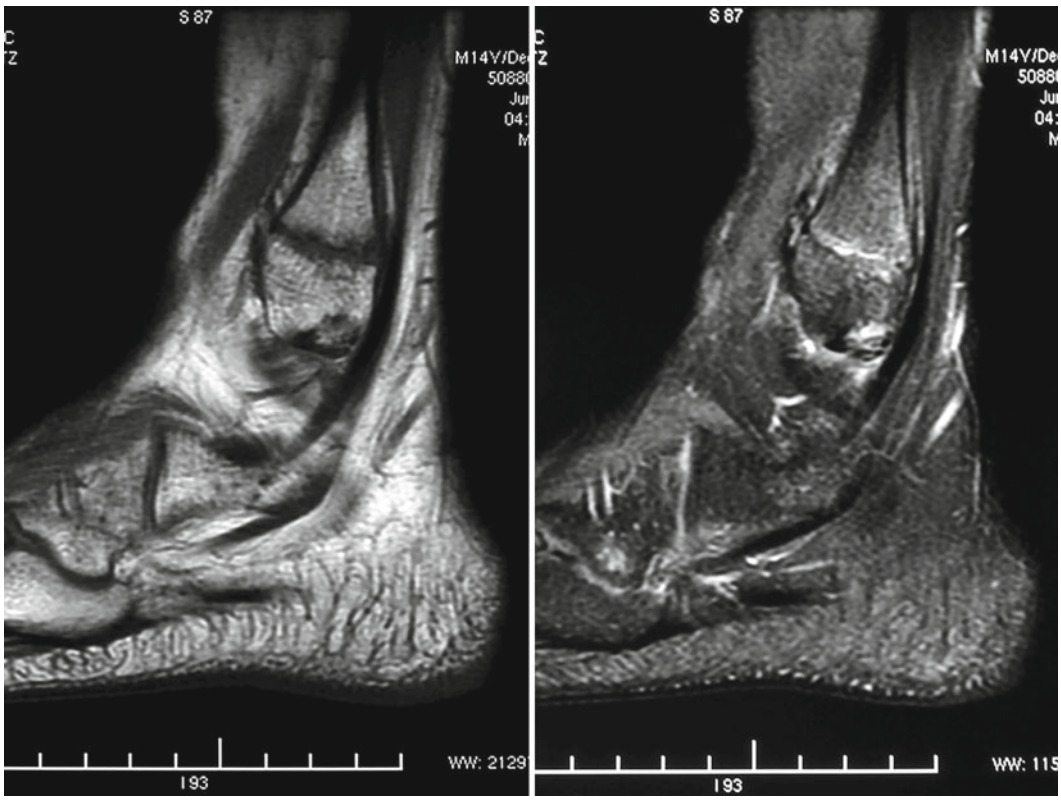

Fig. 9.41 Salter-Harris fracture type I of the distal fibula. Sagittal T1-WI (*left*) and fat sat PD-WI (*right*) of a 14-year-old patient reveal physeal widening (more evident on T1-WI) and edematous changes of the physis and of the adjacent bone marrow (more evident on fat sat PD-WI)

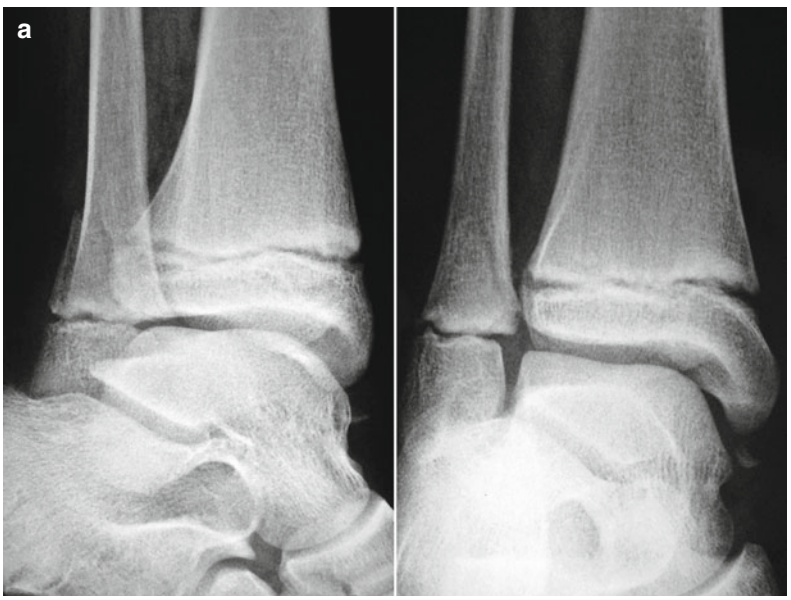

Fig. 9.42 Salter-Harris fracture type II of the distal fibula in an 11-year-old child. Even though a physeal/metaphyseal fracture line is quite evident on oblique views of the ankle (**a**), sagittal T1-WI (**b**, *left*) and fat sat PD-WI (**b**, *right*) demonstrate additional findings, such as marked soft-tissue edema and bone marrow edema pattern

Fig. 9.42 (continued)

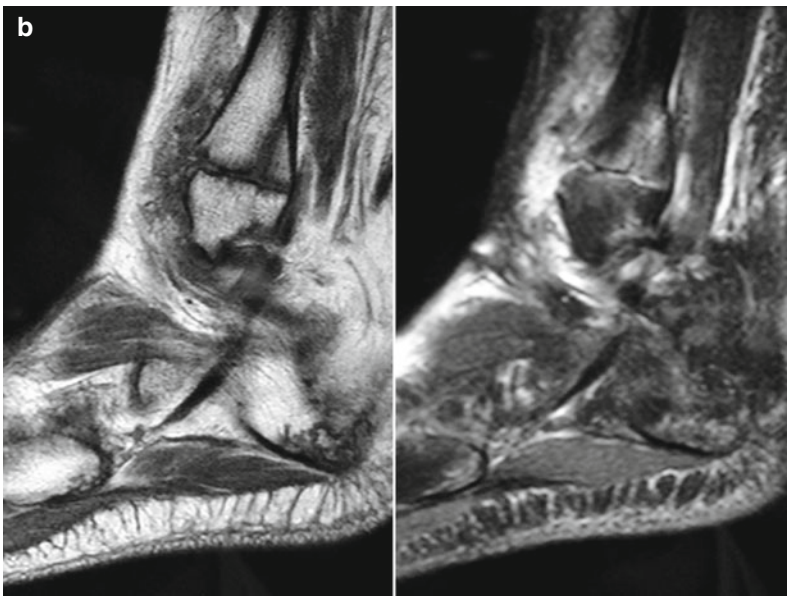

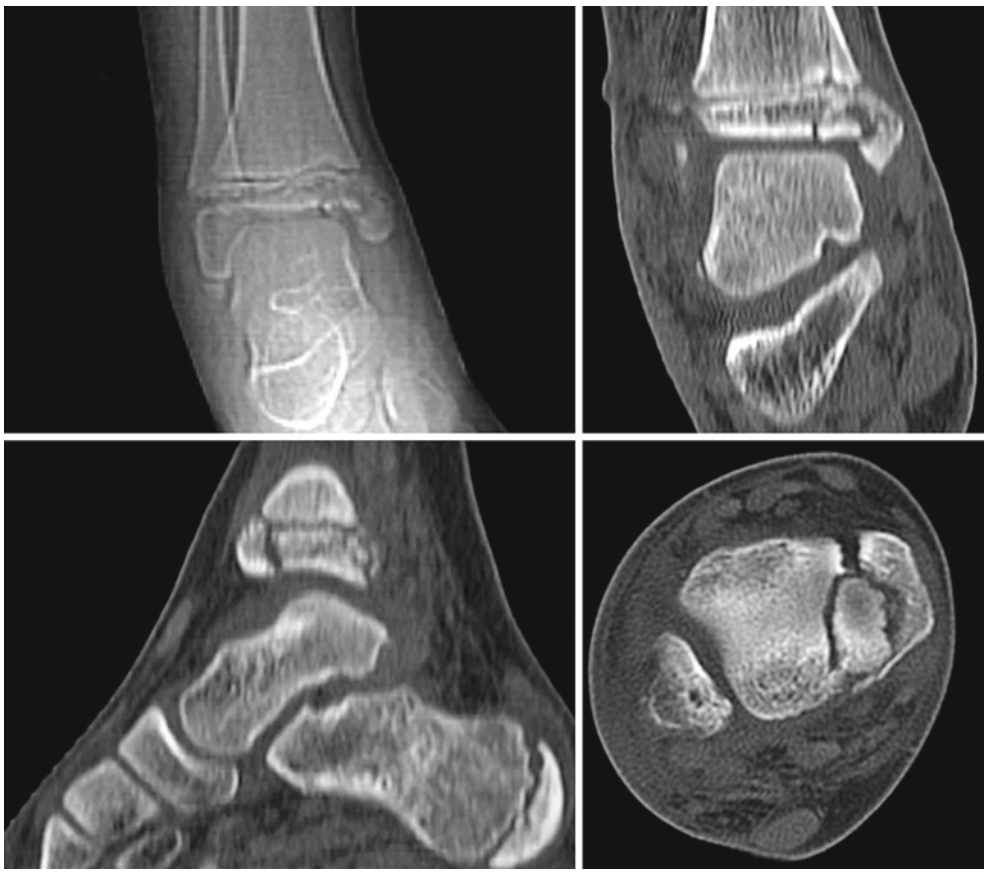

Fig. 9.43 CT scout view (*upper-left image*), reformatted images in the coronal (*upper-right image*) and sagittal (*lower-left image*) planes, and a transverse image (*lower-right image*) of the right ankle of a child who sustained a recent traumatic injury. There is a complex Salter-Harris fracture type IV involving the metaphysis, the physis, and the epiphysis of the tibia, in addition to a fracture of the medial malleolus. CT images are more accurate to demonstrate the real extent of complex fractures like this one

9.5 Traumatic Lesions of the Soft Tissues

Traumatic lesions of the soft tissues in skeletally immature patients are similar to that found in adults on imaging studies. Acute tendon injuries are less frequent and usually less severe in the pediatric group age (Fig. 9.44). Muscle lesions vary from mild strains to high-grade tears. Strains appear on MRI as edematous areas in the affected muscle belly, mostly in the myotendinous junction (Fig. 9.45), while muscle tears present discontinuity of the muscle fibers, either partial or complete, with a hematoma filling the resulting gap. On US, the affected muscle appears heterogeneous, with loss of the normal fibrillar pattern; hypoechogenic material is seen filling muscle tears (Fig. 9.46). Ligaments are more elastic in children and sprains are common, especially in the ankle (Fig. 9.47). Ligament injuries of the knees are relatively infrequent in the pediatric population; however, anterior cruciate ligament (ACL) tears have become more frequent in the last decades as more children and adolescents became engaged in sports practice (Fig. 9.48). In younger children, lesions of the ACL usually involve avulsion of a bone fragment in the tibial insertion (Fig. 9.49). Meniscal tears have also been increasingly reported in skeletally immature patients, and their imaging appearance is similar to that described for adults (Figs. 9.50 and 9.51). Nonetheless, it must be kept in mind that peripheral, transversely oriented linear areas of increased signal intensity in the meniscal substance are common and deprived of significance, probably representing normal vascularity.

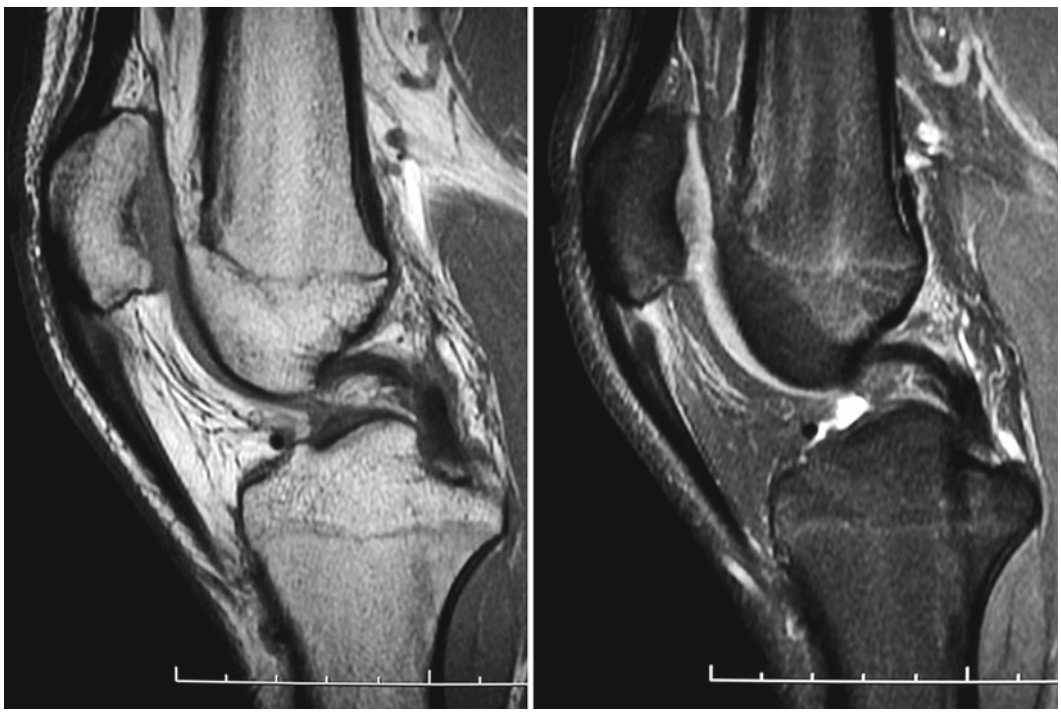

Fig. 9.44 MRI of the right knee of a 16-year-old patient with acute infrapatellar pain during a soccer match. Sagittal T1-WI (*left*) and fat sat PD-WI (*right*) reveal a partial tear of the patellar tendon – which is thickened and heterogeneous – adjacent to its origin, with edema of the Hoffa fat pad and of the bone marrow of the inferior pole of the patella

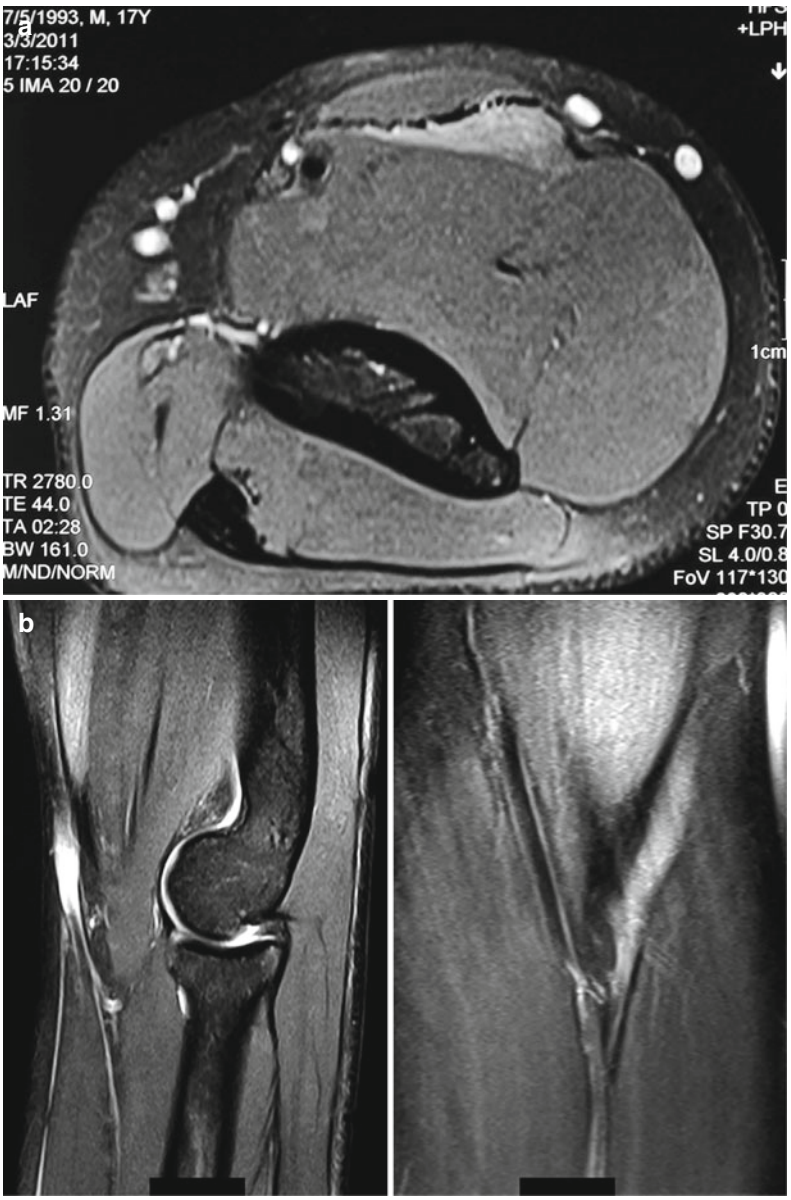

Fig. 9.45 Fat sat PD-WI in the transverse (**a**), sagittal (**b**, *left*), and coronal (**b**, *right*) planes demonstrate edema of the muscle fibers in the distal myotendineous junction of the brachial biceps of a 17-year-old patient, without muscle tear or intramuscular collections, representing a muscle sprain

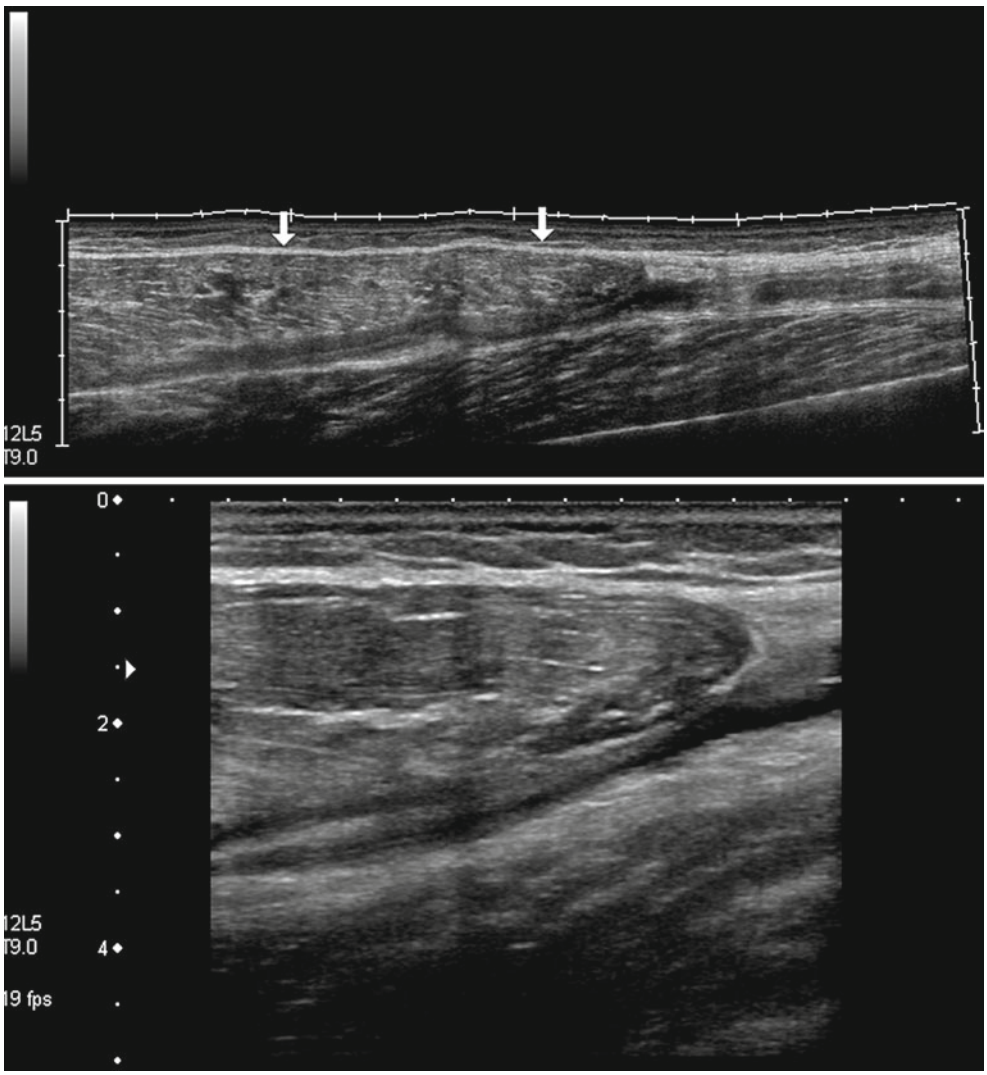

Fig. 9.46 Adolescent with acute pain in the anterior aspect of the right thigh after trauma during a soccer match. The upper image is a longitudinal US scan with extended field of view that demonstrates a complete tear of the rectus femoris, with superior retraction (*arrows*). In the lower image, the inferior portion of the retracted muscle belly is shown in higher detail, with fluid interposed between it and the vastus intermedius

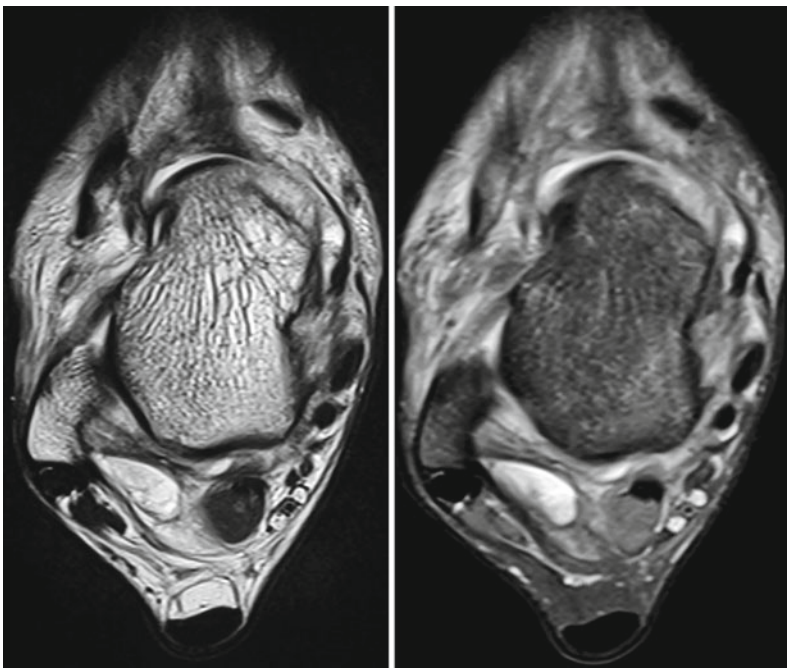

Fig. 9.47 A 15-year-old patient with acute sprain of the right ankle. Transverse T2-WI (*left*) and fat sat PD-WI (*right*) display thickening and heterogeneous signal intensity of the anterior talofibular ligament, without discontinuity of its fibers. Marked edema of the periarticular soft tissues is also seen, as well as joint effusion and fluid in the tendon sheaths

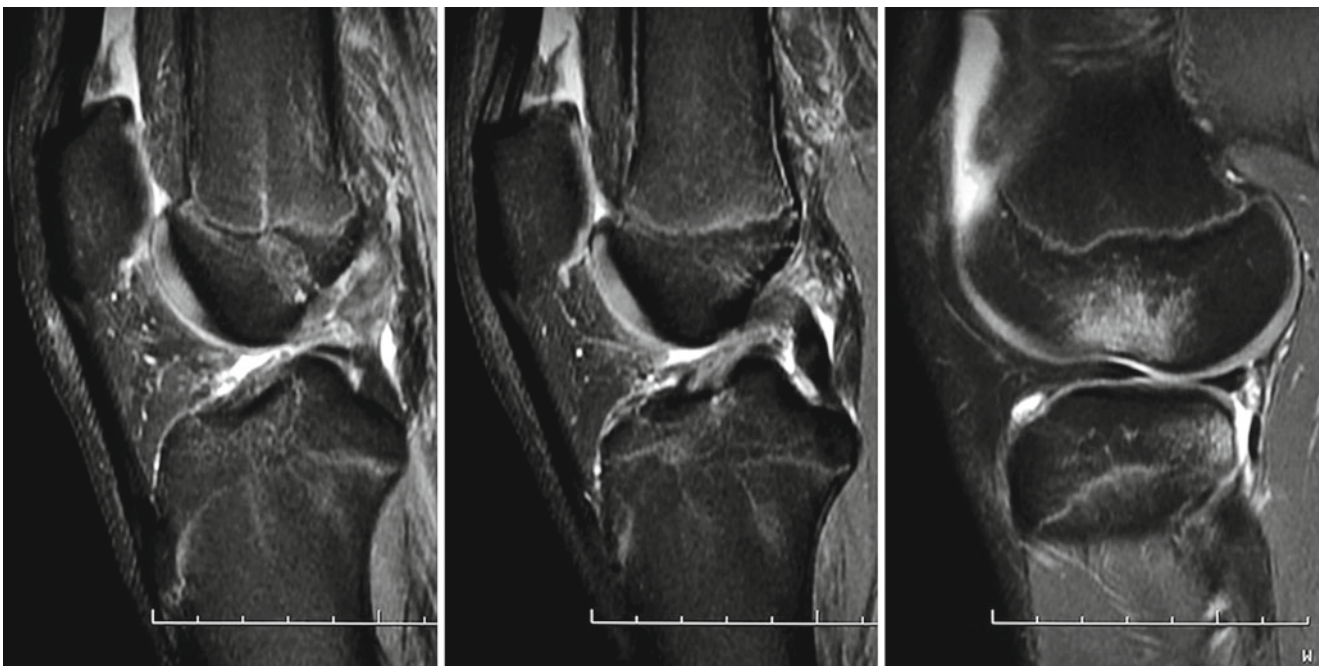

Fig. 9.48 A 16-year-old male seen after knee trauma during a basketball match. Sagittal fat sat PD-WI reveal signs of anterior cruciate ligament tear, including moderate joint effusion, absent visualization of the ligament fibers, typical bone bruises in the lateral femoral condyle and in the lateral tibial plateau, and anterior translation of the tibia. These findings are quite similar to those seen in injuries of the anterior cruciate ligament in adult patients

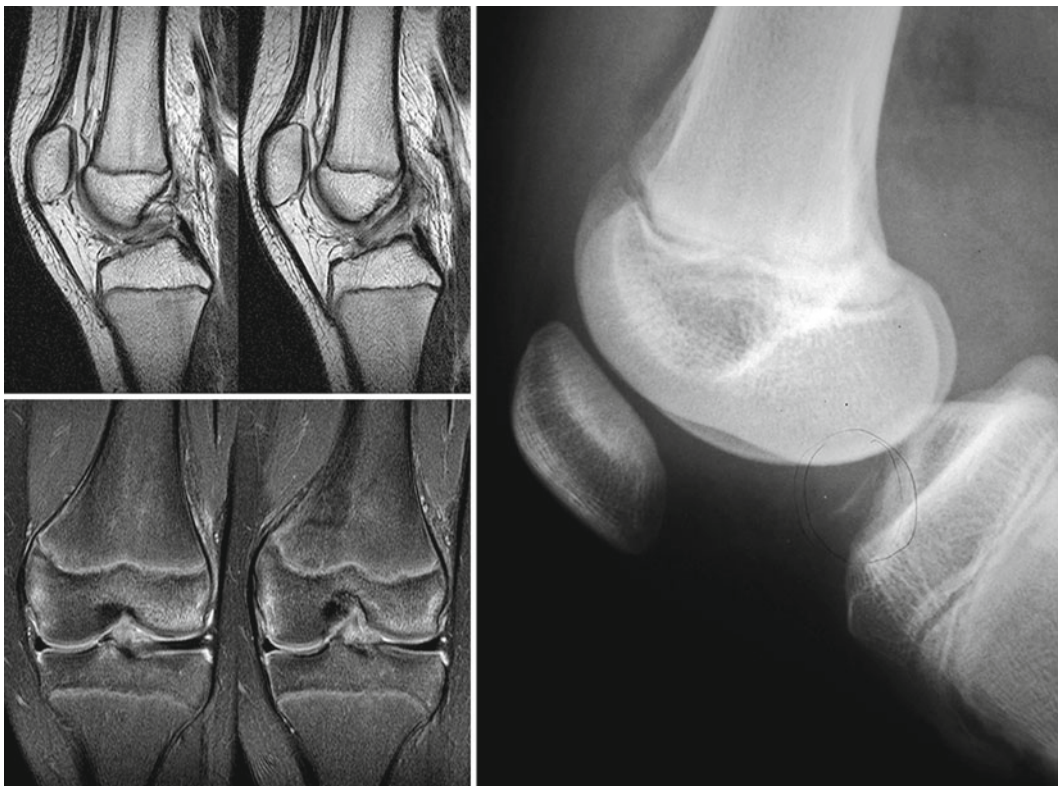

Fig. 9.49 Young child with left knee trauma and clinical evidence of joint instability. At *left*, sagittal T2-WI (*upper row*) and coronal fat sat PD-WI (*lower row*) reveal an intact anterior cruciate ligament. Nonetheless, its tibial insertion is ill-defined, with adjacent bone marrow edema suggesting bone avulsion; subchondral bone marrow edema pattern is also present in the lateral femoral condyle. At *right*, lateral view clearly demonstrates the suspected bone avulsion in the tibial insertion of the anterior cruciate ligament

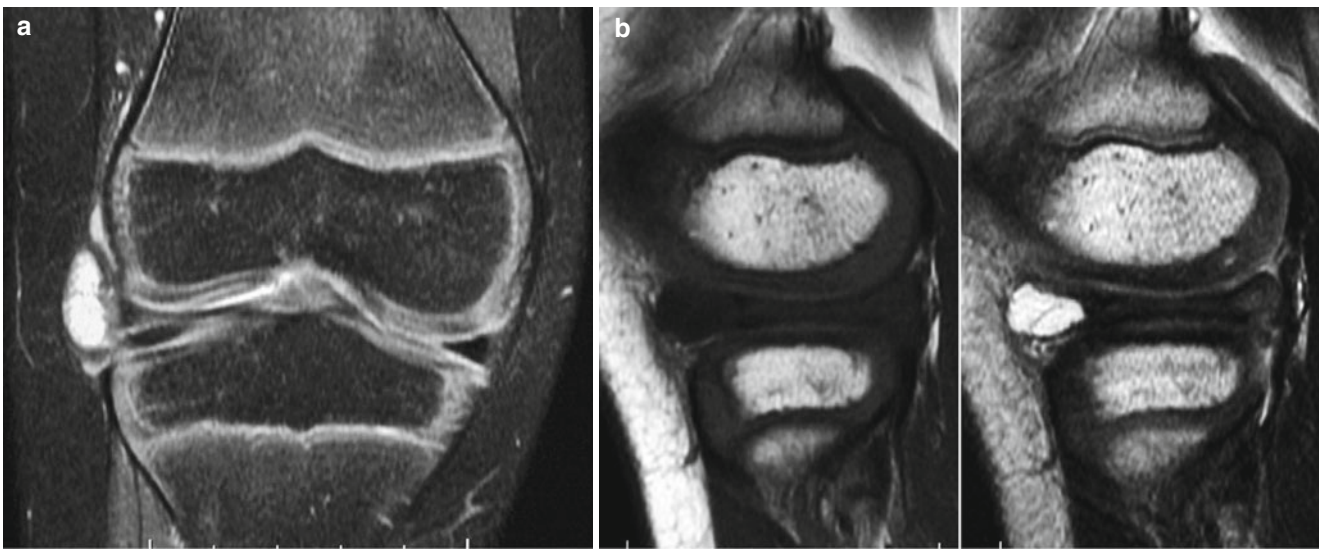

Fig. 9.50 A 6-year-old male with chronic pain in his right knee. Coronal fat sat PD-WI (**a**) and sagittal T1-WI and T2-WI (**b**) disclose a transverse tear across the whole extension of the medial meniscus, with a loculated parameniscal cyst protruding anteriorly and medially. Despite the young age of the child, imaging findings are identical to those of similar lesions seen in adults

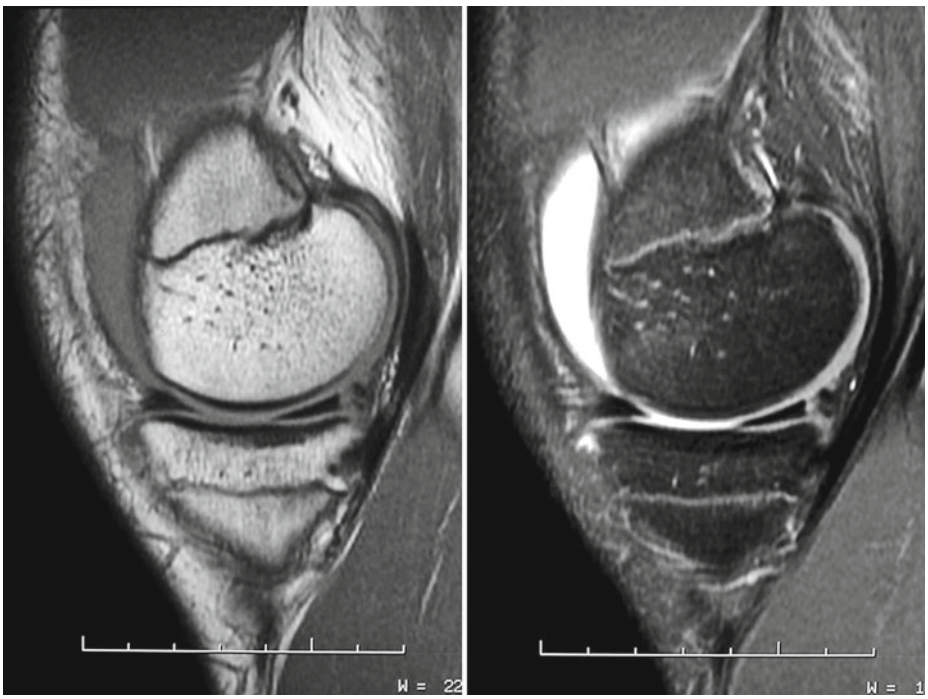

Fig. 9.51 Sagittal T1-WI (*left*) and fat sat PD-WI (*right*) of the right knee of a 16-year-old male. There is a vertically oriented full-thickness peripheral tear of the posterior horn of the medial meniscus. Criteria used to diagnose meniscal lesions in children and adults are essentially the same

9.6 Non-accidental Trauma

Physical abuse is a significant cause of morbidity and mortality in the pediatric population, leading to multisystemic abnormalities that include the musculoskeletal system. It is not infrequent for imaging findings to be the first clues to physical abuse, and some patterns of lesion are characteristic enough to suggest the diagnosis. Nevertheless, communication between the radiologist and the attending physician is paramount in order to include child abuse in the differential diagnosis of pediatric trauma, considering all the legal implications. Inexplicable delay in seeking medical attention, inconsistent clinical history, and discrepancy between the severity of the imaging findings and the informed type of lesion are suspicious signs. More than half of all patients will present evidence of skeletal trauma, even though fractures rarely pose a threat to life in abused children.

Radiographs and bone scintigraphy are the most important imaging studies in the investigation of child abuse. The skeletal radiographic survey is a fundamental screening study, as it investigates each anatomic site separately, including the axial and the appendicular skeleton. An additional survey performed 14 days later may disclose periosteal neoformation and fractures that were not evident previously. Radiographs are able to distinguish recent lesions from old fractures, an important feature as injuries are recurrent in these patients. The overwhelming majority of the fractures in abused children occur before 18 months of life, while most of the accidental osteoarticular lesions take place after age 5. Bone scintigraphy can evidence even subtle fractures or areas of periosteal detachment, but it is limited to demonstrate the classic metaphyseal lesions (see below) or skull fractures. The role of CT in musculoskeletal evaluation of child abuse is limited and it is mostly used as an adjunct to clarify equivocal radiographic findings. MRI and US are only exceptionally used and do not have an established role in this context.

The most important radiographic findings include multiple fractures in different stages of healing, old fractures left untreated (with hypertrophic callus and lack of consolidation), and several areas of periosteal apposition in the metaphyses of the long bones (related to posttraumatic bleeding) (Figs. 9.52 and 9.53). Even though there are no pathognomonic lesions, some patterns of lesion present a high degree of specificity for child abuse. Multiple rib fractures, for instance, mainly when bilateral and symmetric, are very suggestive. The classic metaphyseal lesion (corner fracture) is also highly specific in small children: it is a peripheral fracture of the metaphysis, with a triangular or bucket-handle appearance, representing avulsion of the periosteum and of the immature bone (Fig. 9.53). Corner fractures are more common in the long bones around the shoulders, knees, and ankles. Diaphyseal fractures of the long bones are the most common fractures in physically abused children; spiral or oblique diaphyseal fractures in children with less than 1 year of age present a higher degree of specificity (Fig. 9.53). Epiphyseal separations are strongly associated with child abuse, notably in the distal humerus (Fig. 9.53), even though Salter-Harris fractures are relatively uncommon. Scapular and sternal lesions in small children should also be considered secondary to non-accidental trauma unless proven otherwise (Fig. 9.52). Compressive fractures of the vertebral bodies are more common in the thoracolumbar transition, and fractures of the spinous processes are also very suggestive. In skull fractures, evidence of high-energy traumatic injuries without a compatible clinical history must raise the possibility of physical abuse (Fig. 9.53). The most important condition to be considered in the differential diagnosis is osteogenesis imperfecta, in which, in addition to multiple fractures, there are marked osteoporosis and a larger than usual number of Wormian bones. The clinical history, the physical examination, and a careful analysis of the radiographs usually allow safe differentiation between osteogenesis imperfecta and child abuse.

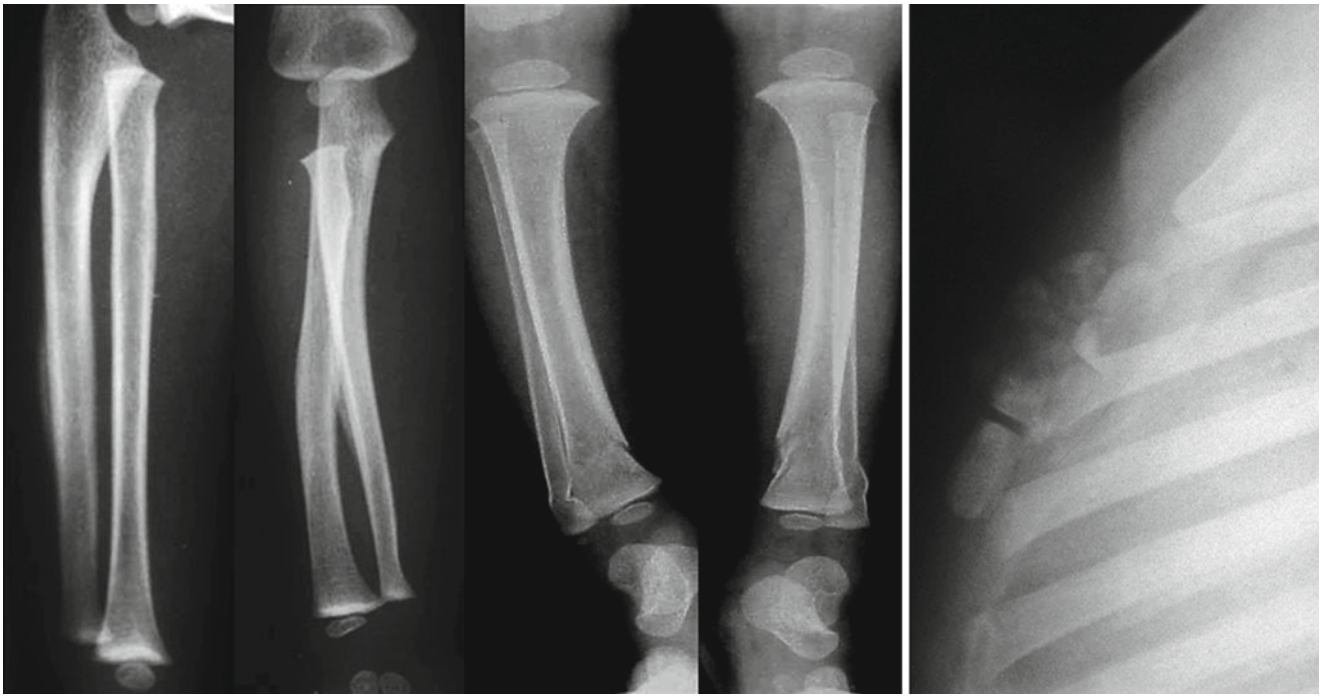

Fig. 9.52 Radiographic findings in two children victims of physical abuse. At *left*, radiographs of the forearms and of the legs display focal areas of periosteal reaction in the mid-diaphyses of the right ulna and of the left radius, with symmetric and bilateral fractures of the distal diaphyses of the tibiae and fibulae. At *right*, lateral view discloses a destructive lesion of the body of the sternum, with ill-defined borders, bone fragmentation, and anterior displacement of its lower portion, related to osteomyelitis (the child was victim of recurrent burns on the anterior portion of the chest, intentionally caused by lit cigarettes)

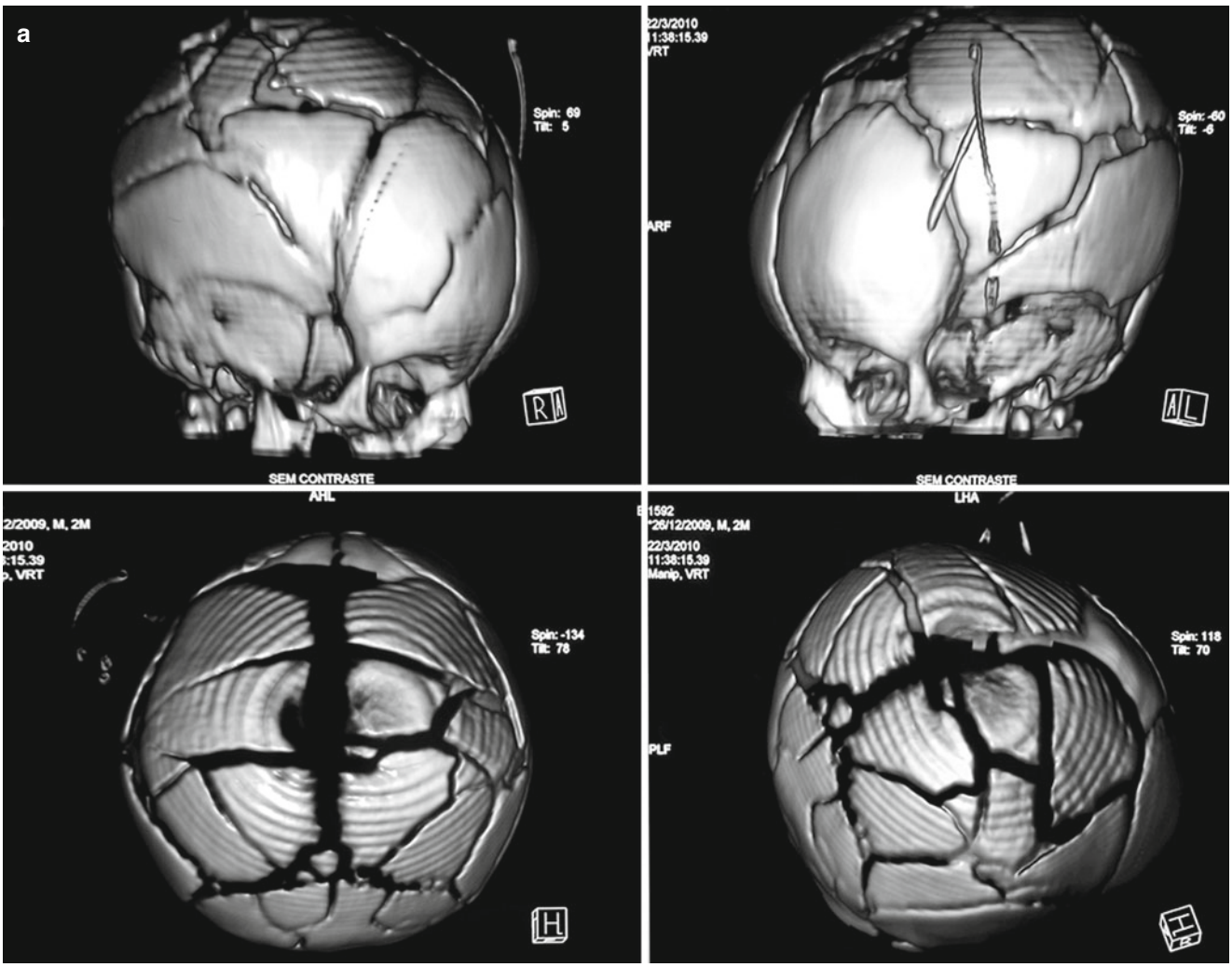

Fig. 9.53 A 2-month-old child admitted to the intensive care unit victim of physical abuse. In (**a**), volume-rendered CT reconstructions demonstrate a complex, multi-fragmented skull fracture that was associated with bilateral subdural collections and brain contusions (not shown). In (**b**), radiographs of the upper limbs of the same child disclose multiple fractures in different stages of healing: spiral diaphyseal fractures of the bones of the left forearm and a transverse fracture of diaphysis of the homolateral humerus (which presents diastasis, angulation, and fragmentation) can be seen, as well as a homolateral supracondylar fracture. There is a complete fracture with gross displacement of the distal portion of the right humerus, as well as thick periosteal reaction in the diaphysis. The distal portion of the right forearm is seen in further detail in (**c**): this image reveals subtle corner fractures in the radius and in the ulna, more evident in the former, in which there is also an incomplete metaphyseal fracture associated with mild bowing (Courtesy of Dr. Marcelo Ricardo Canuto Natal, Hospital de Base do Distrito Federal and Pasteur Medicina Diagnostica – Diagnósticos da America S.A., Brasilia, Brazil)

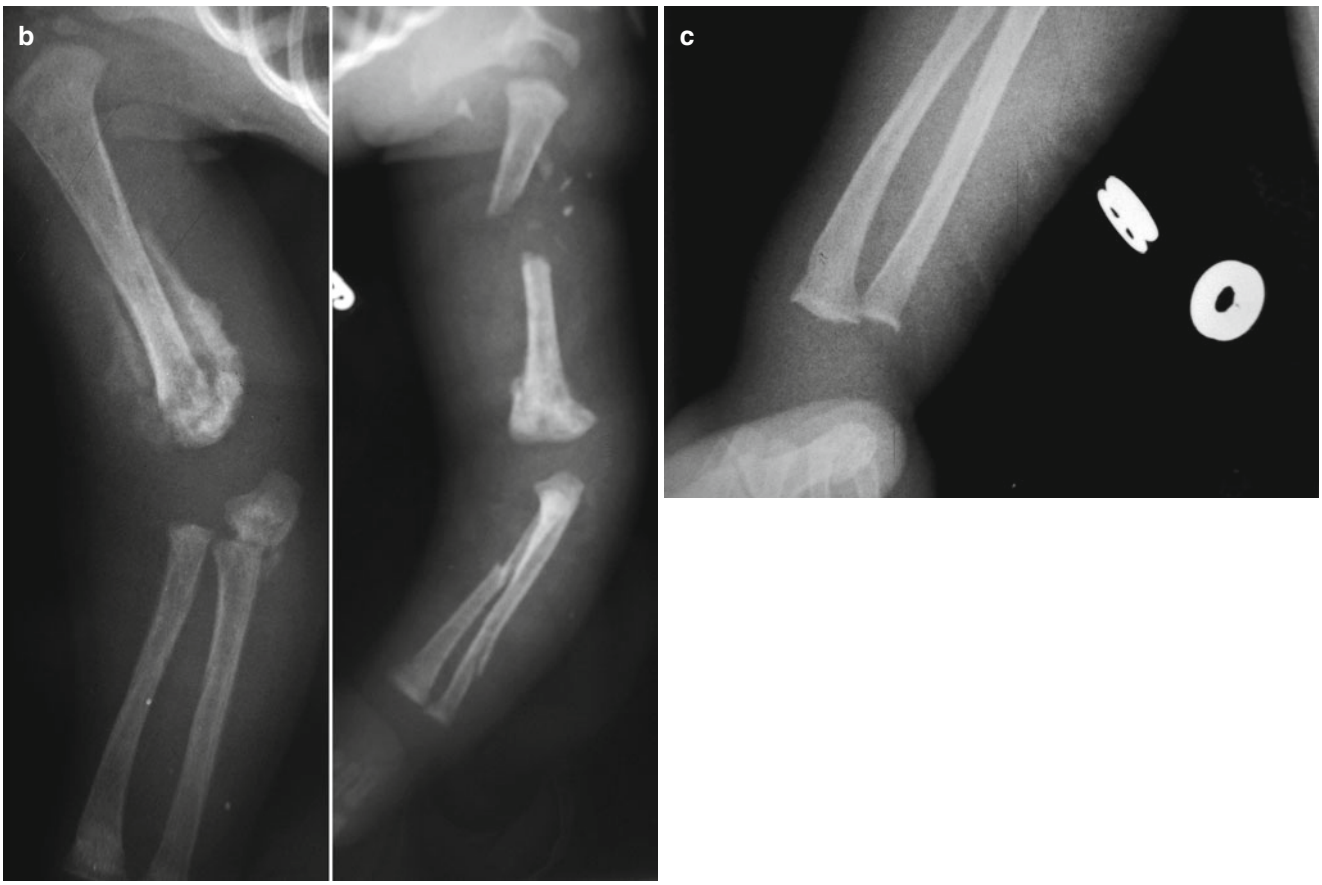

Fig. 9.53 (continued)

Key Points

- Physeal fractures are particularly important because of their potential to cause functional limitation (if the joint surface is affected) and impaired bone growth (damage to the growth cartilage). Salter-Harris classification system divides these fractures into five groups; the prognosis is worst for types III, IV, and V.
- Non-physeal fractures typical of the pediatric population are more common in the forearm, including buckle fractures, greenstick lesions, and plastic deformation. Greenstick fractures deserve special attention because of increased risk of refractures.
- Elbow fractures are the most relevant joint fractures of the upper extremity in children, including supracondylar fractures, fractures of the lateral condyle of the humerus, avulsion fractures of the ossification centers, Monteggia's fracture, and Galeazzi fracture.
- In children, joint fractures are found less often in the lower extremities if compared to the upper extremities, affecting the knees and the ankles in most cases.
- The imaging appearance of the traumatic lesions of the soft tissues in children is essentially the same of those seen in adults. Full-thickness tears of tendons and ligaments are less common in children than in adult patients.
- The radiographic skeletal survey is crucial in the investigation of children with suspected physical abuse. The most important findings include multiple fractures (especially when symmetric and/or in different stages of healing), classic metaphyseal lesions, fractures in atypical sites, and multiple areas of periosteal reaction.

Recommended Reading

Carr KE (2003) Musculoskeletal injuries in young athletes. Clin Fam Pract 5(2):385–415

Carson S, Woolridge DP, Colletti J, Kilgore K (2006) Pediatric upper extremity injuries. Pediatr Clin North Am 53(1):41–67

Chambers HG (2003) Ankle and foot disorders in skeletally immature athletes. Orthop Clin North Am 34(3):445–459

Davis KW (2010) Imaging pediatric sports injuries: lower extremity. Radiol Clin North Am 48(6):1213–1235

Ecklund K, Jaramillo D (2001) Imaging of growth disturbance in children. Radiol Clin North Am 39(4):823–841

Emery KH (2006) Imaging of sports injuries of the upper extremity in children. Clin Sports Med 25(3):543–568

Emery KH (2009) MR imaging in congenital and acquired disorders of the pediatric upper extremity. Magn Reson Imaging Clin N Am 17(3):549–570

Laine JC, Kaiser SP, Diab M (2010) High-risk pediatric orthopedic pitfalls. Emerg Med Clin North Am 28(1):85–102

Lane WG (2003) Diagnosis and management of physical abuse in children. Clin Fam Pract 5(2):493–514

Mulligan ME (2000) Ankle and foot trauma. Semin Musculoskelet Radiol 4(2):241–253

Nimkin K, Kleinman PK (2001) Imaging of child abuse. Radiol Clin North Am 39(4):843–864

Sanchez TR, Jadhav SP, Swischuk LE (2009) MR imaging of pediatric trauma. Magn Reson Imaging Clin N Am 17(3):439–450

Sofka CM, Potter HG (2002) Imaging of elbow injuries in the child and adult athlete. Radiol Clin North Am 40(2):251–265

van Rijn RR, Sieswerda-Hoogendoorn T (2012) Educational paper: imaging child abuse: the bare bones. Eur J Pediatr 171(2): 215–224

White N, Sty J (2002) Radiological evaluation and classification of pediatric fractures. Clin Ped Emerg Med 3(2):94–105

Sports-Related Musculoskeletal Lesions in Pediatric Patients

10

10.1 Introduction

Children and adolescents have become more and more involved in sports practice, whether competitive or purely recreational. The association of skeletal immaturity and intense physical activity renders this group age especially prone to musculoskeletal lesions. Generally speaking, chronic lesions are more common in pediatric athletes than those related to acute trauma. The latter, caused by the sudden action of high-energy forces, usually do not pose a diagnostic dilemma, while chronic osteoarticular lesions caused by repetitive trauma of low intensity may mimic articular diseases. This chapter will discuss some of the most frequent sports-related lesions, such as the different forms of apophysitis, osteochondritis dissecans, stress-related physeal lesions, and stress fractures.

10.2 Apophysitis

An apophysis is an ossification center that – unlike the epiphysis – does not contribute to longitudinal bone growth; instead, it serves as an insertion site for tendons, being especially subjected to traction forces and anomalous stress. In addition, the apophyseal physes are inherently weaker and more vulnerable to traumatic lesions than the adjacent bones and tendons. These lesions may be represented by acute apophyseal avulsions at the level of the growth plate, or by chronic apophysitis, which is an inflammatory process typical of skeletally immature athletes related to excessive traction and microavulsions at the bone/cartilage interface. The latter is commonly found during growth spurts, and it may be considered a non-displaced transphyseal stress fracture (Salter-Harris type I – see Chap. 9). Patients with chronic apophysitis present insidious local pain that worsens with physical activity, as well as tenderness and soft-tissue swelling over the inflamed apophysis.

In acute avulsion fractures, radiographs show a bone fragment with incompletely corticated borders in the soft tissues adjacent to the expected apophyseal site, with no need for additional investigation, even though magnetic resonance imaging (MRI) allows for a more precise and detailed assessment (Fig. 10.1). Radiographs are often normal in patients with early-stage apophysitis, while those with chronic apophysitis often exhibit apophyseal fragmentation and enlargement, physeal widening, and periosteal reaction (Fig. 10.2), which are also well demonstrated on computed tomography (CT) (Fig. 10.3). It is important to have in mind that irregularity and fragmentation may also be found in normal apophyses as a developmental variant, which is deprived of significance if there are no clinical manifestations. On ultrasound (US), chronically inflamed apophyses usually present increased size and heterogeneous vascularity; there may be swelling of the adjacent soft tissues as well, and the tendon may appear thickened, hypervascular, and hyperechogenic. Magnetic resonance imaging (MRI) is the most sensitive and specific method for evaluation of chronic apophysitis, showing an edematous apophysis of increased size that often presents post-gadolinium enhancement; edematous changes are also found in the adjacent bone marrow, in the physis, and in the surrounding soft tissues (Figs. 10.4 and 10.5). Physeal widening may be subtle or marked, and even apophyseal avulsion is found in severe cases (Figs. 10.4, 10.6, and 10.7). Chronic apophysitis may present a misleading appearance on imaging and simulate an aggressive process, with mass effect, marked periosteal reaction and exuberant bone neoformation, in addition to significant bone marrow edema and soft-tissue swelling (Fig. 10.4). Correlation between clinical data and imaging findings is crucial in order to avoid unnecessary biopsies, as that the histopathological picture may lead to an erroneous diagnosis of sarcoma.

Several apophyses may be affected in the pelvis and in the hips, such as the iliac crest, the anterior superior and anterior inferior iliac spines, the ischial tuberosity, and the

S.L. Viana et al., *Joint Imaging in Childhood and Adolescence*,
DOI 10.1007/978-3-642-35876-0_10, © Springer-Verlag Berlin Heidelberg 2013

greater trochanter. Apophysitis of anterior inferior iliac spine is more prevalent in countries where soccer is more popular, resulting from excessive traction exerted by the tendon of the direct head of the rectus femoris. Apophysitis around the hip typically does not affect individuals under age 13, given that the apophyseal ossification centers usually appear between 13 and 15 years of age and fuse between 16 and 18. Inclusion of both hips in the field of view is recommended for CT and MRI coronal and axial images, as comparative analysis of the apophyses maximizes the diagnostic capabilities of these methods (Figs. 10.1, 10.2, 10.3, 10.4, 10.6, and 10.7). Old healed lesions frequently lead to deformity of the affected apophysis, which displays density/signal intensity similar to those of the normal bone (Fig. 10.8).

Osgood-Schlatter disease (OSD) is a traction apophysitis of the insertion of the patellar tendon in the tibial tubercle. It is more frequent in male athletes between 10 and 15 years of age, occurring bilaterally in 20–30 % of the cases. In addition to the above-mentioned classic radiographic findings (Fig. 10.9), heterotopic intratendinous ossification is also common, as well as fluid distension of the deep infrapatellar bursa (Figs. 10.5, 10.10, and 10.11). Residual bone deformity and/or persistence of an intratendinous ossicle in the distal portion of the patellar tendon can be found after healing and may cause chronic pain (Fig. 10.12).

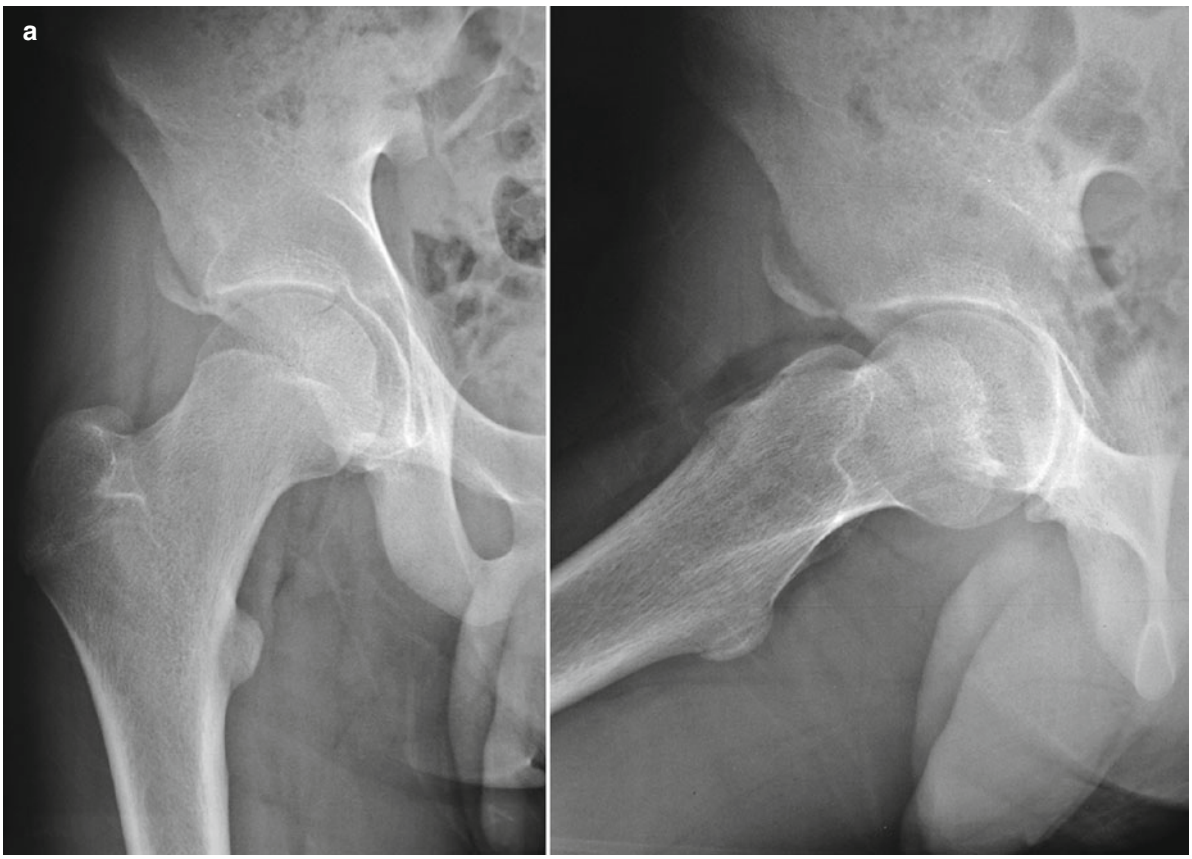

Fig. 10.1 In (**a**), radiographs of the right hip of an adolescent with acute avulsion of the anterior inferior iliac spine show a partially corticated bone fragment in the soft tissues adjacent to the apophyseal site, without evidence of chronic apophysitis. In (**b**), MRI of another patient demonstrates similar findings, with acute avulsion of the same apophysis and mild displacement, without signs of chronic inflammation. T1-WI (*upper row*, *left*) and T2-WI (*upper row*, *right*) demonstrate increased signal intensity of the periapophyseal soft tissues, related to posttraumatic hemorrhage, while sagittal fat sat T2-WI (*lower row*) reveal extensive soft-tissue edema and allow for an accurate estimate of the extent of the avulsion. Transverse T1-WI (**c**) and fat sat T2-WI (**d**) of the pelvis of the same patient disclose a large hematoma deeply situated relative to the right iliac muscle, containing a fluid-fluid level (Fig. 10.1a; courtesy of Dr. Marcelo Coelho Avelino, Medimagem, Teresina, Brazil)

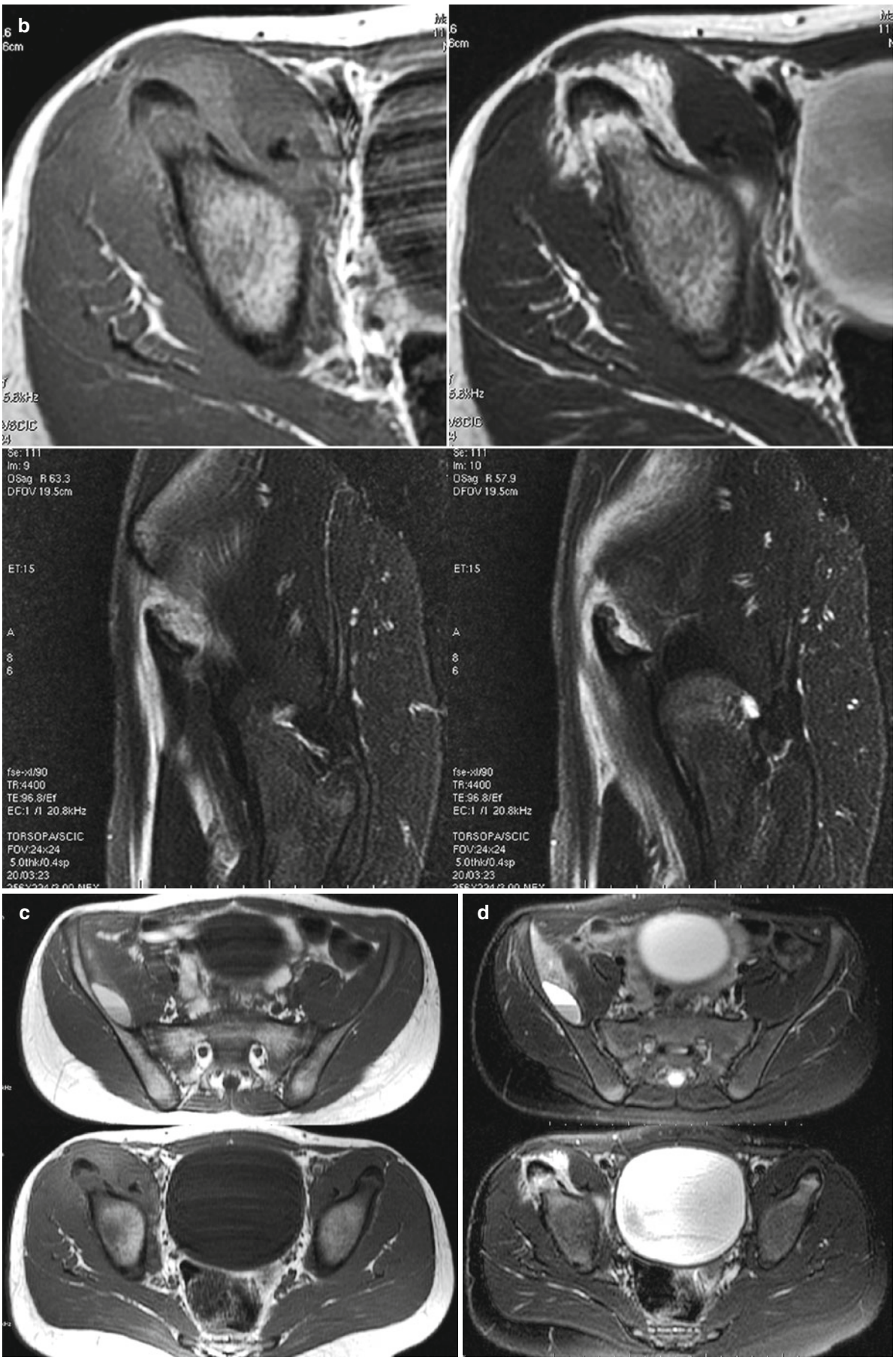

Fig. 10.1 (continued)

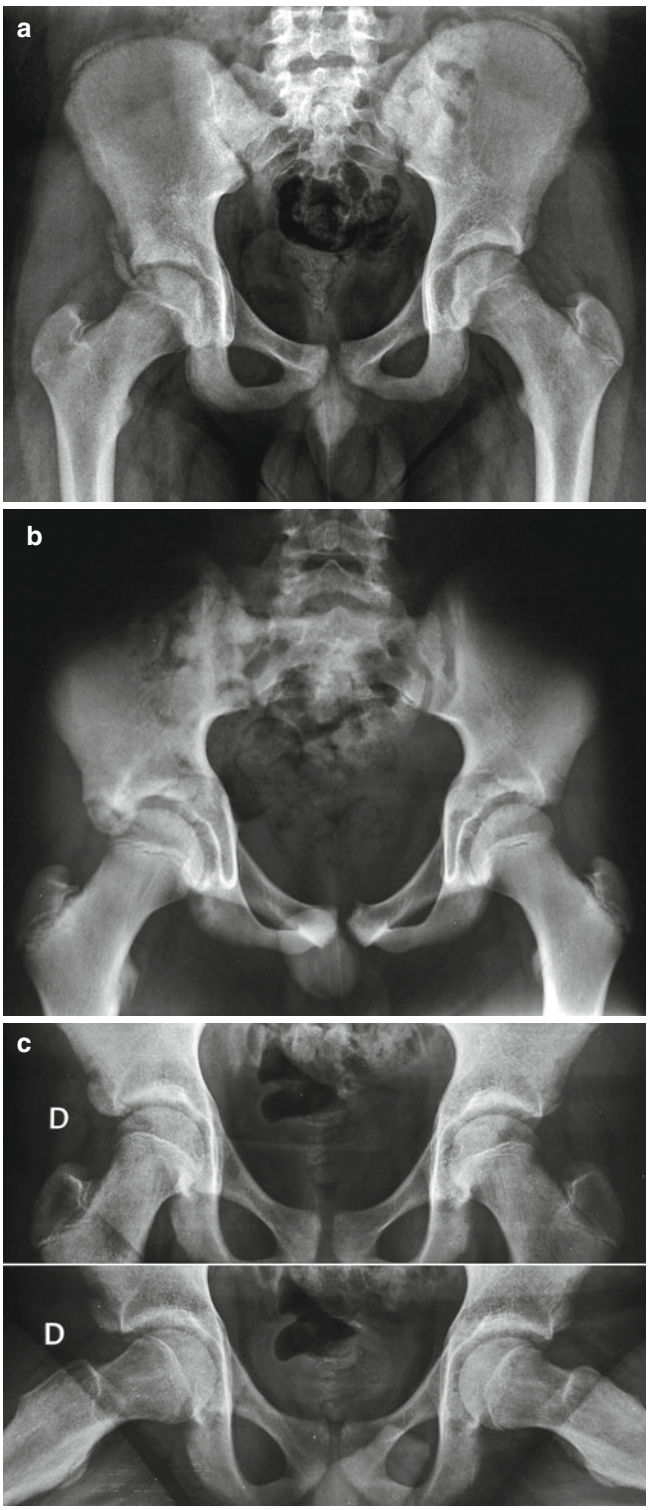

Fig. 10.2 Radiographs of three distinct patients with right-sided chronic apophysitis of the anterior inferior iliac spine displaying different appearances of this condition on imaging. All of them evidence increased size and abnormal shape of this apophysis. In (**a**), periosteal reaction and bone neoformation are evident, which are notably absent in the acute lesion of Fig. 10.1a. In (**b**), the apophysis has a pseudotumoral appearance, with bone deformity, metaphyseal remodeling, and physeal widening. In (**c**), despite the obvious increase of the apophyseal size, bone neoformation/remodeling is absent

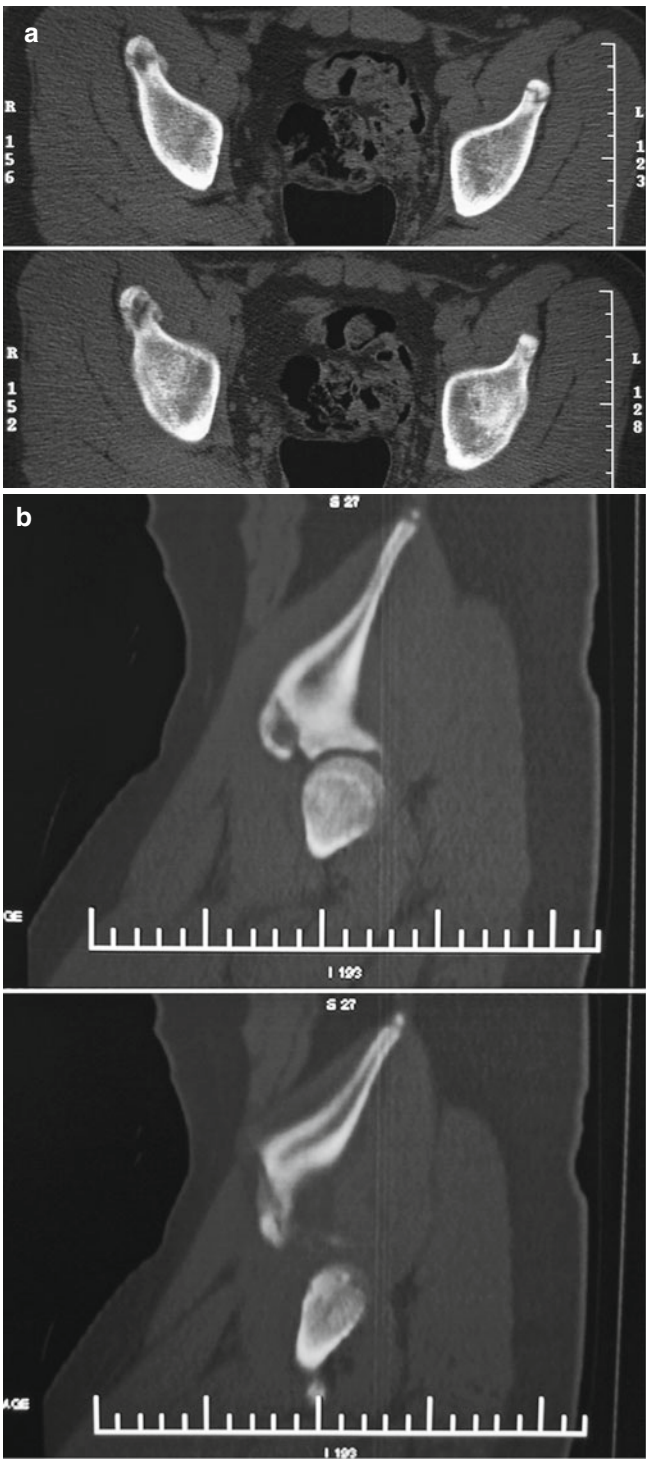

Fig. 10.3 CT of the pelvis of a 14-year-old soccer player. Transverse images (**a**), sagittal reformatted images (**b**), and volume-rendered reconstruction (**c**) display increased size of the apophysis of the right anterior inferior iliac spine, with physeal widening and bone neoformation. Apophysitis is more evident when the affected apophysis is compared to the contralateral one

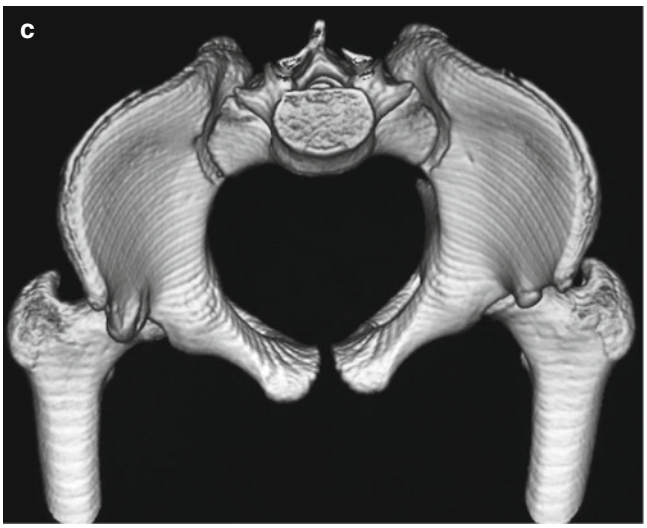

Fig. 10.3 (continued)

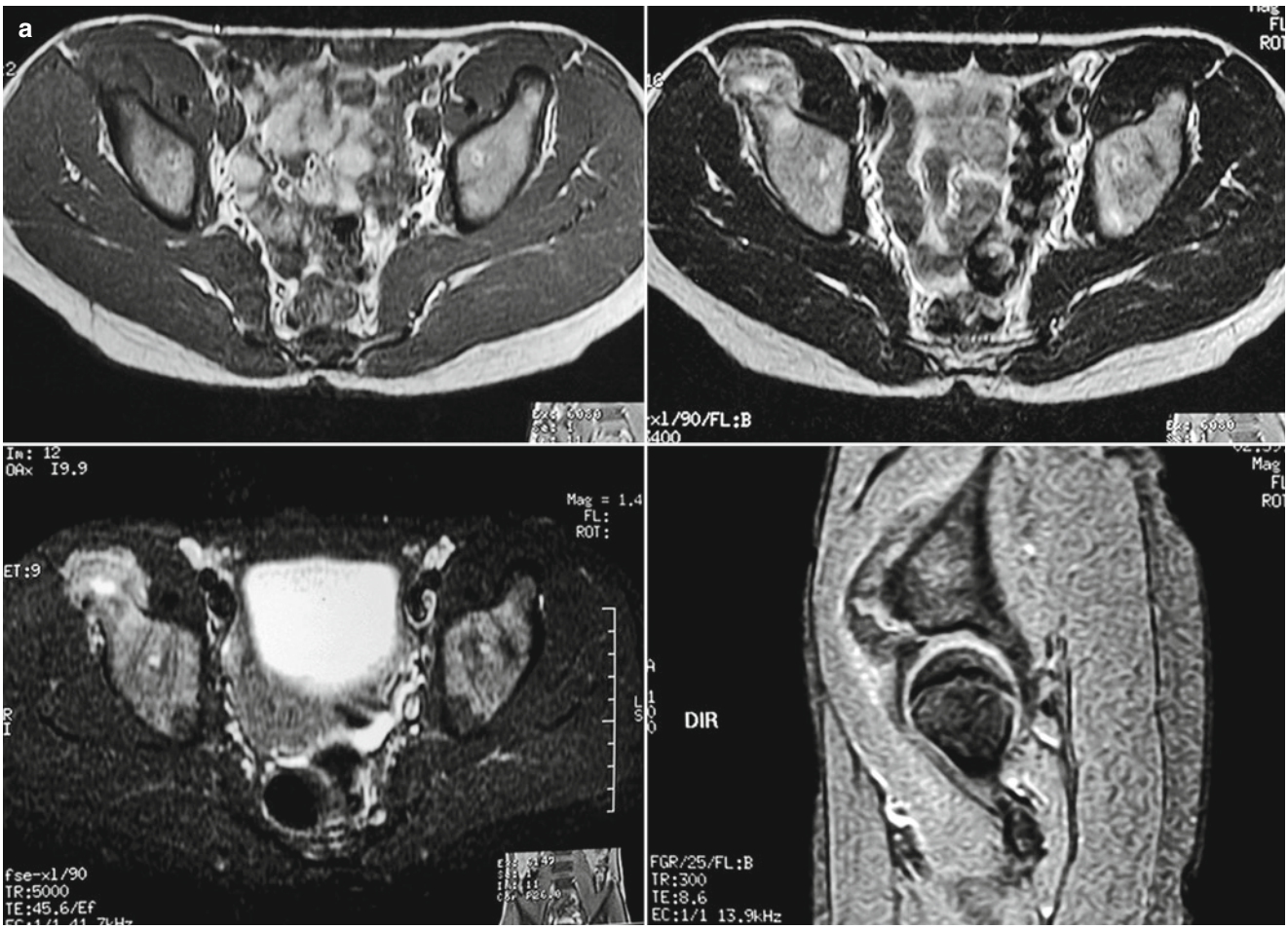

Fig. 10.4 In (**a**), transverse T1-WI (*upper-left image*), T2-WI (*upper-right image*), and STIR image (*lower-left image*) reveal findings similar to those of the patient of Fig. 10.3; MRI, however, is able to detect edematous changes of the bone marrow and of the soft tissues, which are related to chronic inflammation and not evident on CT. Sagittal gradient-echo image (*lower-right image*) is useful to demonstrate increased size and irregular contours of the affected apophysis, as well as physeal widening. In (**b**), post-gadolinium fat sat T1-WI (*upper row*) display enhancement of the above-mentioned edematous areas, while CT images (*lower row*) evidence solid and thick periosteal neoformation, which is difficult to demonstrate on MRI

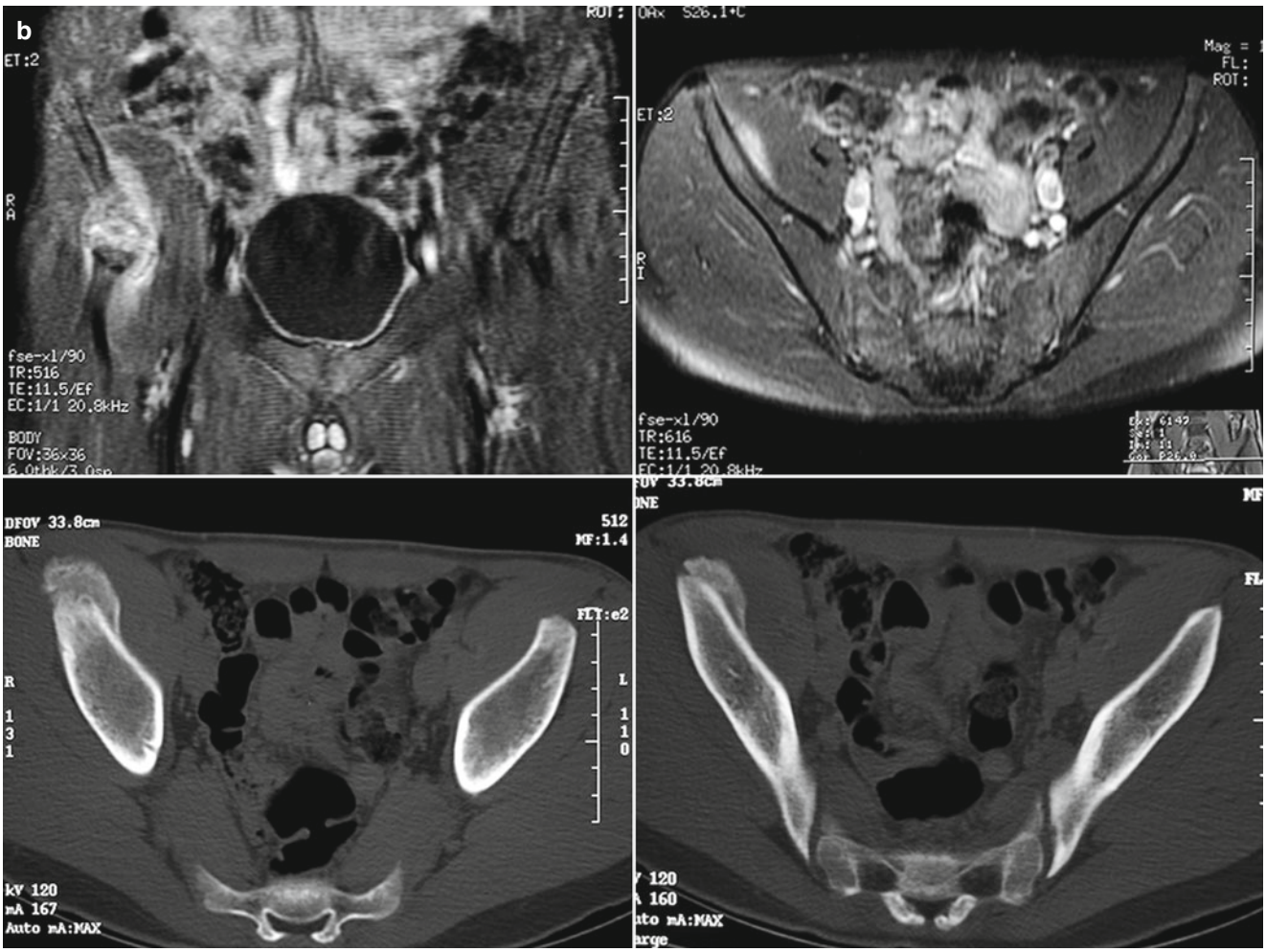

Fig. 10.4 (continued)

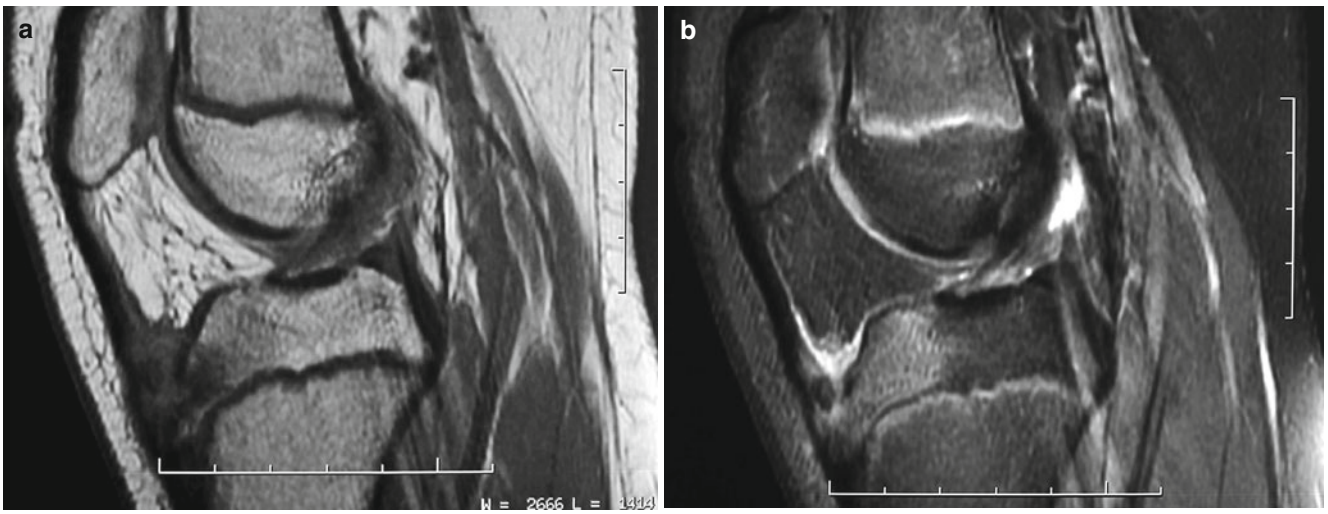

Fig. 10.5 Sagittal T1-WI (**a**), fat sat PD-WI (**b**), and post-gadolinium fat sat T1-WI (**c**) of a patient with apophysitis of the tibial tubercle show bone fragmentation in addition to thickening and heterogeneity of the distal portion of the patellar tendon. In addition, there is fluid distension of the deep infrapatellar bursa and edematous changes of the bone marrow and of the adjacent soft tissues, which show enhancement on post-contrast images

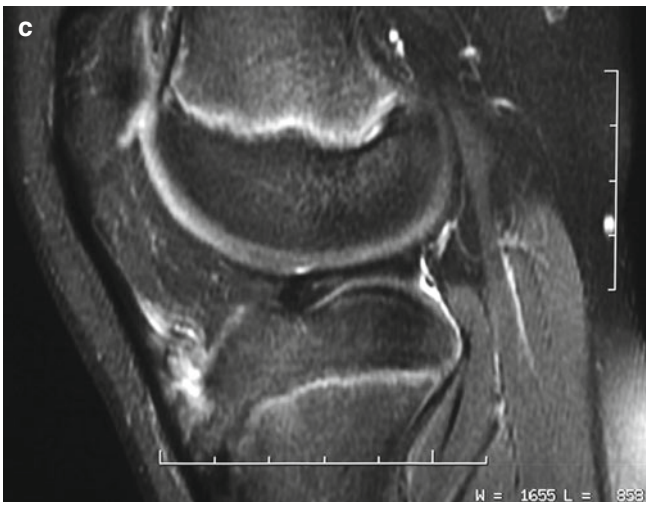

Fig. 10.5 (continued)

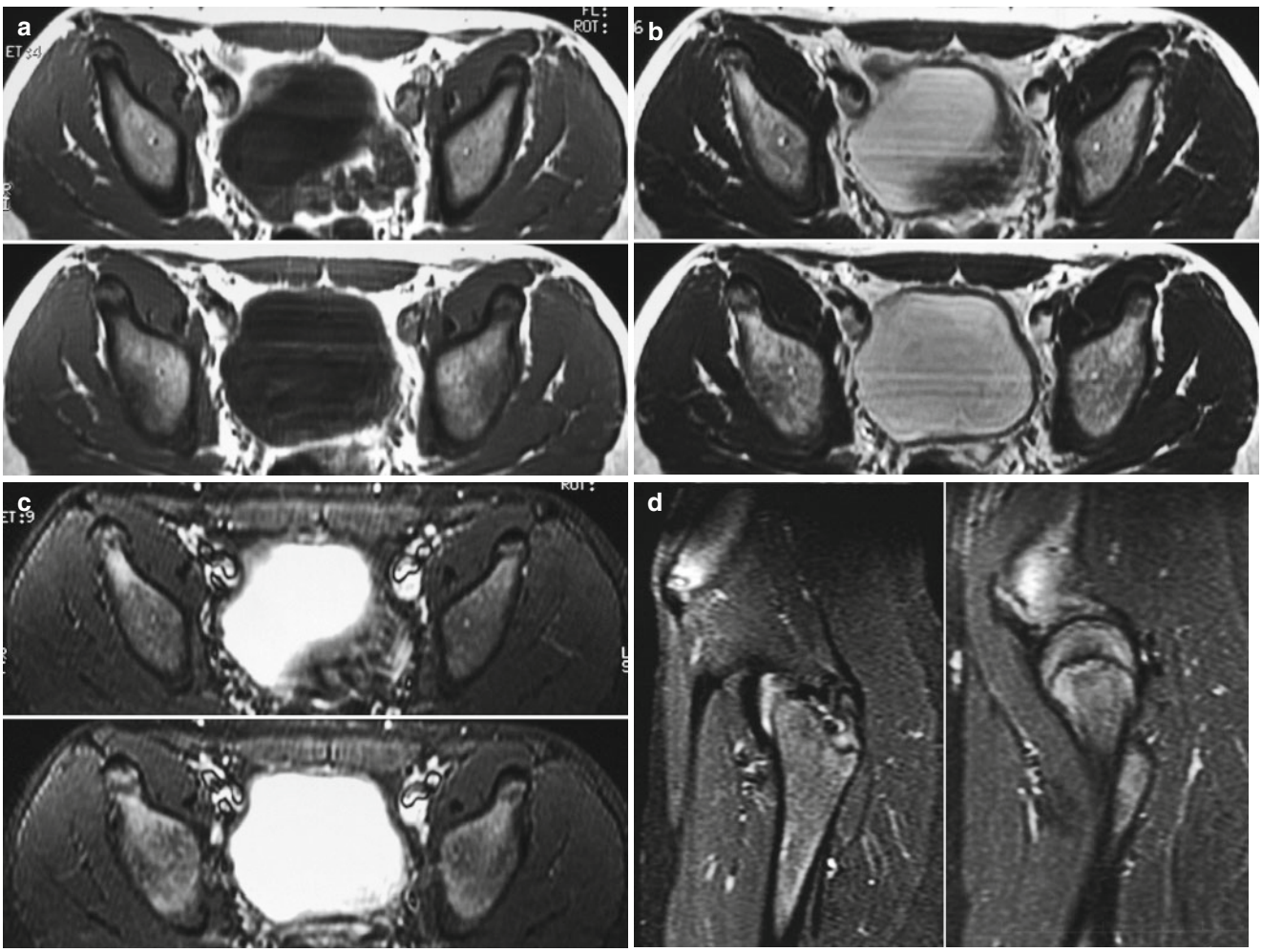

Fig. 10.6 MRI of the hips of a 14-year-old adolescent with chronic apophysitis of the right anterior inferior iliac spine. Transverse T1-WI (**a**), T2-WI (**b**), and fat sat T2-WI (**c**) reveal subtle increase of the size of the affected apophysis and adjacent bone marrow edema, which are absent in the opposite side. In (**d**), sagittal fat sat T2-WI demonstrate widening and increased signal intensity of the right physis, in addition to the above-mentioned findings

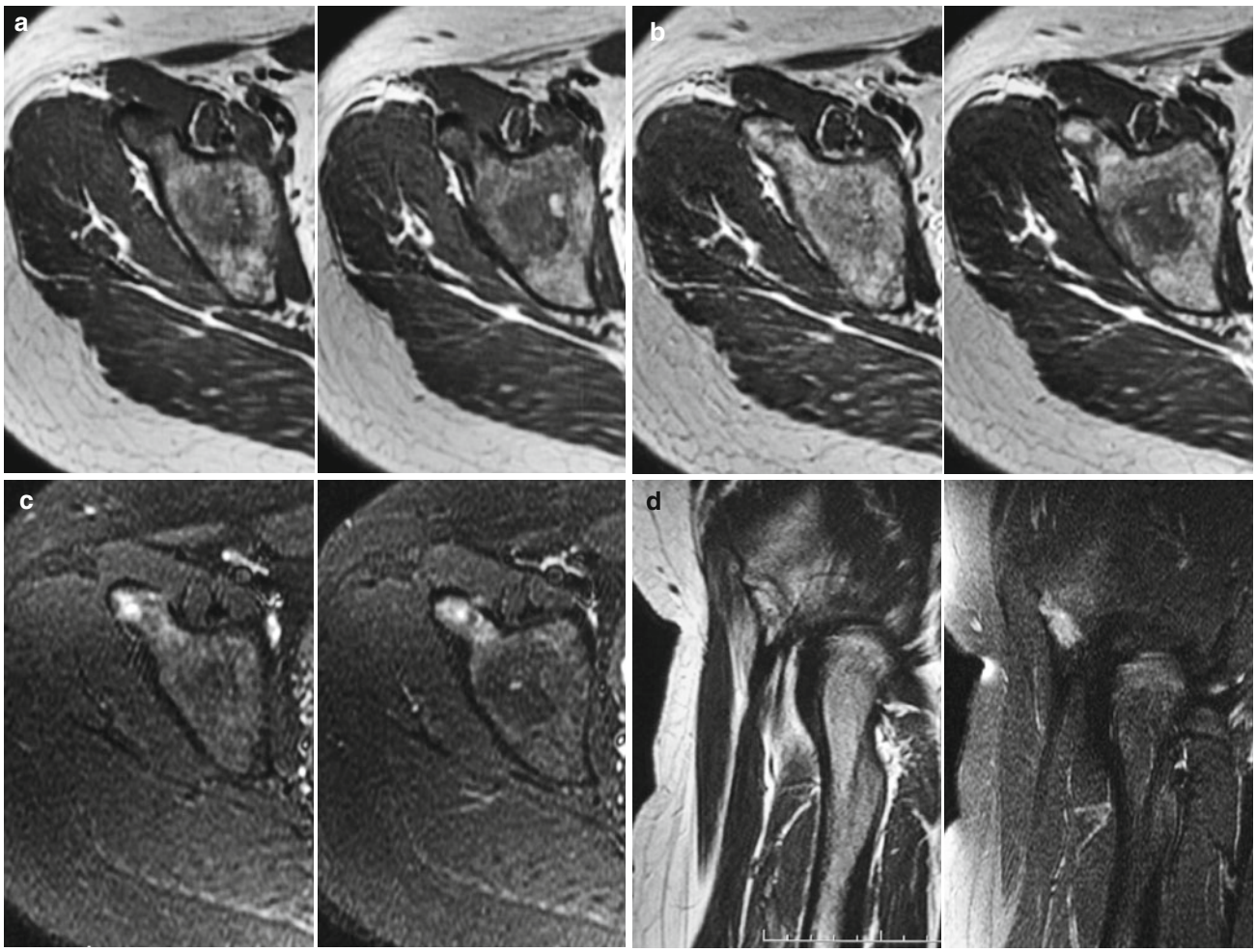

Fig. 10.7 A 15-year-old patient with chronic inguinal pain at right due to chronic apophysitis of the anterior inferior iliac spine. Transverse T1-WI (**a**), T2-WI (**b**), and STIR images (**c**) and sagittal T2-WI and fat sat T2-WI (**d**) display findings very similar to those of the patient of Fig. 10.6, unless for absence of significant physeal widening

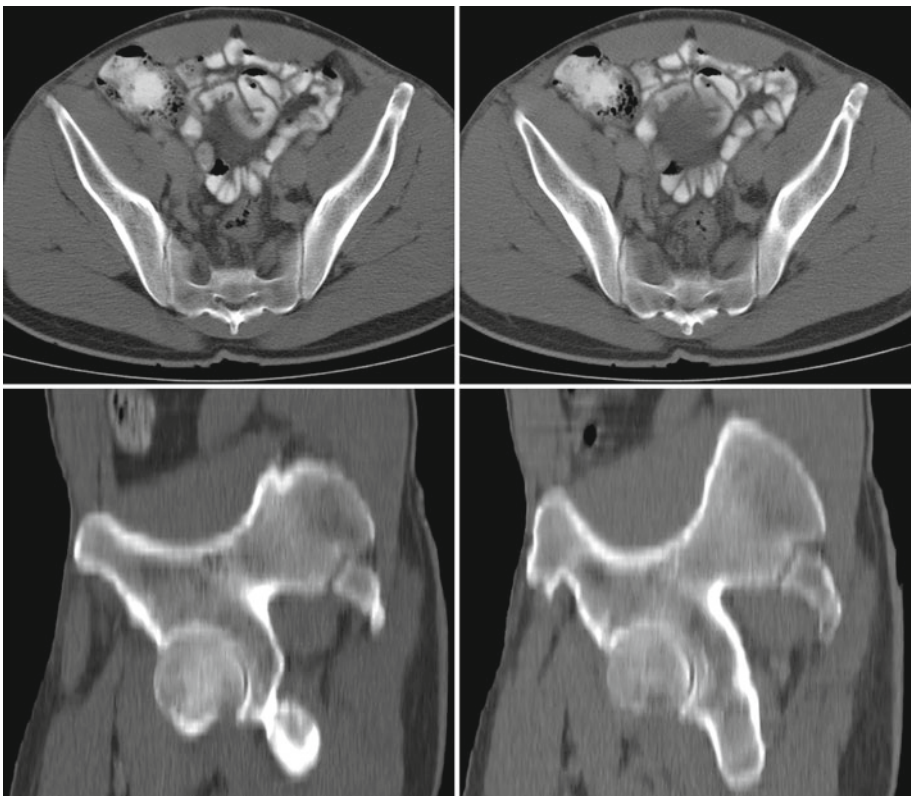

Fig. 10.8 Bone deformity related to an old healed lesion of the left anterior superior iliac spine, incidentally found during an abdominal CT scan of a 36-year-old male (former soccer player during the adolescence). On transverse images (*upper row*), there is prominence of the apophysis, with a bony protuberance that is also evident on a sagittal reformatted image (*right lower image* – compare with the normal apophysis in the *left lower image*)

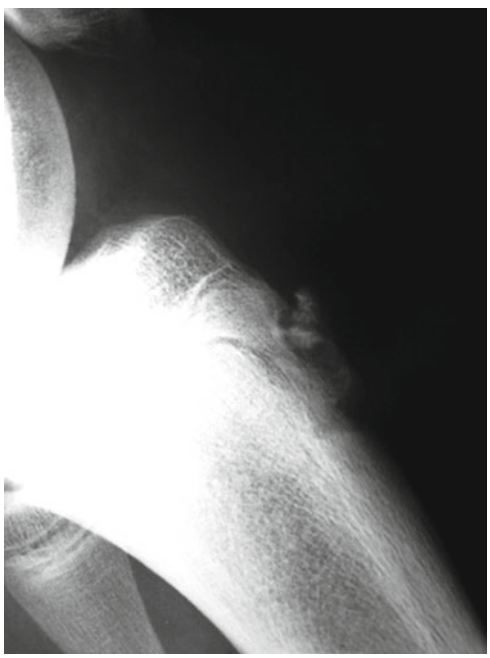

Fig. 10.9 Lateral view of the left knee of a child with OSD showing fragmentation and sclerosis of the tibial tubercle

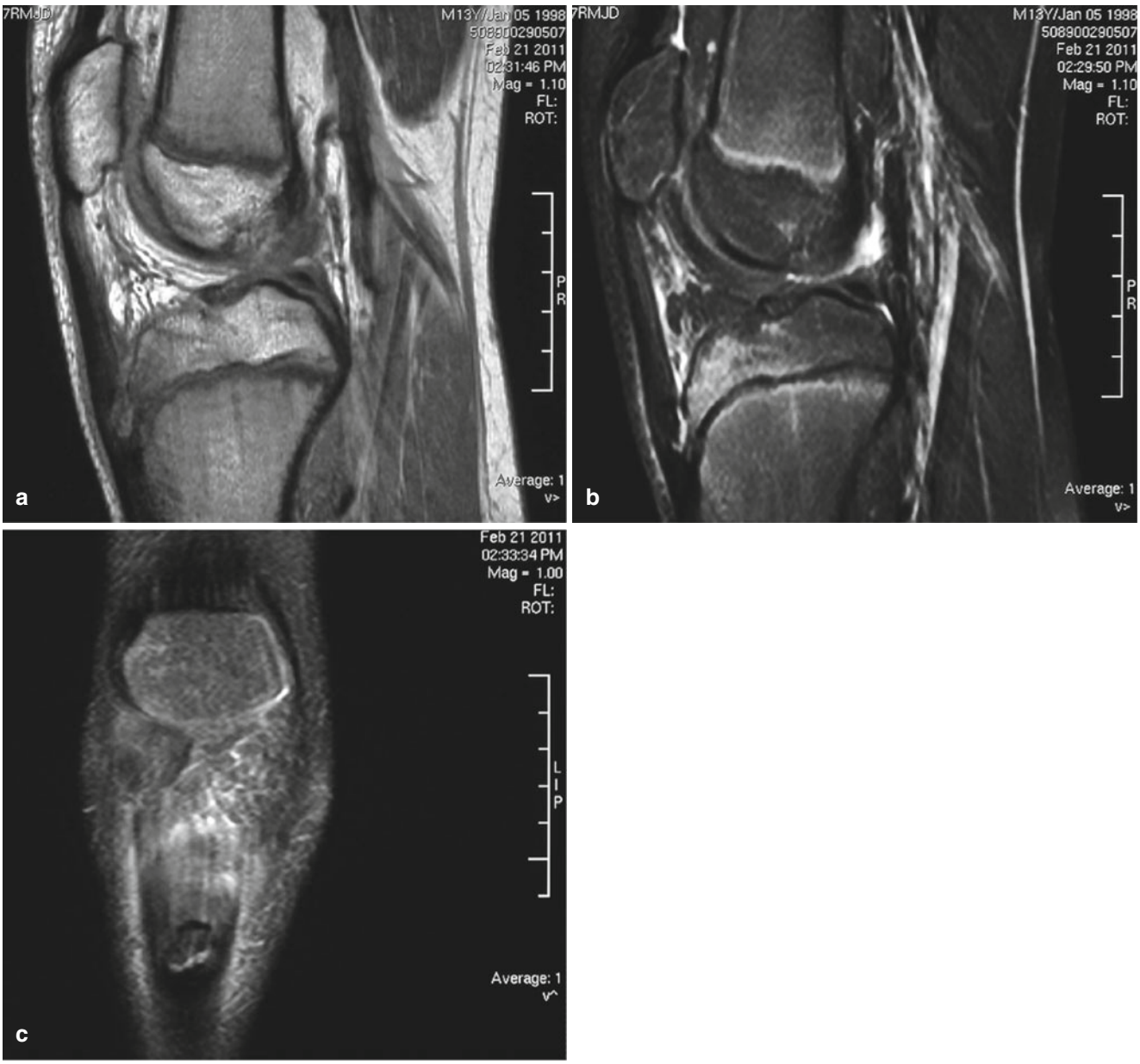

Fig. 10.10 MRI of the right knee of a 13-year-old child with OSD. Sagittal T1-WI (**a**) and fat sat T2-WI (**b**) and coronal fat sat T2-WI (**c**) display fragmentation of the apophysis of the tibial tubercle and extensive bone marrow edema pattern, as well as edema of the infrapatellar fat pad and thickening of the distal portion of the patellar tendon

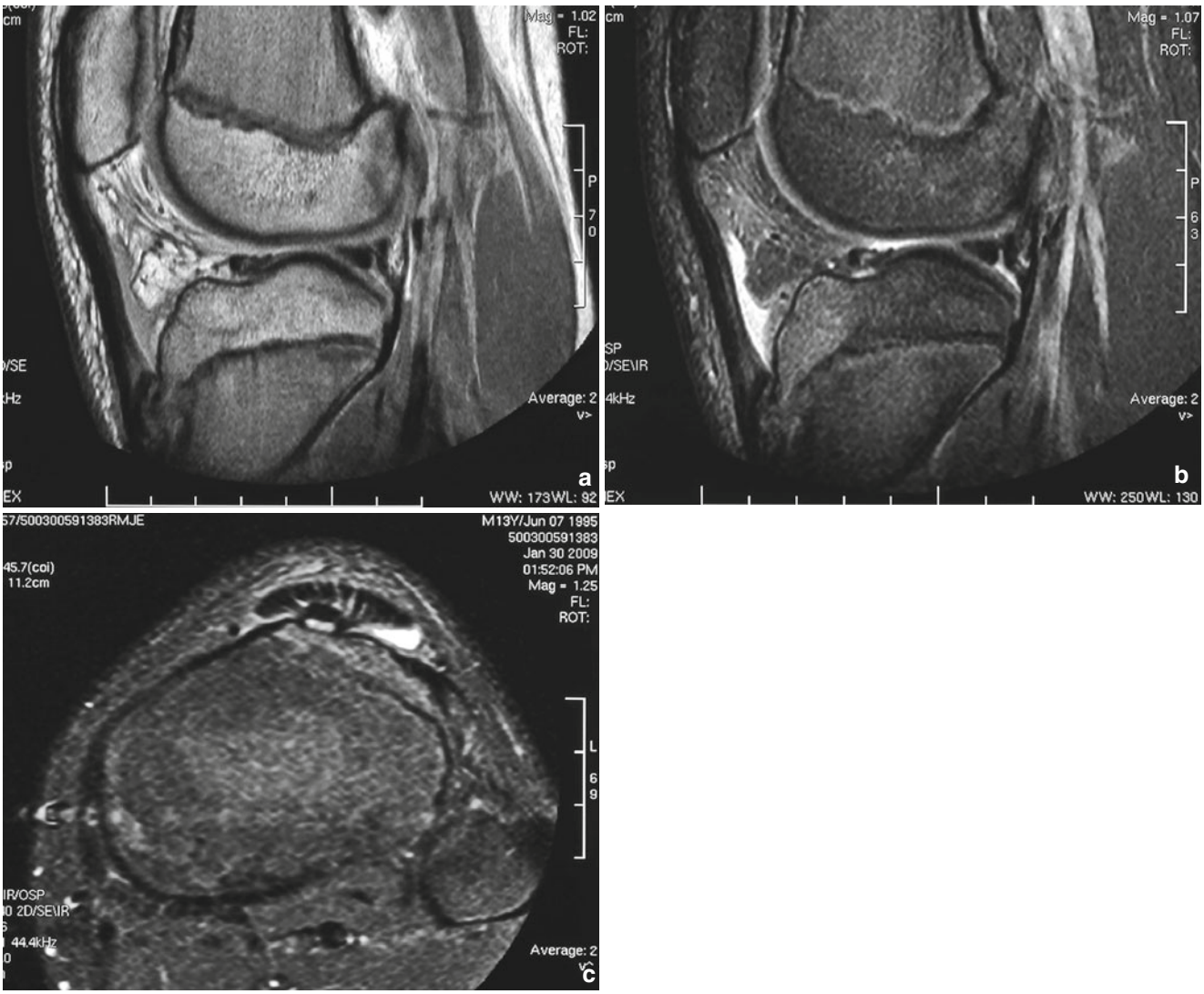

Fig. 10.11 A 13-year-old patient with OSD. In addition to the findings above described for the patient of Fig. 10.10, sagittal PD-WI (**a**) and STIR image (**b**) and transverse STIR image (**c**) disclose fluid in the deep infrapatellar bursa

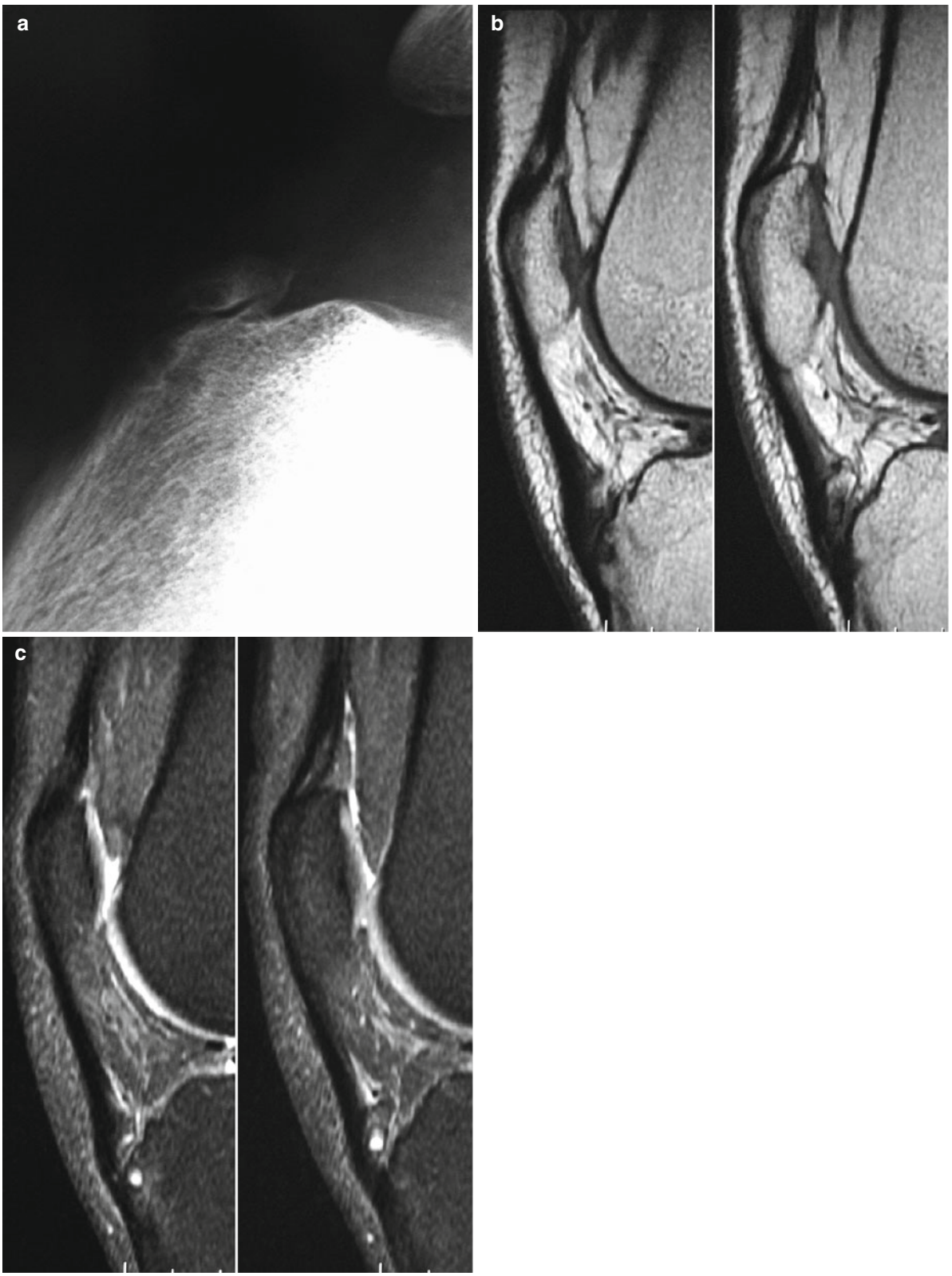

Fig. 10.12 Lateral radiograph (**a**) and sagittal T1-WI (**b**) and fat sat PD-WI (**c**) of an adult with late-stage sequelae of OSD complaining of anterior knee pain. There is an ossicle projected over the distal portion of the patellar tendon, with irregularity of the tibial tubercle. MRI corroborates the radiographic findings, demonstrating cystic/edematous changes of the bone marrow of the tibial tubercle and of the ossicle, as well as thickening of the distal patellar tendon and edema of the adjacent soft tissues

Sinding-Larsen-Johansson disease (SLJD) is a reaction to traction at the inferior pole of the patella, more common in males between 9 and 12 years old, mainly those involved in jumping, gymnastics, and kicking sports. Strictly speaking, the inferior patellar pole is not an apophysis; nonetheless, the etiology and the inflammatory response to traction are identical to those seen in classic apophysitis. Imaging findings include bone fragmentation and inflammation in the inferior pole of the patella, occasionally associated with ossification of the proximal portion of the patellar tendon (Figs. 10.13, 10.14, and 10.15). Tendinopathy/partial tear of the patellar tendon (Fig. 10.16) and patellar fractures are the main differential diagnosis.

Sever's disease is the inflammation of the calcaneal apophysis, adjacent to the insertion of the Achilles tendon. It is more common in males with less than 11 years of age, occurring bilaterally in up to 60 % of the patients. Pain worsens with physical activity and can be reproduced upon latero-lateral compression of the heel. As stated above, even though the classic findings of apophyseal fragmentation and sclerosis are present, the same findings may be found in normal individuals; additionally, recent works indicate that radiographs are not necessary in the workup as they have no real influence in the diagnosis or in therapeutic decision making. Similarly, bone marrow edema pattern may be found in the calcaneal apophysis of symptomatic and asymptomatic children on MRI. Therefore, there is no characteristic imaging pattern for this disease and the diagnosis is primarily a clinical one.

Most of the sports-related lesions of the elbow in skeletally immature athletes are related to activities that cause repetitive valgus stress, such as baseball pitching or gymnastics. This overload lead to the so-called little leaguer's elbow, an apophysitis of the medial epicondyle that is more frequently found in children from 9 to 14 years of age. Imaging plays a secondary role, given that this condition is usually obvious on clinical examination and treatment is conservative. In addition to the aforementioned classic findings, the valgus stress may also cause osteochondral lesions in the capitulum and early physeal closure. Nevertheless, it has been described that the same apophyseal findings can be seen in asymptomatic athletes, so that the "little leaguers' elbow" may be the painful end of a spectrum of response to anomalous stress; caution is advised to avoid valuing too highly imaging findings that may be deprived of significance. MRI is more useful to rule out alternative causes of pain, such as ligament lesions.

Still in the context of apophysitis, a related condition is the segmented (bipartite, tripartite, or multipartite) patella, an anatomical variant in which one or more ossification centers are not incorporated to the body of the patella. These ossification centers are most often superolateral, bridged by a fibrocartilaginous synchondrosis. Even though this condition is often asymptomatic, it may occasionally become painful, probably due to chronic stress related to the insertion of the quadriceps tendon. The resulting anomalous mobility leads to subchondral marrow edema, and degenerative changes are occasionally present in the fibrocartilaginous interface (Fig. 10.17).

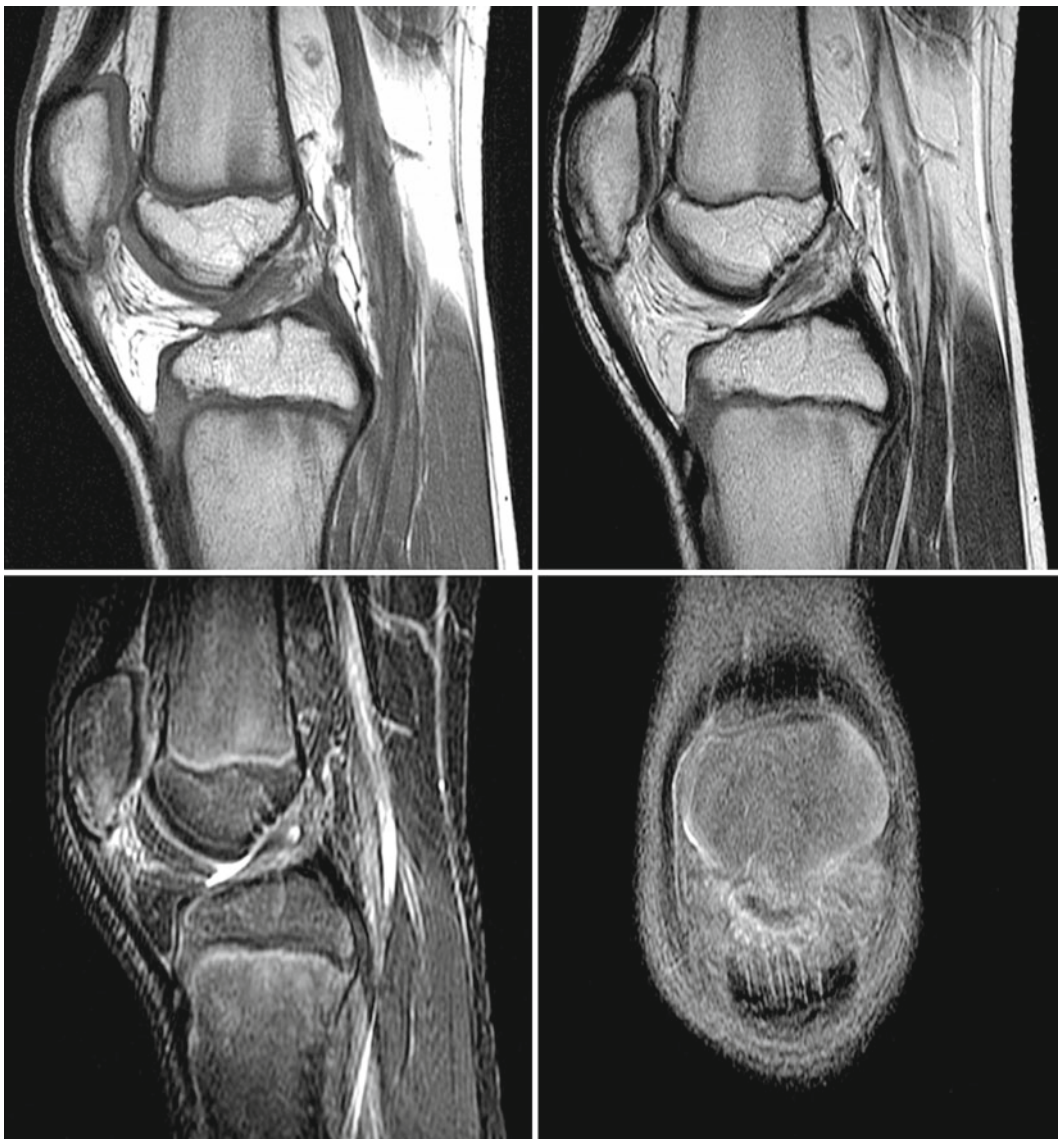

Fig. 10.13 MRI of the left knee of an 11-year-old soccer player with SLJD. Sagittal T1-WI (*upper-left image*), T2-WI (*upper-right image*), and STIR image (*lower-left image*) and coronal fat sat PD-WI (*lower-right image*) display bone marrow edema and fragmentation of the inferior pole of the patella; edema is also seen in the infrapatellar fat pad

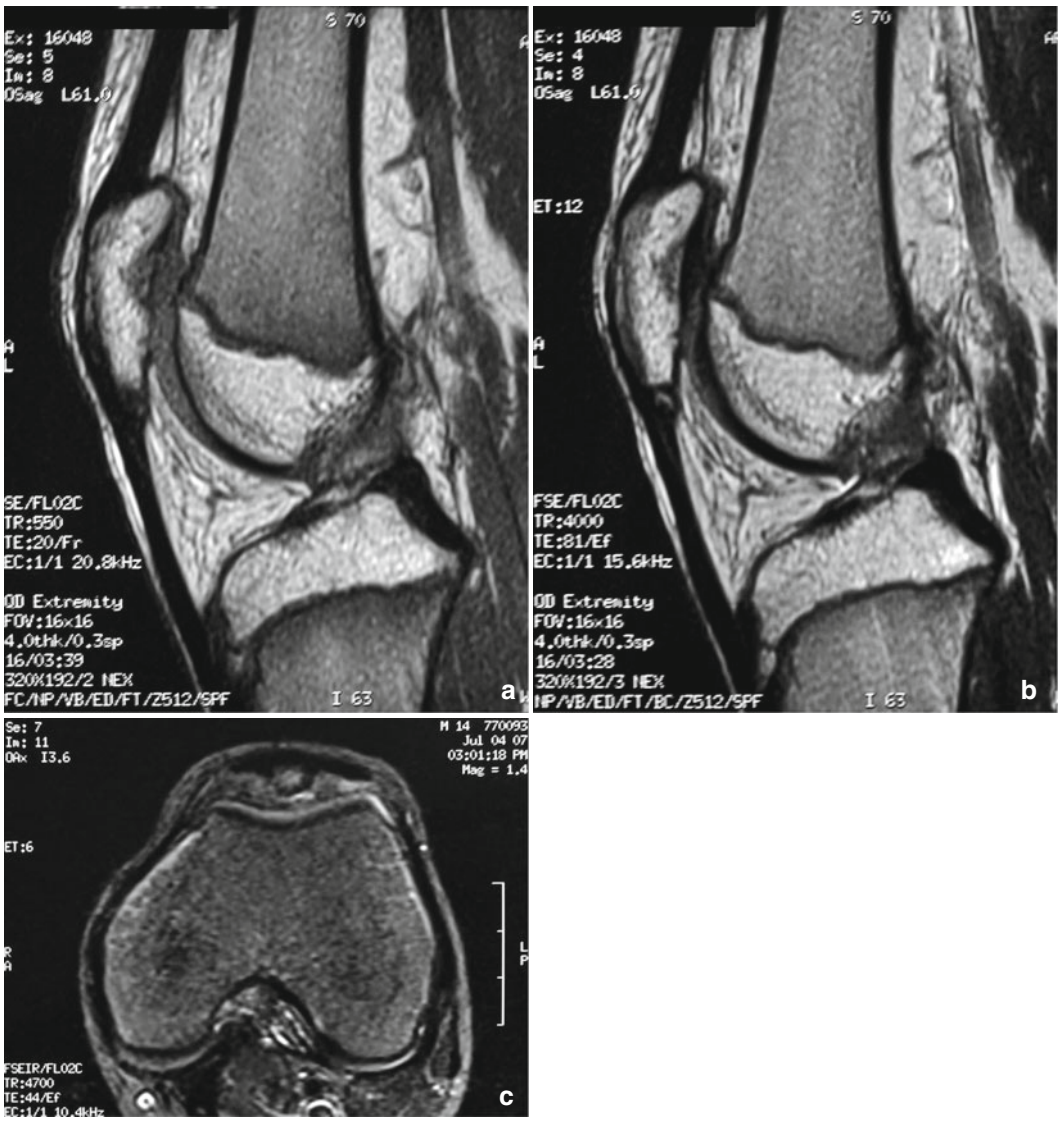

Fig. 10.14 Sagittal T1-WI (**a**) and T2-WI (**b**) and transverse STIR image (**c**) of a 14-year-old patient with SLJD display bone fragmentation, more evident than that observed in the patient of Fig. 10.13. Nonetheless, the edematous changes are less prominent and almost exclusively confined to the avulsed bone fragment. Subtle thickening of the proximal patellar tendon is also present

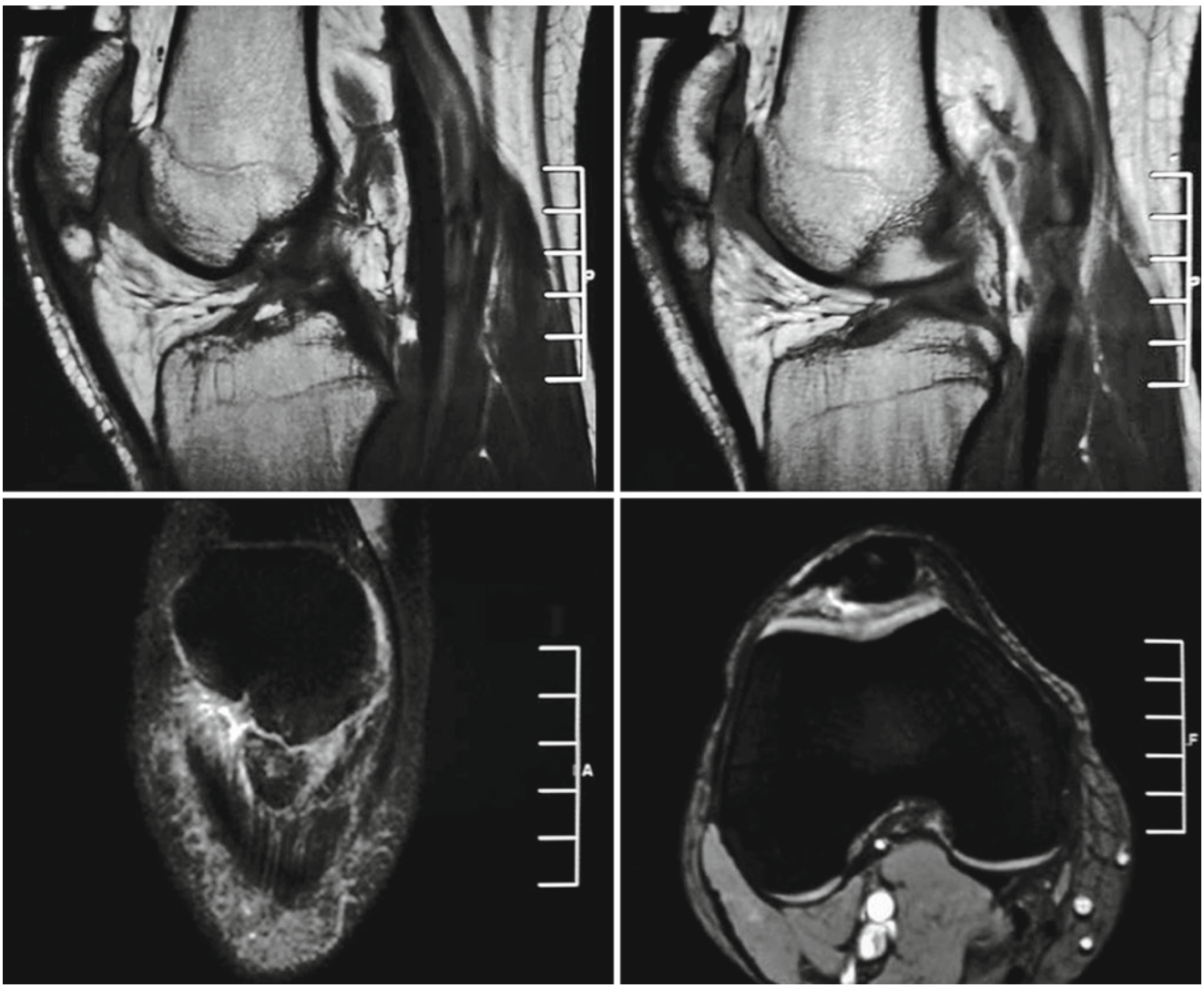

Fig. 10.15 A 27-year-old patient with symptomatic sequelae of SLJD. MRI discloses chronic avulsion of a large bone fragment with corticated borders adjacent to the inferior patellar pole, as well as thickening of the proximal patellar tendon and edema of the adjacent soft tissues

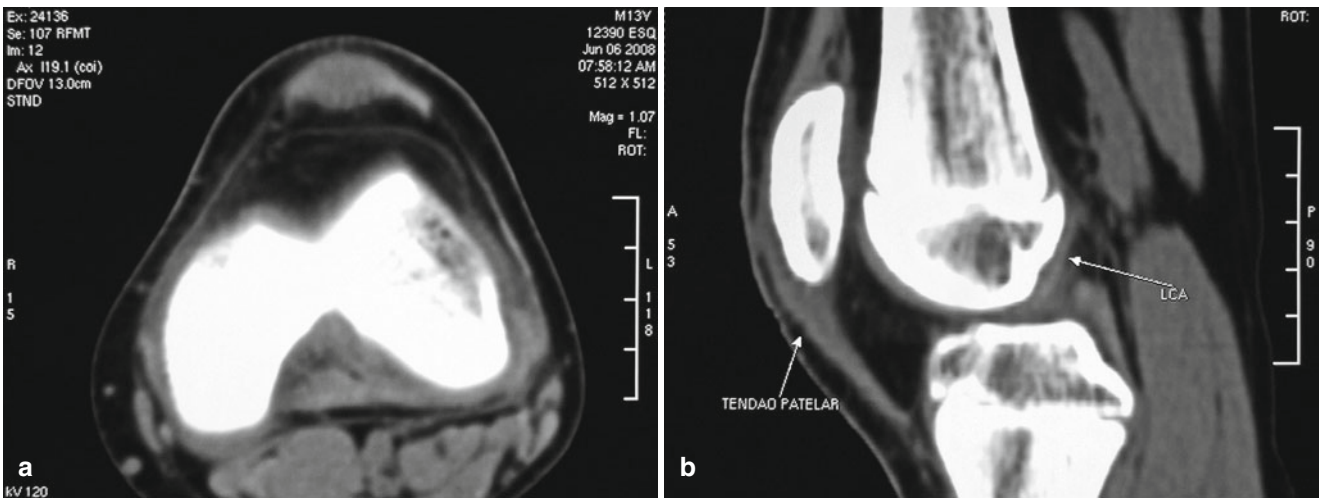

Fig. 10.16 Transverse CT image (**a**) and sagittal reformatted image (**b**) of a 13-year-old runner with left infrapatellar pain disclose thickening and focal hypodensity of the proximal patellar tendon due to tendinopathy, without abnormalities of the adjacent bone or of the soft tissues

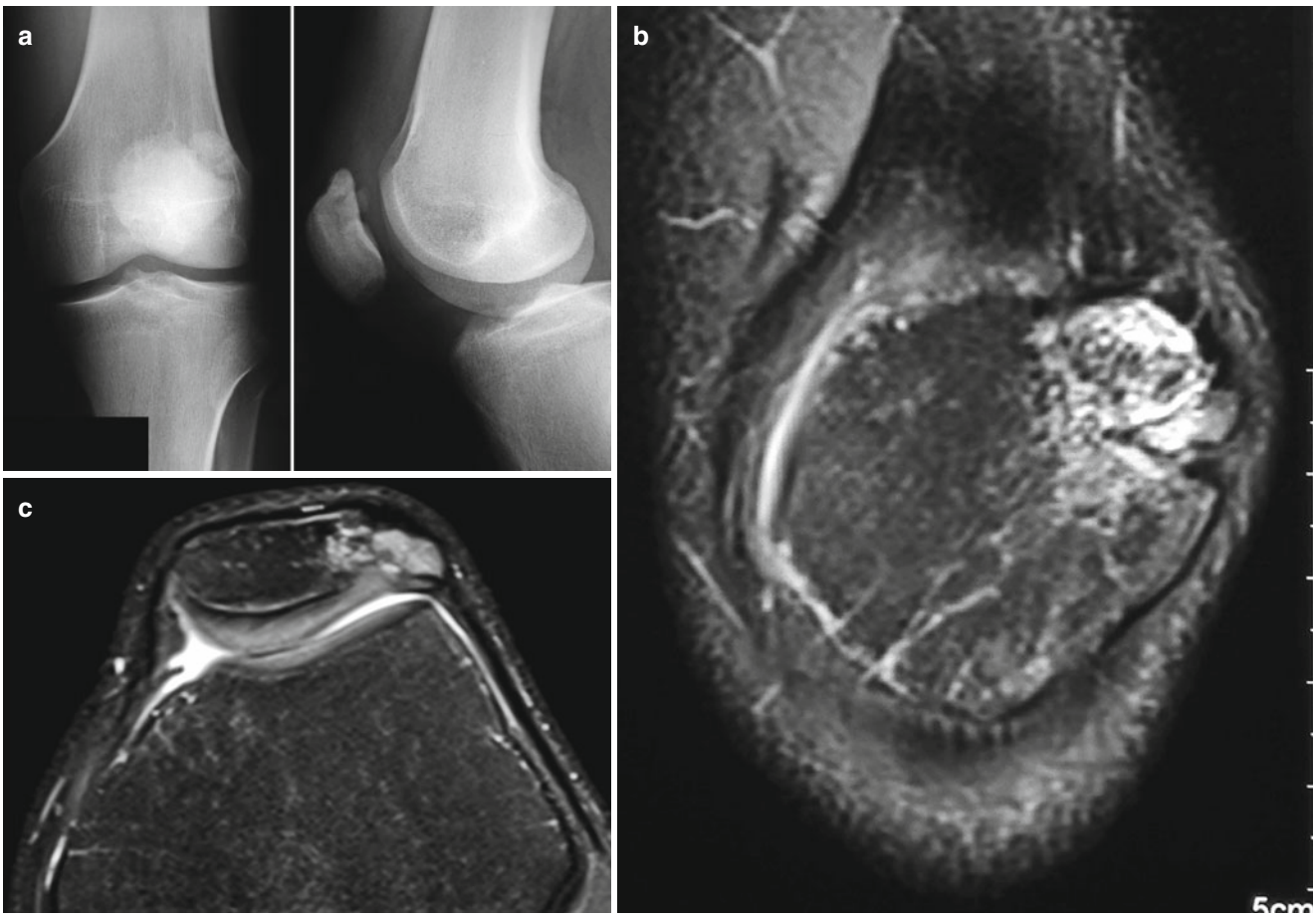

Fig. 10.17 Symptomatic tripartite patella in a 17-year-old athlete. Radiographs of the left knee (**a**) demonstrate two superolateral ossification centers not incorporated to the body of the patella. Coronal (**b**) and transverse (**c**) fat sat PD-WI display bone marrow edema pattern adjacent to the synchondrosis, which presents increased signal intensity

10.3 Osteochondritis Dissecans

Osteochondritis dissecans (OD) is an umbrella term that encompasses a heterogeneous group of focal osteochondral lesions in which there is delamination/sequestration of a bone fragment adjacent to the articular surface, with secondary involvement of the overlying cartilage. This fragment may be unstable and eventually become disconnected, leading to the development of loose bodies. The juvenile form occurs before skeletal maturity and is often found in athletes, probably related to repetitive trauma. Prognosis for juvenile OD is much better than that of the adult form, with more stable fragments and good response to conservative measures. MRI instability criteria present some variation among the different joints but, for the most part, large lesions, perilesional cyst-like lesions, abnormal signal intensity and/or cartilaginous defects in the overlying cartilage, and increased (or fluidlike) signal intensity on T2-WI in the interface fragment/host bone are suggestive of instability, especially if present in combination. Nonetheless, considering the more benign evolution of juvenile OD if compared to the adult forms, it has been suggested that is more prudent to take these criteria as indicators of increased risk instead of absolute markers of instability

OD of the knee is prototypical. Approximately 75 % of the cases affect the medial femoral condyle, typically in its mesial portion, and bilateral disease is found in up to one-third of the patients. OD of the lateral condyle and of the patella is far less frequent, and OD of the tibial plateaus is only sporadic. Most patients are males around 12–13 years old. The classic radiographic appearance is that of a lenticular lucency adjacent to the articular surface, occasionally containing bone fragments (Figs. 10.18, 10.19, and 10.20). Even though mineralized loose bodies may be detected in unstable, displaced lesions, radiographs are not able to assess the stability of in situ osteochondral fragments (Figs. 10.18, 10.19, and 10.20). Besides detecting the aforementioned radiographic findings earlier and with further detail, CT is the best imaging method for the detection of mineralized loose bodies, although it is also limited for the assessment of the stability of in situ frag-

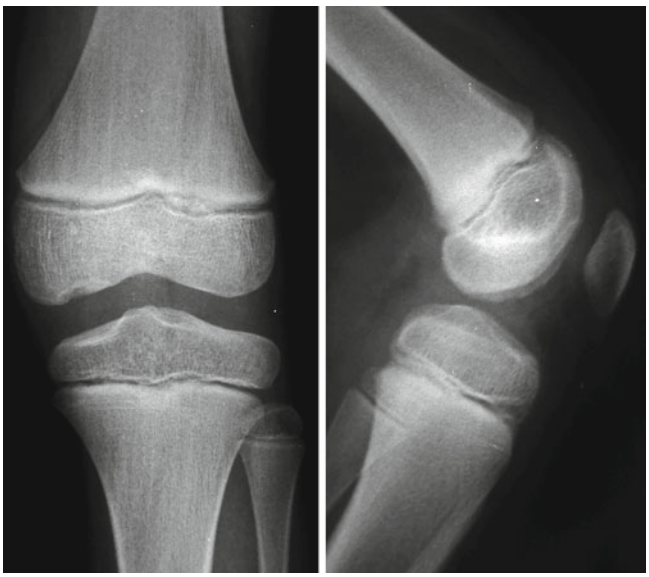

Fig. 10.18 OD of the medial femoral condyle of the left knee. Radiographs demonstrate a subchondral lucency in the mesial portion of the affected condyle containing small bone fragments, more evident in the anteroposterior view

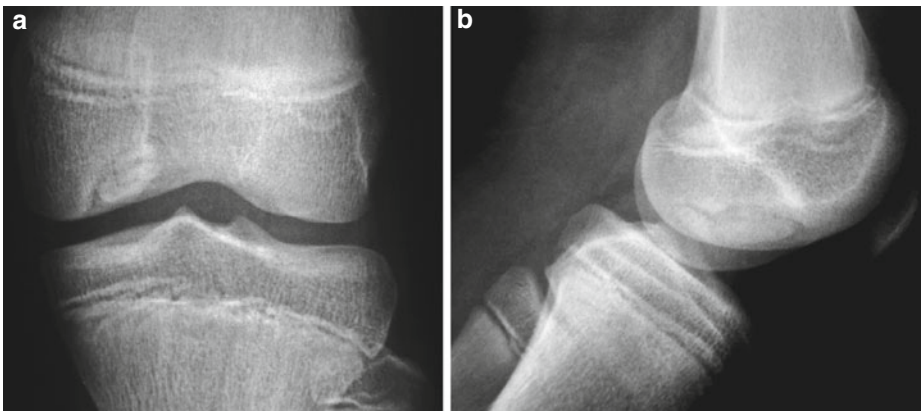

Fig. 10.19 Anteroposterior (**a**) and lateral (**b**) views of the left knee demonstrating OD of the medial femoral condyle. The lesion and the in situ bone fragments are larger than those seen in the patient of Fig. 10.18

ments. MRI can determine the real size of the subchondral lesion, estimate the status of the overlying cartilage, detect intra-articular loose bodies, and, most of all, demonstrate signs of fragment instability. The osteochondral lesion is usually well delimited and presents variable signal intensity, surrounded by bone marrow edema (Figs. 10.21, 10.22, and 10.23). Small lesions (<1 cm) that present evident continuity with the host bone are more probably stable. On the other hand, in addition to the above-mentioned criteria, the presence of bone fragments larger than 1 cm, multiple and/or larger (>5 mm) perilesional cyst-like lesions, and cartilaginous defects larger than 5 mm have all been described as indicative of increased risk of instability (Fig. 10.24). Intra-articular loose bodies and/or an "empty" osteochondral bed filled with synovial fluid indicate advanced OD, no matter the affected joint (Figs. 10.25 and 10.26). MR-arthrography and CT-arthrography are reserved for selected cases, mostly if the findings of non-contrast studies are equivocal, as both are able to disclose irregularity/discontinuity of the overlying cartilage and loose bodies; instability of in situ fragments is present if there is penetration of the intra-articular contrast in the bone/fragment interface.

The term osteochondral lesion of the talus encompasses both OD and osteochondral fractures of this bone: even though the former arises out of repetitive microtrauma and the latter are related to acute traumatic injuries, both fall within the same disease spectrum. These lesions are most common in boys during the second decade of life, affecting mainly the posterior third of the medial convexity and the

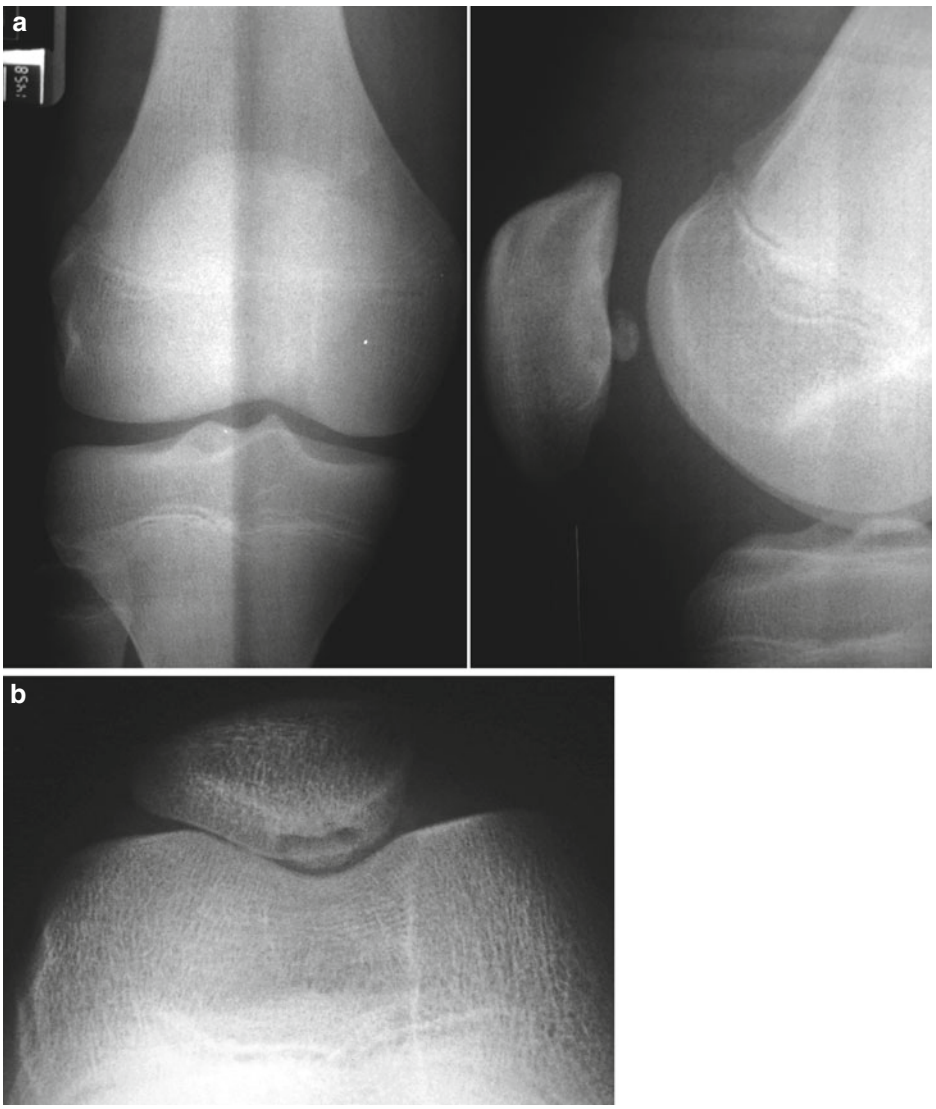

Fig. 10.20 Anteroposterior and lateral views of the knee (**a**) disclose bone fragments adjacent to the articular surface of the patella, related to OD (see Fig. 10.25). However, radiographs are not suitable to assess the stability of the lesion. In another patient, axial view of the patella (**b**) demonstrates more properly the osteochondral bed and the in situ bone fragments, but, once again, it is not possible to evaluate their stability

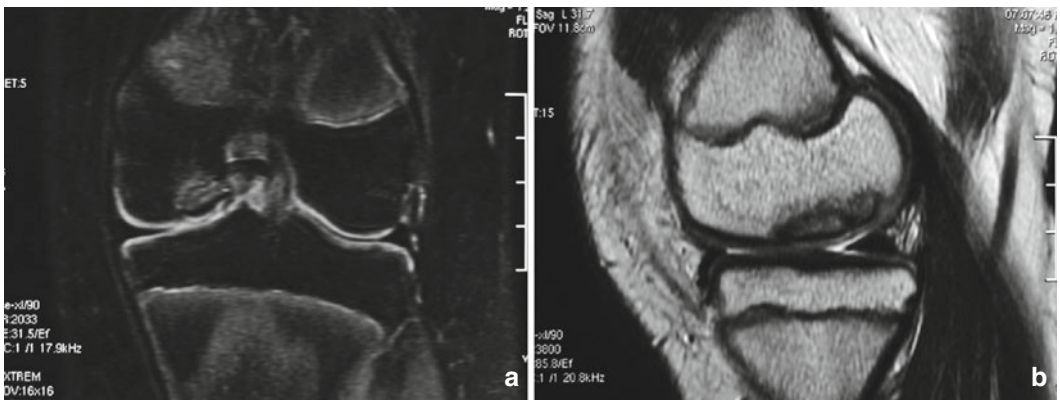

Fig. 10.21 Coronal fat sat PD-WI (**a**) and sagittal T2-WI (**b**) of the left knee of a patient with OD of the medial femoral condyle. There is an in situ bone fragment displaying heterogeneously high signal intensity in (**a**) and low signal intensity in (**b**). Adjacent bone marrow edema is also present, as well as a subtle hyperintense halo surrounding the fragment in (**a**). The overlying cartilage is irregular, with heterogeneous signal intensity

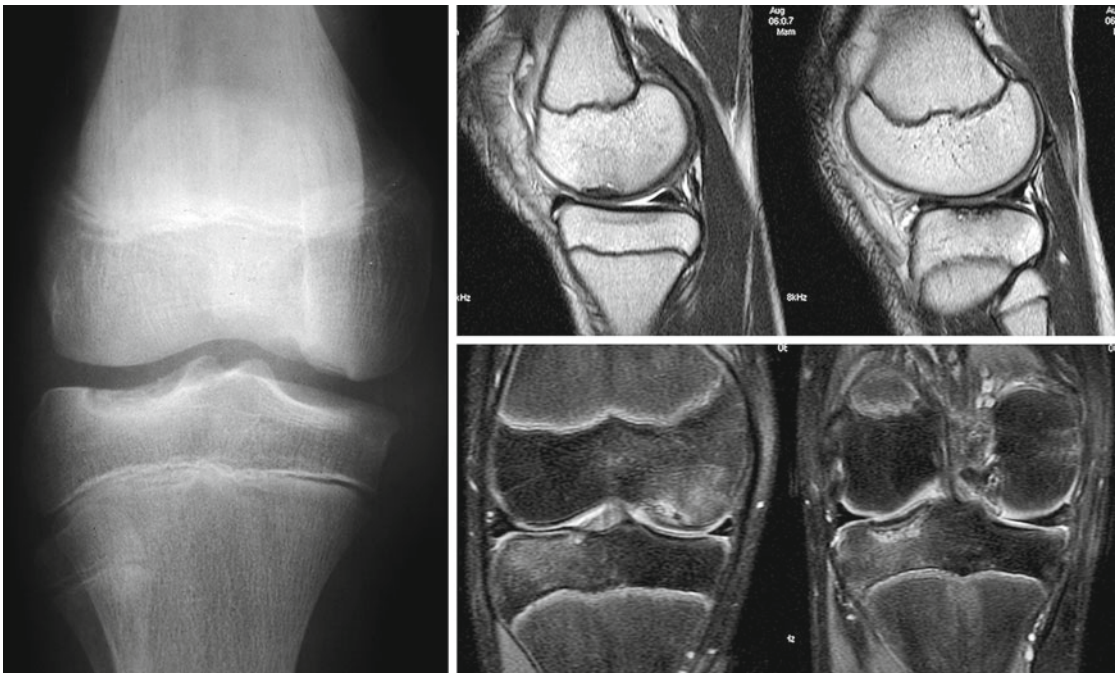

Fig. 10.22 Multifocal OD of the right knee affecting the medial femoral condyle and the lateral tibial plateau. Anteroposterior view (*left*) demonstrates typical subchondral lucencies, with in situ bone fragments. At right, sagittal T2-WI (*upper row*) and coronal fat sat PD-WI (*lower row*) reveal that the bone fragments have heterogeneous signal intensity, with preservation of the overlying cartilages. Cyst-like lesions are seen along the interfaces between the fragments and the host bones. The interfaces are hyperintense on both sequences

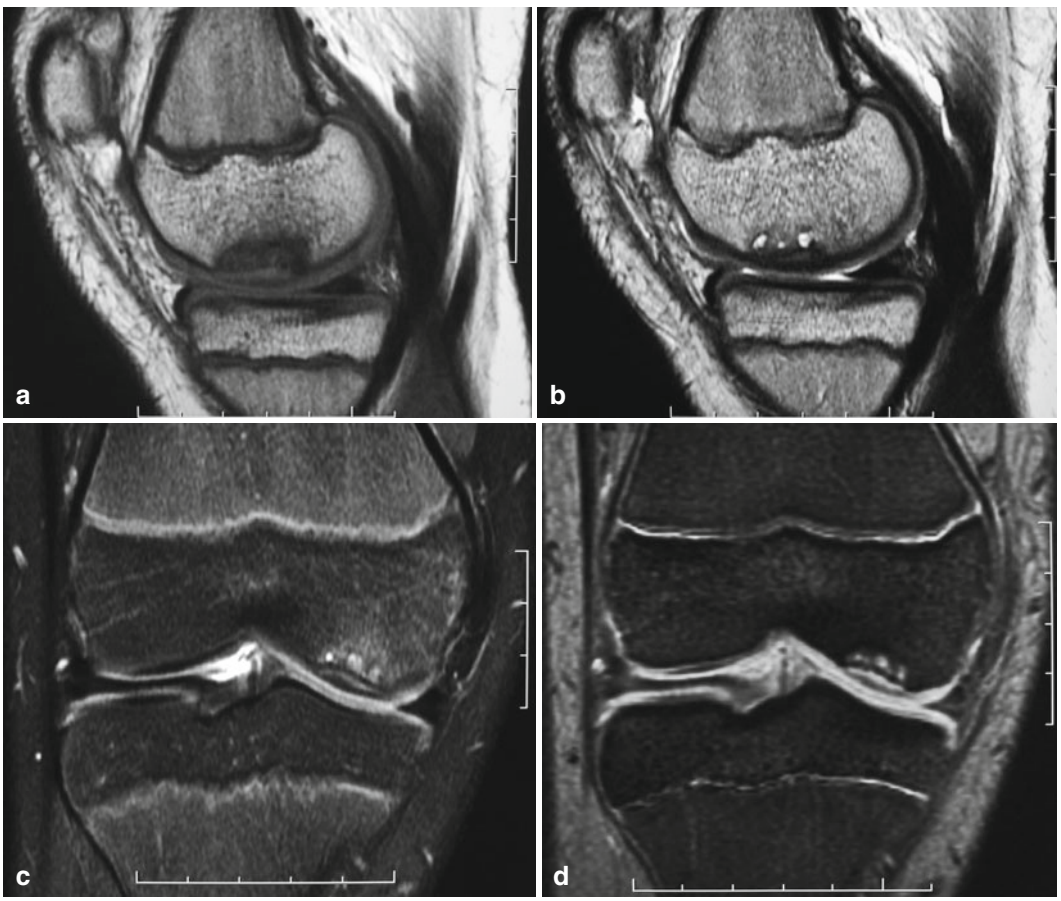

Fig. 10.23 Sagittal T1-WI (**a**) and T2-WI (**b**) and coronal fat sat PD-WI (**c**) and gradient-echo image (**d**) of the knee of an adolescent with OD of the medial femoral condyle. The fragment presents variable signal intensity in the different sequences, with adjacent bone marrow edema and multiple small cysts along the interface fragment/host bone

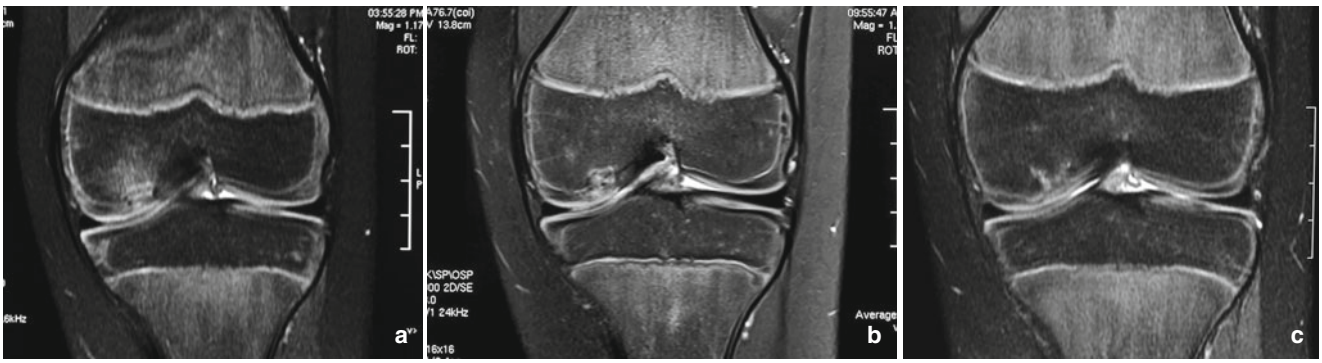

Fig. 10.24 Coronal fat sat PD-WI of the left knee acquired in intervals of 1 year, from age 7 to age 9. The first image (**a**) evidences OD of the medial femoral condyle with an in situ bone fragment of high signal intensity, surrounded by bone marrow edema, as well as hyperintensity in the interface fragment/host bone and heterogeneous signal intensity of the overlying cartilage. The second image (**b**) reveals involution of the bone marrow edema and heterogeneous signal intensity of the fragment and of the cartilage, while the third image (**c**) demonstrates virtually complete incorporation of the bone fragment 2 years later, emphasizing the relative importance of the classic signs of instability in the juvenile form of OD

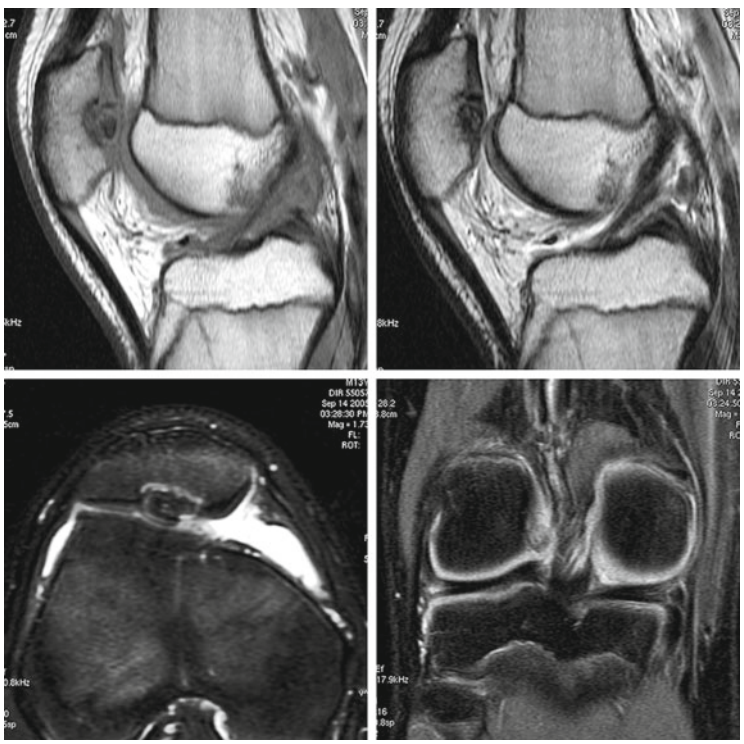

Fig. 10.25 Sagittal T1-WI (*upper-left image*) and T2-WI (*upper-right image*) and fat sat PD-WI in the transverse (*lower-right image*) and coronal (*lower-left image*) planes of the right knee of the same patient of Fig. 10.20. There is OD of the patella with in situ bone fragments that display low to intermediate signal intensity in all sequences, surrounded by a hyperintense halo on fat sat PD-WI. The overlying cartilage is irregular and heterogeneous. A cartilaginous loose body undetectable on radiographs can be seen posterolateral to the anterior cruciate ligament, with intermediate signal intensity on T1-WI and low signal intensity in the other sequences

middle third of the lateral convexity of the talar dome, appearing as rounded subchondral lucencies on radiographs and CT (Fig. 10.27). Their appearance on MRI is quite similar to that above described for OD of the knee (Figs. 10.27, 10.28, 10.29, and 10.30). MR-arthrography, CT-arthrography, and high-resolution MRI sequences are more important in OD of the ankle and the elbow than in the knee, as the articular cartilages are thinner in the former and difficult to evaluate with routine protocols (Fig. 10.27). The validity of intravenous gadolinium to distinguish fluid from granulation tissue in the fragment/bone interface and to determine the viability of the bone fragment in OD of the ankle and elbow is not established (Fig. 10.30).

Panner disease and OD of the capitulum are the most important lesions of the lateral compartment of the elbow in skeletally immature athletes. Despite their similar clinical presentation (pain, edema, and tenderness in the lateral aspect of the joint), they are distinct conditions that affect distinct age groups, with distinct prognoses. Panner disease is an osteochondrosis of the capitulum that usually occurs in children between 7 and 12 years old. It is a benign, self-limited process, not associated with development of loose

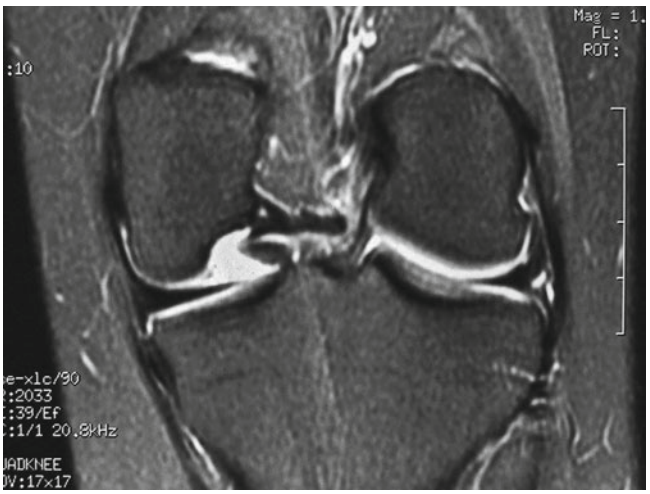

Fig. 10.26 Chronic OD in a 21-year-old patient. Coronal fat sat PD-WI reveals an "empty" osteochondral bed in the medial femoral condyle, filled with synovial fluid, as well as a large loose osteochondral body adjacent to the intercondylar notch

bodies. Conservative treatment yields good results, the prognosis is excellent, and the epiphysis regains its normal appearance with growth. On the other hand, OD affects mainly males between 12 and 16 years of age, during the final stage of ossification of the capitulum. Prognosis for OD of the elbow is worse than that for OD of the knee, with more frequent development of osteoarthritis, chronic pain, and functional limitation. The radiographic appearance of Panner disease may be quite exuberant, with bone fissures, irregularity/flattening of the capitulum and intertwined areas of bone rarefaction, and sclerosis. It affects the epiphysis as a whole, in contradistinction to what occurs in OD (which is usually confined to the anterolateral portion of the epiphysis). MRI displays diffuse bone marrow edema in the affected epiphysis, with an intact overlying cartilage, even though MRI is not necessary in most cases of Panner disease, given its benign clinical course. In OD, there is a well-defined subchondral lucency that may be associated with flattening of the articular surface and bone fragmentation (Fig. 10.31);

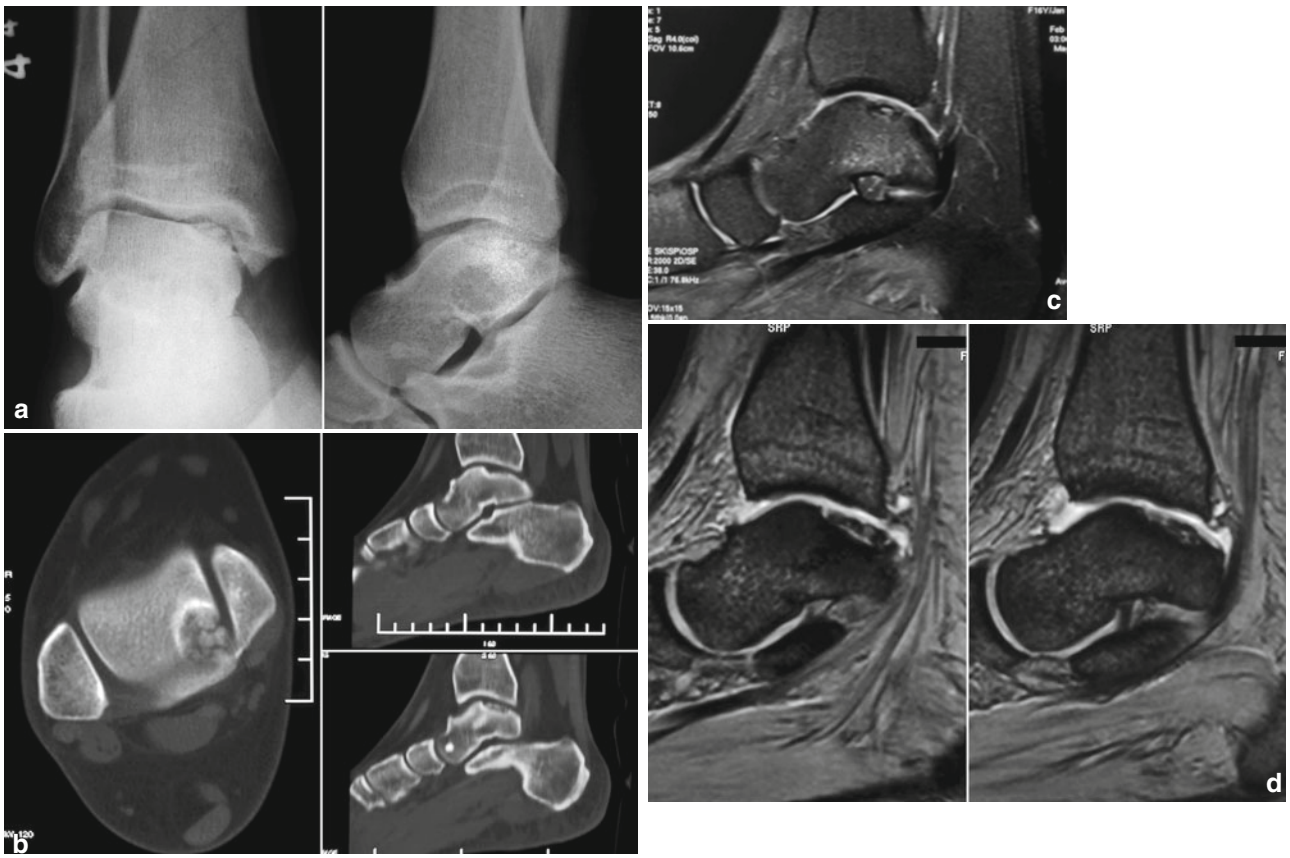

Fig. 10.27 Radiographs (**a**) and CT images (**b**) of the right ankle of a 16-year-old female with OD of the talus. The radiographs evidence a subchondral lucency in the posteromedial convexity of the talar dome, containing bone fragments, which is clearly demonstrated on CT. Nonetheless, none of these methods allows obtaining accurate information about the overlying cartilage or concerning the stability of the lesion. Sagittal fat sat PD-WI (**c**) and 3D gradient-echo images (**d**) reveal adjacent bone marrow edema pattern (more evident in **c**) and thinning/irregularity of the overlying cartilage (more clearly seen in **d**), without signs of frank instability

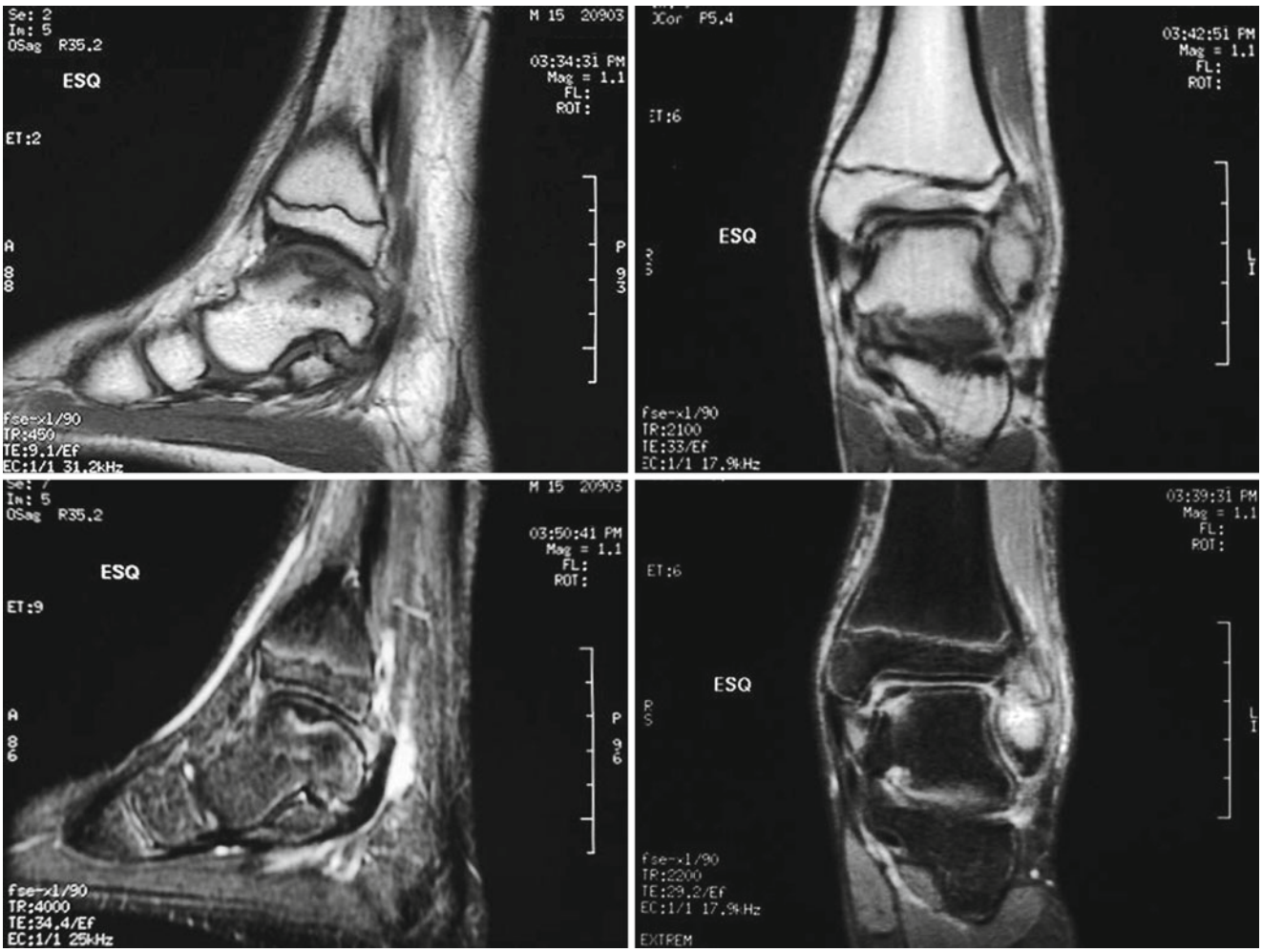

Fig. 10.28 MRI of the left knee of a 15-year-old male soccer player with persistent joint pain 2 months after a traumatic episode. At *left*, sagittal T1-WI (*upper image*) and fat sat T2-WI (*lower image*) and, at *right*, coronal PD-WI (*upper image*) and fat sat PD-WI (*lower image*). There is an osteochondral lesion in the medial convexity of the talar dome with an in situ fragment, surrounded by bone marrow edema. Bone marrow edema is also seen in the lateral malleolus (contrecoup lesion), with swelling of the periarticular soft tissues

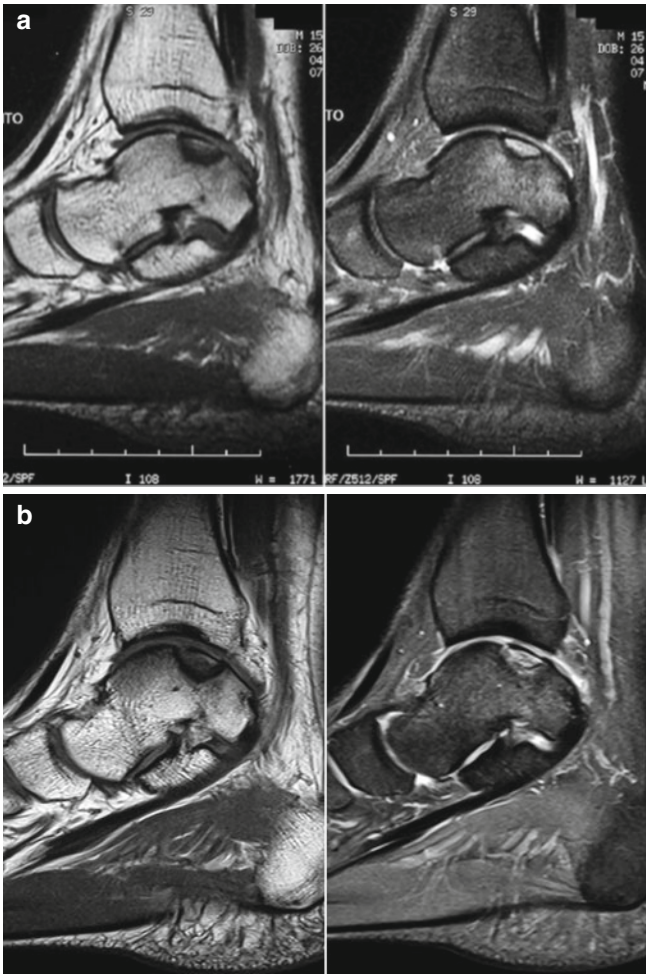

Fig. 10.29 Evolution of juvenile OD of the talus. Sagittal T1-WI (*left images*) and fat sat PD-WI (*right images*) acquired at age 15 (**a**) and age 22 (**b**) reveal an in situ bone fragment in both studies. Despite the edematous changes of the bone fragment and the irregularity of the articular cartilage in (**b**), the stability of the lesion after 7 years of conservative treatment emphasizes the more benign nature of juvenile OD if compared to the adult form

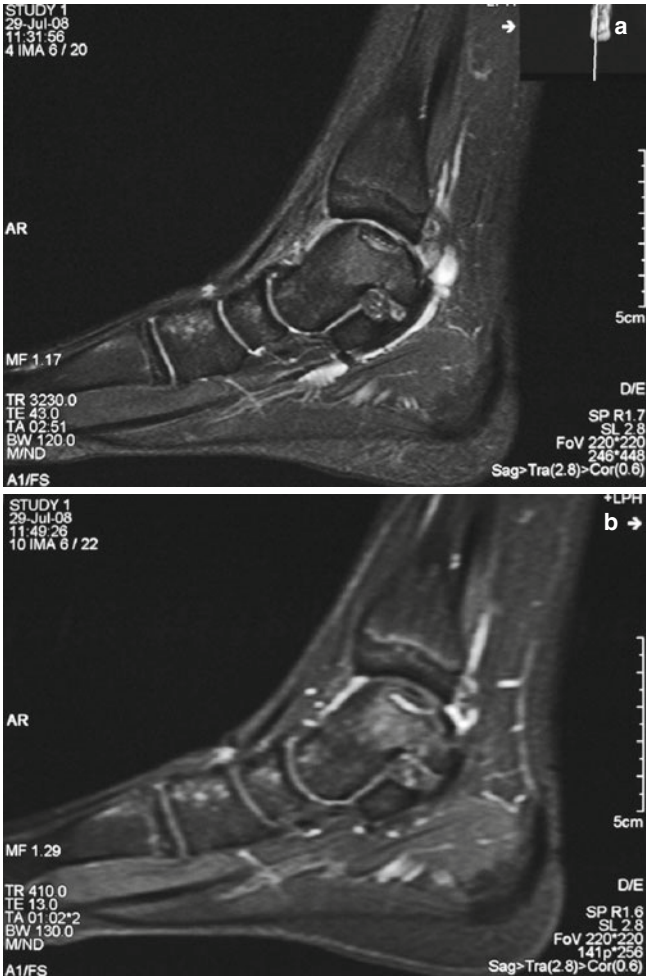

Fig. 10.30 A 14-year-old elite-level female gymnast. Sagittal fat sat T2-WI (**a**) and post-contrast fat sat T1-WI (**b**) demonstrate OD of the medial convexity of the talus. There is continuity between the bone fragment (which presents post-gadolinium enhancement) and the host bone. Enhancement is also present in the fragment/host bone interface, which appears hyperintense on fat sat T2-WI. Perilesional bone marrow edema is present, also seen in the tarsal bones, the latter representing a response to the anomalous stress related to the sports practice

when present, loose bodies are found more often in the olecranon fossa. MRI is quite sensitive, and abnormal findings are present even if radiographs are still normal. The signal intensity of the lesion is variable, and it is important to keep in mind that even sclerotic lesions may appear hyperintense on T2-WI (Fig. 10.31). Just like in other joints, a perilesional halo of increased (or even fluidlike) signal intensity on T2-WI and cysts in the fragment/bone interface have been described as indicative of increased risk of instability for in situ lesions.

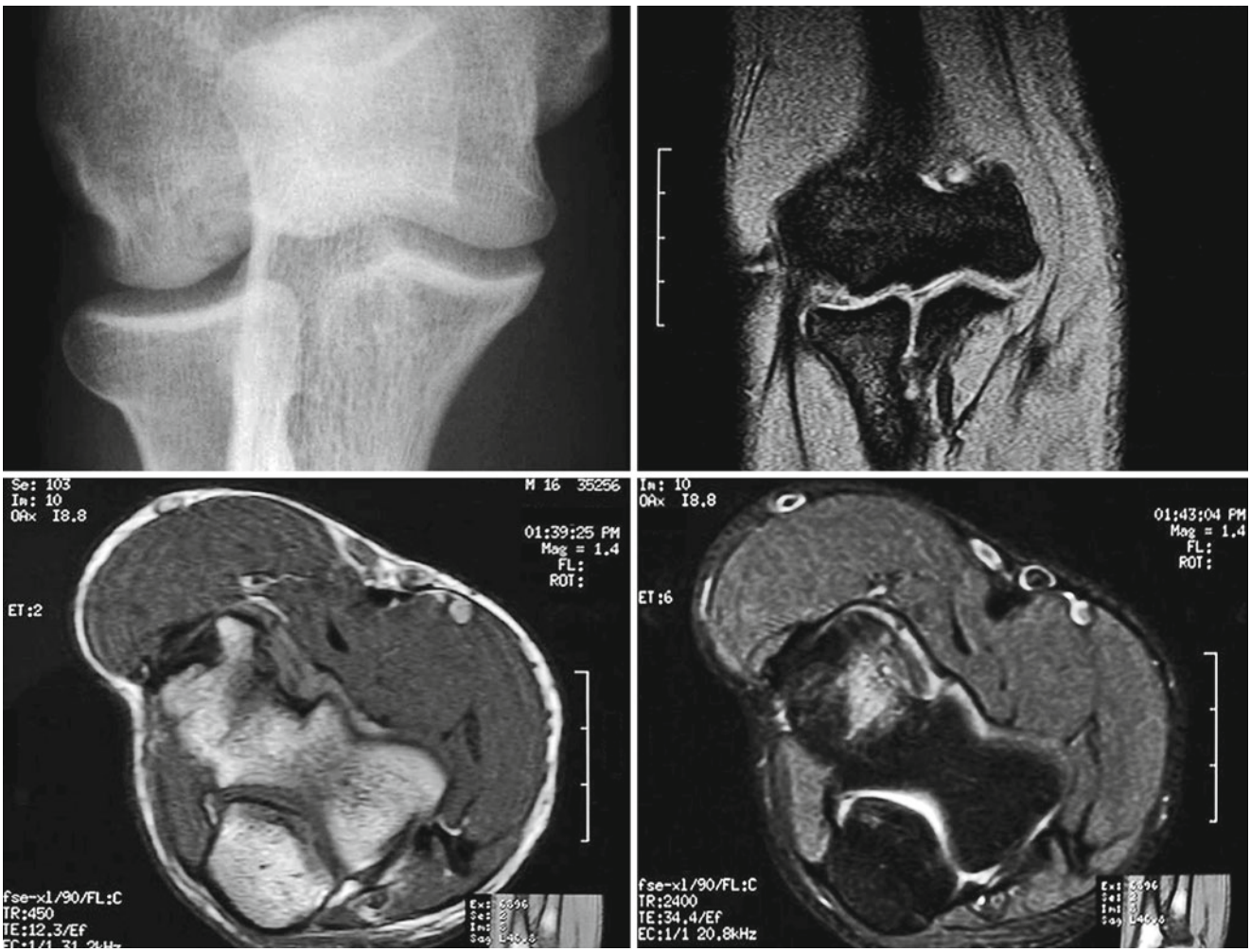

Fig. 10.31 A 16-year-old patient with OD of the capitulum. Anteroposterior view (*upper-left image*) discloses a subchondral lucency in the capitulum, containing bone fragments. Coronal gradient-echo image (*upper-right image*) and transverse T1-WI (*lower-left image*) and fat sat PD-WI (*lower-right image*) demonstrate that the bone fragment is predominantly hypointense on T1-WI and heterogeneous on PD-WI, surrounded by bone marrow edema pattern. The interface with the host bone appears hyperintense on PD-WI, with a small cyst-like lesion in the adjacent cancellous bone

10.4 Stress-Related Physeal Injuries

The term "little leaguer's shoulder" is used to describe a peculiar lesion of the growth plate of the proximal humerus related to overuse/anomalous stress, considered a non-displaced form of epiphysiolysis (Salter-Harris fracture type I). It is more common in athletes between 11 and 16 years old, mainly baseball pitchers. These children present pain and tenderness in the lateral aspect of the shoulder, which worsens with physical activity. Radiographs may be normal or there may be widening of the proximal humeral physis, with osteopenia, bone fragmentation, sclerosis, or cyst-like lucencies along the physis, mainly in its lateral portions. Comparison with the contralateral shoulder is useful in subtle cases, and correlation between clinical and radiographic data is usually sufficient for the diagnosis. MRI demonstrates physeal widening (with increased signal intensity on T2-WI), edema of the metaphyseal bone marrow, and, occasionally, periosteal stripping and edema of the adjacent soft tissues (Fig. 10.32). A similar condition is the so-called gymnast wrist, a type of sports-related injury of the physis of the distal radius that is also considered a non-displaced Salter-Harris fracture type I. Imaging findings are similar to those above described for "little leaguer's shoulder"; however, premature physeal closure may occur in patients with severe injuries, leading to positive ulnar variance and increased risk of late development of ulnar impaction syndrome.

Slipped capital femoral epiphysis (SCFE) is a transphyseal fracture of the proximal femur that leads to posteroinferior slippage of the ossification center of the femoral head relative to its metaphysis, in contradistinction to the non-displaced Salter-Harris fractures type I described in the

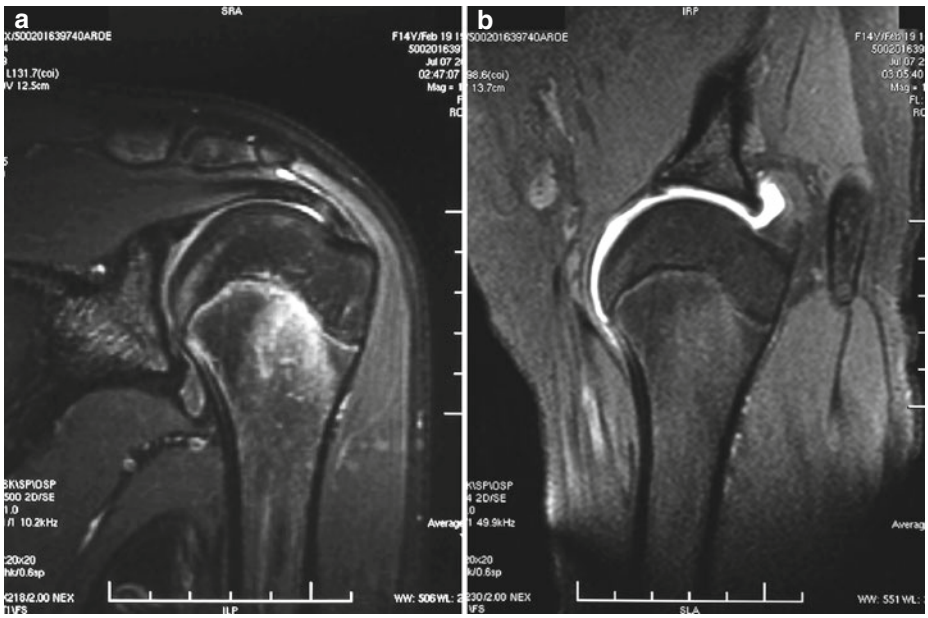

Fig. 10.32 MR-arthrography of the left shoulder of a 14-year-old female complaining of pain and tenderness on the lateral aspect of this joint (little leaguer's shoulder). Coronal fat sat T2-WI (**a**) and fat sat T1-WI in abduction and external rotation (**b**) reveal metaphyseal bone marrow edema radiating from the physis, which presents mild lateral widening, more evident in (**b**) (Courtesy of Dr. Daniel Sa, Image Memorial – Diagnosticos da America S.A., Salvador, Brazil)

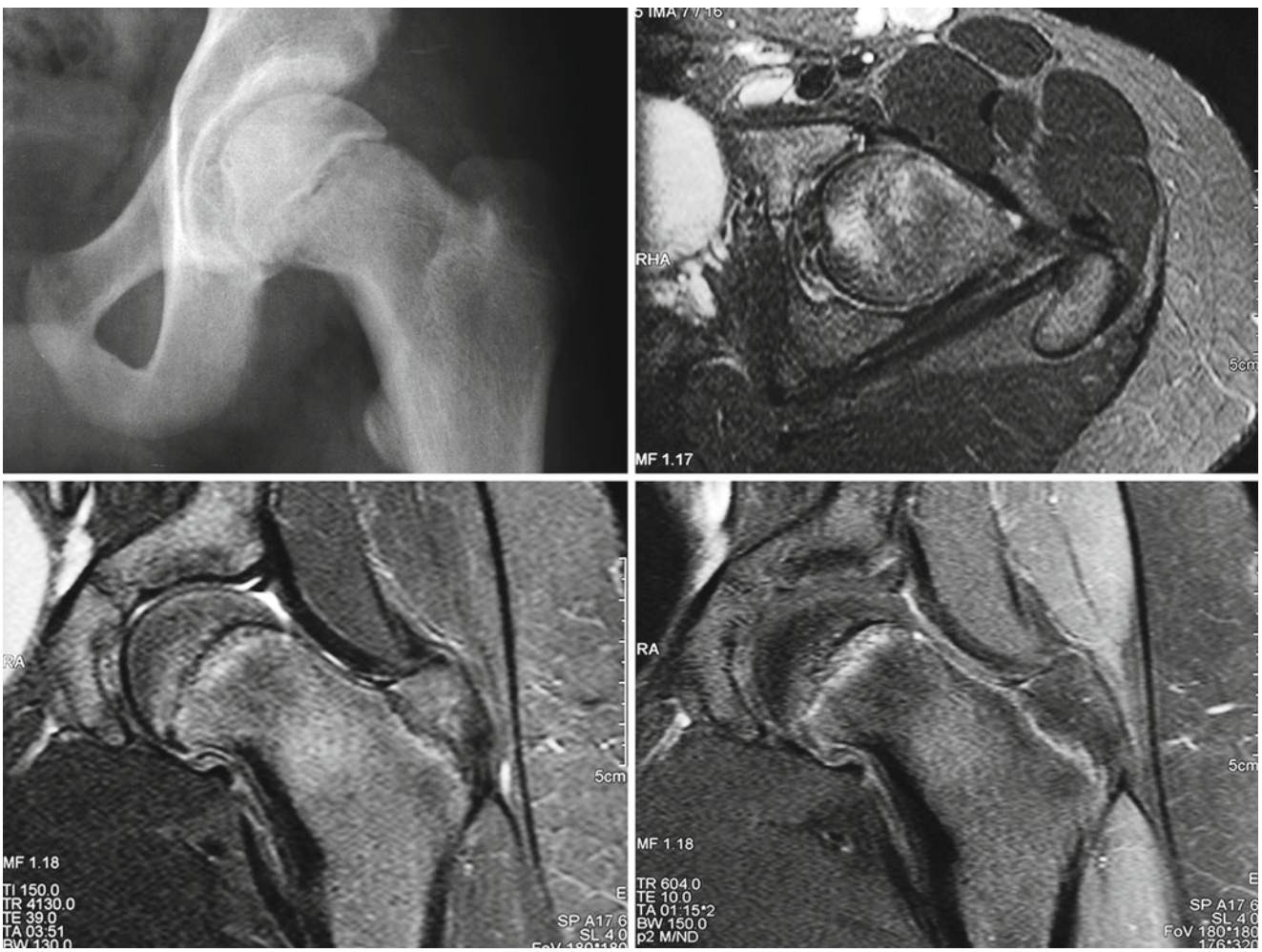

Fig. 10.33 Left-sided SCFE. Radiograph of the left hip (*upper-left image*) demonstrates that an imaginary line drawn along the lateral cortex of the femoral neck does not intersect the femoral epiphysis. Transverse STIR image (*upper-right image*) and coronal STIR image (*lower-left image*) and post-gadolinium fat sat T1-WI (*lower-right image*) evidence posteroinferior slippage of the epiphysis, with juxtaphyseal bone marrow edema and physeal widening. Post-gadolinium enhancement is evident both in the physis and in the edematous bone marrow

previous paragraph. SCFE is more frequent in males between 10 and 16 years old, notably in obese individuals. Approximately 20 % of the cases are bilateral at presentation, even though up to 50 % of all patients may eventually develop bilateral SCFE. These patients present with inguinal pain, limping, and internal rotation of the affected limb. Early diagnosis is paramount to stop disease progression and reduce the risk of complications such as joint deformity, osteoarthritis, and osteonecrosis; confirmation of the clinical hypothesis with imaging is mandatory. The earliest radiographic sign is a slight step-off at the level of the physis, more evident on the lateral view. In normal patients, a line drawn along the superior border of the femoral neck in the anteroposterior view (Klein's line) should intersect the lateral portion of the femoral epiphysis. In SCFE, the femoral head is positioned below this line, and the lower its position, the higher the degree of epiphyseal slippage (Fig. 10.33). Widening and blurring of the physis may also be present in the anteroposterior view, with superimposition of the posteriorly displaced epiphysis over the femoral neck. As slippage advances, there is remodeling of the anterosuperior femoral metaphysis and development of a bone callus in the posterior portion of the femoral neck, which is more evident on CT (Fig. 10.34). CT is also useful to evaluate late-stage deformities related to SCFE (Fig. 10.35). On MRI, the diagnosis of SCFE relies on the recognition of the deformity at the level of the head/neck transition and on the presence of bone marrow edema pattern centered at the physis (Figs. 10.33 and 10.36). Radiographic findings may be transposed to coronal images, which also show absent intersection between Klein's line and the femoral head (Fig. 10.33). The inclusion of both hips in the field of view of MRI images allows for early recognition of contralateral epiphysiolysis (which must be sought before epiphyseal displacement occurs) and avascular necrosis.

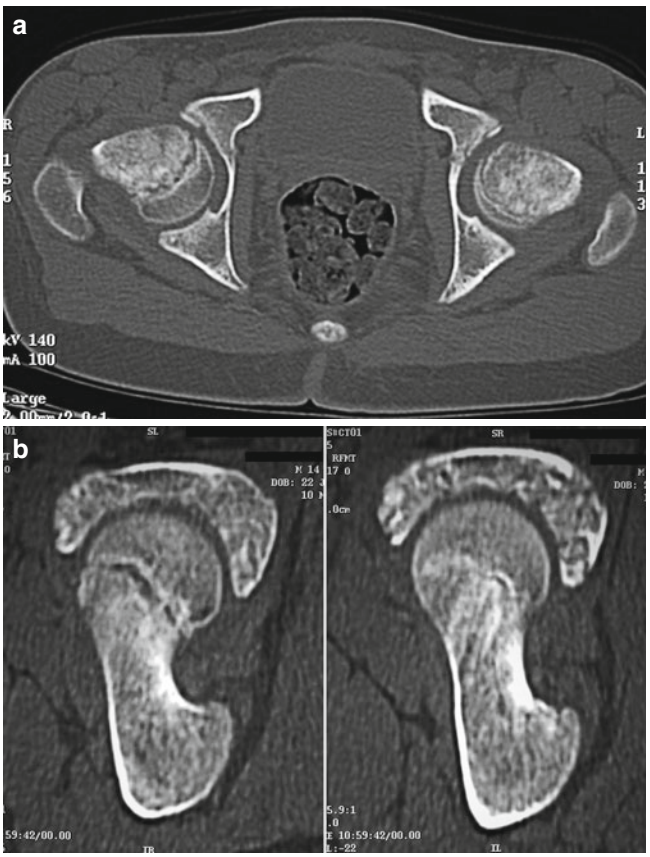

Fig. 10.34 Bilateral SCFE in a 14-year-old patient. Transverse CT image (**a**) and sagittal reformatted images (**b**) reveal posteroinferior slippage of the proximal femoral epiphyses, more important at right, where physeal widening is more evident. Thickening of the posterior cortices of the femoral necks is also evident on sagittal images

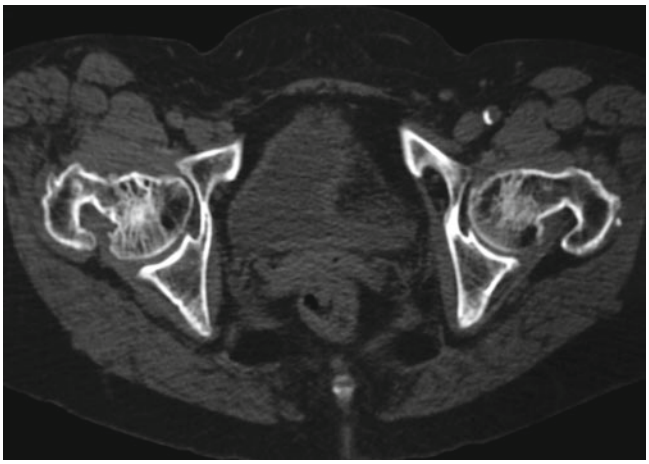

Fig. 10.35 CT scan of the pelvis of an elderly patient with late-stage sequelae of bilateral SCFE. There is deformity of the proximal femora, with marked retroversion of the femoral heads and secondary osteoarthritis (note the remarkable similarity with Fig. 10.34a)

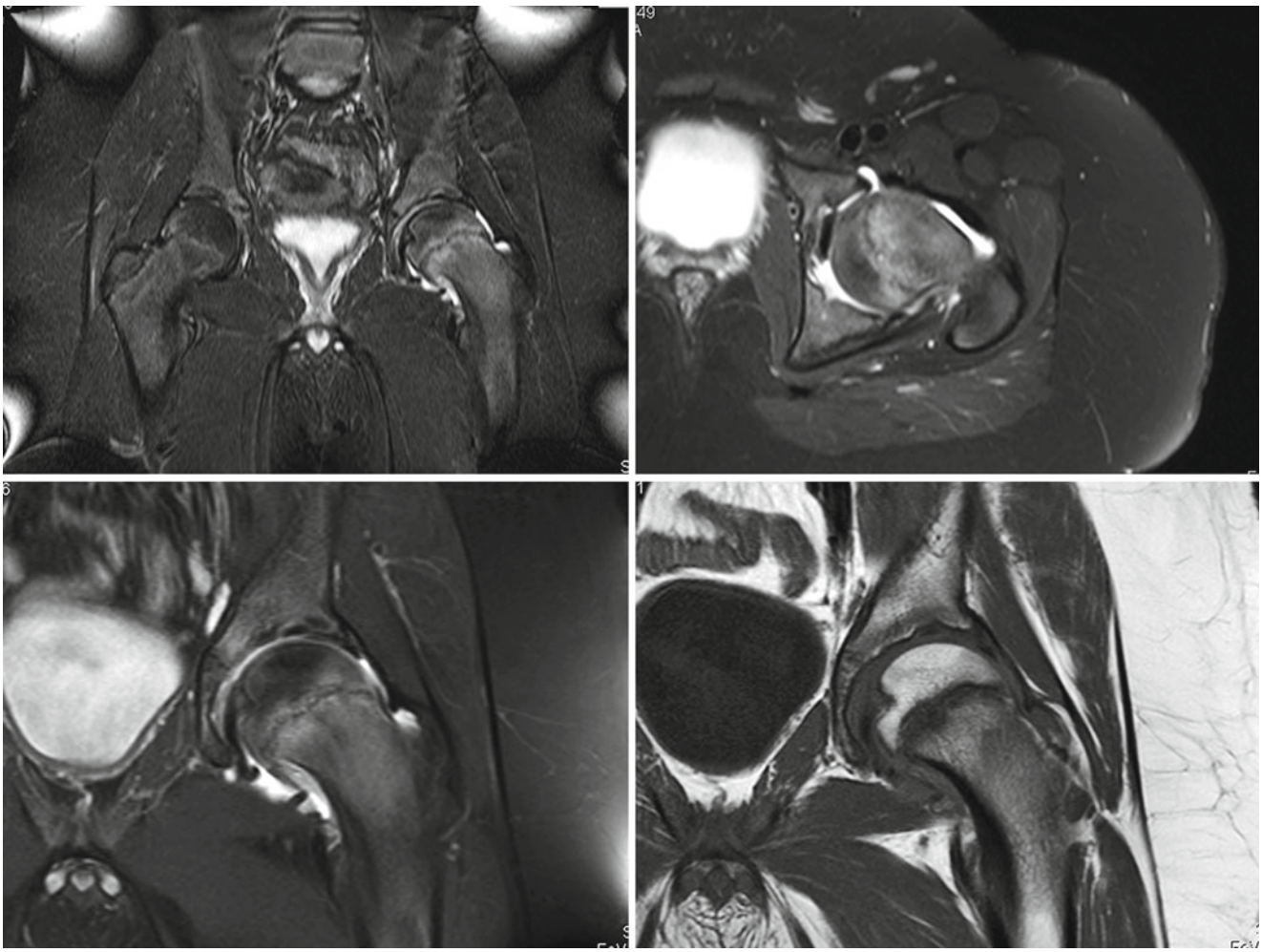

Fig. 10.36 Left-sided SCFE in a 13-year-old adolescent. The *upper-left image* (coronal fat sat PD-WI including both hips) demonstrates bone marrow edema centered about the left physis that is absent in the contralateral hip, associated with joint effusion. Transverse fat sat PD-WI (*upper-right image*) and coronal fat sat PD-WI (*lower-left image*) and T1-WI (*lower-right image*) show posteroinferior slippage of the proximal femoral epiphysis and physeal widening, as well as the above-described juxtaphyseal bone marrow edema

10.5 Stress Fractures

Stress fractures (SF) in skeletally immature patients occur most often during the second half of adolescence, frequently associated with running sports. These fractures result from the action of forces of submaximal intensity on an otherwise normal bone, which are chronic and repetitive but less intense than those necessary to cause acute fractures in a single event, without recovery time between the stressing episodes. SF are more common in the lower limbs, mostly in the tibiae (50–75 % of the cases), followed by the metatarsals and the fibulae. The patients complain of pain of low intensity that worsens with physical activity, occasionally associated with limping. Correlation with clinical data is crucial, especially in children, given the relatively low incidence of stress fractures in this group age.

Radiographs are insensitive – only 10–25 % of the patients will present radiographic abnormalities at presentation, and 2–4 weeks are necessary for them to become evident. In addition, up to half of the patients will never ever develop radiographic findings. Focal cortical lucencies, endosteal thickening, sclerosis of the trabecular bone, and periosteal reaction are the most common findings. In long bones, the fracture line appears as a linear lucency crossing the cortex, while a sclerotic band perpendicular to the trabeculae is seen in predominantly trabecular bones, such as the calcaneus (Fig. 10.37). The same findings are evident on CT, which may be useful in some cases, mostly as an alternative for patients who cannot undergo MRI; however, CT is not a first-line imaging method for the assessment of SF in pediatric patients.

MRI is the method of choice to confirm or to rule out the possibility of SF when radiographs are negative, with sensi-

tivity and specificity near to 100 %, and to distinguish fractures from other causes of pain, whether located in the bone or in the soft tissues. In the early stages, there is increased signal intensity along the periosteum on T2-WI, without abnormalities of the subjacent bone. Stress reaction (pre-fracture events) is characterized by edematous changes of the bone marrow and of the soft tissues, without a well-delimited fracture line (Fig. 10.38). The fracture line appears as a linear band of low signal intensity in all sequences, which is irregular and surrounded by bone marrow edema, often associated with periosteal reaction (Fig. 10.39). Post-contrast enhancement is seen in the edematous areas.

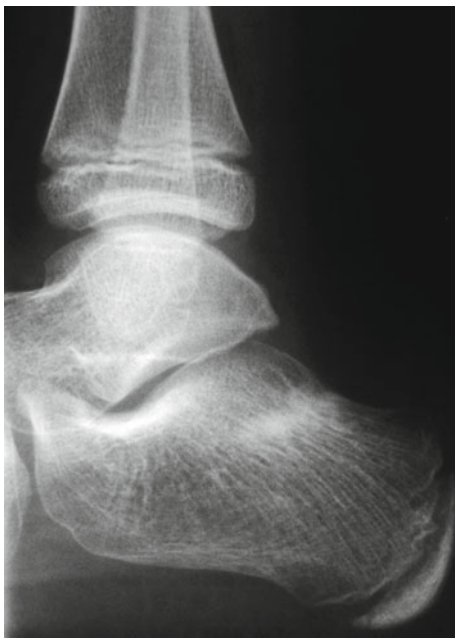

Fig. 10.37 Stress fracture of the calcaneus in a skeletally immature patient. There is a band of sclerosis perpendicular to the bone trabeculae, typical of stress fractures in this site

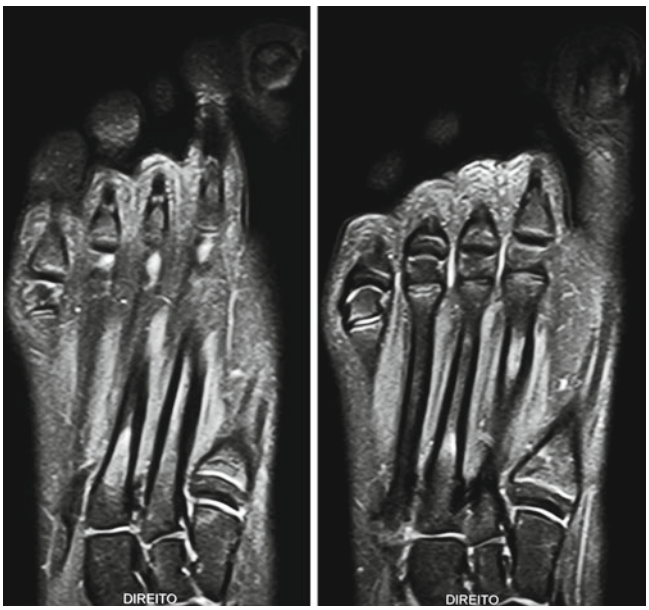

Fig. 10.38 An 11-year-old ballerina complaining of pain in both feet. Transverse fat sat T2-WI of the right foot disclose several areas of bone marrow edema from the first to the third metatarsals, with focal thickening of the medial cortex of the second one, without discernible fracture lines. Multiple foci of bone marrow edema were also present in the left foot (not shown) due to stress reaction related to physical activity

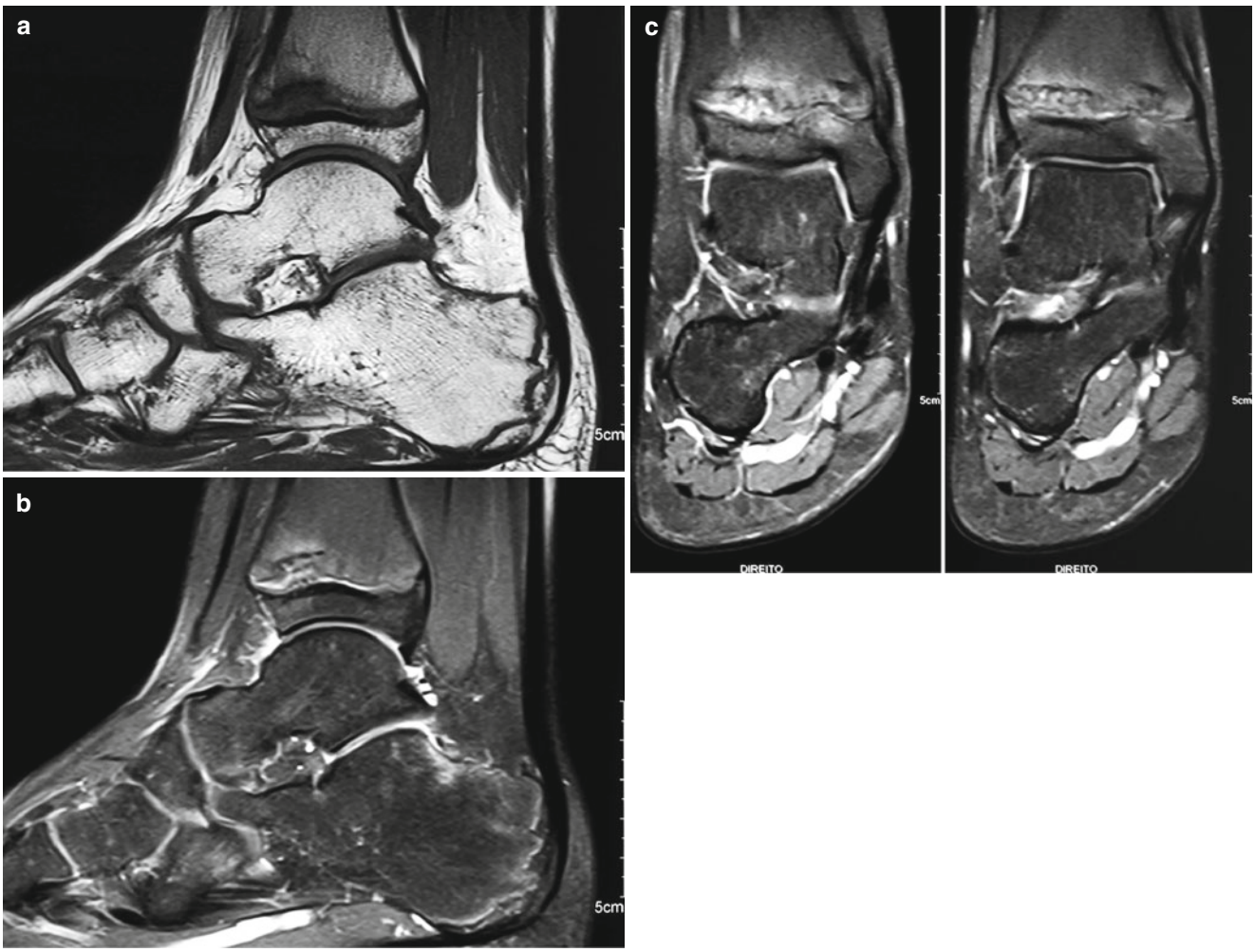

Fig. 10.39 A 12-year-old soccer player with pain in the right ankle that got worse with physical activity. Sagittal T1-WI (**a**) and fat sat T2-WI (**b**) and coronal fat sat T2-WI (**c**) demonstrate an anterolateral fracture line in the trabecular bone of the distal tibial metaphysis, coursing parallel to the growth plate and reaching the lateral cortex, surrounded by bone marrow edema. These findings are typical for a stress fracture

Key Points

- Imaging findings are very similar in the several forms of chronic apophysitis. Radiographs and CT show fragmentation, heterogeneity, and increased size of the affected apophysis; physeal widening and periosteal reaction are often present. On US, there is increased vascularity, edema of the surrounding soft tissues, and structural changes in the adjacent tendons. MRI discloses an apophysis of increased size, with bone marrow edema and post-gadolinium enhancement; inflammation is also present in the metaphyseal bone marrow, in the physis, and in the surrounding soft tissues. Imaging findings may simulate aggressive lesions.
- Juvenile OD presents similar imaging findings in different joints. Radiographs and CT demonstrate a subchondral lucency that may contain bone fragments, but these methods are not able to accurately assess the stability of in situ fragments. MRI is both sensitive and specific, being able to diagnose the lesion and estimate its stability. Findings suggestive of instability include large-sized lesions, perilesional cyst-like areas, increased signal intensity on T2-WI in the interface fragment/host bone, abnormal signal intensity of the overlying cartilage, and large cartilaginous defects, with some variation in these criteria depending on the affected joint. Intra-articular loose bodies and the presence of an "empty" osteochondral bed are safe indicators of advanced OD. Even though MR-arthrography and CT-arthrography can establish if a lesion is stable or unstable beyond any doubt, their use is usually reserved to selected cases.
- Little leaguer's shoulder, gymnast wrist, and slipped femoral capital epiphysis (SCFE) are stress-

induced physeal lesions (Salter-Harris fractures type I, non-displaced in the humerus and in the radius and displaced in the femur). In the lesions of the upper extremity, there is physeal widening with bone fragmentation and rarefaction along the physis, as well as edematous changes of the bone and of the soft tissues on MRI. In SCFE, there is posteroinferior displacement of the proximal femoral epiphysis and bone marrow edema pattern centered at the physis.

- Radiographs are fairly insensitive for the assessment of stress fractures; fracture lines appear as linear lucencies that cross the cortex in the long bones, commonly associated with periosteal reaction, while in predominantly trabecular bones they appear as sclerotic bands coursing perpendicular to the trabeculae. MRI is both sensitive and specific, displaying increased signal intensity on T2-WI along the periosteum in the initial stages, without abnormalities of the subjacent bone. Stress reactions are characterized by edematous changes in the bone and in the soft tissues that lack a well-defined fracture line. The fracture appears as an irregular band of low signal intensity in all sequences. Post-contrast enhancement is seen in the edematous areas and in the periosteal reaction.

Recommended Reading

Arnaiz J, Piedra T, de Lucas EM, Arnaiz AM, Pelaz M, Gomez-Dermit V et al (2011) Imaging findings of lower limb apophysitis. AJR Am J Roentgenol 196(3):W316–W325

Cassas KJ, Cassettari-Wayhs A (2006) Childhood and adolescent sports-related overuse injuries. Am Fam Physician 73(6):1014–1022

Davis KW (2010) Imaging pediatric sports injuries: lower extremity. Radiol Clin North Am 48(6):1213–1235

Davis KW (2010) Imaging pediatric sports injuries: upper extremity. Radiol Clin North Am 48(6):1199–1211

Dwek JR (2009) The hip: MR imaging of uniquely pediatric disorders. Magn Reson Imaging Clin N Am 17(3):509–520

Emery KH (2006) Imaging of sports injuries of the upper extremity in children. Clin Sports Med 25(3):543–568

Frick SL (2006) Evaluation of the child who has hip pain. Orthop Clin North Am 37(2):133–140

Kerssemakers SP, Fotiadou AN, de Jonge MC, Karantanas AH, Maas M (2009) Sport injuries in the paediatric and adolescent patient: a growing problem. Pediatr Radiol 39(5):471–484

Kijowski R, Tuite MJ (2010) Pediatric throwing injuries of the elbow. Semin Musculoskelet Radiol 14(4):419–429

Patel CV (2009) The foot and ankle: MR imaging of uniquely pediatric disorders. Magn Reson Imaging Clin N Am 17(3):539–547

Patel DR (2010) Stress fractures: diagnosis and management in the primary care setting. Pediatr Clin North Am 57(3):819–827

Polousky JD (2011) Juvenile osteochondritis dissecans. Sports Med Arthrosc 19(1):56–63

Sanchez R, Strouse PJ (2009) The knee: MR imaging of uniquely pediatric disorders. Magn Reson Imaging Clin N Am 17(3):521–537

Sanchez TR, Jadhav SP, Swischuk LE (2009) MR imaging of pediatric trauma. Magn Reson Imaging Clin N Am 17(3):439–450

Soprano JV (2005) Musculoskeletal injuries in the pediatric and adolescent athlete. Curr Sports Med Rep 4(6):329–334

Imaging Assessment of the Pediatric Spine: Selected Topics

11

11.1 Introduction

The spine of children and adolescents is frequently affected by diseases, some of them inherent to skeletally immature patients, such as juvenile idiopathic arthritis and Scheuermann's disease, and others that are nonspecific of the pediatric group but present peculiarities when children are affected, such as isthmic spondylolisthesis and spondylodiscitis. Awareness of the imaging presentation of these conditions is paramount to the differential diagnosis and to guide therapeutic decision making. Some musculoskeletal disorders that present spinal involvement are discussed elsewhere in this book and will not be discussed in this chapter.

11.2 Juvenile Idiopathic Arthritis

The spine is involved in a significant percentage of the patients with juvenile idiopathic arthritis (JIA), mostly in the upper cervical segment (facet joints) and in the craniovertebral junction. Similar to peripheral JIA, vertebral disease is related to synovial inflammation/hyperemia, pannus formation, and osteocartilaginous destruction. Radiographs are limited in the assessment of the arthritic spine due to the complex anatomy of this region, superimposition of bone structures, and low sensitivity to soft-tissue abnormalities. Computed tomography (CT) and magnetic resonance imaging (MRI) are the most useful imaging methods in spinal JIA: MRI is very suitable to evaluate the spinal cord and the nerve roots and to estimate the activity of inflammation, while CT is quite appropriate for bone and joint assessment.

Arthritic facet joints show narrowing of the joint spaces and erosions of the articular surfaces, with post-contrast enhancement in the inflamed tissues (Figs. 11.1 and 11.2); when present, ankylosis is found mainly in C2–C3 (Figs. 11.2, 11.3, 11.4, and 11.5). Synovitis of the atlantoaxial joint may lead to erosions of the odontoid peg, joint laxity, and vertebral instability. On radiographs, an interval of more than 5 mm between the posterior cortex of the anterior arch of C1

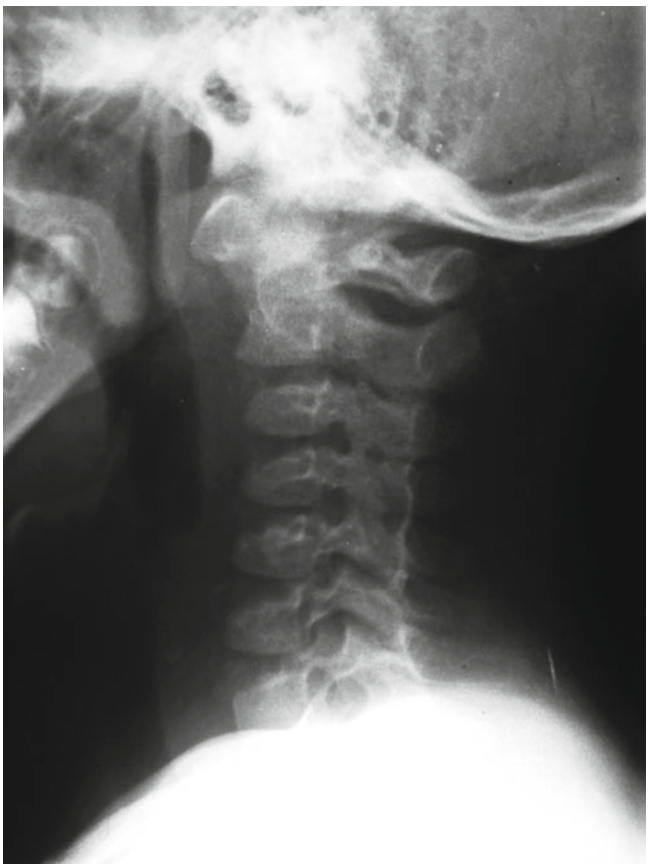

Fig. 11.1 Young child with active JIA in the cervical spine. Lateral radiograph disclose irregularity of the facets from C2 to C5, related to erosive joint disease, with minimal anterior slippage of C2. There is also atlantoaxial instability, with an increased interval between the anterior arch of C1 and the odontoid peg

S.L. Viana et al., *Joint Imaging in Childhood and Adolescence*,
DOI 10.1007/978-3-642-35876-0_11, © Springer-Verlag Berlin Heidelberg 2013

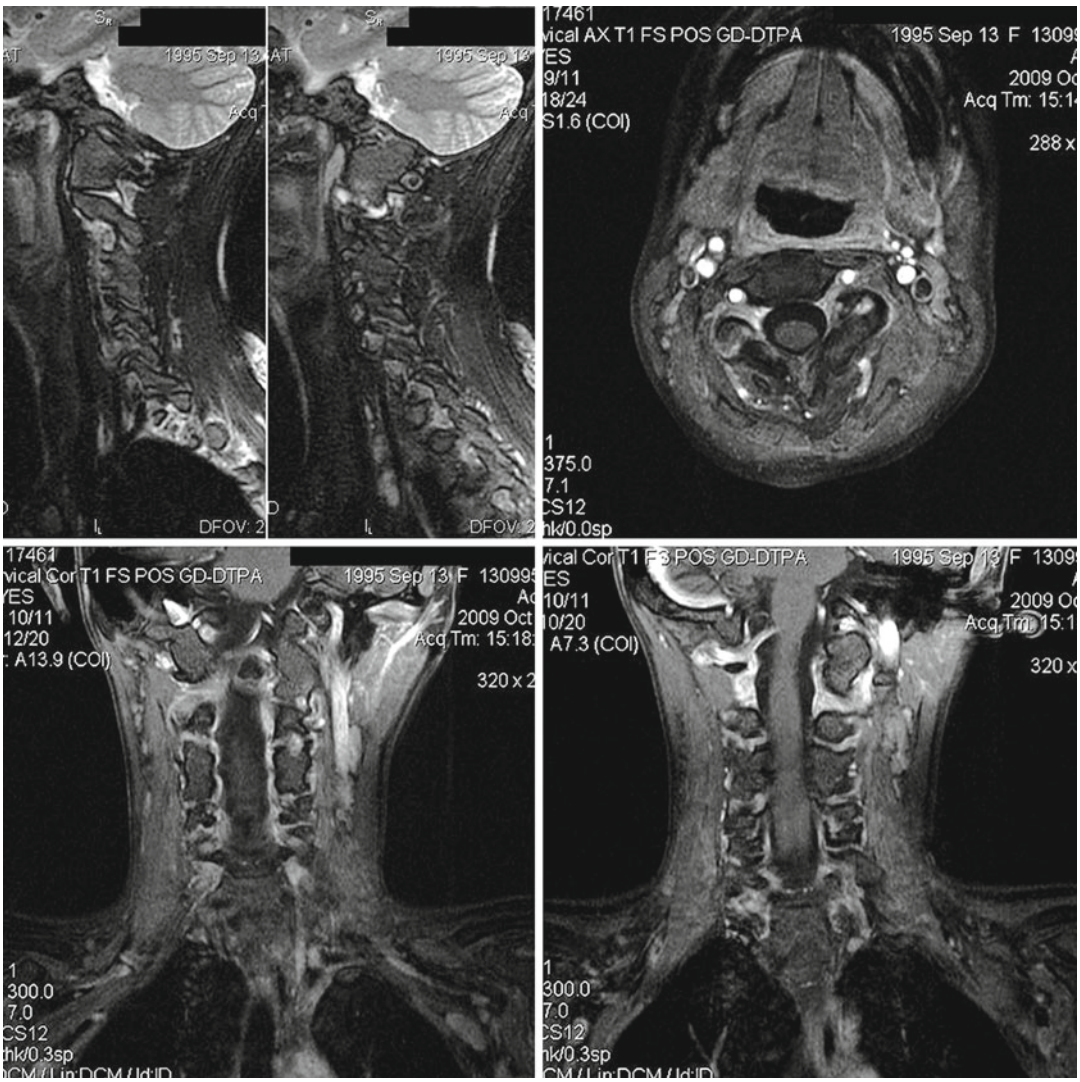

Fig. 11.2 Contrast-enhanced MRI of the cervical spine of a 13-year-old female with active JIA. Sagittal fat sat T2-WI (*upper-left image*) and post-gadolinium fat sat T1-WI in the transverse (*upper-right image*) and coronal (*lower row*) planes reveal ankylosis of the facet joints in C4–C5. Erosions and post-contrast enhancement are seen in C2–C3 and C3–C4 at left and in C5–C6, bilaterally (Courtesy of Dr. Christiane Maria França Coimbra, Hospital Universitario de Brasilia – UnB, Brasilia, Brazil)

and the anterior cortex of the odontoid is considered abnormal (Figs. 11.1 and 11.6); lateral views of the cervical spine in flexion and extension are useful for assessment of instability. Additional findings include sub-axial subluxation (between the second and the seventh cervical vertebrae, also related to arthritis of the facet joints) and basilar invagination (related to occipitoatlantoaxial arthritis). Calcification of the soft tissues and of the vertebral ligaments is common, as well as reduced height of disk spaces (Figs. 11.3 and 11.4). Squaring and hypoplasia of the cervical vertebrae, related to chronic inflammation, are typical of long-standing JIA (Fig. 11.4).

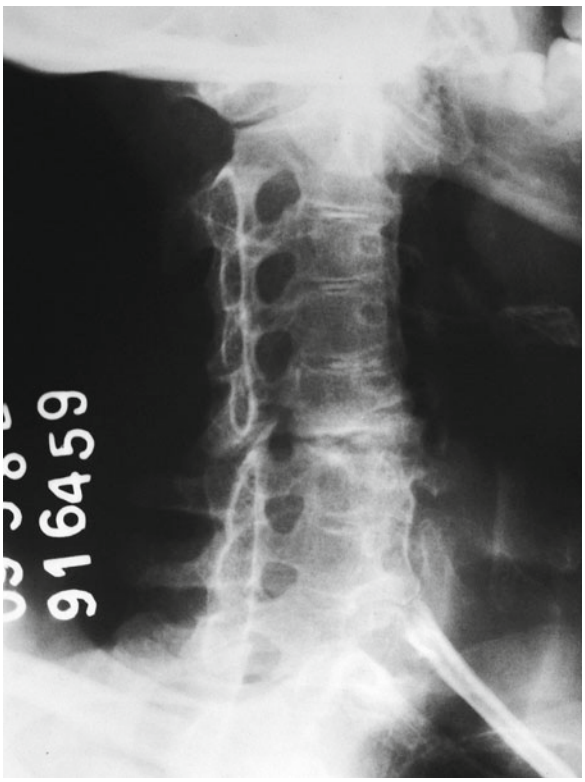

Fig. 11.3 Oblique radiograph of the cervical spine of a patient with long-standing JIA reveals extensive ankylosis of the facet joints. However, there is sparing of C5–C6 level, in which premature and atypical spinal degeneration can be seen, related to excessive solicitation of the only cervical segment with preserved mobility. Calcification of the nucleus pulposus is present in several disks, notably from C2 to C5

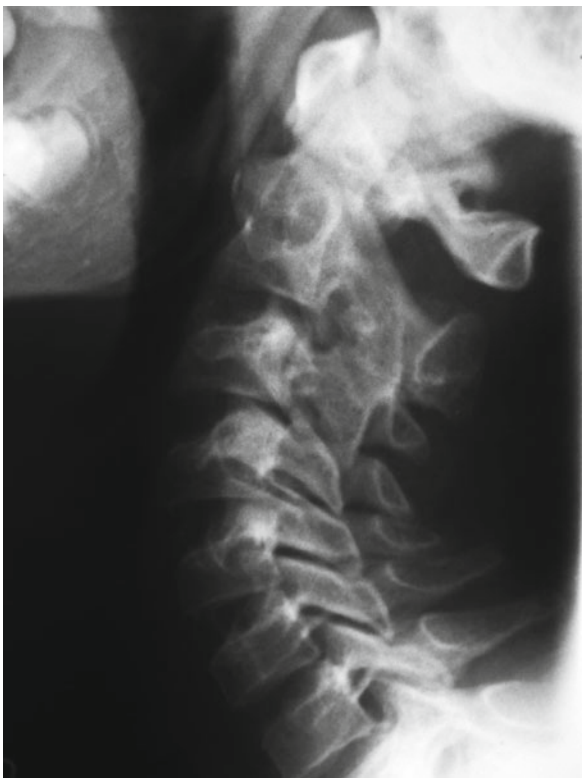

Fig. 11.5 Ankylosis of the facet joints in C2–C3 can be seen in this lateral view of the cervical spine of a child with JIA. Note the normal appearance of the facet joints below this level, with regular and smooth surfaces, in contradistinction to those seen in the child of Fig. 11.1

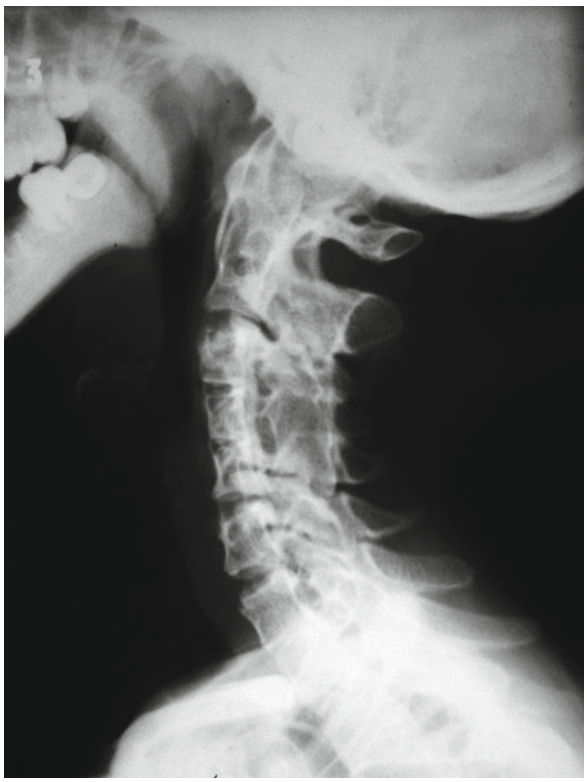

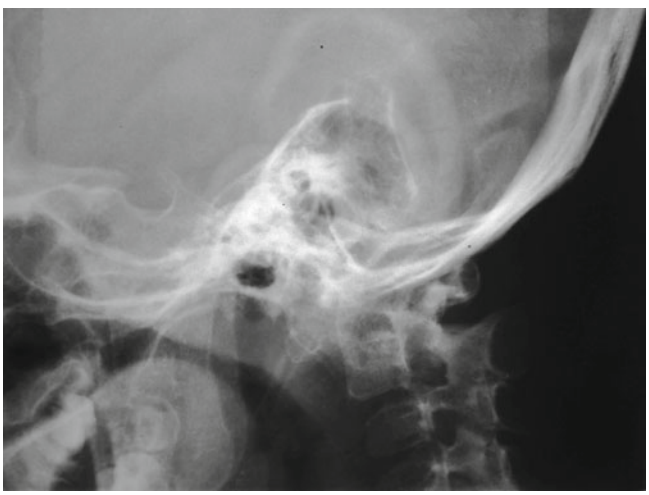

Fig. 11.6 Lateral view (hyperflexion) of the craniovertebral transition of a patient with JIA demonstrating C1–C2 instability, with anterior translation of the atlas relative to the odontoid

Fig. 11.4 Classic radiographic findings of long-standing spinal JIA. There is vertebral hypoplasia from C3 to C7, with squaring of the vertebral bodies and facet joint ankylosis, the latter more evident between C3 and C5. Ankylosis of the median atlantoaxial joint is also present, as well as reduced height of the disk spaces and peripheral disk calcifications from C3–C4 to C5–C6

11.3 Bacterial (Pyogenic) Spondylodiscitis

Discitis and vertebral osteomyelitis are different facets of the same process, namely, spondylodiscitis, which is more frequently found in the lumbar spine. Discitis, which is one of the ends of this spectrum, is more common in children from 6 months to 5 years old. Predominance of primary discitis in small children is probably due to trapping of septic emboli in the vessels of the cartilaginous portion of the disk, as these vessels tend to disappear with growth. On the other hand, vertebral osteomyelitis is the spinal counterpart of classic metaphyseal osteomyelitis, corresponding to up to 2 % of all cases of bone infection. It occurs mainly in older children (around age 7), resulting from hematogenous spread or from contiguous dissemination. Pyogenic infection of the spine is an aggressive and rapidly destructive process that may lead to acute neurologic damage and long-term complications. Timely diagnosis – before radiographic changes appear – is critical in order to start antibiotic therapy as soon as possible.

Imaging is usually necessary to confirm the clinical hypothesis of vertebral infection. Pyogenic spondylitis typically involves two adjacent vertebral bodies and the disk in between; this pattern of involvement appears on radiographs as reduced height of the affected disk space, ill-defined vertebral endplates, and bone erosions, which evolve very quickly once they become evident (Figs. 11.7 and 11.8). Even though this constellation of findings is virtually diagnostic in a child with strong clinical suspicion, it may take from 2 to 6 weeks for them to become apparent, and this delay renders radiographs inadequate for the assessment of initial disease. Bone scintigraphy becomes positive early in the course of the spinal infection, but MRI has similar sensitivity and superior resolution, being the latter the method of choice for early diagnosis. There is bone marrow edema adjacent to the affected endplates, with bone erosions and loss of cortical definition (Figs. 11.9 and 11.10). The affected disk presents reduced height, heterogeneous signal intensity, and post-gadolinium enhancement, the latter also found in the edematous bone marrow (Figs. 11.9 and 11.10). Intravenous gadolinium is indispensable, as the inflamed tissues enhance on post-contrast images: this feature is very helpful to estimate the real extent of the soft-tissue component, mostly paravertebral and epidural phlegmons and/or abscesses (Figs. 11.9, 11.11, and 11.12). Abscesses appear as well-delimited fluid collections with low

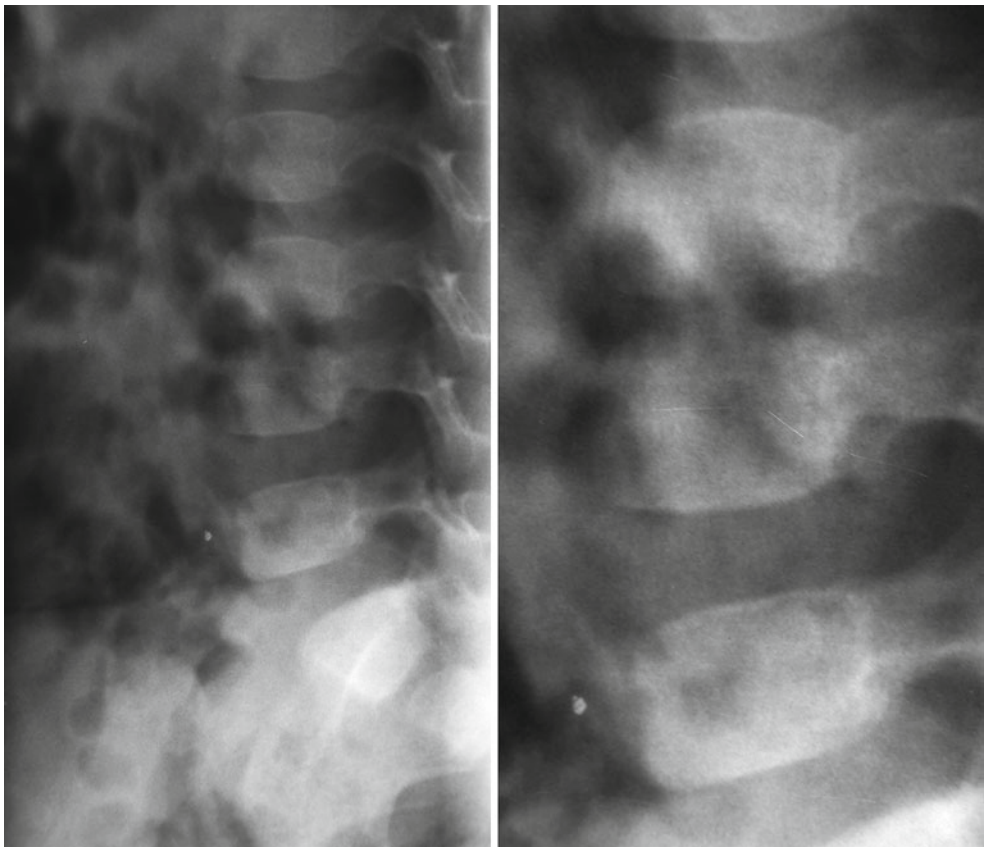

Fig. 11.7 L3–L4 pyogenic spondylodiscitis in a young child. Lateral radiograph reveals reduced height of the corresponding disk space, with loss of definition of the adjacent vertebral endplates (Courtesy of Dr. Marcelo Ricardo Canuto Natal, Hospital de Base do Distrito Federal and Pasteur Medicina Diagnostica – Diagnosticos da America S.A., Brasilia, Brazil)

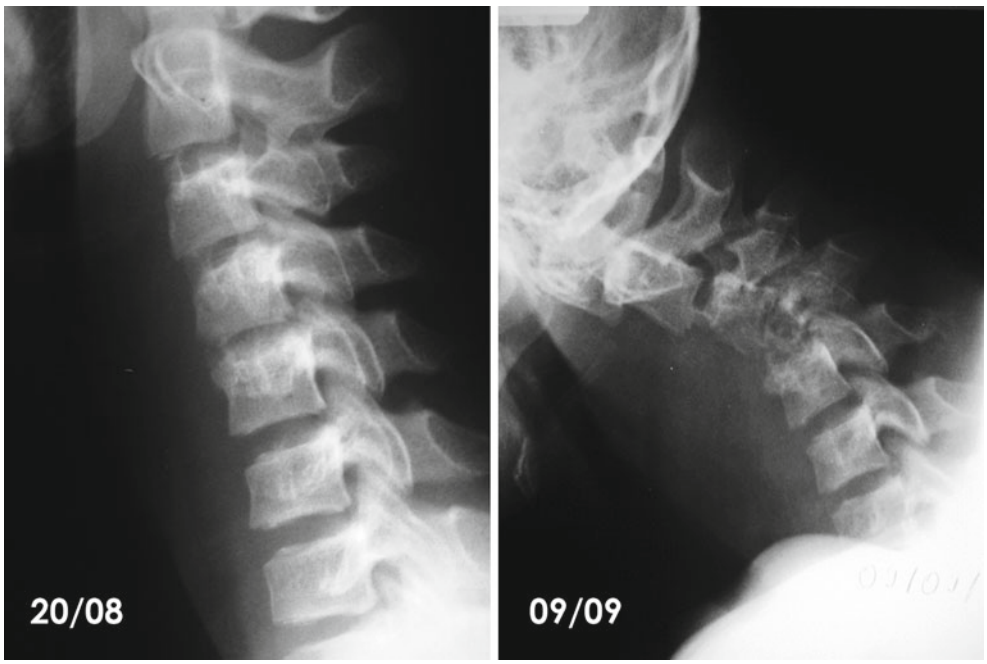

Fig. 11.8 Lateral radiographs of the cervical spine of a 13-year-old child with pyogenic spondylodiscitis, taken 20 days apart. The first radiograph (*left*) shows reduced height of C4–C5 disk space, with loss of definition of the upper endplate of C5 and swelling of the prevertebral soft tissues. The second radiograph (*right*) demonstrates rapid evolution of the infectious process, with angular deformity of the spine centered about C4 (related to bone destruction, collapse, and anterior wedging of this vertebral body), marked osteoporosis of the vertebral bodies from C3 to C5, and reduced height of the corresponding disk spaces. In addition, there is swelling of the prevertebral soft tissues leading to compression of the pharyngeal air column

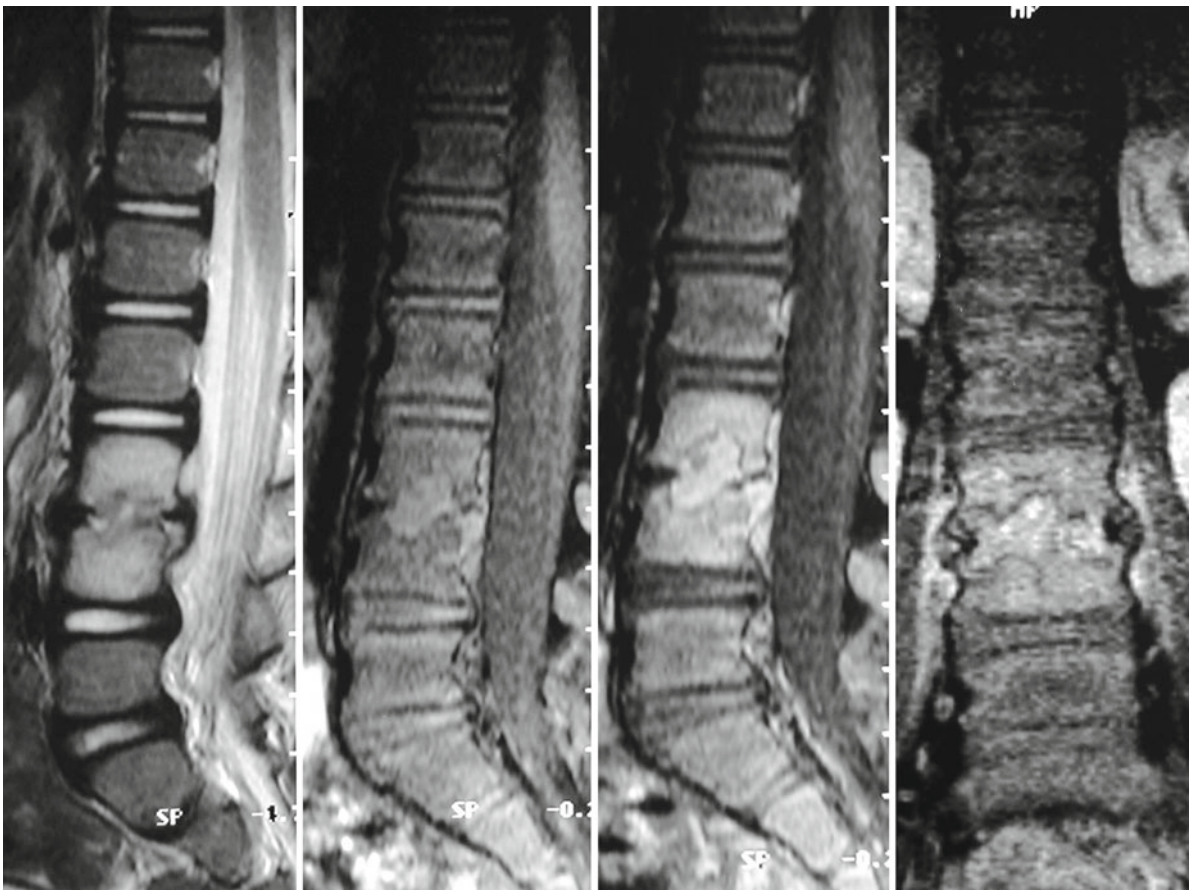

Fig. 11.9 Sagittal T2-WI (*first image*) and fat sat T1-WI (*second image*) of an 11-year-old female with pyogenic discitis in L3–L4 reveal reduced height and abnormal signal intensity of the affected disk, with destruction of the adjacent endplates and extension of the infectious process to the contiguous vertebral bodies. There is extensive bone marrow edema pattern surrounding the areas of bone destruction. A small subligamentous collection can be seen posterior to the vertebral body of L4. Sagittal (*third image*) and coronal (*fourth image*) post-gadolinium fat sat T1-WI demonstrate enhancement of the osteodiscal focus of infection, of the subligamentous abscess, of the areas of bone marrow edema, and of the edematous paravertebral soft tissues (Courtesy of Dr. Marcelo Ricardo Canuto Natal, Hospital de Base do Distrito Federal and Pasteur Medicina Diagnostica – Diagnosticos da America S.A., Brasilia, Brazil)

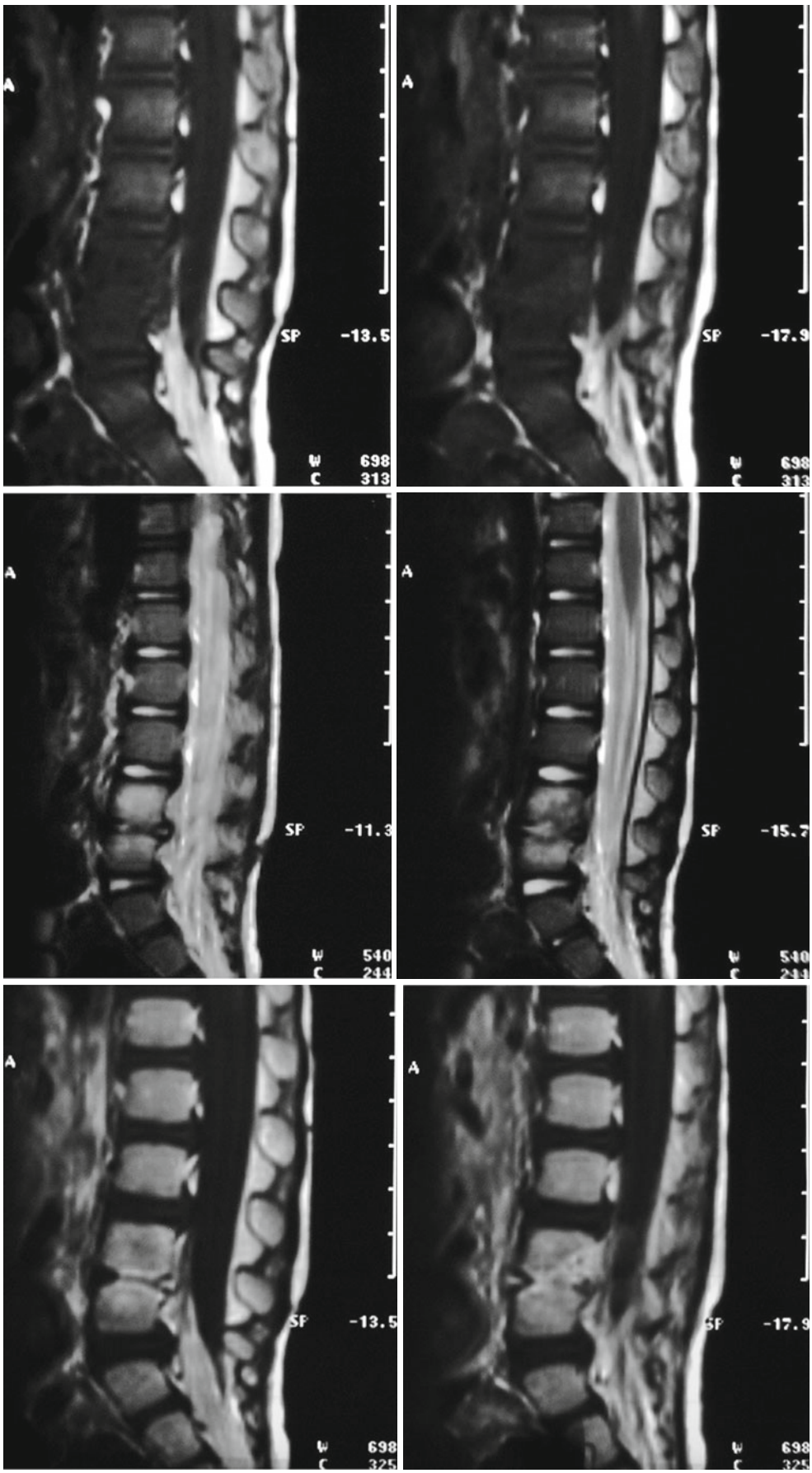

Fig. 11.10 L4–L5 pyogenic discitis. Sagittal T1-WI (*upper row*), T2-WI (*central row*), and post-contrast T1-WI (*lower row*) disclose diffuse reduction of the height of the affected disk, which presents abnormal signal intensity in all sequences. There is destruction of the adjacent endplates and bone marrow edema pattern. Post-gadolinium images demonstrate diffuse and intense enhancement of the infected disk and of the adjacent bone (Courtesy of Dr. Marcelo Ricardo Canuto Natal, Hospital de Base do Distrito Federal and Pasteur Medicina Diagnostica – Diagnosticos da America S.A., Brasilia, Brazil)

signal intensity on T1-WI, high signal intensity on T2-WI, and peripheral post-contrast enhancement, while phlegmons are ill-defined areas of altered signal intensity with diffuse post-gadolinium enhancement (Figs. 11.9, 11.11, and 11.12). In general, the walls of bacterial abscesses are thicker and more irregular if compared to tuberculous abscesses. MRI is also useful to monitor treatment response, given that regression of soft-tissue abnormalities and fatty replacement of the formerly edematous bone are reliable indicators of cure. Nowadays, contrast-enhanced CT is a second-line method in the evaluation of pyogenic spondylodiscitis in children, as its diagnostic accuracy is lower than that of contrast-enhanced MRI (Figs. 11.12 and 11.13), being used essentially as a diagnostic alternative when the latter is not available or contraindicated. Gas bubbles or gas-fluid levels virtually exclude the possibility of tuberculosis and are indicative of the bacterial nature of the infectious process.

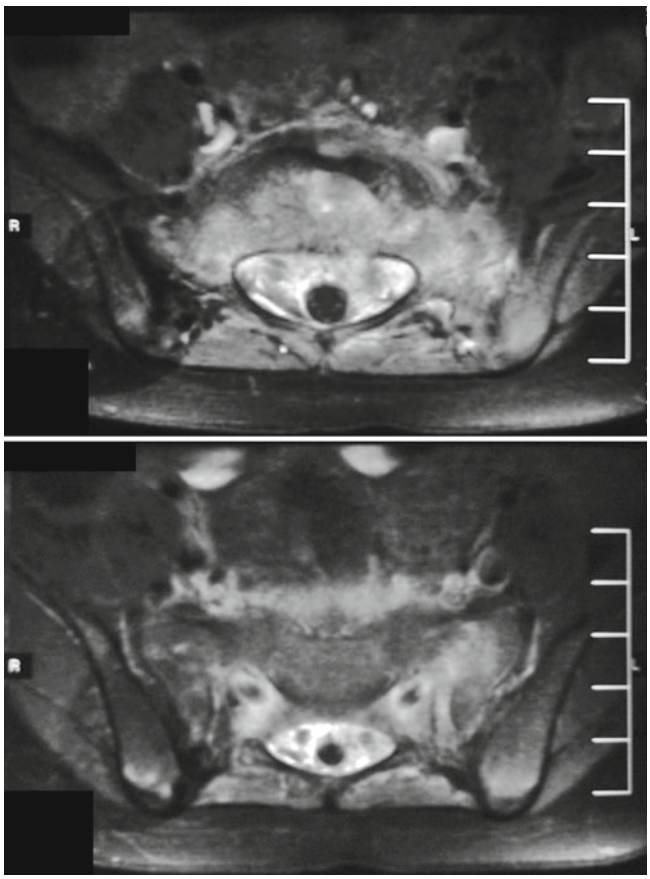

Fig. 11.11 Transverse post-gadolinium fat sat T1-WI of a 3-year-old child with L5–S1 bacterial spondylodiscitis. There is diffuse enhancement in the affected disk, in the bone marrow of the adjacent vertebrae, in the prevertebral and paravertebral soft tissues, and in the epidural space. Despite the extensive involvement of the epidural space, the absence of fluid collections and the diffuse – instead of circumscribed – appearance of such involvement favor phlegmon over abscess in this case

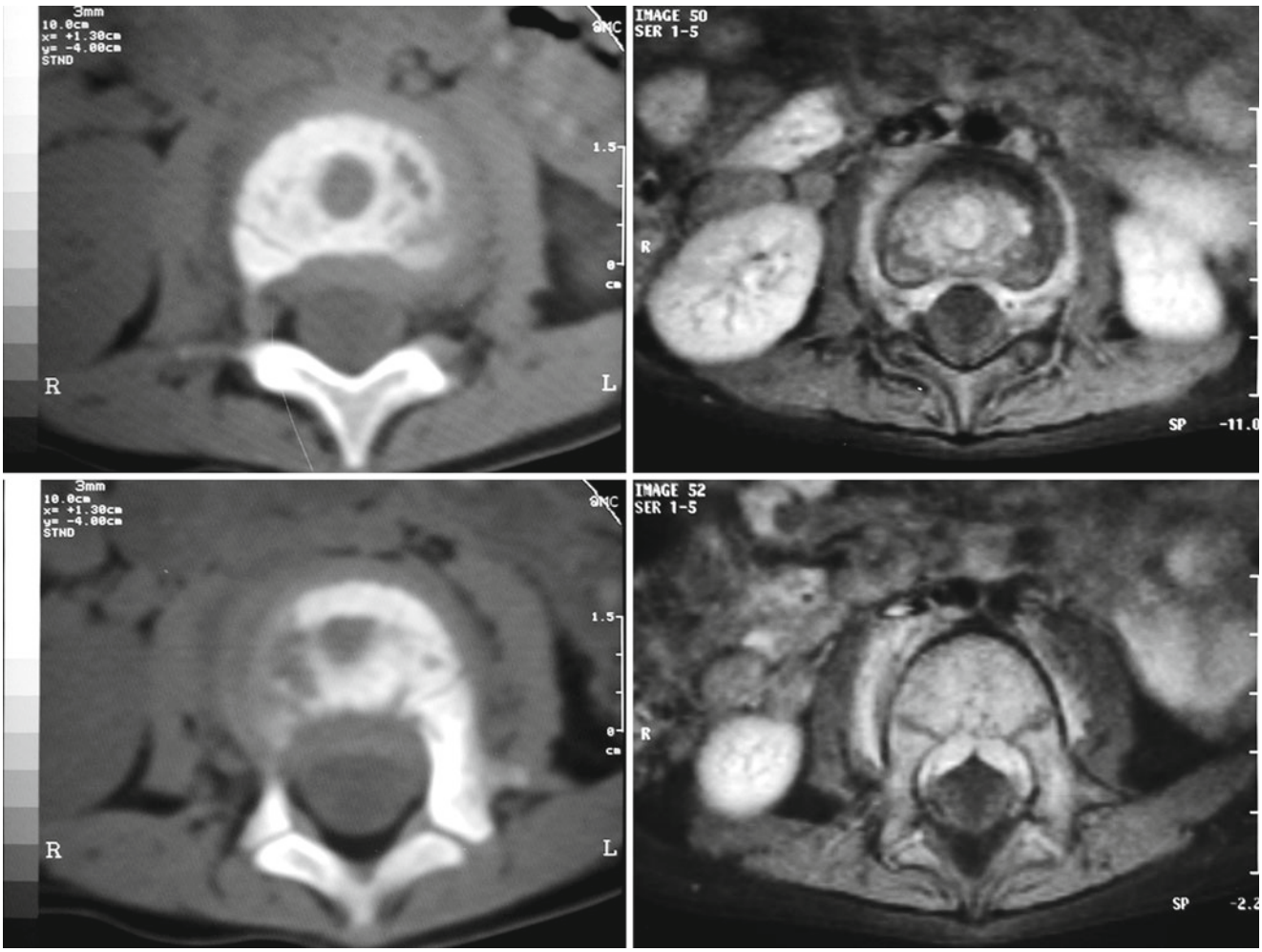

Fig. 11.12 Transverse CT images (*left*) and post-gadolinium fat sat T1-WI (*right*) acquired approximately at the same levels in a child with pyogenic spondylodiscitis of the upper lumbar spine. Despite the excellent resolution of CT for bone structures, allowing for accurate assessment of the destruction of the vertebral endplates, the evaluation of soft-tissue abnormalities is poor if compared to that obtained with MRI. In the latter, in addition to bone destruction and post-contrast enhancement of the bone marrow, there is also enhancement of epidural and paravertebral soft tissues, extending to the foramina, surrounding the emergent nerve roots and leading to anterior compression of the thecal sac (Courtesy of Dr. Marcelo Ricardo Canuto Natal, Hospital de Base do Distrito Federal and Pasteur Medicina Diagnostica – Diagnosticos da America S.A., Brasilia, Brazil)

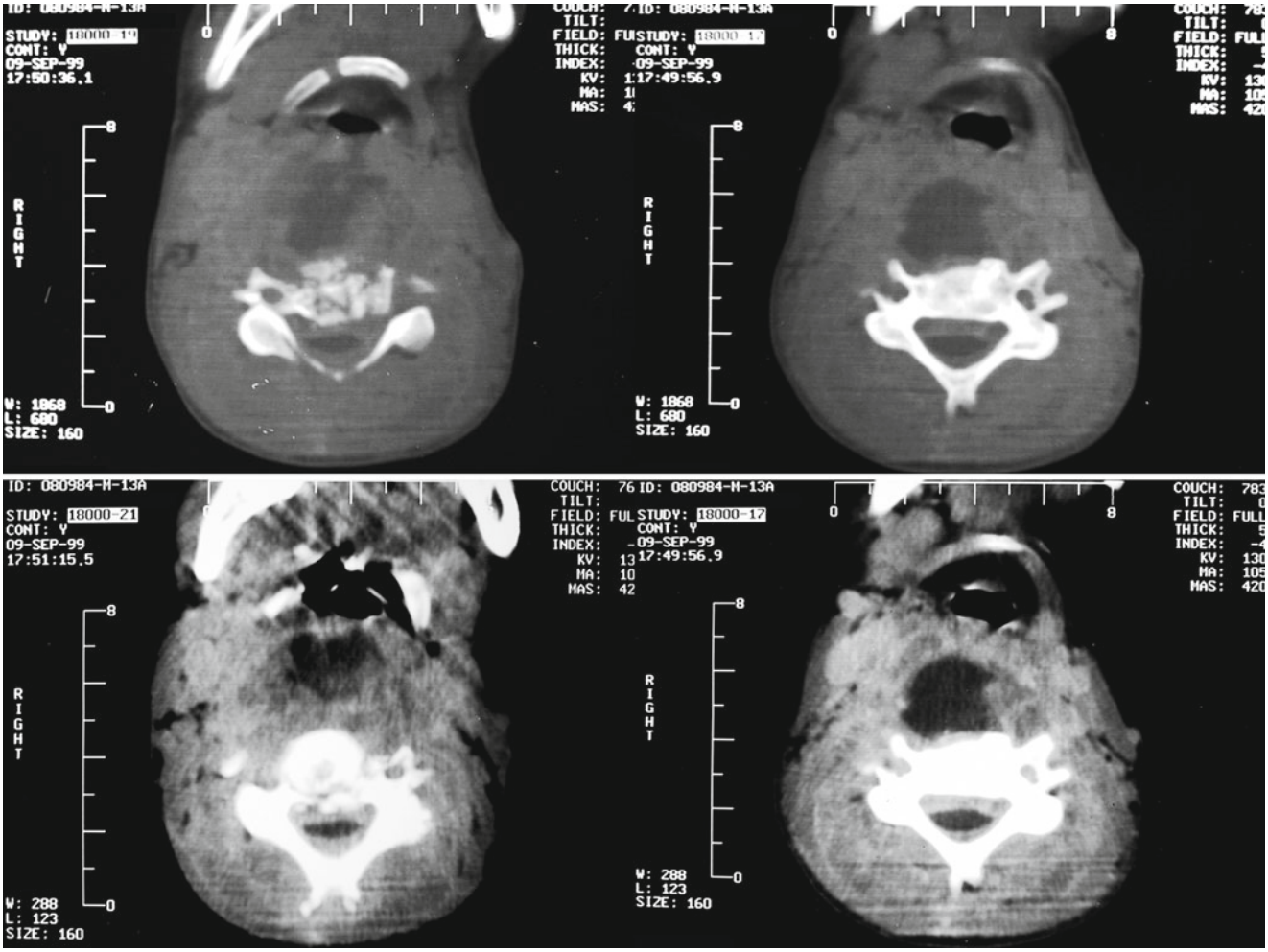

Fig. 11.13 Contrast-enhanced CT of the neck of the same patient of Fig. 11.8, performed on the same day of the second radiograph. There is obvious destruction of the body of C4 (*left images*), with bone fragments extending to the spinal canal. A large retropharyngeal abscess is also seen, displacing the pharyngeal air column (*right images*). In addition, there is obliteration of the cervical fat planes (with diffuse post-contrast enhancement) and increased density of the epidural space, leading to the circumferential compression and deformation of the thecal sac

11.4 Spinal Tuberculosis

Tuberculosis (TB) remains a significant public health issue, mostly in developing countries. TB was discussed in further detail in Chap. 6, in which arthritic involvement of peripheral joints was the main subject. Tuberculous spondylodiscitis accounts for more than half of all cases of musculoskeletal TB. It is most often a secondary infection caused by hematogenous spread from a primary extraskeletal focus, with a chronic and insidious course; less than 50 % of the patients present concomitant pulmonary tuberculosis. Vertebral deformities caused by spinal TB are relatively common, notably kyphosis/kyphoscoliosis. It may be difficult to distinguish spinal TB from pyogenic spondylodiscitis, either clinically or on imaging, and both must always be considered in the differential diagnosis of infectious spondylitis. As in bacterial spondylodiscitis, the earlier the institution of treatment, the better the outcome, especially if the diagnosis is made before significant structural damage is present.

Radiographs may be normal in early disease. The lower thoracic spine and the thoracolumbar transition are the most affected segments (Fig. 11.14); isolated involvement of the thoracic spine favors TB over bacterial infection. The infection usually begins in the anterior portion of the vertebral body, adjacent to the disk, and disseminates to the disk itself, to the paravertebral soft tissues, and to adjacent vertebrae, deep to the anterior longitudinal ligament. This pattern of dissemination is very characteristic and may lead to involvement of multiple vertebral levels, which are frequently noncontiguous, with preserved vertebral bodies in between. Due to the absence of proteolytic enzymes, reduction of the height of the infected disk is less pronounced and occurs later if compared to classic bacterial spondylodiscitis, in spite of the extensive bone destruction that is a hallmark of spinal TB (Fig. 11.15); bone sequestra may also be present. Extension to the paravertebral soft tissues leads to development of tuberculous abscesses, which appear as fusiform masses on radiographs. Sinus tracts in atypical locations – such as the groins or the buttocks – may be present if the iliopsoas muscles are involved, due to distension of their bursae (Fig. 11.15). In late-stage spinal TB, there may be fragmentation, wedging, and collapse of the vertebral bodies, with

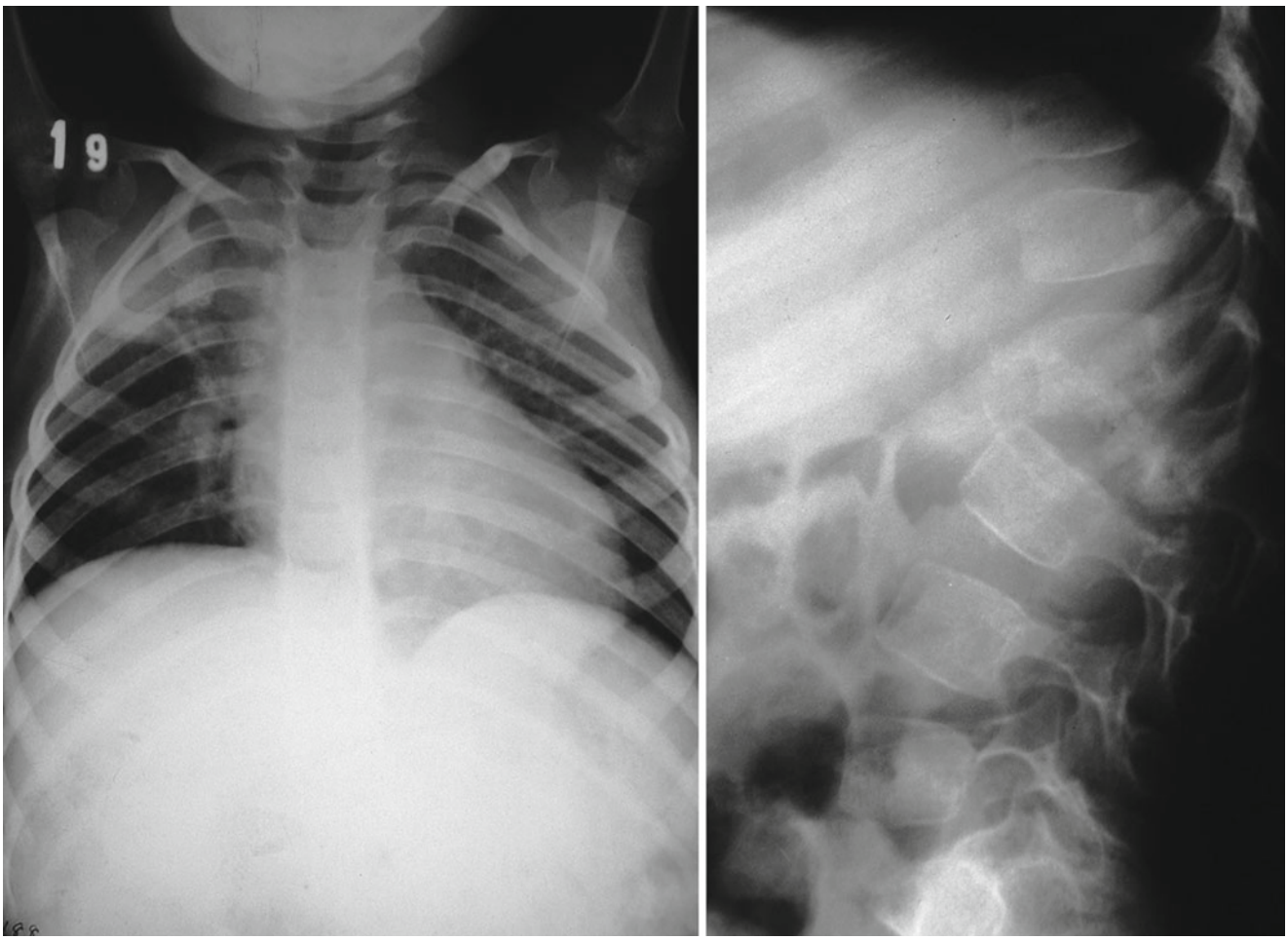

Fig. 11.14 Chest X-ray of a young child (*left*) disclosing opacity of the right upper lobe, due to pulmonary tuberculosis. The *right image* is a lateral radiograph of the lumbar spine of the same patient, demonstrating collapse of the vertebral body of L2, with angular deformity of the spine and destruction of the inferior endplate of L1. A paravertebral soft-tissue mass with peripheral calcifications is also present. Tuberculous spondylodiscitis

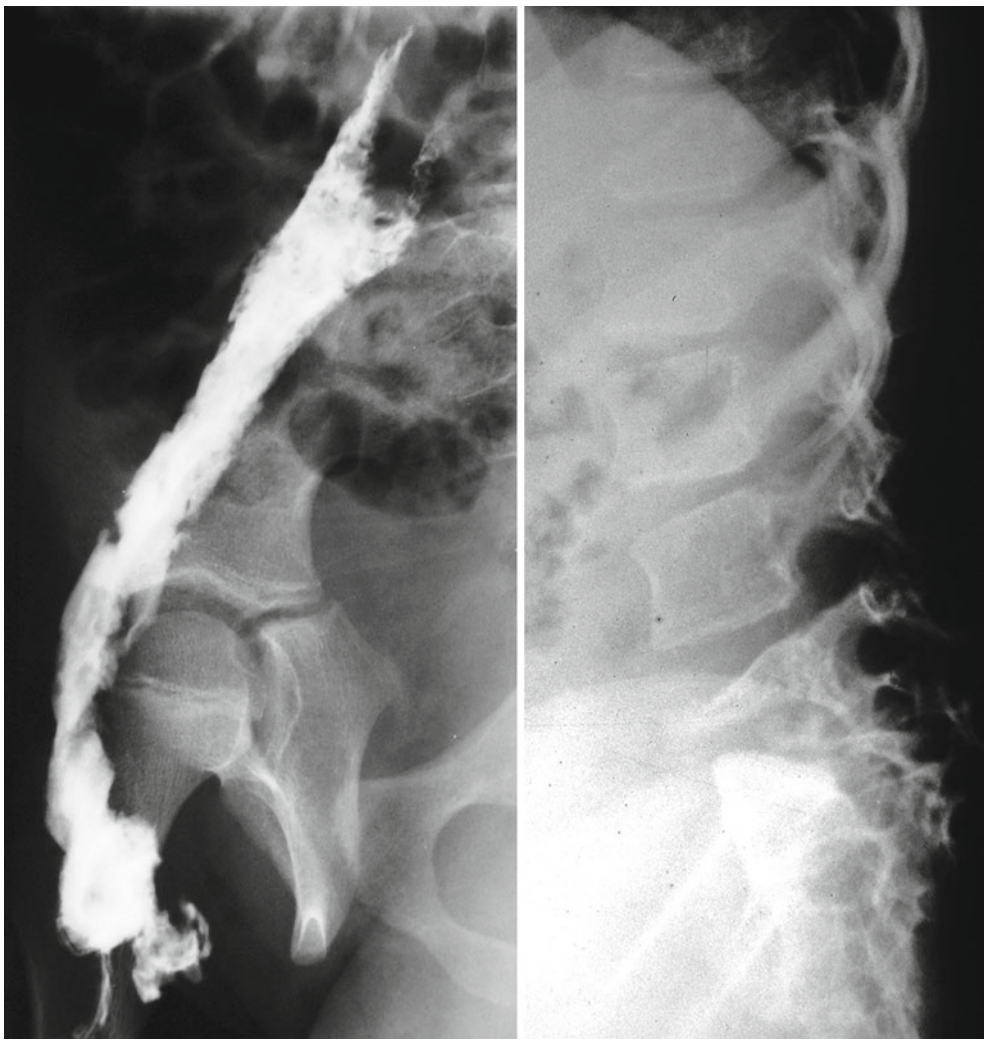

Fig. 11.15 Child presenting a fistulous orifice in the right groin and caseous discharge. Fistulography with injection of iodinated contrast (*left image*) discloses opacification of the iliopsoas bursa. The primary site of disease is located in L2–L3, with collapse and anterior wedging of L2 and destruction of the superior endplate of L3 (*right image*). The disk space is relatively preserved, in spite of the advanced degree of bone destruction. Vertebral tuberculosis and tuberculous iliopsoas bursitis

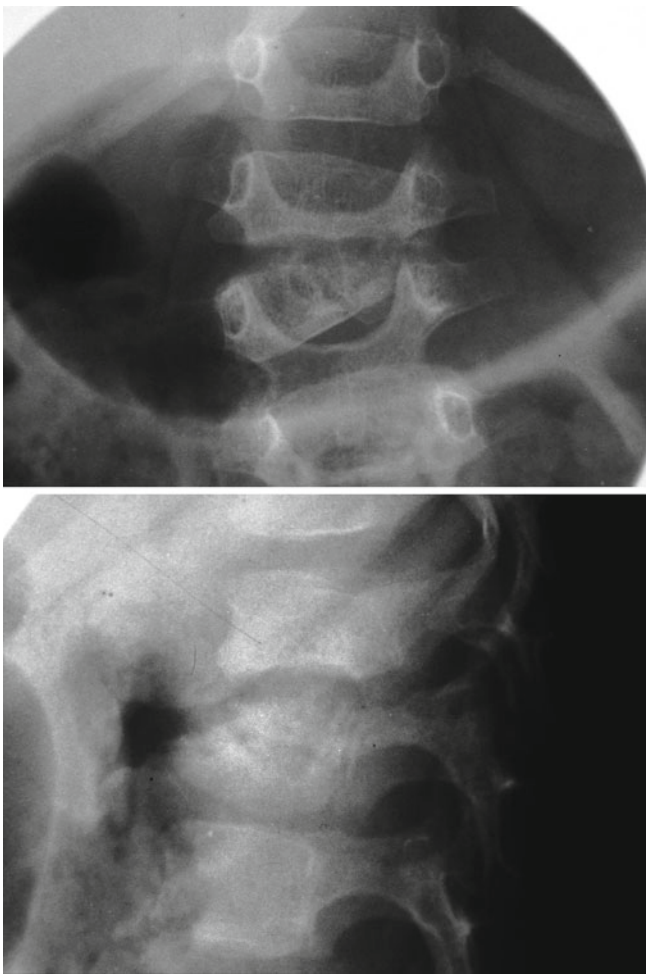

Fig. 11.16 L1–L2 tuberculous spondylodiscitis. Radiographs of the upper lumbar spine display reduced height of L1–L2, with destruction of the adjacent endplates and extensive osteolysis of L2, whose vertebral body presents left anterolateral wedging and right tilting

progression of the thoracic kyphosis and development of gibbus deformity (Figs. 11.14, 11.15, 11.16, and 11.17). Though rarely found, involvement of the vertebral arch suggests tuberculous spondylitis instead of pyogenic infection.

CT is the best method for bone assessment, demonstrating sclerosis and bone destruction earlier than radiographs can do (Fig. 11.18). CT is also the method of choice to reveal soft-tissue calcifications typical of chronic musculoskeletal tuberculosis. Moreover, CT is one of best methods for image-guided invasive procedures in the spine (Fig. 11.18). MRI is superior to CT in the assessment of the spinal cord and nerve roots and to monitor the evolution of the infection. MRI becomes abnormal 4–6 months prior to the appearance of radiographic findings in spinal TB. In the acute phase, bone marrow changes are very similar to those found in pyogenic spondylitis, including bone marrow edema pattern and post-gadolinium enhancement. In chronic tuberculous osteomyelitis, however, the bone marrow has a protean appearance, presenting variable signal intensity. Discitis leads to decreased signal intensity in the affected disk on T2-WI, with loss of the hyperintensity typical of healthy children. Soft-tissue abscesses display peripheral enhancement on post-gadolinium images, and their walls are most often thinner and smoother if compared to those found in bacterial infections (Fig. 11.19). As previously mentioned, involvement of multiple spinal levels strongly suggests tuberculous infection and MRI is especially suitable to demonstrate this pattern of disease, with subligamentous spread along several vertebral bodies and/or to the adjacent soft tissues (Fig. 11.19). Extension to the spinal canal, with occasional development of epidural abscesses, may lead to compression of the spinal cord or of the nerve roots and neurological compromise (Fig. 11.19).

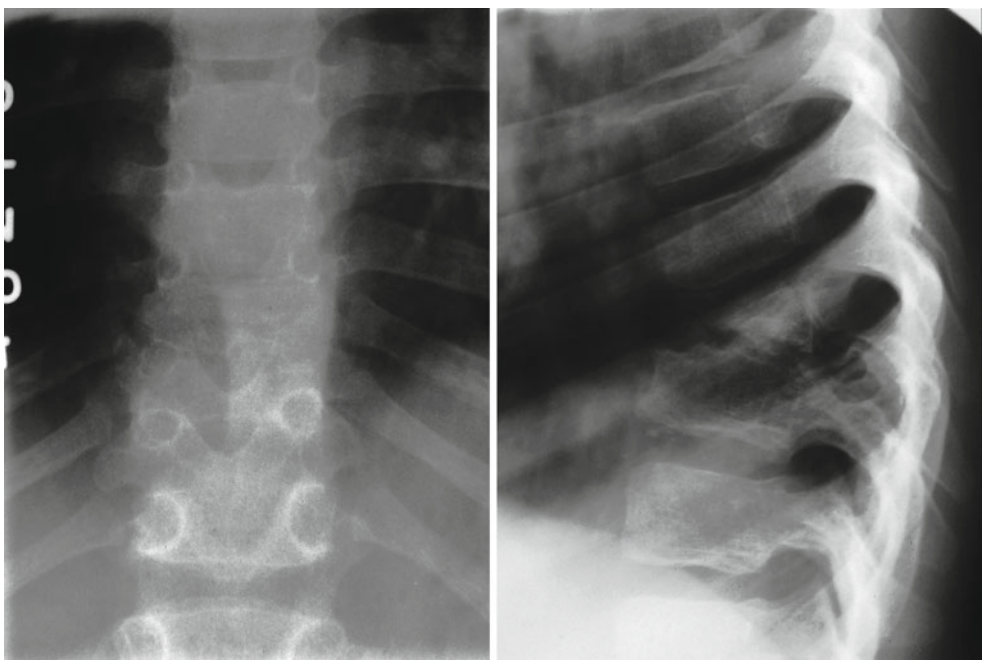

Fig. 11.17 Spinal tuberculosis affecting the lower thoracic segment. Radiographs demonstrate collapse of T9, with extensive bone destruction and anterior wedging of this vertebral body, leading to accentuation of the normal kyphosis. The superior endplate of T10 is eroded and irregular, with reduced height of the corresponding disk space

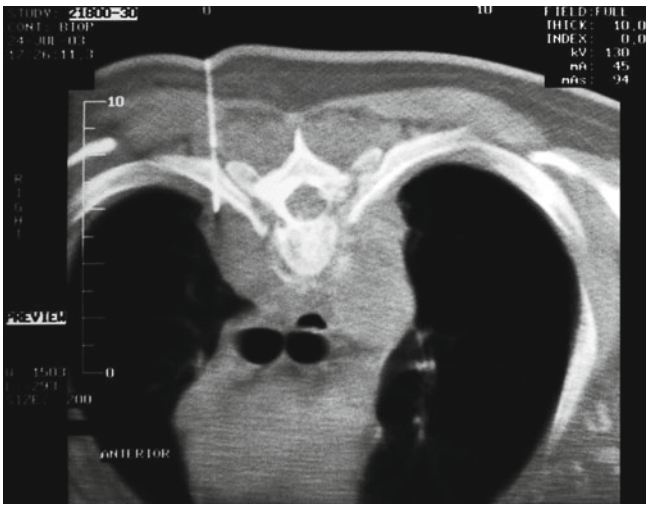

Fig. 11.18 CT-guided aspiration of a right paravertebral abscess in a patient with tuberculous spondylodiscitis of the thoracic spine. The patient is lying in the prone position and the needle is located inside the abscess. There is extensive destruction of the vertebral body and of part of the vertebral arch of this thoracic vertebra. A paravertebral abscess is also seen at left, adjacent to the descending aorta

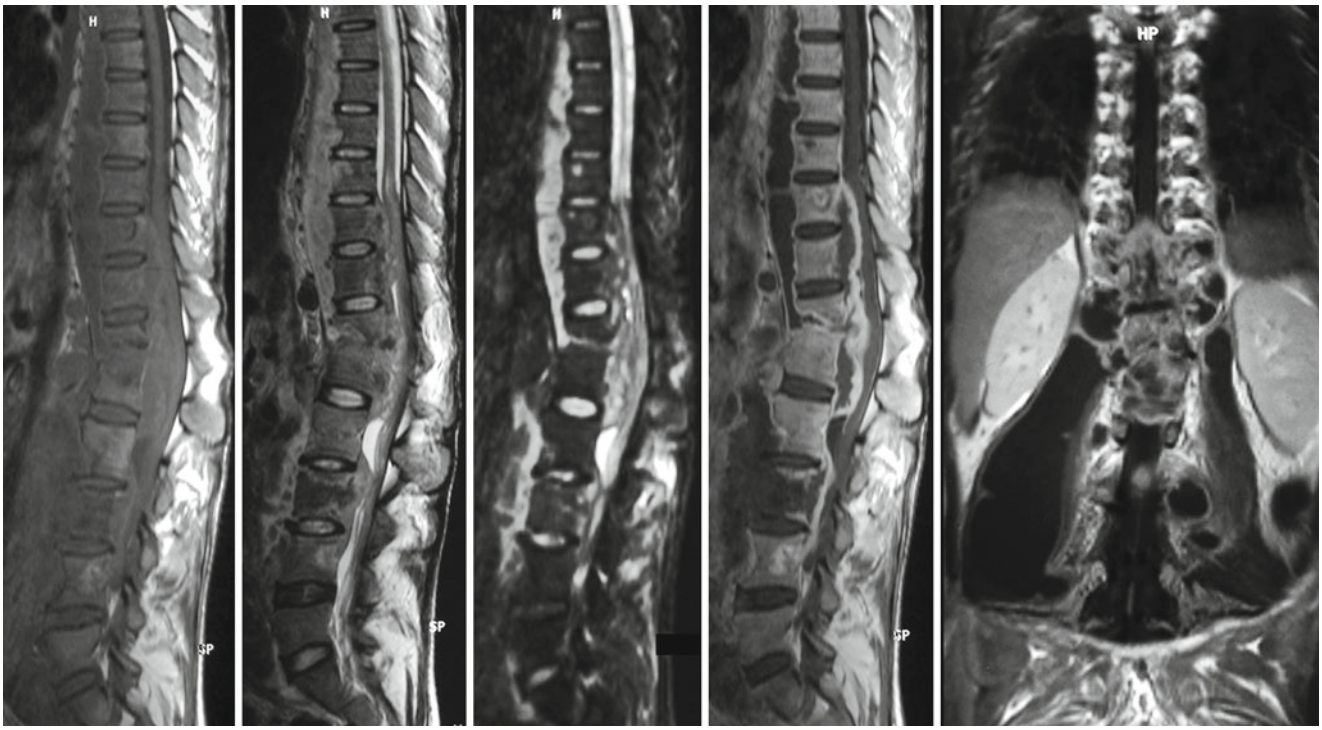

Fig. 11.19 Tuberculous spondylodiscitis. Sagittal T1-WI (*first image*), T2-WI (*second image*), STIR image (*third image*), and post-gadolinium T1-WI (*fourth image*) demonstrate reduced height and abnormal signal intensity of the intervertebral disk of T12–L1, with vanishing of the cortical bone of the adjacent endplates and partial collapse of the vertebral bodies, mainly of T12. Large discontinuous abscesses are seen in the prevertebral and paravertebral soft tissues, as well as in the anterior epidural space, predominantly hypointense on T1-WI and heterogeneous on T2-WI, with peripheral post-contrast enhancement. The epidural abscess leads to spinal cord compression and extends from T10 to L4. The fifth image is a coronal post-gadolinium T1-WI that demonstrates large bilateral abscesses of the iliopsoas muscles

11.5 Spondylolysis

Spondylolysis is a common cause of back pain in children and adolescents, though it may as well be asymptomatic. It is a defect in the *pars interarticularis* (also called isthmus), the region of the lamina located between the superior and the inferior articular processes. This defect may lead to spondylolisthesis, which consists in displacement – anterior, in most cases – of the affected vertebra in relation to the vertebrae below. Spondylolysis is rare in young children and its incidence increases with age. L5 is the affected level in the vast majority of the patients, and the condition is most often bilateral. Generally speaking, there are two forms of spondylolysis: dysplastic and acquired. The former is related to abnormal vertebral development – affecting mainly the vertebral arch – that predisposes to elongation and rupture of the isthmus. The latter, on the other hand, is related to abnormal stress/repetitive strain, commonly associated to sports activities, leading to a stress fracture. In dysplastic spondylolysis, classic findings include focal discontinuity of the bone with sclerotic or corticated borders. The spectrum of findings of the acquired form varies from a stress reaction not associated with bone discontinuity to incomplete stress fractures or, in its typical presentation, complete fractures with obvious bone defects. Incomplete lesions may eventually evolve to consolidation and healing, which is not usual for complete fractures. Besides detecting the bone defect itself, imaging studies aim to distinguish acute from chronic lesions and, in the former, monitor their evolution. Instead of mutually exclusive, imaging methods are complementary and synergistic in the assessment of spondylolysis.

Radiographs are the first line of investigation, even though they are limited for spinal assessment and a significant fraction of the cases will present normal results, especially in acute or incomplete forms. In addition, radiographs are unable to demonstrate the inflammatory component that may be present. Hypoplasia and posterior wedging of the vertebral body in the affected level are common in dysplastic lesions, as well as spina bifida occulta and/or dysplasia of the laminae. Oblique and lateral views are the most sensitive, demonstrating an obvious bony defect or, in less exuberant cases, localized areas of osteopenia or sclerosis (Fig. 11.20). Lateral views are particularly useful for estimating the severity of spondylolisthesis (Fig. 11.21). The Meyerding grading system is widely accepted and categorizes the lesions from I to IV according to the degree of vertebral slippage relative to the endplate below (up to 25, 26–50, 51–75, and more than 75 %, respectively). In grade V spondylolisthesis (also called spondyloptosis), the affected vertebra slips entirely off the vertebra beneath it.

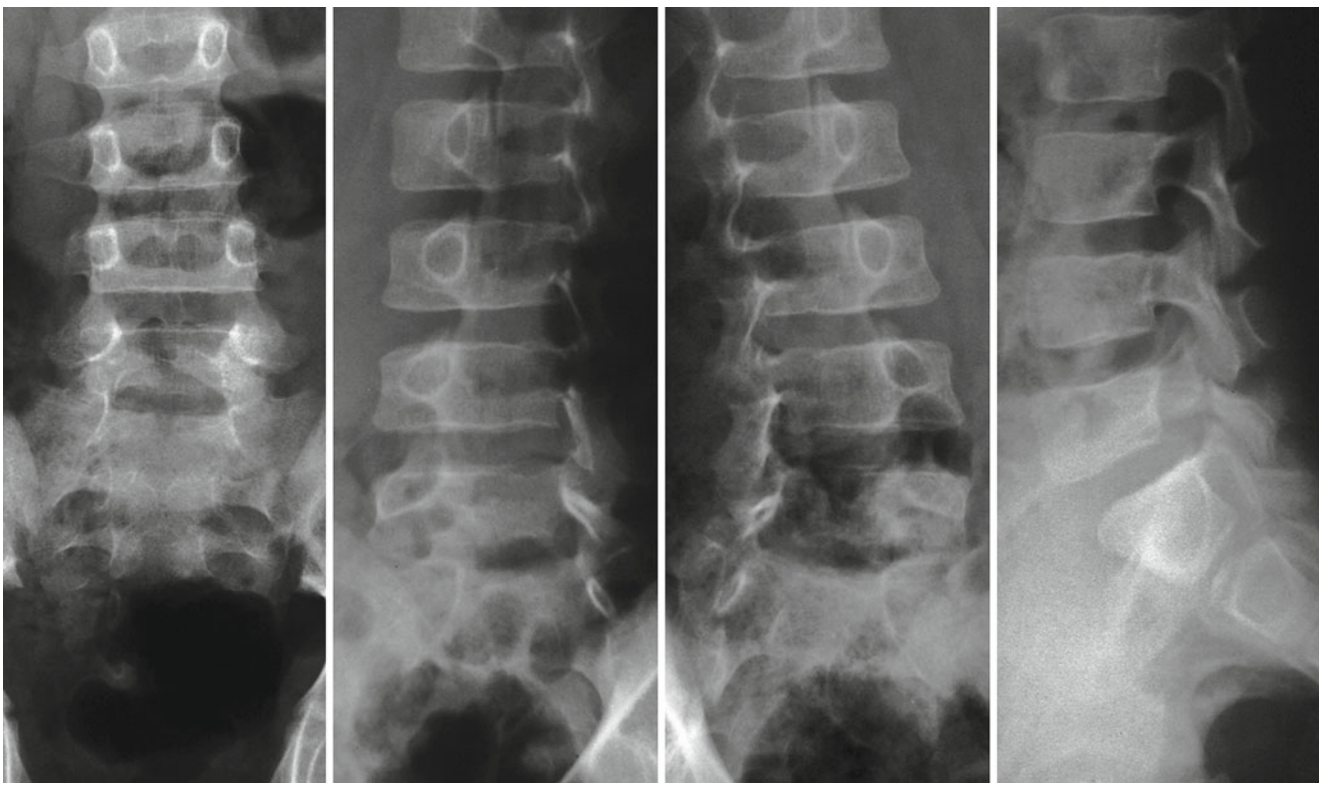

Fig. 11.20 Radiographs of the lumbar spine of a young child with spondylolysis of L5, more evident in the lateral view (*last image*), and slight anterior spondylolisthesis. Mild hypoplasia of this vertebral body is also present, as well as spina bifida occulta in L5 and S1

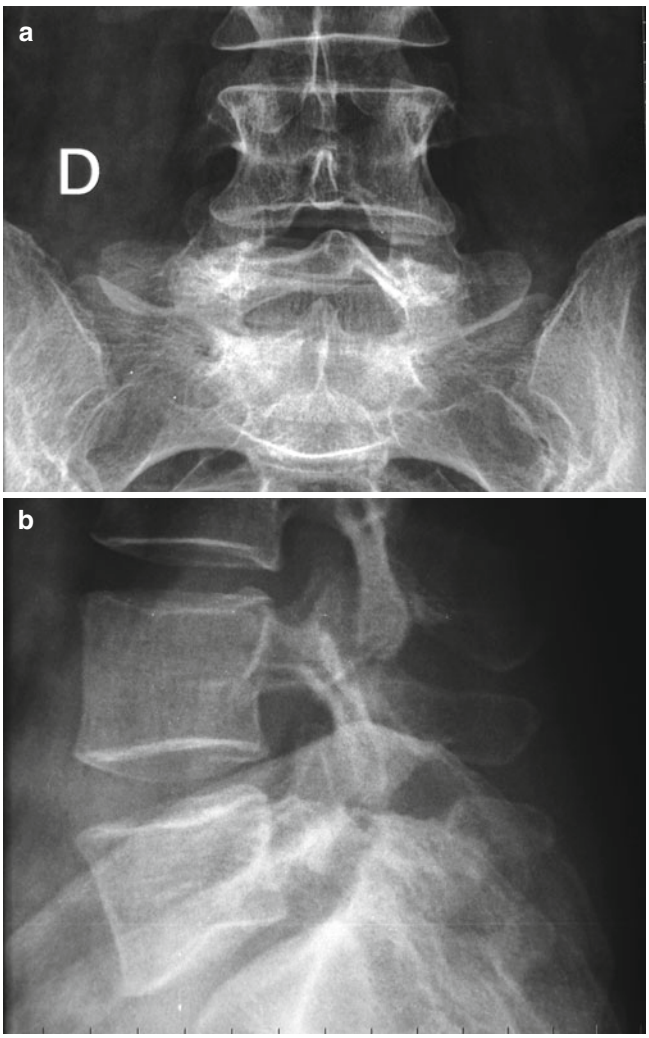

Fig. 11.21 Anteroposterior (**a**) and lateral (**b**) views of the lower lumbar spine of an adolescent with low back pain. A dysplastic left lamina of L5 can be seen in the anteroposterior view, while the lateral radiograph reveals a bony defect of the *pars interarticularis* and grade I anterior spondylolisthesis

Bone scintigraphy is highly sensitive to detect metabolically active lesions, though it is very limited to diagnose chronic/inactive lesions. Increased uptake will be present way before the appearance of radiographic abnormalities, even if there is only stress reaction without fracture. Nevertheless, further investigation is necessary in most cases of abnormal uptake in order to establish the diagnosis, and scintigraphy has been virtually abandoned in favor of MRI, which has similar sensitivity but presents superior anatomical resolution and specificity.

CT is the best method to assess bone anatomy, to demonstrate the bony defect and to estimate the degree of spondylolisthesis, being also useful to monitor the consolidation of acute lesions in serial studies. In the transverse plane, the affected vertebra displays an "incomplete ring" appearance, with discontinuity of the cortical ring in all images obtained (Fig. 11.22). The spondylotic defect is transversely oriented on axial images, commonly presenting irregular borders and bone fragmentation, lacking the oblique orientation typical of the facet joints. CT scanners in current use are able to demonstrate the bone defect in any spatial plane on reformatted images or volume-rendered reconstructions, obviating the need for scans obtained with reverse gantry angle, which were recommended in the past (Fig. 11.22). Chronic lesions present sclerotic/corticated borders, which are notably absent in acute/incomplete lesions (Figs. 11.22 and 11.23). However, CT is insensitive in demonstrating the inflammation component and is not as good as MRI in assessing the relationship between the nerve roots and the bony structures.

Even though spondylolysis can be virtually ruled out if an intact *pars interarticularis* is seen on MRI, this method is less accurate than CT to demonstrate the spondylotic bone defect. Given that false-positive results for spondylolysis are not uncommon with MRI, equivocal cases must be confirmed with CT. Nevertheless, MRI is unsurpassable to demonstrate edematous changes of the bone marrow and of

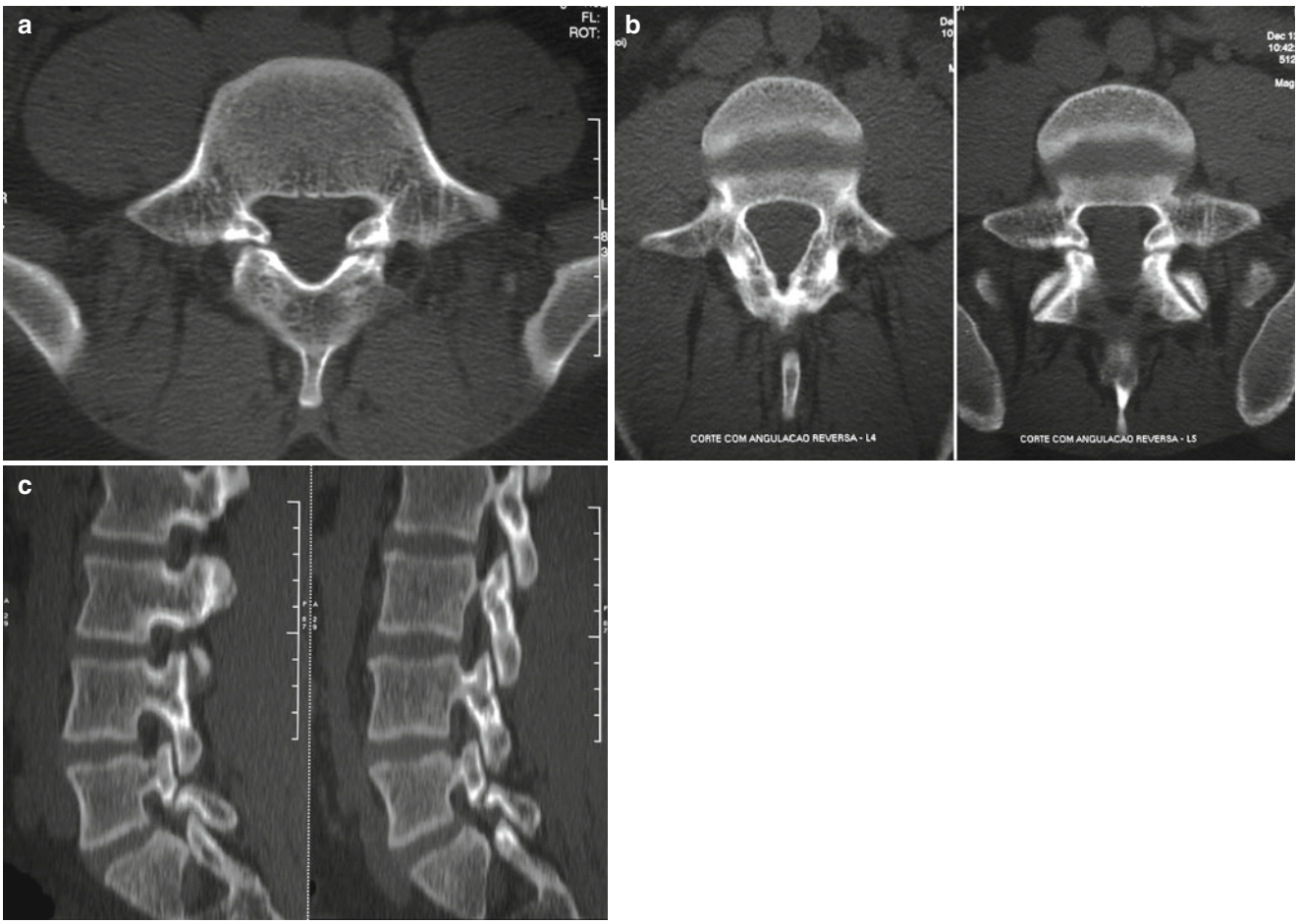

Fig. 11.22 CT of an adolescent with chronic low back pain. In (**a**), transverse image reveals bilateral and symmetric bony defects with sclerotic borders in the vertebral arch of L5. Images acquired with reverse gantry angle (**b**) confirm the discontinuity of the cortical ring of L5 (*right image*), in opposition to the intact ring seen in L4 (*left image*). The technique shown in (**b**) became obsolete as the scanners in current use allow for demonstration of spondylolysis with reformatted images obtained in the exact plane of the bone defect (same patient, **c**). Note the corticated borders of these lesions, indicative of chronic evolution, and compare the isthmi of L5 with the normal ones in the vertebrae above. Spondylolisthesis is absent

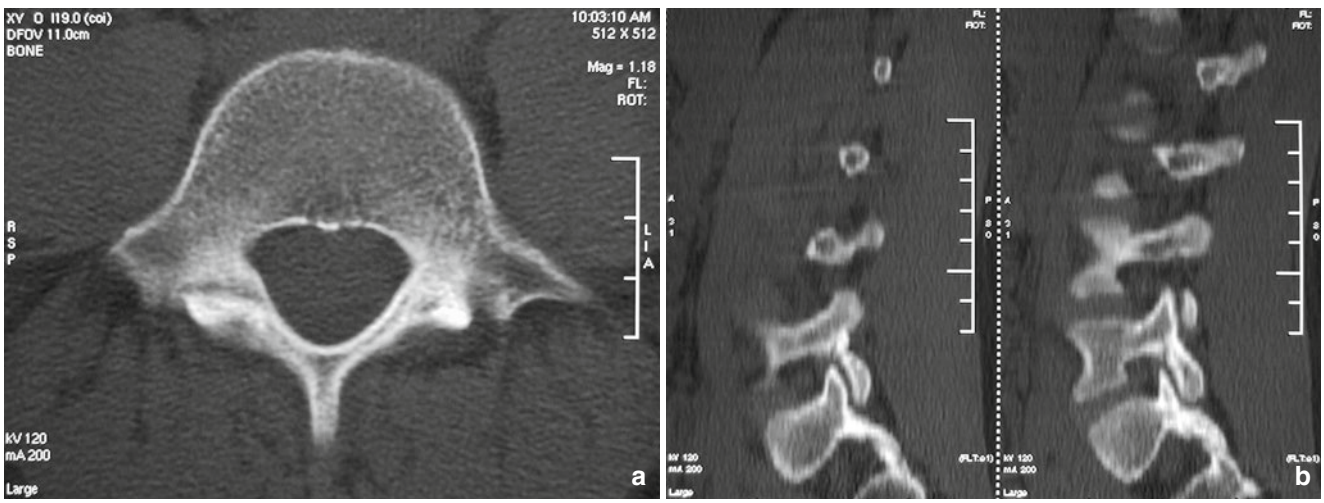

Fig. 11.23 Male adolescent judo player complaining of subacute right lumbar pain. Transverse CT image (**a**) and oblique sagittal reformatted images (**b**) reveal incomplete and unilateral right-sided spondylolysis of L5, involving only the inferior cortex and not associated with spondylolisthesis

the soft tissues, which are indicative of active inflammation (Fig. 11.24). It may be difficult to distinguish stress reactions without fracture from incomplete and/or acute bone defects on MRI with routine protocols, and 3D sequences have been advocated by some authors for this specific purpose (Fig. 11.25). Chronic lesions often present fatty replacement of the adjacent bone marrow and sclerosis of the borders of the bony defect (Figs. 11.24 and 11.26). If there is spondylolisthesis, the spinal canal shows increase of its anteroposterior diameter, with "pseudobulging" of the disk immediately below on axial images (corresponding to exposure of the disk beneath the slipped vertebra – Fig. 11.27), findings that may be also observed on CT. Spondylolisthesis may also cause foraminal stenosis and compression of the emerging nerve roots, which are usually clear on MRI (Figs. 11.26, 11.27, and 11.28).

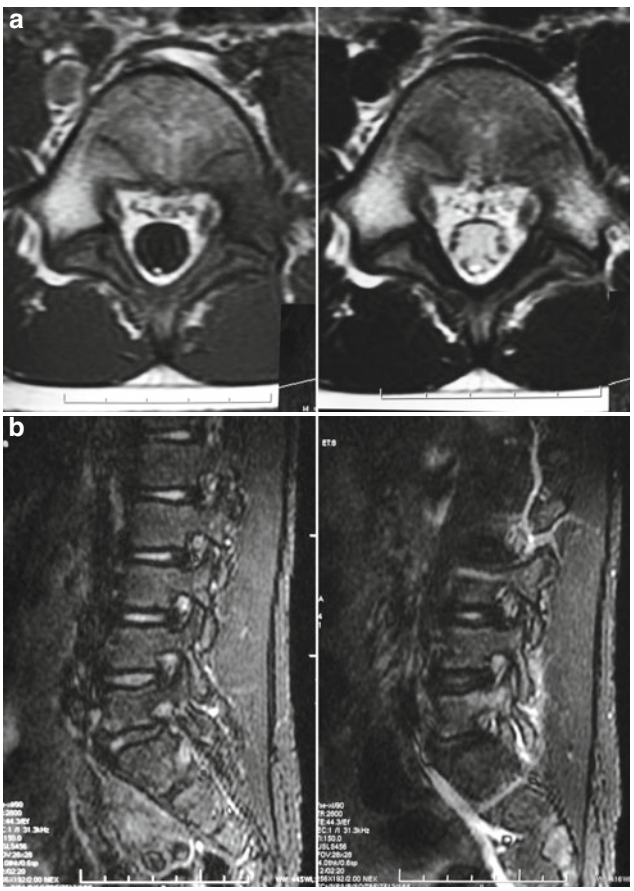

Fig. 11.24 Male adolescent complaining of low back pain of chronic evolution, with exacerbation in the last 10 days. In (**a**), transverse T1-WI (*left*) and T2-WI (*right*) display increased signal intensity on both sequences in the bone marrow of the right pedicle of L5, representing fatty replacement. On the other hand, there is low signal intensity on T1-WI and high signal intensity on T2-WI in the left pedicle, related to bone marrow edema. Sagittal STIR images (**b**) demonstrate hypointensity of the bone marrow of the right pedicle of L5 (*first image*) and hyperintensity in the left pedicle and in the homolateral facets (*second image*), mirroring the findings of (**a**). The inferior articular facet of L4 and the superior articular facet of S1 at left also exhibit bone marrow edema pattern. A small amount of fluid is seen in the right facet joint in L4–L5 and in the left ones in L4–L5 and L5–S1, with diffuse edema of the soft tissues adjacent to the latter. Complete bone defects are present in the isthmi of L5 but are much less conspicuous than those seen on CT images in previous figures. MRI findings are compatible with bilateral spondylolysis of L5, of chronic evolution at right and acute at left

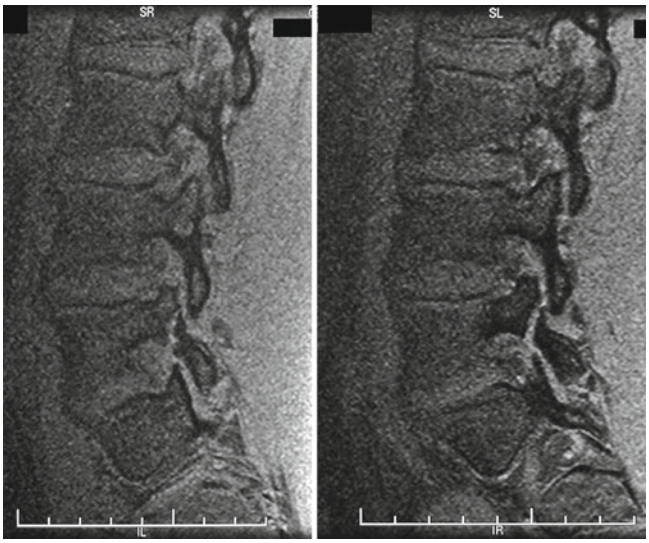

Fig. 11.25 A 3D gradient-echo sequence with sagittal reformatted images at the level of the facet joints of L5 (same patient of Fig. 11.24). The bony defects are much more evident in this sequence: note the irregular borders of the right-sided spondylolysis (*first image*), typical of chronic lesions, in contradistinction to the comparatively smoother borders of the acute left-sided defect (*second image*)

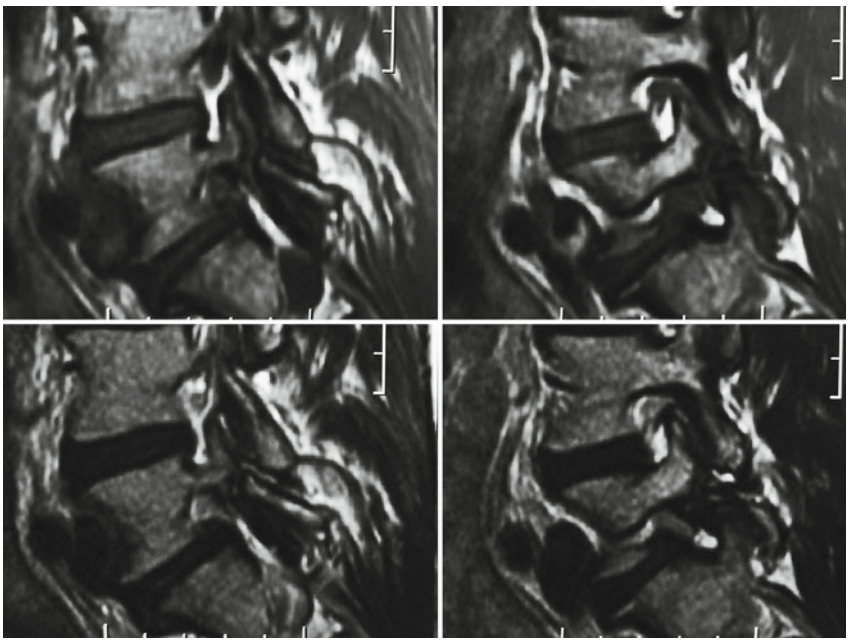

Fig. 11.26 Sagittal T1-WI (*upper row*) and T2-WI (*lower row*) disclosing left-sided spondylolysis of L5, associated with grade I spondylolisthesis and homolateral foraminal narrowing leading to stretching of the emerging nerve root. The bony defect presents corticated borders and fatty replacement is seen in the adjacent pedicle, which are indicative of chronic evolution

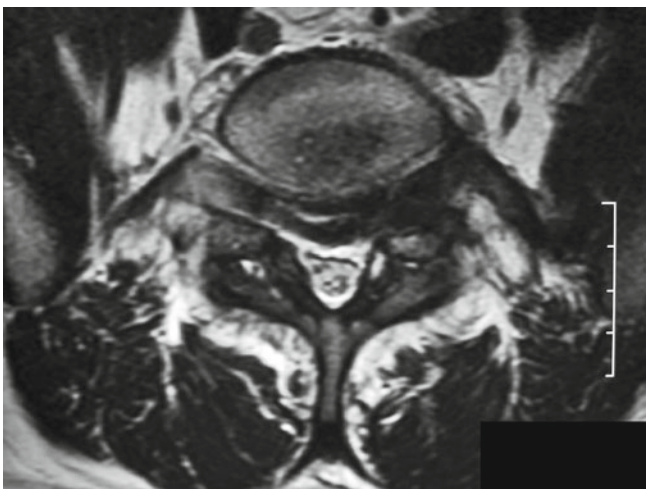

Fig. 11.27 Transverse T2-WI at the level of L5 in a patient with spondylolysis and spondylolisthesis. The bony defects appear as transversely oriented clefts that interrupt the vertebral arch, with anterior translation of the vertebral body and exposure of the disk immediately below ("pseudobulging"). There is narrowing of both foramina, mainly at left

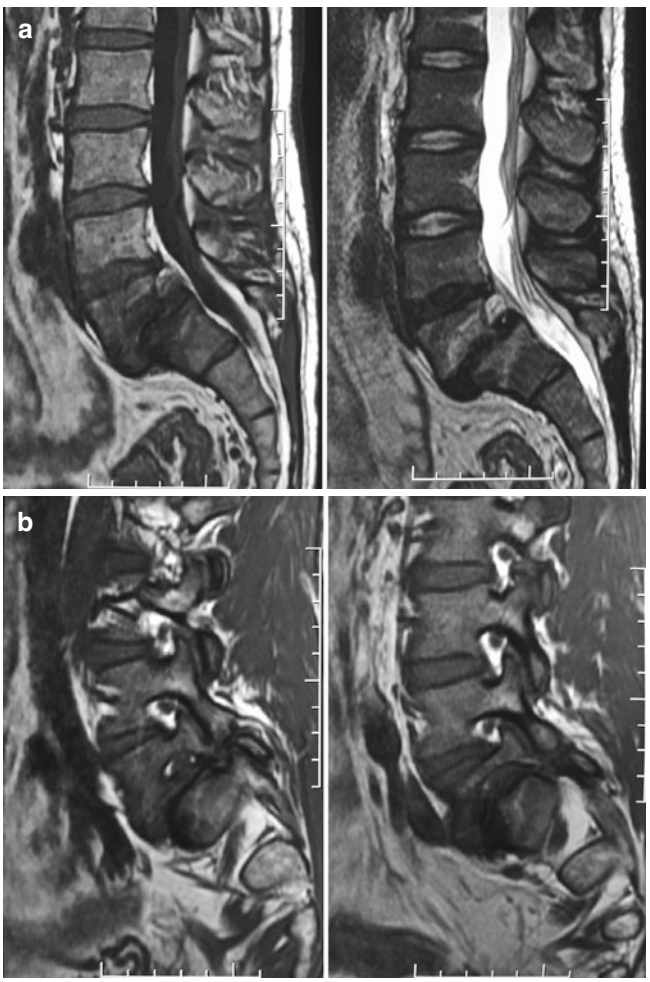

Fig. 11.28 Sagittal (**a**) and parasagittal (**b**) T1-WI and T2-WI of the lumbar spine demonstrating spondylolysis of L5 with grade II spondylolisthesis and marked foraminal stenosis in L5–S1. Hypoplasia and posterior wedging of the body of L5 are present, along with reduced height and low signal intensity of the intervertebral disk of L5–S1 and edematous changes of the bone marrow of the contiguous endplates. Stretching of nerve roots and osteodiscal changes related to abnormal vertebral mobility are the probable causes of pain

11.6 Scheuermann's Disease

Juvenile thoracic kyphosis, widely known as Scheuermann's disease, is a structural kyphosis of unknown cause that involves the thoracic or thoracolumbar spinal segments, typically found in adolescents from 12 to 15 years old. Most cases present minimal deformity and are virtually asymptomatic. There is slow progression of the deformity, which ceases after skeletal maturation. Classic radiographic criteria include (1) thoracic kyphosis with an angle of more than 45°, (2) wedging of more than 5° affecting at least three vertebral bodies adjacent to the apex of the kyphotic curve, and (3) irregularity of the vertebral endplates, commonly associated with Schmorl's nodules and reduced height of the adjacent disks (Fig. 11.29). Nonetheless, in the less severe form of the disease, there is no significant kyphosis and the morphologic abnormalities of the vertebrae may be confined to the lumbar spine or to the thoracolumbar transition (Fig. 11.30). Even though bone changes are usually evident on radiographs, CT and MRI may be useful in selected cases, mainly to rule out alternative causes of dorsalgia (Figs. 11.29, 11.30, and 11.31). Awareness of the imaging appearance of Scheuermann's disease allows avoiding diagnostic confusion in the setting of spinal trauma.

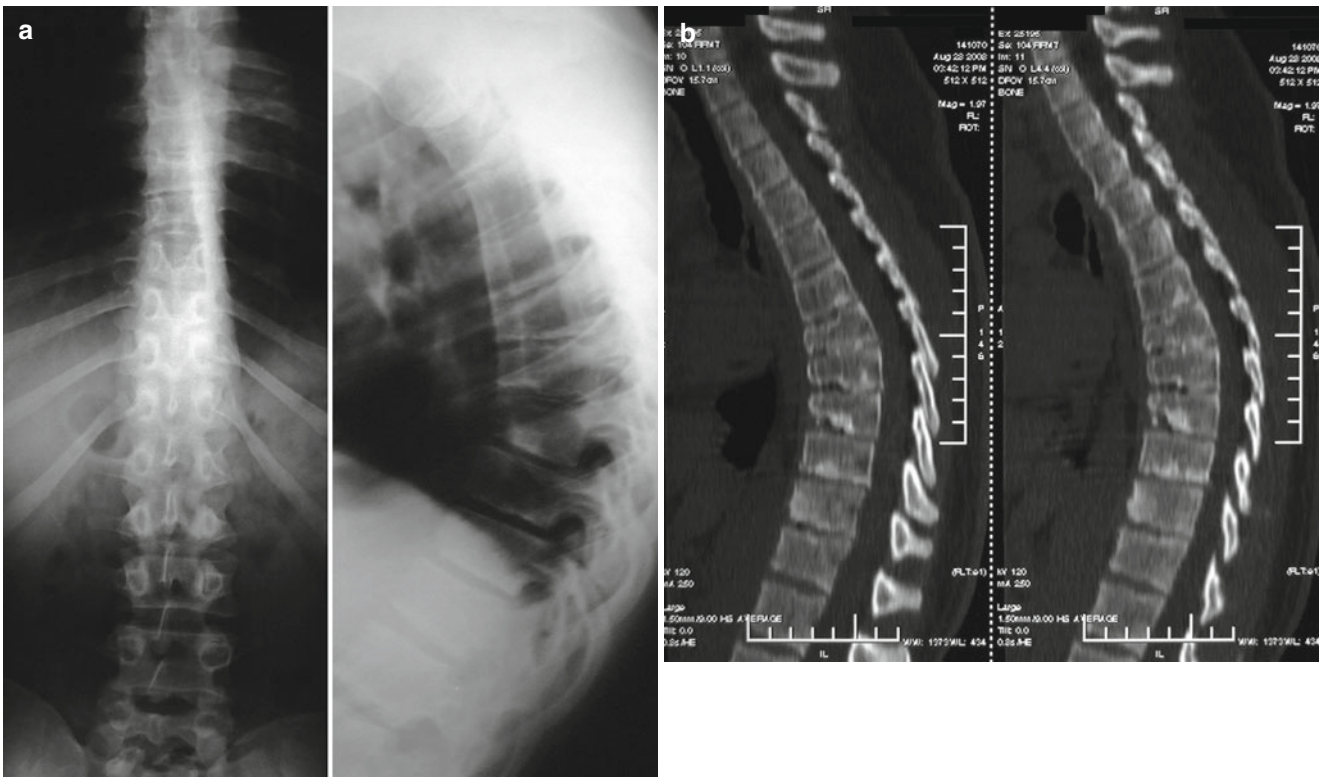

Fig. 11.29 Radiographs (**a**) and sagittal reformatted CT images (**b**) of the thoracic spine of an adolescent with Scheuermann's disease. Thoracic kyphosis is present, due to anterior wedging and reduced height of the vertebral bodies from T7 to T9. The endplates are irregular, presenting subchondral sclerosis from T6 to T11

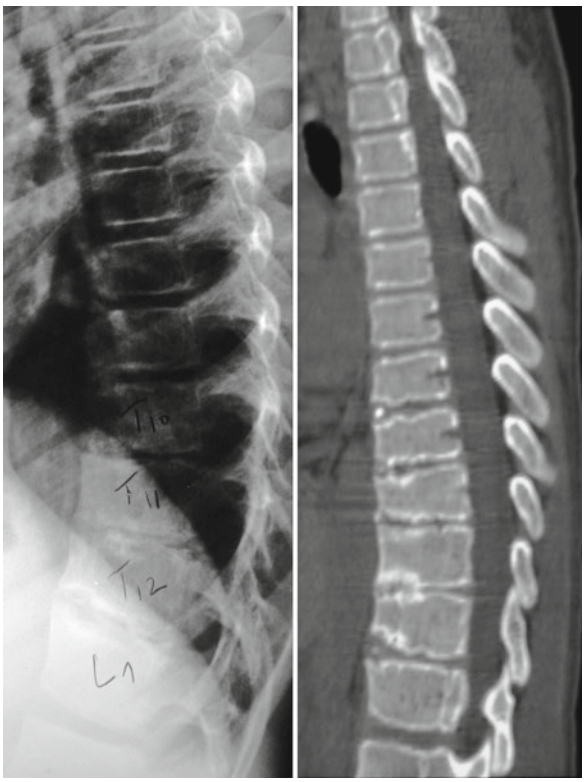

Fig. 11.30 Male adolescent with mild form of Scheuermann's disease. Lateral radiograph (*left*) and sagittal reformatted CT image (*right*) demonstrate findings similar to those observed in the patient of Fig. 11.29 from T9 to T12; nonetheless, in spite of wedging and reduced height of the vertebral bodies of T9, T10, and T12, no significant kyphosis is present

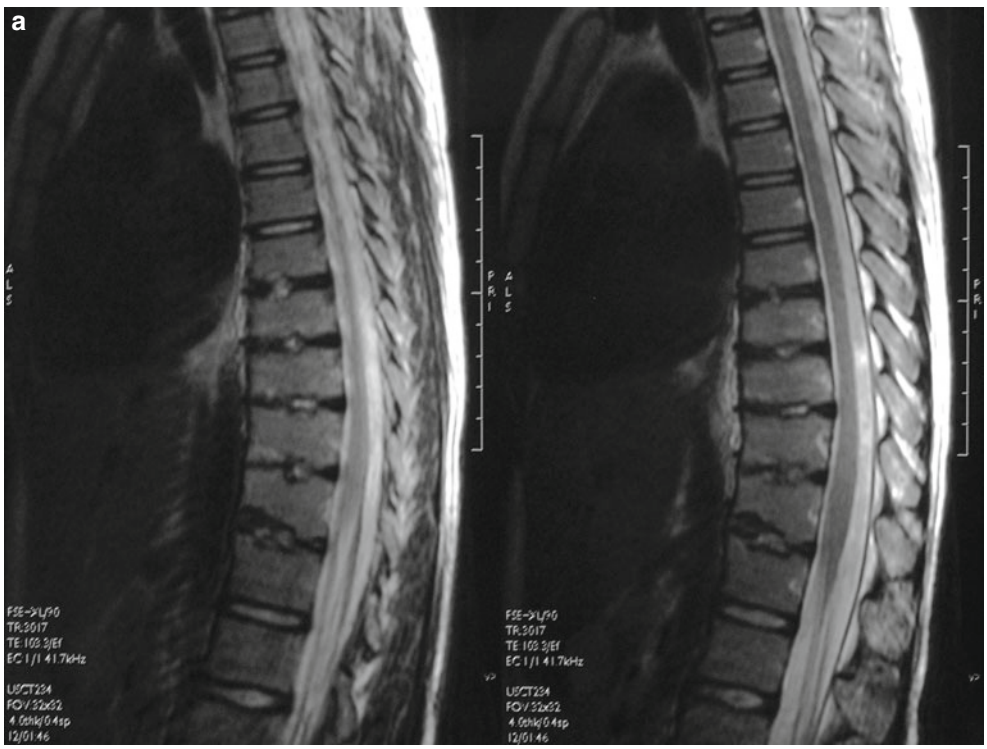

Fig. 11.31 MRI of the same patient of Fig. 11.30, sagittal T2-WI (**a**) and post-gadolinium fat sat T1-WI (**b**). In addition to the previously described findings, there is reduced height of the disks in the affected segment, with loss of the normal signal intensity on T2-WI, as well as minimal subchondral enhancement adjacent to the endplates of T8 and T9

Fig. 11.31 (continued)

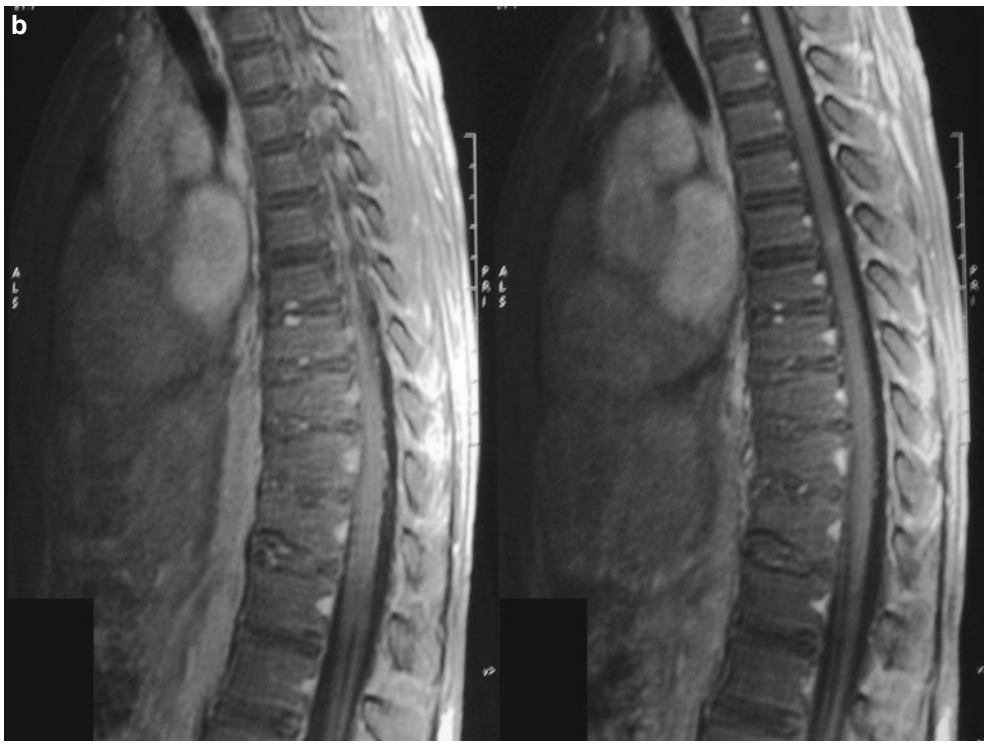

Key Points

- Spinal JIA affects most often the cervical spine, notably the craniovertebral transition and the facet joints. Narrowing of the joint spaces, erosive changes, and vertebral instability are common. Ankylosis, disk calcifications, and morphologic abnormalities of the vertebral bodies are late findings.
- Bacterial spondylodiscitis is an aggressive and rapidly progressive condition, with imaging abnormalities centered about the intervertebral disk and the adjacent endplates, leading to cortical destruction and reduction of the disk height. The lumbar spine is the most frequent site of involvement. MRI is the best method for early diagnosis, being useful to assess the extent of the infection and to monitor the response to treatment.
- Reduction of disk height is less prominent and occurs later in tuberculous spondylodiscitis if compared to bacterial spondylodiscitis. Anterior subligamentous dissemination is a characteristic feature and may lead to involvement of multiple, noncontiguous spinal levels, notably in the thoracic segment and in the thoracolumbar transition. Marked bone destruction and paravertebral soft-tissue abscesses are also common. MRI is the most sensitive and accurate imaging method.
- Spondylolysis is a bony defect of the *pars interarticularis*. Radiographs are equivocal in many cases and CT is the best imaging method to demonstrate the defect, whether complete or incomplete. Even though MRI presents a low positive predictive value for spondylolysis, it is the only imaging method able to demonstrate edematous changes of the bone marrow and of the soft tissues, which are associated with active inflammation and pain.
- In its classic form, Scheuermann's disease is a structural kyphosis that occurs in adolescents, associated with vertebral wedging, irregularity of the vertebral endplates, Schmorl's nodules, and reduced height of the intervertebral disks. Radiographs usually suffice for the diagnosis, and CT and MR are exceptionally used.

Recommended Reading

Campbell RS, Grainger AJ, Hide IG, Papastefanou S, Greenough CG (2005) Juvenile spondylolysis: a comparative analysis of CT, SPECT and MRI. Skeletal Radiol 34(2):63–73

Endén K, Laiho K, Kautiainen H, Arkela-Kautiainen M, Belt E, Kauppi M (2009) Subaxial cervical vertebrae in patients with juvenile idiopathic arthritis – something special? Joint Bone Spine 76(5):519–523

Faingold R, Saigal G, Azouz EM, Morales A, Albuquerque PA (2004) Imaging of low back pain in children and adolescents. Semin Ultrasound CT MR 25(6):490–505

Frank G, Mahoney HM, Eppes SC (2005) Musculoskeletal infections in children. Pediatr Clin North Am 52(4):1083–1106

Hong SH, Choi JY, Lee JW, Kim NR, Choi JA, Kang HS (2009) MR imaging assessment of the spine: infection or an imitation? Radiographics 29(2):599–612

Johnson K (2006) Imaging of juvenile idiopathic arthritis. Pediatr Radiol 36(8):743–758

Kapetanos GA, Hantzidis PT, Anagnostidis KS, Kirkos JM (2006) Thoracic cord compression caused by disk herniation in Scheuermann's disease: a case report and review of the literature. Eur Spine J 15 (Suppl 5):553–558

Kerssemakers SP, Fotiadou AN, de Jonge MC, Karantanas AH, Maas M (2009) Sport injuries in the paediatric and adolescent patient: a growing problem. Pediatr Radiol 39(5):471–484

Kjellberg H, Pavlou I (2011) Changes in the cervical spine of children with juvenile idiopathic arthritis evaluated with lateral cephalometric radiographs. Angle Orthod 81(3):447–452

Laine JC, Kaiser SP, Diab M (2010) High-risk pediatric orthopedic pitfalls. Emerg Med Clin North Am 28(1):85–102

Pruthi S, Thapa MM (2009) Infectious and inflammatory disorders. Magn Reson Imaging Clin N Am 17(3):423–438

Ranson M (2009) Imaging of pediatric musculoskeletal infection. Semin Musculoskelet Radiol 13(3):277–299

Shikhare SN, Singh DR, Shimpi TR, Peh WC (2011) Tuberculous osteomyelitis and spondylodiscitis. Semin Musculoskelet Radiol 15(5):446–458

Sofka CM, Bogner E (2008) Imaging of juvenile rheumatoid arthritis. HSS J 4(1):71–73

Teo HE, Peh WC (2004) Skeletal tuberculosis in children. Pediatr Radiol 34(11):853–860

Selected Dysplastic and Developmental Abnormalities of the Immature Joint

12

12.1 Introduction

Developmental abnormalities and skeletal dysplasias comprise one of the most controversial, extensive, and complex subjects in pediatrics. This miscellaneous chapter will provide a concise review of imaging findings in selected conditions that are particularly prone to affect the immature joint. This selection is inevitably arbitrary and includes abnormalities of the bones and of the soft tissues, based mostly in their frequency, their clinical relevance, their importance for the differential diagnosis, and the potential impact of imaging for their diagnosis and management. Pseudotumoral articular and periarticular dysplastic conditions (such as focal fibrocartilaginous dysplasia and dysplasia epiphysealis hemimelica) are discussed in Chap. 6.

12.2 Madelung's Derformity

Madelung's deformity is an uncommon anomaly characterized by shortening of the distal forearm, which presents a bayonet (or "dinner fork") configuration, and palmar displacement of the wrist. This condition is more frequent in females in late childhood or in adolescence, presenting with pain, joint deformity, and/or limited range of motion. It may be an isolated finding or may be associated with dysplastic syndromes, like dyschondrosteosis (Léri-Weill syndrome, an autosomal dominant mesomelic dwarfism, in which Madelung's deformity is often bilateral). Its origin is probably related to abnormal growth of the volar and medial portion of the physis of the distal radius due to the presence of an anomalous structure named Vickers' ligament, a fibrous band that tethers the lunate and/or the triangular fibrocartilage complex to the distal radius.

Typical radiographic findings include dorsal bowing and shortening of the radius, which presents volar and ulnar angulation of its distal surface, and a triangular appearance of the distal radial epiphysis; lateral angulation and posterior dislocation of the distal ulna are also present (Fig. 12.1). The proximal carpal row has a wedge-like configuration, conforming to the altered shape of the distal surfaces of the radius and ulna (Fig. 12.1). Vickers' ligament itself has been described with ultrasonography (US), computed tomography (CT), or magnetic resonance imaging (MRI), mostly with the latter, inserting at the gutter-like deformity of the distal radius (Fig. 12.2).

12.3 Proximal Femoral Focal Deficiency

The term proximal femoral focal deficiency (PFFD) refers to a rare congenital anomaly that classically presents abnormal development and shortening of the proximal femur and deficient development of the hip joint, occurring unilaterally in most patients. PFFD encompasses a broad spectrum of developmental changes, varying from hypoplasia to complete aplasia of the proximal femur; the severity of the acetabular dysplasia correlates strongly with the extent of the deformity of the femoral head, which is often associated with subtrochanteric varus deformity. Other malformations of the affected limb may also be found, such as tibial shortening and fibular hemimelia.

Until the advent of modern imaging methods, diagnosis and staging were based on radiographic findings and on conventional arthrograms. Aitken's radiographic classification subdivided PFFD in subtypes, varying from A (less severe, characterized by a short femur with a well-formed femoral head, normally articulated with the acetabulum) to D (very severe, with absence of the femoral head and of the acetabulum) (Fig. 12.3). However, radiographs are unable to demonstrate the non-mineralized epiphyseal cartilage and the non-ossified connection that may be present between the femoral head and the distal portion of the bone (Figs. 12.3 and 12.4). MRI is the most important imaging method for preoperative assessment of PFFD, mostly in small children, as it is able to demonstrate noninvasively the anatomy of

S.L. Viana et al., *Joint Imaging in Childhood and Adolescence*,
DOI 10.1007/978-3-642-35876-0_12, © Springer-Verlag Berlin Heidelberg 2013

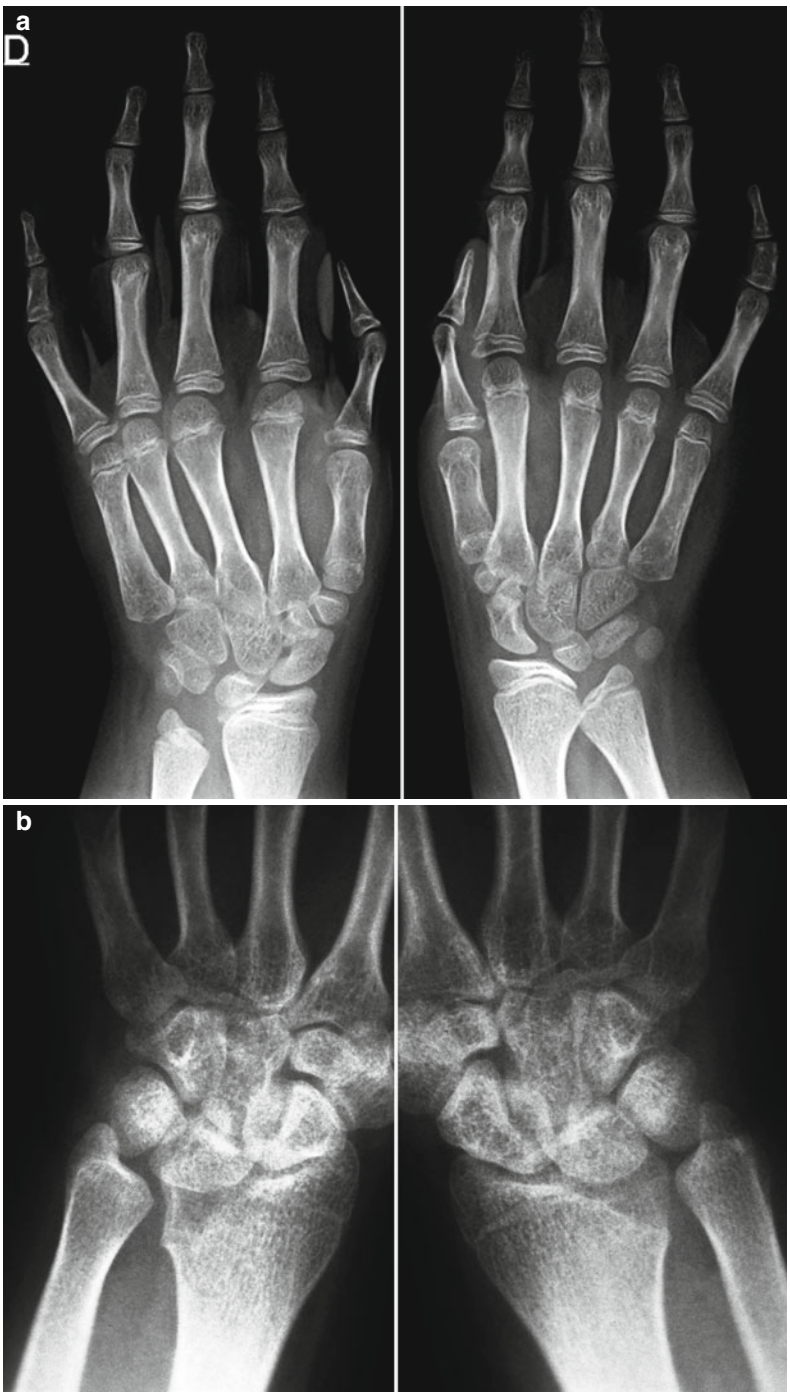

Fig. 12.1 Radiographs of hands and wrists of a child (**a**) and radiograph of the wrist of an adolescent (**b**), both with bilateral Madelung's deformity. These images show medial inclination of the distal articular surfaces of the radii, with volar deviation more prominent in (**b**). The typical ulnar deformity is more marked in (**a**). There is abnormal alignment of the bones of the proximal carpal rows, allowing them to conform to the altered configuration of the distal epiphyses of the forearms. The distal radial epiphyses appear triangular in (**b**)

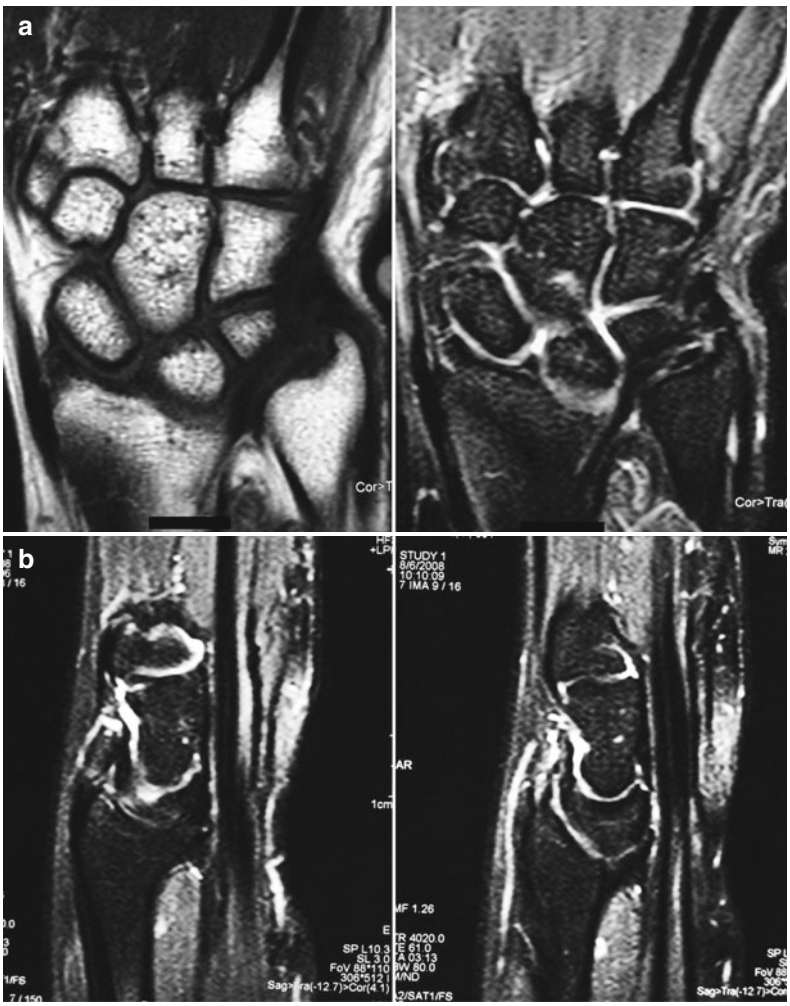

Fig. 12.2 Coronal T1-WI and fat sat T2-WI (**a**) and sagittal fat sat T2-WI (**b**) of the left wrist of a patient with Madelung's deformity. The typical appearance of the distal radius is quite evident, with medial and volar angulation of the articular surface and bayonet-like configuration. Vickers' ligament appears as a band of low signal intensity in both sequences tethering the triangular fibrocartilage complex and the lunate bone to the deformed radial epiphysis. A skin marker can be seen adjacent to the ulnar styloid, indicating a palpable lump due to dorsal subluxation of the distal ulna

the abnormal femur, rendering conventional arthrograms obsolete. Furthermore, MRI can discriminate if the connection between the diaphysis and the femoral head is osseous (signal intensity similar to that of the normal bone), fibrous (hypointense in all sequences), or fibrocartilaginous (hyperintense on T2-WI, similar to the cartilage). The integrity of the physis is also accurately assessed: absence of the provisional calcification zone has been described as an indicator of physeal dysfunction (Fig. 12.5). In addition, MRI can assess the articular relationships and demonstrate other osseous and soft-tissue abnormalities. Even though US is also potentially useful, MRI provides a global assessment of the joint (and of the limb) that US is unable to offer, especially considering the complex and multiple malformations often associated.

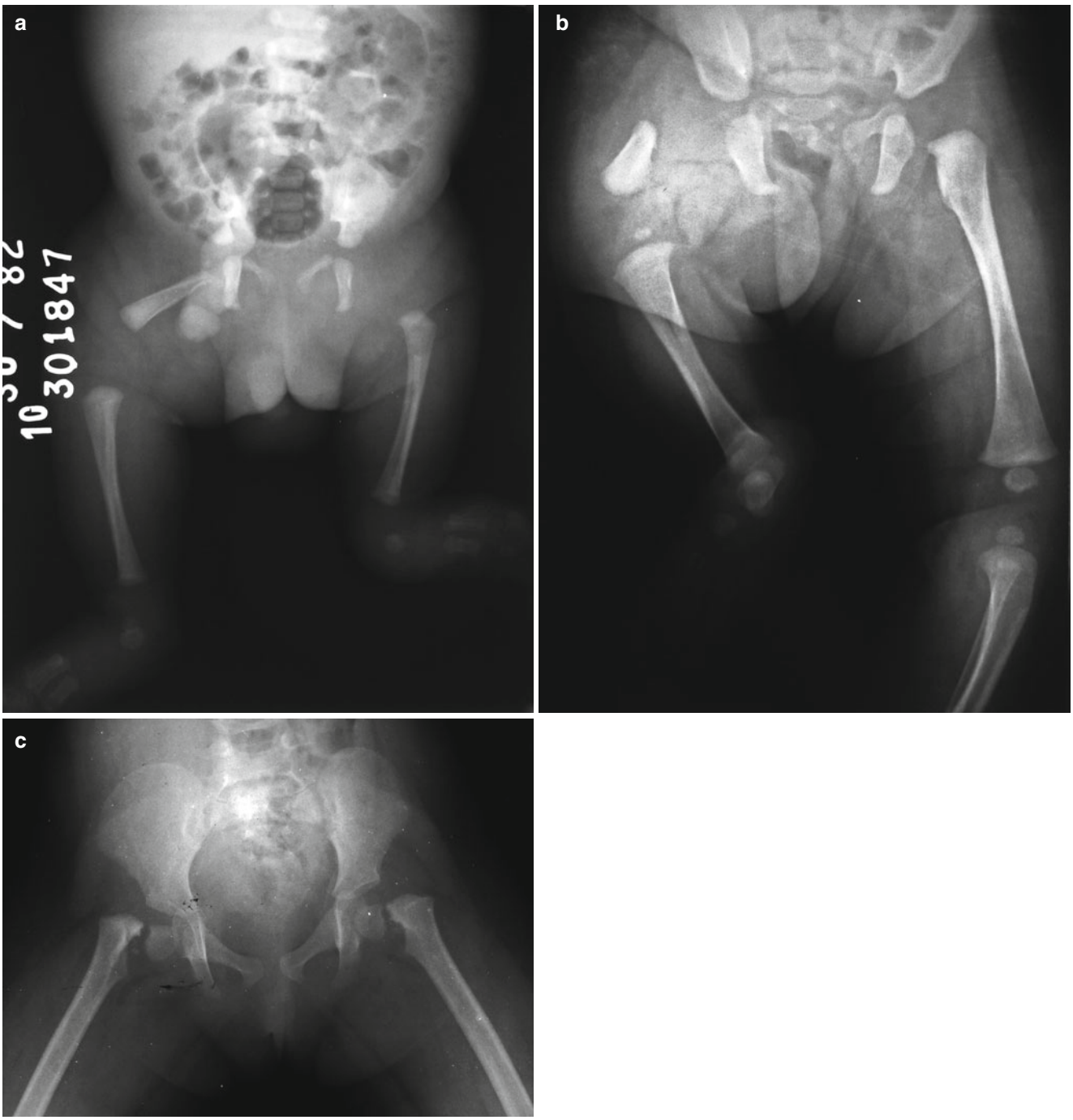

Fig. 12.3 Radiographs of the lower limbs of different patients with PFFD demonstrating the variable severity that this condition may present. In (**a**), both acetabula are markedly dysplastic, with no signs of ossification of the left femur and homolateral thigh shortening; the ipsilateral fibula is also malformed. In (**a** and **b**), the right femora are short and present tapering, pointed upper ends, notably in the latter image, which also displays homolateral acetabular dysplasia, cranial migration of the femoral diaphysis, and absence of the right fibula. In (**c**), there is symmetric and bilateral varus deformity of both femora, with mildly shallow acetabula and cone-shaped femoral heads. Figure (**d**) shows shortening and subtrochanteric varus deformity of the right femur, with acetabular dysplasia and reduced size of the homolateral femoral head; the right fibula is absent

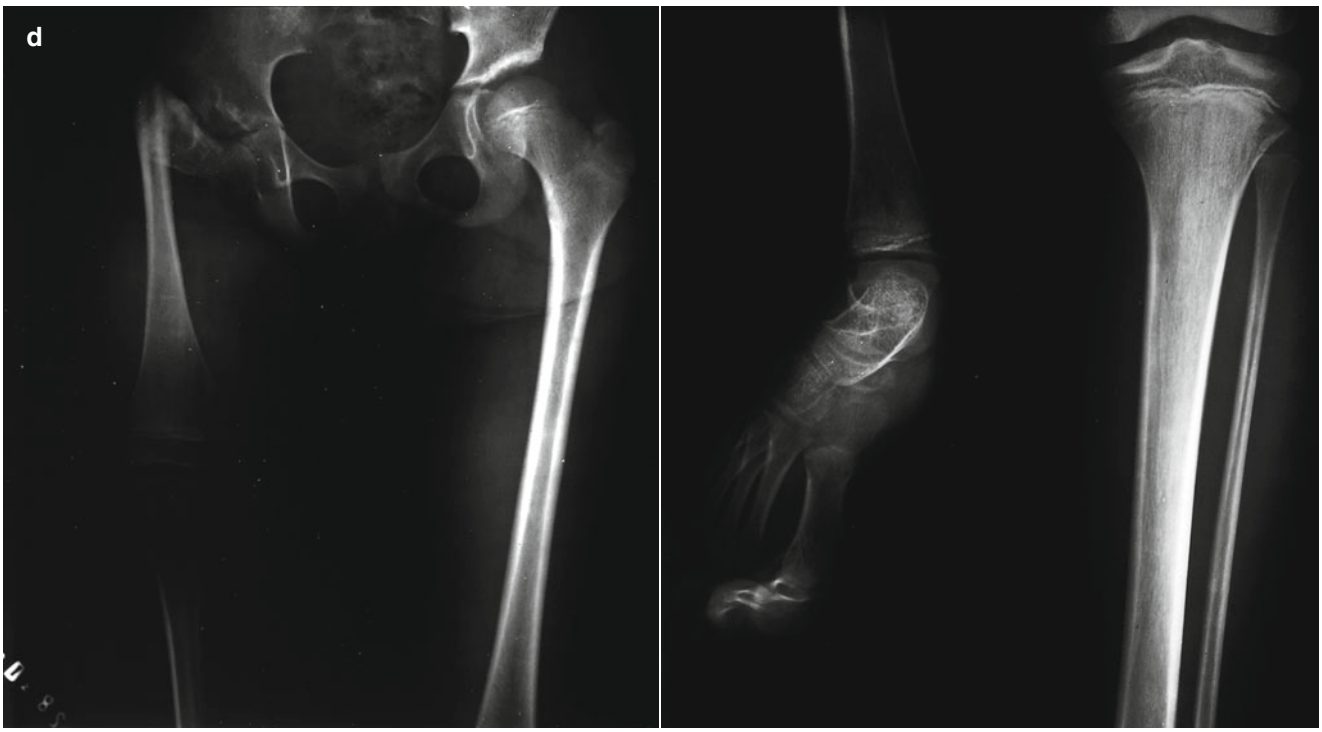

Fig. 12.3 (continued)

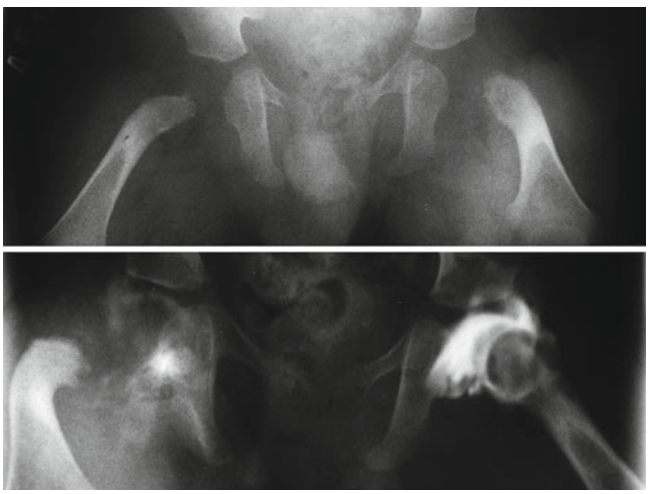

Fig. 12.4 In the *upper image*, pelvic radiograph reveals shortening and bending of both femora, with bilateral metaphyseal irregularity. The acetabula are reasonably well formed, an indirect sign of the presence of the femoral heads. However, as the epiphyseal cartilages are not yet ossified, this study is unable to provide accurate information about them. Conventional arthrograms (*lower image*) delineate the contour of the femoral epiphyses, confirming that they are really present and contained within the acetabula. These images have only historical value, as arthrograms became obsolete after the advent of MRI

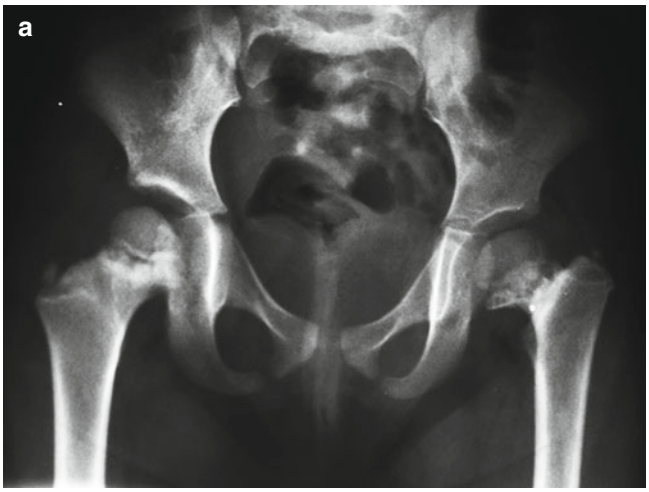

Fig. 12.5 Pelvic radiograph (**a**), coronal T1-WI (**b**, *upper row*), and post-gadolinium fat sat T1-WI (**b**, *lower row*) of the hips of a child with PFFD. Radiograph shows deficient development of the femoral head and neck at left, with homolateral varus deformity; at right, there is sclerosis and irregularity of the proximal femoral metaphysis. MRI demonstrates that the provisional calcification zone is present at right, seen as a metaphyseal line of low signal intensity, and ill-defined at left

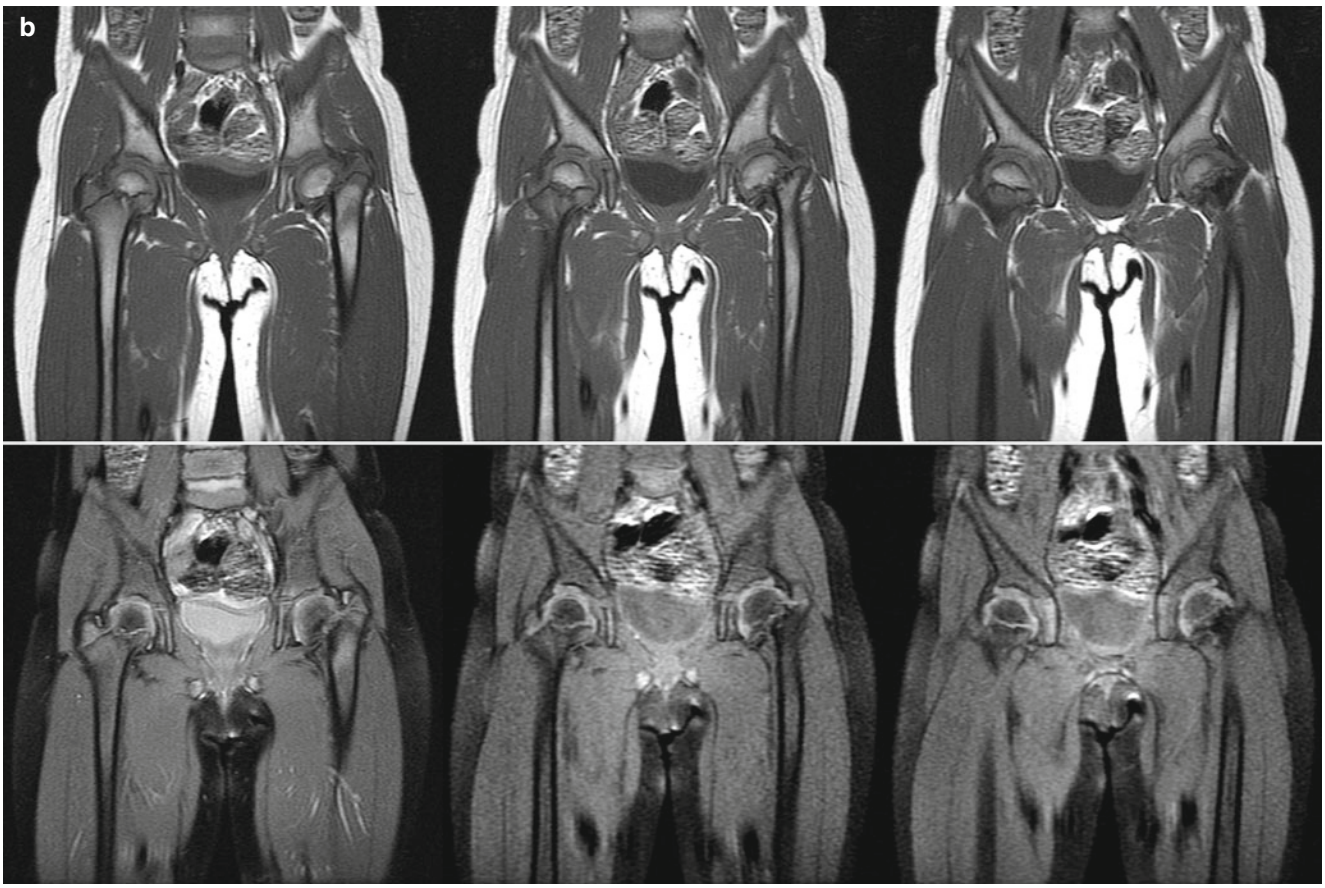

Fig. 12.5 (continued)

12.4 Developmental Dysplasia of the Hip

Instead of a single disease, developmental dysplasia of the hip (DDH) comprises a wide spectrum of congenital malformations that have in common an abnormal relationship between the femoral head and the acetabulum. These conditions may vary from stable and mildly dysplastic hips to frankly dysmorphic and dislocated coxofemoral joints. Females are affected in the overwhelming majority of the cases, and bilateral disease occurs in approximately 20 % of the patients. The diagnosis is essentially a clinical one, which is usually suspected immediately after birth; delayed recognition is associated with worse prognosis and long-term sequelae (Fig. 12.6). Nevertheless, most "dislocatable" hips (especially those detected in the first 4–6 weeks of extrauterine life and not associated with an abnormally shaped acetabulum) are deprived of significance and will stabilize spontaneously, resulting from physiologic postnatal tissue laxity. There is no evidence to support disseminated use of imaging in the screening of DDH, as there is a wide "gray zone" of findings of uncertain significance between the normal hip and clear-cut DDH, so that excessive use of imaging may increase the rate of false-positive diagnoses. Indications for imaging evaluation include, among others, inconclusive physical examination, preoperative assessment, and follow-up of treatment.

The usefulness of radiographs for early diagnosis is quite restricted; nevertheless, markedly dysmorphic acetabula and frank dislocations may be evident even in newborns (Fig. 12.7). Considering that the femoral heads begin to ossify only after 4–6 months of extrauterine life, radiographs are very limited in small children, as the epiphyseal cartilages will be undetectable until then. There are some classic lines drawn in the anteroposterior view of the pelvis that are used to estimate the relationships of the hip joint. Shenton's line is an imaginary arch connecting the medial contour of the femoral neck with the superior contour of the obturator foramen; discontinuity of this arch is an indicator of joint dislocation. Hilgenreiner's line is horizontal and drawn tangentially to the superior aspect of both triradiate

cartilages, while Perkins' line is perpendicular to the former, tangential to the lateral edge of the acetabulum. In normal children, the femoral heads (or their expected location) should be inferior and medial to the intersection of Hilgenreiner's and Perkins' lines, and lateral/superior migration is indicative of dislocation (Figs. 12.7 and 12.8). In dysplastic hips, the femoral head may be smaller and/or show delayed ossification if compared to the normal contralateral one (Fig. 12.8).

US is the preferred imaging method for diagnosis and follow-up of DDH during the first 6 months of life, becoming gradually less sensitive and more difficult to perform as the femoral head ossifies. This imaging modality is largely used to confirm reduction of dislocation in children treated with orthotic devices, such as the Pavlik harness, being also able to evaluate joint stability in real time. However, factors such as subjective interpretation, limited reproducibility, and operator-dependent nature must be kept in mind, as well as the relatively high rate of false-positive diagnoses. The static Graf method is widely disseminated, using two angles drawn in a single coronal image for assessment of DDH (Fig. 12.9), emphasizing the morphology of the hip. The alpha angle measures the osseous acetabular roof angle (slope of the acetabulum), while the beta angle, less important, is indicative of the acetabular cartilaginous roof coverage. There is mild dysplasia if the alpha angle is between 50 and 59°, moderate between 43 and 50°, and severe if the angle has less than 43° (Fig. 12.9). The normal beta angle has less than 55°. The original classification proposed by Graf is complex, with several subdivisions based on the appearance of the anatomic landmarks and on the values of alpha and beta angles. Nevertheless, recent works have recommended a simplified approach, emphasizing descriptive terms related

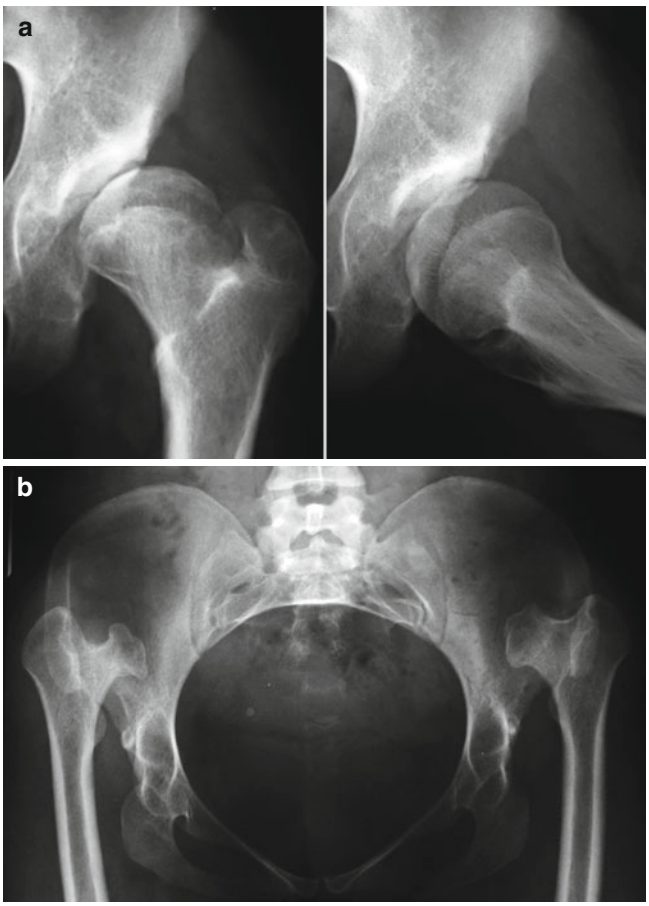

Fig. 12.6 In (**a**), radiographs of the left hip of a child with DDH shows articular incongruity, with a shallow and dysplastic acetabulum associated with a dysmorphic and laterally subluxated femoral head. In (**b**), pelvic radiograph of a 28-year-old female with bilateral DDH shows bilateral coxa vara and posterosuperior dislocation of the femoral heads, which are markedly deformed. Both acetabula are poorly developed

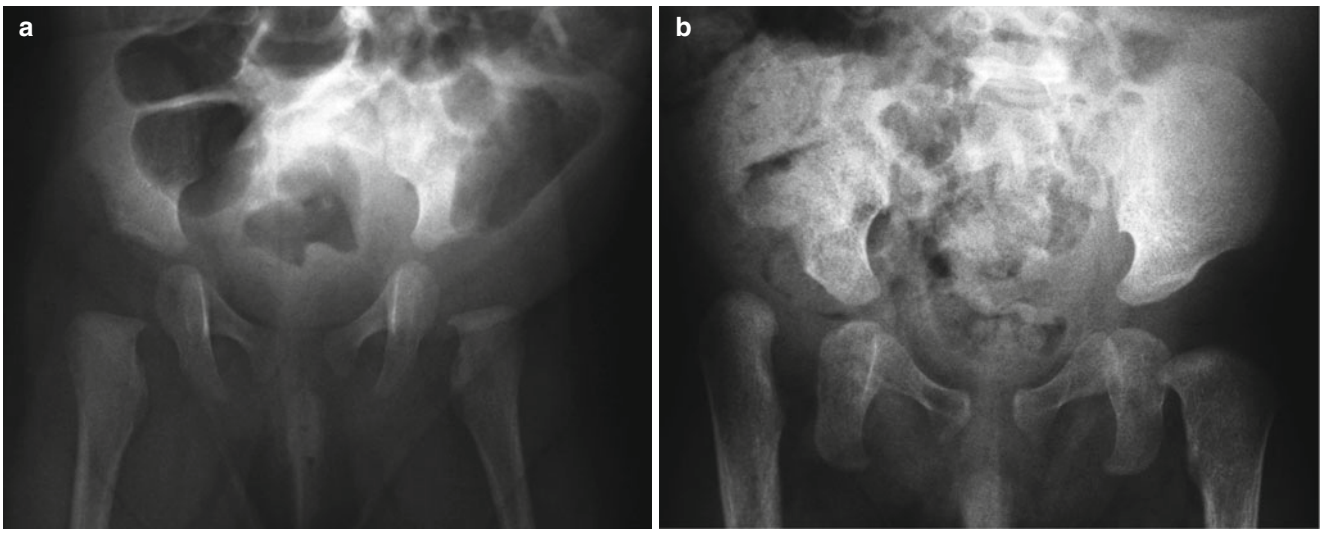

Fig. 12.7 Pelvic radiographs of two distinct patients with DDH. Shenton's line is broken in both hips in (**a**), with mild lateralization of the right metaphysis and homolateral acetabular hypoplasia. In (**b**), the right hip shows signs of frank dislocation, with cephalic migration of the femur and hypoplasia of the acetabulum; discontinuity of Shenton's line is seen in the left hip, as well as mild acetabular hypoplasia. The real position of the femoral heads can be only inferred at radiographs, as they are not yet ossified

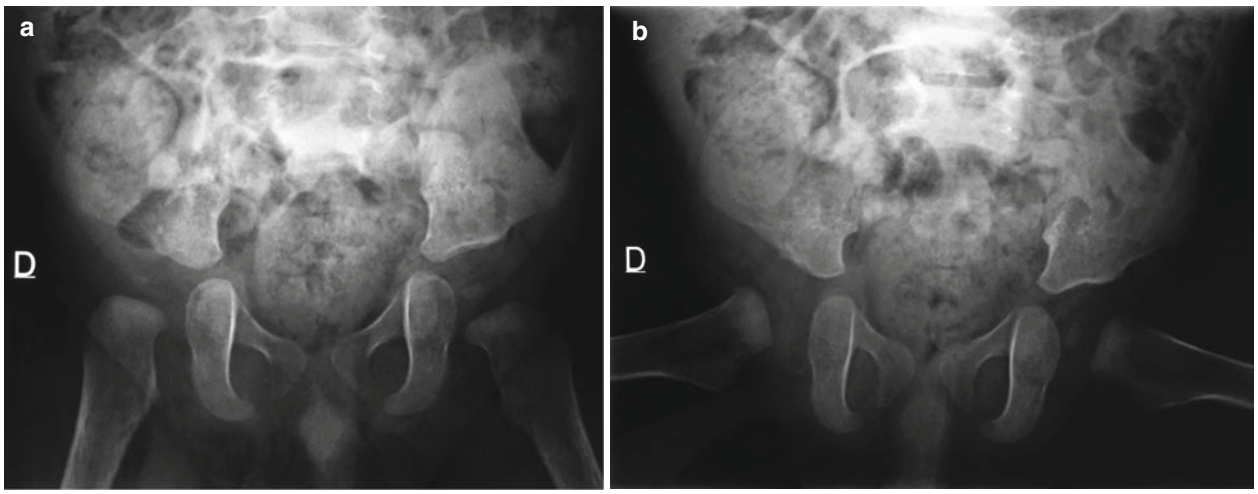

Fig. 12.8 DDH at right. Pelvic radiographs reveal that the ossified portion of the right femoral epiphysis is smaller and presents delayed development if compared to the contralateral one. The right epiphysis is out of the inferomedial quadrant delimited by the intersection of Perkins' and Hilgenreiner's lines. Shenton's line is clearly discontinuous at right, with hypoplasia of the homolateral acetabulum

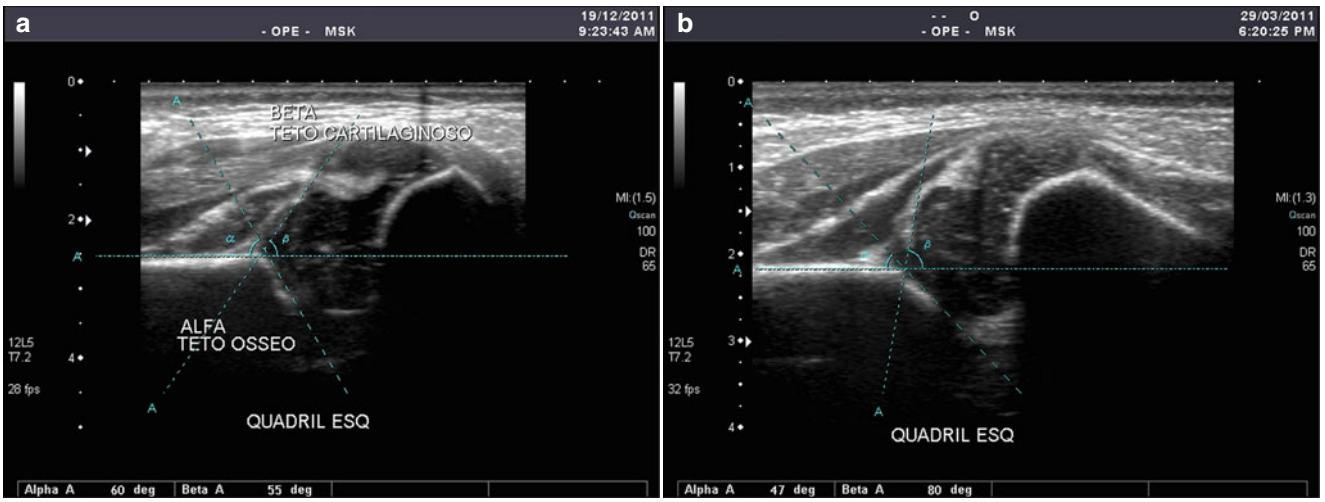

Fig. 12.9 In (**a**), US of the left hip of a newborn reveals normal values for the angles measured with Graf's static method (see text). In (**b**), DDH is present, with reduction of the alpha angle and increase of the beta angle

to the dysplastic changes and to the degree of dislocation of the femoral head, with less emphasis in the angles, given their limited reproducibility. The dynamic (real-time) technique proposed by Harcke is popular in the USA, allowing for assessment of hip stability by examining the joint in rest and under stress (pushing the femur posteriorly) in both the coronal and transverse planes; in normal patients, only minimal posterior subluxation of the femoral head is acceptable under stress.

CT and MRI are exceptionally used in the assessment of DDH. The most important indications include presurgical planning and follow-up of patients with casts after surgery or closed reduction to confirm that the procedure was successful (Fig. 12.10). MRI is also able to demonstrate hypertrophy and/or interposition of soft-tissue structures that may occasionally preclude closed reduction. Avascular necrosis is a potential complication of reduction, and MRI is the optimal imaging method for its diagnosis.

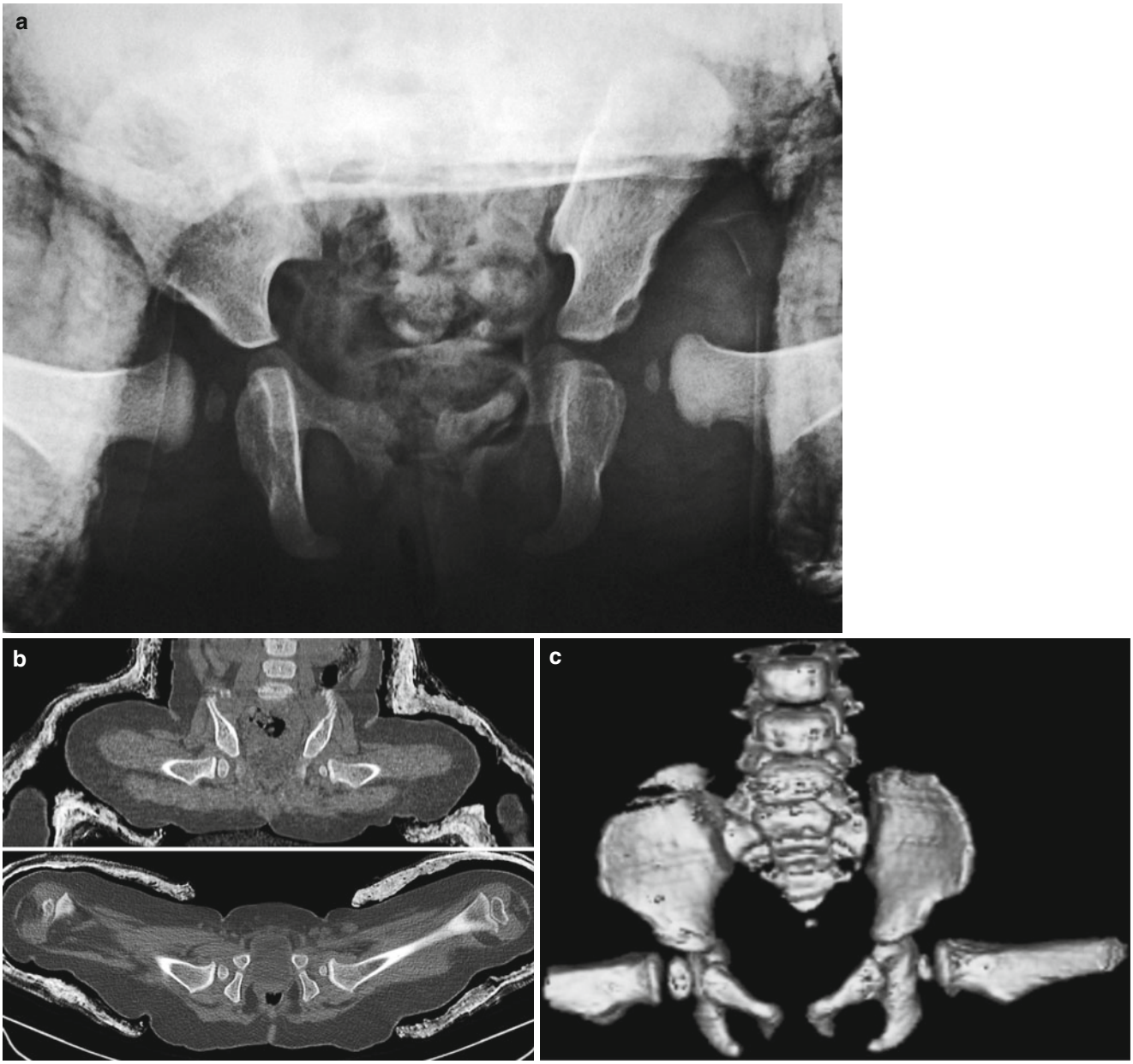

Fig. 12.10 Even though marked acetabular hypoplasia and asymmetric growth of the femoral heads are clearly seen, radiographs alone are unable to provide an accurate evaluation about how successful was closed reduction of hip dislocation after cast placement (**a**). CT of a distinct patient who underwent a similar procedure displays the articular relations in a safe and noninvasive way, in multiplanar reformatted images (**b**) and volume-rendered reconstruction (**c**); left-sided hypoplasia of the acetabulum and of the femoral head are present, more evident in (**c**)

12.5 Dorsal Defect of the Patella

The dorsal defect of the patella (DDP) is an anatomic variant that is present in approximately 1 % of the population. Although often asymptomatic, DDP may occasionally cause pain and patellofemoral symptoms. The defect is typically superolateral, along the articular surface of the bone, appearing on radiographs and CT as a small, well-delimited cortical lucency that is often surrounded by sclerosis (Figs. 12.11 and 12.12). MRI discloses a focal depression of the osseous surface that may be occasionally surrounded by bone marrow edema. The overlying cartilage is most often intact, although in some cases thinning or fraying may be found (Fig. 12.12).

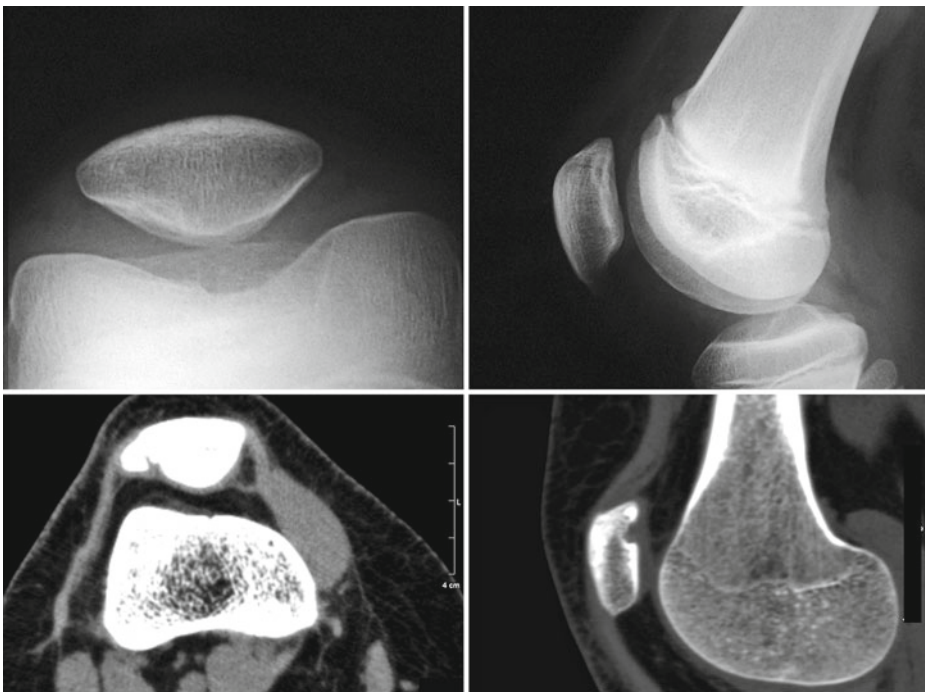

Fig. 12.11 Radiographs (*upper row*) and CT images (*lower row*) of two distinct patients with DDP demonstrates similar findings: a well-defined cortical defect in the superolateral portion of the articular surface of the patella, with subtle depression of the overlying cartilage on CT (Courtesy of Dr. Pablo Picasso Coimbra, Clinica Boghos Boyadjian, Fortaleza, Brazil)

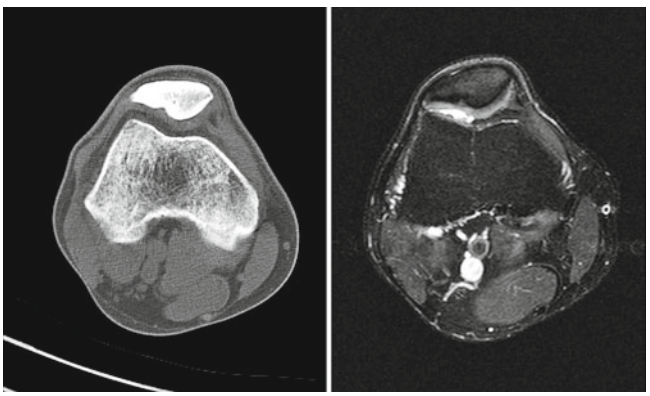

Fig. 12.12 Transverse CT image (*left*) and fat sat T2-WI (*right*) of the right knee of the same patient. There is bone sclerosis adjacent to the superolateral cortical defect, more evident on CT, as well as thinning of the articular cartilage, whose signal intensity is heterogeneous on MRI. Dorsal defect of the patella

12.6 Transient Lateral Patellar Dislocation

The term transient lateral patellar dislocation (TLPD) refers to an acute luxation of the patella, which presents spontaneous and immediate reduction in most cases and frequently goes unnoticed. It is more frequent in children between 9 and 15 years of age. Anatomic variants – such as patella alta, lateral patellar subluxation, lateral patellar tilt, and shallow/dysplastic trochlea – are frequently found, predisposing to chronic patellofemoral instability and recurrent dislocations.

Radiographic findings are subtle and include synovial effusion and soft-tissue swelling, which are often associated with abnormal patellofemoral morphology; avulsion fractures and/or cortical deformities may also be present, better demonstrated with CT (Figs. 1.15c, d, 12.13, and 12.14). MRI is the best imaging modality for assessment of TLPD: some classic signs allow to diagnose previous dislocation even if the articular relationships are normal when the study is performed. Joint effusion is very common, often hemorrhagic. Areas of bone marrow edema at the inferomedial portion of the patella and along the external surface of the lateral femoral condyle ("kissing contusions"), chondral/osteochondral lesions, injury of the medial soft-tissue restraints of the patella, and dysplastic changes of the patellofemoral joint are indicative of TLPD, especially when found in conjunction (Figs. 12.15 and 12.16). Bone marrow edema pattern may still be present several months after the episode of instability, even if there is complete involution of soft-tissue edema (Fig. 12.16). Intra-articular loose bodies are often present (Figs. 1.15, 12.13, and 12.15) and injuries of ligaments and menisci may be found in almost one-fourth of pediatric patients. The aforementioned predisposing structural abnormalities of the patellofemoral joint are better seen with CT and MRI (Figs. 1.15, 12.13, 12.14, 12.16, and 12.17). Many angles, lines, and relations have been described for assessment of patellofemoral instability in adults, but for most of them, there is insufficient evidence to support their use in pediatric patients.

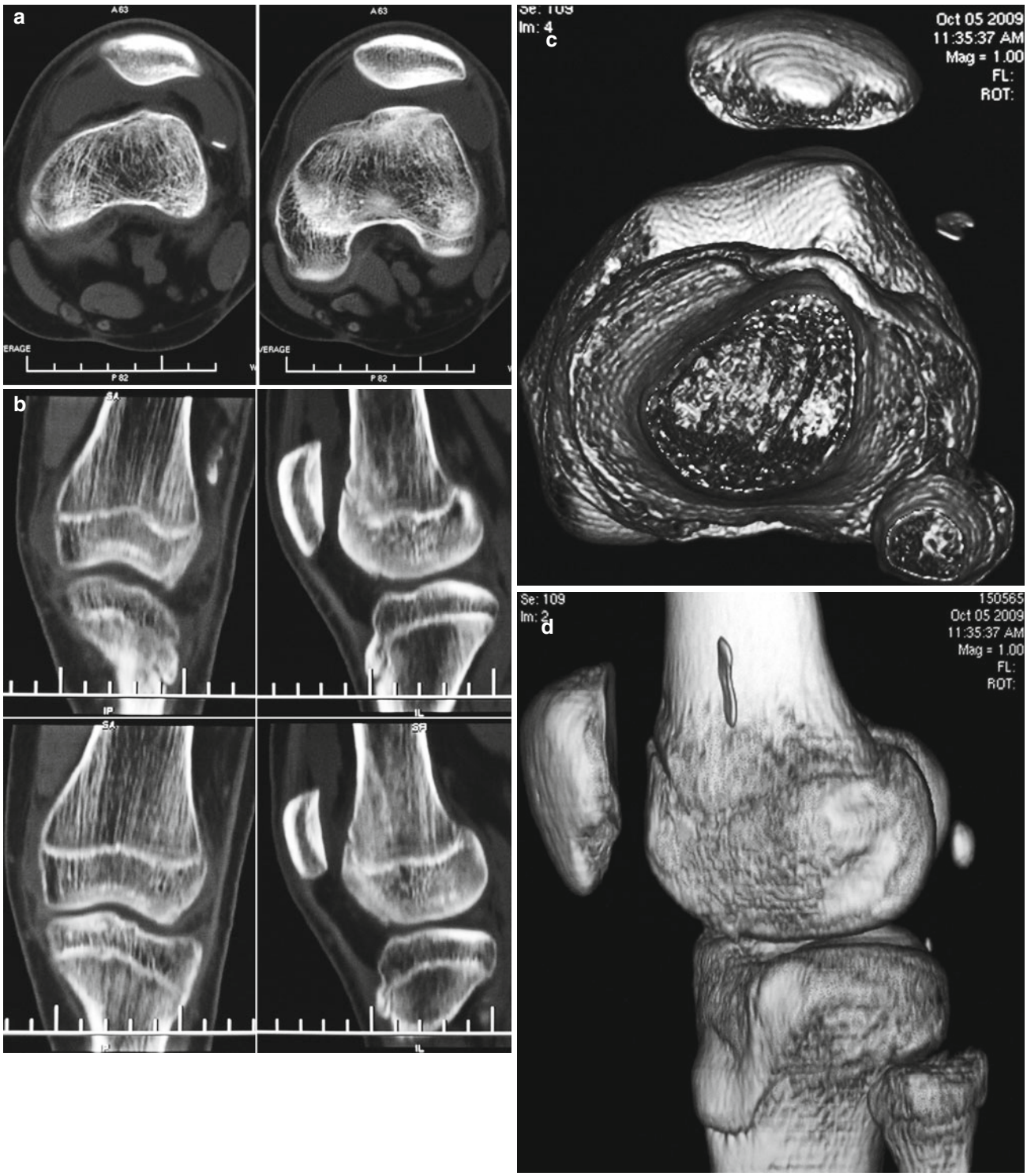

Fig. 12.13 CT of the left knee of an 11-year-old male with acute transient lateral patellar dislocation (images in the transverse (**a**), coronal, and sagittal planes (**b**) and volume-rendered reconstructions (**c** and **d**)). The transverse images display joint effusion and an osteochondral loose body in the lateral recess of the suprapatellar pouch, as well as marked trochlear dysplasia and lateral subluxation of the patella. In addition to the aforementioned findings, reformatted images and volume-rendered reconstructions reveal cortical irregularity along the anterior aspect of the lateral femoral condyle (donor site of the osteochondral fragment, avulsed during an episode of patellofemoral instability)

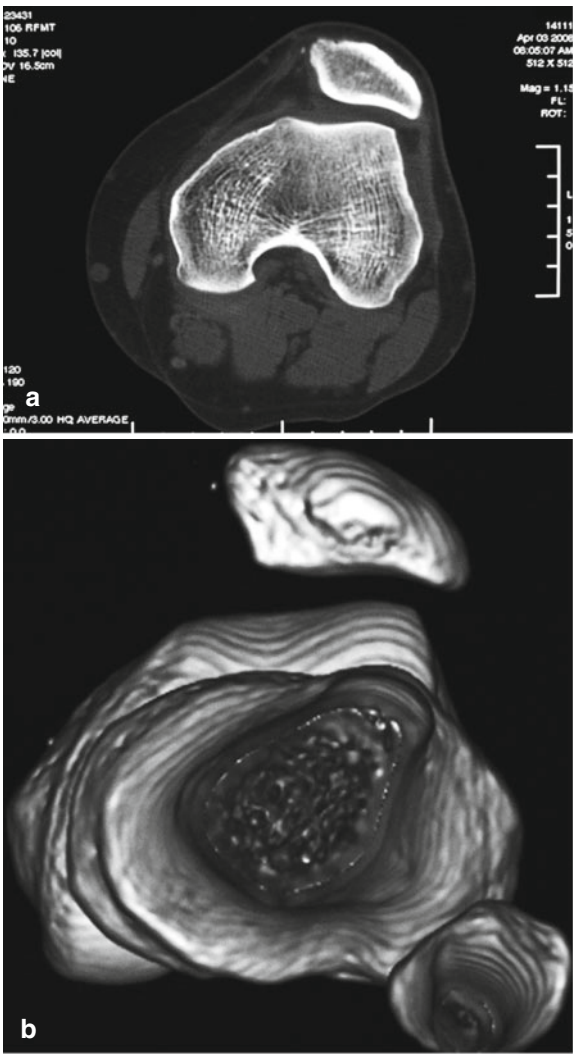

Fig. 12.14 Transverse CT image (**a**) and volume-rendered reconstruction (**b**) of the left knee of an adolescent with chronic patellofemoral instability and recurrent patellar dislocation. The trochlea is shallow, associated with patellar tilt and subluxation. There is also a small avulsed bone fragment adjacent to the site of insertion for the medial patellar retinaculum, as well as irregularity of the adjacent cortex

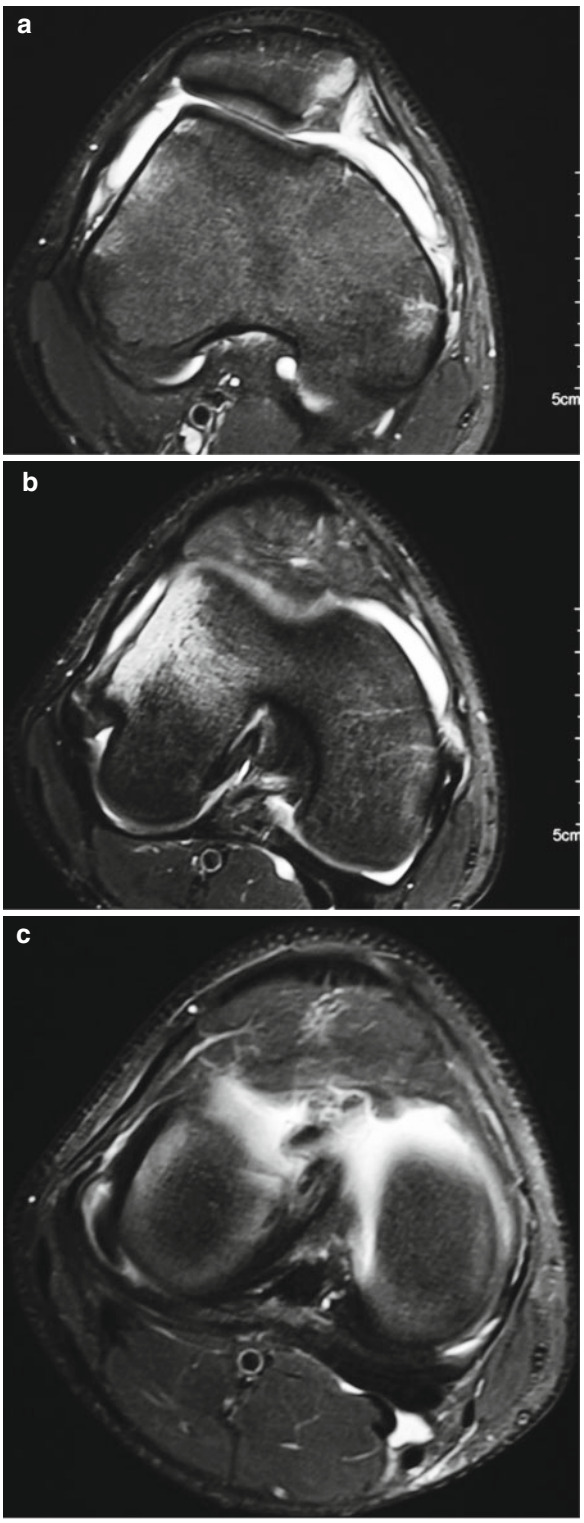

Fig. 12.15 Transverse fat sat T2-WI of the right knee of an adolescent with a recent episode of acute lateral patellar dislocation. Typical "kissing contusions" with bone bruises are seen in the medial patellar margin and in the outer surface of the lateral femoral condyle, in addition to joint effusion and a small popliteal cyst. Partial tear of the medial retinaculum, adjacent to its patellar insertion, can be seen in (**a**). There is an osteochondral lesion on the medial facet of the articular surface of the patella, more evident in (**a**), with detachment of a hypointense osteochondral fragment, which is anteriorly situated relative to the distal segment of the anterior cruciate ligament in (**c**). Even though MRI is superior in demonstrating soft-tissue abnormalities and bone marrow edema, CT is more adequate for the detection of loose bodies with bone fragments (see Fig. 12.13)

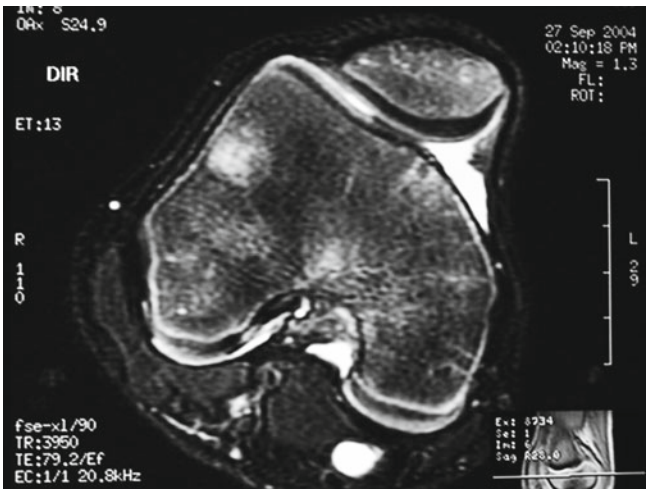

Fig. 12.16 MRI of the left knee of a 13-year-old male with chronic patellofemoral instability, not reporting recent episodes of dislocation. Transverse fat sat T2-WI reveal small joint effusion, trochlear dysplasia, and a subtle area of bone marrow edema in the lateral femoral condyle, reminiscent of a patellar dislocation occurred several months earlier. A small popliteal cyst is also present

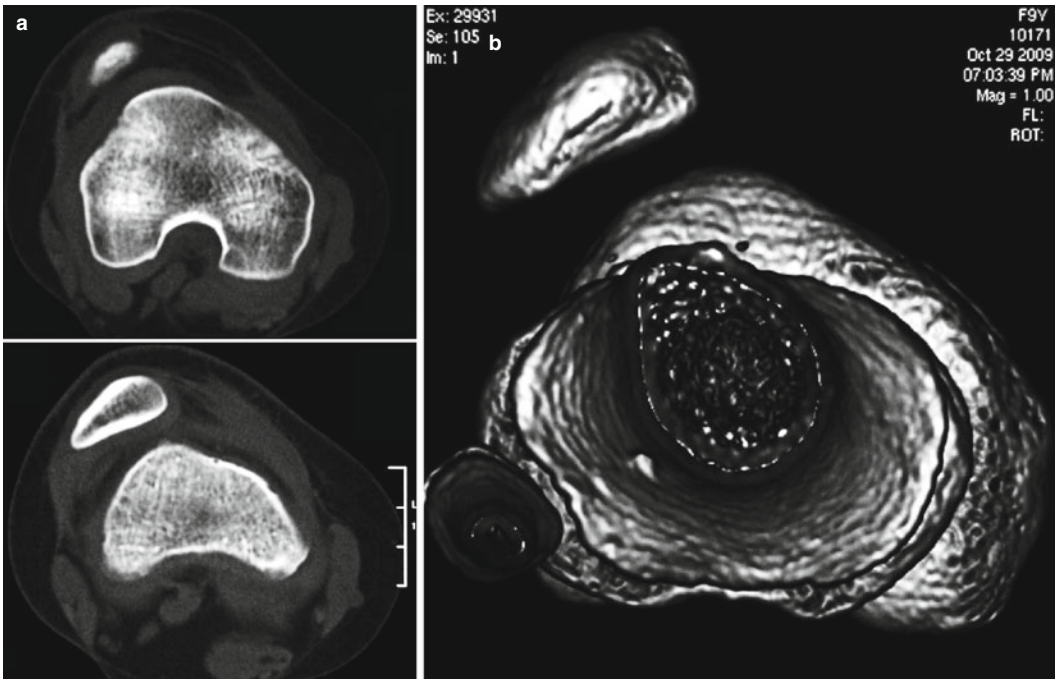

Fig. 12.17 CT of the right knee of a 9-year-old girl with chronic patellofemoral instability. Transverse images (**a**) and volume-rendered reconstruction (**b**) display marked patellofemoral incongruity, with a convex trochlear surface and obvious lateral subluxation of the patella

12.7 Popliteal Cyst

Popliteal cyst (or Baker's cyst) is, in fact, a collection of synovial fluid within the bursa located between the medial gastrocnemius and semimembranous muscles. Even though popliteal cysts are relatively uncommon before skeletal maturity, they can be found in any age group, being often asymptomatic and presenting spontaneous resolution in children. US and MRI are equally good for this diagnosis, even though the latter is superior in the evaluation of the knee as a whole. Regardless the imaging method, the cyst appears as an oval or rounded fluid-filled structure in the posteromedial soft tissues of the knee, with a beak-like projection pointing to the interval between the above-mentioned muscles (Figs. 12.15, 12.16, 12.18, and 12.19). Thin septa within the cyst are often found, which are deprived of significance (Fig. 12.19). Complicated cysts, however, like those associated with inflammation, hemorrhage, or infection, may show synovial thickening, intracystic debris, marked post-contrast enhancement, and/or increased flow on Doppler US (Fig. 12.18). Cyst rupture is relatively rare in children.

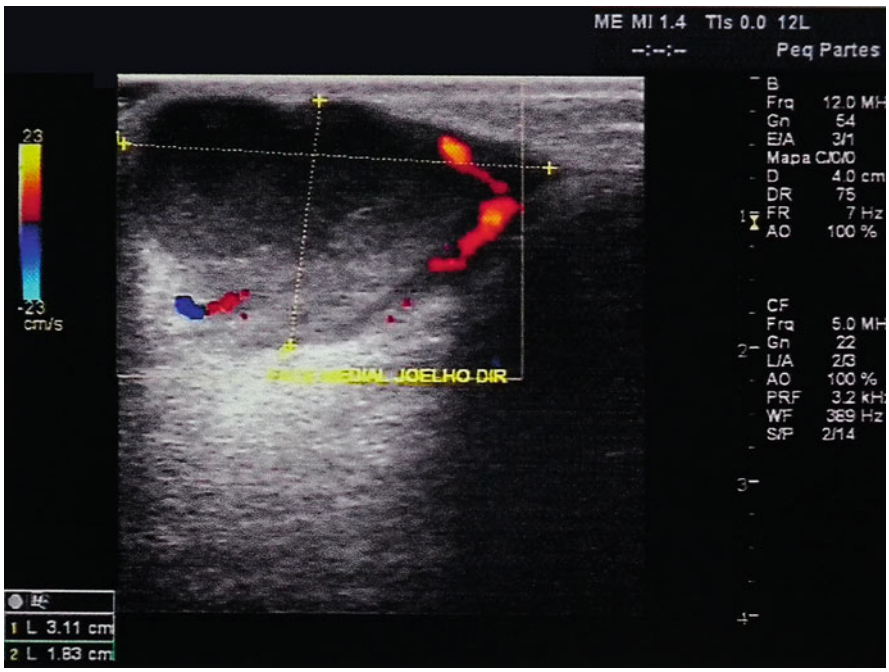

Fig. 12.18 US of the popliteal fossa of a patient with juvenile idiopathic arthritis. There is a popliteal cyst with its characteristic "beak" pointing to the space between the medial gastrocnemius and the semimembranous. The cyst presents heterogeneous content, with synovial thickening and hyperemia on Doppler, related to the subjacent arthritis (Courtesy of Dr. Maria Montserrat, Clinica Montserrat, Brasilia, Brazil)

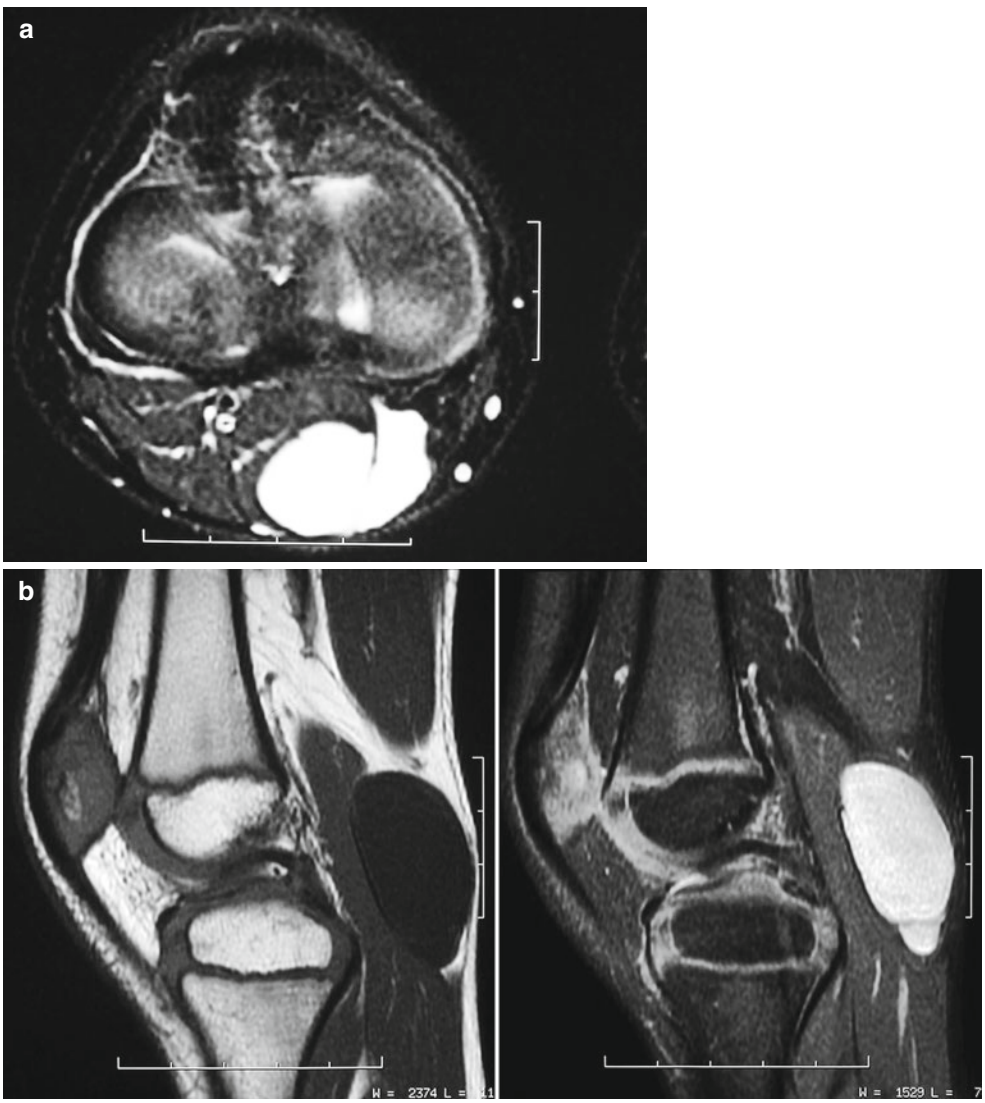

Fig. 12.19 Popliteal cyst in the right knee of a 7-year-old male. Transverse fat sat T2-WI (**a**) and sagittal T1-WI and PD-WI (**b**) demonstrate a cystic lesion in the soft tissues of the popliteal fossa, with a neck between the medial gastrocnemius and the semimembranous tendons. Intracystic septa can be seen, usually deprived of significance

12.8 Discoid Meniscus

The discoid meniscus is dysplastic and unusually large, with loss of the semilunar configuration found in normal menisci, presenting increased diameter and thickness. The condition is bilateral in up to 20 % of the patients, and the lateral meniscus is involved in the overwhelming majority of the cases. The dysplastic changes may involve the meniscus as a whole, forming a complete disk of fibrocartilage that covers the tibial plateau, or may be incomplete. Even though many patients are asymptomatic, others may present with snapping, limited range of motion, and pain.

Radiographs are insensitive, although subtle and nonspecific findings may be occasionally encountered, such as widening of the joint space, hypoplasia of the lateral femoral condyle, meniscal calcifications, and hypoplasia of the tibial spine (Fig. 12.20). MRI is the preferred imaging modality, showing a larger-than-normal meniscus with continuity between the anterior and posterior horns (bow tie shape) in at least three contiguous sagittal slices (Fig. 12.20). Coronal images show the abnormally large meniscus advancing toward the intercondylar notch, often covering of more than 50 % of the surface of the tibial plateau (Figs. 12.20 and 12.21). Abnormal signal intensity is commonly seen in the meniscal substance, related to myxoid degeneration. Meniscal tears are occasionally present, most often of the horizontal type, and parameniscal cysts may also be found (Figs. 12.21 and 12.22).

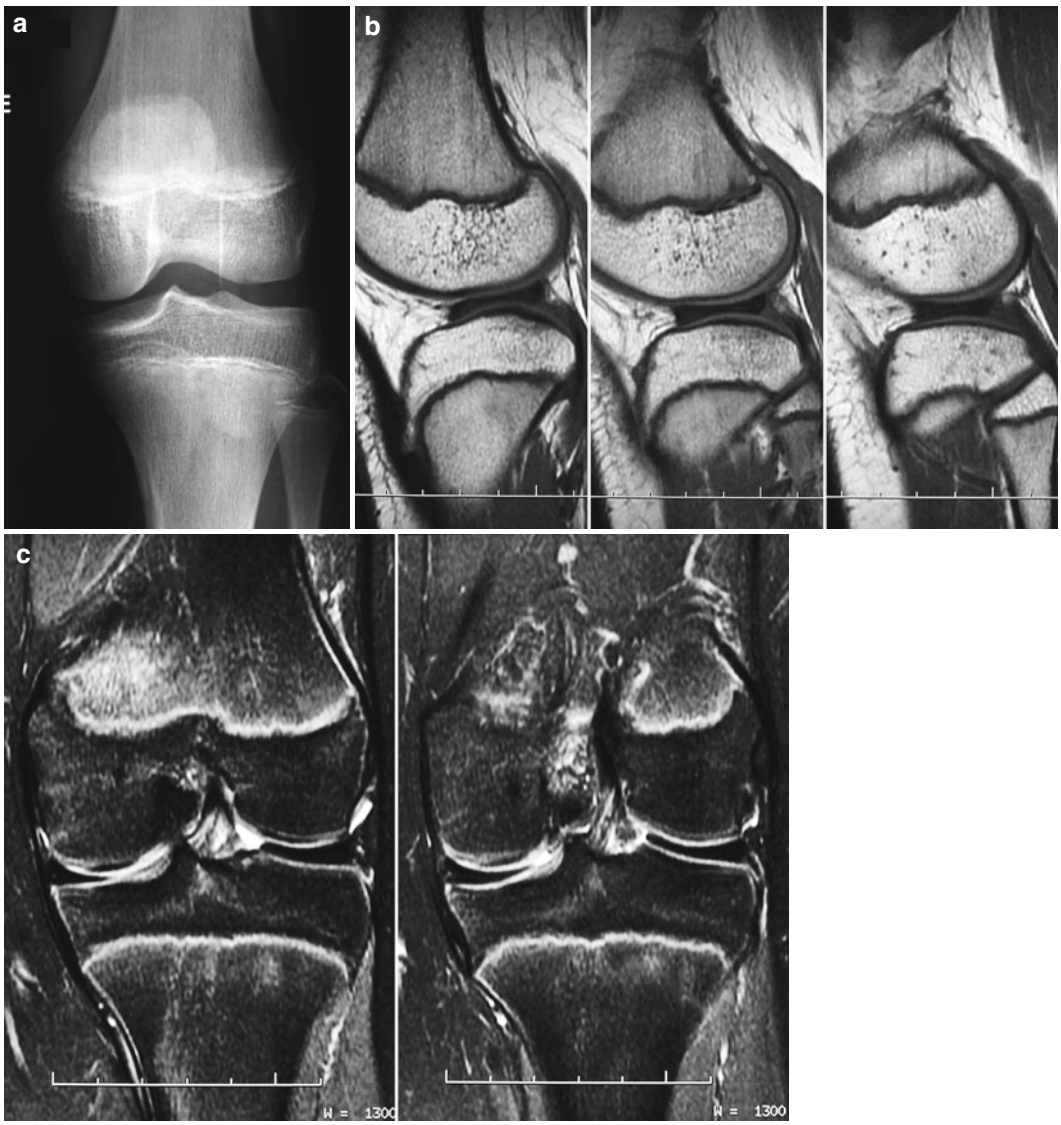

Fig. 12.20 An 11-year-old boy with pain and a clicking sensation on the lateral compartment of his left knee. Anteroposterior view (**a**) reveals widening of the lateral joint space, with hypoplasia of the lateral tibial spine and of the lateral femoral condyle. Sagittal T1-WI (**b**) demonstrate continuity across the anterior and posterior horns of the lateral meniscus (bow tie appearance) in three contiguous slices, while coronal fat sat PD-WI (**c**) show increased meniscal dimensions, covering the full extent of the articular surface of the corresponding tibial plateau. Discoid meniscus

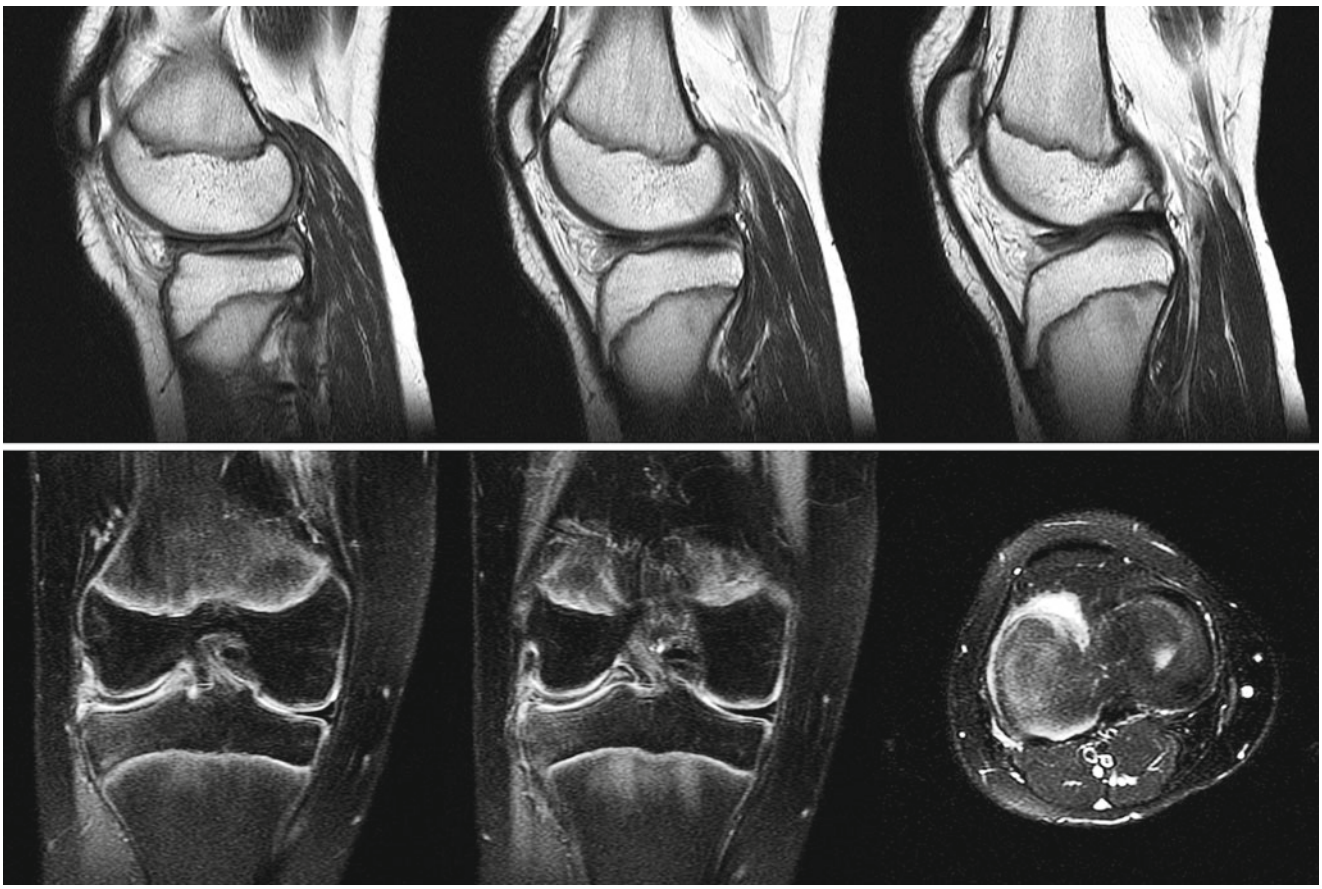

Fig. 12.21 Tear of a discoid meniscus associated with parameniscal cyst. Sagittal T2-WI (*upper row*) and fat sat PD-WI in the coronal and axial planes (*lower row*) show a discoid meniscus whose configuration is similar to that seen in Fig. 12.20. However, in the present case there is a horizontal tear extending from the posterior horn to the anterior horn, in addition to a heterogeneous parameniscal cyst protruding to Hoffa fat pad

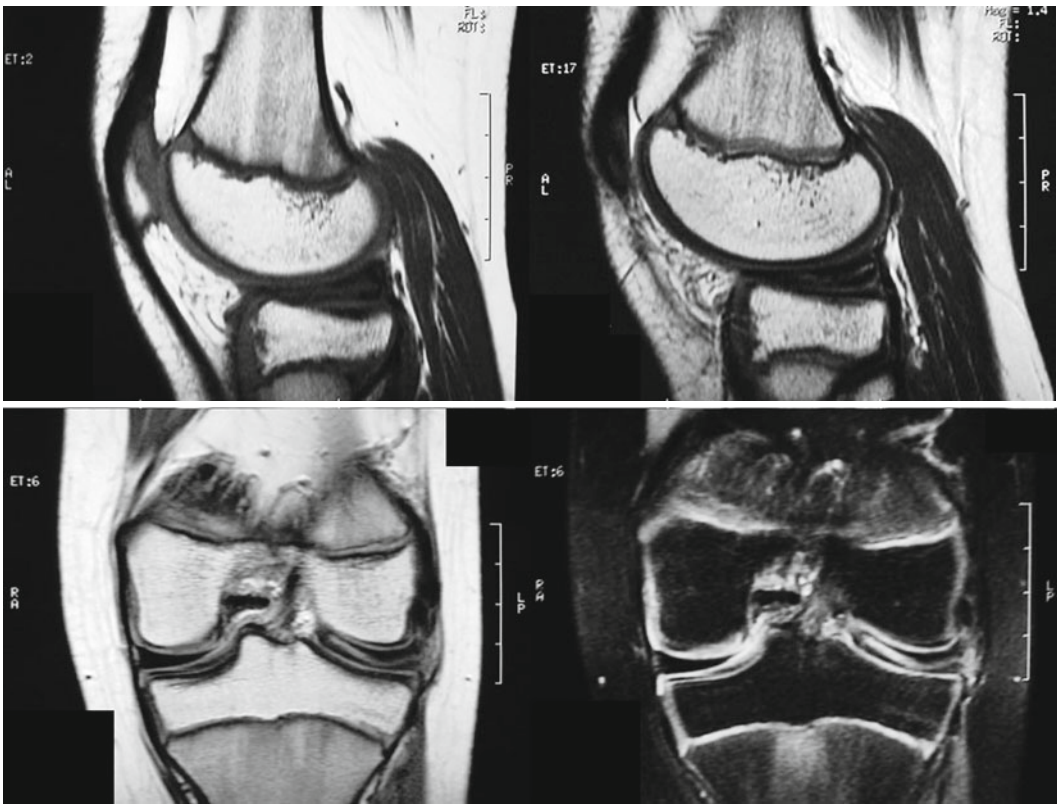

Fig. 12.22 An 11-year-old boy with pain in the lateral compartment of the left knee and limited range of motion. Sagittal T1-WI and T2-WI (*upper row*) and coronal PD-WI and fat sat PD-WI (*lower row*) reveal an incomplete discoid meniscus and a horizontal tear, with a small parameniscal cyst protruding laterally

12.9 Blount's Disease

Blount's disease (infantile tibia vara) is a developmental abnormality that affects the medial portion of the proximal tibia of small children. Classic radiographic findings – also seen with CT – include varus deformity of the proximal tibia, widening and irregularity of the medial portion of the tibial physis, heterogeneous ossification of the proximal tibial epiphysis (which may appear triangular, with medial slope of the articular surface), and prominent beaking of the medial metaphysis (Fig. 12.23). Bilateral and symmetric involvement is not infrequent, and there may be limited motion, joint instability, and early-onset osteoarthritis. Transphyseal bridges may also be present and limb-length discrepancy is common. MRI is a useful adjunct, especially to detect abnormalities of the epiphyseal cartilage and of the menisci, as well as physeal bridges (Fig. 12.24).

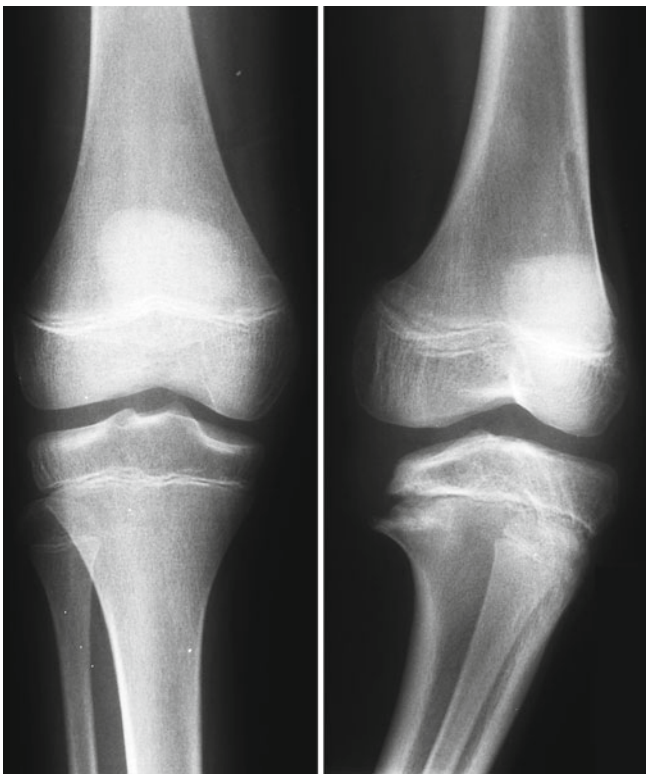

Fig. 12.23 Anteroposterior views of the knees of a child with left-sided Blount's disease. There is varus deformity of the left proximal tibia, with "beaking" of the medial portion of the corresponding metaphysis and hypoplasia of the medial tibial plateau. The medial tibial physis is widened and irregular, with thickening of the adjacent diaphyseal cortex

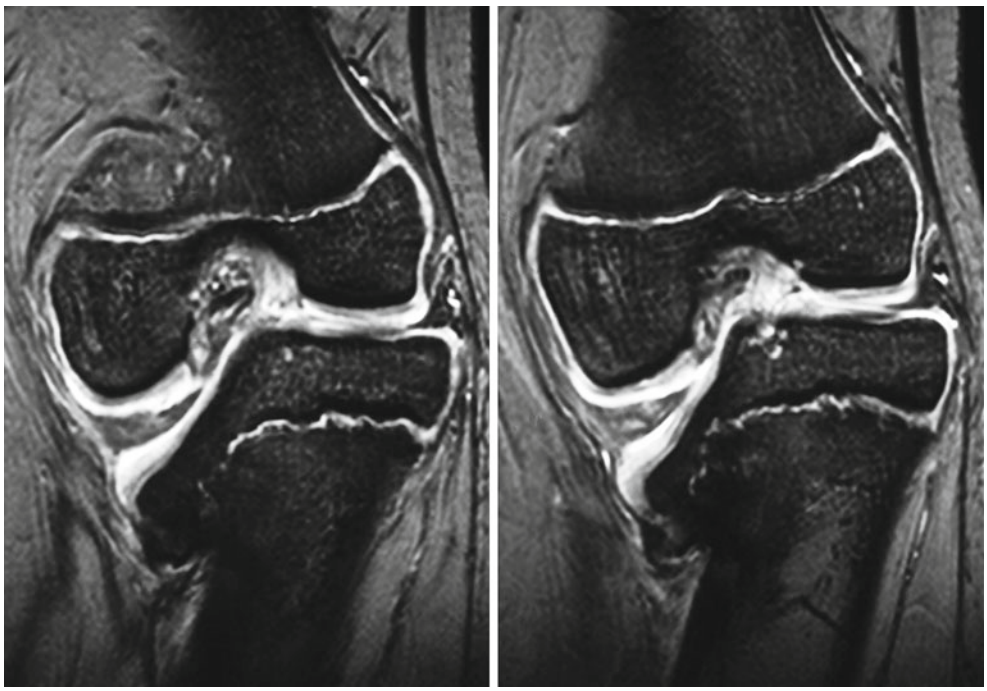

Fig. 12.24 Coronal gradient-echo images of the left knee of a child with Blount's disease. The imaging findings are quite similar to the radiographic picture described in Fig. 12.23. Nevertheless, MRI is more accurate for physeal assessment (notice the medial transphyseal bone bridge) and in the evaluation of structures that are not detectable on radiographs, such as the epiphyseal cartilage (which is thicker in the medial tibial plateau if compared to the lateral) and the menisci (notice the dysplastic appearance of the medial meniscus, which is enlarged and shows abnormal signal intensity)

12.10 Congenital Clubfoot

Congenital clubfoot is one of the most common congenital anomalies of the feet. It is a complex three-dimensional deformity, with equinism of the hindfoot and adduction of the forefoot; bilateral involvement is found in up to 50 % of all patients. The foot should be positioned as close to the anatomic position as possible on imaging studies. Radiographs are the mainstay of evaluation for patients with congenital clubfoot: there is a decrease in the talocalcaneal angle (whose normal range varies from 20 to 40° in the anteroposterior view and from 35 to 50° in the lateral view), with adduction of the forefoot, varus deformity of the hindfoot, medial subluxation of the tarsal navicular bone, and elevation of the calcaneus (Fig. 12.25). CT is very popular because of its multiplanar capabilities, depicting the altered anatomic relationships in a way that is easily understandable by non-radiologists with reformatted images and volume-rendered reconstructions. Nevertheless, MRI is superior in the evaluation of the soft tissues and in the assessment of the non-mineralized cartilaginous anlage of the bones.

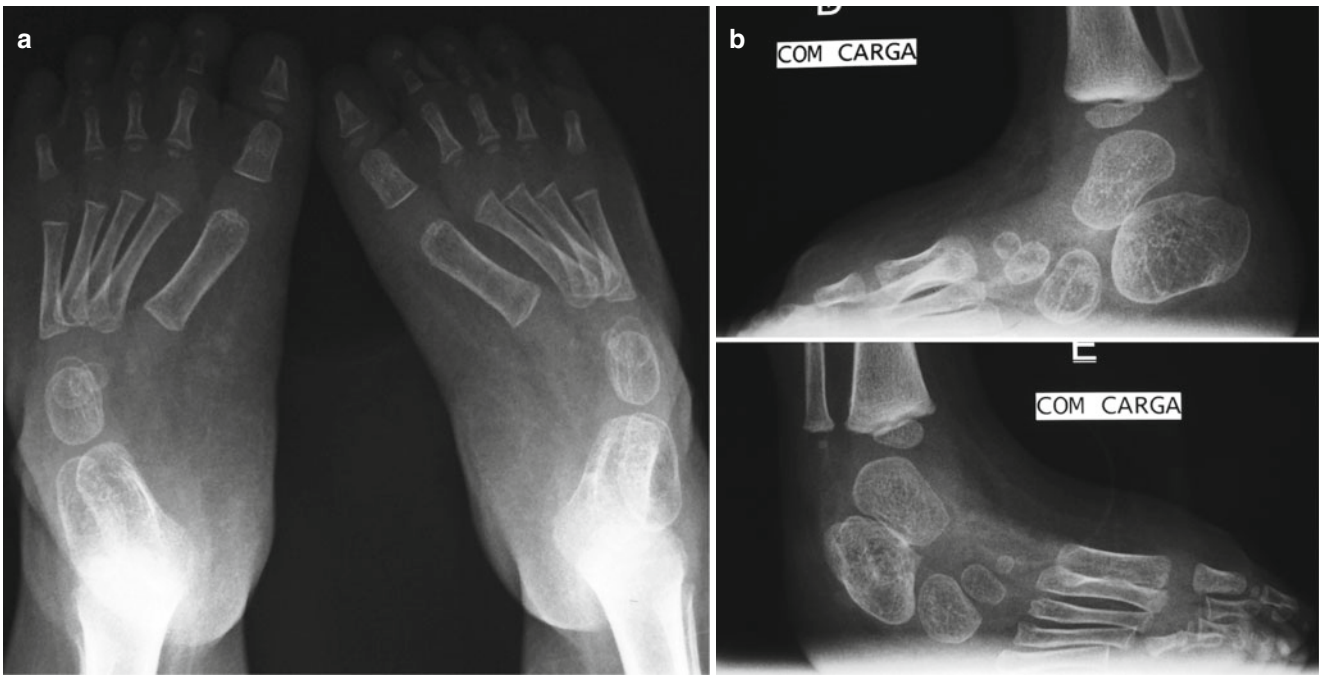

Fig. 12.25 Anteroposterior (**a**) and lateral (**b**) views of a child with bilateral congenital clubfoot. There is adduction of the forefeet with varus deformity of the hindfeet, as well as elevation of the calcanei and decrease of the talocalcaneal angle

12.11 Freiberg's Disease

Freiberg's disease is a condition related to repetitive microtrauma and vascular compromise, classically involving the head of the second metatarsal (or, less often, the third). These factors lead to the development of an osteochondral fracture on the articular surface of the metatarsal head, with subsequent bone collapse and osteonecrosis. The disease is more frequent in female adolescents, and bilateral involvement occurs in up to 10 % of all cases. Initially, radiographs may show widening of the adjacent metatarsophalangeal joint space, mostly related to synovial effusion. In time, radiographic/computed tomographic findings characteristic of osteonecrosis (such as heterogeneous bone density, bone fragmentation/resorption, and cystic changes) eventually appear, with deformation and flattening of the metatarsal head in late-stage disease (Fig. 12.26). Bone scintigraphy demonstrates decreased uptake during the early stages and increased uptake after the onset of bone healing. Early MRI findings include joint effusion and periarticular soft-tissue edema, with nonspecific bone marrow edema pattern in the affected bone marrow. As the bone becomes sclerotic, low signal intensity is seen in all sequences.

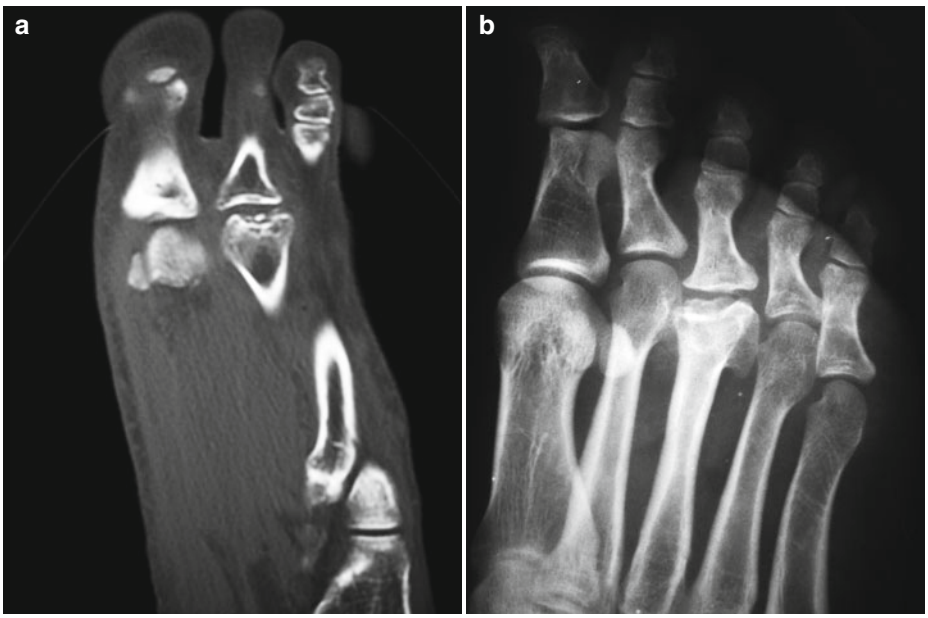

Fig. 12.26 Transverse CT image (**a**) and oblique view (**b**) of the forefeet of two distinct adolescents with Freiberg's disease. In (**a**), there is collapse of the articular surface associated with mild deformity of the second metatarsal, as well as remodeling of the adjacent articular surface of the proximal phalanx. In (**b**), advanced disease is found in the third metatarsal head, with marked bone collapse and prominent remodeling of the base of the proximal phalanx

12.12 Tarsal Coalition

Tarsal coalition is an abnormal bridging across two or more tarsal bones due to defective segmentation of the primitive mesenchyme, whose estimated prevalence is around 1–3 %. Three major types are found: fibrous (syndesmosis), cartilaginous (synchondrosis), and osseous (synostosis). More than one coalition can be found in the same extremity, and bilateral disease occurs in up to half of the patients. Calcaneonavicular and talocalcaneal coalitions are the most common forms, responsible for 90 % of the cases. Talocalcaneal coalitions involve more frequently the middle facet, at the level of the sustentaculum tali. Coalitions usually become symptomatic by the end of childhood or during early adolescence, presenting with a painful, rigid flatfoot and/or repetitive ankle sprains.

On radiographs, bony coalitions present continuity of the cortex and of the medullary bone between the affected structures, while non-ossified coalitions usually appear as narrow and obliquely oriented joint spaces, whose surfaces are irregular and dysmorphic, commonly associated with subchondral sclerosis and cysts (Figs. 12.27 and 12.28). However, due to the anatomic complexity of this region, radiographs alone are often insufficient for accurate evaluation. CT is the best imaging modality for assessment of bone anatomy, demonstrating the aforementioned radiographic findings in further detail (Figs. 12.29, 12.30, 12.31, 12.32, and 12.33). On MRI, an ossified coalition appear as a continuous bar that is isointense to the adjacent bones, while a cartilaginous coalition show an interposed band of signal intensity similar to that of the cartilage (Fig. 12.33) and a fibrous coalition display low signal intensity in all sequences (Fig. 12.34). Edematous changes of the juxtaarticular bone marrow and of the soft tissues are frequently present (Figs. 12.33 and 12.34).

Radiographic demonstration of talocalcaneal lesions may be difficult due to superimposition of osseous structures. Dysplastic enlargement of the surfaces of the sustentaculum tali and of the adjacent talus may be seen on the axial view (Fig. 12.27). Secondary signs must be sought on lateral views: although less reliable, such signs, when present, give support to the clinical hypothesis. Talar "beaks" are found both in talocalcaneal and in calcaneonavicular forms, mostly in the former (Figs. 12.35 and 12.36). The sustentaculum tali is hypoplastic/dysplastic, with loss of its polyhedric appearance (Fig. 12.31) and abnormal inclination of the joint space, better seen on CT and MRI (Fig. 12.34). The middle facet must always be seen on adequately positioned radiographs in normal individuals, but not in patients with coalition ("absent middle facet sign" – Fig. 12.34). The so-called C sign is characterized by a curved line extending from the talar dome to the sustentaculum tali (Figs. 12.35 and 12.36), resulting from flattening of the plantar arch and abnormal talocalcaneal orientation.

Calcaneonavicular lesions are easier to detect on radiographs, mostly on oblique views (Fig. 12.28). The anterior process of the calcaneus is vertically oriented and abnormally enlarged; the "anteater sign" is a secondary sign of calcaneonavicular coalition represented by elongation and hyperplasia of this structure, whose extremity shows a polygonal appearance, similar to the nose of an anteater, seen on oblique and lateral views (Fig. 12.28). The navicular bone may appear hyperplastic and laterally elongated, showing loss of its normal alignment with the talar head on anteroposterior views (Fig. 12.28).

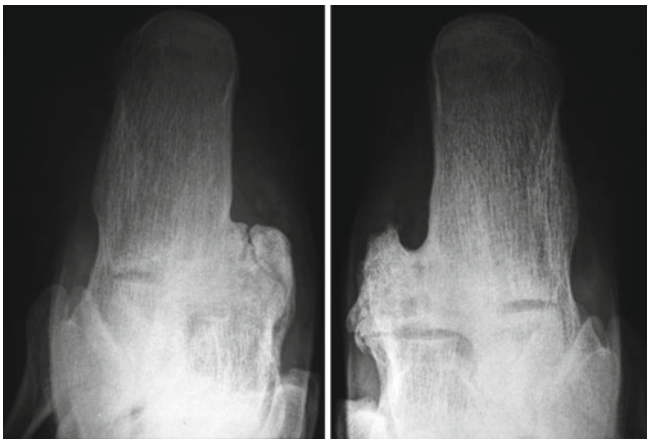

Fig. 12.27 Axial views of both calcanei in a patient with bilateral talocalcaneal coalition. The middle facets are obliquely oriented and narrowed, with irregularity of the joint surfaces. The sustentaculum tali and the talus are deformed

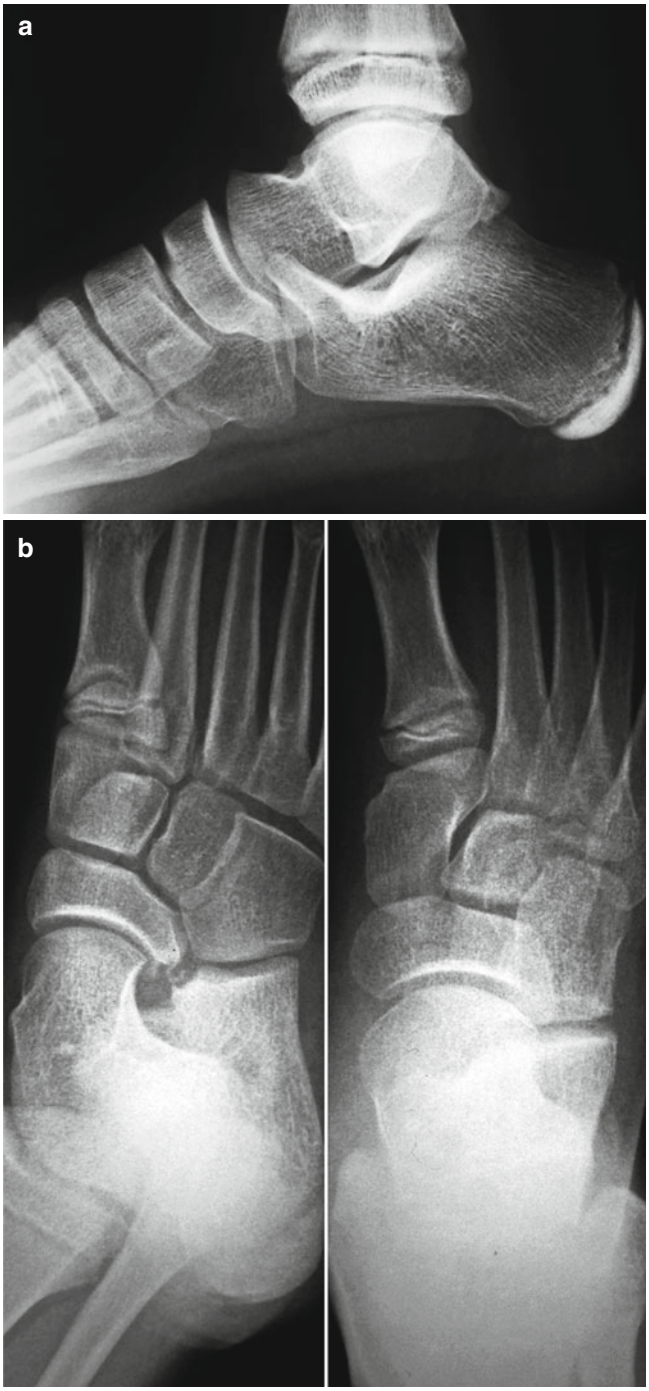

Fig. 12.28 Lateral (**a**), oblique, and anteroposterior (**b**) views of the left ankle of a child with calcaneonavicular coalition. The lateral view shows that the anterior process of the calcaneus is abnormally elongated and tubular ("anteater sign"), as well as a small dorsal talar "beak." The coalition can be seen in the oblique view, with lateral prominence of the navicular bone. Both the lateral portion of the navicular and the anterior calcaneal process are irregular, with bone fragmentation adjacent to the articular surfaces. The lateral prominence of the navicular is also evident in the anteroposterior view

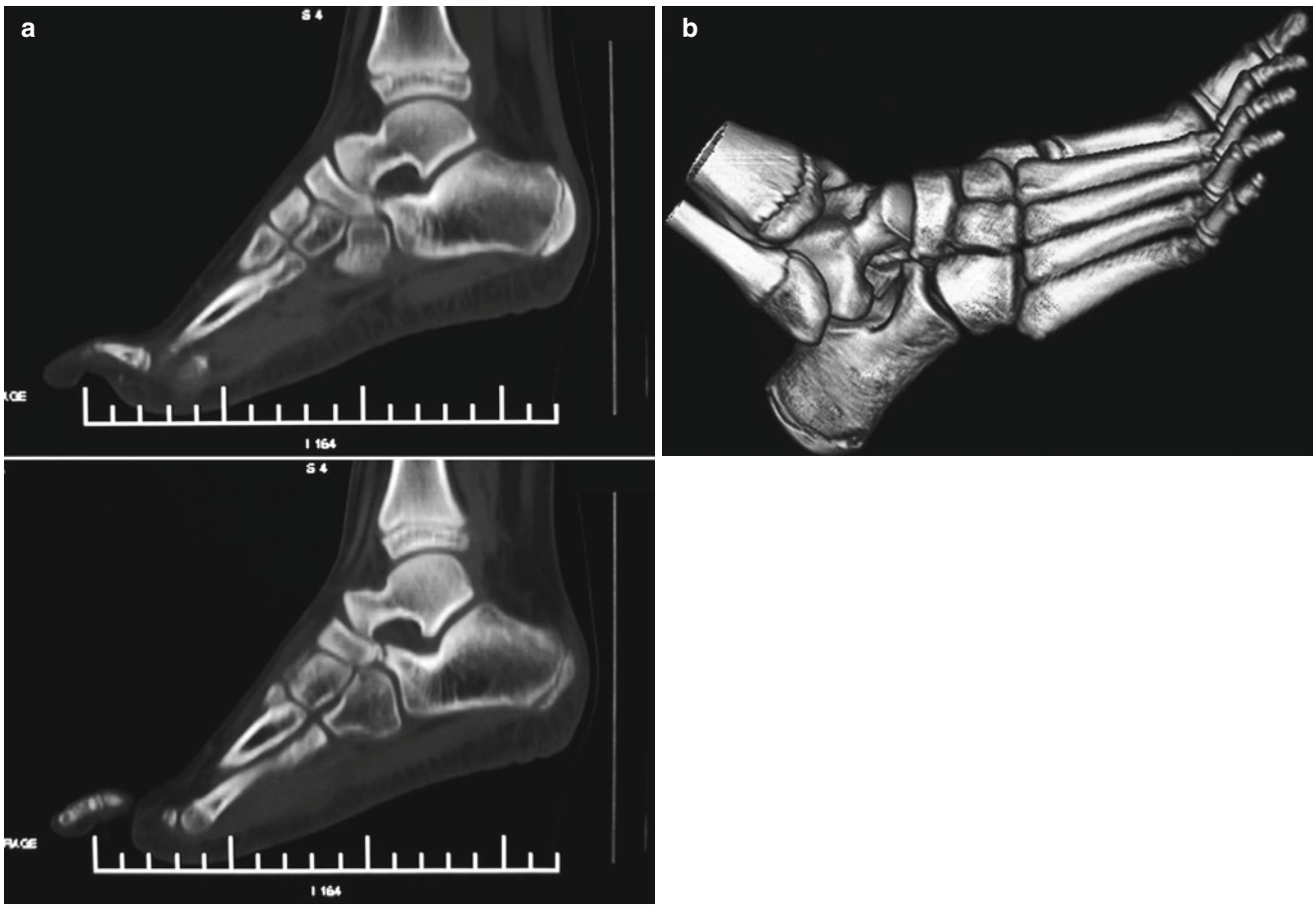

Fig. 12.29 Sagittal reformatted CT images (**a**) and volume-rendered reconstruction (**b**) of the same foot of Fig. 12.28. The above-described findings are depicted with superior anatomic detail. Although the coalition is clearly non-ossified, it is not possible to determine if it is fibrous or cartilaginous in nature with CT

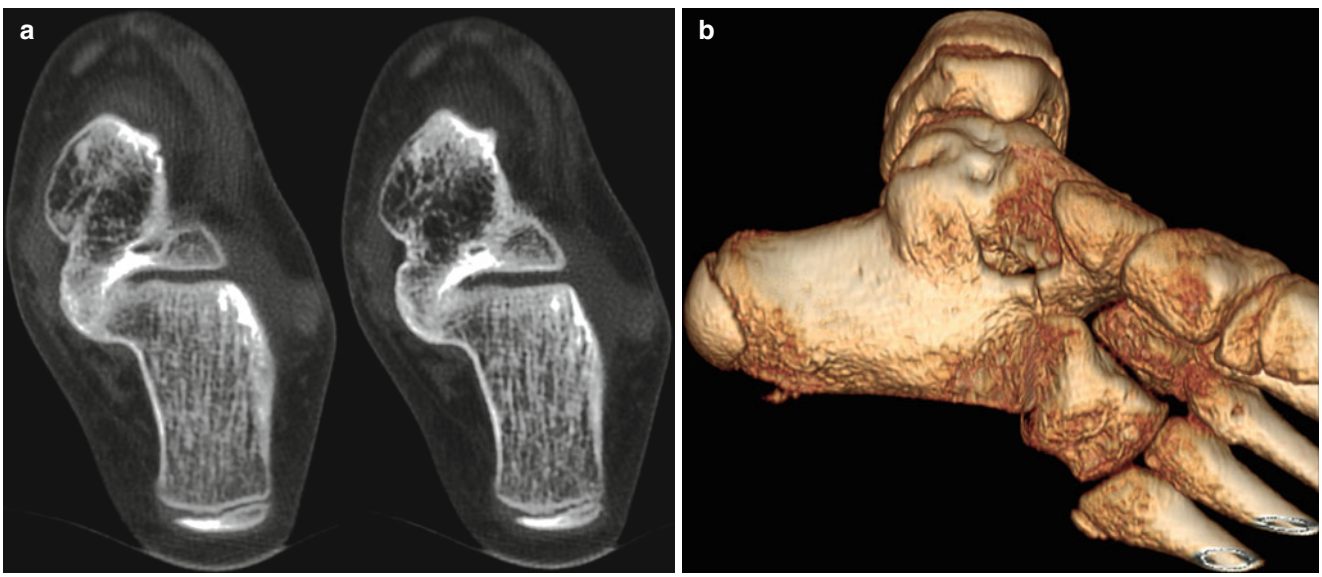

Fig. 12.30 Transverse CT images (**a**) and volume-rendered reconstruction (**b**) of the left ankle of a child with osseous talocalcaneal coalition. There is a bony bridge in the middle facet of the subtalar joint, with seamless continuity of the cortices and of the cancellous bone of the talus and of the calcaneus

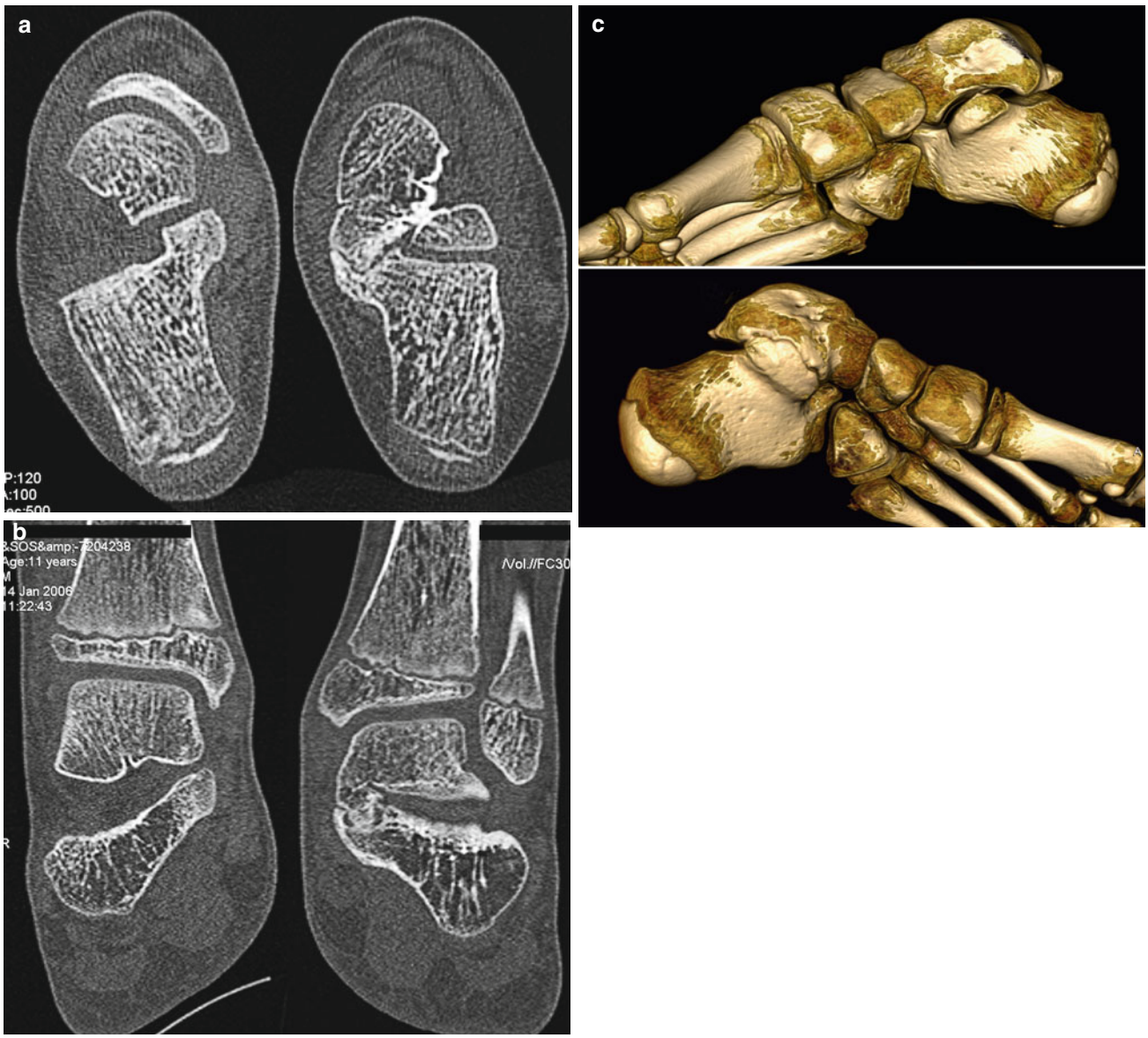

Fig. 12.31 Transverse image (**a**), coronal reformatted image (**b**), and volume-rendered reconstructions (**c**) of a CT scan of the ankles of an 11-year-old male with non-ossified talocalcaneal coalition at left. Compare the normal anatomy of the right subtalar joint with the abnormal contralateral one. There is hypoplasia of the left sustentaculum tali, with loss of its typical polyhedric appearance, as well as enlargement of the adjacent talus. Both bones show rounded contours, with narrowing of the corresponding joint space, irregular articular surfaces, and mild subchondral sclerosis

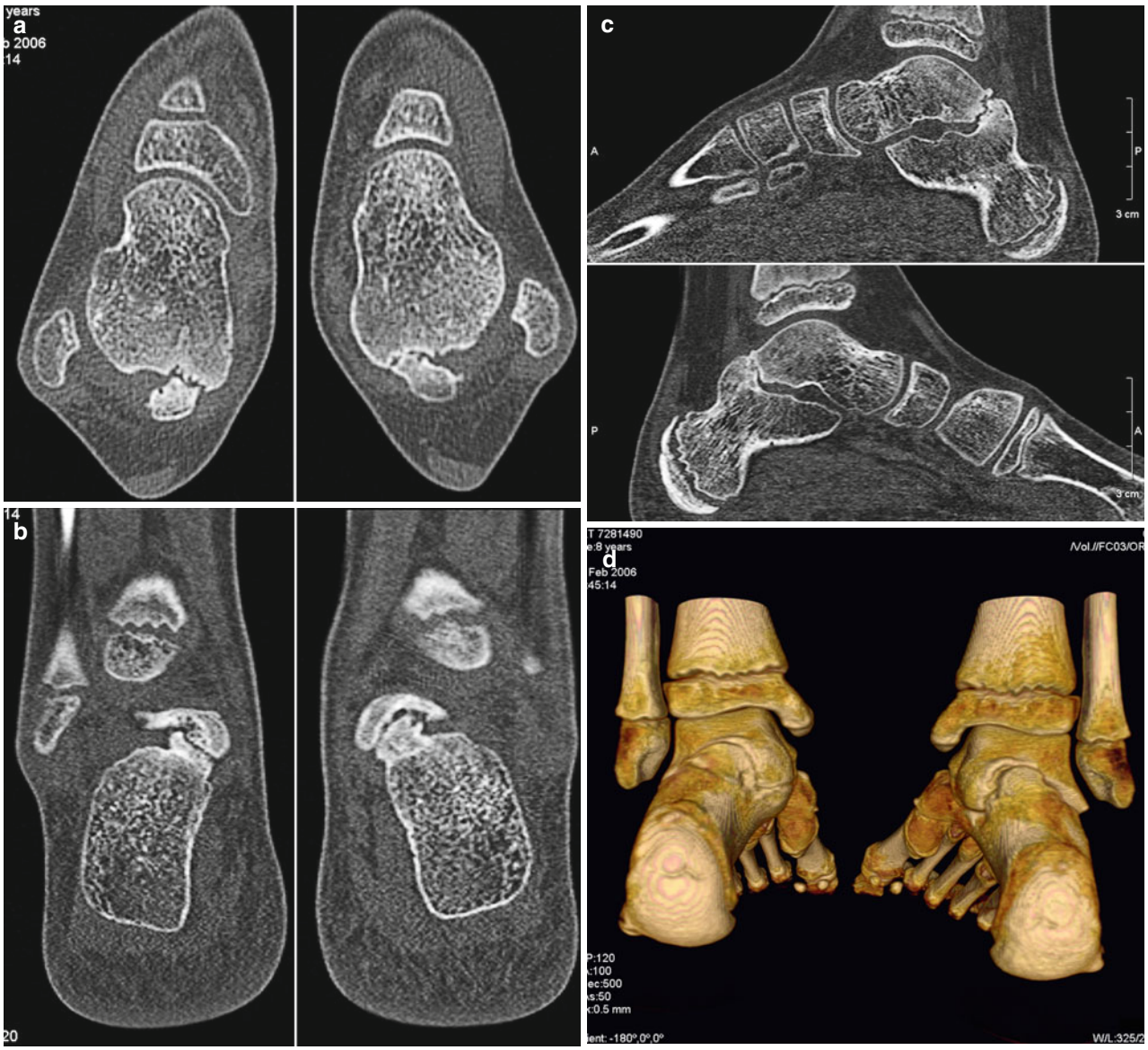

Fig. 12.32 Bilateral talocalcaneal coalition involving the posterior facets (a very rare location) can be seen on a CT scan in this 8-year-old male. Transverse (**a**), coronal (**b**), and sagittal (**c**) reformatted images and volume-rendered reconstruction (**d**) reveal findings similar to those above described for coalition of the middle facet in Fig. 12.31: narrowed joint spaces, irregularity of the articular surfaces, hypertrophy of the articular margins, and subchondral sclerosis

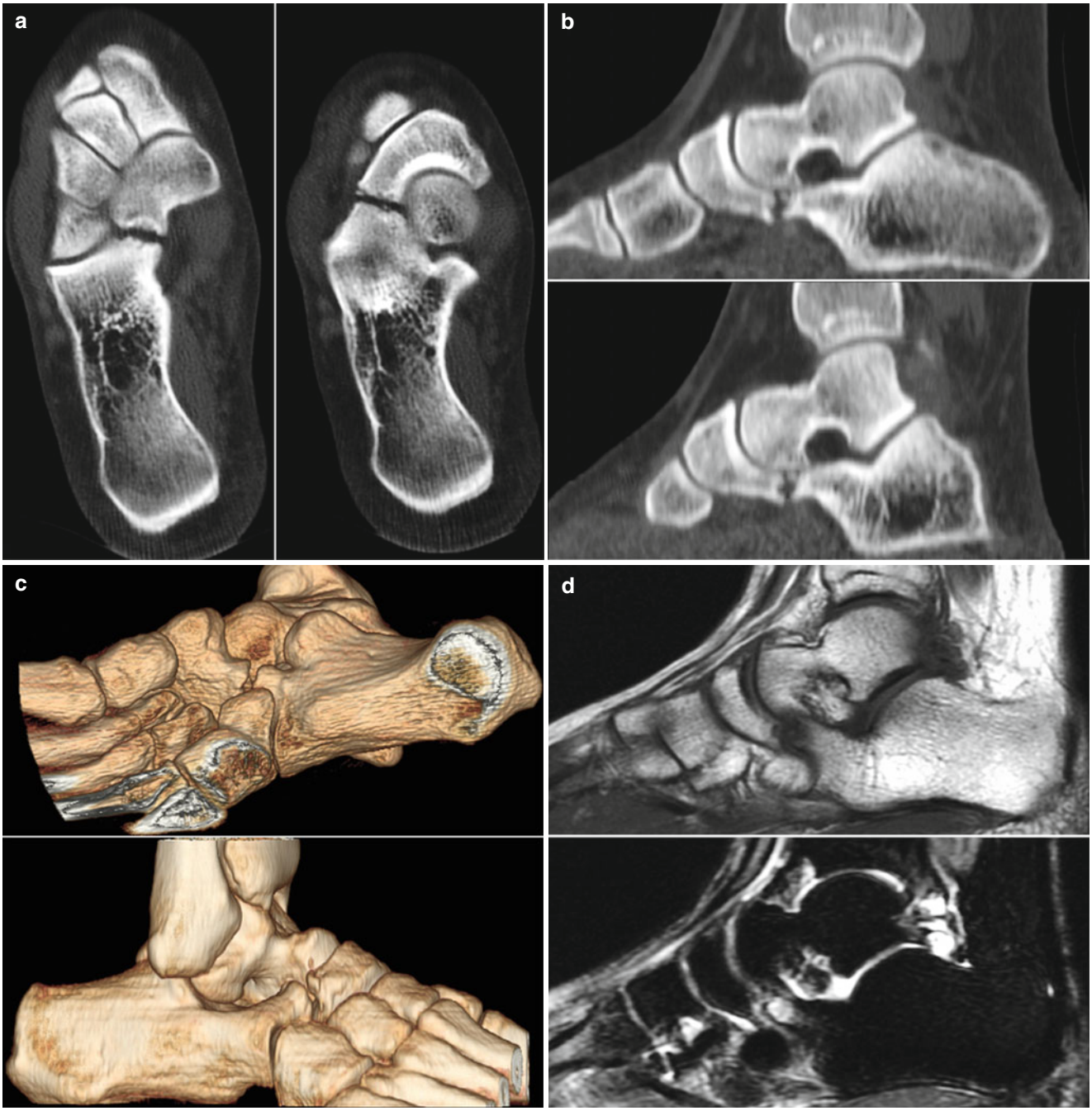

Fig. 12.33 CT scan of a 17-year-old adolescent with calcaneonavicular coalition. Transverse (**a**) and sagittal (**b**) images and volume-rendered reconstructions (**c**) demonstrate very clearly the abnormal anatomy, particularly the elongated anterior process of the calcaneus, which have a polygonal appearance on 3D images ("anteater sign"). Nevertheless, just like in Fig. 12.29, though is quite obvious that the coalition is non-ossified, CT alone cannot define if it is fibrous or cartilaginous. However, sagittal T1-WI and fat sat T2-WI (**d**) and transverse T1-WI (**e**, *left*) and T2-WI (**e**, *right*) show signal intensity similar to that of cartilage within the coalition (hypointense on T1-WI and hyperintense on T2-WI), establishing the cartilaginous nature of the lesion. In (**d**), bone marrow edema pattern is evident in the anterior calcaneal process, in addition to fluid within the tarsal sinus and in the tibiotalar joint

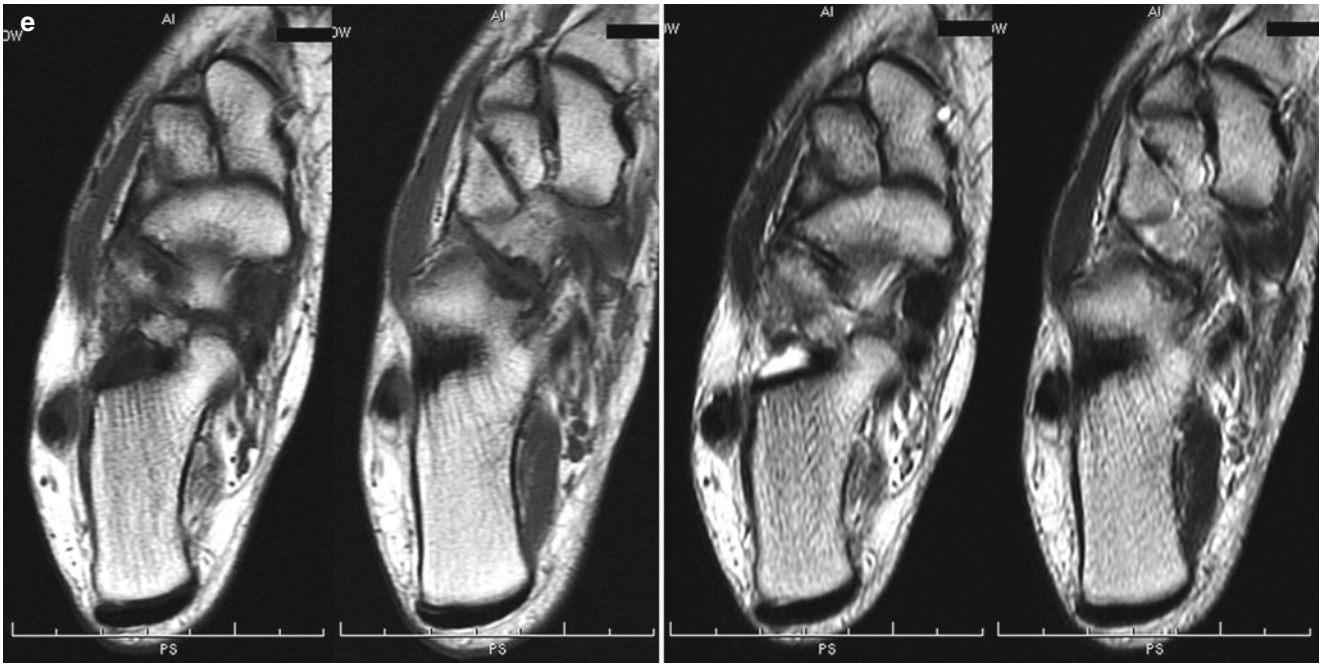

Fig. 12.33 (continued)

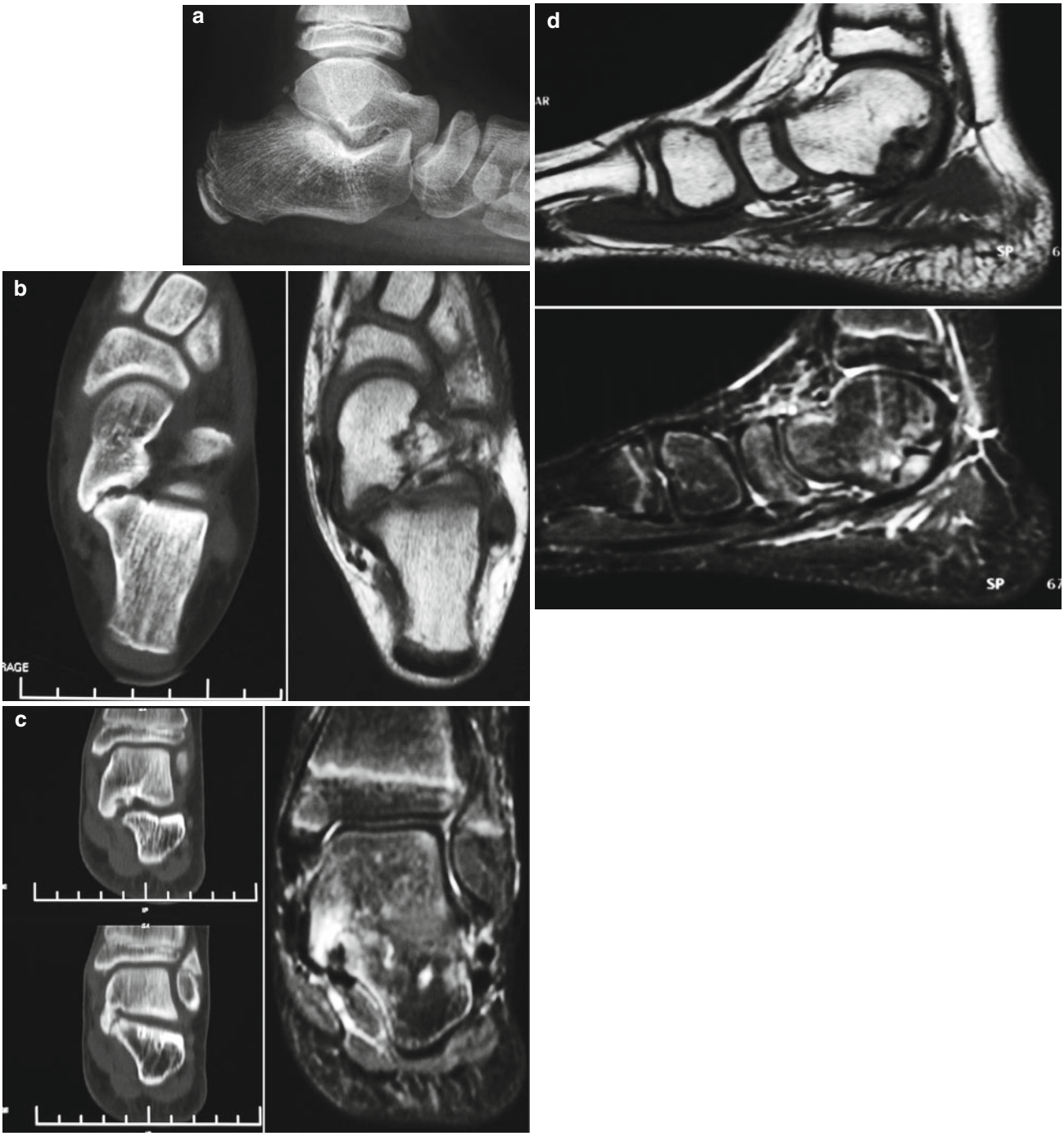

Fig. 12.34 Imaging evaluation of the left ankle of an 8-year-old boy with talocalcaneal coalition. Lateral radiograph (**a**) shows flattening of the plantar arch and absence of the image corresponding to the middle facet. Figures (**b** and **c**) compare CT (*left images*) and MRI (*right images*) sections obtained in similar levels in the transverse and coronal planes. Even though the coalition is well demonstrated on both studies, CT is superior in delineating bone anatomy, while MRI has the unique ability to reveal subchondral bone marrow edema pattern. In (**d**), sagittal T1-WI (*upper image*) and fat sat T2-WI (*lower image*) show low signal intensity in the involved joint space in both sequences, which is typical for fibrous coalition

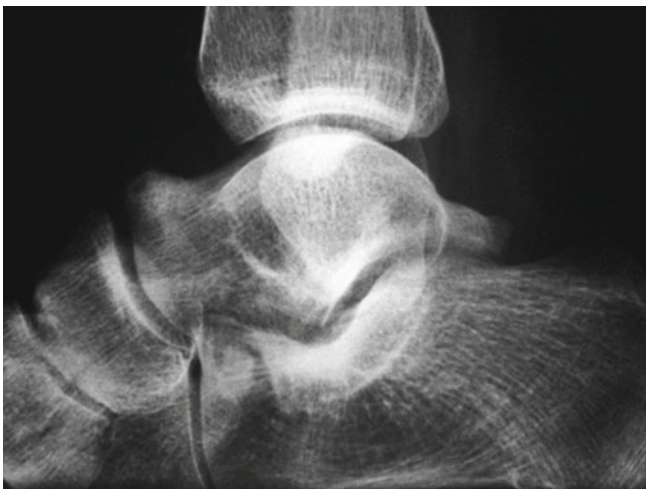

Fig. 12.35 Lateral view of the right ankle of a 19-year-old male showing indirect signs of talocalcaneal coalition. The "C sign" is present, as well as a large talar beak

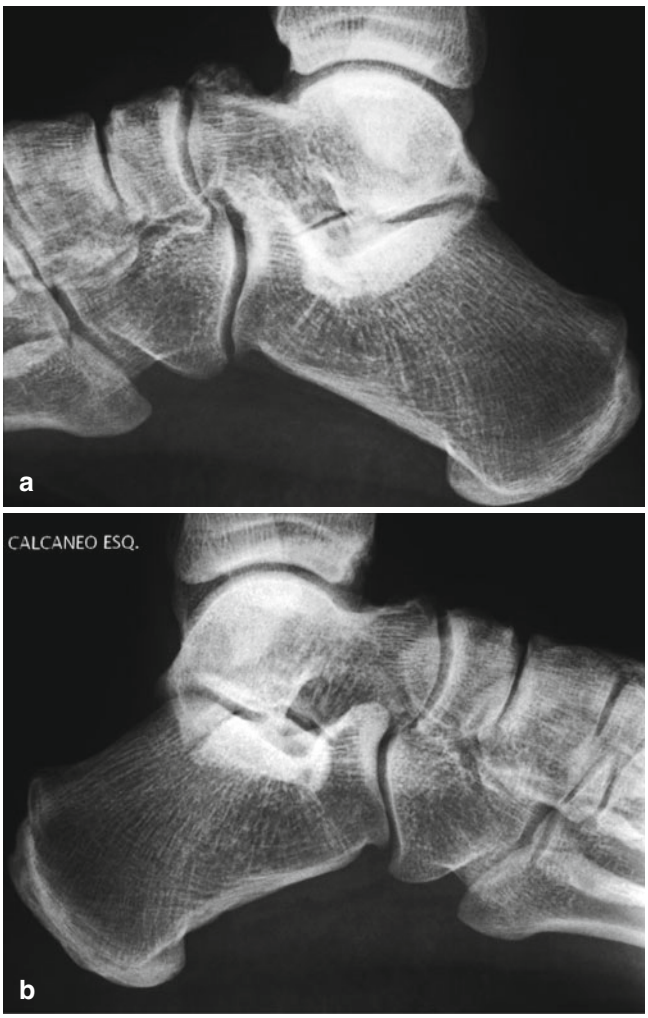

Fig. 12.36 Lateral radiographs of the ankles (right (**a**) and left (**b**)) of an adolescent with bilateral talocalcaneal coalition. The same findings present in the patient of Fig. 12.35 are seen, with some variations. There is bone fragmentation associated with the talar beak in the right ankle, while the "C sign" is discontinuous at left, in its posterior portion

12.13 Spondyloepiphyseal Dysplasia and Multiple Epiphyseal Dysplasia

Spondyloepiphyseal dysplasia (SED) and multiple epiphyseal dysplasia (MED) are skeletal abnormalities that share some clinical and imaging similarities, even though they are different conditions, with distinct inheritance patterns. Both are heterogeneous groups of hereditary skeletal dysplasias that have in common dysplastic involvement of the epiphyses, mild dwarfism, and normal intelligence. Clinical and radiographic manifestations are absent at birth in most cases of SED and MED, becoming evident during skeletal growth. Typical findings in SED include vertebral deformities (hump-shaped mounds of bone in the central and posterior portions of vertebral endplates) and platyspondyly (Figs. 12.37, 12.38, and 12.39), with progressive disk space narrowing, discal calcifications, and atlantoaxial instability due to odontoid hypoplasia. In addition, shortening of the long bones is also present, as well as abnormal shape of the epiphyses of the hips and of the knees, which are bilateral and symmetric (Figs. 12.37, 12.38, and 12.39). The femoral head remains completely cartilaginous in patients with SED until approximately 5 years of age, with gradual development of coxa vara (Figs. 12.37, 12.38, and 12.39); maturation of the secondary ossification centers of the knees is also severely delayed. There is overgrowth of the medial femoral condyles leading to gradual and progressive development of genu valgum (Fig. 12.38). In MED, there is anomalous endochondral ossification with bilateral and symmetric hypoplasia of the epiphyseal cartilages of the tubular bones, more severe in the hips and the knees, although the shoulders, elbows, ankles, and wrists may also be affected (Figs. 12.40, 12.41, and 12.42). Varus or valgus deformities can be found in the knees (Fig. 12.41), as well as mild acetabular hypoplasia. The limbs are relatively short relative to the trunk, and shortening of the tubular bones of hands and feet is also common. Maturation of the secondary ossification centers is delayed and the ossified epiphyses appear fragmented, closely resembling Legg-Calvé-Perthes disease (Fig. 12.43). When present, a double-layered patella (divided in anterior and posterior segments) is highly suggestive of recessive MED. Vertebrae are usually normal or exhibit subtle abnormalities, such as Schmorl nodes or irregularity of the endplates. Patients with MED tend to develop coxa vara (Figs. 12.41 and 12.44), and slipped capital femoral epiphysis may also occur.

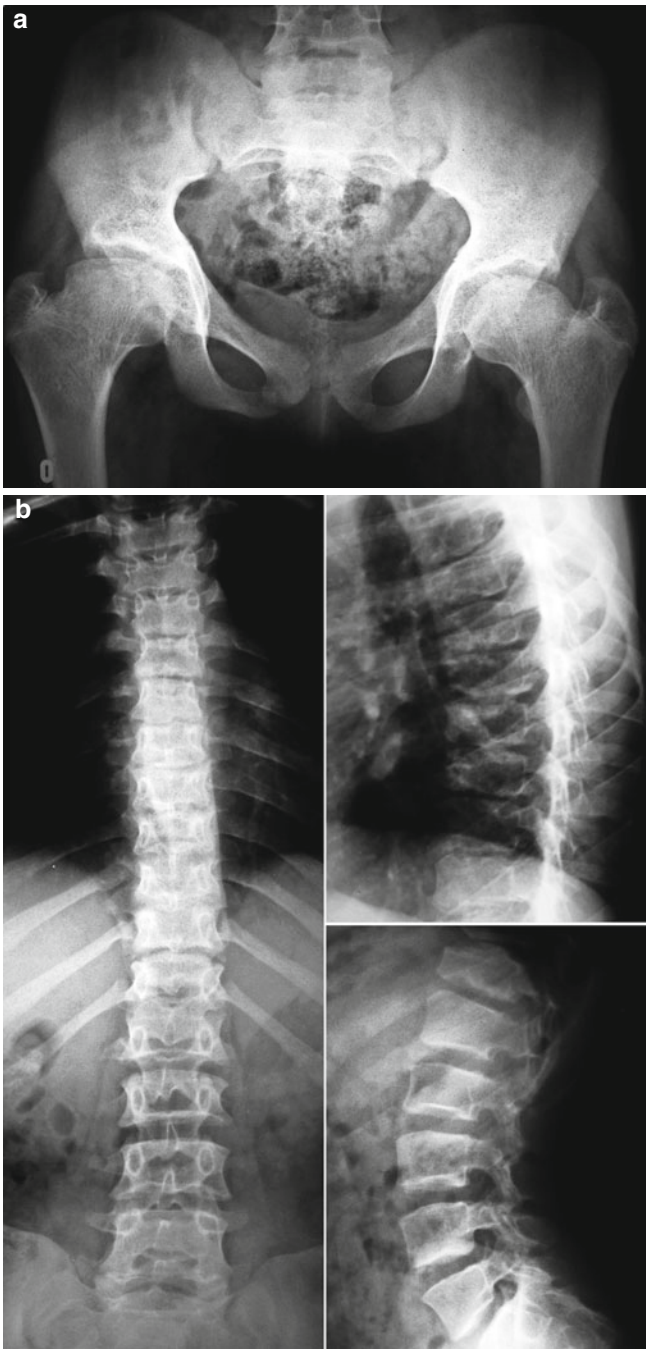

Fig. 12.37 Radiographs of a child with SED. In (**a**), there is bilateral and symmetric deformity of the femoral heads, which are flattened and widened, as well as remodeling of the acetabula and bilateral coxa vara. Platyspondyly can be seen in radiographs of the thoracolumbar spine (**b**), as well as reduced height of the disk spaces and vertebral deformities (mounds of bone in the central and posterior portions of the endplates). Findings are more prominent in the dorsal spine

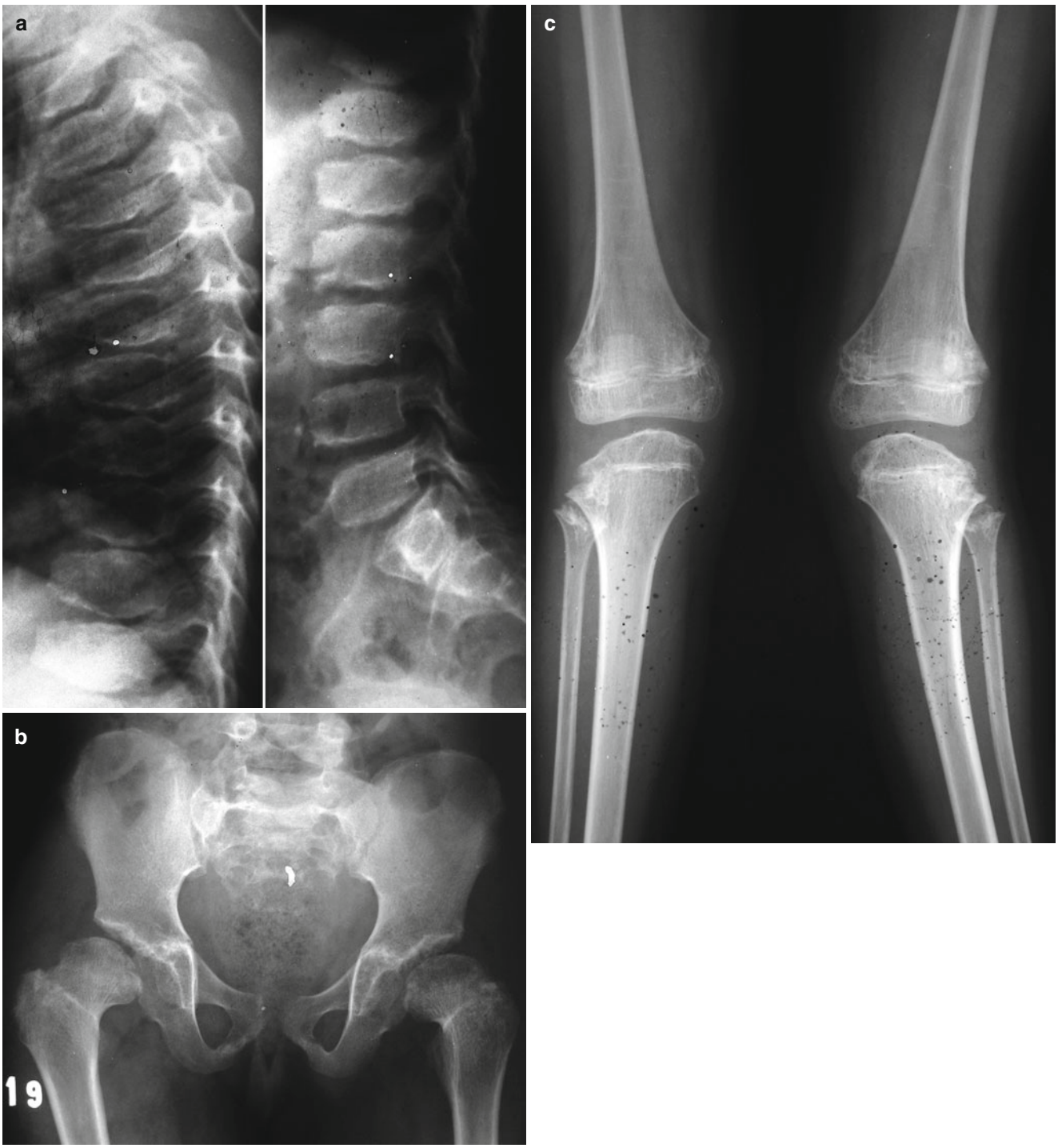

Fig. 12.38 Radiographs of the thoracolumbar spine (**a**), of the pelvis (**b**), and of the knees (**c**) of a child with SED. Spinal changes similar to those described in Fig. 12.38 are seen, with most extensive involvement of the lumbar spine in this patient. The epiphyses of the proximal femora are deformed, with coxa vara, marked acetabular dysplasia, and bilateral coxofemoral subluxation. Anteroposterior view of the knees displays abnormal morphology of all epiphyses, with overgrowth of the medial femoral condyles and bilateral valgus deformity, as well as metaphyseal flaring

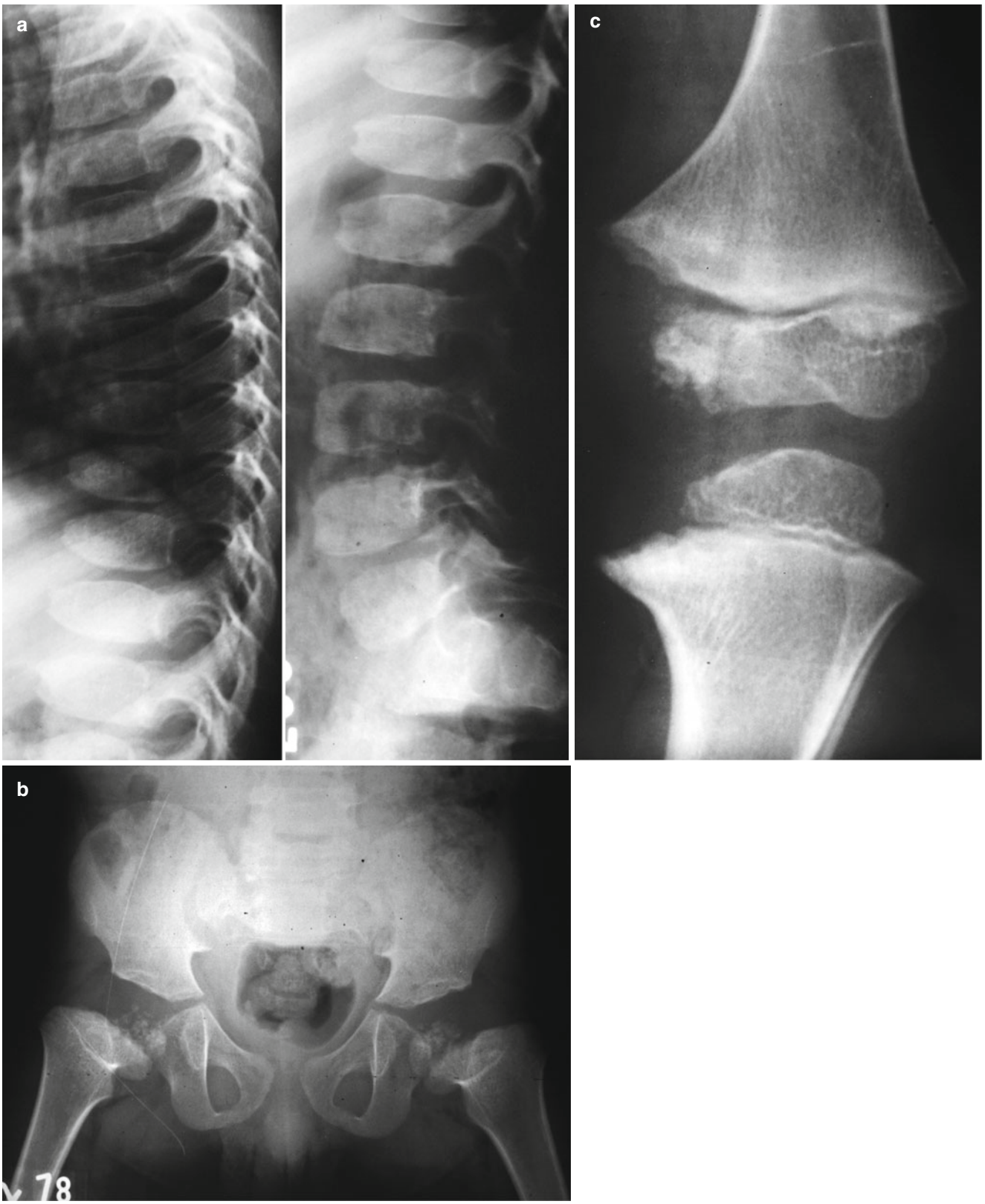

Fig. 12.39 In this child with SED, radiographs of the thoracolumbar spine (**a**) show the typical vertebral deformity seen in previous patients. The height of the intervertebral disk spaces is relatively preserved because this is a younger child. Pelvic radiograph (**b**) reveals bilateral coxa vara and fragmentation of the proximal femoral epiphyses. The same epiphyseal findings are seen in the distal femur, involving the medial femoral condyle (**c**), with deformity of the proximal tibial epiphysis and metaphyseal flaring

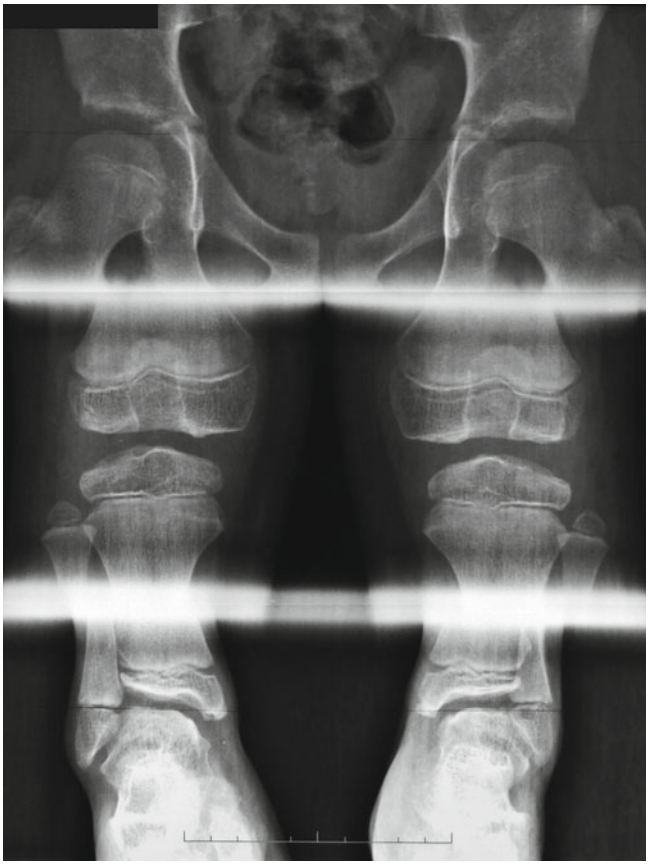

Fig. 12.40 Scanogram of a patient with MED. There are bilateral and symmetric morphologic abnormalities involving the hips, the knees, and the ankles. Marked flattening of the femoral heads and condyles is present, as well as irregularity of the tibiotalar articular surfaces, with spheroid appearance of the talar domes and remodeling of the distal tibiae (ball-in-socket configuration)

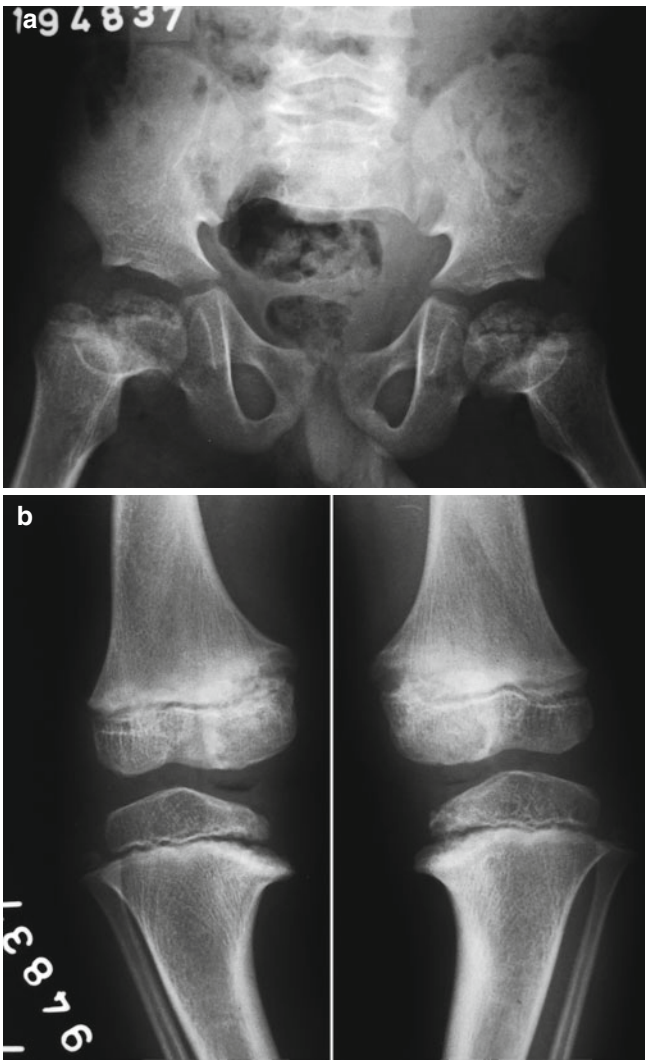

Fig. 12.41 Radiographs of the pelvis (**a**) and of the knees (**b**) of a child with MED. The proximal femoral epiphyses have a stippled, mulberry-like appearance, with bilateral coxa vara. Symmetric and bilateral varus deformities of the knees are also present, with malformed epiphyses and metaphyseal flaring

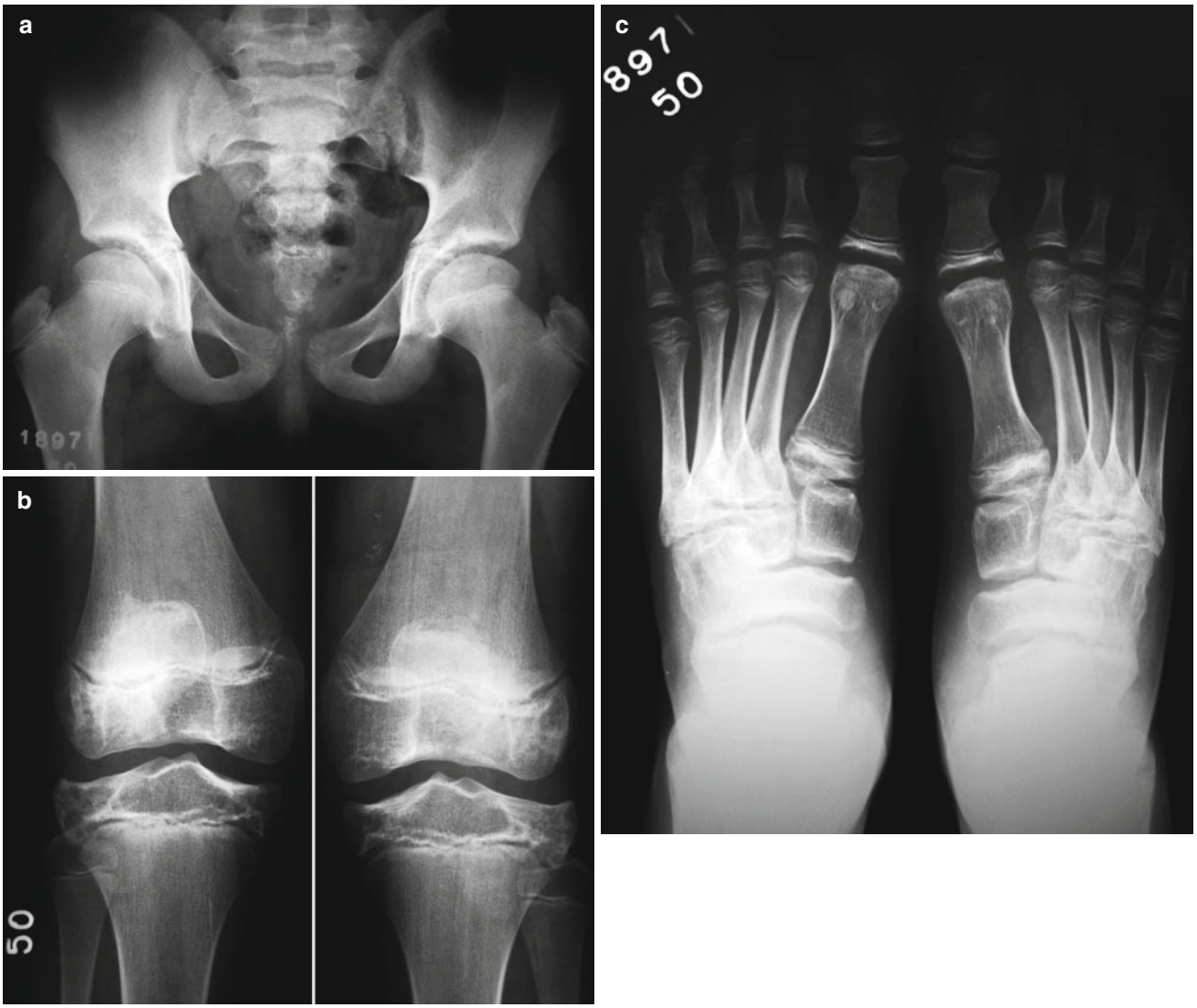

Fig. 12.42 Multiple skeletal abnormalities in a child with MED. In (**a**), there is bilateral and symmetric flattening of the femoral heads. Altered epiphyseal morphology is also seen in the distal femora and in the proximal tibiae in (**b**), with heterogeneous ossification and flattening of the articular surfaces. There is epiphyseal flattening of the metatarsal (**c**) and metacarpal (**d**) bones; morphologic abnormalities can be seen in the epiphyses of the first toes and in the distal radii and ulnae. In (**e**), marked irregularity of the epiphyses in the right tibiotalar joint is evident, with incongruity of the joint surfaces. The secondary ossification centers of the capitula appear fragmented in (**f**), notably at left, with sclerosis of the fragments at right

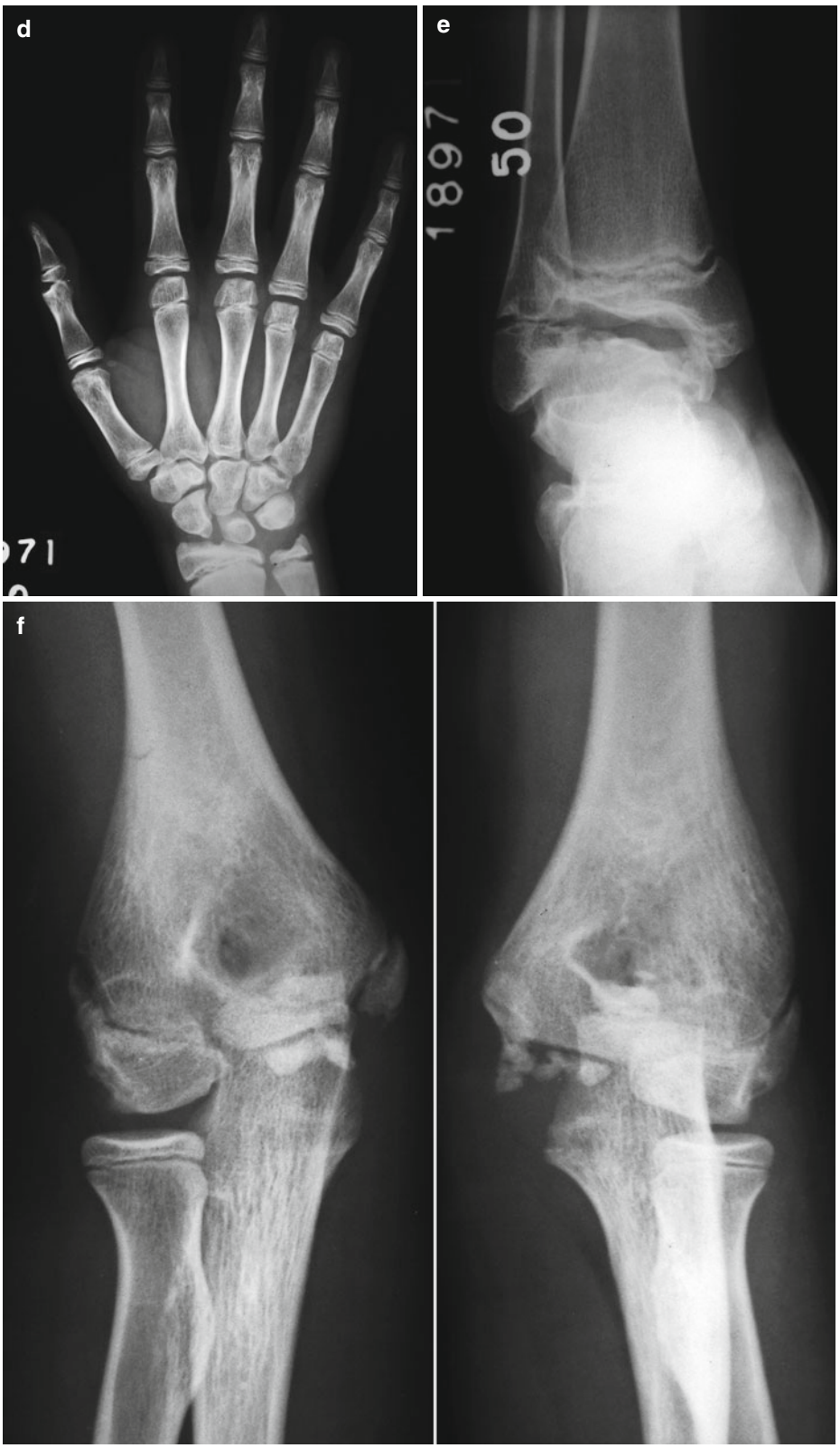

Fig. 12.42 (continued)

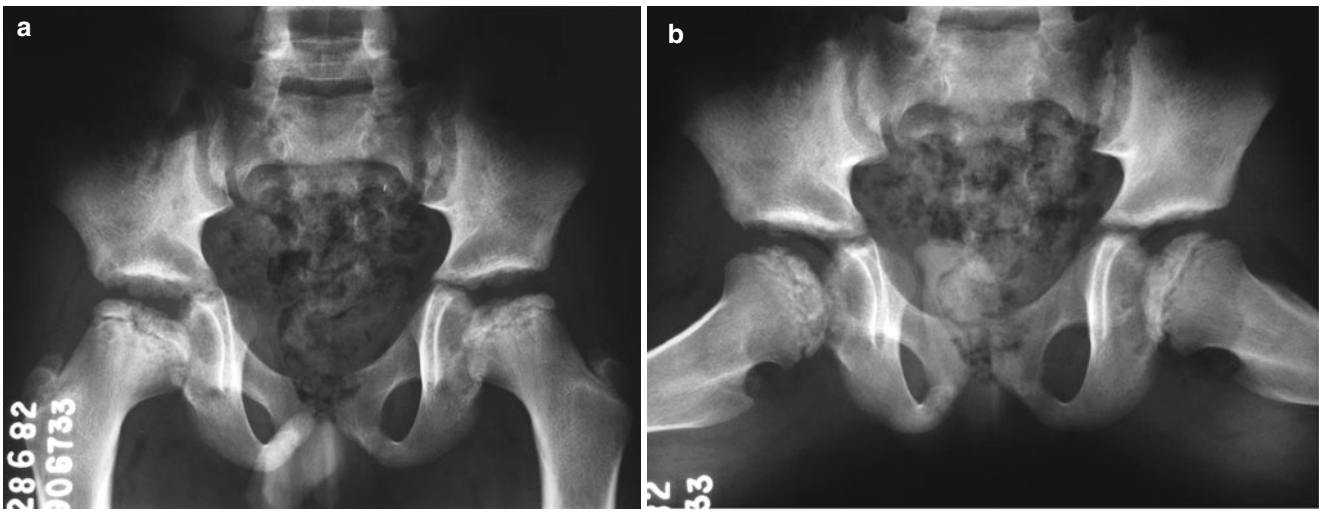

Fig. 12.43 Fragmentation and flattening of the femoral heads in MED may closely resemble Legg-Calvé-Perthes disease, as seen in these radiographs. However, bilateral involvement of the epiphyses of several joints at the same time allows for a safe differential diagnosis in most cases

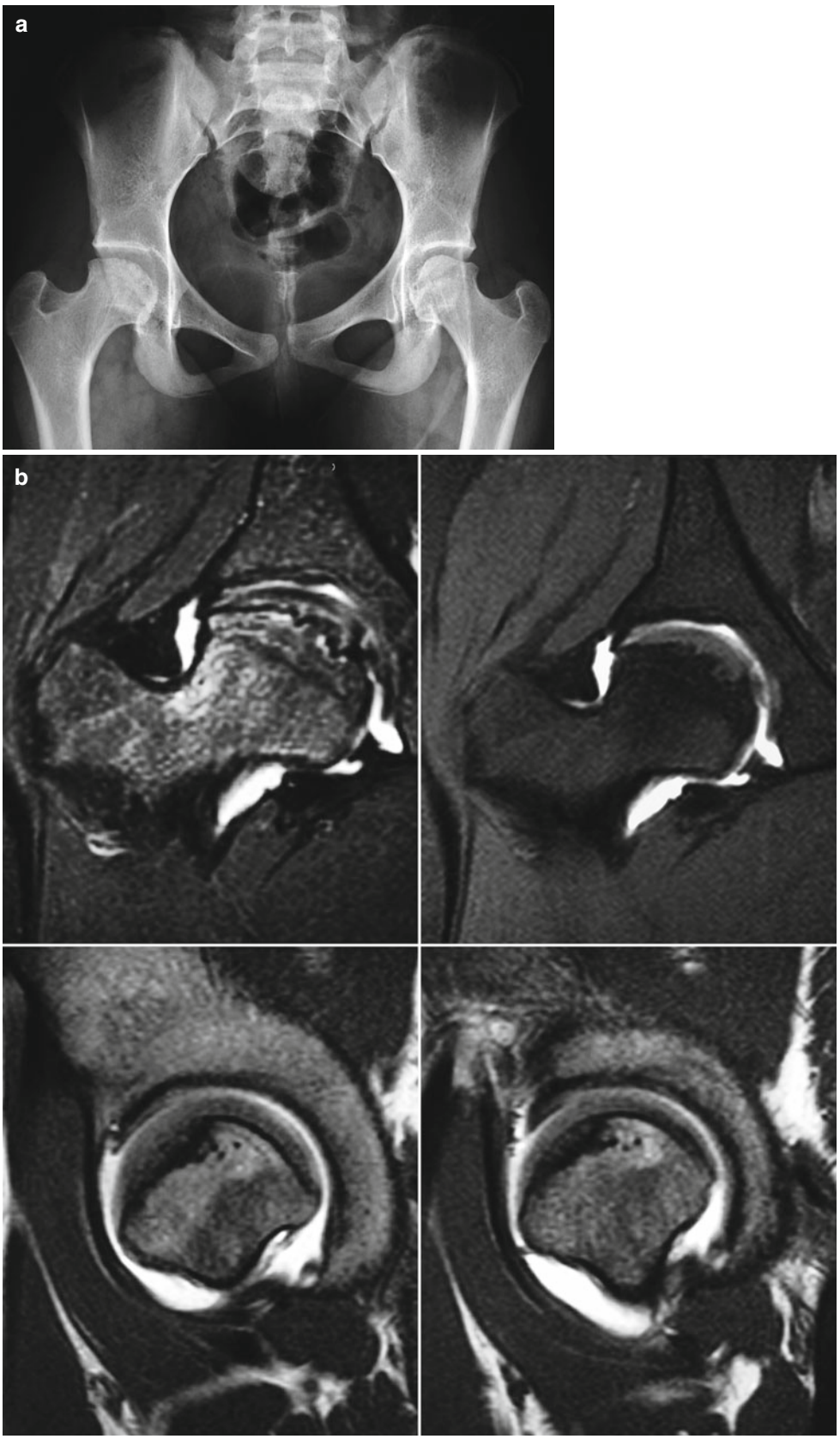

Fig. 12.44 Pelvic radiograph (**a**) and MR-arthrography of the left hip (**b**) of an adolescent with MED. Radiographic findings include marked deformity of the femoral heads and bilateral coxa vara. Despite the irregularity of the epiphyses and the apparent incongruity of the hips on the radiograph, MR-arthrography demonstrates that the cartilaginous component of the joints is preserved, with smooth contours. Nevertheless, premature osteoarthritis must be kept in mind as a frequent complication of MED

Key Points

- Madelung's deformity is characterized by a complex V-shaped deformity of the distal radius and ulna and wedging of the bones of the proximal carpal row. Vickers' ligament, an anomalous band of fibrous tissue tethering the lunate bone and the triangular fibrocartilage complex to the distal radius, is better seen with MRI.
- Typical features of PFFD include shortening of the proximal femur and deficient development of the hip joint. Radiographs alone are not able to demonstrate the non-ossified components of this malformation, such as the immature epiphysis; therefore, MRI is the method of choice for imaging evaluation.
- DDH comprises a spectrum of congenital anomalies that have in common an abnormal relation between the acetabulum and the femoral head, which may vary from mildly dysplastic hips to frankly dysmorphic and unstable joints. The diagnosis is essentially a clinical one, but imaging is helpful in selected cases. US is the most useful study, notably during the first 6 months of life. CT and MRI are usually reserved for follow-up assessment of reduction, in order to evaluate its effectiveness.
- DDP appears on radiographs and CT as a well-defined lucency located on the superolateral corner of the articular surface. MRI is useful in demonstrating bone marrow edema and cartilaginous abnormalities, which are occasionally present.
- TLPD is often associated with patellofemoral morphologic abnormalities, which are more evident on CT and MRI. MRI is the preferred imaging method, showing joint effusion, avulsion fractures, "kissing contusions," osteochondral lesions, and injuries of the medial patellar restraints.
- The popliteal cyst is a collection of synovial fluid within the bursa between the medial gastrocnemius and semimembranous muscles. US and MRI are equally good, showing a rounded fluid-filled structure in the posteromedial soft tissues of the knee.
- The discoid meniscus is larger than normal and abnormally shaped, almost invariably found in the lateral compartment. MRI is the most useful study, demonstrating continuity of the anterior and posterior horns in at least three contiguous sagittal slices and excessive meniscal coverage of the tibial plateau in the coronal images.
- In Blount's disease, there is deformation of the medial portion of the proximal tibial metaphysis leading to progressive varus deformity of the knee. Although radiographs usually suffice for the diagnosis, MRI is superior in demonstrating abnormalities of the epiphyseal cartilage, transphyseal bridging, and meniscal changes.
- On radiographs, there is a decrease in the talocalcaneal angle in congenital clubfoot, with adduction of the forefoot, varus deformity of the hindfoot, medial subluxation of the navicular, and elevation of the calcaneus. CT and MRI are not routinely used.
- Freiberg's disease is an osteochondrosis of the metatarsal head (most commonly the second). Radiographic findings include signs of avascular necrosis of the affected bone, with eventual deformation and flattening of the articular surface. MRI is able detect the disease earlier, being also useful to rule out alternative causes of pain in the forefoot.
- Tarsal coalitions are characterized by abnormal bridging (osseous, fibrous, or cartilaginous) across tarsal bones. Calcaneonavicular and talocalcaneal are the most frequent types. Radiographs remain an essential part of the investigation, but they are often inconclusive or insufficient. CT is the best method to assess bone anatomy, while MRI can distinguish the several types of bone bridges and demonstrate edematous changes in the adjacent bone marrow and in the soft tissues.
- SED and MED are hereditary skeletal dysplasias that involve the epiphyses, sharing clinical and imaging similarities. Progressive platyspondyly and vertebral deformities are typical of SED and are absent in MED. Morphologic changes of the epiphyses (involving mainly hips and knees) are present in both conditions, usually bilateral and symmetric. Delayed bone maturation, coxa vara, and early-onset osteoarthritis may be found both in SED and in MED.

Recommended Reading

Biko DM, Davidson R, Pena A, Jaramillo D (2012) Proximal focal femoral deficiency: evaluation by MR imaging. Pediatr Radiol 42(1):50–56

Carter CW, Kocher MS (2012) Meniscus repair in children. Clin Sports Med 31(1):135–154

Crim J (2008) Imaging of tarsal coalition. Radiol Clin North Am 46(6):1017–1026

de Brito P, Metais JP, Guilley C, Goguey B, de Courtivron B, Sirinelli D (2007) Déformation de Madelung de l'enfant liée à la présence d'un ligament radio-lunaire anormal: à propos de 4 cas. J Radiol 88(12):1887–1892

Dillon JE, Connolly SA, Connolly LP, Kim YJ, Jaramillo D (2005) MR imaging of congenital/developmental and acquired disorders of the pediatric hip and pelvis. Magn Reson Imaging Clin N Am 13(4): 783–797

Harty MP (2001) Imaging of pediatric foot disorders. Radiol Clin North Am 39(4):733–748

Keller MS, Nijs EL (2009) The role of radiographs and US in developmental dysplasia of the hip: how good are they? Pediatr Radiol 39(Suppl 2):S211–S215

Laor T (2008) Musculoskeletal imaging: evaluation of congenital anomalies. Pediatr Radiol 38(Suppl 2):S246–S250

Nalaboff KM, Schweitzer ME (2008) MRI of tarsal coalition: frequency, distribution, and innovative signs. Bull NYU Hosp Jt Dis 66(1):14–21

Neubauer H, Morbach H, Schwarz T, Wirth C, Girschick H, Beer M (2011) Popliteal cysts in paediatric patients: clinical characteristics and imaging features on ultrasound and MRI. Arthritis 2011:751593

Rubenstein JD, Christakis MS (2006) Case 95: fracture of double-layered patella in multiple epiphyseal dysplasia. Radiology 239(3): 911–913

Sanchez R, Strouse PJ (2009) The knee: MR imaging of uniquely pediatric disorders. Magn Reson Imaging Clin N Am 17(3):521–537

Storer SK, Skaggs DL (2006) Developmental dysplasia of the hip. Am Fam Physician 74(8):1310–1316

Umrani SP, Aroojis AJ (2008) Infantile tibia vara: treatment of Langenskiold stage IV. Indian J Orthop 42(3):351–354

Zaidi A, Babyn P, Astori I, White L, Doria A, Cole W (2006) MRI of traumatic patellar dislocation in children. Pediatr Radiol 36(11): 1163–1170